RECENT ADVANCES IN MARINE SCIENCE AND TECHNOLOGY, 2002

NARENDRA K. SAXENA
EDITOR

RECENT ADVANCES IN MARINE SCIENCE AND TECHNOLOGY, 2002

Edited by

Narendra Saxena
Professor & Director
Pacific Mapping Program
School of Ocean and Earth Sciences and Technology
University of Hawai'i
Honolulu, Hawai'i, U.S.A.

TABLE OF CONTENTS

II. COASTAL SCIENCE AND TECHNOLOGY

IV. WORKSHOPS

PREFACE

Recent Advances and Marine Technology, 2002 is the sixth refereed publication of a series based upon papers presented at the Tenth Pacific Congress on Marine Science and Technology (PACON 2002) held in Chiba, Japan, July 21-26, 2002. A unique process was adopted to bring about this refereed publication: session chairs selected papers based on presentations at PACON 2002 and recommended them for possible inclusion in this publication. Each manuscript was reviewed by at least two reviewers. Out of 199 PACON 2002 presentations, 143 papers were recommended by session chairmen, 68 manuscripts were submitted, and finally 55 papers were accepted for this publication.

Since papers dealt in areas of ocean science and technology (OST), coastal science and technology (CST), and marine resource management and development (MRMD), we have tried to group related papers to facilitate the reader's use of this publication. I hope that readers will find this volume of 55 papers useful. Indexes giving the alphabetized list of authors and titles are presented at the end of this volume.

Honolulu   Narendra K. Saxena
April 3, 2003

ONBOARD WAVE MONITORING SYSTEM
BY VIDEO IMAGE PROCESSING

Shigesuke Ishida[1], Yoshifumi Takaishi, Nobuo Kiriya[1], Iwao Watanabe[1],
Tsuyoshi Miyazaki[2], Koichi Masuda[3],
Kohei Ohtsu[4] and Kiyokazu Minami[4]

[1]National Maritime Research Institute, Mitaka, Tokyo, JAPAN
ishida@nmri.go.jp

[2]Japan Marine Science and Technology Center, Yokosuka, Kanagawa, JAPAN

[3]Nihon University, Funabashi, Chiba, JAPAN

[4]Tokyo University of Mercantile Marine, Koto-ku, Tokyo, JAPAN

ABSTRACT

Information of ocean waves is important not only for safe and economical operation of ships but also for ocean environment survey. Recently remote-sensing devices such as altimeters on artificial satellites or radar systems are developed for measuring ocean waves. On the other hand visual observation from merchant ships is still widely carried out. Onboard wave monitoring will be continued because it can detect the waves around the ship immediately. However, to improve the quality of the wave information from merchant ships an onboard device with reasonable price is necessary. With this background a wave monitoring system for merchant ships was contrived, supported by the Program for Promoting Fundamental Transport Technology Research from the Corporation for Advanced Transport & Technology.

The major information of the proposed wave monitoring system is relative wave elevation in some positions along ship hull. The elevation is measured by processing video image taken by CCD cameras. The image processing is based on brightness in the analysis window. For removing the effect of flicker on sea surface, painting of the hull and so on, an ingenious algorithm is developed. For the measurement at night near infrared ray is used.

The relative wave elevation is converted to the absolute elevation in combination with vertical acceleration of the same location. And the wave field around the ship, i.e. wave height, period and direction, is estimated from the elevation of at least three points. The performance of the wave monitoring system was examined by experiments in laboratory and in real sea. In this paper the overview is described.

INTRODUCTION

Wave information is indispensable for the safe and economical navigation of ships and is also important as the information on ocean environment. Recently ocean waves are observed from

artificial satellites. Database of wave height measured by altimeters was published (Young et al. 1996) and the improved resolution and analysis algorithm of SAR (Synthetic Aperture Radar) images are making it possible to detect more detailed wave information then ever (Dankert et al., 2002) while the effort of improving the quality of onboard wave monitoring has been continued to have the real time wave information around ships and offshore structures. Measuring devices, making use of supersonic, radar and so on, are in practical use however, for replacing with visual observation and to get the wave information in wide area of ocean, a system with reasonable price and easy to use is demanded.

With this background an onboard wave monitoring system with a new concept has been developed. In this paper the overview is described. The framework of the research project is shown in Figure 1. The major information of the system is the relative wave motion along ship hull, which is measured by processing video image taken by CCD cameras. For estimating the absolute wave field around the ship, relative wave information from at least three cameras and vertical accelerations of the same positions are combined. The methods for estimating wave directional spectrum from ship motions and RAOs (response amplitude operators) of them are proposed by several researchers (Iseki et al., 1994; Hirayama et al., 1997; Saito et al., 2000; Yoshimoto et al., 1994). However the estimation error of RAOs and the ship motion caused by forces other than waves, for example wind, lead to a serious decline of accuracy. In the proposed wave monitoring system a simpler and more robust estimation method, just for wave height, period and direction, is adopted. Moreover, the proposals for making effective use of the wave monitoring system is within the scope of the research. In this paper the prototype of a navigation support system in heavy weather is shown.
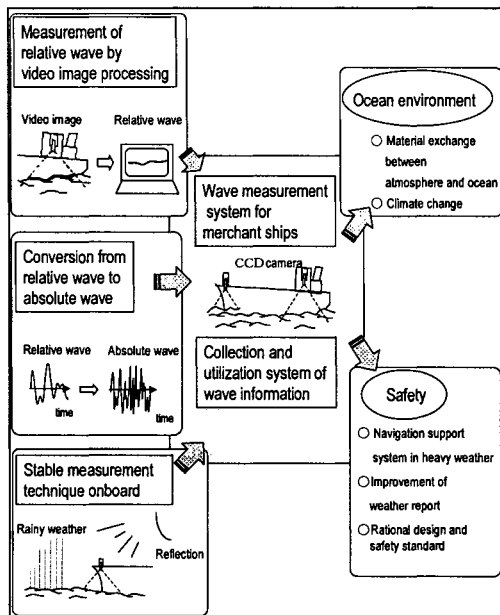
Figure 1. Framework of the project

MEASUREMENT OF RELATIVE WAVE MOTION
BY VIDEO IMAGE PROCESSING

CCD Camera

Figure 2 shows the camera for extracting the intersection line of the ship hull and water surface. Small near-IR (infrared ray) illuminators are equipped. In general CCD has the sensitivity to the light from visible range to near-IR ray. And in order to have a natural picture for human eyes the latter range is eliminated by an optical filter. Here the filter is removed from the camera to make the monitoring system available even at night. In daytime the information by visible light is useful because much information, i.e. red, green, blue and brightness, is included. However, processing all the information is time consuming for the current personal computers. So, only the brightness information is used. The price of the camera is in the same order as the ones for domestic use.
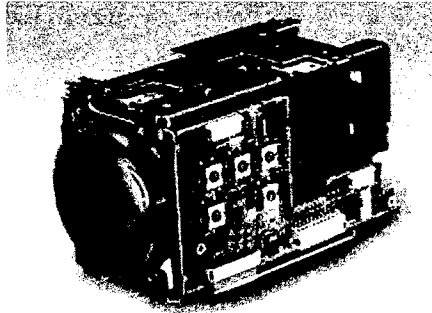
Figure 2. CCD camera

Algorithm of Image Processing

The basic flow of the algorithm is shown in Figure 3. The intersection line between the ship hull and the wave surface is extracted by the change of brightness. This algorithm was confirmed to work well for the pictures taken in a model basin. However the pictures in real sea include some troublesome disturbances like the boundary of painting, change of brightness due to rolling and whitecapping. Figure 4 shows a sample picture of a ship's side. It is recognized that the boundary of painting appears very strongly.

3
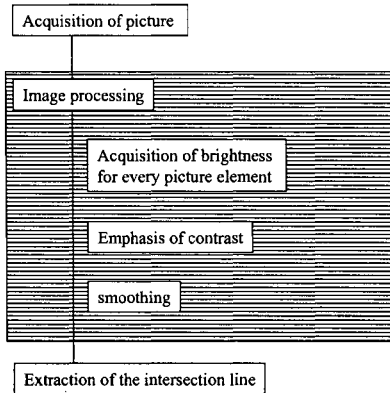
Figure 3. Basic algorithm of video image processing   Figure 4. Brightness of a sample picture
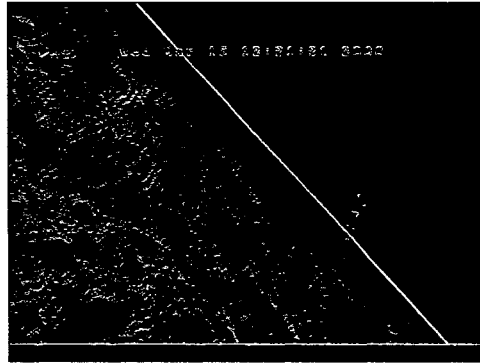
The improved algorithm and the sample pictures are shown in Figures 5 and 6 respectively. At the first stage (pre-processing stage) the standard picture, called Σ-picture, is made by averaging the brightness for 15-20 seconds. Next, the picture at each time step of camera (1/30 seconds), called Δt-picture, is taken. In the analysis window (rectangular window, Fig. 6), the total brightness of Δt-picture is equalized to Σ-picture and the difference of brightness between the two is calculated. Through this processing the effect of brightness change at each instance is reduced and the no-moving parts, e.g. the boundary of painting, are removed. After that the brightness is smoothed to reduce noise. And the area with brightness over a threshold value is extracted as shown by the fourth picture in Figure 6. Finally the highest point of the area is judged to be the water surface. Along these processing the Σ-picture and the threshold value are revised for making them more appropriate. The time for processing one picture is 70 msec. When three cameras are equipped the sampling speed is 4 Hz, which is satisfactory for at-sea measurement.
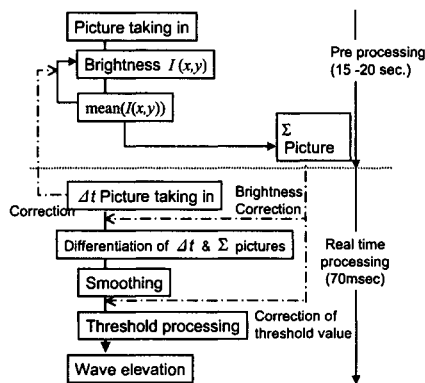
Figure 5. Algorithm of the improved video image processing

4
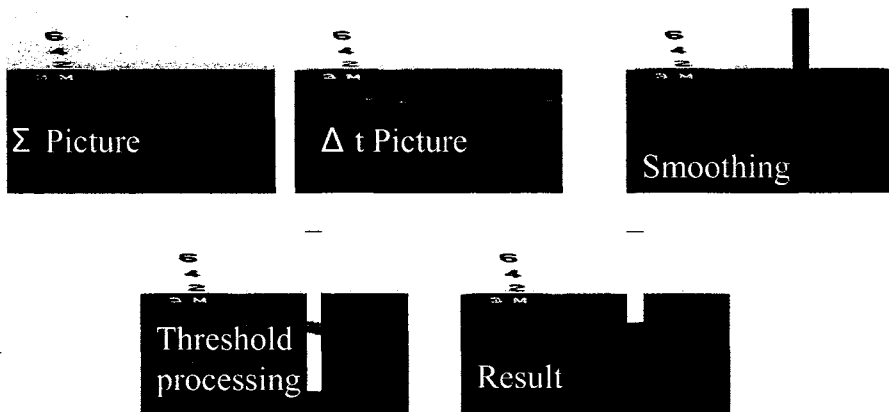
Figure 6.   Pictures of each step of image processing

Accuracy
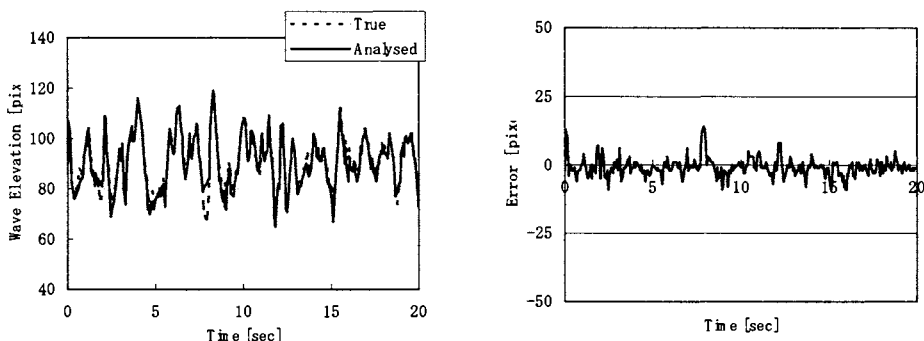
Figure 7.   An example of measured time history (left) and its error (right)

An example of measured time history of relative wave and its error are shown in Figure 7.   In the left figure "True" value is estimated by human eyes on a computer display.   The error is shown in the right as the difference between the two lines.   The standard deviation of the error is 3.3 pixels.   When the camera covers 8 meters, for example, in height of the ship's side wall, the accuracy of the location of water surface is 8[m]/640*3.3 = 4.1[cm] (640 : the resolution of the camera).

ESTIMATION OF WAVE FIELD AROUND THE SHIP

As mentioned in the introduction, some sophisticated methods for estimating wave directional spectrum from ship motions and RAOs of them were proposed. The relative wave motion measured by video image processing, mentioned above, can be used as information for these analyses. However RAOs, for example estimated by strip theory, originally include some error in amplitude and phase, and tend to change by loading conditions, consumption of fuel and operation of anti-rolling devices. Moreover, the ship motion caused by forces other than waves, for example wind and maneuvering, leads to serious error of these analyses.

Conversion from Relative Wave to Absolute Wave

In the analysis proposed in this paper, for avoiding the instability caused by above-mentioned factors, the relative wave motions measured at some positions along the ship's side are converted to absolute waves by subtracting the vertical motions of the cameras. The vertical motions are calculated by double integral of vertical accelerations, or by summation of vertical displacement due to heave, pitch and roll. The influence of inclination on the measured value by vertical accelerometers can be corrected by taking into account the inclination angles of roll and pitch. In displacement calculated from vertical acceleration, drifting or long period deviation from the original mean value can be appeared as the results of accumulation of numerical errors. Such deviation is eliminated by a numerical filter.

By this operation, if the effect of radiation and diffraction waves is small, the amplitudes of RAOs of the converted absolute waves are simplified to unity and the records are treated as the ones from a running wage gauge array. The effect of radiation and diffraction waves are tested by comparing the converted absolute wave on the model ship with those obtained by an array of wave gauges without the model running in the same wave conditions. The results will be presented in the following chapter, in Figure 9.

Estimation of Wave Field from Absolute Waves

It is well known that the wave directional spectrum can be estimated by a wage gauge array, using MLM, MEM, BEM and so on. However the converted record includes some effect of radiation and diffraction waves and when the array is running in following or quartering seas the original wave frequency becomes a three-valued function of the encounter frequency. These factors sometimes lead to an instable estimation. Here a more simple analysis is tried.

The simple analysis just estimates the three quantities of wave, i.e. height, period and direction, based on the geometric relation between a regular wave and wave gauges. From Figure 8 the following equations can easily be derived.

6
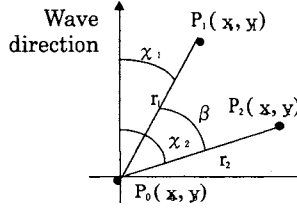
Figure 8 Coordinate system

$$\chi_1 = \tan^{-1}\left[\frac{\cos\beta - \varepsilon_{02}r_1/\varepsilon_{01}r_2}{\sin\beta}\right] \tag{1}$$

$$\lambda = \frac{2\pi r_1 \cos\chi_1}{\varepsilon_{01}} = \frac{2\pi r_2 \cos(\beta+\chi_1)}{\varepsilon_{02}} \tag{2}$$

$$T = \sqrt{2\pi\lambda/g} \tag{3}$$

where ε_{01} and ε_{02} are the phase difference between the records by the wave gauges of P_1 and P_0, P_2 and P_0 respectively. λ and T are the length and period of incident regular wave.

For irregular waves the phase difference is defined as the following relations, i.e

$$\varepsilon_{ij} = \tan^{-1}\{Qu_{ij}(\omega)/Co_{ij}(\omega)\} \tag{4}$$

where $Co_{ij}(\omega)$ and $Qu_{ij}(\omega)$ are the co-spectrum and quadrature spectrum of the cross spectrum of wave records $S_{ij}(\omega)$ at i and j points, respectively.

$$S_{ij}(\omega) = Co_{ij}(\omega) - iQu_{ij}(\omega) \tag{5}$$

As to the wave frequency, the peak frequency of the encounter wave spectrum, ω_p is selected. The mean wave period, T_{01}, is assumed as $0.73T_p$ as the relation at the Pieson-Moskowitz type wave spectrum, where T_p is the wave period corresponding to the peak frequency. The significant wave height is the average value of three points.

In order to investigate the performance of the simple analysis (SA) a model test was carried out in a basin, which has a multi-directional wave generator. The relative wave motions along the side of the model ship were measured by capacitance type sensors because the experiment was just for investigating the performance of the analysis methods. Some estimated results of significant wave height ($H_{1/3}$), wave direction (χ) and mean wave period (defined by the spectrum area and the first moment of spectrum; $T_{01}=0.73T_p$) are shown in Figure 9.

Accuracy
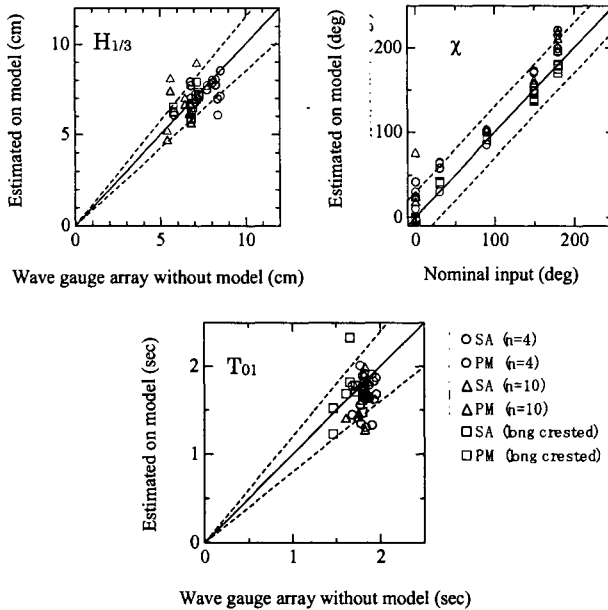
Figure 9.   Estimation of wave parameters by simple analysis (SA) and parametric method (PM) (n : the exponent of directional spreading with the form of $\cos^n \theta$)

In this figure the results estimated by the parametric method (Yoshimoto et al., 1994, see Appendix) (PM), one of the directional spectrum analysis methods, are also included for comparison.   In this analysis the input data is the same as the simple analysis, i.e. the converted absolute waves at three locations.   The broken lines in the figure show the errors of $\pm 15\%$ for $H_{1/3}$, ± 30 degrees for χ and $\pm 20\%$ for T_{01} respectively.   From the figure it is confirmed that most of the estimated results are between the broken lines and that the accuracy of the simple analysis is close to the parametric method as long as the main three parameters of waves are concerned.

WAVE MONITORING SYSTEM

Construction of Wave Monitoring System

The construction of the wave monitoring system is shown in Figure 10, including the navigation support system.   Three cameras are connected to a video board of a personal computer. Instead of three accelerometers, an accelerometer and two angular velocimeters are equipped considering the increase of cameras because this combination of sensors can calculate vertical accelerations of any positions of the ship.
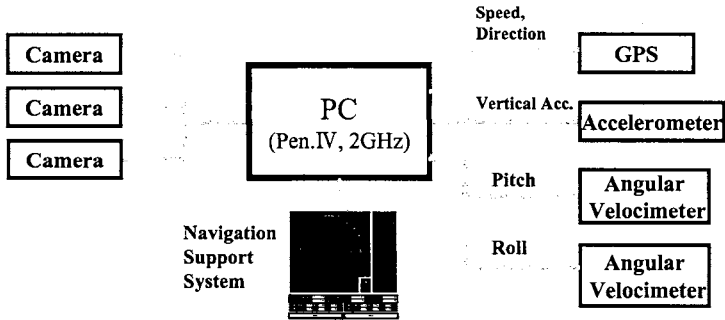
Figure 10.   Construction of Wave Monitoring System

Figure 11 shows the time chart of the system.   The data acquisition and video images processing continues ten minutes and the data is analyzed in five minutes.   The video data is deleted just after detecting the relative wave motions because data saving needs much space of disk and time.
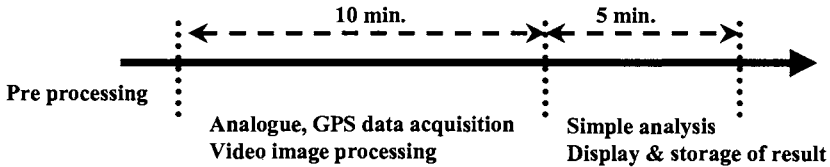
Figure 11.   Time chart of the system

The camera casing and the arm are shown in Figures 12 and 13 respectively.   The casing has a wiper to keep a clean view.   The arm is made foldable because a permanent arm is against regulation.

At-Sea Experiment

The performance of the wave monitoring system was investigated using Shioji-maru, a training ship of Tokyo University of Mercantile Marine.   The principal particulars of the ship, the installation of cameras and the course and velocity of the ship are shown in Table 1, Figures 14 and 15 respectively.
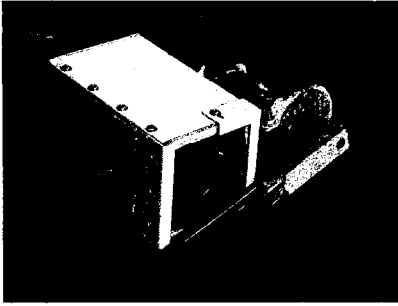
Figure 12.   Camera casing
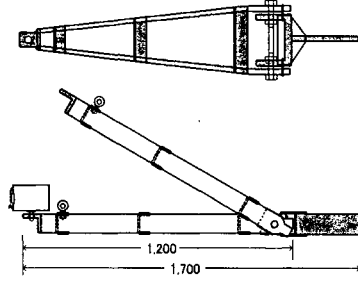
Figure 13.   Camera arm

The main wave at the experiment was estimated by visual observation and hindcasting to be a swell coming from at 80 degrees (almost east) with the height of 1.0 m and the period of 7.0 seconds.   The results by the proposed monitoring system are shown in Table 2.   For comparison the results by the parametric method (PM) with the same input data are also shown in the table within parenthesis.

Table 1
Principal particulars

Loa (m)	49.9
Lpp (m)	46
B (m)	10
D (m)	6.1
d (m)	3
Cb	0.55
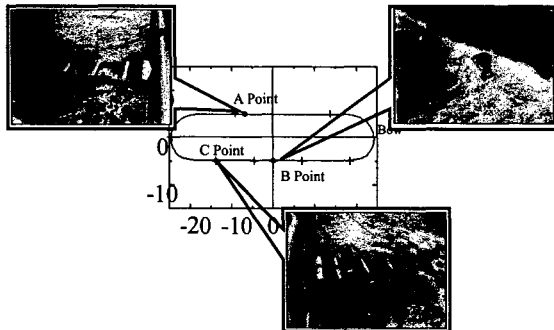
Figure 14.   Installation of cameras
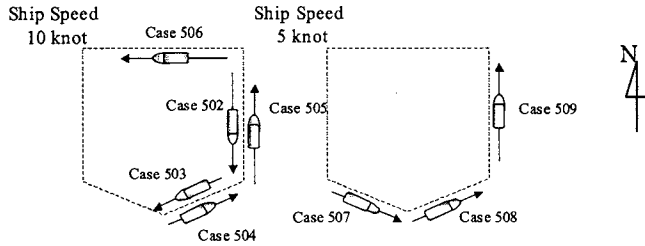
Figure 15. Course and velocity of the ship

Table 2. Estimated results by the wave monitoring system

	$H_{1/3}$ [m]	T_{01} [sec.]	χ [deg]
Case502	1.13 (1.11)	7.09 (8.08)	88 (121)
Case503	1.10 (1.15)	4.87 (7.29)	92 (160)
Case504	1.28 (1.55)	6.18 (8.81)	95 (130)
Case505	1.20 (1.43)	9.43 (7.96)	50 (90)
Case506	1.02 (1.24)	6.19 (7.38)	78 (0)
Case507	1.13 (0.78)	6.28 (7.95)	14 (85)
Case508	1.08 (0.78)	6.79 (10.21)	73 (185)
Case509	1.08 (1.11)	7.69 (10.68)	23 (115)

The agreement of the estimated results is fairly good for wave height. As for the wave period and direction, results somewhat depend on recorded time history and some are apart from the true value. However, the estimation is better than the parametric method and the averaged results are promising.

NAVIGATION SUPPORT SYSTEM

Clarifying the effective use of wave data measured by this system is also within the scope of the project. In this paper a prototype of a navigation support system is proposed. In IMO (MSC Circular 707, 1995), a guidance to avoid dangerous situations in following and quartering seas was adopted. The navigation support system aims at informing the masters to understand the relation between the ship and the waves onboard and helping them avoiding the dangerous situations

The figure in MSC Circular 707 is shown in the left side of Figure 16. The dangerous zone is colored. This figure is called V/T-diagram (V : ship speed, T : wave period). The display of the support system is shown in the right. The ship position is displayed by a flickering circle. This computer is connected to the main computer as shown in Figure 10. From this system the masters easily understand the ship's situation and how to escape from the dangerous condition.

11
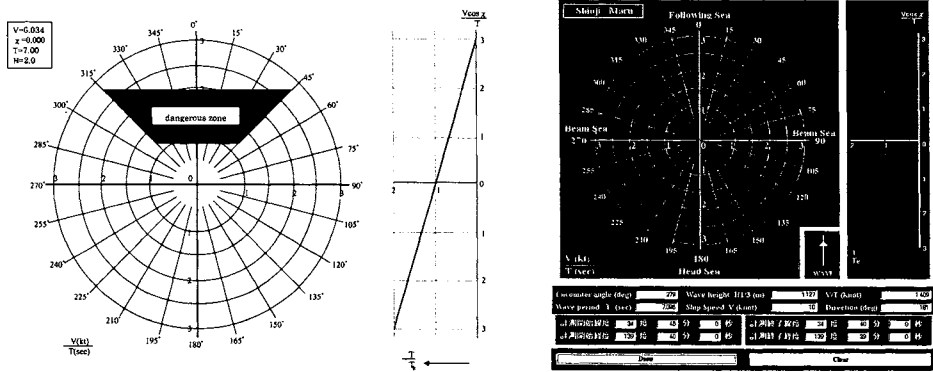
Figure 16.   V/T-diagram in MSC Circular 707 and in the navigation support system

CONCLUSIONS

An onboard wave monitoring system has been developed using relative wave motions along a ship's side, measured by video image processing, as the main information.   For estimating the wave parameters around the ship i.e. height, period and direction, a simple analysis method has been developed.   For promoting the possible use of the system a navigation support system onboard is proposed and a prototype is demonstrated.

The accuracy of video image processing was confirmed to be satisfactory.   The performance of the simple analysis method for estimating three wave quantities was investigated in a test tank. The total performance of the monitoring system was confirmed to be promising through at-sea experiment.   However, these were in limited conditions and it was regrettable that the wave conditions were rather calm.   Moreover the effect of neglecting radiation/diffraction waves in the simple analysis method was not investigated theoretically.   The problem remained for further development is clarifying the performance and limitation in various sea conditions, experimentally and theoretically, especially in heavy weather.

REFERENCES

Dankert, H., Horstman, J. and Rosenthal, W. 2002. Detection of Extreme Waves in SAR Images and Radar-Image Sequence, *Proc. of 21st International Conference of Offshore Mechanics and Arctic Engineering*

Hashimoto, N., Nagai, T., Asai, T. and Sugahara, K. 1993. Extension of Maximum Entropy Principle Method (MEP) for Estimating Directional Ocean Wave Spectrum, Report of the Port and Harbour Research Institute, Vol. 32, No. 1.

Hirayama, T., Minami, K., Hiramatsu, M. and Kawauchi, I. 1997. Development of Hybrid-Type-Onboared-Measuring-System for Directional Wave Spectrum (2nd Report), *Journal of the Society of Naval Architects of Japan*, Vol. 182, pp.217-229.

IMO/MSC. 1995. Guidance for Masters to Avoid Dangerous Situations in Following and Quartering Seas, MSC Circular 707.

Iseki, T. and Ohtsu, K. 1994. Baysean Estimation of Directional Wave Spectra Based on Ship Motions, *Journal of the Society of Naval Architects of Japan*, Vol. 176, pp. 99-105.

Saito, K., Maeda, K., Matsuda, A. and Suzuki, S. 2000. An Estimation of Ocean Wave Characteristics Based on Measured Ship Motions (3rd Report), *Journal of the Society of Naval Architects of Japan*, Vol. 187, pp. 77-83.

Yoshimoto, H. and Watanabe, I. 1994. On the Estimation of Encounter Directional Wave Spectra of Running Ship, Jour. of the society of naval architects of Japan, Vol.176, pp. 107-116

Young,I.R. and Holland,G.J. 1996. Atlas of the Oceans : Wind and Wave Climate, Elsevier Science Ltd.

APPENDIX Parametric Method for Directional Wave Spectrum Analysis

Parametric method (PM) is a general term of the methods for estimating directional wave spectrum by expressing the spectrum through a parametric model. In this appendix the summary of a PM for measurement on running ships (Yoshimoto et al. 1994) is described. In this method the parametric model of EMEP (Extended Maximum Entropy Principle) (Hashimoto et al., 1993) has been adopted and the directional wave spectrum $S(\omega_e, \chi)$ is expressed as follows,

$$S(\omega_e, \chi) = \exp\left\{ a_0 + \sum_{n=1}^{N} a_n \cos n\chi + b_n \sin n\chi \right\} \tag{A-1}$$

ω_e : encounter angular frequency, χ : encounter angle of hull and wave
a_0, a_n, b_n : parameters of the model, N : order of the model.

The maximum value of N is determined by the number of measured data. However, the optimum value is selected based on AIC (Akaike Information Criterion). In case of running ships in following seas, the relations between wave frequency ω and encounter frequency ω_e shows complicacy as shown in Figure A-1, where g is gravitational acceleration and V is ship velocity. In this method, parameters are determined with respect to each range, namely Range – I, II and III in Figure A-1.
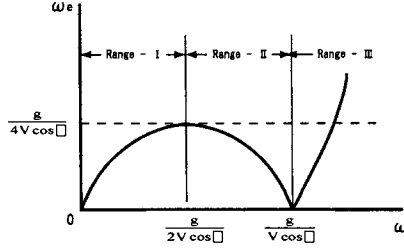
Figure A-1. Relations between wave frequency ω and encounter frequency ω_e

In the analysis, cross spectrum of observed ship responses m and n, $\phi_{mn}(\omega_e)$, is calculated and compared with the parametric model as shown in equation (A-2), where subscript I, II and III correspond to the ranges in Figure A-1 and subscript * means complex conjugate. H_m means RAO of m-th ship response in frequency domain.

$$\varepsilon = \phi_{mn}(\omega_e) - \int_{-\pi}^{\pi} \left\{ H_m^{I^*}(\omega_e, \chi) H_n^{I}(\omega_e, \chi) \times \exp\left\{ a_0 + \sum_{n=1}^{N} a_n^{I} \cos(n\chi) + b_n^{I} \sin(n\chi) \right\} \right.$$

$$+ H_m^{II^*}(\omega_e, \chi) H_n^{II}(\omega_e, \chi) \times \exp\left\{ a_0 + \sum_{n=1}^{N} a_n^{II} \cos(n\chi) + b_n^{II} \sin(n\chi) \right\} \qquad \text{(A-2)}$$

$$\left. + H_m^{III^*}(\omega_e, \chi) H_n^{III}(\omega_e, \chi) \times \exp\left\{ a_0 + \sum_{n=1}^{N} a_n^{III} \cos(n\chi) + b_n^{III} \sin(n\chi) \right\} \right\} d\chi$$

The parameters in equation (A-1) are determined to minimize ε, the estimation error, by Newton-Raphsom method numerically.

14

THE KITE TOWING SYSTEM
(ANTI-SYMMETRICAL TOWING SYSTEM)

Yutaka Terao[1] and Takeo Nikko[2]

[1]Department of Marine Design and Engineering
School of Marine Science and Technology, Tokai University
Shimizu, Shizuoka, Japan
Seagull1@scc.u-tokai.ac.jp

[2]Imabari Shipbuilding Co., Ltd.

ABSTRACT

It is well known that the fishtailing instability or whirling motion occurs when the ship is moored by single point mooring (SPM) system or towed with a single line. Whirling motion is mainly introduced by the instability of the SPM or single line towing system itself, and worsens due to the slack motion. We propose a new towing method and tested, named Kite Towing System (KTS) (Terao et al., 2000), which needs no additional special equipment. This paper shows the analysis of this basic principle and results of numerical results using the newly developed simulation program. From this model and numerical examinations, the stability of the towed hull motion by the Kite Towing System is proved.

INTRODUCTION

If a ship is disabled to navigate due to troubles in engine system or others, it has been the common operation to tow the ship by other ship to a safe coastal area. When towing a ship, stern of the towing ship is connected to bow of the ship to be towed with use of a single towing rope. The towing ship tows the ship to be towed with the propulsion power of the towing ship. During towing a ship, a motion resembling to a swing of pendulum, is created in the yaw direction of the towed ship. This motion is called "whirling motion". This motion is also observed when a ship lies at its moorings.

The causes of generating the "whirling motion" are known such as the relationship between ship speed and wind force, the shape of the bow of the ship being towed against the propeller stream of towing ship, towing speed and length of towing rope (Inoue et al., 1981, Kijima et al, 1983). When a towing is recognized as the relative flow speed of the ship being towed, the towing can be recognized as the phenomena that the mooring point such as mooring buoy is moving during mooring. The effects of "whirling motion" on the ship being towed are as follows:
1. Problems affecting course stability of both ships
2. Increase of motion area of the towed ship by the "whirling motion"
3. Increase the load to the towing rope due to "whirling motion"

Effect (1) can be improved by elongated the towing rope. However, it may change depending on the type of towing ship and on length of the towing rope. Effect (2) becomes a significant problem when piloting a ship inside a bay or in a narrow water way because the motion area where a towed ship swings around increases, since the distance between a towing ship and a towed ship is set to be longer in many cases for safety reason. Effect (3) can generate a large stress (snap tension) momentarily on a towing rope by the whirling motion and can rupture the towing rope or towing systems. It has been known that these effects tend to appear significantly when towing a damaged ship (Yuhara et al., 1999; Kijima et al., 2000; Hara et al., 2000).

The methods to suppress the "whirling motion" have been investigated in the past. These methods need control energy, or adding resistive equipments. Even though these methods have been used, many accidents of rupturing the towing rope have occurred. Under such circumstances, we recognize necessity of developing a new towing method and mooring method that can suppress the "whirling motion" with simple facility. We have proposed the towing method called "Kite Towing System". As this name indicates, it is the towing system that makes use of the principle that a kite is stabilized in the air when it flies in an open air. If we can suppress the "whirling motion" and can obtain the course stability of ships with this method, we can open possibility of new towing method. We have carried out the towing test using simple model ships in 1998. From this test, we obtained the towing trajectories of towing ship and towed ship, and come to know that the "whirling motion" could be suppressed. Figure 1 shows the Kite Towing System (KTS) schematic view.

In the KTS, using only a single rope to moored point, and tow a ship with bow and stern rope makes practically no problem. However, if the sailing speed of towing ship increases by some reasons, the retracting tension cannot be generated when a single towing rope is used. Because of this, using two towing ropes connecting both ships reduces freedom of motion of both ships, the towing ship and the towed ship, so that relative positional relationship between two ships can be maintained while both ships can turn around freely. In other words, connecting the two ships with two towing ropes like a kite can prevent the "whirling motion". In this method, directions of the bows of the two ships should be directed in an oblique direction towards outside each other. The two towing ropes are connected to the bow and stern of the towing ship. These two towing ropes are crossed each other once to form the towing condition. If difference of angle between the bows of these two ships becomes large, the towing resistance increases and is not desired. However, we place priority on suppression of the "whirling motion" to the resistance.
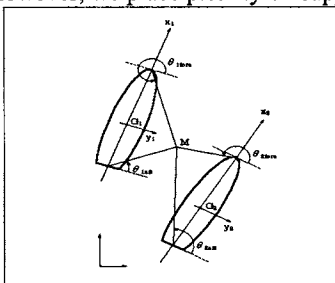
Figure 1. Schematic view of
Kite Towing System
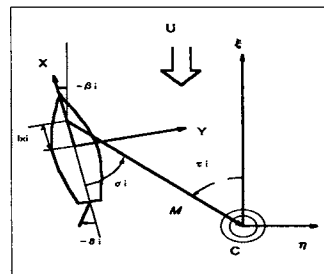
Figure 2. Schematic view of the KTS
balanced towing condition

If any trouble occurs, the towing rope connecting bow of the towing ship and stern of the towed sip can be disconnected to return simply to the conventional towing method.

In this research, we have investigated motions of both of the towing ship and the towed ship with KTS using numerical simulation. We have developed the maneuver motion equation of the two ships and created the hull motion calculation program using the maneuvering motion equation. We have made comparison between motion of the towed ship when it is towed by the conventional towing method and the motion of the towed ship when towed by KTS.

MANEUVERING MODEL

The Mathematical Model of Maneuvering Motion by KTS

Effectiveness of KTS in preventing the "whirling motion" is proved by the model test. We have implemented the numerical simulation using the mathematical model (MMG model (Hirano 1983; Kijima et al., 1992) of maneuverability to confirm the performance of preventing "whirling motion" by KTS.

The hydrodynamic forces that acts on vessel consists of ship type, propeller and rudder configurations while taking various motions in consideration. In addition to the above, the towing force effect is added as the external force term in KTS model. The external force that operates between the towing ship and the towed ship is only the towing rope force and the hydrodynamic force of mutual interference between the two ships is not taken into consideration.

The maneuvering motion equation can be expressed usually as shown below.

$$
\begin{aligned}
(m_i + m_{xi})\dot{u}_i - (m_i + m_{yi})v_i r_i &= X_i \\
(m_i + m_{yi})\dot{v}_i + (m_i + m_{xi})u_i r_i &= Y_i \\
(I_{zzi} + i_{zzi})\dot{r}_i &= N_i
\end{aligned}
\tag{1}
$$

Where i = 1, 2 indicates that 1: Towing ship and 2: Towed ship. At the same time, $(m_1 + m_{x1})$ indicates the hull muss and apparent added mass in the x direction, and $(m_1 + m_{y1})$ indicates the hull mass and apparent added mass in the y direction. $(I_{zz1} + i_{zz1})$ indicates the hull and apparent added moment of inertia.

In addition, the external force that is applied to the hull can be expressed as shown below.

$$
\begin{aligned}
X_i &= X_{Hi} + X_{pi} + X_{Ri} + X_{Ti} \\
Y_i &= Y_{Hi} + Y_{Ri} + Y_{Ti} \\
N_i &= N_{Hi} + N_{Ri} + N_{Ti}
\end{aligned}
\tag{2}
$$

The subscript $_H$, $_P$ and $_R$ indicate hydrodynamic terms that acts on the hull, propeller and rudder and $_T$ indicates the towing force by the towing rope. The term of interaction forces that are generated among the main hull, propeller and rudder, are included in this expression in addition to each of the hydrodynamic forces.

Hydrodynamic Forces That Act on Main Hull

The hydrodynamic force that acts on hull can be expressed as follows.

$$X_{Hi} = -m_{x_i}u_i\dot{\beta} + \left(m_{yi} + X_{vr_i} \right)v_i r_i - X(u_i)$$

$$Y'_{Hi} = Y'_{\beta_i}\beta_i + Y'_{r_i}r'_i + Y'_{\beta_i\beta_i}\beta_i|\beta_i|$$
$$+ Y'_{r_i r_i}r'_i|r'_i| + \left(Y'_{\beta_i\beta_i r_i}\beta_i + Y'_{\beta_i r_i r_i}r'_i \right)\beta_i r'_i$$

$$N'_{Hi} = N'_{\beta_i}\beta_i + N'_{r_i}r'_i + N'_{\beta_i\beta_i}\beta_i|\beta_i|$$
$$+ N'_{r_i r_i}r'_i|r'_i| + \left(N'_{\beta_i\beta_i r_i}\beta_i + N'_{\beta_i r_i r_i}r'_i \right)\beta_i r'_i$$

(3)

$$Y'_{Hi} = Y_{Hi} \Big/ \frac{1}{2}\rho L_i d_i U_i^2$$

$$N'_{Hi} = N_{Hi} \Big/ \frac{1}{2}\rho L_i^2 d_i U_i^2$$

(4)

Where Y'_{Hi} and N'_{Hi} are the dimensionless coefficients and can be expressed as follows. These motion derivatives are determined with the use of MMG's method.

Tension by Towing Ropes

In the KTS method, the two towing ropes connect the towing ship and the ship to be towed together. Where the force of towing rope connected to bow is expressed as T_{fore_i} and connected to stern is expressed as T_{aft_i}. θ_{fore_i} and θ_{aft_i} that indicate angle between the hulls X-axis and towing rope. When the towing force is divided into the X-Y component, it can be expressed as follows.

$$X_{Ti} = T_{i\_fore} \sin\left(\theta_{i\_fore}\right) + T_{i\_aft} \sin\left(\theta_{i\_aft}\right)$$
$$Y_{Ti} = T_{i\_fore} \cos\left(\theta_{i\_fore}\right) + T_{i\_aft} \cos\left(\theta_{i\_aft}\right)$$
$$N_{Ti} = \frac{1}{2}L_i T_{i\_fore} \cos\left(\theta_{i\_fore}\right) + \left(\frac{1}{2}L_i\right)T_{i\_aft} \cos\left(\theta_{i\_aft}\right)$$

(5)

Steady-State Balanced Conditions in KTS

We use the suffix i = 1, 2, which identified both hull, and assumed that both ships are sailing side-by-side with the forward speed U. When the ship 1 is assumed to be the towing ship and takes the orthogonal coordinates (ξ,η). The vertical axis ξ is taken same direction as U and the forces of the two ships in the x direction are balanced by the engine power of the towing ship as shown in Figure 2. The balanced forces in the h direction is expressed as follows:

$$F_{\eta 1}^{U} \otimes F_{\eta 2}^{U}$$

(6)

The status of the ships going straight ahead in the ξ direction with forward speed U is maintained. Then, (β_i) (j=1,2) are determined immediately. The positional relationship between the two ships during towing should satisfy the following Equation (7) when the moment N_p generating the towing force T, cancels the turning moments of the two ships.

$$N_p = l_{x2}|T|\sin|\sigma_2|$$
$$= -N_2(-\beta_2)$$
$$\therefore l_{x2} = \frac{N_2(\beta_2)}{|M|\sin|\sigma_2|}$$

(7)

Where β_i indicate the drifting angle, δ_i indicate the rudder angle and σ_i indicate the towing rope directional angle. Lx is the length up to the Yaw point of application of force. When the above relationship is satisfied, the relationship between the two ships can be maintained by KTS without using the turning moment that is generated by the rudder force. Moreover the rudder force can balance the deviation forces.

DESIGN OF THE KTS TRAJECTORY SIMULATOR

The numerical simulation model using the non-linear maneuvering model, proposed by MMG is installed. Runge-Kutta-Gill method is used for the time step motion calculation. The towing rope is assumed as a linear spring model for simplification of numerical calculation. When the initial length of a towing rope is T_{li_j0} and length of the towing rope after the time t seconds is T_{li_j}, and also spring constant of the towing tope is K_{i_j} (j = 1: aft, 2: fore), the tension applied to the towing rope can be expressed by the following equation (8). Calculated rope tensions are non-dimentionalized as Equation (9). Therefore negative towing force means less towing force is calculated compared to the initial tension.

$$T_{i\_j} = K_{i\_j}(Tl_{i\_j} - Tl_{i\_j0})$$

(8)

$$T\_Force' = Tension \Big/ \frac{1}{2}\rho LdU^2$$

(9)

Our system is developed using Delphi 5 and developed simulator is shown is Figure 3. The simulator initial conditions are given as a data file and used for calculation. The rudder angle, simulation processing time, integration step-size and switching between normal towing method and KTS can be entered with the use of GUI of window. Thus, the normal towing method and KTS are compared so that suppression effect of the "whirling motion" by KTS is numerically proved. At the same time, comparison of motion characteristics under different initial conditions such as length of towing rope, etc., change of tension applied to the towing rope and change of fluid force acting on vessel are investigated too.

The towing ship is assumed to be a bulk carrier and the towed ship is assumed to be an ordinary cargo ship. Main principal dimensions are shown in Table 1.

RESULTS OF CALCULATION

First, result of this simulation and result using actual ship are compared. Regarding the heading angle (Fig. 5) and the change in ship advanced speed (Fig. 6), the result of numerical simulation and actual ship sea trial data are very close. However, there is a difference in the turning trajectories in Figure 4. We could have improved matching of data of the two results in the turning trajectories if we have modified the hydrodynamic models and the hydrodynamic force

derivatives. However, as we thought that the above discrepancy would create no problem when we apply the result of the simulation to find the tendency of the "whirling motion". Therefore we have performed our analysis without changing anything.

Table 1. Principal dimensions

Ship	Towing Ship	Towed Ship
Kind of Ship	Bulk	Cargo Ship
Loading Condition	Ballast	Ballast
Hull Data		
L (m)	230	160
B (m)	32.2	23.5
d (m)	7.24	5.2
τ (m)	1.05	3.78
Cb	0.82	0.6
Cm	0.95	0.88
Cpa	0.75	0.8
Cwa	0.9	0.9
∇ (m3)	4.40E+04	1.17E+04
lcb (%)	-2.17	-3.13
m (kg)	4.51E+07	1.20E+07
mx (kg)	1.44E+06	2.28E+05
my (kg)	2.40E+07	7.84E+06
Izz (N-m)	8.47E+10	9.88E+09
izz (N-m)	9.07E+10	1.42E+10
Rudder		
AR (m2)	34.8	22.1
hr (m)	6.9	3
λ	1.38	1.57
Propeller	AU 4-55	
D (m)	9.7	5.7
P/D	0.71	1.14
n (rps)	1.95	0
tp	0.2	0
Z	4	4
Rope coefficient		
fore (N/m)	1.00E+05	1.50E+05
aft (N/m)	1.00E+05	1.50E+05
Start condition		
Us (m/s)	6.5	5.5
rs (rad/s)	0	0
β s (rad)	0	0
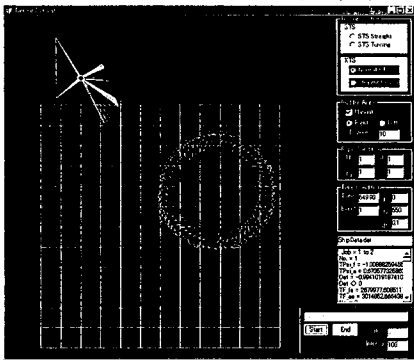
Figure 3. A sample of trajectory
simulation (KTS: δ = 10 deg)
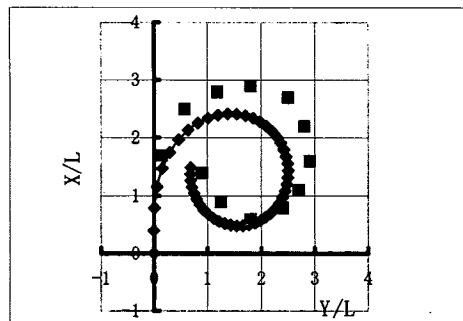
Figure 4. Comparison of the turning
trajectories (δ = 35 deg; ■:Exp,◆:Cal.)
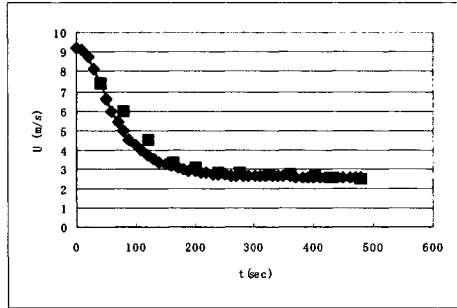
Figure 5. Comparison of the velocity of the heading angle (δ = 35 deg; ■:Exp,◆:Cal)
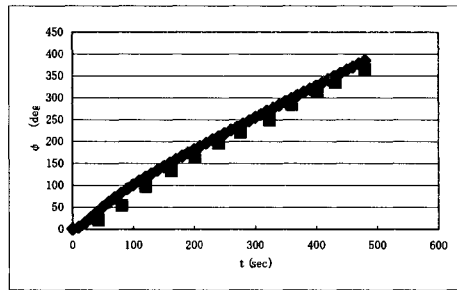
Figure 6. Comparison of advanced speed (δ = 35 deg; ■:Exp,◆:Cal)
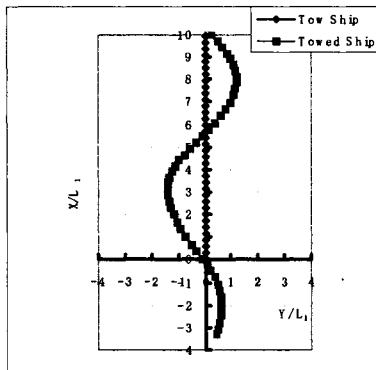
Figure 7. Calculated trajectories of Normal Towing System

Figure 7 shows trajectories of centers of gravity of both ships when both ships are going straight ahead using the normal towing method. Figure 8 shows positions centers of gravity and trajectories of mooring points of both towing and towed ships. Coordinates are non-dimentionalized by the length of the towing ship. Figures 9 and 10 indicate time histories of relative heading angle between bows of the towing ship and the towed ship. It is apparent that the "whirling motion" is generated when the ordinary towing method is used and amplitude of the "whirling motion" decreases when the Kite Towing System is used.

It shows that towing forces and moments are not balanced at the initial stage, but the ships will go straightforward without using any rudder force. They will turn after some time passed. Turning of both ships occurs because the balanced position between two ships changes so that the amount of hydrodynamic forces is changed and both ships are pulled each other by the towing rope tension.

If towing is started from the steady-state position where towing force is balanced, the steady going-straight-ahead performance can be explicitly improved. However, it is difficult to estimate the steady-state equilibrium position beforehand in the situation of actual towing, therefore in the practical operations, the maneuver with the use of rudder force to some extent is expected. Figures 11 and 12 show the time history of tension that acts on the towing rope. When KTS is used, the dynamic tension such as snap tension does not occur. Once the steady state towing is maintained, the KTS towing tension reduced soon.

Changing the rudder angle from -35 degrees to +35 degrees in steps of 5 degrees performs the turning test of KTS. When the rudder angle is a positive, the ships turn to the right that is the "inside towing method" (turn-around radius of the towed ship is inside the turn-around radius of the towing ship). In the contrary, when the rudder angle is the negative, the ships turn around by the "outside towing method". The turn-around loci at the rudder angle +15 degrees and -15 degrees are shown in Figure 13. Relative heading angle between the towing ship and the towed ship is shown in Figure 14. When turning in the right and left with the same rudder angle are compared, it is seen in the figures that the turning radius in the case of left turn (outside towing method) becomes larger. This phenomenon is important in the actual operation. Even in the single turning operation, the hydrodynamic forces acting on the towing hull changes due to the change of the turning radius changes.
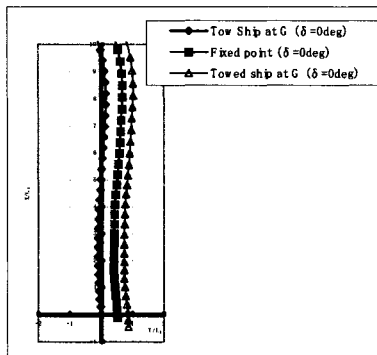
Figure 8. Calculated trajectories of KTS ($\delta = 0$ deg)
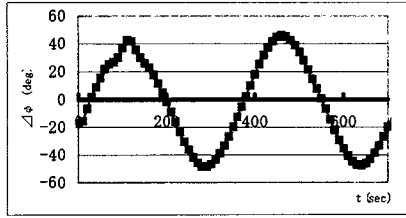
Figure 9. Time history of the relative heading angle (Normal Towing System $\delta = 0$ deg)
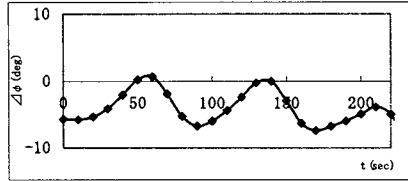
Figure 10. Time history of the relative heading angle (KTS: $\delta = 0$ deg)
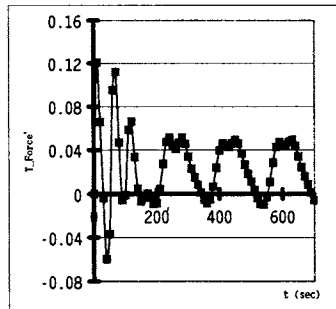
Figure 11. Calculated towing tension of Normal Towing System
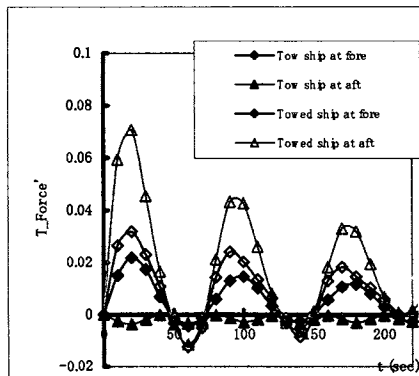
Figure 12. Calculated towing tension of KTS
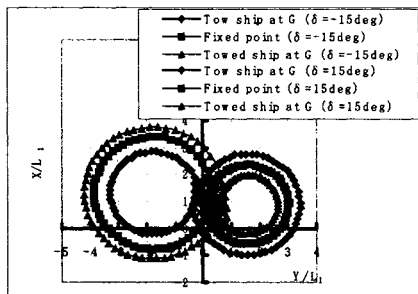
Figure 13. Calculated trajectories of KTS ($\delta = \pm 15$ deg)
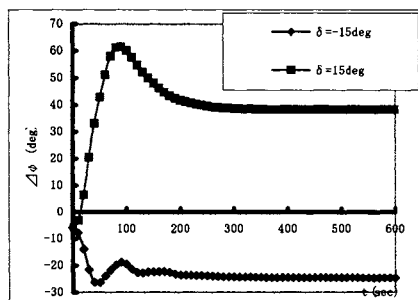
Figure 14. Time history of the relative heading angle (KTS: $\delta = \pm 15$ deg)

CONCLUSION

From the above result, the Kite Towing System has the function of suppressing the "whirling motion" and reduces the snap tension that occurs at the towing rope. We also come to know that the tension on the respective ropes decreases because the two ropes are used.

The future research remains are closer to the actuality. Our rope restoring force model is the linear spring model. Because of this, calculation time is reduced and length of the towing rope, the balancing position could have been maintained easily to the neutral position. In practice, the calculation with the use of non-linear spring model is more natural and necessary. We will continue our research by further developing calculations in such aspects and at the same time the quantitative model tests or actual sea trials should be performed and compared with the result of this study.

REFERENCES

Hara, S., K. Yamakawa, K. Hoshino and K. Yulkawa. 2000. On the Towing of Damaged Ships J. Kansai Soc., N.A, Japan, No. 233, March; 71-78.

Hirano, M. 1983. On Calculation Method of Ship Maneuvering Motion at Initial Design Phase JSNAJ, No. 147; 144-153.

Inoue, S., M. Hirano, K. Kijima and J. Takashina. 1981. A Practical Calculation Method of Ship Maneuvering Motion. ISP, Vol. 28, N0. 325;207-222.

Kijima, K. and Y. Wada 1983. Course Stability of Towed Vessel with Wind Effect. JSNAJ, No. 153;117-153.

Kijima, K., K. Maekawa and K. Tanaka. 1992. The Directional Stability of Tow and Towed Vessels in Shallow Water, *J. West Japan Soc.*, N.A., Japan, No. 84, 1992;85-96.

Kijima, K., T. Kishimoto and K. Suenaga. 2000. On the Towing Characteristics of Disabled Ship. *J. West Japan Soc.*, N.A, Japan, No. 100;17-29

Terao, Y. and T. Nikko. 2000. A Basic Study of The Kite Towing System (Anti-Symmetric Towing Method) *J. Kansai Soc.*, N.A, Japan, No. 234, September; 109-113.

Yuhara, K., K. Hoshino, S. Hara, and K. Yamakawa. 1999. Dynamic forces acting on capsized vessel with geometric configuration and its towing method, JSNAJ, No. 186;145-156

CLIMATE CHANGE IN THE NORTHEAST ASIA AND NORTHWEST PACIFIC DURING 20TH CENTURY

Vladimir Ponomarev[1], Dmitrii Kaplunenko[1], Vladimir Krokhin[2] and Hajime Ishida[3]

[1]V.I. Il'ichev Pacific Oceanological Institute
Vladivostok, Primorskii Krai, RUSSIA
ponomarev@poi.dvo.ru

[2]Far Eastern Regional Hydrometeorological Research Institute
Vladivostok, Primorskii Krai, Russia

[3]Faculty of Engineering, Kanazawa University
Kanazawa, Ishikawa, JAPAN

ABSTRACT

This paper describes major patterns of centennial/semi-centennial climatic tendencies of surface air temperature and precipitation in the Northeast Asia in 20th century, as well as, sea surface temperature (SST) in the Northwest Pacific in the second half of the century. Linear trend of monthly mean precipitation and air/water temperature is estimated using two statistical methods. First one is least squares method with Fisher's test for significance level. Second method is nonparametric robust method based on Theil's rank regression and Kendall's test for significance level applicable to dataset with abnormal distribution function typical for precipitation time series. Consistency of tendencies in surface air temperature, precipitation, and SST, their seasonality, differences in continental, marginal and coastal areas, as well as, in subtropic and subarctic zones are revealed and discussed.

INTRODUCTION

Recent examination of global and hemisphere changes in annual mean surface air temperature, precipitation (Bradley et al., 1986; Vinnikov et al., 1990) and SST (Casey and Cornillon, 2001) in the 20th century have shown statistically significant global warming (Vinnikov et al., 1990; Folland et al., 2001) and precipitation increase in latitude band 35°-70°N over land areas (Bradley et al., 1986; Vinnikov et al., 1990). It is increasing in late 20th and dominating in moderate latitudes (40°- 60°/55°N) and subarctic zone (55°/60°-70°N) (Folland et al., 2001; Kondratiev and Demirchan, 2001). Climatic tendency of annual mean and winter warming during 20th century over Northeast Asia and Far-East found in (Arakawa, 1957; Rankova and Gruza, 1998; Varlamov et al., 1998 and so on) are in agreement with major conclusions on climate change in northern hemisphere mentioned above. At the same time, it was shown that precipitation tendencies over the former Soviet Union and Russian Far-East in the 20th century are unstable and insignificant (Rankova and Gruza; 1998; Dashko et al., 1997). Statistical significance of precipitation trend in Japan estimated earlier is quite similar. For example, precipitation decrease from 1948 to 1985 (Matsumoto and Yanagimachi, 1991) was not

confirmed later by using extended dataset for the next decade (Tase and Nakagawa, 1996). It seams to be due to substantial decadal (Nakamura et al., 1996 and others) and interdecadal (Minobe and Mantua, 1999) oscillations in the extratropic North Pacific and East Asia. Moreover, distribution function of precipitation time series is usually abnormal. In this case it is more accurate to use nonparametric robust method for estimation of trend and its statistical significance (Gan, 1995; Krokhin, 1997, 2001). Our paper is also focused on application of this method for precipitation data set. The aim of this study is to reveal consistency of climatic tendencies in surface air temperature, precipitation and SST, as well as their seasonality and difference in the continental and marginal, subtropic and subarctic zones of the area studied.

OBSERVATION DATA AND STATISTICAL METHODS

The linear trends of surface air temperature and precipitation in the 20th century and second half of the century are estimated for each month of a year in the wide continental area of the extratropic Asia east of 55°E, from Ural Ridge to the coastal areas of the Northwest Pacific and Alaska Peninsula. Semi-centennial tendency of the monthly mean SST in the Northwest Pacific region extended to the west of 180E is examined for the second half of the 20th century. Dataset of monthly mean grided SST also covers East China, Japan, Okhotsk and Bering Seas. Thus, the climate change in the wide latitude band from the North Tropic to the coast of Arctic Ocean is estimated. Monthly mean time series of air temperature and precipitation at the meteorological stations were selected for the area studied from data bases of NOAA Global History Climatic Network (USA), RIHMI-WDC (Russia) and JMA (Japan) for the period of instrumental observations since late 19th century to 2000. To outline the details of climate change associated with extreme cooling or warming in winter and summer, we also used the daily time series of surface air temperature at some meteorological stations. Two monthly datasets of the Northwest Pacific SST on different grids were selected from: (1) - WMU/COADS World Atlas of Surface Marine Data NOAA/NESDIS/NCDC CD-ROM, 1994 of time series since 1945 till 1989 with horizontal resolution 1°x1°; (2) - JMA data base of time series since 1946 till 2000 with horizontal resolution 2° x 2° for the ocean area 15°- 65°N, 110° - 180°E. Initial time series of air temperature, precipitation and JMA SST have missing data. To use complete datasets missing data of the time series in each months was implemented by the statistical method of incomplete multivariate data analyses (Schafer, 1997) using EM and AM algorithms.

Two methods of the linear trend estimation are applied. First one is based on least-squares (LS) method, Pirson's regression and Fisher's test for statistical significance level. Second one is nonparametric robust (NR) method (Holander and Wolfe, 1973; Hettmansperger, 1984), based on Theil's rank regression and Kendall's test for statistical significance level (Bendat and Piersol, 1986). The NR method should be applied to time series with abnormal distribution function typical mainly for precipitation time series. It does not demand the assumption that function of distribution is Gaussian. In this case the rank statistics is used to determine both linear regression and its significance. The NR method was earlier applied to examine trends of precipitation in Canada and northeastern USA (Gan, 1995), as well as, in Russian Far East for a warm season (Krokhin 1997, 2001). To estimate trends of surface air temperature, precipitation and SST we have applied both LS and NR methods to all of time series independently on distribution function of datasets.

CLIMATIC TENDENCY IN SURFACE AIR TEMPERATURE

Large-scale areas of warming and cooling in the Northeast Asia, their seasonality are revealed for both whole period of instrumental meteorological observations and second half of the 20th century by using two statistical methods of linear trend estimation. Sign and statistical significance of semi- centennial air temperature trend for the second half of the 20th century are shown in Figure 1 for winter and summer months. The area studied is most covered by observation data for this period.
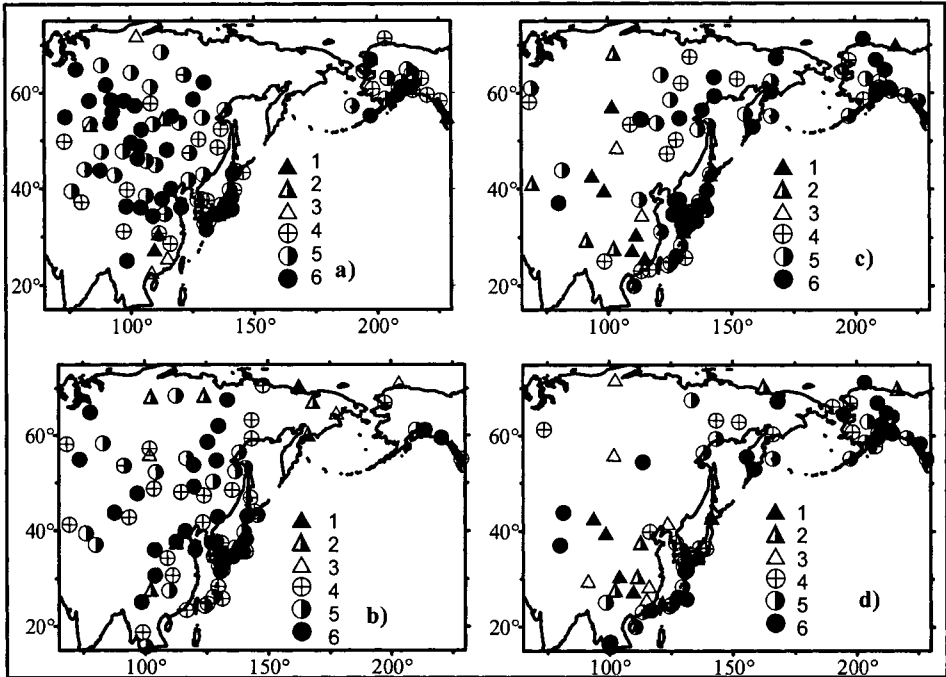
Figure 1. Negative (1, 2, 3) and positive (4, 5, 6) tendencies of surface air temperature with significance levels: 90% (3,4), 95% (2,5) and 99% (1,6) in December (a), January (b), June (c), and July (d) for the time series since 1945 till 2000

A semi-centennial warming of high significance level 99% (Fig. 1) in the second half of the 20th century is clear recorded over subtropic Pacific marginal zone (Korean Peninsula, Japanese Islands) all the year round, over Kamchatka Peninsula in summer, spring, and fall, and at the Pacific side of Alaska Peninsula in most months. Weak semi-centennial warming is also found over Chukchi Peninsula, but only in summer months. Significant semi-centennial cooling in the Northwest Pacific marginal area is found only in southeast subtropic continental area adjacent to the East-China Sea in latitude band 25°-35°N (Figs. 1a, c, d). Negative air temperature trend of 95%-99% significance level occurs in latitude band 25°-35°N in June and July, as well as in 25°-30°N band it occurs in August, September, November, December, March and April. The

29

significant centennial cooling in other months is also typical for this latitude band but mainly in the offshore continental area. Most substantial seasonality of semi- centennial air temperature trends is found in continental area 35°-55°N, 90°-110°E. As shown in Figure 1, seasonality of climatic trend in this large-scale area is characterized by warming in winter and cooling in summer. Positive temperature trend in this area is most significant and expanded in December – March, and negative one expands in June - September with maximal significance in June - July. Correspondently, differences between monthly mean air temperature in June and December, July and January, August and February substantially decreases in this continental area both in 20th century and second half of the century. The substantial difference of the air temperature tendencies in the offshore continental area and marginal zone of the Northwest Pacific is also manifested. It seems to be due to amplification of ocean impact to the mid-latitude Asian continental areas, as well as, with long-term anomaly of the Asian monsoon system.

Statistically significant centennial warming (1° - 3°C/90 years) from the beginning of 20th century till 1990 or 2000 also occurs over marginal subtropic Northwest Pacific throughout a year, over subarctic coastal area in most months, and over arctic marginal zone only in some months, particularly, in December, January, July and August. Centennial trend in offshore area of mid latitude continental Asia also shows warming in winter and cooling in summer (Ponomarev et al., 2001). So, centennial and semi-centennial trends of surface air temperature are similar and stable. At least, at the meteorological stations where period of instrumental observations is more than 100 years (Japan, Korea, Russia) sign and significance of centennial trend do not substantially depend on a period of time series varied from 73 to 120 years. Similar patterns of linear trends in the area studied were found for datasets of monthly mean air temperature since beginning of instrumental observations in late 19th century until 1990 or since 1917 until 1990 (Ponomarev et al., 2001). It is also in agreement with tendencies of annual/seasonal mean surface air temperature and other climatic characteristics estimated for Japan and Russia by many authors, particularly by Arakawa (1957), Rankova and Gruza (1998), Varlamov et al. (1998) and others. On the whole, significant warming of both centennial and semi-centennial scale predominates in a cold period of a year in a broad mid-latitude continental zone north of 35°-40°N (Fig. 1a).

CLIMATIC TENDENCY IN PRECIPITATIONS

Statistically significant (95-99%) trends of precipitations for the second half of the 20th century (1945-2000) are revealed in large-scale areas of the Northeast Asia for each month of a year. This result is not in agreement with conclusion on statistically non-significance of precipitation trends estimated earlier by traditional LS method by Dashko et al. (1997), Rankova and Gruza (1998) and others. Sign and statistical significance of semi-centennial trend of monthly precipitations in each season are shown in Figure 2. Increase of precipitation in the second half of 20th century is found in large-scale continental areas of the Northeast Asia predominating in October - May in moderate and arctic latitude zones. Typical monthly precipitation rise of high statistical significance level (99%) there is 0.2-0.4 mm/year, and maximal values are in range of 1.4-1.7 mm/year at some Russian meteorological stations in the continental area of moderate latitudes.
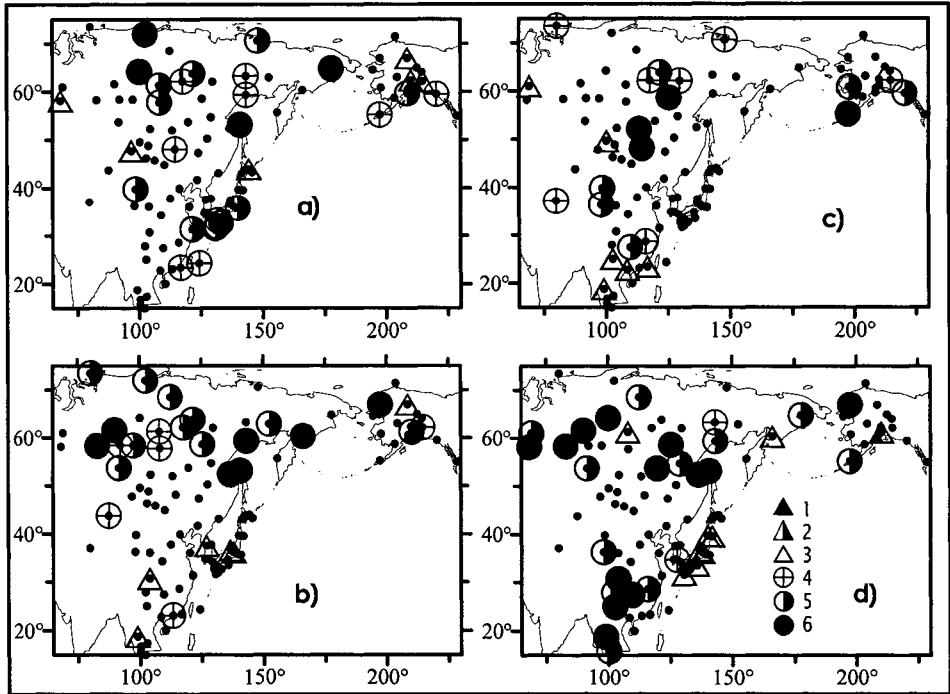
Figure 2. Negative (1, 2, 3) and positive (4, 5, 6) tendencies of precipitation sum with significance levels: 90% (3,4), 95% (2,5) and 99% (1,6) in March (a), October (b), June (c), and January (d) for the time series since 1945 till 2000

In October - February positive semi- centennial trend of monthly precipitation sum occurs east of 55°E in the whole latitude band 45°-70°N, but in March, May and June it occurs in the area east of 100E in the same latitude band. In February positive precipitation trend of high significance level (99%) also occurs in tropical and subtropical marginal area east of 95°-100°E adjacent to the East-China Sea, where the air temperature trend in this month is also positive. Week negative precipitation trend in this subtropical area is found in May and October, and only at some meteorological stations it takes place in the period from July to September. Bands of positive precipitation trend in summer months are stretched out from southwest to northeast, parallel to the Northwest Pacific marginal zone as well as (Fig. 2c). In June positive precipitation trend occupies area along Pacific and Bering Sea coast of Alaska and offshore band stretching out from continental area adjacent to the East-China Sea to the arctic coast of the East-Siberian Sea. So, positive patterns of precipitation and air temperature trends are very similar in the continental area of the Northeast Asia. Warming accompanies precipitation rise there. This result is close to conclusion on the accompanying centennial trends of global/ hemisphere means air temperature and precipitations (Bradley et al., 1986; Vinnikov et al., 1990; Kondratiev and Demirchan, 2001 and others). Weak negative trend of precipitation is found in Japan south of Hokkaido and in Russian Primorye region adjacent to the Northwest Japan Sea. In this area of the NW Pacific marginal zone centennial and semi-centennial warming accompanies

precipitation decrease. Relatively week (>90% significance level) negative precipitation trends of both centennial and semi-centennial (Figs. 2c, d) scales are found over Kyushu and Honshu Islands in September, October, December and January. Similar trends with low significance level (<90%) are found in Russian Primorye region for most months (Krokhin, 2001).

Significant positive precipitation trend occurs in Kyushu and Honshu Islands: centennial trend in May, semi-centennial in March (Fig. 2a). In the subarctic zone (Hokkaido, Sapporo) centennial increase of precipitation with high significance level (95-99%) occurs in January, February, March and August, and decrease of precipitation occurs in May, June and July. Thus, seasonality of precipitation trend over Japanese Islands is significant, and shows opposite patterns of trend in subtropic and subarctic zones. It can be conditioned by storm track change like in ENSO signal and decadal oscillation (Nakamura et al., 1997). Trends estimated by Nonparametric Robust (NR) method are more objective with greater reliability than LS method in case of precipitations. About 50% of precipitation time series even for whole period of instrumental observation has abnormal distribution function usually with substantial positive skewness and sometimes an abnormal kurtosis. Difference between statistical significance of centennial precipitation trends in Japan estimated by NR and LS methods is demonstrated in Figure 3.
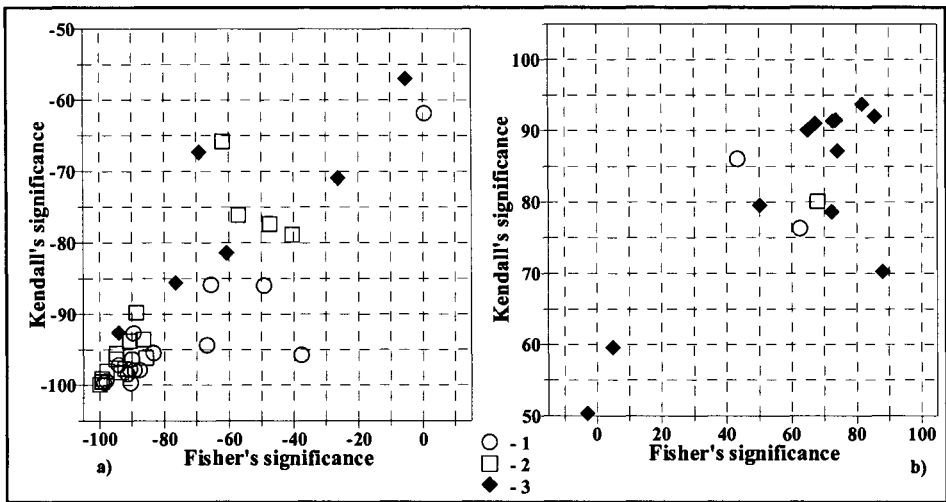
Figure 3. Statistical significance level (%) of negative (a) and positive (b) centennial (1900-2000) trends of monthly precipitation in Japan for October (1), December (2), and May (3) estimated by LS method with Fisher's test and by NR method with Kendal's test for significance level. A negative value of in axis (a) means negative trend.

The principal difference and similarity between trend and its significance estimated by two methods depends on distribution function, mainly, on its skewness and kurtosis. Statistical significance of precipitation trends determined by NR method is higher, than that calculated by LS method in all cases of abnormal skewness and kurtosis in distribution function.

CLIMATIC TENDENCY IN THE NORTHWEST PACIFIC SST

The trend of the annual mean SST of the World Ocean in 5° longitude-latitude bins was earlier analyzed by Casey and Cornillon (2001) for the period 1942 – 1993. In comparison with (Casey and Cornillon, 2001) we revealed regional details of high seasonality in SST tendency in the Northwest (NW) Pacific for the second half of 20th century (1945-2000), estimating linear trend in grid 2°x2° for each month of a year. The SST trends, for two months of both winter and summer seasons, are shown in Figure 4, demonstrating high seasonality.
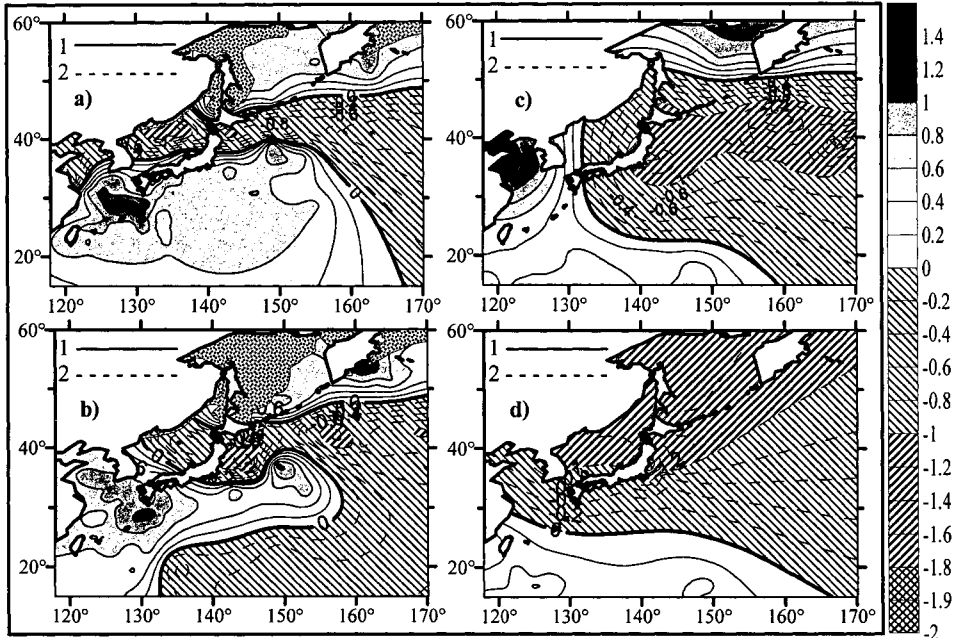
Figure 4. Positive (curve 1) and negative (curve 2) increment (°C) of linear trend in SST (JMA) since 1946 until 2000 in January (a), February (b), July (c), and August (d). Ice coverage in marginal seas is filled by special pattern

Seasonality of SST trend is similar to that of surface air temperature trend over the Northeast Asia (Fig. 1). Semi-centennial warming in SST dominates in November - January (Fig. 4a), and cooling dominates in July (Fig. 4c) – September. It is important that warming tendency in November-December takes place, at first, in western tropic and subtropic area including west Philippine Sea, East-China Sea, Kuroshio region, at second, it occurs in the northwestern subarctic Pacific. Warming in cores of both pools are most significant (99%) and highest (0.8-1.3°C per 55 years) in December. In this month subarctic pool of warming occupies offshore Oyashio region off the Kuril Islands, as well as areas adjacent to western Aleutian Islands and Kamchatka Peninsula. Most significant positive trend in the Northwest Pacific SST occupies indeed largest area in December. In January subtropical warming pool expands northeastward to Kuroshio Extension and transition zone south of subarctic front (Fig. 4a). In January - February the subarctic pool of warming also shifts northeastward to the southwest Bering Sea and ocean

area adjacent to the north Kamchatka (Figs. 4a, b). At the same time, in January significant trend of cooling occurs in the latitude band 39°- 45°N east of Tsugaru Strait and Hokkaido Island, extending eastward. This area of long-term cooling is associated with Oyashio, its intrusion and subarctic frontal zone. In February the pool of cooling occupies most of the western subarctic gyre, dominating in the Oyashio Intrusion and western core of the subarctic gyre. In March-May it expands substantially southward, occupying northeast area of the subtropic gyre. Pool of cooling also expands in subarctic gyre in spring, becomes deepest in July, and occupies NW Pacific north of 30°N in August with maximum negative SST trend in the Japan and Okhotsk seas, being weak and insignificant in subtropical area and transitional zone.

Features of both SST trends and dynamics of the Japan Sea are very close to that in the Northwest Pacific. Warming in winter SST occurs in south subtropic region adjacent to Korean Strait and north subarctic area adjacent to Tatarskii Strait, but cooling pool occupies central sea area associated with the subarctic gyre and subarctic frontal zone where intermediate low salinity water forms through the subduction mechanism in late fall and winter. Subtropic gyre in the Japan Sea spins up in late 20th century, which follows from observation data analyses and modeling results presented in (Trusenkova, Ponomarev and Ishida, this volume). Anomalous increased heat transport from the western subtropic Pacific and East-China Sea to the Japan Sea accumulates in its intermediate and deep waters (Ponomarev and Salyuk, 1997; Ponomarev et al. 2000, 2001), but semi-centennial trend in SST of subarctic gyre is negative. Physical mechanism of the SST cooling in the Northwest Pacific subarctic gyre, accompanying warming in Kuroshio region seems to be similar to physics of circulation and climate change in the Japan Sea.

CONCLUSION

Climatic tendencies in Northeast Asia in the 20th century are characterized by significant warming in winter and cooling in summer over offshore continental area west of 120-110°E in mid and moderate latitudes. Difference between summer and winter surface air temperature significantly decreases in this continental area during 20th century and its second half. Warming tendency being characteristic throughout a year for the area east of 110°120°E accompanies precipitation increase in this area of moderate latitudes. Thus, continental climate in moderate latitudes of the Northeast Asia becomes closer to marine climate. Positive air temperature trend occupies marginal land area adjacent to the Northwest Pacific practically all the year round, with the exception of subtropic continental area adjacent to the East China Sea. Warming tendency in fall and winter accompanies precipitation decrease in Japan and Russian Primorye Region adjacent to the Northwest Japan Sea. Significant precipitation reduce in Japan takes place in October, December and January, with the exception of subarctic area (Hokkaido Island) where precipitation slightly increases in December-March and in August, but decreases in May-July.

Statistically significant positive SST trend in Kuroshio region and in the northwest area of the Pacific subarctic gyre dominates from November - February, accompanying warming in the continental and marginal areas of the Northeast Asia. At the same time, semi-centennial negative SST trend occurs in the Oyashio region and occupies southwestern area of subarctic Pacific gyre. On the whole, temperature contrast in subtropic Western Pacific increases, while air temperature contrast over East Asia decreases during second half of the 20th century.

Climatic patterns typical for subtropics shift northward in the East Asia, and duration of cold period of a year decreases in marginal subarctic zone and continental area of moderate latitudes.

REFERENCES

Arakawa, H. 1957. Climatic change as revealed by the data from the Far East. *Weather*. 12(2):46-51.

Bendat, J.S. and A.G. Piersol. 1986. *Random data: analysis and measurement procedures*. New York: John Wiley & Sons Publications.

Bradley, R.S., H.F. Diaz, J.K. Eischeid, P.D. Jones, P.M. Kelly, and C.M. Goodess. 1986. Precipitation Fluctuations over Northern Hemisphere Land Areas since the Mid-19th Century. *Science*. 237:171-175.

Casey, K. S. and P. Cornillon. 2001. Global and Regional Sea Surface Temperature Trends. *Journal of Climate*. 14:3801-3818.

Dashko, N.A., S.M. Varlamov, E.X. Khan, and E.S. Kim. 1997. Variability of precipitation above coast of the Japan sea. *Meteorologiya i Gidrologiya* (in Russian) 12:12-24.

Folland, C. K., N. A. Rayner, S. J. Brown, T. M. Smith, S. S. Shen, D. E. Parker, I. Macadam, P. D. Jones, R. N. Jones, N. Nicholls, and D. M. H. Sexton. 2001. Global temperature change and its uncertainties since 1861. *Geophysical Research Letters*. 28(13):2621-2624.

Gan, Th. 1995. Trends in air temperature and precipitation for Canada and north-eastern USA. *Int. J. Climatology*. 15(10):1115-1134.

Hettmansperger, Th.P. 1984. *Statistical inference based on ranks*. New York - Chichester - Brisbane – Toronto – Sigapore: John Wilew & Sons Inc. Publications.

Holander, M. and D. Wolfe. 1973. *Nonparametric statistical methods*. New York - Brisbane - Toronto – Sigapore: John Wilew & Sons Inc. Publications.

Kondratiev, K. Ya. and K. S. Demirchan. 2001. Earth climate and "Kioto Protocol" (in Russian). *Vestnik Rossiyskoy Akademii Nauk* (In Russian) 71(11):1002-1009.

Krokhin, V.V. 1997. About some methods of statistical data processing of the monthly sums of precipitation. (in Russian) *Trudy DVNIGMI Collection of papers of the Far East Regional Hydrometeorological Institute*. St. Petersburg: Hydrometeorological Press, 148:116-127.

Krokhin, V.V. 2001. On the precipitation trends over the Russian Far East in a warm season. *Reports of International Workshop on the Global Change Studies in the Far East", Sept. 7-9, 1999*. Vladivostok: Dalnauka. TEACOM Publication. 7(1):111-122.

Matsumoto, J. and H. Yanagimachi. 1997. Long-term variations of precipitation and snow depth in Japan. *Environ. Change and Gis. Intern. Symp.,* Asahikawa, Japan, Aug. 28.-1991:431-444.

Minobe, S. and N. Mantua. 1999. Interdecadal modulation of interannual atmospheric and oceanic variability over the North Pacific. *Progress Oceanography.* 43:163-192.

Nakamura, H., G. Lin, and T. Yamagata. 1997. Decadal climate variability in the North Pacific during the recent decades. *Bull. American Meteorol. Soc.* 78(10):2215-2225.

Ponomarev, V.I. and A.N. Salyuk. 1997. The climate regime shifts and heat accumulation in the Sea of Japan. *Proceedings of CREAMS'97 Symp.* Jan. 26-31, 1997. Fukuoka: 157-161.

Ponomarev, V.I., E.I. Ustinova, A.N. Salyuk, and D. D. Kaplunenko 2000. Climate variation in the Japan Sea and adjacent area in 20th century. (In Russian) *Izvestiya TINRO (Collection of papers Trans. Pacific Res. Fish. Center).* 127 (2):20-36.

Ponomarev, V., D. Kaplunenko, and H. Ishida. 2001. Centennial and semi-centennial climatic tendencies in the Asian continental and Pacific marginal areas. *Bulletin of Japan Sea Research Institution.* Kanazawa University. Japan. 32:77-90.

Rankova, E.Ya. and G.V. Gruza. 1998. Indicators of climate change for Russia. *Meteorologiya i Gidrologiya* (in Russia) 1: 5-18. (Translated into English).

Schafer, J. L. 1997. *Analysis of incomplete Multivariate data.* London: Chapman&Hall Publications.

Tase, N. and S. Nakagawa. 1990. Spatial and temporal characteristics of precipitation in Japan. Long-term trends of annual precipitation. *Annual Report Institution Geosciences Univ. Tsikuba.* 16:553-572.

Trusenkova, O., V. Ponomarev, and H. Ishida. 2002. Heat transport to the Northwest Japan Sea: simulation with the MHI model. In *this volume.*

Varlamov, S.M., Y.S. Kim, and E.Kh. Han 1998. Recent variations of temperature in East Siberia and in the Russian Far East. *Meteorologiya i Gidrologiya* (in Russia) 1:19-28. (translated into English).

Vinnikov, K. Ya., P. Ya. Groisman, and K. M. Lugina. 1990. Empirical Data on Contemporary Global Climate Changes (Temperature and Precipitation). *Journal of Climate.* 3(6): 662-677.

HEAT TRANSPORT TO THE NORTHWEST JAPAN SEA: SIMULATION WITH THE MHI MODEL

Olga Trusenkova[1], Vladimir Ponomarev[1] and Hajime Ishida[2]

[1]V.I. Il'ichev Pacific Oceanological Institute
Vladivostok, Primorskii Krai, RUSSIA

[2]Faculty of Engineering, Kanazawa University
Kanazawa, Ishikawa, JAPAN
trolia@poi.dvo.ru

ABSTRACT

Circulation, heat transport, and air – sea heat fluxes in the Japan Sea are simulated for two climatic regimes of mid and late 20th century. The MHI numerical model (Shapiro et al., 1998) is applied for simulations. Two short-term experiments are performed for the external and initial conditions of the 1950s or 1990s based on meteorological and oceanographic observations. Simulation results suggest that re-distribution of the Tsushima Current transport between western and eastern branches and thermal regime of the northwest Japan Sea is highly affected by conditions of decreased baroclinicity in the 1950s or increased baroclinicity in the 1990s. Intensification of the simulated East Korean Warm Current (western branch) in 1999 associated with increased baroclinicity facilitates heat transport to the western and central sea area. In winter, heat loss at the sea surface and convection depth is decreased in 1999, compared to 1950.

INTRODUCTION

Wintertime interdecadal warming in the atmosphere over many regions of Northeast Asia, in particular over the adjacent Japan Sea area is supported by numerous observational evidence (Ponomarev et al., 2001a and refs. therein). It can be demonstrated by the increase of wintertime air temperature over the Japan Sea from 1950 to 1990, reconstructed from data of 20 meteorological stations around the Sea (Fig. 1a). Warming is especially high (up to 5°C for January (Fig. 1a)) over the northwest Japan Sea off Vladivostok, an area of increased wintertime air – sea heat turbulent flux (Kawamura and Wu, 1998) and of deep winter convection (Talley et al., 2002). Conditioned by atmospheric warming, potential temperature has increased in thermocline and deep water of the Japan Sea from mid to late 20th century (Ponomarev et al., 2001a and refs. therein).

In our previous studies, we focused on modeling of circulation patterns in the Japan Sea, associated with climate change (Ponomarev et al., 2001b; Trusenkova et al., 2003). The purpose of this paper is to numerically simulate an impact of climate change on heat content and transport in the sea. The results on circulation are only briefly discussed with regard to their contribution to heat advection and air – sea turbulent heat flux.

SETUP OF NUMERICAL EXPERIMENTS

The MHI model (Shapiro, 1998) is a primitive equation model in isopycnic coordinates under hydrostatic, Boussinesq, and β-plane approaches. It is a good tool for simulating jet currents, fronts, and winter convection by entrainment/subduction and layer outcropping devices. In the MHI model, seawater temperature, salinity, and buoyancy are allowed to vary horizontally in any layer, facilitating simulation of subduction and variation of water properties throughout the sea. Stable vertical stratification is maintained by introduction of "base" buoyancy to constrain buoyancy variations in inner layers: a layer outcrops if buoyancy gets out of its base limits; density variations in the upper layer are unbounded. The upper mixed layer model incorporates the balance of turbulent kinetic energy. Air - sea heat and freshwater fluxes are calculated by considering the complete (non-linear) heat balance and prescribed precipitation.

Table 1. Experimental setup

	1950 Experiment	1999 Experiment
Model domain	127° – 142°E, 34° - 52°N	
Inflow ports	Western and Eastern Tsushima Channels	
Outflow ports	Tsugaru and La Perouse (Soya) Straits	
Horizontal resolution	1/8°; 10 km W – E, 14 km N - S	
Number of layers	7	8
Time step	5 min	
Starting date	1st of January	1st of June
Bi-harmonic viscosity	10^{17} cm^4/s equivalent to 10^5 cm^2/s for the 1/8° mesh	
Harmonic diffusivity	10^7 cm^2/s	
Diapycnal diffusivity	$5 \cdot 10^{-6}$ cm/s equivalent to $2.5 \cdot 10^{-2}$ cm^2/s (for 50 m thick layer)	
Base buoyancy (cm/s^2)	∞, 2, 1.6, 1.3, 1, 0.8, 0	∞, 2.4, 1.8, 1.4, 1.05, 0.87, 0.8, 0
Data for initial interfacial surfaces	R/V "Vityaz" 3rd cruise, January – February 1950	cruises of R/Vs "Roger Revelle" and "Prof. Khromov", June – August 1999
Inflow transport	Sinusoid with extreme values of 3Sv/2Sv for September/March	
Outflow transport	Divided between Tsugaru and La Perouse Straits as 2 : 1	
T and S of inflow water	From monthly climatology	
Air – sea fluxes:		
Wind stress	Neglected (set equal to zero)	
Freshwater flux	Neglected (precipitation balanced by evaporation; no runoff)	
Net downward radiative flux	From climatology; seasonally varied but constant over the sea	
Turbulent heat flux	Calculated from bulk formulas	
Sea surface temperature	Temperature of the upper layer calculated by the MHI model	
Surface air temperature	Monthly mean for 1950	Monthly mean for 1990
Wind speed	5 m/s, constant in time and space	
Air relative humidity	0.7, constant in time and space	

The model domain covers the Japan Sea from Tsushima Island to Tatarsky Strait; model bottom topography is presented in Figure 1b. Two short-term experiments are performed (integration up to three years; results are discussed for August and February of the third year) for the external and initial conditions of 1950s and 1990s based on meteorological and oceanographic

observations. The experimental setup is basically the same as in (Trusenkova et al., 2003); model domain, simulation parameters, and data used are summarized in Table 1. Initial interfacial surfaces are taken as isopycnals corresponding to base buoyancy of the layers. In both cases, initial interface topography (shown in (Figs. 1b, c; Trusenkova et al., 2003)) exhibits doming structure typical for the cyclonic gyre in the northwest Japan Sea and large-scale depression in the subtropical area. Features specific for the climatic regimes are consistent with decreased baroclinicity in the Japan Sea in 1950s or increased baroclinicity in 1990s. Initial layers are isopycnic with uniform temperature and salinity within every layer.

The difference between two climatic regimes is analyzed, associated with change of buoyancy forcing at the sea surface. As inflow transport and water characteristics in the Tsushima Strait are the same, air temperature and SST (temperature of the model upper layer) are two parameters affecting air – sea heat flux which vary in time and space and are different for both experiments. Air temperature is subjected to climate change and SST depends upon circulation in the Japan Sea and air – sea heat flux. Wind stress is usually considered as principal forcing for numerical models. However, principal features of the Japan Sea general circulation, such as the separation of the western boundary current from the coast and formation of the cyclonic gyre, can be explained by surface thermal forcing only, with surface cooling and wind stress acting in the same way (Seung, 1992). Ekman transport and Ekman pumping is neglected due to the lack of direct wind forcing in our experiments. Realistic large-scale and mesoscale circulation can be simulated this approach (Trusenkova et al., 2003).

Figure 1. Air temperature increase (°C; for January) from 1990 to1950 (a) and model domain and bottom topography (b; m; hatches downhill, contours every 250m) for the Japan Sea

RESULTS OF NUMERICAL EXPERIMENTS

Simulated circulation and heat content and advection in the Japan Sea

The general circulation in the Japan Sea is realistically simulated in both experiments; current velocity is shown in Figures 4 and 5 in (Trusenkova et al., 2003). It is consistent with circulation schemes derived from observations such as (Sizova, 1961) and simulations by other models, such as (Yoon and Kawamura, 2002). The cyclonic gyre simulated in the northwest Japan Sea and Tatarsky Strait is characterized by sea surface depression (Figs. 2, 5) and by doming structure in topography of interfacial surfaces between layers (Figs. 6, 7; Trusenkova et al., 2003). The cyclonic gyre is intensified in the 1950 Experiment, compared to 1999: sea

surface height (SSH) difference between its center and the subtropical area is of about 24-28 cm in the former case and 16-20 cm in the latter case (Fig. 2; Trusenkova et al., 2003).
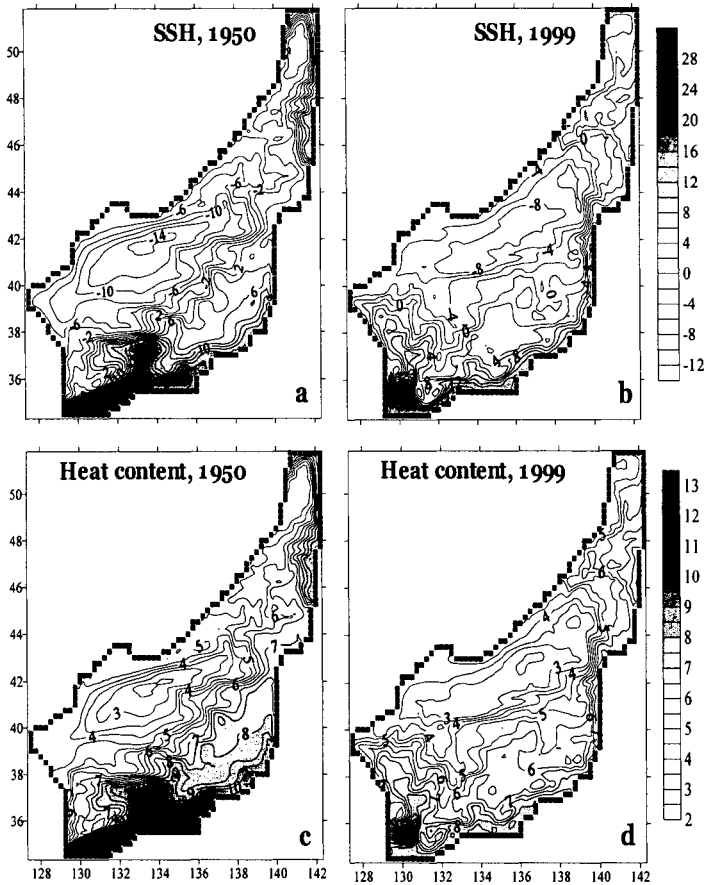
Figure 2. Sea surface height (cm; a, b) and heat content of the upper (250 m) baroclinic layer (10^9 J/m^{-2}; c, d) in summer (August 1) for the 1950 (a, c) and 1999 (b, d) Experiments

Simulated branches of the Tsushima Warm Current carry subtropical water from the Tsushima Strait northward to the northeast Japan Sea and Tatarsky Strait, where buoyant water is seen as elevation of the sea surface (Fig. 2). Anticyclonic circulation off La Perouse Strait is reproduced in geostrophic currents by Sizova (1961). The eastern branches of the Tsushima Current are intensified in the 1950 Experiment, while the western branch, the East Korea Warm Current (EKWC) flowing northward along the Korean coast is intensified in the 1999 Experiment (Trusenkova et al., 2003). The sea surface elevation associated with the EKWC develops as far north as 40°N in the western sea (westward of 131°E) in 1999 (Fig. 2b), while sea surface depression associated with the cyclonic gyre reaches as far south as 37°N in 1950 (Fig. 2a). The simulated circulation pattern in the northwest Japan Sea for 1999 is in agreement with

observational evidence from satellite imagery and ship measurements. Observed warm streamers and eddies originating from the EKWC penetrate as far north as 42°N (westward of 132°E; Danchenkov et al., 1997). With direct wind forcing, anticyclonic wind stress curl over this area caused by adjacent land orography can strengthen the anticyclonic circulation.
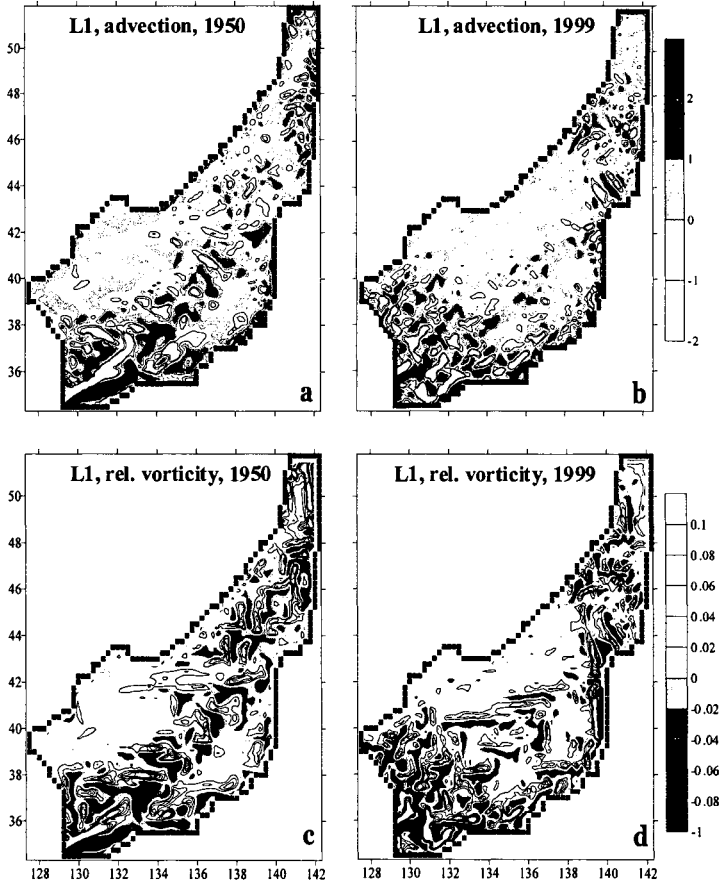
Figure 3. Horizontal heat advection (10^3 wt/m^2; a, b) and relative vorticity (10^{-4} s^{-1}; c, d) in the upper layer (summer) for the 1950 (a, c) and 1999 (b, d) Experiments

The first and second (eastern) branches of the Tsushima Warm Current flow along the Honshu coast over the shelf and slope (Kawabe, 1982). In our experiments they are simulated as a single stream or separate jets (Trusenkova et al., 2003). Besides, in both cases a meandering jet is simulated in the interior southeast region over the Oki Bank (centered at 133°E, southward of 37°30′N in Fig. 1b) and Yamato Rise (centered at 134°E, southward of 40°30′N in Fig. 1b). It is clearly seen in current velocity (Figs. 4, 5; Trusenkova et al., 2003) and also as a ridge of increased SSH (Figs. 2a, 2b, 5a, 5d). The presence of warm water and temperature fronts in this

41

area is supported by observational evidence; temperature patterns reveal considerable interannual and mesoscale variability (Kawabe, 1982).

Westward branches of the Tsushima Current Extension flow across the sea off the eastern to western coast in the northern Japan Sea and southern Tatarsky Strait. The westward jets are simulated along 42°-43°N, 44°N, 45°N, 46°N, and, in summer 1999, along 46°30'-47°N (Trusenkova et al., 2003). Cyclonically bended contours correspond to these jets in the SSH distribution (Figs. 2a, 2b, 5a, 5d). The westward current across the Japan Sea off the Tsugaru Strait is reproduced in geostrophic circulation by Sizova (1961) and has already been simulated by numerical models (Ponomarev et al., 2001b; Yoon and Kawamura, 2002).

Distribution of heat content of the upper (250 m) baroclinic layer closely follows circulation patterns in both cases (Fig. 2). Heat content is low inside the subarctic gyre in the northwest Japan Sea and northern Tatarsky Strait and high in the southeast region of warm currents (Fig. 2). Heat content is lowest (of $2.3 \cdot 10^9$-$2.35 \cdot 10^9 J/m^2$) in the center of the cyclonic gyre (around 133°-133°30'E, 41°30'-42°N with lowest SSH) in 1950, while in 1999 heat content inside the cyclonic gyre is above $2.4 \cdot 10^9 J/m^2$. In the southeast Japan Sea heat content is higher in 1950: it is more than $10.0 \cdot 10^9 J/m^2$ in the anticyclonic meander over the Oki Bank with extreme sea surface elevation over 20 cm (Fig. 2). In contrast, the western Japan Sea (westward of 132°E) is warmer in 1999: heat content is over $5.0 \cdot 10^9 J/m^2$ as far north as 39°30'N, while it is under $4.5 \cdot 10^9 J/m^2$ as far south as 38°-39°N in 1950 (Figs. 2c, d). Contrast in heat content between the subarctic and subtropical regions is higher in 1950 due to intensification of the cyclonic gyre.

Heat advection is estimated from the horizontal advective terms of the transport equation for temperature. Positive advection is highest within mesoscale circulation features associated with warm currents, such as anticyclonic meanders and eddies. In both experiments patterns of heat advection closely match patterns of relative vorticity. The latter also has extreme values within mesoscale features (Fig. 3). In the 1950 Experiment, heat is mostly advected from the Tsushima Strait northward in the eastern Japan Sea (Fig. 3a). In contrast, in the 1999 Experiment, northward heat advection is higher in the western Japan Sea (Fig. 3b). Chains of anticyclonic eddies seen as curved belts of high positive advective heat flux and of anticyclonic vorticity form eddy streets considered as an important device of heat transport. Eddy streets were documented in infrared satellite images of the northwest and central Japan Sea (Danchenkov et al., 1997). As, with the present spatial and temporal resolution (Table 1), simulated eddies do not move, heat is advected by mesoscale currents associated with them. In both experiments, heat is advected to the northwest Japan Sea from the east with the westward branches of the Tsushima Current Extension. Curved patches of positive advection coincide with the current jets across the sea in the 42°-44°N band in summer 1950 and in the 45°-47°N band in summer 1999 (Fig. 3).

Wintertime air – sea heat fluxes and convection

In both experiments large-scale spatial patterns of wintertime turbulent (sensible and latent) heat flux (Fig. 4) simulated under constant wind speed forcing are consistent with ones based on observation data, such as in (Kawamura and Wu, 1998), estimated under synoptic wind forcing.

These patterns should be associated with the difference between air temperature and SST (temperature of the model upper layer). Disagreement in some areas and quantitative underestimation of simulated heat fluxes are due to values adopted for wind speed, relative humidity, and climatic upward longwave radiation. Wintertime heat loss at the sea surface is high in the subtropical area of warm currents and higher SST and in the northern Japan Sea and Tatarsky Strait of lowest air temperature; latent heat flux is highest in the south and sensible heat flux is highest in the north (Figs. 4, 5). Sensible heat flux exceeds latent flux in the area northward of 40°-41°N in 1950 and northward of 42°-43°N in 1999, as cold air cannot hold much moisture. An excess of sensible over latent flux is reported by Kawamura and Wu (1998) for the area northward of 44°N and area of increased flux off Vladivostok.
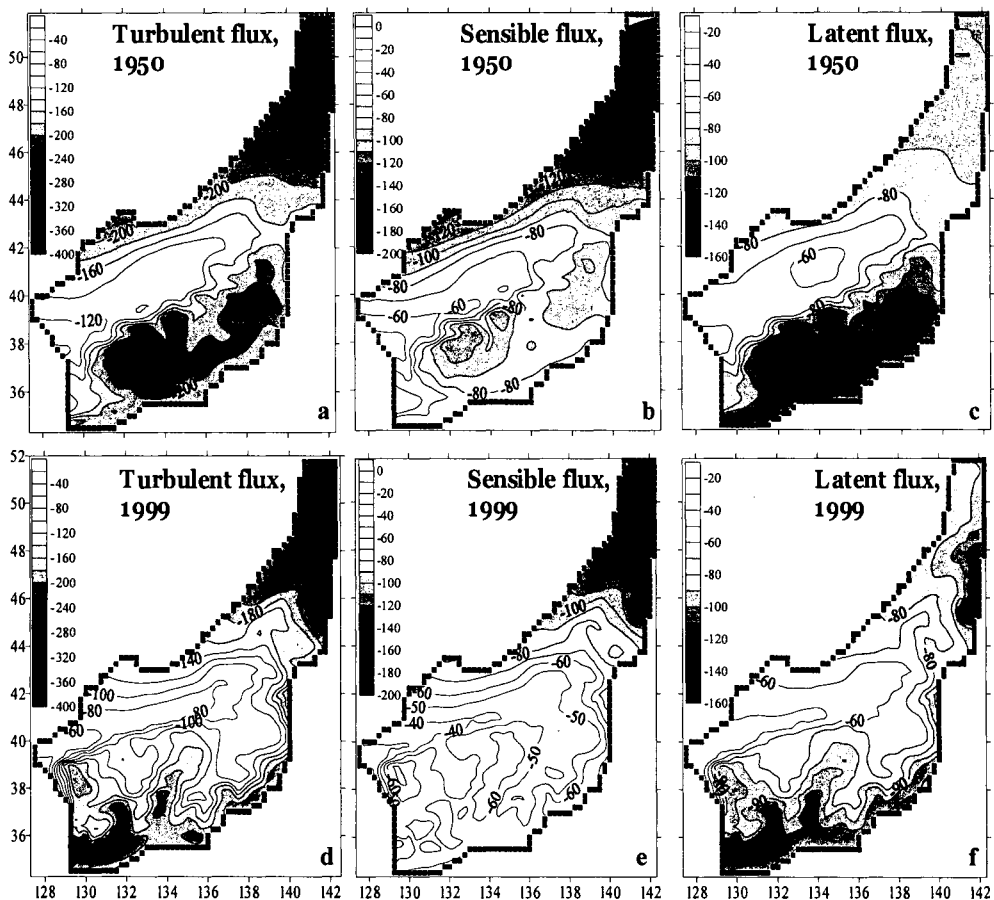
Figure 4. Wintertime net turbulent (a, d), sensible (b, e), and latent (c, f) heat flux (wt/m^2) on February 1 for the 1950 (a, b, c) and 1999 (d, e, f) Experiments

Heat flux is low inside the cyclonic gyre, due to low SST (Figs. 4, 5). The area of minimum flux, decreasing westward, is stretched out along the southern subarctic front associated with the

EKWC Extension, with the lowest flux off the Korea coast (Fig. 4). This pattern is in agreement with (Kawamura and Wu, 1998). Turbulent heat flux, especially due to sensible flux, is increased in the area adjacent to Vladivostok (Fig. 4) due to low air temperature caused by strong winter monsoon wind from continental Asia, although according to Kawamura and Wu (1998) "the flux center" off Vladivostok is shifted eastward. In the subtropical area, simulated patterns of net turbulent heat flux resemble patterns of SSH and upper layer temperature in both experiments (Figs. 4, 5). In the 1999 Experiment, tongues of increased heat flux are simulated in the southern Japan Sea: along the Honshu Island, in the central region centered at 134°E, and in the western area. A tongue-shaped area of increased turbulent fluxes centered at 133°E appears over the Oki Bank in Kawamura and Wu (1998). Eastward shift of simulated flux maximum can be explained by variability of currents in this area (Kawabe, 1982).

In winter air - sea turbulent heat flux averaged over the sea, although underestimated in both experiments, is higher in 1950 than in 1999, namely 110 wt/m^2 versus 74 wt/m^2 for February. Wintertime latent and sensible fluxes are higher in the 1950 Experiment over most of the sea area, with two exceptions. In 1999 the western Japan Sea is occupied by warm surface and intermediate water associated with the intensified EKWC even in winter, while in 1950 the cyclonic gyre extends to 37°N, as seen from SSH distribution (Figs. 5d, a). Therefore, heat loss is increased in this area in the 1999 Experiment (Figs. 4b, e). In the eastern Japan Sea, branches of warm currents penetrate farther north in 1999 than in 1950, as seen from SSH distribution (Figs. 5d, a). In winter surface water is warmer in the area off La Perouse Strait (Figs. 5e, b) and air – sea heat flux is increased in 1999, compared to 1950 (Figs. 4d, a).

Wintertime patterns of SSH, upper layer temperature, and convection depth match each other, with sharp fronts in convection depth along the current jets (Fig. 5). Convection penetrates to greater density in the interior of cyclonic gyres due to isopycnal doming. Simulated surface density is higher in the interior than at the margins of the cyclonic gyre: it is $27.12\sigma_\theta$ versus 26.83-$26.87\sigma_\theta$ for 1950 and $27.02\sigma_\theta$ versus $26.98\sigma_\theta$ for 1999. However, the convection depth is increased at the cyclonic gyre margins (Fig. 5). According to recent (winter 2000 and 2001) observations in the Japan Sea, evidence of deep convection is found at the southwest margin of the cyclonic gyre close to the subarctic front and at the northwest margin over the underwater seamount called Siberia (Talley et al., 2002). Compared to observations, the simulated SST is too high and convection depth and surface density are too low due to underestimated heat loss at the sea surface.

Convection simulated in the northwest Japan Sea was more intense in 1950 than in 1999 due to the higher heat loss at the sea surface and the intensified cyclonic gyre. However, in the interior of the cyclonic gyre, SST simulated under constant wind seed forcing is lower in 1999 than in 1950, with lower convection depth in 1999. This decrease is consistent with negative wintertime SST trend in the subarctic Japan Sea and Northwest Pacific found in observations (Ponomarev et al., 2003). On the contrary, simulated surface salinity in the cyclonic gyre interior is higher in 1950 than in 1999: 33.9-33.95 ppt versus 33.8-33.85 ppt. This increase implies that entrainment and upward buoyancy flux from the sea interior to the surface layer is higher in 1950 than in 1999, consistent with the intensified cyclonic gyre.

44
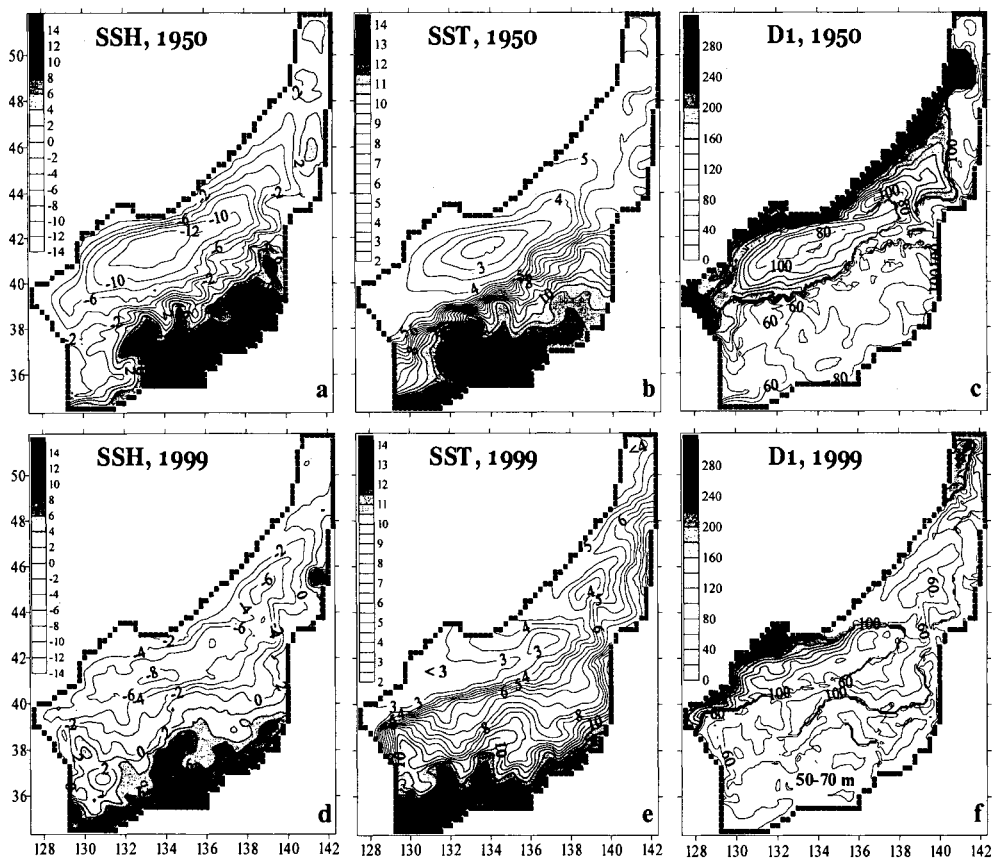
Figure 5. Sea surface height (cm; a, d), upper layer temperature (°C; b, e), and convection depth (m; c, f) on February 1 for the 1950 (a, b, c) and 1999 (d, e, f) Experiments

CONCLUSIONS

Inflow transport across the Tsushima Strait is redistributed in favor of the eastern branches of the Tsushima Current in conditions of decreased baroclinicity in the mid 20th century and in favor of the western branch (East Korea Warm Current; EKWC) in conditions of increased baroclinicity in the late 20th century. The EKWC intensified in the 1990s supplies heat to the northwest Japan Sea, in contrast with the situation in the 1950s characterized by southeastward expansion of the intensified cyclonic gyre. In both cases, heat is advected to the northwest Japan Sea from the east with the westward branch of the Tsushima Current Extension. Realistic large-scale spatial patterns of wintertime turbulent heat flux from the Japan Sea surface to the atmosphere are simulated under constant wind speed forcing. Wintertime heat loss at the sea surface was higher in the cold conditions of the mid 20th century over most of the Japan Sea, with the exception of the western Sea and an area off La Perouse Strait where heat loss is higher in the late 20th

century. In the climatic conditions of the mid 20th century, winter convection in the northwest Japan Sea was facilitated by the intensified cyclonic gyre. Further research of modeling of the Japan Sea circulation will be implemented under forcing of synoptic winds.

REFERENCES

Danchenkov, M.A., V.B. Lobanov, and A.A. Nikitin. 1997. Mesoscale eddies in the Japan Sea, their role in circulation and heat transport. In *Proceedings of CREAMS'97 International Symposium, January 26-31, 1997, Fukuoka, Japan*, 81-84.

Kawabe, M. 1982. Branching of the Tsushima Current in the Japan Sea, Part I. Data analysis. *J. Oceanogr. Soc. Japan*. 38(4): 95-107.

Kawamura, H., and P. Wu. 1998. Formation mechanism of the Japan Sea proper water in the flux center off Vladivostok. *J. Geophys. Res*. 99(C12): 25081-25091.

Ponomarev, V.I., D.D. Kaplunenko, and H. Ishida. 2001a. The 20th century climate change in the Asian-Pacific Region. In *Oceanography of the Japan Sea, Proceedings of CREAMS'2000 International Symposium*, edited by M.A. Danchenkov, 129-136. Russia, Vladivostok: Dalnauka.

Ponomarev, V.I., O.O. Trusenkova, and L.D. Talley. 2001b. Simulation of the Japan Sea circulation in summer 1999 using the MHI layered model. In *Oceanography of the Japan Sea, Proceedings of CREAMS'2000 International Symposium*, edited by M.A. Danchenkov, 104-111, Vladivostok: Dalnauka.

Ponomarev, V.I., D.D. Kaplunenko, V. Krokhin, and H. Ishida. 2003. Climate change in the Northeast Asia and Northwest Pacific during 20th century. In *this volume*.

Seung, Y.H. 1992. A simple model for separation of East Korean Warm Current and formation of North Korean Cold Current. *J. Oceanological Society Korea*. 27(3): 189-196.

Shapiro, N.B. 1998. Formation of the Black Sea general circulation considering stochastic wind stress. *Marine Hydrophysical Journal* (In Russian), 6: 26-40.

Sizova, Yu.V. 1961. The Japan Sea circulation. In *General features of the Japan Sea geology and hydrology*, edited by V.N. Stepanov, 146-154 (in Russian). Moscow: Ac. Sci. USSR Publ.

Talley L.D., V. Lobanov, V. Ponomarev, A. Salyuk, P. Tishchenko, I. Zhabin, and S. Riser. 2002. Deep convection and brine rejection in the Japan Sea. *Science* (submitted).

Trusenkova, O., V. Ponomarev, and H. Ishida. 2003. Impact of climate change on circulation patterns in the Japan Sea. *Journal of Hydraulic, Coastal and Environmental Engineering, JSCE* (in print).

Yoon, J.H., and H. Kawamura. 2002. The formation and circulation of the intermediate water in the Japan Sea. *Journal of Oceanography*, 55(2): 197-211.

GLOBAL EDDY-RESOLVING SIMULATION BY THE EARTH SIMULATOR: BRIEF REPORT ON THE FIRST RUN

Hirofumi Sakuma[1], Hideharu Sasaki[1], Keiko Takahashi[1], Takashi Kagimoto[2], Toshio Yamagata[2,3] and Tetsuya Sato[1]

[1]Earth Science Program, Earth Simulator Center
Yokohama, Kanagawa, JAPAN
sakuma@es.jamstec.go.jp

[2]Variation Research Program, Institute for Global Change Research
Yokohama, Kanagawa, JAPAN

[3]Department of Earth and Planetary Science, Graduate School of Science
The University of Tokyo, Tokyo, JAPAN

ABSTRACT

The outcomes of the first test run on a global eddy-resolving simulation using the Earth Simulator are reported briefly in this short paper. The aim of the first run is to assess not only computational performance of our newly tuned code for the machine but also an overall physical performance in reproducing basin scale characteristics of currents and temperature fields together with important mesoscale eddy activities in the world ocean. One of the noteworthy accomplishments of the first run is the fact that the Earth Simulator enables us to complete a time integration of a 50-years-long global eddy-resolving simulation in less than half a month, which would accelerate greatly high-resolution climate modeling studies from now on.

INTRODUCTION

Among the key elements that determine the basic properties of the general circulations of the world ocean, nonlinear scale interactions between mesoscale eddies and basin scale circulations affecting the global statistics of heat, momentum and tracer transports are challenging research subjects to which enormous computational power of the Earth Simulator is of great help. Setting this as an initial goal of our Earth Simulator Initiative, we have developed a MOM3-based high performance OGCM code optimized for our machine. Physical performance of ocean models using the Bryan (1969) formulation adopted in MOM-3 have been extensively checked so far by many research groups in the world and high-resolution performances of the model were investigated notably by Semtner-Chervin (1992) and Fu and Smith (1996). Those studies revealed that the model can reproduce comprehensive three-dimensional structures of ocean circulations, some of them are fairly correct but some are rather inaccurate. Well known persistent problems relating to a high-resolution issue are sluggishness of simulated circulations and improper separation points of the western boundary currents and those are expected to be improved with higher resolution in both the horizontal and vertical directions (Chao et al., 1996).

Simulated oceanic fields are not only dependent upon the physical performances of a given model but also on the quality or appropriateness of the data imposed as boundary forcing including bathymetry and attempts of successful global eddy resolving simulations are relatively new time consuming efforts in which the above two factors are carefully evaluated. A major obstacle to perform a global eddy-resolving simulation is the fact that an effective execution of such a simulation is not possible due to the insufficient computational capability of available machines. However, the situation has been drastically changed with the advent of the Earth Simulator together with an optimized OGCM code for it. Our machine enables us to complete a decadal-long (near) global eddy-resolving simulation with horizontal resolution of 0.1 degree in several days and it gave us a great impetus to start out on high-resolution simulation studies on climate variability. As a first step towards such studies, we set up a series of basic numerical experiments to assess the computational and physical performances of our newly developed code. The aim of this short paper is to report the main outcomes of the first experiment in which the choice of scheme options, model parameters and types of boundary forcing were made on a rather trial basis. Nevertheless, the overall characteristics of the simulated fields turned out to be quite realistic, especially improved are two drawbacks mentioned above, namely, the sluggishness of the currents and separation points of the Kuroshio and the Gulf Stream. In what follows, our code optimization strategy and sustained performance of a newly developed MOM3-based OGCM are briefly explained in section one. Section two covers the outline of the computational settings of our first experiment, and in section three we will assess the overall physical performances of our code putting emphasis on fine structures our high-resolution simulation could reproduce. Brief summary and future plans are given in the summary section.

CODE OPTIMIZATION AND COMPUTATIONAL PERFORMANCE

To attain high performance of our eddy resolving code, a number of different optimization technique have been utilized considering distinctive characteristics of the Earth Simulator. First of all, each routine must be vectorized to improve the performance on vector machines. In addition, we applied such common techniques as inline expansions, loop merging, loop unrolling/rerolling together with re-ordering in order to reduce the number of calling procedures and to make the averaged length of do-loops longer. In some cases, techniques of loop fission/splitting and loop fusion are reintroduced in a balanced manner.

As the first step of optimization, we attempted to make the vector ratio of almost all routines to exceed 99.5 percent. Attained the maximum value of averaged vector length, vector ratio and value of the total flops are indicated in Table 1, where the maximum vector length and peak performance for each processor are 256 and 8 Gflops respectively.

Table 1: Routine-wise vector length, ratio and the total flops elapsed

Main computation [routine names]	CPU time (%)	MFLOPS	Vector Ratio	Ave. Vector Length
baroclinic computation [baroclinic]	14.3	4900.7	99.8	240.0
vertical mixing with implicitly [invtri]	13.0	3374.6	99.6	240.0
barotropic computation [expl_freesurf]	11.0	4902.6	99.7	240.0
Unesco_density [unesco_density]	8.4	5202.2	99.8	256.0
computation with biharmonic [delseq_velocity]	7.5	4255.7	99.7	240.0
main computation of tracers [tracer]	7.1	5025.9	99.8	240.0
calculate advection velocities [adv_vel]	4.2	4838.7	99.6	240.0
construct diagnostics [diagt1]	2.6	3801.6	99.5	243.0
computation of normalized densities [statec]	2.4	6613.0	99.8	240.1

We employed one dimensional domain decomposition in the meridional direction, in which parallelization procedure is limited by the number of employed latitudinal circles, namely, the maximum number of CPUs to be used for a near global domain extending from 75°S to 75°N is 1500 provided that the meridional resolution is 0.1 degree. Each processor is assigned computation in zonal strips. The number of meridional grid points in a zonal strip depends on the number of processors. As the number of processors increases, the meridional extent of a strip becomes comparable to or smaller than a halo region, which means that some measures are necessary to reduce computational burdens especially in the halo regions. To this end, we employed micro-tasking techniques for intra-node parallelization while inter-node communications were achieved via MPI library to get the best communication performance on the Earth Simulator. Using 188 nodes, the sustained performance of our aggregate code turned out to be 2.75 Tflops, which is 23% of the peak performance. The horizontal and vertical resolutions we employed to get this performance are 1/10 degree and 54 levels respectively. The other details of our simulation settings are given in the following section. Our tuning effort is still going on and, as the result, the latest parallel efficiency reached to 99.9% and 30 days integration is completed in 1395 seconds of wall clock time, which allows us to execute 100 years integration within 20 days.

SIMULATION SETTING

The computational domain covers a near-global region extending from 75°S to 75° North. The horizontal resolution and the number of vertical levels we employed are 1/10° and 54 respectively. The thickness of vertical layers increases with depth starting with 5 m (the depth of the upper-most grid point is at 2.5 m depth) and the maximum depth of our model ocean is 6,065m. Model bottom topography was interpolated from 1/30° "OCCAM Topography" dataset we obtained by courtesy of GFDL, which was originally created by the OCCAM project at the Southampton Oceanography Centre. The upper boundary forcing of the momentum heat and salinity fluxes are specified by using monthly mean NCEP (Kistler et al., 2001) to reanalysis data with surface salinity restoring to climatological value. At the northern and southern artificially introduced boundaries, we introduced the restoring zones with three degrees meridional width in which temperature and salinity fields are also restored to their monthly climatological values. The annual mean temperature and salinity fields obtained from World Ocean Atlas 1998 (henceforth WOA98; Antonov et al., 1998a, 1998b, 1998; Boyer et al., 1998a, 1998b, 1998) are

used as an initial condition for density field and initial current velocity is set to zero at all levels. To suppress grid-scale noises we introduced a scale-selective damping of Bi-harmonic type and for the vertical mixing, KPP scheme (Troen et al. 1986, Large et al, 1994) is employed. In the present version of the model, no sea ice model is implemented yet.

VERIFICATION OF SIMULATED RESULTS

(1) Sea surface temperature and height fields

Since sea surface temperature (SST) field directly reflects a seasonal meridional migration or variation of temperature field affected by small scale eddy activity, we present a snapshot of SST field first in Figure 1a as a concise but informative figure that tells us what our eddy-resolving simulation looks like, while Figure 1b gives a monthly mean observational field of the corresponding month with a horizontal resolution of 1 degree. We see that basin scale SST patterns together with such mesoscale features as the existence of ubiquitous eddy activities, the Kuroshio's meandering and the Gulf Stream paths with the right separation latitudes, Natal pulses in the Agulhas Current and herringbone structures of the Legeckis waves in the eastern tropical Pacific are well reproduced in our simulation.
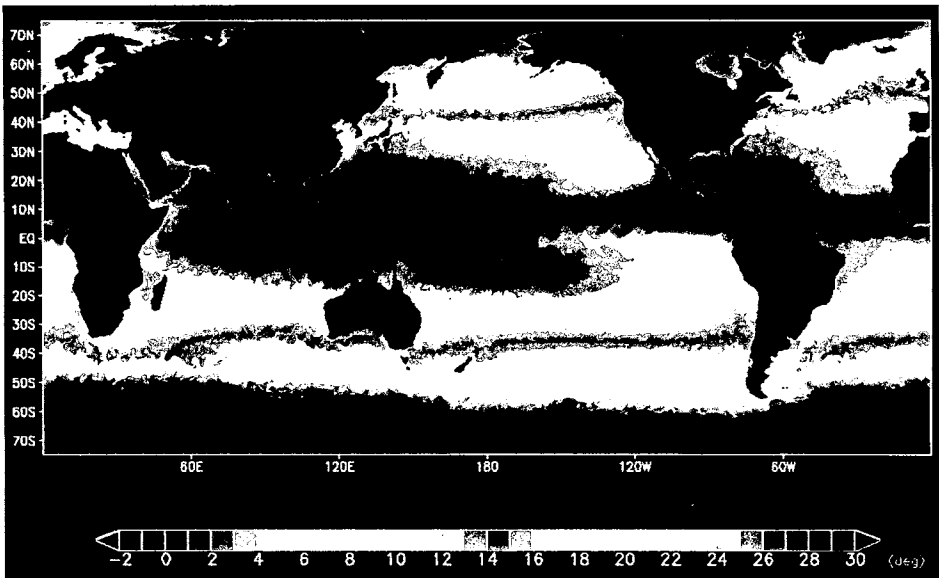
Figure 1a. A snapshot field of sea surface temperature in 15 October at 45th model year
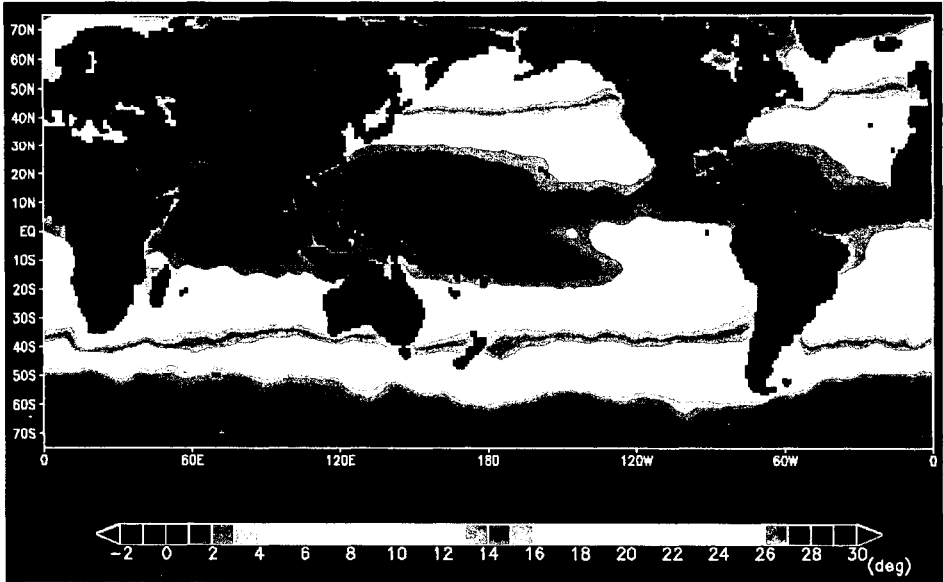
Figure 1b. Observational monthly mean sea surface temperature in corresponding month

Depicted in Figure 2 is the annual mean sea surface height (SSH) field obtained from our simulation. We can clearly see that, consistent with a simple geostrophic relation, the SSH in the subtropics is higher than that in the subpolar region and the lowest SSH appears in the southern flank of the strong Antarctic Circumpolar Current. A zonal band of lower SSH can be noticed along 7°N in the Pacific, which corresponds to the boundary between the North Equatorial Current and the North Equatorial Countercurrent and we can say that the basin-wide pattern of the mean SSH field is simulated well. Note, however, that these features are also well reproduced in numerous other simulations reported so far with much coarser horizontal resolution so that they are insensitive to the explicit representation of mesoscale eddies. One of the intriguing features in Figure 2 is the existence of a fine frontal structure associated with the boundary between the Kuroshio Extension and the Oyashio current systems in the North Pacific.
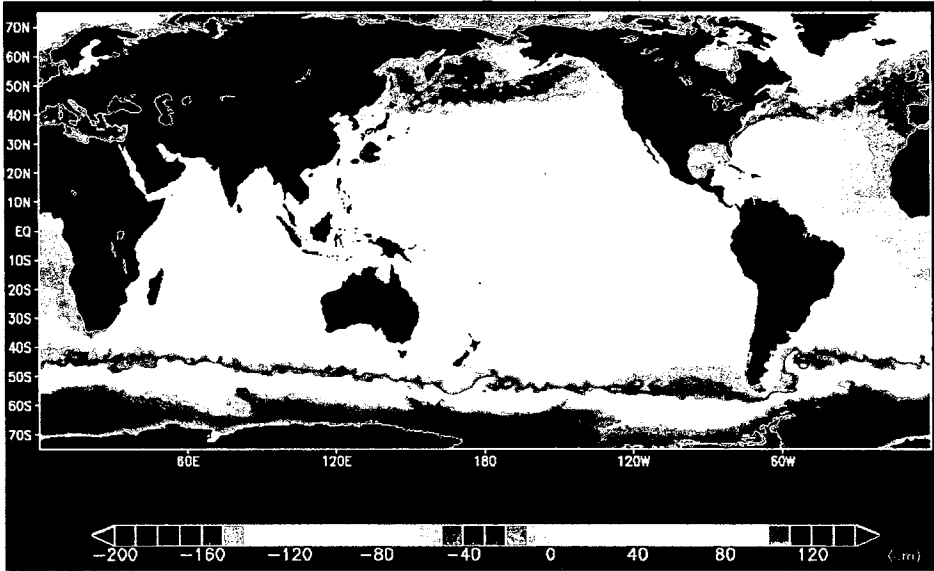
Figure 2. Simulated annual mean sea surface height

Three major fronts can be seen to the east of 160°E, two of them merge in the region extending from 140°E to 160°E and the other corresponds to the sub-arctic front. This fine frontal structure is similar to the observed one discovered by the satellite AVHRR (Advanced Very High Resolution Radiometer) infrared imagery (Fig. 1 of Mitchell et al., 1996) in which they showed the existence of multiple thermal fronts in the North Pacific aligned in the zonal direction. Using hydrographic observational data, Mizuno and White (1983) also identified this bifurcated structure of the former fronts, namely, the Kuroshio Extension bifurcates at 37°N, 163°E and the northern branch extends along the Shatsky Rise to reach 40° North. This is one of the striking features that the present high horizontal resolution model successfully simulates. In fact, this frontal structure was not simulated well by relatively coarser resolution models (e.g. Kagimoto and Yamagata, 1997; Mitchell et al., 1996).

Another feature seemingly reproduced well by our high horizontal resolution of the model can be seen in SSH variability fields. Figure 3 shows the root-mean-square variation of the SSH anomaly. The variability maxima (~ 40 cm) appear in the western boundary current regions such as the Kuroshio/Kuroshio Extension, the Gulf Stream/the North Atlantic Current, the Malvinas Current and the Agulhas Current and also along the Antarctic Circumpolar Current. For example, in the Kuroshio Extension region, a high SSH variability region extends from Japan coast to the date line in forming a zonal band. This is mostly due to the path variation of the Kuroshio Extension (Mizuno and White, 1983).
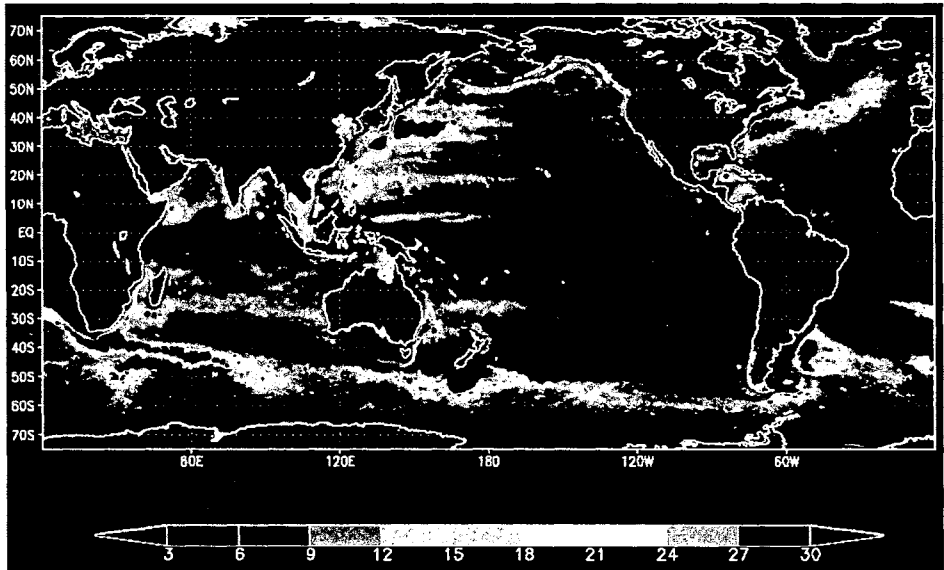
Figure 3. Root-mean-square variation of sea surface height anomaly

Fairly high SSH variability regions are also seen along 20°N and 6°N in the western Pacific. Locations of these high SSH variability regions in the Pacific are observationally confirmed by the satellite altimetry (Le Traon and Orgor, 1998; Qiu, 1999). In the North Atlantic, the region where energetic eddy activities are reflected in high SSH variability extends from the Cape Hatteras to the Irminger basin. The amplitude of the maximum variability is almost the same as the observed one (Le Traon and Orgor, 1998) though its meridional extent is somewhat broader in the Gulf Stream extension region than the observational counterpart. In short, we may safely say that the present simulation reproduced observed SSH variability quite well. We think that this success is partly attributable to the employed high resolution not only in the horizontal (Smith et al, 2000) but also in the vertical direction (Schmitz and Holland, 1986).

(2) Vertical cross section of the equatorial Pacific
As a validation of zonally varying current structures and associated thermocline depth and salinity distribution around the equator, we compared simulated fields with observational ones (Fig. 2 of Wyrtki and Kilonsky, 1984).
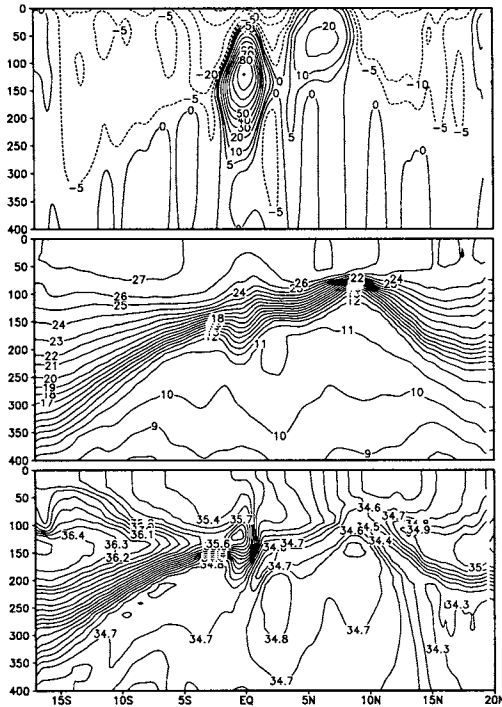
Figure 4. Simulated vertical cross sections of zonal velocity, isotherm and salinity along the Hawaii-Tahiti line

Simulated annual means of the zonal current velocity, isotherm and salinity distributions are given in the upper, middle and lower panels in Figure 4. Those fields given in Figure 4 are the annual mean at tenth model year and no substantial changes were noticed in the following 40 years. The horizontal and vertical extents of the equatorial undercurrent are in good agreement with the observation and the maximum velocity appeared around the depth of 150 m reaches 80 cm/s, which is a little bit weaker than the observed value. The flow patterns extending to the northern and southern flanks of the undercurrent are also well simulated. The thermocline structure given in the middle panel, especially its accentuated contour intervals is very close to the observed structure except for the magnitude of meridional gradient around 5°N~10° North. As to salinity field in the bottom panel, we noticed that the overall distribution pattern does not deviate considerably from the observational one. A closer inspection shows, however, that just the north of the equator there exists a thin lower salinity tongue extending downward at the depth around 200 ~ 250 m and we are now checking whether it is the outcome of numerical noises or not. In spite of the existence of those detailed structures, we think that our simulation is successful in reproducing realistic vertical profiles of velocity, temperature and salinity fields and that the success is due not only to the employed high horizontal resolution but to high vertical resolution.

(3) Meridional heat transport
Realistic meridional heat transport is difficult to simulate with low horizontal resolution model in which mesoscale eddy parameterization is not incorporated (Böning et al., 1995). Figure 5 shows the annual mean meridional heat transport calculated from our eddy-resolving model. The maximum poleward heat transport in the northern and southern hemispheres turned out to be about 1.5 PW between 10 - 30°N and about 0.7 PW between 10 - 15°S respectively. Thus simulated meridional heat transport pattern is not symmetric to the equator, while direct estimates based on hydrographic observations (Hastenrath, 1982; Talley, 1984) and the indirect one using satellite radiation and atmospheric reanalysis data (Trenberth and Solomon, 1994) also suggest an anti-symmetric pattern but with a lesser degree. This discrepancy is possibly due to the underestimation of the southward heat transport in the South Pacific and/or the Southern Indian Ocean (Figs. 5c, 5d), though the southward heat transport in both the Pacific and the Indian Ocean derived from the model is within the range of observed values.

The large latitudinal change of the heat transport can be seen in 8-10°S in the Pacific and the Indian Ocean (Figs. 5c, 5d). The amplitude reaches to about 0.9 PW, which is comparable to the northward heat transport by the Gulf Stream in the North Atlantic (Fig. 4b). This indicates that the Indonesian Throughflow carries such a huge amount of heat from the Pacific to the Indian Ocean and possibly affects the climate over the Indian Ocean. In the North Atlantic, the meridional heat transport between 20 - 36°N is approximately 1 PW, which is similar to the estimation from the hydrographic observation (Fig. 4b). Such a large heat transport is attributed mostly to the northward transport of the warm water by the Gulf Stream/the North Atlantic Current and to the southward transport of cold North Atlantic Deep Water forming the Deep Western Boundary Current. Böning et al. (1995) showed that the horizontal resolution is one of the crucial factors for a reliable estimate of the meridional heat transport. Actually, heat transport in that region simulated with a coarse horizontal resolution of 1° turned out to be only 0.7 PW, while the same model with mesoscale eddy parameterization (e.g. Gent and McWilliams, 1990) can reproduce the northward heat transport of about 1 PW, which is comparable to the one obtained in our eddy-resolving simulation.
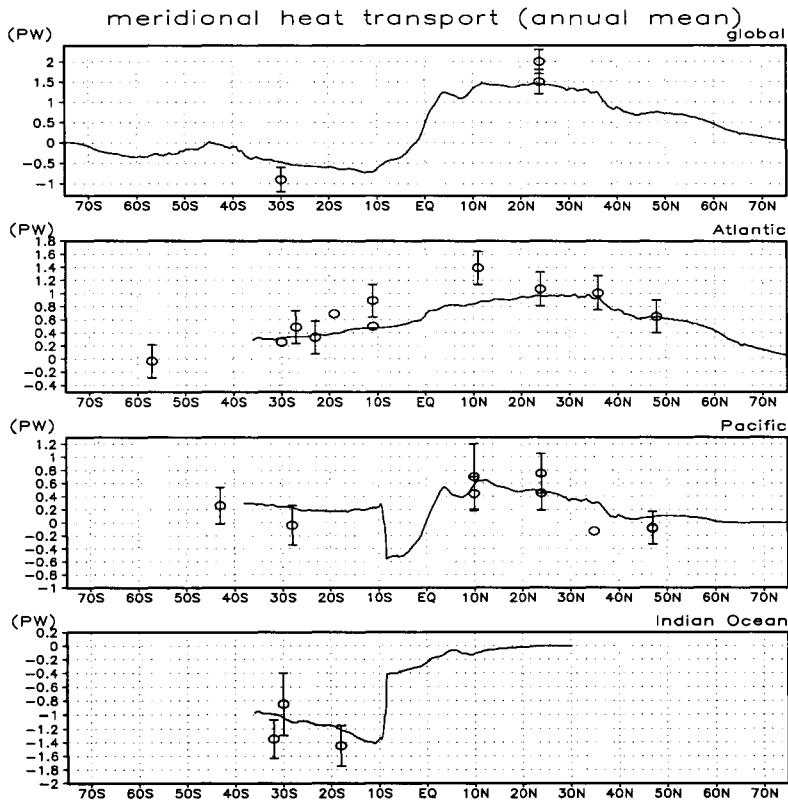
Figure 5. Simulated annual mean heat transport, global(a), Atlantic(b), Pacific(c) and Indian Ocean(d). Circles with error bars indicate the estimated heat transport from the hydrographic observations based on Hall and Bryden (1982), Holfort and Siedler (1997), Macdonald and Wunsch (1996), Rintoul and Wunsch (1991), Roemmich and McCallister (1989) and others referenced in Trenberth and Caron (2001)

SUMMARY

The computational as well as partial physical performances of our MOM3-based OGCM loosely optimized for the Earth Simulator were briefly presented here. A major achievement of the present work was to demonstrate a superior computational ability of the Earth Simulator in performing a time consuming eddy-resolving simulation on the (near) global domain. A fifty-years-long integration was completed for the first time within a tolerable period of about two weeks and there is room for further improvement in computational performance. We can say that the overall feature of simulated fields is pretty good in the sense that the anticipated improvements associated with eddy activities are actually reproduced in our simulation together with a fine frontal structure we referred to in the section above.

56

As was mentioned in the introduction, the outcome presented here is the result of the first test simulation for which further parameter tunings and implementation of advanced computational schemes are to be planned. It is fair to say that quite a few detailed water mass characteristics we looked into are not well simulated due possibly to the compound misrepresentations arising from the inadequate modeling of sub-grid scale processes and highly problematical forcings we employed in our simulations. Those detailed water mass properties are influenced considerably by mixing processes occurring at unresolved small scale and are difficult to reproduce well by OGCM simulations. The main target of the second run is to evaluate the sensitivity of the parameterized mixing processes on model parameters together with the different forms of boundary forcings in order to improve gross features of surface mixing/boundary layers as well as water mass properties as much as possible within the frame work of our model dynamics.

REFERENCES

Antonov, J. I., S. Levitus, T. P. Boyer, M. E. Conkright, T. D. O'Brien and C. Stephens, 1998a: World Ocean Atlas 1998 Vol. 1: Temperature of the Atlantic Ocean, NOAA Atlas NESDIS 27, U. S. Government Printing Office, Washington, D.C.

Antonov, J. I., S. Levitus, T. P. Boyer, M. E. Conkright, T. D. O'Brien and C. Stephens, 1998b: World Ocean Atlas 1998 Vol. 2: Temperature of the Pacific Ocean, NOAA Atlas NESDIS 28, U. S. Government Printing Office, Washington, D.C.

Antonov, J. I., S. Levitus, T. P. Boyer, M. E. Conkright, T. D. O'Brien and C. Stephens and B. Trotsenko, 1998: World Ocean Atlas 1998 Vol. 3: Temperature of the Indian Ocean, NOAA Atlas NESDIS 29, U. S. Government Printing Office, Washington, D.C.

Boyer, T. P., S. Levitus, J. I. Antonov, M. E. Conkright, T. O'Brien and C. Stephens, 1998a: World Ocean Atlas 1998 Vol. 4: Salinity of the Atlantic Ocean, NOAA Atlas NESDIS 30, U. S. Government Printing Office, Washington, D. C.

Boyer, T. P., S. Levitus, J. I. Antonov, M. E. Conkright, T. O'Brien and C. Stephens, 1998b: World Ocean Atlas 1998 Vol. 5: Salinity of the Pacific Ocean, NOAA Atlas NESDIS 31, U. S. Government Printing Office, Washington, D. C.

Boyer, T. P., S. Levitus, J. I. Antonov, M. E. Conkright, T. O'Brien and C. Stephens and B. Trotsenko, 1998: World Ocean Atlas 1998 Vol. 6: Salinity of the Indian Ocean, NOAA Atlas NESDIS 32, U. S. Government Printing Office, Washington, D. C.

Böning, C. W., W. R. Holland, F. O. Bryan, G. Danagasoglu and J. C. McWilliams, 1995: An overlooked problem in model simulations of the thermohaline circulation and heat transport in the Atlantic Ocean, *Journal of Climate*, 8:515-523.

Bryan, F. O. and R. D. Smith, 1998: Modelling the North Atlantic circulation: From eddy-permitting to eddy-resolving, *Int. WOCE Newsletter*, 33:12-14.

Chao, Y., A. Gangopadyay, F. O. Bryan, and W. R. Holland. 1996. Modelling the Gulf Stream system: How far from reality? *Geophysical Research Letters,* 23:3155-3153.

Fu, L. L. and R. D. Smith 1996: Global ocean circulation from satellite altimetry and high-resolution computer simulation. *Bulletin of the American Meteorological Society,* 77:2625-2636.

Gent, P. R. and J. C. McWilliams, 1990: Isopycnal mixing in ocean circulation models, *Journal of Physical Oceanography,* 20:150-155.

Hastenrath, S., 1982: On meridional heat transport in the world ocean, *Journal of Physical Oceanography,* 12:922-927.

Hall, M. M. and H. L. Bryden, 1982: Direct estimates and mechanisms of ocean heat transport, *Deep-Sea Research,* 29:339-359.

Holfort, J. and G. Siedler, 1997: The heat and mass transport in the south Atlantic, *The WOCE International Newsletters.* 28:3-5.

Kagimoto, T. and T. Yamagata, 1997: Seasonal transport variations of the Kuroshio: An OGCM Simulation, *Journal of Physical Oceanography,* 27:403-418.

Kistler, R., E. Kalnay, W. Collins, S. Saha, G. White, J. Woollen, M. Chelliah, W. Ebisuzaki, M. Kanamitsu, V. Kousky, H. van den Dool, R. Jenne and M. Fiorino, 2001: The NCEP-NCAR 50-year reanalysis: Monthly means CD-ROM and documentation, *Bulletin of the American Meteorological Society,* 82:247-268.

Large, W. G., J. C. McWilliams and S. C. Doney, 1994: Oceanic vertical mixing: A review and a model with a nonlocal boundary layer parameterization, *Reviews of Geophysics,* 32:363-403.

Le Traon, P.-Y. and F. Ogor, 1998: ERS-1/2 orbit improvement using TOPEX/POSEIDON: The 2cm challenge, *Journal of Geophysical Research,* 103:8045-8057.

Macdonald, A. M. and C. Wunsch, 1996: Oceanic estimates of global ocean heat transport, *The WOCE International Newsletters,* 24:5-6.

Mitchell, J. L., W. J. Teague, G. A. Jacobs and H. E. Hurlburt, 1996: Kuroshio Extension dynamics from satellite altimetry and a model simulation, *Journal of Geophysical Research,* 101:1045-1058.

Mizuno, K. and W. B. White, 1983: Annual and interannual variability in the Kuroshio current system, *Journal of Physical Oceanography,* 13:1847-1867.

Qiu, B., 1999: Seasonal eddy field modulation of the North Pacific Subtropical Countercurrent: TOPEX/Poseidon observations and theory, *Journal of Physical Oceanography,* 29:2471-2486.

Rintoul, S. R. and C. Wunsch, 1991: Mass, heat oxygen and nutrient fluxes and budgets in the North Atlantic Ocean, *Deep-Sea Research*, 38:Suppl. 1A, 355-377.

Roemmich, D. and T. McCallister, 1989: Large scale circulation of the North Pacific Ocean, *Progress in Oceanography*, 22:171-204.

Schmitz, W. J., Jr. and W. R. Holland, 1986: Observed and modeled mesoscale variability near the Gulf Stream and Kuroshio Extension, *Journal of Geophysical Research*, 91:9624-9638.

Semtner, A. J., and R. M. Chervin. 1992: Ocean general circulation from a global eddy-resolving model. *Journal of Geophysical Research,* 97:5493-5550.

Smith R. D., Maltrud, M. E., 2000: Numerical Simulation of the North Atlantic Ocean at 1/10 degrees. *Journal of Physical Oceanography*, Vol. 30, 1532-1561.

Tally, L., 1984: Meridional heat transport in the Pacific Ocean. *Journal of Physical Oceanography*, 14:231-241.

Trenberth, K. E. and J. M. Caron, 2001: Estimates of meridional atmosphere and ocean heat transport, *Journal of Climate*, 14:3433-3443.

Trenberth, K. E. and A. Solomon, 1994: The global heat balance: heat transports in the atmosphere and ocean. *Climate Dynamics*, 10:107-134.

Troen, I. B. and L. Mahrt, 1986: A simple model of the atmospheric boundary layer; Sensitivity to surface evaporation, *Boundary Layer Meteorology*, 37, 129-148.

Wyrtki, K. and B. Kilonsky, 1984: Mean water and current structure during the Hawaii-to-Tahiti shuttle experiment. *Journal of Physical Oceanography,* 14:242-254.

A MODEL OF CRUSTAL UPHEAVAL BY OCEAN WATER LOADING AND ITS APPLICATION

Shigehisa Nakamura

Wakayama, JAPAN

ABSTRACT

A theoretical model is introduced for realizing a coastal upheaval by an ocean water loading. An increase of the ocean water loading can be expected by the resultant effect of the global warming, which might be caused by the climatological warming and glacial melting which must be resulted by the recent human activities after utilizing the fossil fuels and with producing the artificial chemical products which affect strongly the earth's environment. This model is a simple linearized elastic model of a thin plate assumed to be equivalent to the existing tectonic plate on the earth. This model plate is for demonstrating and evaluating upheaval just around the coastal zone. A set of the differential equations for an equivalent elastic thin plate is solved with consideration of several equivalent parameters specifying the elastic constants. The solution under some assumed conditions suggest that the ocean water loading is effective to give a set back of the coastline. In this work, an additional brief note on time factor is given though the model is for an upheaval pattern. The solution might be well applied for some other geophysical problems, for example, on dynamical understanding of an existing profile of geographic section and on a dynamical mechanism to realize what process is possible at forming a co-seismic upheaval pattern.

INTRODUCTION

A theoretical model is introduced for realizing a coastal upheaval by ocean water loading. This model might give us a key to get a dynamical understanding of what could be expected as a final stage of the threat of an increasing sea level caused by ocean water loading. This ocean water loading is considered to be caused mainly by resultant effect of the global warming. The global warming is essentially one of the important factors of climatology. The climatological process of the global warming must be controlled by the natural variations of the solar beam on the earth's surface and by the artificial impacts of the man-made products appeared and increased after the recent human activities after utilizing the fossil fuels and finding the industrial chemical products. It is now widely known that these impacts are resulted to the growth of the ozone layer in the polar upper layer by the artificial effect. Then, we have to consider here these

products, which might surely be found in the ocean in near future. Several products are discussed in a scope of environmental problems in relation to the factors, for example, carbon dioxide but CFC (Chrolo-Fluoro-Carbonate) or NOx, SOx, and the other fine particulate materials. Nevertheless, in this work, simply a dynamical problem is considered for considering the final stage of the global warming. The term of this global warming might concerns directly to the climatological problem, though the author's interest is mainly in the problem of the crustal upheaval caused by the global warming.

In this work, a linearized model of the author's interest is introduced first for an elastic thin plate that could be taken as an equivalent crust. This crust is considered to be a part of the existing tectonic plate on the earth. This model plate is for demonstrating and evaluating crustal upheaval just around the coastal zone. A set of the differential equations for the equivalent elastic thin plate is introduced to formulate the interested problem in this work with considering several equivalent parameters specifying the elastic constants. The solution under some assumed condition suggests that the ocean water loading is effective to give a set back of the coastline. The solution might be well applied for some other geophysical problems, for example, on a dynamical understanding of an existing profile of a geographic section in the coastal zone, and on a key to a dynamical mechanism of a forming process of a co-seismic upheaval pattern. In this work, a brief note on time factor is given.

GENERAL CRUSTAL PATTERN IN COASTAL ZONE

Looking at the natural topography in the coastal zone, it can be seen a mountain range along the coast line with a continental shelf and a trough between the coast line and the deep sea area in several locations of the coastal zone around the existing continents.

This natural pattern of the topography in the coastal zone stimulates us the natural scientists to raise a problem for geographic or other related scientific fields. In fact, it is hard to consider the time-span of any process of the topographic formation by using a simple spatial model. There is a long history of the researches in the past in the related fields (i.e., geography, geology, geomorphology, geodesy, geophysics, and others), so that it would be hard to introduce and list up here all of the contributions. These contributions should be referred in the other publications, and no list is shown except what are directly referred in this work.

Regarding the mathematical theory of the elastic earth, Jeffreys (1952) has published his classic theory after Love's (1927) treatise on the mathematical theory of elasticity.

Regarding the process of crustal upheaval, it is necessary to take a geological time scale rather than any other time scales utilized in the existing fields of, for example, meteorology, climatology, oceanography, seismology, and etc. There is no current dynamical research available on the time-span of the process of crustal upheaval. We merely understand that crustal motion and its resulting change take place very slowly. Research on plate tectonics includes, for example, Care (1976) on scale of tectonic phenomena, as well as Daivies (1999) and Richard et al. (2000).

Recent climatological studies have also focused on global trends (see, for example, Clark et al., 1994, 2000) on the basis of a two-dimensional ocean-climate model considering the thermal effect of atmospheric temperature increase on the seawater column in the world. Watt (1977) also noted sea level rise. Singer (1999) and Nakamura (1999) introduced some notes in relation to what had been reported in Houghton's publication on IPCC (1990).

Once, Nakamura (2001) has studied on crustal upheaval in a coastal zone in relation to an expected increased loading of the oceanic water on the crust after global warming and glacial melting.   A comment in a public brochure motions that a future crustal rebound, as a result of an unloading effect of a melting glacier, is possible.   Thus, future study of such a reversal possibility of crustal upheaval is warranted.

LINEALIZED ELASTIC MODEL

Assuming an elastic plate in a coastal zone instead of a shell covering the earth, a crustal upheaval can be taken as a problem of the elastic plate.   The thickness of the crust is less than one hundredth of the earth's radius. So then, this assumption is reasonable.

For convenience, the plate is assumed to be of uniform and homogeneous (thickness, H, and density, ρ).   Then, it becomes easy to formulate the problem for this study. Formulating technique for this purpose is essentially same as that for the classic problem on elastic bodies (see, for example, Love, 1892; Jeffreys, 1852; Officer, 1974; Nakamura, 2001).   The surface of the plate, then, is taken as the horizontal reference (O-x in Fig. 1) with a static loading of the semi-infinite oceanic layer (thickness Ho and density ρ_o on the plate.
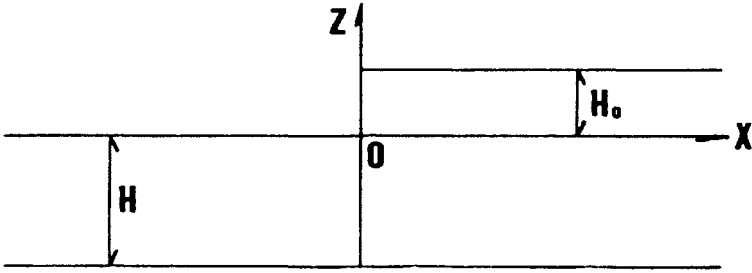
Figure 1.   A simple linealized model of crust just around a coastal zone with a loading of a semi-infinite ocean water to the crust in the gravitational field. Notations H and H₀ are for thickness of model crust and ocean.

When a quasi-equilibrium state of the crust is assumed, the crustal upheaval can be obtained by solving a formulated equation such as that for the classic problem of elastic bodies.   The vertical displacement (w) of the crust surface by loading is reduced from the equations of motions for the elastic body with some assumptions.   In this case, the reduced equation is written as follows:

$$D[d^4w/dx^4]=Z, \qquad (1)$$

Where,

$$Z= \rho_0 gH_0 - \rho gw, \qquad (2)$$

And D(flexural rigidity of the plate) is

$$D=(1/12)[E H ^ 3 / (1 - \sigma ^2)], \qquad (3)$$

where, E is the Young modulus, and σ is the Poisson ratio. Introducing Lame's two constants, λ and μ, the two parameters, E and σ are written as (cf. Officer, 1974; Nakamura, 2001):

$$E= \mu [3 \lambda + 2 \mu]/[\lambda + \mu], \qquad (4)$$

And,

$$\sigma = \lambda /[2 \lambda + \mu]. \qquad (5)$$

EFFECT OF OCEANIC WATER LOADING

Using the model in Figure 1, vertical displacement of the crustal surface (w) may be written as:

$$w = [S_0 H_0] [2 - \exp(Gx) \cos(Gx)] \qquad \text{for} \quad x>0, \tag{6}$$

and,

$$w = [S_0 H_0] [\exp(Gx) \cos(Gx)] \qquad \text{for} \quad x<0, \tag{7}$$

where the initial crustal surface is assumed to be located on the line L-N in Figure 2, and the Z axis is taken to be upward positive.
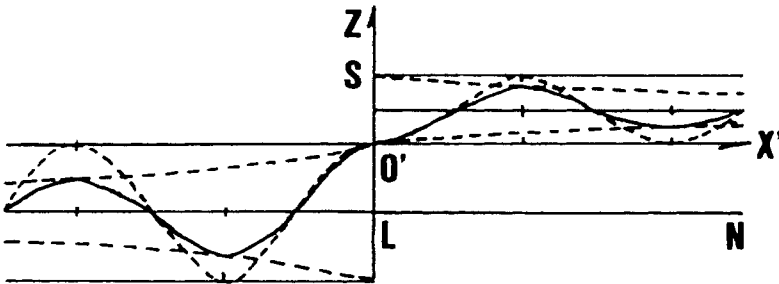
Figure 2. Negative upheaval (solid line) as a combined function of a simple harmonic function and exponential functions (dotted lines) referring to the reference sea level (L-N).

Denoting the densities of the crust as ρ and of the sea water as ρ_0, then,

$$G^4 = \rho H/(4D), \tag{8}$$

$$S_0 = \rho_0/\rho, \tag{9}$$

And, then, the distance between the crest to the next crest L' is written as follows:

$$L' = [(4/9) \rho g] [E H^3], \tag{10}$$

Where, $G = 2\pi/L'$.

If we denote $S=2S_0$ (referring to the line L-N in Fig. 2), then, it is easily understood that the crustal surface pattern can be illustrated by a solid line of an undulation curve as shown in Figure 2. This pattern may be given as a product of exp (Gx) and cos (Gx). Taking that S=0'

at x=0, and using (4) and (5), then, the vertical displacement of the crustal surface is shown by the solid line. The pattern of the solid line in Figure 2 is the final equilibrium state of the crustal surface after the loading of the model ocean water as assumed in Figure 1. This might be similar to a corresponding geodetic isostacy (cf. Officer, 1974).

TROUGH AND RIDGE

In order to clarify what we are interested, the specific pattern of the solid line is shown as a function w with a variable x (Fig. 2). The value of w is the vertical displacement of the crustal surface, and this can be taken as negative upheaval (Fig. 3). The pattern of the negative upheaval demonstrates the crustal surface near the coast (around the discontinuous place of the model ocean water loading). The pattern of the negative upheaval relative to the sea surface may be, for example, as that relative to the initial flat state L-N (Fig. 2). This pattern shows that a significant negative upheaval is seen by a loading to form a trough offshore and a minor positive upheaval is seen on landside after loading to form a ridge. As for the location of the coastline, the initial coastline, assumed to be located at the edge of the model ocean loading, is shifted horizontally to the side of the model land (Fig. 1). What is noted above is the specific result caused by the loading of the model ocean on the model crust.
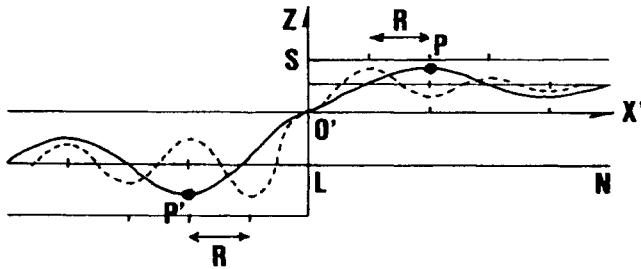
Figure 3. Negative upheaval for a given value of $G=G_0$ (solid line) and that of $G=2G_0$ (dotted line). Location of maximum (P) and minimum (P') for $G=G_0$ shifting as much as R relative to the origin of the coordinate (O') with the reference sea level (L=N).

Formation of an offshore trough is caused by the loading effect of the static ocean water on the elastic crust. As for the positive upheaval of the crustal surface, it can be seen at a little distance on the land side of the crust, that is, on the side of x>0 in Figures 2 and 3. This means that it is possible to find a mountain ridge just adjacent to the coastline after the loading effect of ocean water. This shows also that the coastline moves to the landside of the model in Figure 1. If the thickness of the model ocean water is increased, then, amount of the upheaval is amplified without any change of the shifted location of the coastline.

In Figure 3, it is shown what shifting of the trough and ridge can be expected when the value of G is twice of the value initially assumed in the above solution. The solid line is the same as that for the solution reduced first in this work, and the dotted line shows the solution for the value of 2G.

In this case, the location of the trough at x=P should shift to x= P − R, and, the location of the first maximum of the upheaval at x=P' should shift to x= P' + R (Fig. 3).

When $G=G_0$ at x=P and G=0 at x=0, the relationship between G_0 and R for an arbitrary value of x' (in the range of 0<x'<P) is given (Fig. 4). This shows that the slope between the trough and the ridge becomes steeper when the value of G becomes smaller. It should be noted That $G' = \rho H/(4D)$, and D= $(1/12)[E^3]$ $[1 - \sigma^2]$. Hence, the value of G is determined by the parameters ρ of and D, and the value of D is determined by the parameters E, H and σ. These parameters should be taken as the equivalent parameters for the model in this work.
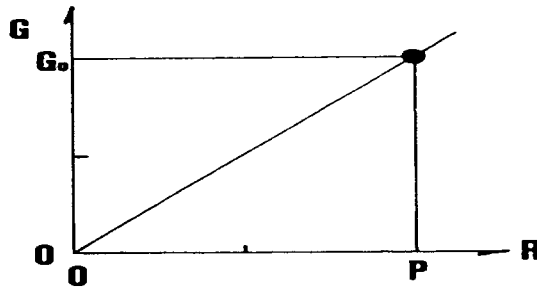
Figure 4. Shift R from P for $G=G_0$ at the same phase of the simple harmonic function

Now, it might be helpful to introduce a nominal set of the equivalent parameters, for convenience, for realizing what could be expected in the existing crustal upheaval pattern (Nakamura, 2001).

Adding to the above, it is necessary to remind that the actual crust existing on the earth, has a very complicated geological structure in fact. Nevertheless, the model in this work is aimed for a macroscopic response of the crustal upheaval so that only a dynamical response of the model with a set of the equivalent elastic parameters. Although, the value of these parameters would not be same to the corresponding elastic constants of any one of the materials consisting the actual crust.

Officer (1974) provides some numerical case studies that help us to understand what we see. For Lame's two constants, it is assumed that $\lambda = \mu = 3.3$ x 10 ^10Pa (= 10 x 10^11 cgs), where the dimension of Pa corresponds to [N/m^2] (= 10 g/sec^2/cm)

When H=100 km, the value of L' is obtained for the above specific parameters as 196 km(=L').
When H=150 km, then, L'=265 km, and when we take the value as H=200 km then L'=329 km.
These three values of L' show that the slope between the trough and ridge becomes steep when
the value of L' is large.   This shows that the coastline recedes much more when the value of H
is larger.   Then, it could be a case of set back of the coastline.

If we put the values of H=150 km and L'=265 km, then, the pattern of the model crustal upheaval
might be taken to be similar to the pattern as seen in a part of the actual coastal area.   That is,
for example, as is noted by Nakamura (2001), for a meridional cross section of the crustal
surface or the geographical land surface in the neighboring area covering the Nankai Trough and
Kii Peninsula through Kushimoto.

LOADING EFFECT OF SEA LEVEL RISE TO CRUST

In a case of that considering for the relation between the vertical displacement w and the sea
level rise in the ocean, it must be helpful to apply the above model.

Looking at the solution expressed as in (6) or (7), the maximum of the expected crustal upheaval
is simply controlled by the factor $[S_0 H_0]$.   When the densities of the seawater and of the crust
as a plate in the model are $\rho_0 = 1.03$ and $\rho = 3.3$, and the expected sea level rise is $H_0 = 125$ m
for the case of that the value of $[S_0 H_0]$ is 39 m.

When the value of H_0 is increased, the locations of the trough and ridge in the model are
unchanged, and the slope between the trough and ridge becomes steep. In this case, the location
of the coastline would never change (Fig. 2).

For some case with several possible factors affecting to the sea level rise, it can be considered
that there is a threat of a set back of the coastline.   Hence, we should be careful, in considering
the related problems, to see the location of the coastline and to know the horizontal shifts of the
trough and ridge.   It is also necessary to consider the vertical displacement of the crustal
surface.

Although this work may be helpful for our dynamical understanding of the crustal upheaval, the
pattern of the crustal surface in the coastal zone should be studied more at any actual case with
careful consideration of what parameters are more actively controlling the solution.   In fact, any
one of the existing plates on the earth has a boundary so that it might be more practical to
introduce several additional factors for obtaining a more realistic solution of an advanced model.

Now, it can be seen well that the solution in this work may give an essential suggestion to the actual process of the crustal upheaval in practice.

APPLICATION TO UNDULATING CRUST

With the above solution, it is interesting to consider about an application of the model introduced in this work in order to realize a secular upheaval of datum level in relation to a local case of the past tsunamigenic earthquakes as the actual seismic events.

One of the specific examples is the case at a couple of the earthquakes in 1944 and 1946.   This case might be helpful to give a dynamical understanding of the crustal upheaval around the seismic events.

In order to show a typical geodetic process around the seismic events, an illustration of the geodetic surveys before and after the seismic events in a specific area are shown in Figure 5. The curve X shows a pre-seismic pattern of the crustal surface, and each of the curves Y and Y_0 shows co-seismic pattern around an island (Fig. 5).   The curve X is the crustal upheaval pattern in 1929 relative to the geodetic reference of 1887, and the curve Y is for that in 1950 relative to the reference of 1929, though the curve Y_0 is that in 1950 relative to that in 1887.   The illustration as shown in Figure 5 was first appeared in the publication which was a notice to the hazardous earthquakes written by Kenzo Sassa (1951).
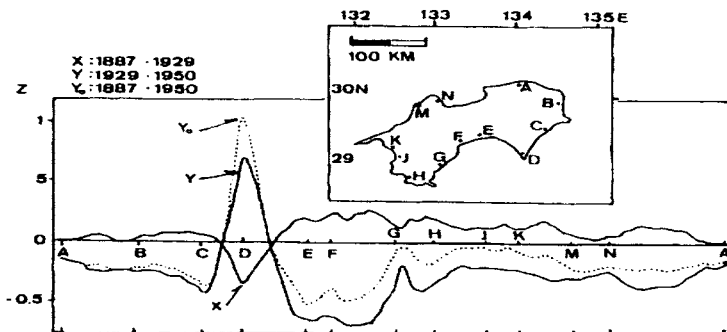
Figure 5. Geodetic process around a couple of the earthquakes
(The survey line is along the coastline of an island. Relative crustal upheavals X, Y, and Y_0 are shown.)

Now, consider one of the co-seismic patterns in Figure 5 for convenience.   When the pre-seismic pattern is expressed by a function Z= F(S, T) with a distance S from the reference

station A, and the co-seismic pattern is for a function Z= F(S, T'), then, the difference of the two functions may be the crustal upheaval pattern around the couple of the seismic events. That is,

$$DZ(S; T, T') = F(S, T') - F(S, T),$$ (11)

Where T'>T. Referring to the functions F(S, T') and F(S, T), it can be considered a corresponding pattern along a meridional line for convenience.   When a meridional line passing the station A on the geodetic survey line (Fig. 5), is considered, then, a pattern of crustal upheaval along the meridional line could be drawn boldly.

As for the bold crustal upheaval pattern or the topographical pattern along the meridional line passing the station A and D, the pattern along the line as the X axis can be shown as shown at the top in Figure 6.   In this case, the distance S in (11) should be read as X, and, DZ(X; T, T') = F(X, T') – F(X, T).

Assuming an identified forcing at the seismic events to give some difference of the crustal upheaval along the X axis, it can be seen an undulating crust surface (mid Fig. 6).
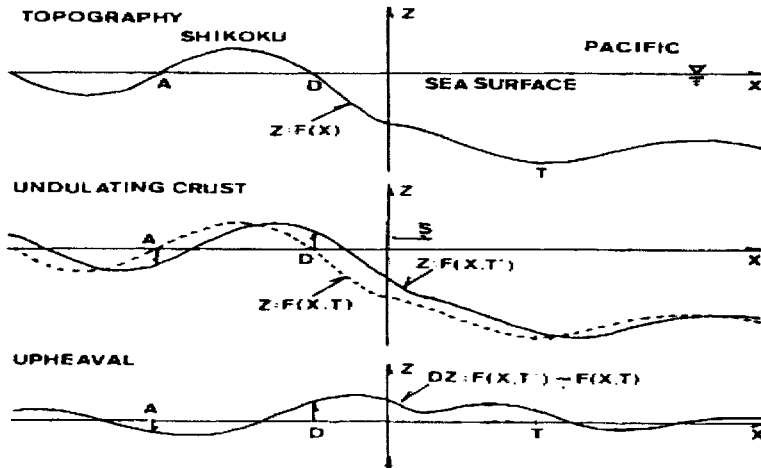
Figure 6.   A consistent model of undulating crust around a couple of the earthquakes

Then, the pattern of DZ as a function of X may be shown as that at the bottom in Figure 6. When this pattern is taken to corresponding to the pattern in the range between the positions X for D and A, then, it can be taken that a consistent trend to the pattern as seen in the range between the stations D and A is found with a background of a dynamical theory.   Here, it is necessary to see that the consistent pattern can be obtained simply by an elastic modeling even

70

though a couple of the seismic events might exhaust some energy at each event of the seismic fault formation.

This may be one of the important keys to have a final solution of the hazardous tsunamigenic earthquake.

NOTICE TO SATELLITE ALTIMETRY

There might be an idea to utilize an available satellite altimetry for detecting crustal upheaval in practice with a careful processing of the data for obtaining the crust surface pattern as a topographical pattern, even though the satellite altimetry at present has only a short history in the fields of geophysical sciences, especially, in the interdecadal problems of geophysical processes. Recent advance of the satellite altimetry has been reported and its data set is supplied for application to the geographical mapping of the land surface and on the sea surface in a certain precision referring to the geoid, which is taken as the reference at present. Nevertheless, the author has unfortunately not yet any information about whether the accuracy of the satellite altimetry is satisfiable at applying it to the evaluation of the sea level in the coastal zone. Hence, it is hard to consider that the interannual variations of the sea levels at the tide stations can be equivalent to the satellite altimetry variations at the corresponding tide station. Now, we have to require that the accuracy of the available satellite altimetry would be equivalent to that of the tidal stations on the coast for the specific geophysical research purposes.

In the case as shown in Figure 6, the existing and available data set of the geodetic survey is used. This geodetic data set was obtained for about one hundred years, though the author used the data set for the time period from 1888 to 1950 in this work. This geodetic data set is obtained in a certain high precision by using the advanced geodimeters with the well-trained and skilled survey groups consisted by the geodetic specialists.

The satellite altimetry is yet under an improving stage in the scope of geodetic sciences, especially, for the problems concerning on the crustal upheaval in the coastal zone as the author has studied.

Therefore, it should be aware in fact that the accuracy of the available satellite altimetry at present in the coastal zone cannot be satisfiable for the purpose of studies on the problems of undulating crust in the coastal zone.

Adding to the above, it should be noticed that it is necessary to take a long time for compilation of the data of the global satellite altimetry for the author's purpose in this work. It should be

required the accurate and precise data set of the advanced satellite altimetry for more than several ten years.

A more advanced technique in future is also expected for active practice of the result of the author's works and of the related contributions in the field of geodesy and geophysical sciences.

CONCLUSIONS

A theoretical model is introduced for realizing a crustal upheaval in the coastal zone by the active effect of possible water loading to the crust. The increase of the ocean water loading can be expected as a resultant effect of the global warming, i.e., as the effects of the climatological warming and glacial melting on the earth's surface. The model is a simple linealized elastic model of a thin plate assumed to be equivalent to the existing tectonic plate or the crust covering the earth. This model plate is for demonstrating and evaluation an expected crustal upheaval just around the coastal zone. A set of the differential equations for an equivalent elastic thin plate is solved with some equivalent elastic constants specifying the properties of the model plate. The solution under some assumed conditions suggests that the ocean water loading is effective to give a set back of the coastline. The solution is essentially for a final equilibrium crustal pattern. Then, the author has given a brief note on time factor for convenience. This solution may be well applied for obtaining a key to some other geophysical problems, for example, for a dynamical understanding of an existing profile of geographic section and of a dynamical mechanism about a process of a co-seismic crustal upheaval pattern. An additional notice to satellite altimetry is given for detecting the crustal upheaval in the coastal zone in practice.

REFERENCES

Care, S.W. 1976. *The expanding earth*: Developments in geotectonics 10, Amsterdam, Elsevier Science Pub. Co.

Clark, P.U., R.S. Webb and L.D. Keigwin (eds.) 1999. *Mechanism of global climate change at millennial time scales*, Geophysical Miograph Series Vol. 12, Washington D.C., American Geophysical Union.

Davies, G.D. 1999. Dynamic Earth: Planets, plumes and mantle convection, New York, Cambridge University Press.

Harvey, L.D.D. 1994. Transient temperature and sea level response of a two-dimensional ocean climate model to green house increases, *Jour. of Geophysical Res., 99, 18447- 18466.*

Harvey, L.D.D. 2000. *Global warming*, Harlow, Essex, UK, Pearson Education Ltd.

IPCC 1990. *Climate change*: The IPCC scientific assessment, eds. By J.T. Houghton, New York, Cambridge University Press.

Jeffreys, H. 1852. The earth, its origin, history, and physical constitution, 3rd ed., New York, Cambridge University Press.

Kenzo Sassa, K. 1951. *Dai-Jishin (Hazardous Earthquakes)*, Athenai Ser.161, Tokyo, Kobundo.

Love, A.E.H. 1892. A treatise on the mathematical theory of elasticity, New York, Cambridge University Press.

Nakamura, S. 1990. Secular upheaval of datum level in relation to tsunamigenic earthquake, *Marine Geodesy*, 14, 117-141.

Nakamura, S. 1999. *The planetary earth in the 21st century: A scientific view of future*, Tanabe, Wakayama, Japan, Nakamura Publishers and Maruzen Press.

Nakamura, S. 2001. A crustal upheaval in a coastal zone after ocean water loading, *Marine Geodesy*, 24, 229-235.

Officer, C.B. 1974. *Introduction to theoretical geophysics*, New York, Springer-Verlag.

Richard, M.A., R.G. Gordon, and R.D. Van der Hilst (eds.) 2000. *The history and dynamics of global plate motions*, Geophysical Monograph Series.121, Washington DC, American Geophysical Union.

Singer, S.F. 1999. Human contribution to climate change remains questionable, *EOS (Transaction of American Geophysical Union), 80(16), 183-187.*

Watt, R.G. 1997. *Engineering response to global climate change: Planning a research and development agenda*, Boca Raton, FL, USA, Lewis Publishers-CRC Press.

MOTION ANALYSIS OF OFFSHORE FLOATING UNIT FOR 1MW CLASS OTEC PLANT

Hideyuki Niizato[1], Shin Okamura[2], Sadayuki Jitsuhara[3] and Yasuyuki Ikegami[4]

[1]Hitachi Zosen Corporation
Osaka, JAPAN
niizato@hitachizosen.co.jp

[2]Universal Shipbuilding Corporation, Tokyo, JAPAN
[3]Xenesys Inc., Tokyo, JAPAN
[4]Institute of Ocean Energy, Saga University, Saga, JAPAN

ABSTRACT

In this paper, the offshore floating unit for 1MW class OTEC (Ocean Thermal Energy Conversion) plant that can be stably and safely in severe environmental conditions is proposed. The proposed offshore floating unit has octagon column shape of 24 m diameter and 29 m height, and is moored by four points with hybrid mooring system of steel chains and wires. A flexible riser pipe of 700 m long is equipped at the bottom of platform. In order to confirm whether it is safe, nonlinear hull/mooring coupled dynamic analysis of the designed offshore floating unit is carried out in the time domain and it is evaluated the characteristics of motion in severe environmental condition like a typhoon. Environmental condition was decided in consideration of the return period of 100-year storm based on the observed data over the long period of time of ocean space. In the dynamic analysis, first of all, hydrodynamic coefficients are calculated by using the singularity distribution method (References). In considering viscous influence, drag coefficient is calculated by using CFD (Computational Fluid Dynamics). Since the mooring force has strong nonlinear characteristics, the equations of motion are solved in the time domain by means of the Lunge-Kutta-Gill method. Dynamic analysis of the designed riser pipe is carried out, too. As a result of calculation, the motions of an offshore floating unit for OTEC plant were very small. The present designed offshore floating unit for OTEC plant will be brought to realization.

INTRODUCTION

In offshore activities, examples of the hanging-off riser pipes are numerous such as a pipe for ocean thermal energy conversion. The motions of an offshore floating unit for OTEC plant with the flexible hanging-off riser pipes are very complex dynamic behavior. Many researchers have investigated the offshore floating structure with flexible riser. Allan T. Maris et al (1980) discussed the analysis and design of the Cold-Water Pipe for the OTEC-1MW power plant system. H. Maeda et al (1991) investigated into the dynamic behaviors of a deep water utilization system composed of a two-point moored barge equipped with machineries and cold water pipe attached to the barge. A. Tahar (2002) calculated nonlinear hull/mooring/riser coupled dynamic analysis of a classic spar designed for 6,000-ft water depth in the time domain. Y.B. Kim et al (2002) numerically simulated to investigate the characteristics of nonlinear behaviors and hull/mooring/riser dynamic coupling for tanker-based FPSO. A. Bando et al (2002) investigated into the hydrodynamic phenomena of eight-shaped oscillating flexible risers for upwelling deep ocean water. H.I. Park et al (2002) investigated into the transverse

vibrations of a highly flexible free hanging pipe in water by top end oscillations by means of experiment.

The purpose of this paper is to calculate motions of the offshore floating unit for OTEC plant under the severe environmental conditions. First of all, in the ocean field at the water depth of 1,000 m, the basic plan of the floating structure with riser pumping up deep ocean cold seawater is shown. Next, it calculated dynamic analysis of the designed floating unit with riser pipe in the time domain. Finally, the displacement of riser pipe was calculated as the dynamic analysis.

Environmental conditions

In the design of an offshore floating unit for OTEC plant, in order to set up the Environmental conditions, we have to assume the ocean field in which a structure is installed. Moreover, in the design of structure, mooring equipment, etc., the following typical state was taken into consideration in various operation states; Operation condition and Survival condition where, environmental condition of a survival state is given to the safety of the structure as severest external conditions, and was decided in consideration of the return period of 100 year storm based on the observational data over the long period of time of the ocean field. Where, the ocean field: the East China Sea buoy near Japan, because of the severe environmental conditions such as the typhoons in summer and the monsoons in winter. Based on the above, the environmental conditions in this study were summarized on the Table 1.

Table 1.   Environmental conditions

Sea state	Survival
Significant wave height	15 (m)
Mean wave period	14.6 (sec.)
Designed wind velocity	50 (m/s)
Current	1.15 (m/s)

Table 2.   Principal measurements and plants of the offshore floating unit, respectively

Displacement	7684 (ton)
Height	29 (m)
Breadth	24 (m)
Draft	19 (m)
Length of riser	700 (m)
Outer diameter of riser	1.5 (m)
Thickness of riser	15 (mm)

Generation of electric power	600kw
The amount of flow for surface water	5000m³/h
The amount of flow for deep ocean water	4500m³/h
Flow velocity in a riser pipe	0.71m/s

Designed the offshore floating unit for OTEC of an octagon column shape

There is a buoy of spar type set upright (long and slender form like a stick) as what was considered not to oscillate in the severe ocean field. Based on the concept of the form of spar type, OTEC plant equipment and accommodation field were secured as design conditions, and it was decided for construction purposes to adopt the structure of Semi-Submergible type octagon column shape formula that has easy form. Moreover, since the center of gravity becomes low

with a riser and a meta-center becomes large, the characteristics of motion that were excellent in wave are expectable. The general arrangement of the offshore floating unit is shown in Figure 1 and principal measurements and plants are shown in Table 2.

The offshore structure consists of floating unit, mooring systems and riser. The inside of floating unit consists of the power generation plant, an engine room, an electric room, accommodation and ballast rooms.
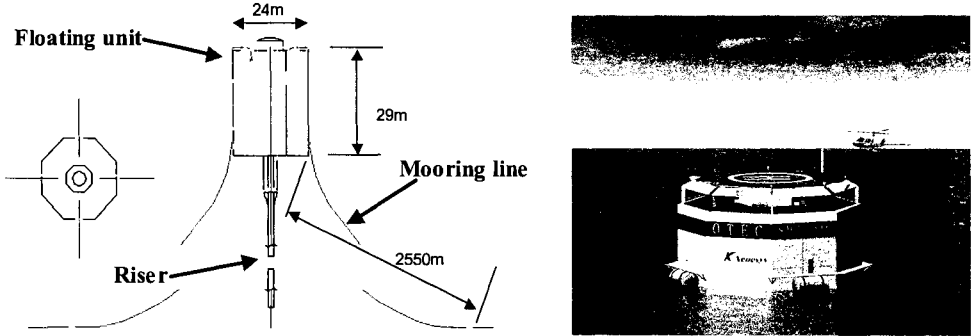
Figure 1.   General arrangement of the offshore floating unit

CALCULATION OF MOTIONS

Equations of motion
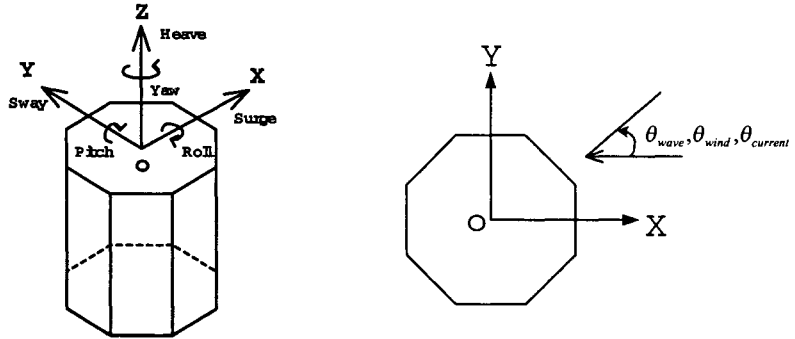
Figure 2.   Descartes coordinate systems

Figure 2 is shown in Descartes coordinate systems.

The equation of motion of the offshore floating unit for OTEC plant is written as follows.

$$(M + A)\ddot{\eta}(t) + B\dot{\eta}(t) + C\eta(t) + N|\dot{\eta}(t)|\dot{\eta}(t) = D(\eta(t)) + F(t)$$

(1)

Where,

$$M = \begin{pmatrix} M_{11} & \cdots & 0 \\ \vdots & \ddots & \vdots \\ 0 & \cdots & M_{66} \end{pmatrix} \quad A = \begin{pmatrix} A_{11} & \cdots & A_{16} \\ \vdots & \ddots & \vdots \\ A_{61} & \cdots & A_{66} \end{pmatrix} \quad B = \begin{pmatrix} B_{11} & \cdots & B_{16} \\ \vdots & \ddots & \vdots \\ B_{61} & \cdots & B_{66} \end{pmatrix} \quad N = \begin{pmatrix} N_{11} & \cdots & 0 \\ \vdots & \ddots & \vdots \\ 0 & \cdots & N_{66} \end{pmatrix}$$

$$C = \begin{pmatrix} C_{11} & \cdots & C_{16} \\ \vdots & \ddots & \vdots \\ C_{61} & \cdots & C_{66} \end{pmatrix} \quad D(\eta(t)) = \begin{pmatrix} D_1(\eta(t)) \\ \vdots \\ D_6(\eta(t)) \end{pmatrix} \quad F(t) = \begin{pmatrix} f_1(t) \\ \vdots \\ f_6(t) \end{pmatrix} \quad \eta(t) = \begin{pmatrix} \eta_1(t) \\ \vdots \\ \eta_6(t) \end{pmatrix}$$

$$F(t) = F_e(t) + F_w(t) + F_d(t) + F_c(t) \tag{2}$$

Where, M shows the total mass of floating unit, A shows added mass coefficients, B shows damping coefficients, C shows restore coefficients, N shows the drag coefficients in consideration of viscous influence, D shows the tension the tension acting on mooring lines, F shows the external forces. Like equation (2), the external forces involve wave exciting force, wind force, wave drift force and current force η is displacement of motions.

Calculation method

Added mass coefficients, damping coefficients and wave forces are calculated by making use of the singularity distribution method. This is a method of solving the integration equation that made the unknown the strength of the singular point. Using the Green's function, it distributes a source on the surface of floating unit in the singular point. In order to distribute a source, the mesh is constructed on the surface of floating unit. Added mass coefficients are shown Figure 3, damping coefficients are shown Figure 4 and wave exciting force coefficients are shown Figure 5.
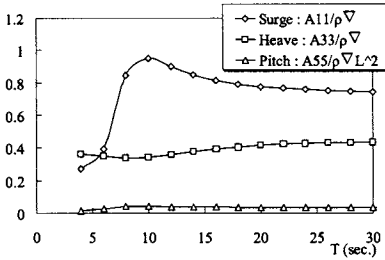
Figure 3.　Added mass coefficients　　　　Figure 4.　Damping coefficients
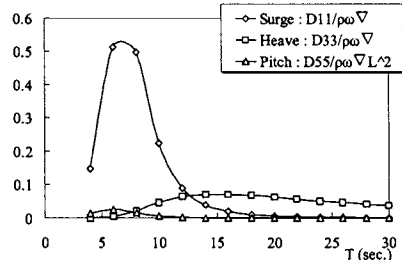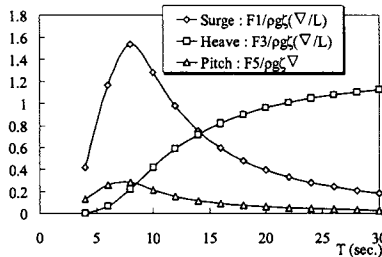
Figure 5.　Wave exciting force coefficients

78

External force is taken as the amount of irregular change that changes with time history. It is assumed that motions of floating unit are small displacement. Therefore, a wind drag coefficient, a current force coefficient, etc. give a fixed value. The solution method of the equation of motion uses Runge-Kutta-Gill method.

Calculation conditions

In the present dynamic analysis in the time domain, in order to evaluate motion when the maximum external force acts on floating unit, all external force shall be given in the same direction. Therefore, in the present calculation, θ_{wave}, θ_{wind} and $\theta_{current}$ are equals to zero degree.

Wave exciting force
Exciting force is found using wave height. The time series of wave height are obtained by carrying out inverse Fourier transform about wave spectrum. In the present study, the modified Pierson-Moskowits type spectrum is used about a wave spectrum.

Wind force
Wind force is found using wind velocity. The time series of wind velocity are obtained by carrying out inverse Fourier transform about wind spectrum. The wind force coefficient is set up from the shape of floating unit on the water surface, and the time series of wind force is calculated based on an obtained time series of wind velocity. In the present study, the Hino type spectrum is used about a wind spectrum.

Current force
Current velocity is made into the fixed value, without changing with time history. Therefore, in motion calculation of this simulation, current force serves as a fixed value.

Drag force
In consideration of viscous influence, drag coefficient is found using Computational Fluid Dynamics.

Tension acting on mooring lines
Other, calculate about acting on mooring line of one point with hybrid mooring system of steel chains and wires.

Riser motion
The influence of mutual interference of the offshore floating unit and the riser is not taken into consideration. The forced oscillation was given as the maximum motions of the offshore floating unit on the top of the riser about the motion analysis of riser in the hang-off mode because the value of maximum motions is enough in a design stage.

Flow field around the floating unit

In order to consider motion of floating unit in the inside of the ocean, it is necessary to estimate the drag coefficient in consideration of viscous influence of octagon shapes. Here, the flow field visualization of the computational result using CFD (Computational Fluid Dynamics) is shown. Where, about computational conditions, the flow velocity is 0.5m/s, Reynolds number is 1.179×10^7, Node number is 25904. In Figure 7, the Karman's vortex under the influence of

viscous has occurred.   If Karman's vortexes generate, the floating unit receives the force of a flow and the right-angled direction by turns.   Then, if this frequency is in agreement with a natural frequency, a resonance phenomenon will be caused.   This becomes easy to occur a noise and an oscillation of floating unit. As a result of calculation, Pressure distributions are shown in Figure 6 and Velocity vectors are shown in Figure 7.   At T=1240s, time series of drag and lift coefficients are shown in Figure 8.   Therefore, drag coefficient is 1.4.
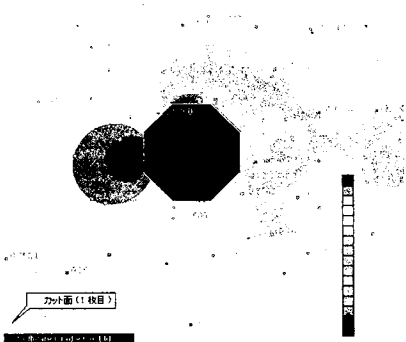
Figure 6.   Pressure distributions
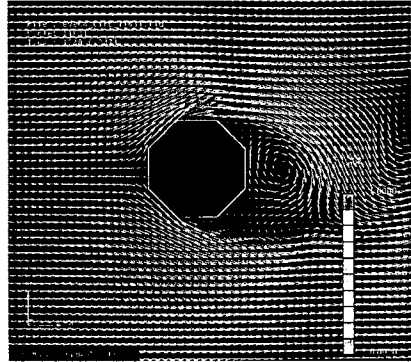
Figure 7.   Velocity vectors
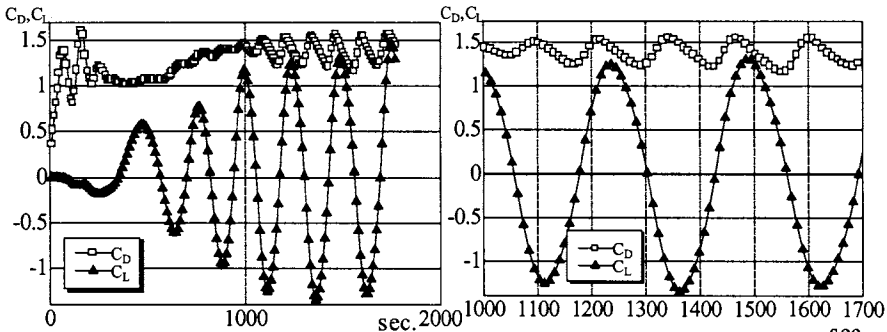
Figure 8.   Time series of drag and lift coefficients, respectively (at T=1240s)

Characteristics of motion for only floating unit

Before considering the response of the floating unit system containing a mooring system, first of all, the characteristic of motion at the floating unit simple substance was examined.   The response in regular waves without mooring lines (RAO) is shown in Figure 9.   The horizontal axis expresses the wave period and the vertical axis expresses the amplitude of motion per wave amplitude of 1.0m.
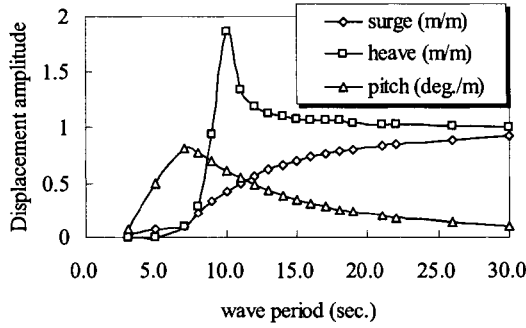
Figure 9.   Response in regular waves

Mooring Characteristics

In the present, the mooring system is four points with Hybrid mooring system of steel chains and wires.   The length of the mooring line is 2,550 m and the rapture load is 950tf.   In order to calculate the response of the floating unit with mooring line, the mooring characteristic per a mooring (Fig. 10).   Figure 10 illustrates that the horizontal axis is the distance horizontal movement from stillness point and the vertical axis is the tension of a horizontal component. About centerline, the distance of horizontal movement from stillness point equals zero.   Initial tension acting floating unit is 30tf.   This state is that the Figure 11 illustrates (the stillness point).

When the distance horizontal movement from stillness point is greater than or equal to zero (the moving distance of floating unit increases gradually to positive direction), the horizontal tension will increase.   According to Figure 11 this state is the right side of stillness point state.   On the other hand, when the distance horizontal movement from stillness point is smaller than or equal to zero (when the moving distance of floating unit increases gradually to negative direction), the horizontal tension will decrease.
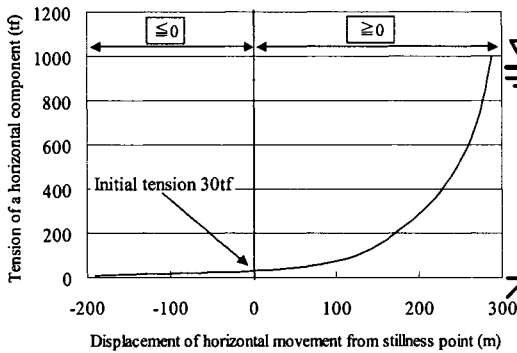
Figure 10.   Characteristics of mooring line   Figure 11.   Stillness point
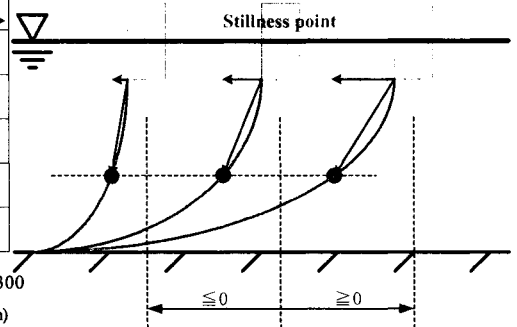
RESULT AND DISCUSSION IN A TIME DOMAIN ANALYSIS

Results of the time history response analysis of floating unit

Motions of the floating unit

Figure 12 shows the results of time history of motions of a floating unit. About calculation condition, the significant wave height is 15 m and the mean wind velocity is 50m/s. That is to say the environmental condition is Survival state.

According to Figure 12, sequentially from the top, Surging motion, Heaving motion, and Pitching motion are shown. Table 3 shows a result of statistics analysis at these time series. The value is positive semi amplitude in time series. Figure 12 and Table 3, first of all, time series of surging motion shows that the floating unit moves in the flow direction 150 m and is oscillating with the significant value of 6.4 m in the surging direction in the position. Time series of heaving motion shows that the floating unit is oscillating with the significant value of 6.75m in the vertical direction in the position. Finally, time series of pitching motion shows that the floating unit is oscillating with the significant value of 1.94 (deg.) at the pitching direction in the position. Therefore, maximum positive semi amplitude of a pitching motion in time series is 3.4 degrees.

Tension acting a mooring line

Figure 13 shows the results of time history of tension acting on a mooring line. Sequentially from the top, the time series are shown in terms of next their parameters; the tension acting on the mooring lines, the horizontal distance from an anchor point to a mooring point and the vertical distance from the seabed to a mooring point.

Table 4 illustrates as a result of statistics analysis at these time series. These values are positive semi amplitude in time series. Table 4 is the result of statistics analysis at the time series of tension of a mooring line. Sequentially from the left, the value that the mean value of positive semi amplitude is added to the mean value of time series, the value that the significant value of positive semi amplitude is added to the mean value of time series and the value that the maximum value of positive semi amplitude is added to the mean value of time series.

From these results, it turns out that the tension acting on one mooring line is about 160tf at the maximum, and it is much less than the rapture load, 950tf, of one mooring line. That means the maximum tension acting on one mooring line is about 17% of a rapture load. Second, this is the result of statistics analysis of the time series of the horizontal distance from an anchor point to a mooring point. When the offshore floating unit is in the state of stillness, this distance is 2,092 m. If it subtracts 2,092 m of distance in the state of stillness from 2,213 m of maximum distance, it set to about 121 m. This value indicates the maximum horizontal moving distance. Third, this is the result of statistics analysis of the time series of the vertical distance from the seabed to a mooring point. When the offshore floating unit is in the state of stillness, this distance is 981 m. If it subtracts 981 m of distance in the state of stillness from 993 m of maximum distance, it set to about 12 m. This value indicates the maximum vertical moving distance.

Surge ... **Tension of a mooring line** ... **Heave** ... **Horizontal distance** ... **Pitch** ... **Vertical distance**
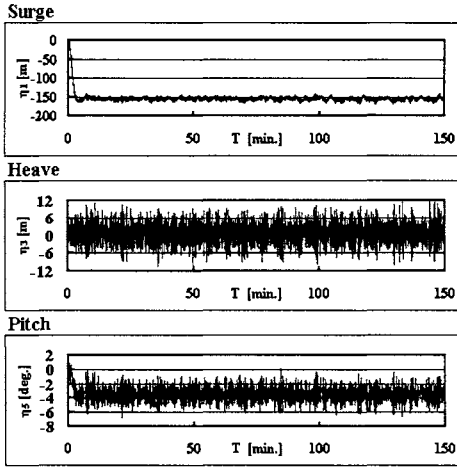
Figure 12.   Time history of motions   Figure 13. Time history of tension of moored line
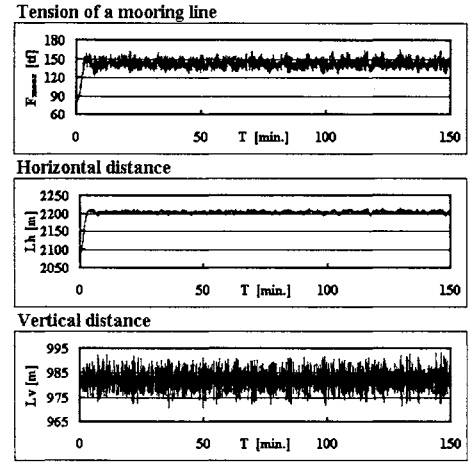
Table 3.   Static analysis of motions

	Mean value	Significant value	Maximal value
Surge (m)	3.48	6.40	13.19
Heave (m)	4.27	6.75	10.87
Pitch (deg.)	1.19	1.94	3.40

Table 4.   Static analysis of mooring line

	Mean value	Significant value	Maximal value
Tension of mooring line (tf)	150.64	155.47	165.97
Horizontal distance (m)	114.78	117.50	121.65
Vertical distance (m)	5.68	8.22	12.37

Results of displacement response analysis of riser

About the motion analysis of riser in the hang-off mode, the forced oscillation was given as the maximum motions of the offshore floating unit on the top of the riser.   The analysis method of the riser motion the equation of motion of the riser is found by means of Finite Element Method. The external forces are found from Morison's equation.   The equation of motion of the riser is written as follows.

$$(M + A)\ddot{\eta} + B\dot{\eta} + C\dot{\eta}|u + v - \dot{\eta}| + K\eta = 0.25C_M\rho\pi D^2\dot{u} + 0.5C_D\rho(u + v)|u + v - \dot{\eta}|$$

Where, M shows the matrix of total mass of the riser, A shows the matrix of added mass, B shows the matrix of damping, C shows the matrix of restore force, K shows rigid matrix, η is displacement of motions of the riser. ρ shows the density of fluid, u and $\dot{u}$ show the matrix of the velocity and acceleration of water particle, respectively. v shows the matrix of the flow velocity. D shows the outer diameter of the riser. C_M and C_D show the mass coefficient and the drag coefficient, respectively.   Where the values of C_M and C_D are 2.0 and 1.17, respectively. The solution method of the equation of motion of the riser uses Runge-Kutta method.

83

About the calculation, the forced oscillation on the top of riser was given as the motions of the offshore floating unit in wave. As a result of analysis, Riser is behavior in the range from 0.0m to 7.0m in the surging direction. The calculation results of riser motion are shown in the Figure 14. The breadth of floating unit is twenty-four meters. Then, the maximum displacement of riser motion is about 29% of breadth of floating unit. Therefore, the riser and the mooring lines are not entangled.
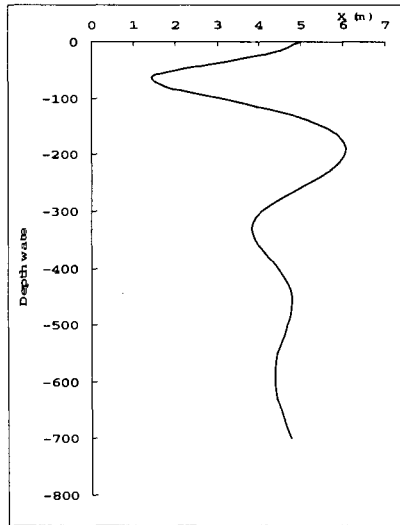
Figure 14.   Calculated distributions of horizontal displacement of riser

CONCLUSIONS

As a result of the calculation of motions about the offshore floating unit for OTEC plant with riser in a time domain analysis in the sever environmental conditions of survival state aimed at the East China Sea, the following knowledge was acquired.

Maximum positive semi amplitude of a pitching motion in time series is 3.4 degrees. Therefore, since the behavior of floating unit is very small, the plant equipments for OTEC do not break down.

Maximum tension acting on one mooring line is about 17% of rapture load. Therefore, a mooring line is not damaged.

Maximum displacement of riser motion is about 29% of breadth of floating unit. Therefore, riser and mooring lines are not entangled.

Motion characteristic of the designed offshore floating unit for OTEC plant was able to obtain the very good calculation result. Therefore, in the present, designed offshore floating unit for OTEC with hanging-off riser has enough reality under the severe environmental conditions.

REFERENCES

Faltinsen, O.M., and F.C. Michelsen 1974. *Motions of Large Structure in waves at Zero Froude Number,* Marine Vehicles.

Allan T., Maris, J., and Randolph Paulling. 1980. Analysis and Design od the Cold-Water Pipe (CWP) for the OTEC System with Application to OTEC-1, *Marine Technology*, Vol.17, 281-289

Ramsden, Harold D. 1983. Conversion of the USNS Chepachet to the OTEC-1 Platform, *Marine Technology*, Vol.20, 64-70

Kinelski, Eugene H. 1985. Ocean Thermal Energy Conversion Heat Exchangers: A Review of Research and Development, *Marine Technology*, Vol.22, 64-73

Hong, Sub. 1994. Three-Dimensional Static Analysis of Flexible Risers by a Lumped-Mass Method, International Offshore and Polar Engineering Conference.

Hong, Sa Y. and Sup Hong. 1996. Motion Simulation of a Floating Structure Coupled with Mooring Lines, International Offshore and Polar Engineering Conference.

Tahar, A., Z. Ran, and M.H. Kim. 2002. Hull/mooring/Riser Coupled Spar Motion Analysis with Buoyancy-Can Effect, International Offshore and Polar Engineering Conference.

Kim, Y.B. and M.H. Kim. 2002.Hull/Mooring/Riser Coupled Dynamic Analysis of a Tanker-Based Turret-moored FPSO in Deep water, International Offshore and Polar Engineering Conference.

Bando, Akiyoshi, Koji Otsuka, and Yoshio Ikeda. 2002. Experimental Study of an 8-shaped Oscillating Flexible Riser, International Offshore and Polar Engineering Conference.

Zhang, Xinyu and Jun Zou. 2002. Coupled Effects of Risers/Supporting Guide Frames on Spar Responses, International Offshore and Polar Engineering Conference.

IMPROVEMENT OF WAVE POWER ECONOMY BY TERMINATOR BACKWARD BENT DUCT BUOY WITH CYLINDER DUCT

Y. Masuda[1], A. Thakker[2], T. Lewis[3] and Xi. Liang[4]

[1]The Pacific Society
JAPAN

[2]Wave Energy Research Team, University of Limerick, IRELAND

[3]University of Cork, IRELAND

[4]Guangzhou Institute of Energy Conversion
Chinese Science Academy, CHINA

ABSTRACT

It is commonly established that wave power has a higher power density than wind power. The wave energy power generation device which makes use of air turbine was developed from navigational buoy and from test of Kaimei.

A new device "Backward Bent Duct Buoy" developed and was found that conversion efficiency was ten times greater that found from Kaimei. Also, the mooring force was significantly reduced. It was found from the water tank test, based on single float, that terminator BBDB can absorb wave power in wide width of wave front. Test on two and three floats terminator were conducted. Based on the results, wave power generator cost in open sea was estimated to be 10 Euro Cent in high power wave density wave sites, such as Ireland (60 KW/m) by 1: 36 scale three floats terminator BBDB model. Also, it was estimated the cost to be 15 Cent Euro in low power wave density, such as Japan (10 KW/m) by 1: 25 scale model.

CHARACTERISTIC OF WAVE POWER

Solar power (150 watts/square meter) is highly concentrated to wave power through wind blow on wide sea surface, and it is transmitted as swell from far distant area. Table 1 shows wind and wave conditions with fully developed sea state.

Table 1. Comparison of wind power and wave power by wind speed

(Wind speed U m/s)	(Wave height Hs m)	(Wave period Second)	(Wave Power KW/m)	(Wind Power KW/ square meter)
5.1	0.55	3.3	5	0.08
10.3	2.3	6.6	16	0.67
15.4	5.0	9.9	120.2	2.3
20.6	9.0	13.2	520	5.4
25.7	14.0	16.5	1600	10.0

In the case of 15 m/s wind speed, wave power through 1 m width is equal to solar power of 500 square meters, and wind power of 50 square meters. Wind power is proportional to wind speed cubed. While fully developed wave power is to wind speed raised to the fifth Power. It is evident that wave power concentrates wind power in dramatic proportions. Therefore use of wave power will be a much better way than solar or wind usage.

Wave power density in the world is shown in Figure 1. High wave power such as 60 KW /m is reported in Ireland, low wave power such as 10 KW/m is reported in Japan and middle wave power such as 20 KW/m is reported in many islands including Hawaii. It is desired to generate electric power economically in not only high wave power areas (60 KW/m. Ireland), but also in low wave power area (10 KW/m such as Japan).

Symbol of Fig.1 is
☐——0-15 KW/m ▨——15-30 KW/m ▧ —30-45 KW/m
▨——45-60 KW/m ▨——over 60KW/m
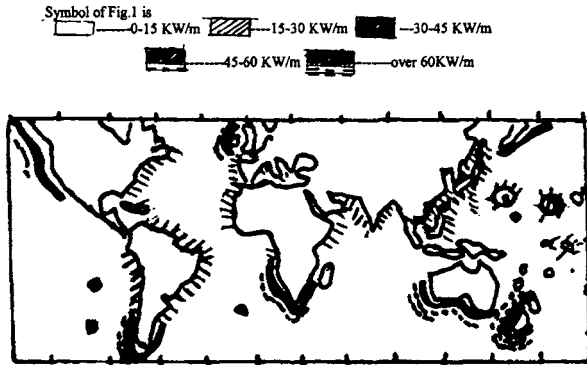
Figure 1. Wave power power distribution in the world
(produced by USA National Climate Center)

VARIOUS WAVEPOWER GENERATOR

There have been various wave power devices studied: the Oscillating Water Column (OWC) with floating buoy (Fig. 2), Center pipe Buoy (Fig. 3) Kaimei Buoy (80 m long, 12 m wide.)

Figure 2.   Center pipe Buoy   Figure 3.   Ship shape Kaimei Buoy
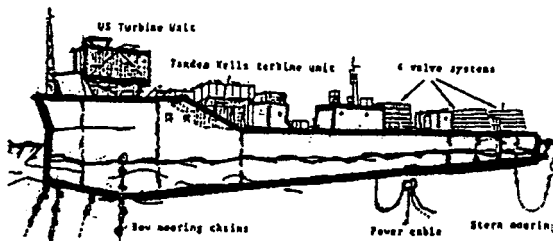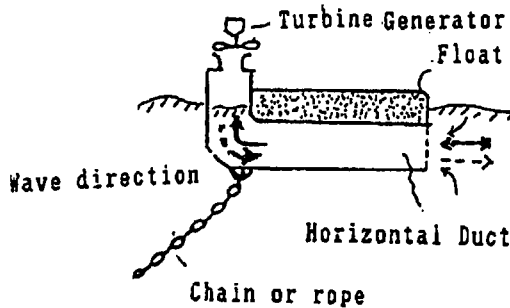
Figure 4.   Original Single Float BBDB Model

Kaimei sea test was conducted at Yura Japan Sea from 1976 to 1984.   Safety and long life of wave power device were confirmed, but conversion efficiency from wave power to air output was not good enough.   In order to improve the efficiency, Backward Bent Duct Buoy (BBDB) was proposed.   As shown in Figure 4, BBDB has an air chamber in the bow, and the duct is bent to backward, it opens to the stern. Air output per the same area of air chamber improved power ten times higher than Kaimei.   The Buoy length was decreased to 30%, and mooring force was decreased significantly by function of oscillating water in the bent duct.

Mighty Whale (Fig. 5) is another type that has Frontward Bent Duct.   It was tested by JAMSTEC for the past four years on the Pacific side of Japan.   This buoy is 50 m long and 30 m wide. The test by JAMSTEC will finish soon

At this time a 200 KW project named B2D2 (same as BBDB) started in Ireland by Dr Tony Lewis of Cork University.   We wish to support this Ireland's test.   After this single BBDB study, Terminator BBDB will be studied to use wider width of wave front.
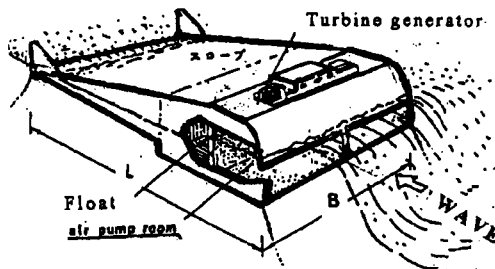
Figure 5.   Mighty Whale

CHARACTERISTIC OF OPEN SEA WAVE

Open sea waves are irregular waves.   Let's call 1/3 of the average highest significant waves Hs. We observe that Hs and wavelengths L have characteristics constant Hs/L.   Wave scatter

89

diagram from the Japan Sea and North Atlantic is shown in Figures 6 and 7. Highest wave is distributed in line of Hs/L=1/20 by dotted line. Average power wave is distributed in line of Hs/L=1/40 by solid line. It is a very important wave characteristic that average power wave in Figures 6 and 7 are same. These are the basic wave characteristics in most of open seas.
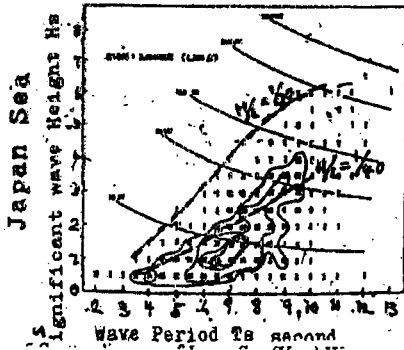
Figure 6. Wave Scatter diagram
of Japan Sea (Yura)
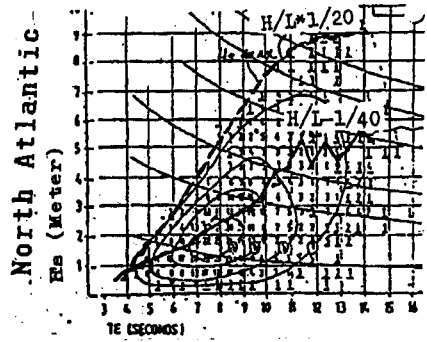
Figure 7. Wave Scatter diagram of North
Atlantic

MODEL TEST

BBDB model tests were conducted in Japan, China, Ireland and India. Chinese model tests were two years ago.
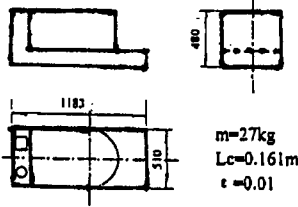
Figure 8. The floating body model 3-3
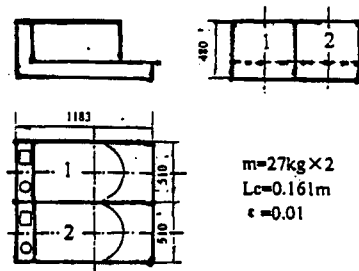
Figure 9. Twin connection Floating body model

90
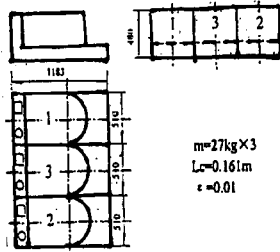
Figure 10. Trinity connection floating body model   Figure 11. Middle model 3-3   Figure 12. Small model 3-3
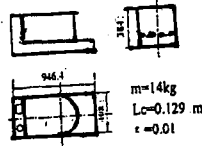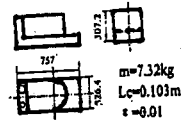
Table 2. Performance of Chinese model's optimal response point to peak periods only

Model plan	Code	Ho (m)	T_{peak} (S)	Hi (m)	ΔP mmAq	N Watts	Q cm^3/s	Hi/Ho	Δ P/Ho	Eff (%)	Eff$_{ave}$ (%)
Model3-3	1·1	0.1	1.25	0.136	38.4	6.342	16.2	1.36	0.384	108.9	
Middle Model3-3	M1·1	0.1	1.1	0.113	37.2	4.787	10.01	1.13	0.372	106	
Small Model3-3	S1·1	0.1	0.96	0.1192	37.7	3.247	7.477	1.192	0.377	102	
Twin Connection Model3-3	2·1·1	0.1	1.25	0.1196	36.1	5.895	14.180	1.196	0.361	92.5	93.85
	2·1·2·			0.1186	41.1	6.066	14.065	1.185	0.411	95.2	
Twin Connection Model3-3	2·3·1	0.1	1.257	0,1234	37.6	6.515	14.695	1.234	0.376	101	103
	2·3·2			0.1019	42.2	6.741	14.364	1.019	0.422	105	
Twin Connection Model3-3	2·4·1	0.1	1.25	0.1329	35.5	6.239	15.575	1.329	0.355	97.9	
	2·4·2			0.1167	39.6	7.575	16.662	1.167	0.396	118.8	
Three Connection Model3-3	3·1·1	0.1	1.257	0.1134	38.9	6.151	13.708	1.134	0.389	95.9	89.4
	3·1·2			0.0939	38.2	5.836	13.462	0.939	0.382	91	
	3·1·3			0.0981	32.9	5.213	13.571	0.981	0.329	81.3	
Three Connection Model3-3	3·3·1	0.1	1.243	0.1174	35.9	5.905	14.341	1.174	0.359	93.2	95.17
	3·3·2			0.1028	36.8	6.564	17.165	1.028	0.368	103.6	
	3·3·3			0.1032	33.5	5.623	14.349	1.032	0.335	88.7	
Three Connection Model3-3	3·4·1	0.1	1.25	0.1296	39	6.998	15.289	1.296	0.39	109.8	104.5
	3·4·2			0.1954	38.8	7.069	14.944	1.054	0.388	110.9	
	3·4·3			0.1093	31.8	5.915	15.333	1.093	0.318	92.8	

OUTPUT ESTIMATION IN OPEN SEA

True line in Figure 13 shows air output by 10 cm constant Wave.   It is 6.9 watts in peak at 1.25 sec, and drops sharply in short and long periods.   For models of single BBDB 1,183 mm long

and 510 mm wide dotted line shows air output by H/L=1/40 which is average wave in open sea, and is 2.2 watts in average wave.   Scale up ratio to open sea from this model is estimated 36 times for the West coast of Ireland.   Buoy is 42.6 m long and 18.36 m wide.   Air output increases to 36 to the power of 3.5(36=279,936) which is equal to 2.2watts x 279,936 =616 KW.
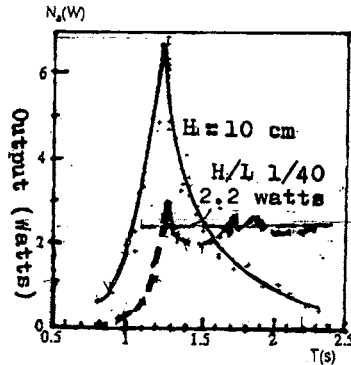
Figure 13. Air output by l0 cm constant wave, and by H/L constant (1/.40) wave

When prototype BBDB is scale up 25 times for low wave power area such as near Japan and Hawai'i.   Buoy is 29.6 m long, 12.75m wide, and 2.2 watt x 78,125=17 2 KW.

MOORING FORCE OF BBDB and TERMINATOR BBDB

Mooring force of BBDB is influenced by direction of duct.   Figure 14 shows mooring force difference by direction of Duct for single float BBDB with cylinder duct (2.4 m long, 0.6 m wide) by 5 cm wave.   Mooring force was 0.3 Kg in backward bent duct condition, and 1.2 Kg in frontward bent duct condition.   Backward can decrease mooring force from 1.2 Kg to 0.3 Kg. This is a function of bending duct, oscillating water in side of the duct. Produces frontward force by changing the water direction at the bent duct.   Mooring force of terminator was measured by wave height 0.1 meter for float number N as shown in Figure 15 is not proportional to N.   It is proportional to the root of N.
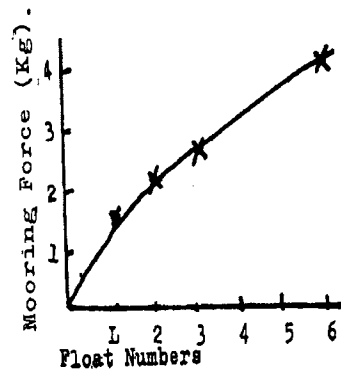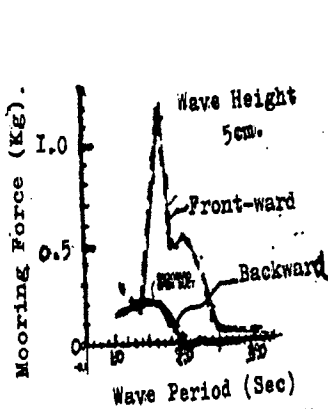
Figure 14. Mooring force of BBDB by direction   Figure 15. Mooring force of Terminator
BBDB by float numbers

TURBINE AND VALVE BOX

Impulse turbine with valve was used in Kaimei. It is consisted of guide vane and rotor as shown
in Figure 16.   Eight turbines were used in Kaimei test.   It operated safely for more than seven
years. The turbines were 1.4 m in diameter.   Constructed of anti-corrosion aluminum.   They
had relatively good performance operating at over 60% efficiency.

Wells turbine was used for this test, but efficiency in high wave conditions was not efficient and
noise problems have not yet improved.   Airflow by wave is oscillates, a check valve mechanism
is necessary to use this impulse turbine.   Two check valve box (three turbine unit) was used in
Kaime from the first year test.   Four check valve box (three turbine unit) was used the following
year, in the second test.
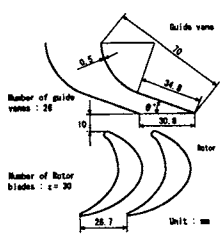
Figure 16. Impulse turbine   Figure 18. Two valve system with turbine
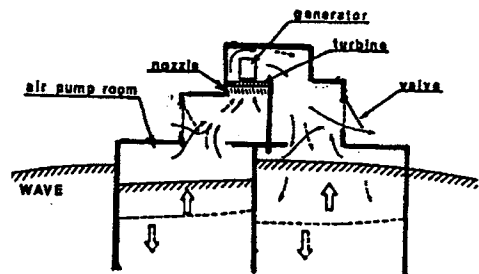
93
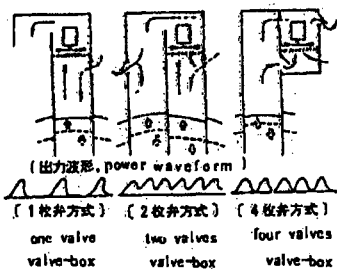
Figure 17. Valve boxes
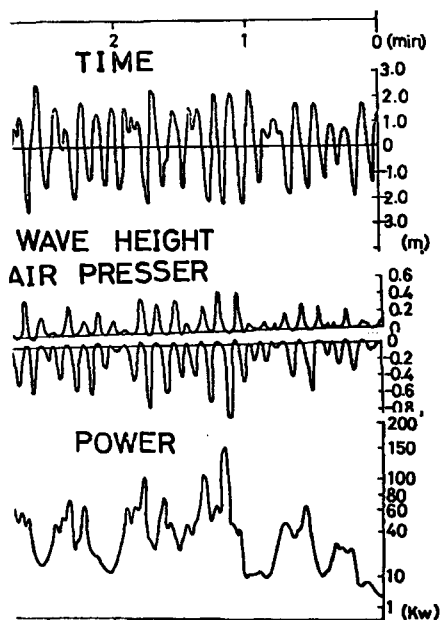
Figure 19. An example of generation by 4 m wave on KAIMEI (2-Valve)

Two-valve box consisted of two air chambers and two check valves. When wave height Hs is 4m. Air pressure was 0.5 m Aq on the plus side and 0.8 m Aq ~0.6 Aq on the minus side as shown in Figure 19. Since Hs=4 m, specific air pressure ratio was 0.13 in plus side, and 0.22~0.15 in minus side, and generated electric power was 40~150kw as shown in Figure 19 (Kaimei generation data). It has minute order output variation by Sea wave characteristic.
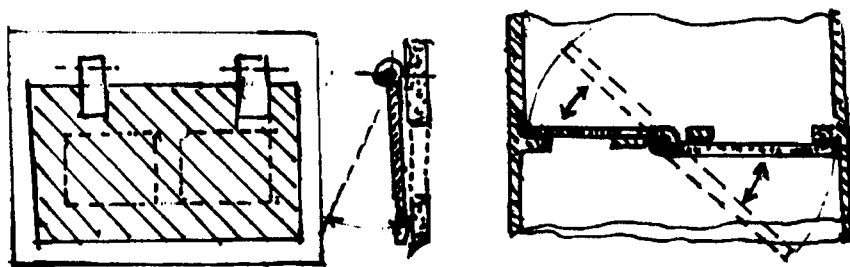
Figure 20. Example of design of Valve (Flat valve and butterfly valve)

Comparing 2-valve box and 4-valve box, output was almost the same. However the 2-valve box had advantage over the 4-valve system. The number of turbines is half of the 4-valve system. The design shown in Figure 20 may be adopted to keep valve safety by throttling the

94

flow of air. Therefore slowing down of the valve turning speed and balancing the two way turning force.

Wells turbine was used to study the elimination of valves. It is very simple. It rotates in the same direction with bi-directional flow of air. But conversion efficiency was low, particularly; efficiency drops in high wave condition by stall characteristic of symmetrical blade turbine. Therefore it will be difficult to use it. Another candidate turbine is Setoguchi turbine developed by Saga University and Limerick University. It has rotor with crescent shaped and two guide vanes in both sides as shown in Figure 21. Recently this turbine was studied by Limerick University. Max efficiency of 46% was obtained. It was lower than impulse turbine.
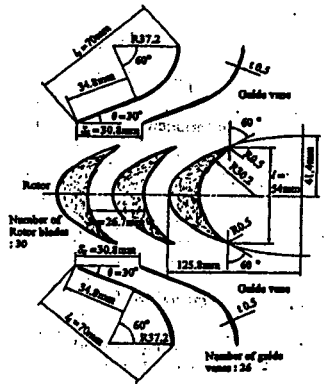
Figure 21.   Setoguchi Turbine

ADAPTATION OF HELLERS GENERATOR

Wave power generator in Isly Island (UK) and Vizihinjam (India) used wound type induction generator with resister controls. Hellers generator is the same to use wound type induction generator, but control is different. Resister, capacitor and reactor are used for control to connect to power grid. Figure 22 shows efficiency of Hellers generator by control method. When it is controlled with resister, efficiency is 60 percent. When it is controlled with resister and capacitor, efficiency is 75 percent. When it is controlled with resister, capacitor and reactor, efficiency is 90 percent.
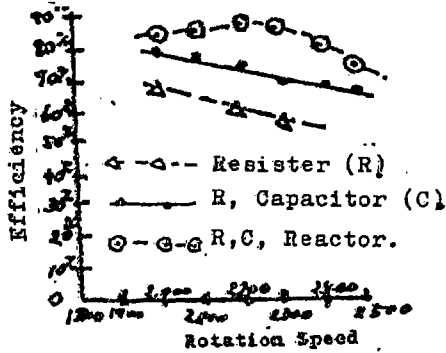
Figure 22. Efficiency of Hellers Generator

ADOPTATION OF CYLINDER DUCT

BBDB with box duct (Fig. 23) was standard shape, but BBDB with cylinder duct (Fig. 24) is an improved shape. Comparison between both shapes is shown in Figure 25 in order to improve economy of wave power in low wave areas such as Japan, BBDB with cylinder duct was adopted. BBDB with box duct (B Buoy) and BBDB with cylinder duct (C Buoy) are compared in specific pressure (Air pressure / Wave height). As shown in Figure 25, Cylinder duct (Fig. 24) has higher air pressure than box duct (Fig. 23) and air output is 170% higher in peak, with 30% higher in average for single float BBDB. The reason of this output difference is the difference between the surface areas of the inner duct. The cylinder duct has a smaller inner surface and movement loss of inner water will be at a minimum.
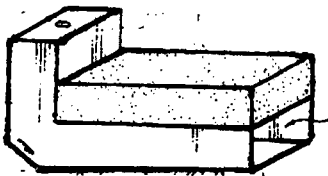
Figure 23. BBDB with box duct (B Buoy)
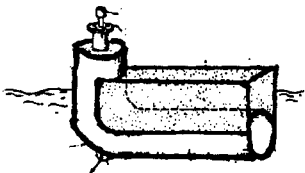
Figure 24. BBDB with cylinder duct (C Buoy)
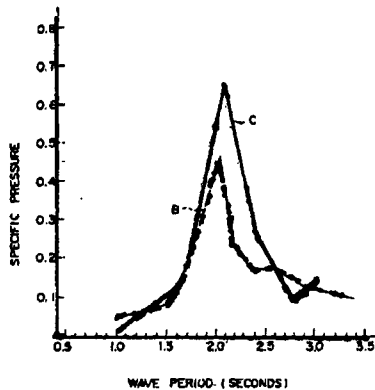
Figure 25. Comparison between B and C Buoy

96

TERMINATOR BBDB

Based on the three floats terminator of Figure 10, two other designs of the terminator were developed (box duct, Fig. 26, and cylinder duct, Fig. 27) for 25 times scale up from the model 1,183 mm long, 510 mm wide.

The three floats terminator with box duct (Fig. 26) has 12 ducts, each duct is 3,187 mm wide, 4,433 mm high and 14.36 square meter per duct times four ducts provide 56.52 square meter / one air turbine, three turbines and twelve ducts with total duct area of 169 square meters including horizontal duct of 29.5 meters long and vertical duct of 7.6 meters high.
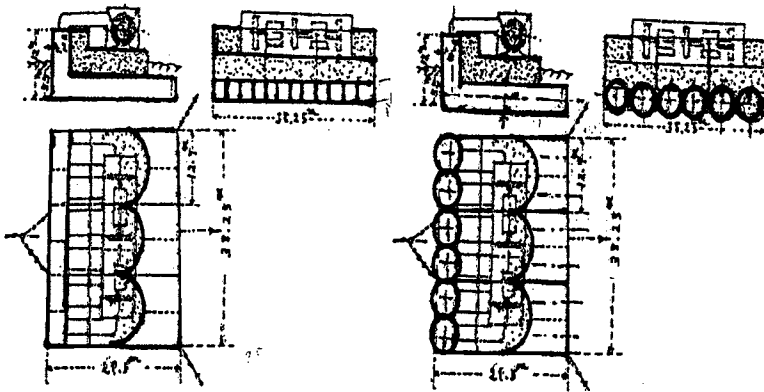
Figure 26. Terminator BBDB with box ducts   Figure 27. Terminator BBDB with cylinder duct

Preparing the Terminator BBDB with cylinder ducts (Fig. 27) has six cylinder ducts that are 6 meters in diameter.   It has 28.36 square meters per one cylinder duct and total of 170 square meters and three turbines.   Steel needed for Terminator BBDB (three floats) with box duct is 12 mm by 6,774.1 square meters of steel plate weighing and 650.3 tons.   Terminator BBDB with cylinder duct needs 5,266.4 square meters, 505.6 ton of steel weight.   Can be decreased by 23% of steel weight, and ship hull construction needed 505.6 ton x 30,0000=151,680,000 yen.

Twenty-five times scale up is suitable size for low wave power area such as Japan Sea, but for high sea such as Ireland, 36 times scale up is better and 1,350 tons of buoy weight is necessary, and construction cost of ship-hull is 1,350 x 300,000=405,000,000 yen.

ECONOMY OF TERMINATOR BBDB

(For high wave area such as Ireland)
   Ship hull construction for Box duct---1,359 tons x 300.000 yen/t=405,000,000 yen
      Turbine (2 m) and generator 3 unit----700,000 yen/unit x 3 =210,000,000 yen
                  Mooring-----------------------100,000,000 yen
                  Cable---------------------------40,000,000 yen
                  Reserve------------------------40,000,000 yen
                         Total   795,000,000 yen
Year cost-------0.13 x 795,000,000 yen=103,350,000 yen per year

When prototype BBDB model is scale up 36 times.   Air output increases to 36 to the power of 3.5(36=279,936) which is equal to 2.2 watts x 279,936 = 616 KW.   Average air output is estimated at 2.2 watts x 279,936 = 616KW per one float, and 1,848 KW by three floats terminator, and electric output 0.5 of it.   In this high sea area, no wave climate is 5%, and three floats terminator generates 616 KW x 3 x 24 h/d x 365 x 0.95 x 0.5 = 8,094.240 KW-h/y.   In this estimation, efficiency of 0.5 is consisted of generator efficiency of 0.9 and turbine efficiency 0.6 and others.

Power Cost-------103 350,000 yen/y / 8,o94,240 KW-h/y = 12.7yen/KWh   = 10.9 Cent Euro /KWh

Similar calculation was reported in Lewis (2000), using a single float BBDB (16 m wide, 40 m long), in Atlantic Wave Condition.   Power Cost was reported 9.3 Cent Euro / KWh.

For low wave area such as Japan and Hawai'i: three floats terminator BBDB (25 times scale up) with cylinder duct is adopted, 172 KW x 3 x 1.3=760.5 KW--- 1,3 is cylinder duct effort.
Year Electric output is 760.5 KW x 24 h/d x 365 d/y x 0.75 x 0.6 x 0.8 =2,698,101 KWh/y
In it. No wave time /y is 0.25 in Japan sea.   Turbine efficiency=0.6.   Generator efficiency 0.9.
                  Ship hull construction------------151,680,000 yen
                  Turbine generator (3 unit)------ 120,000,000 yen
                  Mooring -------------------------- 60,000,000 yen
                  Cable------------------------------ 30,000,000
                  Yen Reserve ---------------------- 30,000,000 yen
                         Total -------------------- 391,680,000 ye

Year cost 0.13 x 391.680,000 yen = 50,918,400 yen/y
Power cost=50,918.400yen/ 2,698,102KWh=18yen/KWH=16 Cent Euro/KWh
      (50% higher power cost than high wave power area)

Since, low wave area has a merit in operation and maintenance than high wave area, and economical wave power use in low wave area become too practical but to do so, scale up ratio must be changed from 36 to 25.   Terminator BBDB can generate higher output by using wave power in wide width of wave front (Masuda et al, 2002; Article, 2001; Masuda et al, 2002).   Terminator will be the best way to get high and smooth electric output.   Nielsen (2002) compared various kinds Wave Power devices, and BBDB was selected as the most economical wave power system in Wave Power Devices studied in Denmark.

REFERENCES

Article. 2001. Terminator BBDB (Backward Bent Duct Buoy) *MAREC Conference* pp. 219-P226. New Castle, UK.

Lewis, Tony. 2002. The Performance of Backward Bent Duct Device B2D2 in Atlantic Wave C condition. Fourth European Wave Energy Conference. pp. 185-193.

Masuda, Y., Y. Kuboki, A. Takker, T. Lewis, X. Liang. 2002. Prospect of Economical Wave Power Electric Generator by the Terminator Backward Bent Duct Buoy (BBDB) *ISOPE 2002* Kitakyushu, Japan.

Masuda, Y., T. Kuboki, T. Setoguchi, X. Liang. 2002. Development of Terminator type BBDB (Backward Bent Duct Buoy) Fourth European Wave Energy Conference. p. E12.

Nielsen, Kim. 2002. The Danish Wave Energy Program Second Year Status (SWAN DK 3) in Atlantic Wave Condition. Fourth European Wave Energy Conference. pp. 312-P324.

PREDICTION METHODS FOR A HYDROELASTIC BEHAVIOR OF AN AIRCUSHION SUPPORTED ELASTIC FLOATING STRUCTURE

Tomoki Ikoma[1], Koichi Masuda[1], Hisaaki Maeda[1] and Chang-Kyu Rheem[2]

[1]Department of Oceanic Architecture and Engineering, College of Science and Technology
Nihon University
Funabashi, Chiba, JAPAN
ikoma@ocean.cst.nihon-u.ac.jp

[2]Institute of Industrial Science, University of Tokyo
Meguro-ku, Tokyo, JAPAN

ABSTRACT

This paper shows the two prediction methods for the analysis of hydrodynamic forces on an aircushion-supported elastic floating structure. One is an approximate method in which the zero draft is assumed and the pressure distribution method is applied, therefore, the problem becomes two-dimensional horizontally. Another applies the three-dimensional source distribution method. There are some areas of free water surface in the aircushions. A behavior of the free surface in the aircushion is directly considered in the analysis of the water pressures or the velocity potentials. In the results the validity of the zero draft assumption is proved. Additionally, a characteristic of the elastic deformation is discussed in head sea conditions. It is found that the elastic deformation is little and the heave motion mode becomes very small when a whole bottom of the floating structure is the aircushion. However, when structural surfaces at the bottom are wide, i.e. not air-supported areas are large, there are some cases that the deformation increases because of the resonance phenomenon. We will investigate the water wave behavior around the floating structure, and from the wave behaviors we will examine the wave drifting forces.

INTRODUCTION

There are some methods for the hydroelastic response reduction on pontoon-type flexible floating structures. One method is the added mass increases due to installation of submerged horizontal plates at part of edge of the structure. Another is a method such as phase of an elastic wave of the flexible structure being shifted to devise a shape of an area of end of the structure. However, the wave drifting force may increase due to reducing the elastic deflection while the above methods can reduce the elastic deflection. Increase of the wave drifting force is possibly a problem for a design of a mooring system.

As a countermeasure, the authors have proposed a very large floating structure with wave energy absorption devices applying the oscillating water column. Its concept was that the device absorbing the wave energy prevented an increase of a reflection wave due to the reduction of the deflection. However, it was very difficult to optimize the device. In addition, the wave

drifting force was not always reduced efficiently because the transmitted wave did not change although the reflected wave decreased. Originally, it was the best method for a reduction of the wave drifting force that the reflection wave makes to decrease and the transmitted wave makes to increase but a pontoon-type flexible structure cannot satisfy the above things simultaneously. However, if only water waves can be transmitted no matter if the structure doesn't deform elastically, the transmitted wave will not decrease. Therefore, it may be possible to reduce the wave drifting force. A type that the above problem may be settled is an aircushion supported floating structure.

The analysis method of hydrodynamic forces and characteristics of a rigid motion of an aircushion supported floating structure were investigated by Pinkster et al. (1998, 2001) and Lee et al. (2000). These investigations were carried out with a three-dimensional problem for the analysis of hydrodynamic forces, however only rigid motion modes were considered in the investigations. Therefore, characteristics of hydroelastic responses of a very large flexible floating structure supported by aircushions have not been concretely discussed.

The present paper shows qualitative characteristics of a hydroelastic deflection of aircushion supporting very large floating structures, and an effectiveness of such floating type is verified. The analysis method and formulations are shown. The pressure distribution method, by Maeda et al. (1996, 2001), is applied. The zero draft is assumed in this method. The pressure change in an aircushion is linearized and a boundary condition of a free surface in an aircushion is directly considered in the analysis of pressures (Ikoma et al., 2002). In this paper, basic characteristics of the elastic deflections of the large aircushion supported elastic floating structures are examined. We examine the hydroelastic behavior of the structures in not only head sea conditions but also oblique sea conditions. We confirm the effectiveness and discuss the behavior of the waves around the floating structure.

THEORY

Equation of pressure in aircushion

Originally, the boundary condition of the general free surface is given as the equilibrium of the pressure between the pressure of the free surface and the atmosphere. In case of the boundary condition on the free surface in the aircushion, the pressure on the free surface is balanced with the compression pressure in the aircushion so far. If the adiabatic compression is assumed to the pressure change in the aircushion, the equation of the pressure can be expressed such as:

$$P_a(t) = \frac{(P_{00} + P_m)V_0^\gamma}{[V_0 - \bar{v}(t)]^\gamma} \tag{1}$$

where, P_{00} stands for the atmospheric pressure, P_m stands for the additional hydrostatic pressure due to sinking by its weight, V_0 is the initial volume of the aircushion; γ is the specific heat ratio (1.4 is used in this study) and $\bar{v}$ stands for the volume varying value of the aircushion. After here, the initial pressure in the aircushion P_0 is expressed as follows:

$$P_0 = P_{00} + P_m \tag{2}$$

The pressure in the aircushion varies non-linearly according to the volume change. Since the hydrodynamic force is analyzed by using the linear theory, it is necessary that the relation between the pressure and the volume change be linearized. If the relation between the volume change and the initial volume of the aircushion could be expressed as follows:

$$V_0 >> \bar{v}(t) \tag{3}$$

The following approximation was possible:

$$\frac{1}{(V_0 - \bar{v})^\gamma} \approx \frac{(1 + \gamma \bar{v}/V_0)}{V_0^\gamma} \tag{4}$$

Therefore, equation (1) can be rewritten as follows:

$$P(t) = P_0 + \frac{\gamma P_0}{V_0} \bar{v}(t) \tag{5}$$

The volume of the aircushion changes according as the water level varies and a ceiling of the aircushion deforms elastically.

Three-dimensional prediction method

The three-dimensional singular point distribution method (3D-SDM) (Maeda et al., 2001) is applied to the analysis of the velocity potentials. In this study, this method is applied to the analysis of a VLFS with the aircushion with the definitions of boundaries shown in Figure 1 using the right hand Cartesian coordinate. The vertical axis z is the positive upward. A region of water mass under the aircushion and surrounded by a skirt is defined as an inner region Ω_A. Outside region of the water mass is defined as the outer region Ω. The area between the inner region and the outer region is continued by a matching boundary. The former includes a free surface in the air chamber. The matching boundary at the bottom outlet satisfies the continuity condition of the velocity potential and the velocity flow. The multi domain method is applied to the 3D-SDM. The free surface in the aircushion satisfies the equation (5).
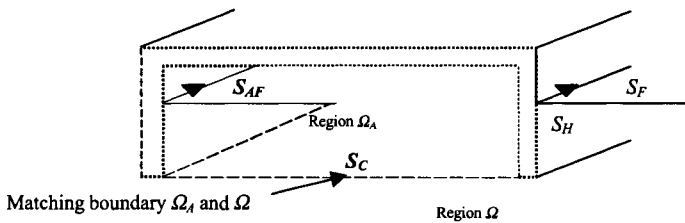
Figure 1. Definitions of boundaries

The Laplace's equation is satisfied in the fluid region:

$$\nabla^2 \phi = 0 \tag{6}$$

Each boundary condition is listed as follows;

$$\phi_z - K\phi = 0 \qquad\qquad \text{on } S_F \tag{7}$$

103

$$\phi_z = 0 \qquad\qquad \text{on } S_B \qquad (8)$$

$$\lim_{R \to \infty} \sqrt{R}\left(\phi_R - ik\phi\right) = 0 \qquad\qquad \text{at } S_\infty \qquad (9)$$

$$\frac{\partial \phi_r}{\partial n} = \hbar \cdot \hbar_r \quad \text{(R-problem)} \qquad\qquad \text{on } S_H \qquad (10)$$

$$\frac{\partial \phi_D}{\partial n} = -\frac{\partial \phi_I}{\partial n} \quad \text{(D-problem)} \qquad\qquad \text{on } S_H \qquad (11)$$

$$\phi_{rO} = \phi_{rA} \qquad \text{(R-problem)} \qquad\qquad \text{on } S_C \qquad (12)$$

$$\phi_I + \phi_{DO} = \phi_{DA} \quad \text{(D-problem)} \qquad\qquad \text{on } S_C \qquad (13)$$

$$\frac{\partial \phi_{rO}}{\partial n} = -\frac{\partial \phi_{rA}}{\partial n} \quad \text{(R-problem)} \qquad\qquad \text{on } S_C \qquad (14)$$

$$\frac{\partial \phi_I}{\partial n} + \frac{\partial \phi_{DO}}{\partial n} = -\frac{\partial \phi_{DA}}{\partial n} \quad \text{(D-problem)} \qquad\qquad \text{on } S_C \qquad (15)$$

$$\phi_z - K\phi + \frac{\gamma P_0}{\rho g V_0} \iint_{A_F} \left(\phi_z + i\omega\Delta z\right) dA = 0 \qquad\qquad \text{on } S_{AF} \qquad (16)$$

Where, subscripts z and R represent the differential due to z or R. And, K is ω^2/g, k is a wave number, $\hbar$ is a normal vector and $\hbar_r$ stands for a mode shape function of the r-th motion mode. Subscripts D and I mean the component of the diffraction or incident wave. P_0 is an initial pressure in the air chamber, V_0 is an initial volume of the air chamber, ρ is fluid density, g is the acceleration of gravity, ω is angular frequency, Δz represents vertical displacement of the water surface in the air chamber and i means a complex number. γ stands for the specific heat ratio, and γ is 1.4 in this study. α represents the complex coefficient, which expresses the phase of the pressure corresponding to the volume change in the air chamber. Therefore, amplitude of α is defined from 0.0 to 1.0. It is possible that this is expressed as the impedance of the orifice. In addition, subscripts O and A in equations (12) to (16) stand for the outer region and the inner region respectively. In the diffraction problem, there is no component of the velocity potential of the incoming wave.

The source density can be obtained solving the integral equation based on the above boundary conditions, and the velocity potentials are obtained later. The integral equation in the air chamber is expressed as:

For Diffraction problem:

$$\frac{\gamma P_0}{\rho g V_0} \iint_{S_{AF}} \frac{\partial \phi_{DA}}{\partial z} dS = \frac{\alpha \gamma P_0}{\rho g V_0} \iint_{S_{AF}} \left(-2\pi \sigma(P) + \iint_{S_A} \sigma(Q) \frac{\partial G_0(P,Q)}{\partial z} dS \right) dS \qquad (17)$$

For Radiation problem of r-th motion modes:

$$\frac{\gamma P_0}{\rho g V_0} \iint_{S_{AF}} \left(\frac{\partial \phi_{rA}}{\partial z} + \eta_r \right) dS = \frac{\alpha \gamma P_0}{\rho g V_0} \iint_{S_{AF}} \left(-2\pi \sigma(P) + \iint_{S_A} \sigma(Q) \frac{\partial G_0(P,Q)}{\partial z} dS + \eta_r \right) dS \qquad (18)$$

Where σ represents the source density, and the Green function in the infinite fluid G_0 is $1/r(P,Q)$, which is a fundamental solution of three-dimensional Laplace's equation.

Application of Pressure Distribution Method

The pressure distribution method (P.D.M) is applied to the analysis of the hydrodynamic forces in this study. In this method, the zero draft is assumed. The variation of the water level in the aircushion is directly considered when the pressures are solved. This is a present approximation method. The coordinate system is illustrated in Figure 2. The boundary plane of the free surface in the aircushion is expressed as S_{AF}.
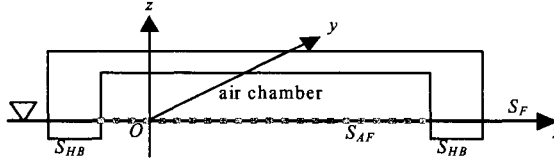
Figure 2. Coordinate system

In the pressure distribution method, the velocity potential Φ and the pressure P are defined as:

$$\Phi(x,y,z;t) = i\omega a\phi \cdot e^{-i\omega t} \tag{19}$$

$$P(x,y,z;t) = -\rho g a p \cdot e^{-i\omega t} \tag{20}$$

where ω is angular frequency, a is wave amplitude, ρ is the fluid density and g is the acceleration of gravity. "i" stands for the complex value $(-1)^{1/2}$. In addition, the velocity potential ϕ is given as follows with Green's function G:

$$\phi(x,y) = -\iint_{S_H} p(x,y) \cdot G(x,y,x',y') dS_H \tag{21}$$

where S_H that is a region of the integration means a boundary of a body bottom.

Then, the boundary condition of the general free surface is expressed as follows:

$$K\phi - \frac{\partial\phi}{\partial z} = 0 \tag{22}$$

In addition, the boundary condition on the body surface, which is a bottom of a floating body on $z=0$ is given as

$$K\phi - \frac{\partial\phi}{\partial z} = p \tag{23}$$

where p is the pressure on the body bottom. K stands for the wave number in case of deep-water condition, and is ω^2/g.

In case of the free surface in the aircushion, the condition of the kinetic equilibrium can be expressed as following linearized Bernoulli's equation:

$$P_a(x,y,0;t) = -\rho\left\{\frac{\partial\Phi(t)}{\partial t} + g\overline{\eta}(t)\right\} \tag{24}$$

where P_a represents the pressure in the aircushion and $\bar{\eta}$ represents the variation of the free surface. The boundary condition such as following equation is derived by considering equation (24) and the kinematical condition:

$$K\phi - \frac{\partial \phi}{\partial z} = p_a \tag{25}$$

Now, since the pressure in the aircushion is obtained by equation (5), equation (25) can be rewritten as:

$$K\phi - \frac{\partial \phi}{\partial z} = p_a$$
$$= -\frac{P_0}{\rho g} \frac{\gamma}{V_0} \cdot v \tag{26}$$

where v is expressed as

$$\bar{v}(t) = a v e^{-i\omega t} \tag{27}$$

By the way, in the pressure distribution method, the boundary integral equation is generally given such as following expression:

$$-\frac{\partial \phi}{\partial z} = \eta(x, y)$$
$$= p(x, y) + K \iint_{S_H} p(x', y') \cdot G(x, y, x', y') dS \tag{28}$$

where S_H means the bottom surface of a floating body and η is defined as:

$$\bar{\eta}(x, y; t) = a \eta(x, y) e^{-i\omega t} \tag{29}$$

Now, if follows is defined

$$p' = \begin{cases} p & \text{on } S_{HB} \\ p_a & \text{on } S_{AF} \end{cases},$$

Equation (28) can be expressed as:

$$\eta(x, y) = p'(x, y) + K \iint_{S_H} p'(x', y') \cdot G(x, y, x', y') dS \tag{30}$$

where, S_H includes S_{HB} and S_{AF}.

So, if an observation point (x, y) is put on S_{HB}, equation (30) becomes

$$\eta(x, y) = p(x, y) + K \iint_{S_H} p'(x', y') \cdot G(x, y, x', y') dS \tag{31}$$

In case that there is the point on S_{AF}, the integral equation can be expressed as follows:

$$\eta(x, y) = p_a(x, y) + K \iint_{S_H} p'(x', y') \cdot G(x, y, x', y') dS \tag{32}$$

One should note that p_a in equation (32) is given by equation (26) too.

Next, the boundary values that are a left term of equation (32) are discussed. The boundary value $\eta(x,y)$ is just the vertical displacement around $z=0$. Therefore, its variable has been a known value in general boundary integral equation methods. However, $\eta(x,y)$ in the aircushion is unknown because we do not have an information of a distraction behavior of the free surface before the problem is solved.

Diffraction problem
In the diffraction problem, the boundary value is usually obtained on the body bottom S_{HB} such as:

$$\eta_S = \eta_I + \eta_D$$
$$= 0 \tag{33}$$

where η_S is the scattering wave, η_I is the incoming wave and η_D is the diffraction wave. Therefore, the following boundary value is given:

$$\eta_D = -\eta_I \tag{34}$$

In the case of the present problem, the diffraction wave is given by the following expression:

$$\eta_D = \eta_S - \eta_I \tag{35}$$

The boundary value of equation (32) is given by equation (35). Therefore, the boundary integral equation on S_{AF} for the diffraction problem can be expressed as:

$$\eta_D(x,y) = p_{Sa}(x,y) + K\iint_{S_H} p'_S(x',y') \cdot G(x,y,x',y')dS$$
$$= \eta_S(x,y) - \eta_I(x,y) \tag{36}$$

accordingly,

$$-\eta_I(x,y) = p_{Sa}(x,y) + K\iint_{S_H} p'_S(x',y') \cdot G(x,y,x',y')dS - \eta_S(x,y) \tag{37}$$

In the above integral equation, a point to which special attention should be paid are that the unknown variable is not only the pressure but also the scattering wave η_S. Then, a following equation is used for another equation,

$$p_{Sa}(x,y) = -\frac{P_0}{\rho g}\frac{\gamma}{V_0} \cdot v(x,y) \tag{38}$$

where, because $v(x,y)$ stands for the volume change of the aircushion, it is obtained by just the variation of the water plane in the aircushion. Therefore, $v(x,y)$ is given by

$$v(x,y) = \iint_{AF} \eta_S(x,y)dS \tag{39}$$

where the integration of equation (39) is carried out in just one aircushion.

From the above formulations, simultaneous equations for the diffraction problem are derived in the following expressions:

$$-\eta_I(x,y) = p_{Sa}(x,y) + K\iint_{S_H} p'_{Se}(x',y') \cdot G(x,y,x',y')dS - \eta_S(x,y) \left|\begin{array}{l} \\ \\ \end{array}\right.$$

$$p_{Sa}(x,y) = -\frac{P_0}{\rho g}\frac{\gamma}{V_0} \cdot \iint_{AF} \eta_S(x,y)dS \qquad \left.\begin{array}{l} \\ \\ \end{array}\right\} \quad \text{on } S_{AF} \qquad (40)$$

The integral equation for the pressure on the body bottom can be expressed such as a formula of equation (31).

Radiation problem
The boundary condition for the radiation problem is usually obtained by just the mode shape functions. Then, the integral equation is obtained as follows:

$$\eta_R(x,y) = p_{ra}(x,y) + K\iint_{S_H} p'_r(x',y') \cdot G(x,y,x',y')dS \qquad (41)$$

where η_R generally represents a mode shape function. However, here, it is the variation of the water plane due to the radiation wave in the aircushion. The radiation wave in the aircushion is unknown in like manner as the diffraction problem. Therefore, η_R is an unknown variable. Equation (27) can be rewritten to

$$0 = p_{ra}(x,y) + K\iint_{S_H} p'_r(x',y') \cdot G(x,y,x',y')dS - \eta_R(x,y) \qquad (42)$$

The expression for the pressure p_a is same as equation (38). Then, the volume change of the aircushion is given by the radiation wave and the deflection of the ceiling of the aircushion. Thus the volume change is expressed as follows:

$$v(x,y) = \iint_{AF} \{\eta_R(x,y) - \Delta z_r(x,y)\}dS \qquad (43)$$

where Δz_r is the vertical displacement of the ceiling, and usually corresponds to the mode shape function $\eta_r(x,y)$ at same place. Because the pressure p_a and the wave elevation η_R are unknown values, the equation becomes the simultaneous equations in the same manner as equation (40). The simultaneous equations are derived as follows:

$$0 = p_{ra}(x,y) + K\iint_{S_H} p'_r(x',y') \cdot G(x,y,x',y')dS - \eta_R(x,y) \left|\begin{array}{l} \\ \\ \end{array}\right.$$

$$p_{ra}(x,y) = -\frac{P_0}{\rho g}\frac{\gamma}{V_0} \cdot \iint_{AF} \{\eta_R(x,y) - \Delta z(x,y)\}dS \qquad \left.\begin{array}{l} \\ \\ \end{array}\right\} \qquad (44)$$

The following integral equation corresponds to the equation for the pressure p on the body bottom

$$\eta_r(x,y) = p_r(x,y) + K \iint_{S_H} p'_r(x',y') \cdot G(x,y,x',y') dS \qquad (45)$$

CALCULATION MODELS

The idealization of the air supported flexible structure is illustrated in Figure 3 however, the draft of the structure is zero in the numerical calculations. Calculation models and wave conditions correspond in real scale. The dimension of calculation models has 1,000 m in length and 200 m in breadth. Mass of the models corresponds to the draft of 2 meters. A bending stiffness per width corresponds to 1.0E+10 Nm^2/m. Angles of the incident wave 0, 30, 60 and 90 degrees. Water depth is 500 m that corresponds to almost deep-water conditions against the calculated waves.

Table 1 shows the principal particular of the aircushion areas of numerical calculation models. Model-0 has no aircushions (i.e., it is a normal pontoon flexible body). Model-1 is supported by just the aircushion (the whole bottom area is an aircushion). Model-2 to Model-5 have two aircushions divided by a buoyant body having width of b and d. In the real numerical calculations, the draft is zero at whole bottom surface.
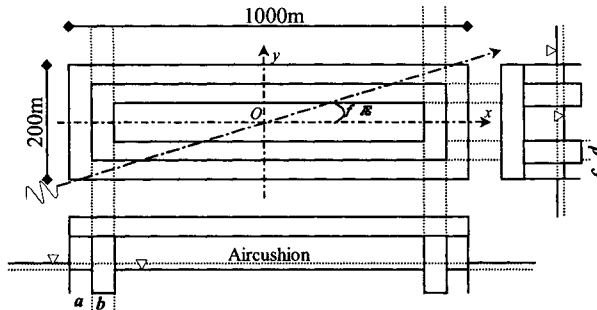
Figure 3.   Idealization of air supported flexible body for numerical calculation

Table 1. Principal particular of aircushion areas of calculation models

	Model.0	Model.1	Model.2	Model.3	Model.4	Model.5
a, c[m]			0, 0	12.5, 12.5	25, 25	50, 50
b, d[m]			25, 25	25, 25	25, 25	25, 25
Inner air chamber [m*m]	0*0	1000*200	950*150	925*125	900*100	850*50

RESULTS AND DISCUSSIONS

Verification of prediction methods

The calculation results of distributions of vertical displacement on y=0 are compared in order to verify the validity of the prediction methods in Figures 4 to 8.   In the three-dimensional method, α equals 1.0.   The height in order to calculate the volume of an aircushion is 5.0 meters.

In all of the figures, deformation characteristics of each model are agreement qualitatively although the both results have slight differences.
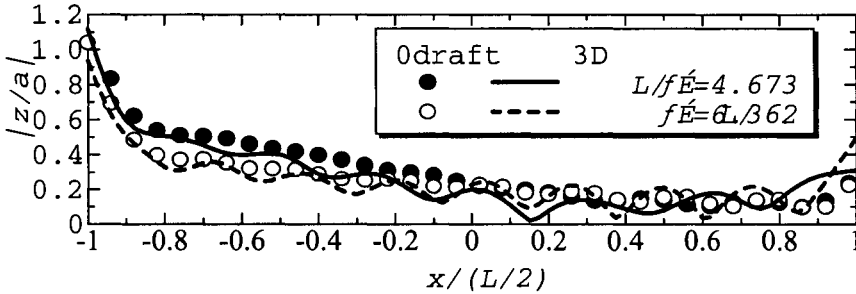
Figure 4.   Comparison between deflection amplitudes of Model-0 calculated by present method and 3-D method on y=0.0
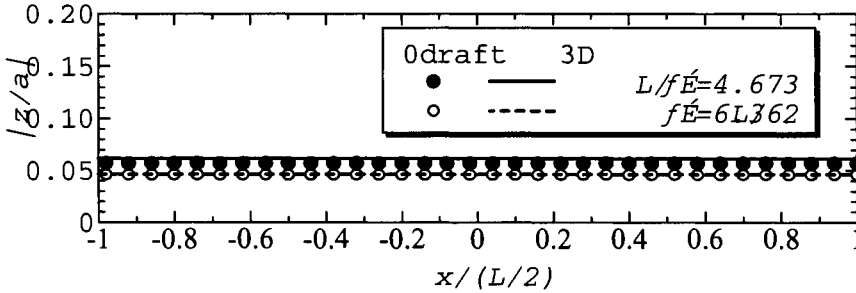
Figure 5.   Comparison between deflection amplitudes of Model-1 calculated by present method and 3-D method on y=0.0
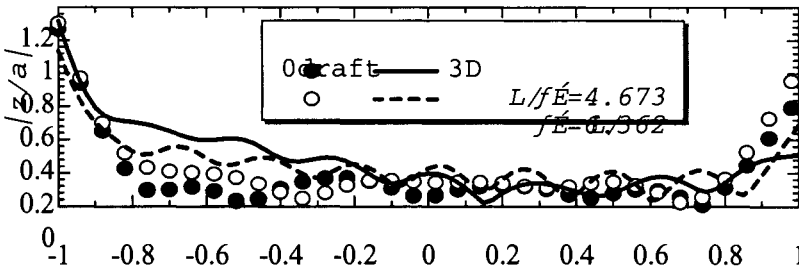
Figure 6.   Comparison between deflection amplitudes of Model-2 calculated by present method and 3-D method on y=0.0
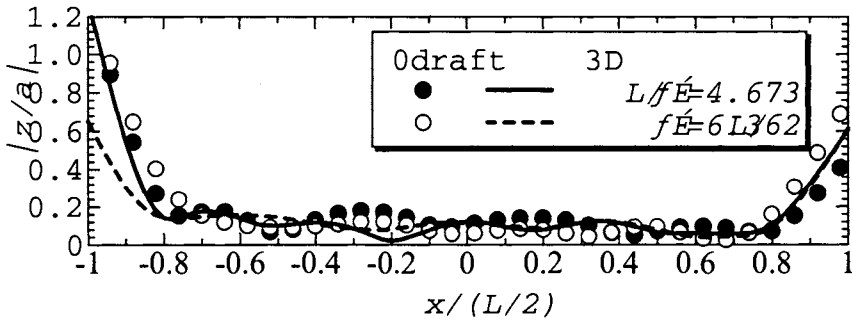
Figure 7. Comparison between deflection amplitudes of Model-3 calculated by present method and 3-D method on y=0.0
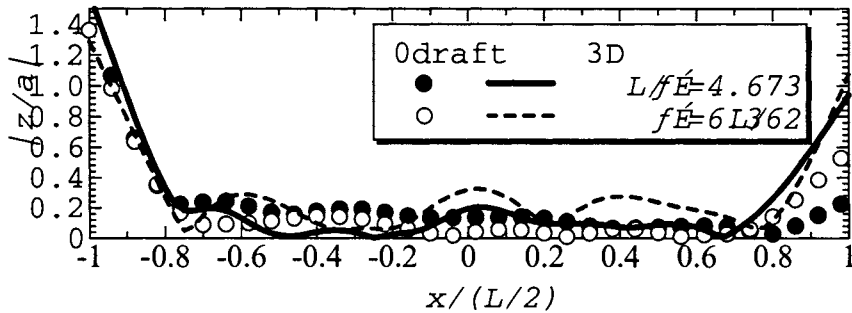
Figure 8. Comparison between deflection amplitudes of Model-4 calculated by present method and 3-D method on y=0.0

Reduction of elastic deflection in head sea conditions

In Figure 9, the comparison of vertical displacement distributions by x direction on y=0.0 is shown in case of L/λ=3.24. Figure 10 shows the results in case of L/λ=12.98. The wave angle is 0 degrees in both results. It can be seen that the motion responses of Model-0 which whole bottom area is the one aircushion are very small in the both wavelength ranges. In Figure 9, the elastic deflection becomes small when the inner aircushion area is wider. However, a characteristic of the deflection of Figure 10 that is shorter waves is reverse as compared with that of Figure 9. The response of Model-5 is smallest in Figure 10. From the deflection characteristic of Model-5 differs greatly from that of Model-3 and Model-4, it is expected that width of outer aircushion to the wavelength influence the elastic deflection greatly.

Figures 11 (a) and (b) show results of the distribution of vertical displacement of Model-1. Model-1 has little motion response in an oblique wave and a beam sea with relatively long waves. The examination on Model-1 is neglected in longer wave ranges because it is expected easily that the response became smaller.
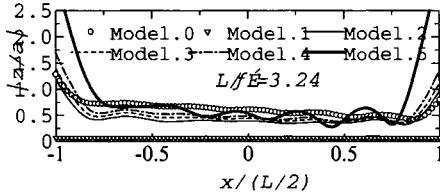
Figure 9. Comparison of deflection amplitude in $L/\lambda=3.24$
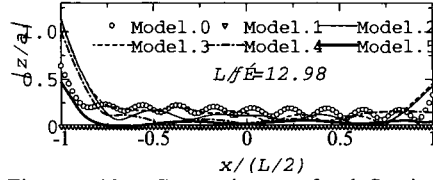
Figure 10. Comparison of deflection amplitude in $L/\lambda=12.98$
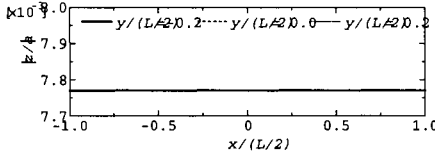
(a) Wave angle is 30 degrees
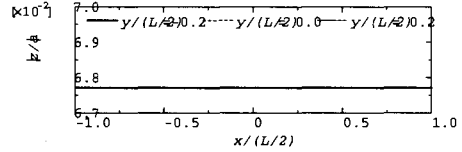
(b) Wave angle is 90 degrees

Figure 11. Deflection distributions of Model-1 in $L/\lambda=4.67$

Behaviors of wave field around floating structures

Counter maps of a wave height distribution around the calculation models are shown in Figure 12 where the results are normalized by height of an incident wave. The behavior of the wave field includes an influence of the elastic deflection of the floating structure. A counter at structure area means amplitude of the elastic deflection. The wavelength corresponds to $L/\lambda=12.98$. The range of the counter maps is from 0.0 to 2.0 other than that of Model-1. In the results of Model-1, the range of the counter maps is expanded since the incident wave is mostly transmitted. In blue colder areas, the wave height is over from maximum value of the counter range.

In the case of Model-1, most waves penetrate. Therefore, Model-1 supported by one aircushion at whole bottom area is an ideal floating type in order to reduce the elastic deflection and the wave drifting force simultaneously.

In the case where the wave angle is 0 degrees, the transmitted wave backward does not become large in Model-2. The transmission of the wave to behind of Model-5 does not become larger that of Model-0. However, the wave scattering is small to transverse directions. Therefore, it can be estimated to be able to reduce the wave drifting force.

It is necessary to narrow the width of the buoyant block or the bulkhead as much as possible in order to reduce the deflection and the wave drifting force. Then, it is thought that division of the aircushion does not become a demerit for the response reduction in order to secure the hydrostatic restoring force.

(a) Model-0

(c) Model-2

(b) Model-1

(d) Model-5
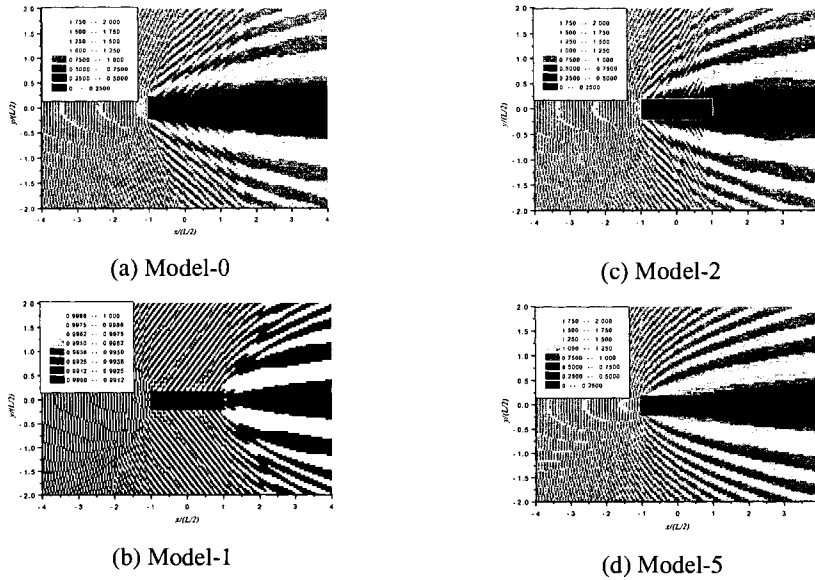
Figure 12. Counter maps of wave around floating structure in 0 deg. wave with L/λ=12.98

CONCLUSIONS

In this paper, two prediction methods for the analysis of the aircushion type VLFS are proposed. From the calculation results we conclude on the aircushion-supported elastic floating structure as follows:

1) The present zero-draft theory is useful for the prediction of the aircushion type VLFS.
2) Model-1 that is an ideal aircushion type is hardly moved in waves. Moreover, it is supposed to be able to reduce the wave drifting force from the results of the counter map of the wave behavior around the floating structure.
3) When the aircushion is divided to outer and inner aircushions, the width of the outer aircushion to a wavelength of an incident wave influences in the elastic deflection strongly. Moreover, the elastic deflection becomes small at mid-ship area when the buoyant block has the width that prevents the water wave into the inner aircushion. Then, the transmitted wave becomes small.
4) It is necessary to narrow the wall as much as possible in order to reduce the elastic deflection and the wave drifting force simultaneously.

ACKNOWLEDGMENTS

REFERENCES

Ikoma, T., Masuda, K., Maeda, H., and Rheem, C.H.. 2002. "Hydroelastic Behavior of Air-Supported Flexible Floating Structures," *Proceedings of The 21st International Conference on Offshore Mechanics and Arctic Engineering*, OMAE'02 in Oslo Norway, ASME, OSU-28090, 2002

Lee, C.H. and Newman, J.N., 2000. "Wave effects on large floating structures with aircushions," *Journal of Marine Structures*, Vol.13, ELSEVIER SCIENCE, pp.315-330

Maeda, H., Masuda, K., Miyajima, S. and Ikoma, T., 1996. "Hydroelastic Responses of Pontoon Type Very Large Floating Offshore Structure," *Proceedings of The 15th International Conference on Offshore Mechanics and Arctic Engineering* (OMAE'96), ASME, Vol. I, pp. 407-414

Maeda, H., Rheem, C.K., Washio, U., Osawa, H., Nagata, Y., Ikoma, T., Fujita, N. and Arita, M. 2001. "Reduction Effects of Hydroelastic Responses on a Very Large Floating Structure with Wave Energy Absorption Devices using OWC System," *Proceedings of The 20th International Conference on Offshore Mechanics and Arctic Engineering* (OMAE'01), ASME, CD-ROM file OSU-5013

Pinkster, J.A., Fauze, A., Inoue, Y. and Tabeta, S. 1998. "The behaviour of large aircushion supported structures in waves," *Proceeding on Hydroelasticity* '98 in Fukuoka Japan, Edited by M. Kashiwagi, pp. 497-506

Pinkster, J.A. and Meevers Scholte, E.J.A. 2001. "The behaviour of a large air-supported MOB at sea," *Journal of Marine Structures*, Vol.14, ELSEVIER SCIENCE, pp. 163-179.

EVALUATION OF HABITABILITY IN VERTICAL MOTION BY PUKARI FLOATING PIER MODEL

Yasutaka Saito[1], Hiroaki Eto[2] and Osamu Saijo[3]

[1]Graduate School of Science & Technology, Nihon University
Chiba, JAPAN
yasu@post.ocean.cst.nihon-u.ac.jp

[2]The Institute of Physical and Chemical Research
Saitama, JAPAN
hiro@atlas.riken.go.jp

[3]Department of Oceanic Architecture & Engineering, Nihon University
Chiba, JAPAN
saijo@ocean.cst.nihon-u.ac.jp

ABSTRACT

For the structural design of floating architectural buildings on which various kinds of environmental loads acts, first, the structural design has to be required to secure the structural safety relating to elapse, deformation, stress and motion. Besides, even if structural safety of buildings is saved, the following problem to be solved will be presented; the oscillation or vibration of floating structure giving uncomfortable feeling to people induced by environmental loads will lose the habitability and efficiency on work. Therefore, the structural design to be considered the physiological and psychological influence to human body becomes particularly essential to evaluate the habitability in the motion of floating structure.

The object of this paper aimed to study the evaluation of habitability for floating oceanic architectural buildings. After having reviewed several standards; ISO (International Standard Organization) describing about vibration and vertical motion, guideline for building vibration in Architectural Institute of Japan and others, we proposed a diagram expressed by four levels for evaluation of habitability in vertical motion. Moreover, we had calculated displacement responses of floating structural model using arranged significant wave in Tokyo Bay. In order to examine the validity of calculation procedure and the evaluation, we plotted the obtained results into the diagram, and summarized the conclusion.

INTRODUCTION

With overpopulation of late years, living space for human beings has been compelled to expand to the ocean. The building on the sea where people aims to live is called oceanic architectural building. It is apparent the environment surrounding those buildings is different from the environmental land. Therefore, in the structural design of oceanic architectural buildings influenced by ocean environment, specifically, environmental loads of wave and wind, its

structural members must be designed to secure the safety for structural damages like collapse, deformation, others. However, even if structural safety has been kept, and if the oscillation or vibration to be uncomfortable to the human beings appears, the habitability and utility of buildings will be hurt. Particularly, in floating oceanic architectural building, the structural design has to be considered with regard to the influence to human body caused by these oscillation and vibration. In this paper, we proposed an analytical procedure of calculation method in terms of load effect of environmental load, wave response analysis of oceanic architectural buildings and the evaluation of habitability in the specified vertical motion except horizontal and rotational motions. Using the floating structural model referred to PUKARI-Pier at Yokohama, MM21, we demonstrated displacement response of its model by wave load, and evaluated the habitability in accordance with that procedure.

THEORY

Limit state design for oceanic architectural buildings

In limit state design of buildings in Japan, two limit states relating to safety on structural performance and utility performance are prescribed by Japanese building code. In addition, another limit state on the habitability of floating architectural buildings has to be considered. This limit state arises from the oscillation of building and vibration caused by wave and wind load. The structural design of oceanic architectural building cannot avoid from the evaluation for habitability is relation to comfortable or uncomfortable feeling induced by the oscillation and vibration. We have shown the classification of limit state design in oceanic architectural building as the followings:

Habitability Limit State – Habitability Level
The limit state belongs to the level which does not hurt habitability due to comfortable or uncomfortable feelings induced by ordinary oscillation and ordinary vibration of the buildings.

Serviceability Limit State – Utility Level
The limit state belongs to the level which does not damage the use of the building, work and operation induced by oscillation, vibration and deformation.

Ultimate Strength Limit State – Safety Level
The limit state means that some structural member is damaged partially or the structure collapses totally by extreme forces.

Load effect and return period

In order to grasp the load effect of environmental load acting on oceanic architectural buildings, the calculation of expected value corresponding to the return period is required. Practically, the expected values of wave height and wave period are needed for wave load calculation. With regard to the return period connecting to the load effect, three levels mentioned as above; habitability level, utility level and safety level, can be listed up. Load effect level and return period of limit state design for oceanic architectural buildings are shown in Table 1.

Habitability Level
It means the evaluation by the level according to closest usual life. The degree of oscillation and vibration of buildings must be grasped by ordinary load occurred everyday. The return period on load effect corresponds to 1-year.

Utility Level
This level is judged by the purpose due to use of buildings, building owner and user. The return period corresponds to two to three times of use period of building.

Safety Level
Assuming that huge typhoon or tsunami hits the structure directly, return period of load effect sets up 50 or 100-year. Its level aims to secure the structural safety.

Table 1. Load effect level and return period

Limit State	Load Effect Level	Return Period
Habitability	Habitability	1-year
Serviceability	Utility	by user
Ultimate Strength	Safety	50,100-year

The ground of 1-year return period can be explained by the evaluation of displacement response in ordinary state of buildings. The utility and safety level are controlled by large magnitude of loads like appearance of once in several decades or several hundred years. One year is defined as the shortest term of climate change in Japan of four seasons. Therefore, its calculation by short period than one year such as several months or half year is not rational. By those reasons, 1-year was adopted as the return period for habitability level.

Evaluation diagram in vertical motion

Most standards and guidelines have dealt with frequency range from 1.0 (Hz) to 100.0 (Hz) with regard to frequencies of buildings on land in vertical direction with reference to the actual earthquake which had happened in the range from 3.0 (Hz) up to 30.0 (Hz). In case of floating oceanic architectural buildings, it must be considered by the motion due to low frequency range less than 1.0 (Hz) of wave period. As to the frequency range from 1.0 (Hz) to 30.0 (Hz), there are many data, for example, Guidelines for the evaluation of habitability to building vibration (AIJ, 1991), Reiher & Meister (AIJ, 1991), ISO standard (ISO 2631/2, 1989) are well known. But, in frequency range between 0.05 and 1.0 (Hz), data are still lacking. Figure-1 shows an evaluation diagram between 0.05 (Hz) and 50.0 (Hz) for habitability in vertical motion, which had been drawn in reference to three represent lines mentioned below.

Line V-1.5 corresponds to the perceptible or imperceptible boundary line for human being (AIJ, 1991).

Line given by Meister and ISO show upper limit for office work and the lower limit for work; Reiher & Meister (AIJ, 1991) and ISO2631/2 "K: 4 of a normal factor" (ISO 2631/2, 1989)

117

Line of V-30 shows the clear perceptible boundary (AIJ, 1991).
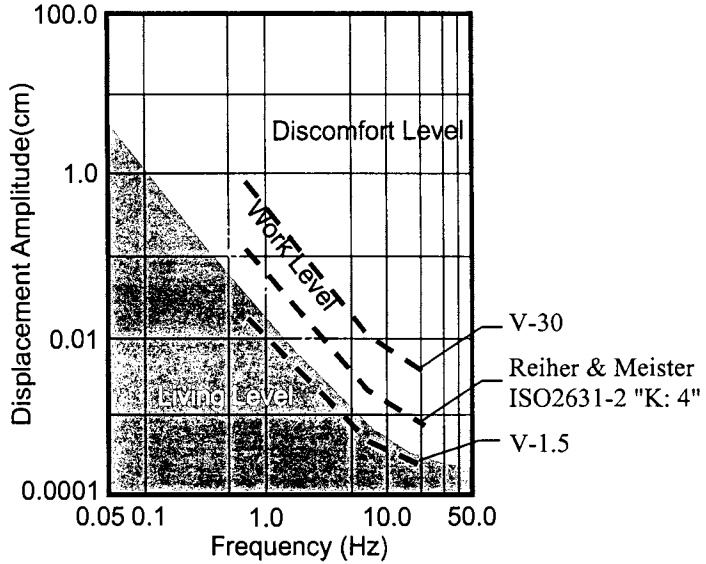
Figure 1.   Evaluation diagram for habitability in vertical motion

Performance level

The evaluation domain of oscillation in vertical direction was classified into three performance levels shown in Figure 1.   Table 2 shows the definition of three performance levels; living level, office work level and work level.

Table 2.   Performance level and definitions

Performance Level	Use	Definition
Living Level	House	The domain where it is comfortable for person not relation in age. Also people don't feel it even if they lie down.
Office Work Level	Office	The domain that does not cause a delay in work by sitting condition. There is difference due to age and duration of stay.
Work Level	Factory	The domain that does not cause a delay in work by standing condition. The work efficiency will not go down even if people suffer from the oscillation.

Procedure of evaluation

The procedure on evaluation for habitability of oceanic architectural buildings is shown.

Step 1. Calculation of 1-year expected value in return period of significant wave by observation data

118

Step 2. Design of oceanic architectural building and grasp the structural characteristic
Step 3. Wave response analysis of the building
Step 4. Evaluation of habitability

In practical, the structural design level in habitability does not accord with the level in habitability satisfied with the use of building, return to Step 2 and trace its procedure repeatedly until satisfaction.

CALCULATION RESULTS

Using floating architectural building model called PUKARI-Pier in Tokyo Bay near Yokohama City, the calculation was done.   In accordance with an evaluation procedure, we calculated that the expected wave (height and period) of 1-year return period and the wave response analysis, and we evaluated the habitability.   Location point for the demonstration and picture of PUKARI-Pier are shown in Figures 2 and 3.

Figure 2.   Location point   Figure 3.   Yokohama MM21 PUKARI-Pier

1-year expected value of wave height and wave period

Wave data for the calculation of 1-year expected value were obtained from NOWPHAS (Nationwide Ocean Wave information network for Ports and HArbourS) for maximum value on daily observation annual report 1991-2000 by Coastal Development Institute of Technology. The expected value of significant wave height was calculated by the linear approximation of the moment method by Gumbel.

Table 3. Significant wave of 1-year return period (Yokohama)

Significant wave	Wave height (m)	Wave period (s)
Average value	0.51	3.48
Maximum expected value	1.42	4.93

With regard to the expected value of significant wave period, after grasping the correlative relation of the dispersion diagrams of wave height and period, and by the approximation line using least squares method, the 1-year expected value was obtained. Table 3 shows the average value and the maximum expected value of significant wave in terms of 1-year return period. 0.51(m) of average significant wave height was obtained at Yokohama point and 3.48(s) of wave period was shown in Table 3. Maximum expected value of the wave height denoted 1.42(m), the wave period was 4.93(s). Significant wave height over 2 (m) and wave period over 10 (s) were not obtained, because its point was located inside Tokyo Bay.

Properties of calculation model

The numerical calculation model for wave response analysis was assumed with reference to size of PUKARI-Pier as shown in Figure 4.
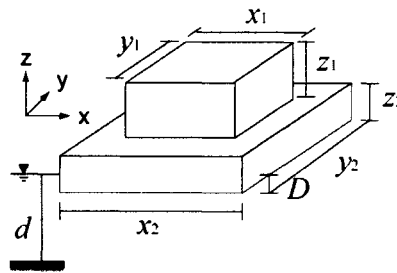
Length of building	x_1, y_1, z_1	(m)	14.4, 14.4, 10.8
Length of floating	x_2, y_2, z_2	(m)	28.8, 21.6, 3.6
Young' modulus	E	(N/m^2)	2.1×10^{11}
Mass per unit volume of structure	ρ_s	(kg/m^3)	8.0×10^3
Draft	D	(m)	2.0
Depth of water	d	(m)	15.5

Figure 4. Calculation model and properties
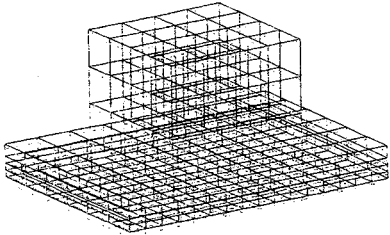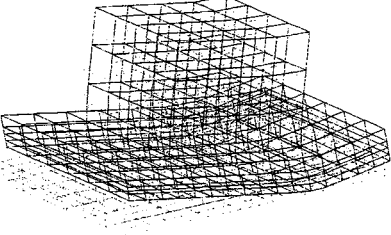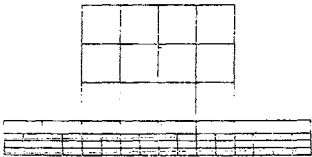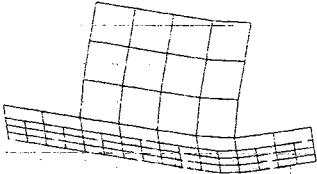
Wave response analysis

Table 4 shows displacement response results by time history expression, displacement amplitude of both bird's-eye view and cross section by average value and the maximum value shown in Table 4. Figure 5 shows incident wave direction, and shows nodal points for the evaluation of habitability on the line AB. Figure 6 shows the displacement amplitude at nodal point 1-5 of roof part of building in vertical direction by average of significant wave (height and period) and the maximum expected value. Figure 7 shows the displacement amplitude at nodal point 1-9 of the base. All of calculations adopted 1-year return period.

Point 1 of the building, logically, showed different results obtained from the average value of significant wave and maximum expected value, because of different magnitude of input wave forces, also it can be seen at base part. But, at Point 5 of the building and Point 7 of the base, those responses induced by the average and maximum obtained the almost same values,

120

respectively. Calculation results at Point 1, 5 and 7 of the base were shown in Table 5 by numerical values. Particularly, concerning to the response of the building, the response results at the incident wave side can be seen, but as approaching to the leeside, the responses of the average and maximum denoted the almost same values. This difference can be judged by different wave period or wavelength.

Table 4. Displacement amplitude of calculation model

	Average Value	Maximum expected value
Bird's-eye view		
Cross-section		
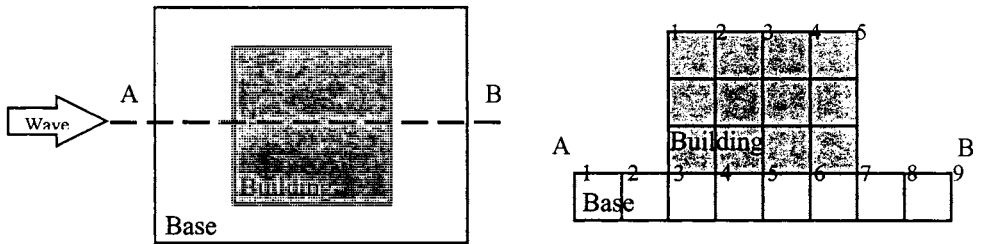
Figure 5. Incident wave direction and nodal point of calculation model

121
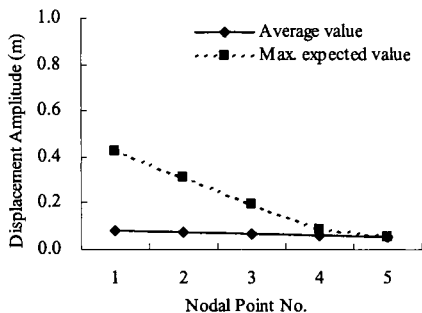
Figure 6. Displacement response of nodal point (Building)
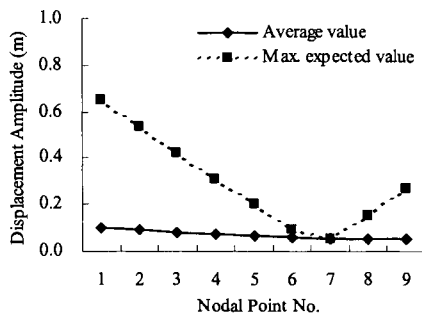
Figure 7. Displacement response of nodal point (Base)

Table 5.　Displacement response of nodal point (Base)

Significant Wave	Displacement (cm)			Frequency (Hz)
	1	5	7	
Average value	10.0	7.0	6.0	0.27
Maximum expected value	65.0	20.0	5.0	0.20

As the third step of the present procedure, using the result at Point 5 of the base, we had evaluated the habitability in vertical motion.

Evaluation of performance level for habitability

After plotting the results shown in Table 5 into Figure 8 of the diagram of performance level domain, the evaluation for habitability in vertical motion was examined.
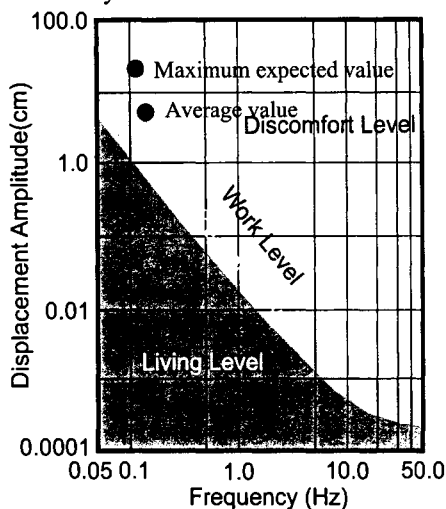
Figure 8.　Performance level domain for evaluation of habitability in vertical motion

122

Present result obtained by 1-year average significant wave indicated 0.07 (m) at 0.27 (Hz), and the evaluation showed the work level. This level may regard not to hurt working condition by standing position. The response result of the displacement by maximum expected value shows 0.20 (m) at 0.20 (Hz) in Table 5, and its result was plotted into discomfort level nearby work level domain.

As the results, the calculation by average expected value of 1-year of the significant wave does not influence the work condition keeping standing position. But the maximum expected value will bring the difficulty to working condition by standing potion, and it can be supposed to make the work efficiency go down by perception of motion.

CONCLUSION

In order to evaluate the habitability for floating oceanic architectural buildings, we have presented and studied as the followings:

(1) Definition of the habitability limit state relating to performance level; dairy living, office work like deskwork and work at factory.
(2) Wave load effect of 1-year return period.
(3) Proposal of an evaluation diagram in vertical motion using published various standards.
(4) The analytical procedure to the evaluation for habitability.

Assuming the floating model, the response calculation was preceded in accordance with present procedure and the validity of its procedure was confirmed. Using these response results, the performance level in vertical motion was evaluated. In calculation results of the floating model at Yokohama, the evaluation showed the work level in vertical motion by 1-year average value of significant wave, and also the other showed the discomfort level by maximum expected wave. In the future, and for the design of oceanic architectural buildings, we consider it is essential to secure the safety not only structural limit state but also the habitability limit state caused by oscillation and vibration, and also for this goal, the estimation of rational load effect in terms of 1-year return period dealing with dairy/ordinary load must be elucidated.

REFERENCES

Adachi, D., Y. Saito and O. Saijo. 2001. Study on Evaluation of Habitability for Floating-Type Oceanic Architecture 1st Report, Evaluation of Vertical and Horizontal Motion, Proceedings of Technical Paper of 44th Annual Meeting of College of Science and Technology Nihon Univ. Session of Ocean Architectural Engineering, Ja-4 pp.658-659 (Written in Japanese).

Architectural Institute of JAPAN (AIJ). 1991. Guidelines for the evaluation of habitability to building vibration (Written in Japanese).

Coastal Development Institute of Technology. NOWHPAS (Nationwide Ocean Wave information network for Ports and HArbourS). observation annual report 1991-2000 (Written in Japanese).

ISO2631/2-1989-02. 1989. Evaluation of human exposure to whole body vibration Part 2-Evaluation of human exposure to vibration in buildings.

Kamekawa, K., Y. Saito and O. Saijo. Study on Evaluation of Habitability for Floating-Type Oceanic Architecture 2nd Report, Case Study by Rigid Body Model, Proceedings of Technical Paper of 44th Annual Meeting of College of Science and Technology Nihon Univ. Session of Ocean Architectural Engineering, Ja-5 pp.660-661 (Written in Japanese).

Masumo, Y., O. Saijo, Y. Saito, H. Eto and K. Kamekawa. 2002. Response Analysis of Floating Artificial Base and Building by Wave Forces, *Proceedings of ESDA2002, 6th Biennial Conference on Engineering Systems Design and Analysis*, ESDA2002/APM-091 pp.1-8.

Saito, Y. and O. Saijo. 2002. Load Effect of Habitability Level acting on Oceanic Architectural Buildings -1-year Expected Wind Speed at 6 Points of Coastal Zone around Tokyo Bay-, *Journal of JACZS* (Japanese Association Coastal Zone Studies) No.14, pp.167-174 (Written in Japanese).

EXPERIMENTAL STUDY ON AT-SEA JOINING METHOD FOR LARGE FLOATING STRUCTURE USING SMA

Kiyoshi Shingu[1], Takashi Mizota[1] and Yoshifumi Takaishi[2]

[1]Department of Oceanic Architecture and Engineering, Nihon University
Chiba, JAPAN
kshingu@shinguu2.cs.cst.nihon-u.ac.jp

[2]Nihon University
Tokyo, JAPAN

ABSTRACT

This study is on secondary drawing and fixing technique in construction of very large floating structures (VLFS) represented as the Mega-Float. In constructing a large floating structure, many units are made in dock separately and towed to the settle region one after another. Under the influence of waves at sea, the units are joined to become a VLFS. Existing methods of joining by secondary drawing and fixing include some problems. To solve these problems and improve safety and construction efficiency, a new technique of joining jig using shape memory alloys (SMAs) are proposed. SMAs have distinct characteristics of shape memory effect and superelasticity controllable by temperature. This paper reports the results of the joining experiment using floating body models. The joining jigs make it possible to combine two remote floating bodies by drawing each other against disturbance of waves, controlling stiffness and transformation of SMAs continuously by Joule heat of electric conduction in the alloys.

INTRODUCTION

In construction of a VLFS, the "at-sea joining" for connecting and integrating separate floating units at a specific sea site is one basic technique of central importance. In the Mega-Float studies validation experiments, which began in 1994, have been executed by Technological Research Association of Mega-Float where various proposals have been executed (1996, 1997, 1998, 1999). A number of units constituting a floating structure are made in docks separately and towed to a specific sea site. These towed units are then joined using proper techniques to avoid the influence of waves, and thereby constructing a large marine floating structure. This study intends to develop a new technique for the secondary drawing and fixing of units in the at-sea joining process. The current secondary drawing and fixing techniques widely used have a number of problems including one likely to have great impact forces on the floating units being rolled and pitched together by external forces such as waves. Finding an appropriate solution to these problems will contribute greatly to the safety and workability of the at-sea joining process. Therefore, we propose a new joining method using SMAs.

125

AT-SEA JOINING

Procedure for At-Sea Joining

In general, an at-sea joining of a large marine floating structure is executed in the following procedure (Shimamune et. al., 1998):

Building floating body units in a dock: Floating body units are built in advance at a dock.
↓
Towing of the dock-built floating body units: Dock-built floating body units are set afloat and then towed to a specified site at sea for installation.
↓
Primary drawing of floating body units: A floating body unit to be newly installed is pulled to the range within tens of centimeters from the final position of the floating body.
↓
Secondary drawing of floating body units: Towed floating body units are placed in contact with each other and then installed at the specified location.
↓
Cutoff and drain of water: Water is cutoff and drained from the floating body units.
↓
Fixing of floating body units: Floating body units are fixed together to enhance their stability.
↓
Welding of floating body units: Floating body units are welded.

It has been proven that in the above process flow, the primary drawing of floating body units can be executed basically in the same manner as the alongside pier procedures for bringing a ship to a quay. The process flow from the secondary drawing of floating body units to the fixing of floating body units is hereafter referred simply to as the "drawing and fixing" process.

Means for Drawing and Fixing

In general, when joining two independently oscillating floating body units together, external forces acting on the joint of these two floating body units can be divided into Fx, Fy, and Fz components of axial forces in the directions of X, Y, and Z, and into Mx, My, and Mz components of moments around each of the three axes, respectively as shown in Figure 1. However, in the drawing and fixing process where waves act as actual external forces, load Fz in the vertical direction, moment Mx in the abutting direction, and load Fy in the horizontal direction each play an important role. In order to join floating body units while enduring these external forces, it is necessary for the floating body units to have a joining jig that has a strength durable enough to withstand the braking force and its reaction force so as to converge the relative motions among the adjacent floating body units gradually, and finally to turn these floating body units into a fixed unit. This joining jig needs to have a guide-like function of converging the relative motions of the floating body units and finally guiding the units to their joining positions, a pressurizing function that applies a force necessary to deal with the guide-like function, and further a function that restrains minute fluctuations of the floating body units during the final stage of fixing.

126
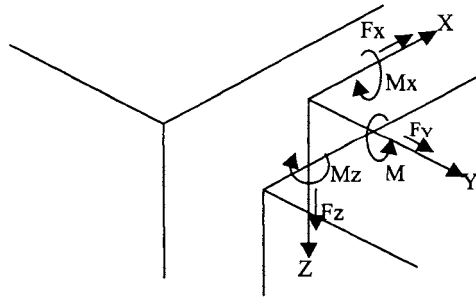
Figure 1. External forces applied to floating body units

AT-SEA JOINING USING SMAs

Fundamental characteristics of SMAs

A SMA can memorize its shapes by heat-treatment for about one hour at a temperature ranging from 300°C to 600°C. Once a SMA is heat-treated to higher than the Af point (Austenaging point, around 120°C in this study), no strain remains in it even when an external force is applied to it (the elastic limit is in a range of 6-8%). Furthermore, at a temperature lower than the Mf point (Martenaging point, around 30°C in this study), when an external force is applied to a heat-treated SMA, apparent plastic strain remains intact in it even after the external force is taken away from it. However, when a SMA is heat-treated to a point higher than the Af point, keeping its apparent elastic strain as it is, the elastic strain is eliminated, and the alloy can restore its original shape. Then, the elastic modulus of the alloy varies continuously with temperature (Industrial Material Center, 1991).

Procedure for At-Sea Joining using SMAs

After a floating body unit to be newly joined to the existing floating body unit at a prescribed site at sea is drawn to a position as near as tens of centimeters at the primary step, SMAs are attached to the new floating body unit at normal temperature (in the martensitic phase). Since the stiffness of the SMAs are slight, the use of the at-sea joining jigs affects fewer of the oscillations of those floating body units. Then, the temperature of the SMAs are raised, the deck of the new floating body unit is made to contact that of the existing floating body unit, the tops of two bodies abutted, water between the two bodies drained, and finally the bottoms abutted. After that, in order to enhance their stability within a few millimeters as required for welding, the temperature of the SMAs of two units is raised to fix the units together.

CHARACTERISTIC TEST OF SMA

Method for measuring the characteristics of the SMAs

We used the characteristics testing equipment shown in Figure 2 for material experiment of the SMA to be used in the joining jig. The measurement and experimental procedure are as follows:
Measurement conditions:
1) Length of sample material: 50 mm
2) Measured length: 80 mm
3) Elongation: 5% (1.5 mm)
4) Temperature measurement interval: 10°C
5) Temperature measurement range 20°C-130°C

Experimental procedure:
(1) Tighten only the upper section of the chuck, mount a SMA sample to the chuck, and then heat the air from the fan to 130°C using a heater, then apply the 130°C air gas to the SMA sample to remove residual stress. (2) While maintaining the above state, tighten the lower section of the chuck to fasten the SMA sample to the chuck and set the elongation 5% of the sample length. Then lower and raise the temperature of the air gas between 130°C and 20°C repeatedly until the maximum and minimum values of the tensile force of the SMA sample become stable and the sample can trace the same hysteresis. (3) Measure the tensile force of the SMA sample using a force gauge while lowering and raising the temperature by 10°C increments between 130°C and 20°Celsius.
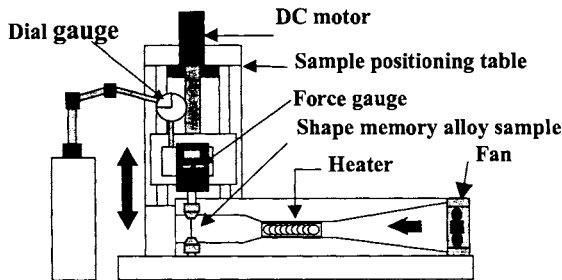
Figure 2. Characteristic testing equipment for shape memory alloy

Result of the characteristics test

The result of the characteristics test for the SMA is shown in Figure 3 in terms of the relationship of "temperature vs tensile force".
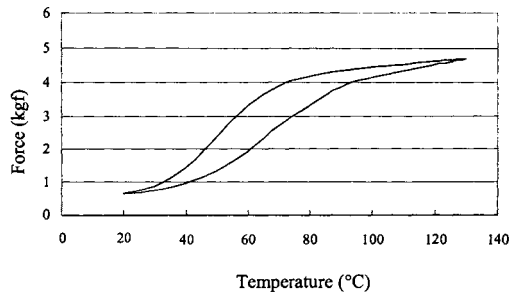
Figure 3. Result of the characteristics test

MODEL EXPERIMENT

Design of drawing jig

In the drawing jig of the SMA, the heat resistance of the SMA must be taken into consideration at two stages. At the first stage, the SMA needs to be able to endure heat-treatment at 500°C in order to enable the SMA to memorize the SMA. At the second stage, the SMA needs to be able to endure a temperature of about 70°C applied for eliminating the apparent strain of the alloy so as to restore the alloy to the original shape that the alloy memorized during the first stage. In this study, since two stages of heat-treatment are executed by electric heating, the insulation of the drawing jig must be taken into consideration at the second stage. We designed the drawing jig considering the above conditions.

MECHANICS OF THE DRAWING JIG

A drawing jig is an apparatus like a pair of *scissors* (Fig. 4). Each edge of the apparatus is hinged to each floating body. *Handgrip-side* edges are combined using SMA. The perimeter of a sheet of a disk, whose center is on the axis of *scissors*, is involved with SMA. The disk is installed so that the length of the SMA will be longer and the jig stroke range wider. In this condition, two floating bodies are separate and distant, and as the stiffness of the SMA is low, the two floating bodies are softly restrained and comparatively free.

Electric conduction makes SMA reach a high temperature and shrink. As the *blades of the scissors* approaches each other gradually, so do the floating bodies. Here, since the stiffness of the SMA become stronger nearly in proportion to temperature rise, restraint force between floating bodies becomes gradually stronger and relative motion reduces. After SMA is heated long enough, the *scissors* are completely closed and the two floating bodies are so close to each other that they can be combined, behaving as if they were one body.

The entire configuration of the drawing jig is shown in Figure 4, of which dimensions are as follows: 1) Height: 175 mm; 2) Breadth: 116 mm; 3) Depth: 46 mm; 4) Drawing distance: 42 mm; 5) Radius of disc: 40 mm.
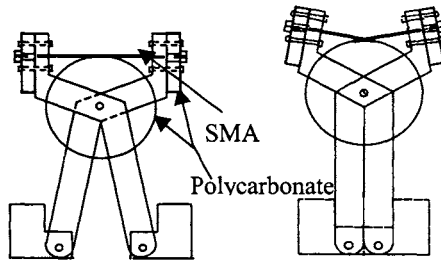
【State of drawing jig loaded with SMA】　　【State of drawing jig during drawing】

Figure 4. Drawing jig

Dimensions of the SMA

Dimensions of the SMA are as follows.
1) Type: Ni-Ti alloy
2) Diameter: 0.4 mm
3) Overall length (when loaded with SMA): 375.20 mm
4) Overall length (when drawing): 361.84 mm
5) Tensile strain (when SMA is linear): 8.9%
6) Electric resistance: $89 \times 10^{-8} \Omega \cdot m$

Polycarbonate

In this study, since the SMA is heat-treated electrically, polycarbonate is used as an insulator. The polycarbonate used has a specific gravity ranging from 1.13 to 1.24, and a heat resistance of about 120° Celsius.

Water Tank Experiment

Floating Body Model
Dimensions of the floating body model, which were assumed to be on a scale of 1/80 of the real one, are as follows.

Scale: Length × width × depth = 1,100 × 600 × 100 (mm)
Material: Acryl　　Draft: 50 mm　　Weight: 28.91 (kgf)

Measuring Method for Floating Body Model Units
The motions of the floating body model units were measured by LED targets attached to the floating body model units at seven positions (points A through G) using sensor heads. Measured data were digitized and stored in a computer.

Layout of Experimental Equipment
The upper sections of floating body model units were equipped with at-sea joining jigs, LED targets, and sensor heads. In order to protect the floating body model units from being drifted by waves, springs and piano wires were laid out over the floating body model units as shown in Figure 5.
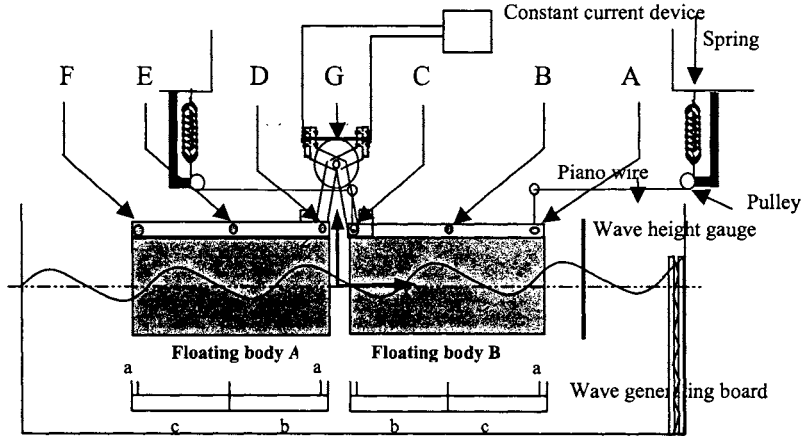
a=25 mm, b=330 mm, c=270 mm

Figure 5. Layout of the experimental equipment (side view) in the water tank (length: 17 m, breath: 9 m, depth: 0.7 m)

Experimental Conditions
Table 1 below shows the experimental conditions. WH in the Table means wave height.

Table 1. Experimental conditions

λ/L	Period (sec)	Frequency (Hz)	Nominal WH (mm)
Still water	∞	0	0
0.80	0.55	1.818	
1.25	0.69	1.440	
2.00	0.88	1.140	25.0
2.50	0.98	1.015	
6.00	1.52	0.658	

Procedures for Measuring the Oscillations of Floating Body Model Units
Carry out wave tests before measuring the motions of the floating body model units. Generate waves using the wave generating board, and switch on the constant current device after five seconds from the start of measurement. After 180 seconds from the start of measurement, switch off the constant current device. The measurement ends when 240 seconds have elapsed after the start of the measurement.

RESULTS OF THE TANK EXPERMENT

The tank experiment resulted in the six parameters as enumerated below.
(1) Positions of the floating body model units in a period between the start of measurement and 2.0 seconds and in the period between 100 seconds and 102 seconds.

131

(2) The relative horizontal displacement, Cx–Dx, between position C of the joint surface of floating body model unit B and position D of the joint surface of floating body model unit A.
(3) The inclinational difference, $\angle DF-\angle AC$, between the inclination $\angle AC$ of the base floating body model unit B and the inclination $\angle DF$ of the floating body model unit A.
(4) The relative vertical displacement, Cz–Dz, between position C of the joint surface of the floating body model unit B and position D of the joint surface of floating body model unit A.
(5) Wave height.
(6) Temperature of the joining jig of the SMA.
Positions of the floating body model units are indicated being shifted at an interval of 10 mm for each time in the z (vertical) direction. Experimental results for $\lambda / L=2$ as part of the results are shown in Figures 6-12.
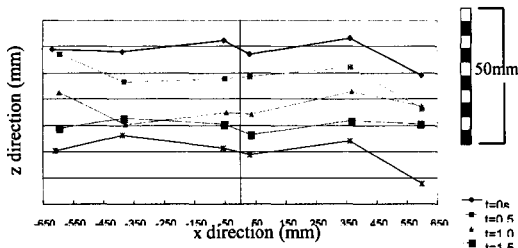
Figure 6. Positions (t=0~2.0s)
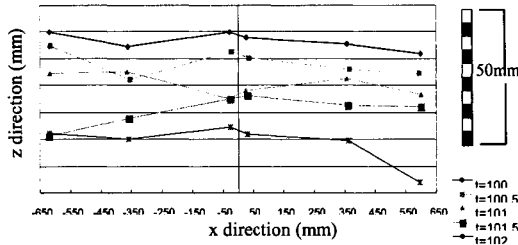
Figure 7. Positions (t=100~102s)
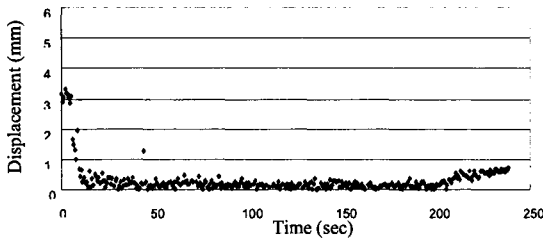
Figure 8. Displacement Cx–Dx

132
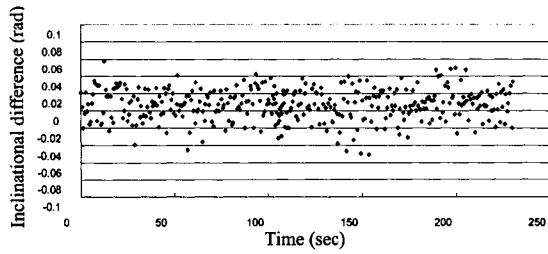
Figure 9. Inclinational difference ∠DF-∠AC
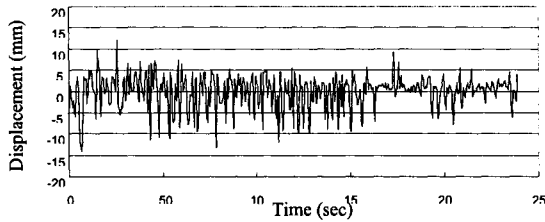
Figure 10. Displacement Cz-Dz
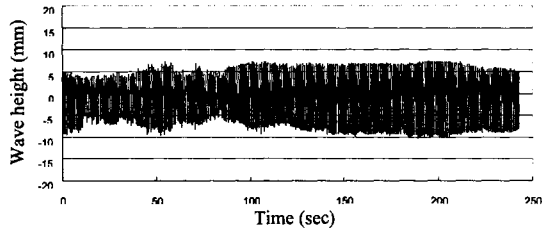
Figure 11. Wave height
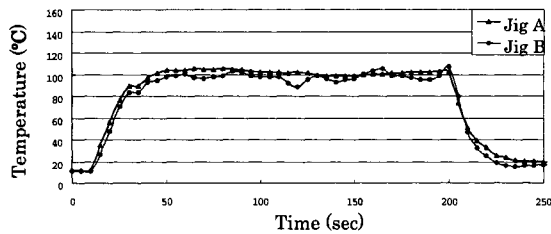
Figure 12. Temperature

DISCUSSIONS

(1) Comparing the position in the period from the start of measurement to 2.0 seconds with that of the period from 100 seconds to 102 seconds, it is understood that two floating body model

units oscillate separately at the start of the measurement, while at 100 seconds from the start of measurement both floating body model units oscillate almost in unison.

(2) From the results of relative horizontal displacements Cx–Dx, it is understood that both floating body model units are drawn to each other by about 40 mm and finally they touch each other as viewed under any condition. From these facts, it has been found out that two floating body model units can be drawn to each other against wave forces by the restoring forces of the SMAs.

(3) From the experimental result revealing that the inclinational differences $\angle DF-\angle AC$ concentrate around 0, it is understood that both floating body model units sustained nearly the same inclination. Further, in this experiment only the upper sections of floating body model units were joined, while their bottom sections were free to oscillate. It is assumed that by applying similar joining jigs to their bottom sections; the whole of both floating body model units can be integrated almost completely.

(4) The results of the relative vertical displacement Cz–Dz indicate a difference of around $\pm 5mm$. This difference is considered to be caused by the inclinations of the floating body model units since position C is distanced horizontally about 55 mm from position D and also considerable vertical noise exists. Further, since the LED target of the position sensor, which was used in this study, measures the target position optically, reflected waves appearing from the water surface are considered to be another source of noise.

(5) The model is assumed to be 1/80 of an actual apparatus:
  Model: 1.10m x 0.6m x 0.1m.
  Actual apparatus: 88m x 48m x 8m.
Incidentally, the unit of Mega-float (Phase I) is as follows: 100m x 20m x 2m.

CONCLUSION

From the above mentioned, we can develop a joining jig using SMAs as a means for an at-sea joining method in the construction of a large marine floating structure.

ACKNOWLEDGMENTS

REFERENCES

Industrial Material Center, 1991. Handbook of Production and Processing of New Materials and New Metals. pp. 535-552. (Written in Japanese).

Shimamune, S., M. Matsuura and S. Nakano, 1998. Afloat Joining Method of Very Large Floating Structures and Response Analysis with a Mathematical Modeling of Joint Mechanism, 14th Ocean Engineering Symposium, The Society of Naval Architects of Japan. pp. 487-494. (Written in Japanese).

Technological Research Association of Mega-Float. 1996, 1997, 1998, 1999. Study Reports of Very Large Floating Type Marine Structures. (Written in Japanese).

CONSTRUCTION OF FLOATING DISASTER PREVENTION BASES AND IMPROVEMENT PROPOSALS BASED ON TRAINING EXERCISES

Hiroichi Tsuruya[1], Masaharu Ikegami[2], Kiyoshi Ikeda[3], Atsushi Fujii[4] and Daisuke Furuta[5]

[1]Institute of Oceanic Research and Development, Tokai University
Shimizu, JAPAN
tsuruya@scc.u-tokai.ac.jp

[2]Yokohama Research and Engineering Office for Port and Airport
Kanto Regional Development Bureau
Ministry of Land, Infrastructure and Transport, JAPAN

[3]Kobe REOPA, Kinki RDB, MLIT, JAPAN
[4]Nagoya REOPA, Chubu RDB, MLIT, JAPAN
[5]Coastal Development Institute of Technology, JAPAN

ABSTRACT

Three types of floating disaster prevention bases (FDPB) have been constructed in 2000 and disposed at the base ports in Tokyo, Ise, and Osaka Bays. The shell structures adopted for the bases are steel, PC-hybrid, and RC-hybrid types. Details of the structures from the construction to the present situation are described. After the completion of FDPD, training exercises have been conducted. Improvement proposals acquired from the experiences are also shown in the present paper.

INTRODUCTION

The Great Hanshin-Awaji Earthquake has occurred at 17 January 1995 and 6,400 people have been killed or missing. Houses partially or completely destroyed in the quake reached 240,954 and the financial cost of total damages are estimated approximately ten trillion Japanese Yen. Because of the heavy damages of infrastructures and buildings, human and urban activities are forced to be stagnant for a long time. Through many types of experiences for relief and restoration works, it has been recognized that the relief activities especially from sea side are quite important and effective especially during about two weeks from just after the occurrence of a disaster to the genuine relief and rescue operations are put into practice.

After the Great Hanshin-Awaji Earthquake, the Ministry of Transport has drawn up the Basic Principle for the Construction of Countermeasures for the Big Earthquake Disaster in Port Area. Based on the principle, the Second, the Third, and the Fifth Port Construction Bureaus of the Ministry of Transport have decided to construct floating disaster prevention bases as complementary

facilities of the high-performance quay walls against earthquake, which had been intentionally constructed but still be insufficient. Because of the reorganization of the central government of Japan in 2001, the Ministry of Transport has changed its name to the Ministry of Land, Infrastructure and Transport, and the Second District Port Construction Bureau to the Kanto Regional Development Bureau, the Third Port Construction Bureau to the Kinki RDB, and the Fifth PCB to the Chubu RDB. The present paper describes the sequence of the construction of three types of floating disaster prevention basis and improvement proposals based on the training exercises.

DESIGN CONCEPT AND STRUCTURE OF THE BASES

Design Concept

The basic design concept of each basis has been explained by Kozawa et al. (2000). Three types of the bases are planned to be disposed in Tokyo, Ise, and Osaka Bays. In a disaster, the floating disaster prevention basis will be towed by a ship to the neighboring stricken district and fully used for relief activities.

The basic design concept of the floating basis learned from the relief activities from seaside at the Hyogoken-nanbu earthquake disaster is as follows (Kozawa et al., 2000):
 (1) Maintain quay walls available for 1,000 DW class vessels,
 (2) Guarantee cargo handling with a 25 ton class truck crane,
 (3) Secure storage space inside the floating structure,
 (4) Secure necessary space for a heliport.

The advantages of a floating structure are that it is unaffected by earthquakes, transportable, and that inside space of it is available. Generally, they are used as a floating wharf for vessels. Once a disaster occurs, it will be taken in tow to the suffering district from the base port and support relief works. Images for the general use and relief works during disaster are expressed in Figure 1.
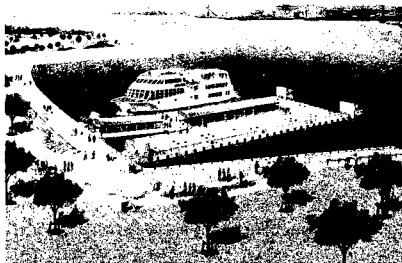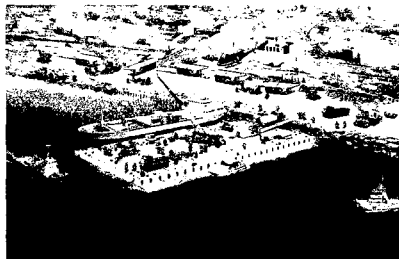
(a) General Use   (b) Relief works During Disaster

Figure 1.   Floating Disaster Prevention Basis

138

Structure

When a disaster occurs, the FDPB should be towed by a ship from the base port to the stricken district. Because the FDPB is different from a normal pontoon, the bottom of the shell is cut up. Required towing performance is given taking into account emergency as significant wave height $H_{1/3}$ = 1.5 m, significant wave period $T_{1/3}$ = 5s, wind speed V = 16m/s, and towing speed 5 knots. Based on the discussion of the committee organized to investigate the basic design of the FDPB, three structure types are proposed for each bays. They are steel type for Tokyo Bay, PC-Hybrid type for Osaka Bay, and RC-Hybrid type for Ise Bay (Fig. 2).

<table>
<tr><td>(a) Tokyo Bay (Steel)</td><td>(b) Osaka Bay (PC-Hybrid)</td><td>(c) Ise Bay (RC-Hybrid)</td></tr>
</table>
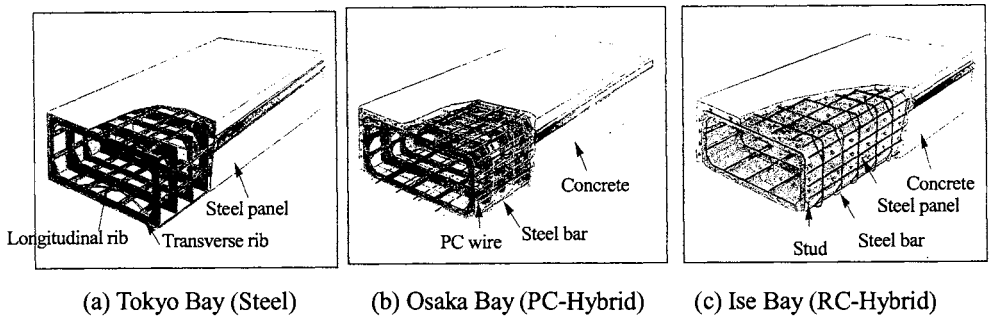
Figure 2.   Basic Structure of FDPB for each Bay

Structure type and size should be appropriately determined according to the site condition and the purpose of usage not only for an emergency but for usual use. The common specification for each structure type is that the length of the float should be 80 m to enable a 1,000 DWT class cargo ship come alongside it. According to the Technical Standards for Port and Harbor Facilities in Japan, the apron width of a pier will be 20 m for 7.5 m berth water depth. Kozawa et al. (2000) have already explained the detailed design conditions and structures. Here we describe the completed FDPBs.

Tokyo Bay
The FDPB is moored at Yokohama Port central harbor for small craft as shown in Figure 3. The size of the FDPB is 80 m in length, 25 m in width, and 4 m in height. Both sides are double decked and serviceable for both small and large vessels. The regular width of an apron for public use is 20 m as described before. Adding 5 m to the fundamental apron width 20 m, the width of the FDPB here is estimated to be 25 m so that mooring pillars do not disturb takeoff and landing for medium and small size helicopters. Inside the floating body, 1,000 tons water for human use can be stored. Usually, it is moored with chains and dolphins with rubber fenders. The weight of the connecting bridge is 50t and that of the hatch for carrying in supporting materials is 4t (totally 5t taking into account the bonding force for waterproof).

139
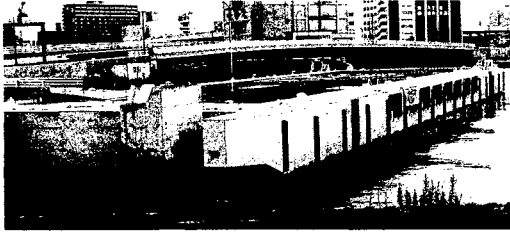
Figure 3.   Double Decked Steel Floating Disaster Prevention Basis (Yokohama Port)

Osaka Bay
The size of the FDPB is 80 m in length, 40 m in width, and 4 m in height.   Ordinary, as both sides of the FDPB can be used as berths for passenger boats, the width is estimated as 40 m taking into account the safety of passengers.   Generally, it is moored at the Universal City Port in Osaka City and used as a wharf for passenger and cruise ships (Fig. 4(a)).

In relief works, cargo handling is possible on both sides of the FDPB as the width of it is 40 meters. It has available space for a large helicopter (35 m*30 m).   Ordinarily, a roof tent for passengers is set.   It introduces combined mooring system of chain and rubber fenders to suppress the motion. Four anchors are prepared as emergency anchoring at the suffering district.   A 25t truck crane and a 4t truck can travel on the deck, and a 4t truck can pass the connecting bridge.   Relief goods can be stored on the deck about 1,600 ton, and that of about 3,000m^3 equivalent to the weight 400t can be stored inside the float.
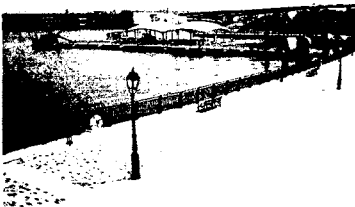
(a) Moored with Chain and Rubber Fenders   (b) Anchor used at Relief Works
Figure 4.   PC-Hybrid Type Floating Disaster Prevention Basis (Osaka Port)
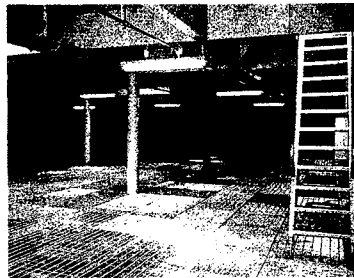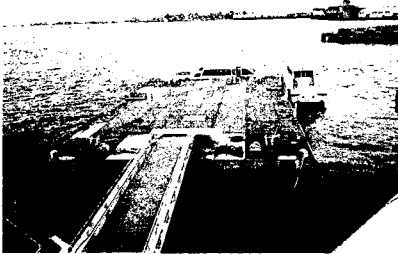
(a) Section B (20m*40m)   (b) Inside of Section A
Figure 5.   RC-Hybrid Type Floating Disaster Prevention Basis (Ise Bay, Nagoya Port)

140

Ise Bay
The structure of the FDPB is RC-Hybrid type. It is separable in two parts, namely A (40m*40m) and B (20m*40m) sections. It can be used as a single structure by linking the two sections with slide guides. The section B and inside view of the section A is shown in Figure 5. The reasons that the RC-Hybrid structure has been selected here are:
a. Rivers inflow to the mooring points and steel structure was prohibited,
b. Joint equipment can be set on side walls (it is impossible for PC-Hybrid),
c. Area of action will be the widest among three bays and it can be moored in shallow area such as -3m (it is impossible for PC-Hybrid structure),
d. Maintenance and alteration of structure are relatively simple.

Table 1 shows the specifications of each FDPB. The PC and RC-Hybrid structures have less displacement during disaster condition than the ordinary condition. In ordinary time, they are used as wharves for passenger and cruise ships. In order to adjust the freeboard as 1 m or 1.1 m for small ships, the displacements are increased in ordinary use to pour water into the ballast tank.

Table 1. Specifications of three bases

Specifications		Tokyo Bay	Osaka Bay	Ise Bay	
Type of Structure		Steel	PC-Hybrid	RC-Hybrid	
Length (m)		80	80	40	40
Width (m)		25	40	40	20
Height (m)		4	4	3.8	3.8
Freeboard (m)	Ordinary	3.3	1	1.5	1.1
	Disaster	2.1	1.5	1.5	1.5
Displacement (t)	Ordinary	1450	9840	3705	2212
	Disaster	3910	8200	3705	1095
Interior Volume (m^3)		2080	2300	1009	686
Necessary Towing Power (H.P.)		3500	13000	10000	5000

TRAINING EXERCISES

After the completion of the floating disaster prevention bases, it is recognized that the regular training exercises are quite important. The procedures to dispatch the FDPB in the case of Osaka Bay, for example, are as follows.

Criteria of action
When devastating disaster such as a big earthquake occurred in some area in which the Disaster Relief Act will be invoked, the anti-disaster headquarters of the prefecture, city, and town will ask the Kinki Regional Development Bureau of the Ministry of the Land, Infrastructure and Transport,

to send the Floating Disaster Prevention Basis for relief works.   The Bureau will make the decision of dispatching the FDPB.

Coverage area
The coverage area of the FDPB is that it can reach in about one day after the completion of the preliminary arrangements and towed in 4 knots/h (7.4 km/h).   In the case of Osaka Bay, almost all the area of the bay will be covered by the above-mentioned restriction.   For example, Kobe Port is 20 km from Osaka Port and it will take about three hours, and Wakayama-Shimozu Port 75 km with approximately 10 hours.

Policy
Required time that the anti-disaster headquarter at the suffering site can use the FDPB will be 48 hours from the request.   It will take one day for the preparation to leave the base port.   At the mooring base port, the connecting bridge is removed and is loaded onto the FDPB with a crane ship. Disconnection of the FDPB from the dolphins is also carried out with a crane ship.   Supporting goods, construction materials and machinery needed at the suffering district are procured and will be loaded to the FDPB.   The route of transportation will be applied to the Japanese Maritime Safety Agency.   It will take one day to tow the FDPB to the suffering district and to moor it at a fixed space.

It is considered that the anti-disaster headquarter will use the FDPB for two weeks after it is dispatched.   The reason is that the quay walls suffered from the Hanshin-Awaji Earthquake almost recovered its function by a rapid restoration works after 14 days of the disaster.   Another reason is that the amount of the land transportation cargo has exceeded that of the sea and air transportation after about 15 days of the disaster.   If the anti-disaster headquarters request the FDPBs staying to extend, it will be possible to extend the time at most one month from the arrival.   The expenditure of money on dispatch will be borne by the anti-disaster headquarter that requested the dispatch.

Results and suggestion obtained from the training exercises
Based on the training exercises conducted on February 5, 2002, at Osaka Port, some comments and suggestions are described below.   As it has passed about one year from the previous exercise, it took much time to release the mooring chains because rust had eaten deeply into the space of pin and anchor shackles.   The work at the narrow space on the dolphin and the requirement of truck crane because of the very heavy weight of mooring chain (about 1.3t) and anchor shackles, also contributed to require a great deal of time for release preparation.   Because of the restriction of the arrangement of wharfs, the four anchor winches of a derrick were moored asymmetrically, and the FDPB should be pulled out carefully between the narrow spacing of about 15 cm clearance on one side surrounded by the four fixed dolphins.   The technique to pull out the FDPB parallel to the normal line of the dolphins is important to avoid the minor collision.   It took much time to bring wires needed for the replacement of connecting bridge and another equipment for the preparation of towing.   One of the reasons is that the shipping of a truck crane is impossible on the wharf.   This time, the tent was left as it is.   In case of emergency, however, opening of a hutch and removal of the tent for the usage of a heliport are needed.   Such points at issue should be carefully considered.

Based on the training exercised conducted on September 1, 2001, at Yokohama Port, some comments and suggestions are described below. It was recognized to prepare the criteria to leave off the work at rough seas. The leave off criteria is as follows:

Wind speed   - 10 m/s or more,
Rain fall   - 20 mm/h or more,
Earthquake   - seismic intensity of 4 or more,
Wave height   - 1.5 m ore more.
Take shelter of the FDPB itself is not necessary.

A 25t hanging rafter crane was used to open the hatch (4.1t) and hanging of temporarily used mooring chains (3.6t/chain). In case of emergency, however, is it possible to provide such a crane promptly? It will be impossible to make lighter the hatches because the upper deck is designed for the 25t truck crane to be able to work on it. Therefore, it is a precondition to prepare hanging crane and necessary equipment before the relief action. As the weight of the connecting bridge is 50t, a large crane will be required. The structure of the bridge is designed to be able to float on the sea and can be towed to the destination. The arrangement of anchor chains under normal conditions is complicated and difficult to release, especially the anchor chains are quite heavy and the structure of dumpers are so complicated. The chains should be small to 78 mm in diameter and the dumpers for chains should be improved to open release type from above and below.

CONCLUSION

With the Great Hanshin-Awaji Earthquake as a turning point, three types of Floating Disaster Prevention Bases have been constructed. They are disposed in Tokyo, Ise, and Osaka Bays. Based on the training exercises and direct experiences, some suggestions and proposals for improving the FDPB system are obtained.

REFERENCES

Kozawa, T., Y. Miyachi , T. Koizumi, K. Wada, and Y. Matsushita. 2000. Provision of Floating Disaster Prevention Basis. In *Proceedings of the Techno-Ocean International Symposium*, 623-628 (623-626. In Japanese). Japan: Techno-Ocean 2000 International Symposium Secretariat, Japan.

BIOLOGICAL ACTIVITIES OF MULTIPLE LECTINS
FROM THE TOXOPNEUSTID SEA URCHINS

Hideyuki Nakagawa[1], Fumihiko Satoh[1], Hitomi Sakai[1],
Hiromi Hayashi[1] and Yasuhiro Ozeki[2]

[1]Department of Life Sciences, University of Tokushima
Tokushima, JAPAN
sea-hide@ias.tokushima-u.ac.jp

[2]Graduate School of Integrated Science, Yokohama City University
Yokohama-Kanagawa, JAPAN

ABSTRACT

The toxopneustid sea urchin, *Toxopneustes pileolus* and *Tripneustes gratilla* have well-developed globiferous pedicellariae with bioactive substances. Two D-galactose-binding lectins (SUL-I and SUL-II) and a heparin-binding lectin (TGL-I) were purified from *T. pileolus* and *T. gratilla* using gel filtration chromatography, affinity chromatography, and reverse-phase HLPC. SUL-I and SUL-II from the large flower-like globiferous pedicellariae of *T. pileolus* are D-galactose-binding proteins with molecular masses 32 kDa and 23 kDa, respectively (Nakagawa et al., 1999a). Furthermore, Contractin A (Nakagawa et al., 1991), a mannose-containing glycoprotein (18 kDa) from the ordinary globiferous pedicellariae of *T. pileolus* is also a novel lectin that causes smooth muscle contraction and relaxation. On the other hand, TGL-I from the small globiferous pedicellariae of *T. gratilla* is a Ca^{2+}-independent heparin-binding protein with a molecular mass of 23 kDa (Nakagawa et al., 1999a). SUL-I and Contractin A induced mitogenic stimulation on murine splenocytes but SUL-II and TGL-I did not. SUL-I had weak cytotoxic activity on murine splenocytes, and promoted chemotaxis of guinea-pig macrophages. SUL-I did not show a sequence homology to the N-terminal 21 amino acid sequence of SUL-II. However, SUL-I is related to fish egg lectins (Tateno et al., 1998; Hosono et al., 1999). On the other hand, SUL-II showed a sequence homology to Contractin A and UT841 from *T. plileolus* (Zhang et al., 2001), which may be a phospholipase A_2-like substance. The present results suggest that the toxopneustid sea urchins might be a resource for invertebrate lectins with an interesting mechanism of action.

INTRODUCTION

Most animal lectins can be classified into two groups: C-type lectins, which are dependent on Ca^{2+} for their carbohydrate binding activity; and galectins, soluble molecules that share characteristic amino acid sequences and specificity for ß-galactoside (Drickamer, 1988; Barondes et al., 1994; Kasai and Hirabayashi, 1996). Although in recent years, some ß-galactoside binding lectins have also been isolated from marine invertebrates (Yokosawa et al., 1986; Ozeki et al., 1991, 1997; Mikheyskaya et al., 1995), it is not clear that they appear to be a family of galectins. The toxopneustid sea urchins, *Toxopneustes pileolus* and *Tripneustes gratilla* have well-developed globiferous pedicellariae with bioactive substances. Some of these

bioactive substances caused deleterious effects such as severe pain, syncope respiratory distress, and loss of consciousness (Fujiwara, 1935; Mendes et al., 1963; Alender et al., 1965; Kimura et al., 1975; Mebs, 1984). We have recently purified a D-galactose-binding lectin (SUL-I) from the large flower-like pedicellariae of sea urchin, *T. pileolus*. SUL-I with a molecular mass of 32 kDa showed chemotactic properties for guinea-pig neurophils (Nakagawa et al., 1996). Although the physiological roles of SUL-I from the large globiferous pedicellariae of *T. pileolus* are unknown, it is suggested that the primary role of pedicellarial lectin may be defense and offense against a foreign body. More recently, we have also isolated a coelomic lectin from the coelomic fluid of *T. pileolus* (unpublished data). It is possible that animal lectins including those within the galectin family may function in a variety of biological processes. Direct evidences for particular functions have recently begun to accumulate for not only vertebrate lectins but also invertebrate lectins. Here we present the results on biological activities of pedicellarial lectins from the toxopneustid sea urchins, *T. pileolus* and *T. gratilla*.

MATERIALS AND METHODS

Toxopneustes pileolus (47 specimens) and *Tripneustes gratilla* (48 specimens) were collected along the coast of Shikoku Island and Okinawa Island Japan, from 1992 through 1996 (Fig. 1). Rabbit blood sample was obtained from Nippon Bio-test Lab. (Tokyo, Japan). Sephadex G-200 gel and heparin-Sepharose CL-6B were obtained from Amersham Biosciences Corp. (New Jersey, U.S.A.). Immobilized D-galactose gel was from Pierce (Illinois, U.S.A.). All the other chemicals were reagent grades.

Isolation of Sea Urchin Lectins
Thirty large flower-like pedicellariae per *T. pileolus* sea urchin specimen (8-10 cm in diameter) were removed with fine forceps. They were extracted with 20 ml of 0.15 M NaCl at 4°C for twenty-four hours. The 20 ml aliquot of each was centrifuged at 12,000 g for twenty minutes and the supernatant was used as the crude lectin extract (Nakagawa et al., 1996). Briefly, for the first step of purification, the crude extract was applied to a Sephadex G-200 column (2.6 x 80 cm) equilibrated with 0.15 M NaCl solution and was eluted with the same solution at a flow rate of 15 ml/hour. Fractions of 10 ml each were collected and analyzed for absorption at 280 nm and agglutinating activity. For the second step of purification, the gel chromatographic fractions (the second protein peak and third protein peak) were dissolved in 150 mm phosphate buffer and placed on an immobilized D-galactose column (1 x 2 cm). The sample was washed with same buffer and was eluted with 100 mM D-galactose in the same buffer. The 2 ml elution fractions were collected and analyzed for absorption at 280 nm and agglutinating activity. Each of the second peaks was pooled. Final purification was achieved by HPLC using a reverse-phase C$_8$ column. Two solvents, 0.1% trifluoroacetic acid (TFA) and acetonitrile in 0.08% TFA were used. The fraction was monitored at 230 nm. The main peaks were pooled and analyzed for agglutinating activity and SDS-PAGE, and then used as the purified sea urchin lectins (SUL-I and SUL-II). In the case of *T. gratilla*, the pedicellarial extract was fractionated as reported previously (Nakagawa et al., 1999a). The venom proteins from the pedicellariae were extracted with 20 ml distilled water at 4°C for twenty-four hours. Twenty ml aliquots of the extract were centrifuged at 12,000 g for twenty minutes and the supernatant was used as the crude lectin extract. The extract was applied to a Sephadex G-200 column equilibrated with 0.15 M NaCl

146

solution containing 10 mM lactose at flow rate of six ml/hour. Final purification was achieved by heparin-Sepharose CL-6B affinity chromatography. The gel chromatographic fraction (the first protein peak) was dissolved in 6.4 mM phosphate buffer saline (PBS), pH 7.2, and placed on a heparin-Sepharose CL-6B column (1 x 2 cm). The sample was washed with PBS and was eluted with 1.0 M NaCl in PBS. The 2 ml elution fractions were collected and analyzed for absorption at 280 nm and agglutinating activity. The second protein peak was collected and used a purified heparin-binding lectin (*Tripneustes gratilla* lectin-I, TGL-I). Contractin A from the ordinary globiferous pedicellariae of *T. pileolus* was purified as reported previously (Nakagawa et al., 1991).

Figure 1. Toxopneustid sea urchins, *Toxopneustes pileolus* (left), *Tripneustes gratilla* (right)

Agglutinating Activity
The agglutinating activity was assayed by using rabbit erythrocytes in microtiter plates. Twenty-five μl of 2% (V/V) suspension of erythrocytes in PBS was added to 50 μl of serial two-fold dilutions of the lectin fractions and purified sea urchin lectins. The plates were incubated at room temperature for one hour. The results were expressed by the minimum concentration of the test solution (μg/ml) required for positive agglutination.

Mitogenesis Assay
The mitogenic activity by murine splenocytes was determined by the cell culture assay using the tetrazolium salt MTT (3-[4,5-dimethylthiazol-2-yl]-2,5-diphenyl tetrazolium bromide). Fresh splenocytes were taken from female ddY mice (30-40 g) and suspended in a RPMI-1640 medium supplemented with penicillin and streptomycin (100 μg/ml and 100 U/ml). The splenocytes with or without concanavalin A (Con A) and lectin fractions were plated in flat-bottomed microtiter plates incubated at 37°C in a humidified atmosphere containing 5% CO_2 for sixty-eight hours. Ten μl of MTT (5 mg/ml) was then introduced in each well and the formazan in the cells was extracted with 10% sodium dodecyl sulfate (SDS). The optical density of each well was measured spectrophotometrically with microplate reader (Bio-Rad, model 450) at 570 nm.

Assays for chemotaxis and phagocytosis
Macrophages were induced by intraperitoneal injection of 1% glycogen solution into male guinea pigs (350-400 g), and collected by centrifugation in PBS (Ohura et al., 1990). The washed cells were resuspended in Dulbecco's modified Eagle's medium (DMEM) and adjusted

147

to a macrophage density of 1 x 10^6 cell/ml. The macrophage cell suspensions were plated in the 96-well plate at 100 μl per well and allowed to stand for one hour. Non-adherent cells were washed out by two washings with Eagle's balanced salt solution (EBSS). One-hundred μl EBSS containing fluorescein conjugated *Escherichia coli* bioparticles adjusted to 1 x 10^7 cell/ml were added to the adherent macrophages. After incubation for one hour at 37°C in a 5% CO$_2$-humidified atmosphere, extracellular fluorescence was quenched by 100-μl trypan blue (0.25g/ml of 13 mM citrate buffer), and the dye was removed. The fluorescence intensity was measured at 485 nm excitation and 530 nm emission using by a Cyto Fluor (PerSeptive Biosystems).

Amino Acid Sequence
The amino acid sequence was determined directly on a Shimadzu PPSQ-10 system protein sequencer.

RESULTS AND DISCUSSION

SUL-I and SUL-II from the large flower-like globiferous pedicellariae of *T. pileolus* are D-galactose-specific lectins with molecular masses 32 kDa and 23 kDa, respectively (Nakagawa et al., 1996, 1999b). On the other hand, TGL-I from the small globiferous pedicellariae of *T. gratilla* is a heparin-specific lectin with a molecular mass of 23 kDa (Nakagawa et al., 1999a). SUL-I induced mitogenic stimulation on murine splenocytes in lower dose ranges such as 0.5 μg/ml. At higher doses SUL-I had an inhibitory effect on the splenocytes. However, SUL-II and TGL-I did not induce significant activity on the splenocytes as shown in Figure 2.
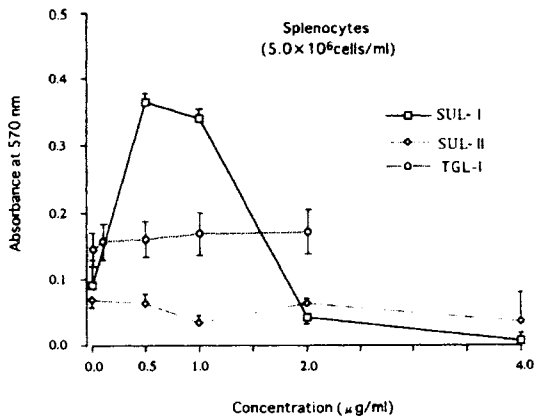
Figure 2. Comparison of mitogen response to SUL-I, SUL-II and TGL-I on murine splenocytes

Further studies of biological activities of SUL-II and TGL-I are in progress for comparison with those of SUL-I. More recently, we found that Contractin A, a mannose-containing glycoprotein (18 kDa) (Nakagawa et al., 1991) is a novel lectin that causes smooth muscle contraction and relaxation. Contractin A also induced mitogenic stimulation on murine splenocytes (data not shown). The dual response to SUL-I was effectively inhibited by 50 mM D-galactose (data not shown). Thus, the data suggest that SUL-I may exhibit mitogenic and inhibitory activities

148

through binding to D-galactose containing carbohydrates that are present on the surface of murine splenocytes. Moreover, it has been suggested that SUL-I binds to D-galactose residues of *Datura stramonium* agglutinin (DSA) to interfere with mast cell activation induced by DSA, a glycoprotein with arabinose and D-galactose residues (Suzuki-Nishimura et al., 2001). Our previous finding revealed that SUL-I induces chemotactic activity of guinea-pig neutrophils (Nakagawa et al., 1996).

In the present study, the chemotactic and phagocytic responses to SUL-I were also examined on guinea pig macrophages. SUL-I had chemotactic and phagocytic activities for guinea-pig macrophages in dose dependent manner (Fig. 3). In human polymorphonuclear leukocytes SUL-I exhibited chemotactic activity (data not shown). Chemotaxis and phagocytosis by leukocytes play an important role in the defense reactions to infection and injury in higher vertebrates. Thus, it is interesting that SUL-I as a chemoattractant may be a useful tool for biomedical research. Sequence analysis of intact SUL-I indicated N-terminal sequence from Ala-1 to Ile-35 (Nakagawa et al., 1999b). SUL-I shows five glycine residues in the sequence region. SUL-II was subjected to partial amino acid sequence analysis. The sequence of 21 residues from the N-terminal was established. The N-terminal amino acid is serine. SUL-II is rich in serine (Table 1). Although SUL-II did not show a sequence homology to SUL-I, it was found to be 45% and 40% homologous to the sequence of Contractin A (Nakagawa et al., 1991) and UT841 from *T. pileolus* (Zhang et al., 2001), respectively. SUL-II, Contractin A and UT841 may be a phospholipase A_2-like substance, because there is a good relationship to the amino acid sequence of phospholipase A_2 (Takasaki et al., 1990).

On the other hand, SUL-I is related to the segment Tyr-Gly-Arg of the rhamnose-binding lectins (SAL and STL2) from fish eggs (Tateno et al., 1998; Hosono et al., 1999). Although physiological roles of multiple lectins from the toxopneustid sea urchins are not well understood, our data suggest an extracellular function for SUL-I and Contractin A that may have wide-ranging effects, and suggest that these lectins can be used as valuable tool for analysis of inflammation, differentiation and development of cells. Further structural studies on SULs, Contractin A and TGL-I are needed to elucidate the biological functions of sea urchin venoms.
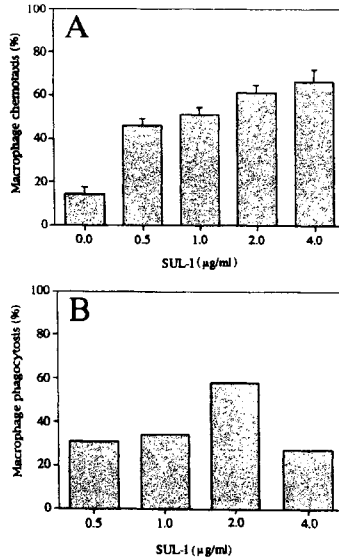
Figure 3. Effect of SUL-I on macrophage chemotaxis (A) and phagocytosis (B)

Table 1. Comparison of partial amino acid sequence of sea urchin lectins and fish lectins

Lectin	Oraganism	Sequence
SUL- I	Sea urchin (*T. pileolus*)	A V G R T X E G K S L D L E X P E G Y I I S V N Y A N Y G A N S P G Y
SUL- II	Sea urchin (*T. pileolus*)	S V I N F G W M S S X V T X X T S X R Y Y
Contractin A	Sea urchin (*T. pileolus*)	S V I N F G W M S S X V T X S T S T R Y N G Y G X Y X G F G G S X T P
SAL	Catfish (*S. asotus*)	A N M I T C Y G D V Q K L H - C E T G L I I V K S S L Y G R
STL 2	Steehead trout (*O. mykiss*)	(2) R V V T C D N G E N V Q F L I C D S G V I F I E R A L Y G R

ACKNOWLEDGMENTS

REFERENCES

Alender, C.B., G.A. Feigen and J.T. Tomita. 1965. Isolation and characterization of sea urchin toxin. *Toxicon*. 3(1):9-17.

Barondes, S.H., D.N.W. Cooper, M.A. Gitt and H. Leffler. 1994. Galectins. Structure and function of a large family of animal lectins. *J. Biol. Chem.* 269(33):20807-20810.

150

Bradford, M.M. 1976. A rapid sensitive method for the quantitation of microgram quantities of protein utilizing the principle of protein-dye binding. *Analyt. Biochem.* 72:248-254.

Drickamer, K. 1988. Two distinct classes of carbohydrate-recognition domains in animal lectins. *J. Biol. Chem.* 263(20):9557-9560.

Fujiwara, T. 1935. On the poisonous pedicellariae of *Toxopneustes pileolus* (Lamark). Annot. Zool. Japan. 15(1):62-69.

Hosono, M., K. Ishikawa, R. Mineki, K. Murayama, C. Numata, Y. Ogata, Y. Takayanagi and K. Nitta. 1999. Tandem repeat structure of rhamnose-binding lectin from catfish (*Silurus astotus*) eggs. *Biochem. Biophys. Acta.* 1472:668-675.

Kasai, K. and J. Hirabayashi. 1996. A family of animal lectins that decipher glycocodes. *J. Biochem.* 119(1):1-6.

Kimura, A., H. Hayashi and M. Kuramoto. 1975. Studies of urchi-toxins: Separation, purification and pharmacological actions of toxinic substances. Japan. *J. Pharmacol.* 25(2):109-120.

Laemmli, U.K. 1970. Cleavage of structural protein during the assembly of the head of bacteriophage T4. *Nature.* 227(259):680-685.

Mebs, D. 1984. A toxin from the sea urchin *Tripneustes gratilla. Toxicon.* 22(2):306-307.

Mendes, E.G., L. Abbud and S. Umiji. 1963. Cholinergic action of homogenates of sea urchin pedicellariae. *Science.* 139(3553):408-409.

Mikheyskaya, L.V., E.V. Evtushenko, R.G. Ovodova, N.I. Belogortseva and Y.S. Ovodov. 1995. Isolasion and characterization of a new ß-garactose-specific lectin from the sea worm *Chaetopterus variopedatus.* Carbohydr. Res. 275:193-200.

Nakagawa, H., A. Tu and A. Kimura. 1991. Purification and characterization of Contractin A from the pedicellarial venom of sea urchin, *Toxopneustes pileolus. Arch. Biochem. Biophys.* 284(2):279-284.

Nakagawa, H., T. Hashimoto, H. Hayashi, M. Shinohara, K. Ohura, E. Tachikawa and T. Kashimoto. 1996. Isolation of a novel lectin from the globiferous pedicellariae of the sea urchin *Toxopneustes pileolus. Adv. Exp. Med. Biol.* 391:213-223.

Nakagawa, H., C. Yamaguchi and H. Hayashi. 1997. Biologically active substances from sea urchins. *J. Natural Toxins.* 6(2):193-202.

Nakagawa, H., C. Yamaguchi, H. Sakai, K. Kanemaru and H. Hayashi. 1999a. Biochemical and physiological properties of pedicellarial lectins from the toxopneustid sea urchins. *J. Natural Toxins.* 8(3):297-308.

Nakagawa, H., C. Yamaguchi, F. Tomiyoshi and H. Hayashi. 1999b. A novel mitogenic lectin from the globiferous pedicellariae of sea urchin, *Toxopneustes pileolus*. *Jour. Chem. Soc. Pak.* 21(3):305-310.

Ohura, K., M. Shinohara, K. Ogata, A. Nishiyama and M. Mori. 1990. Leucocyte function in rats with naturally occurring gingivitis. *Archs. Oral Biol.* 35 Suppl.:185s-187s.

Ozeki, Y., T. Matsui and K. Titani. 1991. Amino acid sequence and molecular characterization of a D-galactose-specific lectin purified from sea urchin (*Anthrocidaris crassispina*) eggs. *Biochemistry.* 30(9):2391-2394.

Ozeki, Y., E. Tazawa and T. Matsui. 1997. D-galactoside-specific lectins from the body wall of an echiuroid (*Urechis unicinctus*) and two annelids (*Neanthes japonica* and *Marphysa sanguinea*). *Com. Biochem. Physiol.* 118B(1):1-6.

Suzuki-Nishimura, T., H. Nakagawa and M.K. Uchida. 2001. D-galactose-specific sea urchin lectin sugar-specifically inhibited histamine release induced by *Datura stramonium* agglutinin: Differences between sugar-specific effects of sea urchin lectin and those of D-galactose- or L-fucose-specific plant lectins. *Japan Journal of Pharmacology.* 85(4):443-452.

Takasaki, C., F. Yutani and T. Kajiyashiki. 1990. Amino acid sequences of eight phospholipase A_2 from the venom of Australian king brown snake, *Pseudechis australis*. *Toxicon.* 28(3):329-339.

Tateno, H., A. Saneyoshi, T. Ogata, K. Muramoto, H. Kamiya and M. Saneyoshi. 1998. Isolation and characterization of rhamnose-binding lectin from eggs of steelhead trout (*Oncorhynchus mykiss*) homologous to low density lipoprotein receptor superfamily. *J. Biol. Chem.* 273(30):19190-19197.

Yokosawa, H., K. Harada, K. Igarashi, Y. Abe, K. Takahashi and S. Ishii. 1986. Galactose-specific lectin in the hemolymph of solitary ascidian, *Halocynthia roretzi*. Molecular, binding and functional properties. *Biochem. Biophys. Acta.* 870:242-247.

Zhang, Y., J. Abe, A. Siddiq, H. Nakagawa, S. Honda, T. Wada and S. Ichida. 2001. UT841 purified from sea urchin (*Toxopneustes pileolus*) venom inhibits time-dependent $^{45}Ca^{2+}$ uptake in crude synaptosome fraction from chick brain. *Toxicon.* 39(8):1223-1229.

DEVELOPMENT OF A HYDRATE-BASED NATURAL GAS TRANSPORTATION SYSTEM

Toru Iwasaki, Yuuichi Katoh, Takashi Arai,
Kiyoshi Horiguchi and Kazuyoshi Matsuo

Mitsui Engineering and Shipbuilding Co., Ltd.
Ichihara, Chiba, JAPAN
iwasakir@mes.co.jp

ABSTRACT

Natural Gas hydrate can contain a lot of gas in it and its production, transport and storage can be made under milder thermal condition than that of LNG. Mitsui Engineering & Shipbuilding Co., Ltd., utilizing such characteristics of natural gas hydrate, is now developing an integrated system for its production, pelletizing, storage, ocean transporting, and gasification. This paper describes the results of our experiments with methane hydrate to verify each component technology such as production, pelletizing, storing and gasification technologies. Through various experiments with such component technologies, the feasibility of the transport system of natural gas hydrate has been confirmed.

INTRODUCTION

Natural gas usage continues to grow in response to the need to cope with global environmental issues while securing a convenient and stable source of energy. Currently, the long distance ocean transport of natural gas to consumer markets is achieved by an integrated Liquefied Natural Gas (hereinafter called LNG) system. However, this system needs huge capital investments for LNG production facilities, LNG carriers and so on, which are economic only with very large-scale gas fields. Accordingly, the development of a simpler, lower cost natural gas transportation system is strongly required to meet the growing worldwide demand for natural gas.

Natural Gas Hydrate (hereinafter called NGH) is a solid substance resembling ice, which sometimes clogs natural gas and crude oil pipelines. Although previously regarded as a nuisance, NGH has been found to have unique characteristics that make it a good candidate as a storage and transport medium for natural gas. In particular, it can be easily made at rather high temperatures compared with LNG and it can contain gas about 160 times its volume. Based upon these characteristics, Gudmundson, Norwegian University of Science and Technology et al published a paper in 1996 introducing a natural gas transportation system based on powdered NGH. The paper reported on the artificial production of NGH using natural gas and water and the storage and transportation of powdered NGH across the sea at a temperature of -15°Celsius. This system results in cost reduction of about 24% compared with the conventional LNG system, especially in terms of the capital investment required.

On the basis of the results reported in the above-mentioned paper, Mitsui Engineering & Shipbuilding Co., Ltd. (hereinafter called MES) is now developing its own high volume, long distance NGH-based natural gas transportation system. The development of the system's process component technology has now reached the stage of concept demonstration using a continuous process pilot plant. This paper introduces the results obtained with each component process such as production, pelletizing, storage and gasification of NGH, which together will compose one continuous system of NGH transportation.

CONCEPT OF AN NGH-BASED NATURAL GAS TRANSPORTATION SYSTEM

Figure 1 shows the NGH-based long distance, bulk natural gas transportation system now being developed by MES. The special feature of this system is the use of compressed powdered NGH pellets for transportation and storage of natural gas. In this system, powdered NGH with particle sizes of dozens of μm - several mm is pelletized into spheres of dozens of mm in diameter. Pelletizing increases both the bulk density of NGH and the packing efficiency during storage in comparison with powdered NGH. Pelletized NGH also has superior fluidity, and therefore its compaction and adhesion decrease, making its handling much easier and enabling time savings in handling for storage on land and in the cargo holds of ocean going carriers. Furthermore, the remarkable reduction in the specific surface area of the pelletized NGH (when compared with that of powdered NGH) is expected reduce the amount of gas dissociation during the storage. In the transportation system (Fig. 1), the natural gas extracted from the gas field is processed to remove the interfused sour gas and later mixed with water to produce NGH. After dewatering, the NGH is pelletized by a pelletizer before being temporarily stored in a tank before being loaded into the storage tanks of a bulk carrier.

On reaching its destination, the pelletized NGH is unloaded and stored temporarily in a storage tank awaiting gasification and subsequent distribution to consumers. Residual dissociation water at the gasification is used as pellet carrier ballast water and is brought back to the loading port where it is used again used for producing NGH. By making each component process faster and more efficiently adapted to mass production, it will be cheaper to both build and operate and hence will enable the exploitation of smaller and currently uneconomic gas fields, thereby increasing the world's usable natural gas reserves.
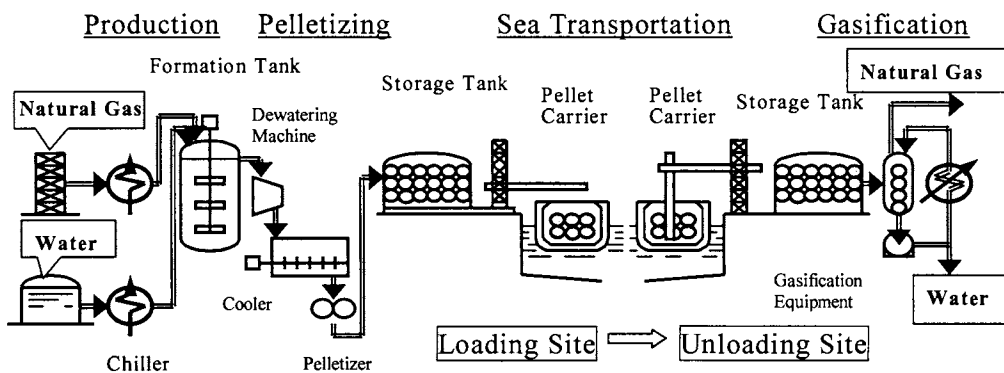
Figure 1. NGH-based Natural Gas Transportation System

154

EXPERIMENTAL STUDIES OF THE SYSTEM'S COMPONENT TECHNOLOGIES

The main components of the NGH pellet transport system technology shown in Figure 1 are: 1) NGH Formation Characteristics, 2) NGH Pelletizing Characteristics, 3) Pellet Storage Stability and 4) Gasification Characteristics. Experimental studies were carried out on each component technology to determine its applicability to a system using methane gas, the main component of natural gas. The results are described hereinafter.

NGH Formation Characteristics

Parameters affecting the formation rate of NGH are formation pressure, super-cooling (the difference between equilibrium temperature and formation temperature) and the contact surface area of gas and water. Of the three NGH formation methods currently used, i.e., the mixing, bubbling and spray methods, a method combining the mixing and bubbling methods was adopted as it can remove formation heat quickly, thereby enabling quick formation of NGH. This paper therefore describes the experimental results obtained with the combined method.

Figure 2 shows the formation tank used to produce the NGH. The tank is a pressure vessel of 10-liter capacity. Figure 3 shows the mixing and bubbling conditions inside the formation tank. Experimental parameters selected were mixing strength, bubbling gas volume and the super-cooling. NGH formation rate was calculated from methane gas flow rate assuming Hydrate Number is 6.2. Figure 4 shows an example of the experimental results which indicates that the amount of NGH formation increases proportionally with the increase in mixing Reynolds number and super-cooling. It is assumed that the increase in the contact surface area of water and gas is caused by the combination of the mixing and bubbling methods, and this, along with the removal of formation heat to maintain super cooling are the keys to the high speed production of NGH. Figure 4 also shows that the amount of NGH formation per initial filling water is about 1.2 kg/h/L, which implies that mass production of NGH with this system is quite feasible.
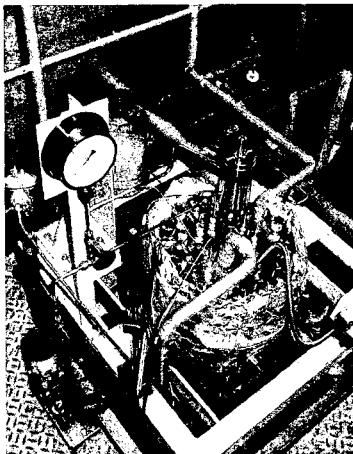
Figure 2. Formation tank

Figure 3. Mixing and bubbling conditions in Formation tank

155
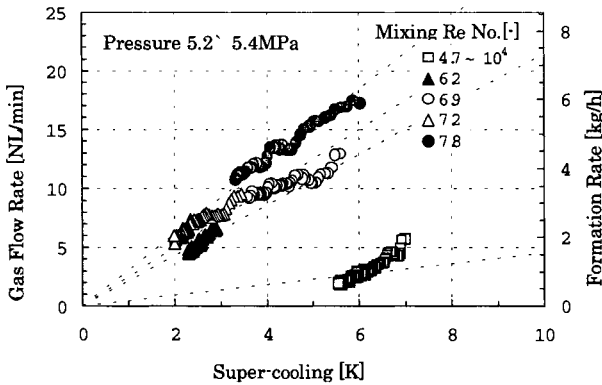
Figure 4. Relation of NGH formation rate and
super-cooling

NGH Pelletizing Characteristics

Figure 5 shows the continuous pelletizer, and Figure 6 shows NGH pellets of φ20 mm made from powdered NGH. Of the three pelletizing methods currently in use, i.e. rolling, fluidized bed and compression molding, compression molding was chosen as it produces pellets with superior strength, which is important during prolonged and loading/unloading as well as producing pellets with a rounder shape. This is important for better fluidity, along with greater pellet homogeneity. Studies of the production method were also made, however, with a view to improving storage and transport efficiencies. As shown in Figure 6, it is confirmed that NGH can be pelletized under several MPa (max.) compression resulting in nearly perfectly round pellets. Separate pellet static collapse tests also confirmed that pellets made under the aforementioned conditions can bear about 0.21 MPa, which is the collapse pressure calculated by the static compression load from the ship's cargo hold top to its bottom and by the oscillation acceleration of the carrier ship. Slight adhesion between pellets was witnessed under loaded conditions typical of storage in a ship's hold, but it is judged that it can be avoided by controlling storage atmosphere properly.
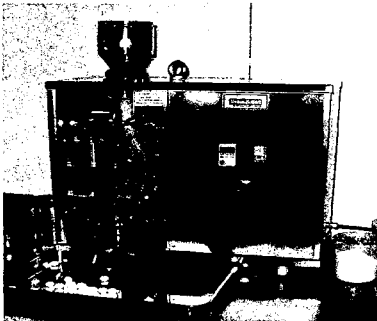
Figure 5. Continuous pelletizer

Figure 6. NGH pellets

156

Stability of Stored Pellets

The biggest concern about mass storage of palletized NGH during ocean transport is dissociation control, or ensuring the stability of the gas contained in the pellets during bulk transport over long periods. With methane hydrate, the equilibrium temperature under atmospheric pressure is about -80°C (Sloan, 1998). In general, NGH dissociates into gas, water or ice at above the equilibrium temperature. However, a self-preservation effect, by which NGH can be kept at above the equilibrium temperature, was announced by Yakushev et.al in 1992. The mechanism of the self-preservation effect is that when NGH formed under high-pressure and low-temperature is brought back to the low-pressure condition, a part of NGH dissociated on its surface forms an ice membrane on NGH which controls the dissociation of inner NGH. Meanwhile, Ebinuma et al. (1992), have announced that if the NGH is scattered onto ice below freezing point, dissociation of NGH is fairly well controlled even under thermodynamically unstable atmospheric pressure conditions, implying the possibility of NGH transport at storage temperatures as high as -15°Celsius. Applying this self-preservation effect, experimental studies were carried out to determine the feasibility of securing stable storage of pelletized NGH over long periods under atmospheric pressure in ten Centigrade minus numbers. Experimental equipment was an 11 ml container filled with pelletized NGH with a pinhole (φ0.8 mm) to eliminate pressure buildup, and the stability of the pelletized NGH was determined by measuring changes in its weight, as a reduction in weight was attributable to gas dissociation. The two-week experiment was to simulate bulk ocean transport of pellet NGH by a carrier ship.

Figure 7 shows the measured weight changes of powdered and pelletized NGH stored at a temperature of -20° Celsius. As can be seen, Figure 7 shows that the pelletized NGH is far more stable than powdered NGH, as pelletized NGH gas dissociation under these conditions was below 0.25wt%/d of total gas weight, which is stable enough for practical use, because this dissociation rate is almost equal to the boil off gas rate of LNG carrier. Figure 8 shows the change in dissociation rate over time at different storage temperatures. Stability due to self-preservation is well maintained between -20°C and -15°C, but a sharp increase in gas dissociation is evident at minus 5° Celsius. Accordingly, it is suggested that NGH pellets formed using the techniques reported herein should be stored at below -15° Celsius.
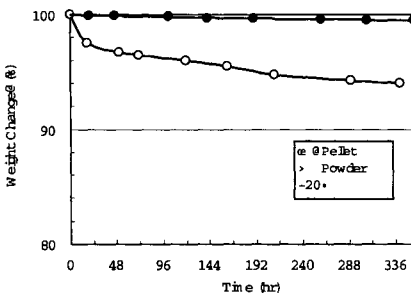
Figure 7. Respective dissociation rate of pellet and powder
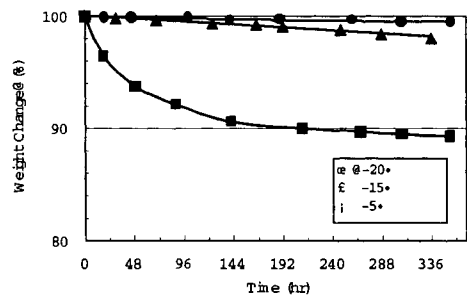
Figure 8. Relation between storage temperature and dissociation rate

157

Gasification Characteristics

As noticed from the self-preservation effect, NGH, when dissociated, makes an endotherm taking heat from the circumference, which means that the NGH itself will be cooled down and gas dissociation eventually decreases. When the gas contained in NGH needs to be utilized, the pellets it need to be heated to accelerate the gas dissociation, the need to respond quickly to changes in gas demand may sometimes require considerable heat energy. Our experiment assumes that the pelletized NGH would be gasified rather rapidly and therefore gasification characteristics were investigated with gasification temperature and pellet size as experimental parameters. Figure 9 shows gasification experimental equipment. Experimental conditions were as follows: Pellets were all of φ20mm. Several pellets were put simultaneously into a gasification tank. Gasification was achieved by heating the water in the tank through the tank shell using a thermostat. The gasification pressure was set at 3.6MPa assuming pressure feeding of gas by pipeline.
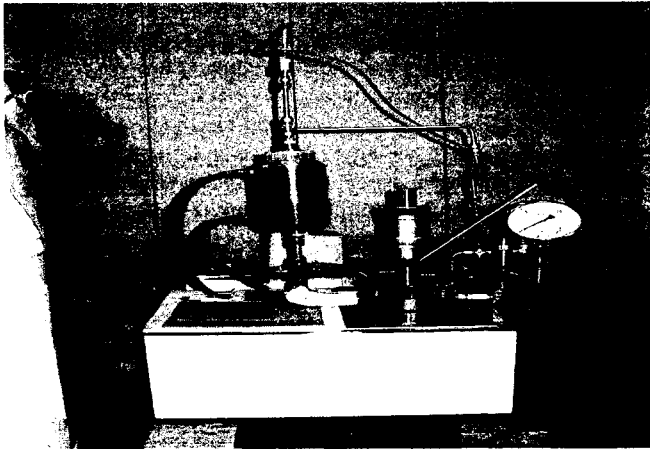
Figure 9. Gasification test equipment

Figure 10 shows how gasification rate changes at 3.6 MPa according to the differences between NGH equilibrium temperature and gasification temperature. Figure 11 shows a comparison of gasification rate between pelletized and powdered NGH by size simulation. Figure 10 shows that gasification gas increases in proportion to the temperature difference between the pellets and the heat medium. This is because calorific transfer to the pellets differs with temperature difference. Figure 11 shows rapider gasification rate for the powdered NGH than for the pellet, which is believed due to differences in surface area to the weight. The pellet gasification rate depends on and is limited by the heat transfer efficiency between the pellets and the heat medium. The experiment also suggests that the adjustment of pellet size by crushing will increase the pelletized NGH gasification
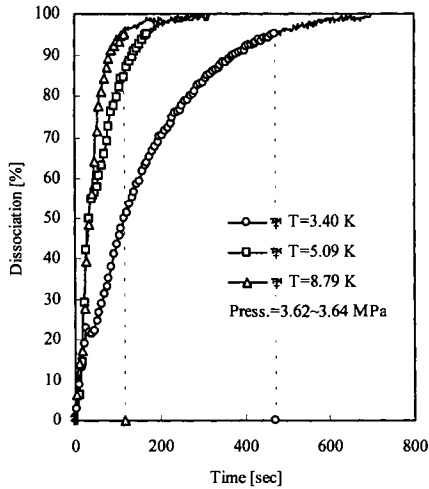
Figure 10. Gasification rate with ΔT
(ΔT: Difference between the equilibrium
temperature and gasification temperature)
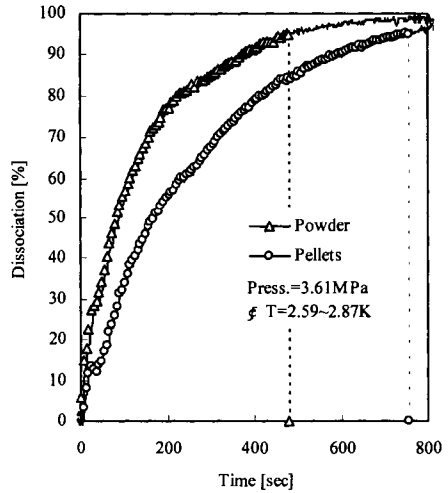
Figure 11. Gasification rate of pellet
and powder

CONCLUSION

The development and confirmation of the effectiveness of the various component technologies in our study has proved that the long distance transportation of natural gas by pelletized NGH is technically quite feasible. MES is now building a pilot plant combining each component of the process such as production, pelletizing, storage, transportation in bulk and gasification into one continuous system. Upon completion of the plant, we will collect more engineering data and scale-up data of the system through various tests and operations and further will proceed to an economic feasibility study. It is our intention and commitment to realize a system for natural gas transport by the Pelletized Natural Gas Hydrate in the near future.

ACKNOWLEDGEMENTS

REFERENCES

Ebinuma, T. and N. Maeno. 1992. Mechanical behaviors of polycrystalline ice containing pressurized gas enclosures, *Physics and Chemistry of Ice*, Hokkaido University Press, Sapporo, Japan.

159

Gudmundsson, J.S. and A. Borrehaug. 1996. Frozen hydrate for transport of natural gas, *Proceedings of 2nd International Conference on Gas Hydrate,* Toulouse, France.

Sloan Jr., E. Dendy. 1998. Clathrate hydrates of natural gas - 2nd ed., rev. and expanded, Marcel Dekker, New York.

Stern, L.A., et al. 2000. Anomalous preservation of pure methane hydrate at 1 atm, *Journal of Physical Chemistry* B, 105, 1756-1762.

Yakushev, V.S. and V.A. Istomin. 1992. Gas hydrates self-preservation effect, *Proceedings of Physics and Chemistry of Ice '91* Symposium, Hokkaido Univ., Sapporo, Japan.

USE OF HYDRATE FOR NATURAL GAS TRANSPORTATION
--- INTRODUCTION OF RESEARCH PROJECT ---

**Hideyuki Shirota[1], Kenjiro Hikida[1], Yasuharu Nakajima[1], Susumu Ota[1],
Tatsuya Takaoki[2], Toru Iwasaki[3] and Kazunari Ohgaki[4]**

[1]Department of Maritime Safety, National Maritime Research Institute
Mitaka, Tokyo, JAPAN
shirota@nmri.go.jp

[2]Mitsui Engineering and Shipbuilding Co., Ltd., Chuo, Tokyo, JAPAN
[3]Mitsui Engineering and Shipbuilding Co., Ltd., Ichihara, Chiba, JAPAN
[4]Osaka University, Toyonaka, Osaka, JAPAN

ABSTRACT

Almost all natural gas consumed in Japan is liquefied at a low temperature below -150°C, and is transported by liquefied natural gas (hereinafter called LNG) carriers. This mode of transportation requires substantial energy consumption for producing LNG. If the 'self-preservation' property of gas hydrate can be utilized economically in addition to its high-density gas containing property, it is possible to store and transport stranded natural gas at higher temperature and lower pressure compared to the conventional LNG method. The authors are pursuing the hopeful prospect that natural gas hydrate (hereinafter called NGH) could be a medium for natural gas transportation, and are examining the properties of hydrate, as well as handling and quality control issues for NGH cargo forms. The authors also found that marine transport of natural gas in the form of natural gas hydrate pellets (NGHPs) would be available, and started the three-year research project last year under the financial support by the Corporation for Advanced Transport & Technology. The project consists of (1) the investigation on microscopic properties of a single NGHP by using laser Raman spectroscopy and plasma replica methods, (2) the evaluation of thermal and mechanical properties of NGHPs, and (3) the conceptual design of an NGHP carrier, i.e., a specially constructed bulk carrier fitted with insulated cargo holds. The authors conducted preliminary self-preservation experiments of pelletized methane hydrate. Both at -5°C and -10°C, only approximately 5% of the theoretically contained gas remained in the MHPs' sets after a lapse of 3 weeks from the base time. On the other hand, at -15°C/-20°C, approximately 0.5 to 0.75 of the theoretically contained gas remained in the MHPs' sets even after a lapse of three weeks from the base time. It is qualitatively assumed that the dissociation rate of the MHPs' set used in the experiment decreased monotonically as the temperature around the set dropped. The MHPs' set dissociated rather slowly at -20°C in the experiments, so it is assumed that the MHP's self-preservation is maintained on the time scale including seaborne transportation. Namely, there is assumed to be every possibility of transporting NGHPs by ship from the viewpoint of hydrate's self-preservation.

INTRODUCTION

The thermodynamic equilibrium temperature below which methane hydrate remains stable at 1 atm methane pressure is about -80° Celsius. In recent years, however, it has been reported that methane hydrate remains metastable under some conditions outside its stability region by Yakushev et al. (1992) and Stern et al. (2001). According to the above groups, methane hydrate may remain metastable at temperatures 50°C to 75°C above its 1atm dissociation temperature.

Or, Gudmundsson et al. (1994) confirmed metastability of methane-ethane-propane hydrate plus ice mixtures, whose composition was selected to represent natural gas from North Sea fields. The metastability of hydrate is usually called 'self-preservation'. Japan has never had abundant indigenous energy resources, and has imported virtually all of its energy supplies. Since the exhaust gas of combusted methane is relatively clean compared to conventional fossil fuels such as coal and oil, natural gas consumption in Japan is expected to rise in the future. According to the government forecast of long-term energy supply and demand, natural gas consumption in Japan will reach about 1.7 times the present consumption in more than 15 years (Max, 2000).

Although a great deal of natural gas is globally transported through pipelines from gas fields to consumer markets, almost all natural gas consumed in Japan is presently liquefied at extremely low temperature below -150°C, and is stored/transported by LNG carrier. However, the energy loss due to liquefaction is rather high in this method; it is reported that the energy loss due to liquefaction accounts for 8.8% of the energy content of natural gas (Tamura et al., 1999). If the 'self-preservation' property of hydrate can be utilized economically in addition to its high-density gas containing property, it is possible to store and transport stranded natural gas at higher temperatures and lower pressures compared to the conventional LNG method. This method has the potential not only for prevention of the energy loss due to liquefaction, but also for reduction of equipment costs for liquefaction and storage.

RECENT RESEARCH ON THE GAS HYDRATE SELF-PRESERVATION EFFECT

Among some reports upon the self-preservation property of gas hydrate which have been submitted thus far, principle papers are interpreted as follows. Yakushev et al. (1992) conducted methane hydrate dissociation experiments at atmospheric pressure by using several samples in different conditions. They observed various dissociation behaviors and preservation periods depending upon humidity, surface/mass ratio in hydrate sample, temperature, light radiation, etc. Preservation periods of some samples ranged from several months to a few years. They suggested that this self-preservation property of gas hydrate occurs because thin ice films, impermeable to gas molecules, form on hydrate surfaces during depressurization and interrupt further dissociation of the hydrate.

Gudmundsson et al. (1994) made mixed-gas hydrate at pressures from 2MPa to 6MPa and at temperatures from 0°C to 20°C, from a 92:5:3 methane:ethane:propane mixture, which should form structure II that is stable to much warmer temperature and lower pressure than structure I methane hydrate. The amount of water converted to hydrate was 27% to 44% in these experiments. Temperature was decreased adiabatically to -18°C at high pressure, and hydrate samples were kept frozen in a freezer for 24 hours. They examined metastability of the hydrate after rapid depressurization to atmospheric pressure, confirming that the samples remained meta-stable at -18°C, -10°C and -5°C at atmospheric pressure and dissociated only slightly in 7 days to 10 days. Based on the experimental results, Gudmundsson et al. (1996) examined natural gas transportation by hydrate from an economical viewpoint. They compared a NGH transportation chain (including production plant, hydrate carriers and re-gasification plant) to an equivalent conventional LNG transportation chain, on the assumption of natural gas transportation of 3.5 billions cubic meters over 5,500 kilometers. As a result, the capital cost of the NGH chain was estimated to be 24% lower than the capital cost of an equivalent LNG chain. In the latest study of Gudmundsson et al. (2000), an NGH slurry (mixture of natural gas hydrate and crude oil) process was also examined using floating production storage and offloading (FPSO) vessel for stranded natural gas utilization.

Stern et al. (2001) conducted thorough experiments on dissociation regions of methane hydrate at atmospheric pressure over the temperature range from -78°C to 17° Celsius. According to Stern et al., there are three distinct dissociation behaviors when the hydrate was removed from its

162

stable field by rapid depressurization. Of them, the regime between -31°C and -2°C has an anomalously slow dissociation rate of hydrate. At the temperature of -5°C, the dissociation percentages within 24 hours and one month after dissociation start were 7% and 50% respectively (confirmed as shown in Stern et al. (2002)), which were the best results of self-preservation. In the latest study of Stern et al. (2002), they stated it is highly probable that ice 'shielding' effects provided by partial dissociation along hydrate grain surfaces are not the primary mechanism for the anomalous preservation behavior observed in rapidly depressurized samples, in the light of SEM imaging of hydrate sample materials and their experimental results on both structure I and structure II gas hydrates.

Also in Japan, Shirota et al. (2002) examined experimentally the influence of dissociation temperature upon pure methane hydrate dissociation between -7.5°C and 0° Celsius. They obtained relatively extremely slow dissociation data within temperature range between -7.5°C and -3°C, which coincided with the report by Stern et al. qualitatively but differed from them quantitatively. They also estimated the period at which all samples finished dissociating at approximately 120 days, and concluded that the estimate seemed to be very promising for practical application of self-preservation property to natural gas storage and transportation. Although some ideas for the mechanism of the hydrate's self-preservation effect have been proposed as stated above, the details of the mechanism are still poorly understood.

RESEARCH PROJECT FOR NATURAL GAS TRANSPORTATION UTILIZING HYDRATE PELLET

Mitsui Engineering & Shipbuilding Co., Ltd. (MES), National Maritime Research Institute (NMRI) and Osaka University had a hopeful prospect that NGH could be a medium for natural gas transportation, examining the properties of hydrate, handling, and quality control for some NGH cargo forms (Takaoki et al., 2002; Nakajima et al., 2002). The authors also found that seaborne transportation of natural gas in the form of natural gas hydrate pellets (NGHPs) would be available, and have started the three-year collaborating research project 'Research on Transportation of Natural Gas Using Gas Hydrate Pellets' under the financial support from the Corporation for Advanced Transport & Technology (CATT) since July 2001. Partial responsibilities of each research group in the project are as follows: MES mainly oversees the conceptual design of a NGHP carrier that is specially constructed with thermally insulated cargo holds. Transportation plans and design of the carrier are considered, including ports of loading/unloading, total amount of transportation per year, number of ships, and capacity. Other elemental systems of the NGHP carrier that are considered include: propulsion systems, cargo handling systems, residual cargo processing systems, explosion prevention systems, evolved gas processing systems, cargo holds, and ballast tanks.

At NMRI, thermal/mechanical properties of NGHPs in bulk are examined. Specific heat and thermal conductivity are measured and evaluated in addition to NGHPs' self-preservation property. Heat transfer and temperature in cargo holds is analyzed by numerical simulation taking into account dissociation heat and phase change effects, and NGHPs' dissociation is estimated based upon experimental data including their compressed conditions. In parallel, safety measures for NGHP carriers are also considered; regulations for transport of dangerous goods are investigated, and necessary safety functions/measures are clarified. The research at Osaka University is focused upon both crystal morphology and surface structure of a single NGHP. In the former, the relation between crystal morphology and stability of the single NGHP due to phase change resulted from contained gas other than methane is investigated using laser Raman spectroscopy. In the latter, dissociation rate and surface structure change of the single NGHP are examined using plasma replica method.

PRELIMINARY SELF-PRESERVATION EXPERIMENTS
OF METHANE HYDRATE PELLETS

The authors have already obtained some meaningful results so far in the research project. From among them, introduced is the result of preliminary self-preservation experiments of pelletized methane hydrate, which were conducted to estimate their self-preservation property. The methane hydrate pellets (MHPs) tested in these experiments were made by MES, using methane hydrate production and pelletization trial machines. The photograph of the MHPs is shown in Figure 1. The MHP is a spherical body with the weight of approximately 3 grams and the diameter of 20 millimeters. Methane hydrate powder was synthesized in mixing method from water and pure methane gas (99.99% purity) at 5.2MPa to 5.4MPa and at the temperature lower by 2K to 7K than the methane equilibrium temperature corresponding to the pressure. After taken out from the mixer, the hydrate powder was kept in a Dewar vessel at roughly -196°C with liquid nitrogen. The hydrate powder was taken out and pelletized one at a time with a trial compressor at atmospheric pressure and at -20° Celsius. No extra heat and no ice were added during the pelletization process. Then, it is supposed that hydrate dissociation partly started and the pellet was a mixture of methane hydrate and ice. Thermal history of the hydrate powder/pellets was not controlled thoroughly, since the machine was developed for the main purpose of NGHPs' high-speed mass production. Manufactured MHPs had been kept in a Dewar vessel at roughly -196°C with liquid nitrogen again until they were used in the experiments.
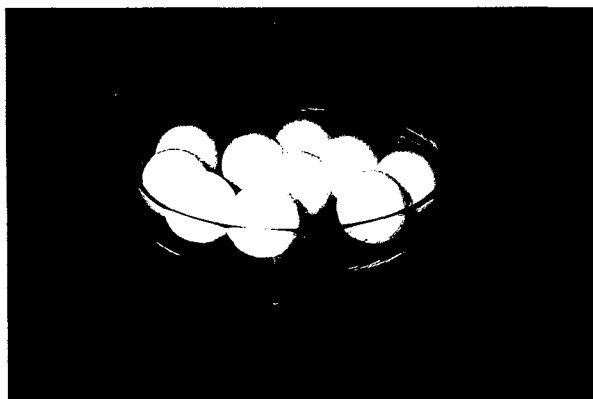
Figure 1. Photograph of methane hydrate pellets

In the experiments, weight change for one set of five MHPs was measured using an electronic balance (the minimum graduation: 1 milligram). Enclosed in a container with small holes, each MHPs' set was stored in a freezer that was kept at -20°C, -15°C, -10°C and -5°C respectively, in order to examine influence of temperature changes upon MHPs' self-preservation property. This temperature variation was specifically chosen to simulate the possible temperature fluctuations of the cargo hold during shipment (Ohta et al., 2002). The measurement period was set at three weeks, simulating a shipment time from natural gas fields in southeastern Asia to Japan, and taking into account storage on land. Shown in Figure 2 is the weight change of MHP's sets, assuming the weight ratio of each one at 'base time' as 100 percent. Here, 'base time' means the time when roughly one hour passed after the MHPs' set was picked out from the container cooled down by liquid nitrogen. As a result, it was confirmed that the lower the set temperature became from -5°C to -20°C, the lower the shrinkage of the MHP's set became.
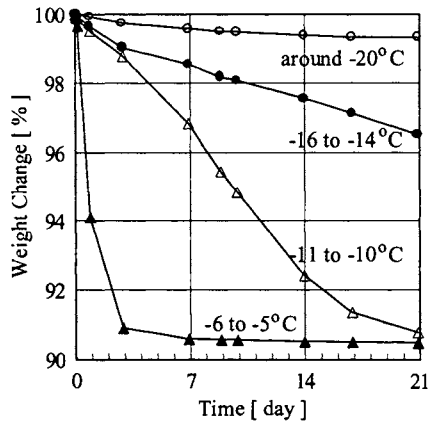
Figure 2. Weight change of MHPs' set

Promptly after the weight change was monitored for three weeks, the remaining MHPs' set was put at a normal temperature. The contained gas weight was measured by decomposing the set into water and methane gas completely, making sure that the water did not evaporate. Supposing that the weight decrease of the MHPs' set is equal to the weight of emitted methane gas, then the contained gas weight at every time can be calculated from the above weight change and the gas weight remained in the set after three weeks from the base time. From these data, dissociation rates of the MHPs' set were estimated. The MHPs were then kept at low temperature/humidity in order to prevent its weight from increasing owing to attached moisture in the air. Then, influence of sublimation was not taken into account.

The results of the contained methane gas measurement are shown in Table 1, and the estimated change of the hydrate ratio for every set temperature is shown in Figure 3. In Table 1, 'State I' means the state at the base time, and 'State II' means the state of the complete dissociation after 3 weeks from the base time. As seen from Figure 3, every MHP included 20% to 28% ice in at the base time. It is assumed that the ice had resulted from both imperfect conversion from water into hydrate in the hydrate synthesis process and part dissociation in the pelletization process. At this stage, it is not clear if the ice existed on the granular scale or as a rind encasing the entire pellet, or both.

Table 1. Results of contained gas measurement

Set Temperature [°C]	-5	-10	-15	-20
Weight of MHPs' Set (State I) [gf]	13.754	13.794	14.809	15.355
Weight of MHPs' Set (State II) [gf]	13.601	13.639	12.933	12.557
Ratio of Contained Methane Gas [%]	0.63	0.64	7.03	10.11
Hydrate Ratio [%]	4.7	4.8	52.5	75.4

165

100

80

Hydrate Ratio [%]

60

40

20

0

around -20°C

-16 to -14°C

-11 to -10°C

-6 to -5°C

0   7   14   21

Time [day]
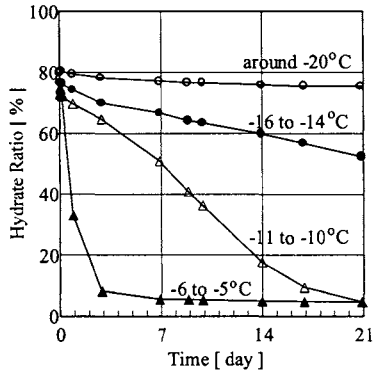
Figure 3. Hydrate ratio change of MHPs' set

Both at -5°C and -10°C, only approximately 5% of the theoretically contained gas remained in the MHPs' sets after a lapse of 3 weeks from the base time. On the other hand, at -15°C/-20°C, approximately 0.5 to 0.75 of the theoretically contained gas remained in the MHPs' sets even after a lapse of three weeks from the base time. It should be added that, the specific characteristics of the MHPs, used in these experiments such as contained methane gas ratio, are expected to be changed (improved) in the future. On the basis of the experimental data, average change rates of the hydrate ratio for three weeks from the base time at each temperature were calculated 47.9%/day at -5°C, 3.7%/day at -10°C, 2.6%/day at -15°C and 0.5%/day at -20°Celsius. According to these results, it is qualitatively assumed that the dissociation rate of the MHPs' set used in the experiment decreased monotonically as the temperature around the set dropped. The complicated temperature-dependence of the self-preservation effect, which Stern et al. pointed out (2002), could not be observed in the experiment. It is inappropriate, however, to discuss the matter at this stage, since the temperature-pressure history in hydrate synthesis/pelletization process was not controlled fully with close attention in our experiments. The MHPs' set dissociated rather slowly at -20°C in the experiments, so it is assumed that the MHP's self-preservation is maintained on the time scale including seaborne transportation. Namely, there is assumed to be every possibility of transporting NGHPs by ship from the viewpoint of hydrate's self-preservation.

CLOSING REMARKS

Regarding self-preservation, there are still a lot of problems to be solved for realization of the NGHP seaborne transportation, such as the estimates of (1) influence of pelletization upon self-preservation, (2) influence of pressure-temperature history in hydrate synthesis/pelletization process upon self-preservation, (3) self-preservation of NGHP (not MHP) (since the dissociation behavior of natural gas hydrate is assumed to be quite different from that of methane hydrate owing to the extremely different conditions required for thermodynamic stability), (4) mechanism of self-preservation effect and so forth. The authors are going to devote all our energies to tackling these problems continuously.

166

ACKNOWLEDGEMENT

REFERENCES

Gudmundsson, J.S., Parlaktuna, M., and Khokhar, A.A. 1994. Storing natural gas as frozen hydrate. SPE Production and Facilities, pp. 69-73.

Gudmundsson, J., and Borrehaug, A. 1996. Frozen hydrate for transport of natural gas, 2nd International Conference on Natural Gas Hydrates, pp.415-422.

Gudmundsson, J.S., Andersson, V., Levic, O.I., and Mork, M. 2000. Hydrate technology for capturing stranded gas, Gas Hydrate, Challenges for the Future, Annals of the New York Academy of Sciences, 912, pp. 403-410.

Max, M. D., 2000, Chapter 18: Hydrate as a future energy resource for Japan, Natural Gas Hydrate in Oceanic and Permafrost Environments, Kluwer Academic Publishers, pp. 225-238.

Nakajima, Y., Takaoki, T., Ohgaki, K. and Ota, S. 2002. Use of hydrate pellets for transportation of natural gas - II - Proposition of natural gas transportation in form of hydrate pellets -, *Proceedings of the 4th International Conference on Gas Hydrates*, pp. 987-990.

Ota, S., Uetani, H. and Kawano, H. 2002. Use of hydrate pellets for transportation of natural Gas - III - Safety measures and conceptual design of natural gas hydrate pellet carrier -, *Proceedings of the 4th International Conference on Gas Hydrates*, pp. 991-996.

Shirota, H., Aya, I., Namie, S., Bollavaram, P., Turner, D. and Sloan, E.D. 2002. Measurement of methane hydrate dissociation for application to natural gas storage and transportation, *Proceedings of the 4th International Conference on Gas Hydrates*, pp. 972-977.

Sloan, E.D. 1998. Clathrate hydrates of natural gases, 2nd Ed, Marcel Dekker, New York.

Stern, L.A. et al., 2001, Anomalous preservation of pure methane hydrate at 1 atm, *Journal of Physical Chemistry* B, 105, pp. 1756-1762.

Stern, L.A., Circone, S., Kirby, S. H., and Durham, W. B., 2002, New insights into phenomenon of anomalous or "Self" preservation of gas hydrates, *Proceedings of the 4th International Conference on Gas Hydrates*, pp. 673-677.

Takaoki, T., Iwasaki, T., Katoh, Y., Arai, T., and Horiguchi, K., 2002, Use of hydrate pellets for transportation of natural gas - I - Advantage of pellet form of natural gas hydrate in sea transportation -, *Proceedings of the 4th International Conference on Gas Hydrates*, pp. 982-986.

Tamura, I., Kagajyo, T., Kuwabara, S., Yoshioka, T., Nagata, Y., Kurahashi, K. and Ishitani, H. 1999. *Proceedings of 15th Energy System/Economics/Environment Conference*. Japan Society of Energy and Resources, pp. 419-423.

Yakushev, V.S. and Istomin, V.A. 1992. Gas-hydrates self-preservation effect, *Physics and Chemistry of Ice*, Hokkaido University Press, Sapporo, pp. 136-139.

NEW GRIDDED DIGITAL BATHYMETRY
FOR THE KURIL-KAMCHATKA REGION

Andrei G. Marchuk[1], Anatoly Yu. Bezhaev[1] and Nikolay I. Seliverstov[2]

[1]Institute of Computational Mathematics and Mathematical Geophysics
Siberian Division, Russian Academy of Sciences, Novosibirsk, RUSSIA
mag@omzg.sscc.ru

[2]Institute of Volcanology, Far Eastern Division, Russian Academy of Sciences
Petropavlovsk-Kamchatsky, RUSSIA

ABSTRACT

In the paper the algorithms and some interface for creating detailed digital regular gridded bathymetry using digital soundings data are described and examples of obtained data for different regions of the Pacific are shown. In calculations of the depth at each grid point, the algorithm uses up to 9 points from data source. They are chosen using two criterions: the first - they must be situated in various sectors (N, NE, E, SE, S, SW, W, NW) from calculating grid-point, and the second - they must be the nearest ones to this point in each sector. Then the spline interpolation is used for defining the depth value in the grid-point. Another algorithm uses linear interpolation for obtaining depth value in the grid-point. The new digital bathymery on the rectangular grid with 1 and 0.5 arc minute resolution has been created for the Kuril-Kamchatka region. These data consist from four rectangular arrays of depth, which cover 200 km zone around the Kuril Islands and Kamchatka from 41.00° up to 61.00° Northern latitude.

INTRODUCTION

Numerical modeling of different oceanologic problems and natural hazards in ocean now is widely used. For such a modeling (for example tsunami waves propagation) the detailed digital bathymetry on a regular grid is required. Now no global gridded bathymetry database with resolution better than five geographical minutes is available for users. Therefore for modeling local tsunamis (or another hazard) it is necessary to obtain somewhere or create detailed digital bathymetry for the regarded area. There are few ways to create such data arrays. There are several bathymetry information databanks now are available for use. One of them is a global database "Marine Trackline Data" of depth's soundings from the vessels (Marine Geological and Geophysical Data from NGDC) that had been collected during a very long period (from the beginning of 20-th century). In some coastal areas location of points from this data set are so dense, that using only this data make it possible to create the regular array of depths with a rather small spatial step (less than one geographical minute). In the areas, where it is not enough points with such a data, it is necessary to take into account additional information about bottom relief. Another possible information about ocean bathymetry is the isolines of depth. The database of depths isolines "GEBCO" (General Bathymetric Chart of Ocean) (GEBCO 97, 1997) is the most

known global digital database, the quality of which is of no doubts. However, the set and density of isolines are rather different for various regions. In the areas, where these isobaths together with echo sounding data of depth cover regarded area with enough densely without "white pots", it is possible to create digital bathymetry of high quality. In those areas, where density of Trackline and GEBCO data is seems to be insufficient, it is necessary to input into computer the isolines of depth and spot data from available bathymetric charts (navigating, fishing or specially prepared). Then the program that developed by the authors can produce the detailed digital bathymetry on the regular grid.

POSSIBLE WAYS FOR CREATING GRIDDED BATHYMETRY

At first we shall consider what kind of information can be used as a source for creating the digital bathymetry on a regular grid. On the bathymetric maps the information about depths is presented as isolines and dot data of depth soundings. A lot of soundings have been collected in a digital form in the databases "Marine Trackline Data" (Marine Geological and Geophysical Data from NGDC) and "Hydrographic Survey Data" (Hydrographic Survey Data, CD-ROM data set). This base contains the data about measurements of depth during cruises of large number of vessels and covers with the data with a various density practically all regions of world ocean. Each element of this database represents trace of a vessel movement (track), along which with a very small step (about hundreds of meters) the values of measurements of depth are presented. In some coastal regions tracks and the soundings are located so close to each other, that only these data would be enough for creation of the regular array of depths with a rather small step (less than one geographical minute). However, in other regions the distances between tracks are so big, that if we take into account only this kind of bathymetry information, it would be insufficient for creating of the qualitative detailed digital bathymetry on a regular grid. Isolines of depth had been collected in another global bathymetric database "GEBCO" (GEBCO 97, 1997), where some isolines of depth are stored in a digital vector form. This database covers all regions of World Ocean. The set of isobaths values in this database depends on region, and alongside with water areas, where this set is rather rich (in the Mediterranean sea, for example, it consists of about 40 values), there are also regions, where density of these isolines is insufficient. Also it is possible to find some other data about depth measurements that is now not available for a wide range of the users.

Here we shall describe some ways of creating of the arrays of depths on a regular grid using available bathymetric data. These arrays then can be used for mathematical simulation of processes in ocean. David Sandwell made the attempt to use for a gridded digital bathymetry creating the gravimetric data obtained from a satellite (Smith and Sandwell, 1997). Using this kind of data and the depth sounding data, he has constructed global two-minute gridded digital bathymetry. However, the matching of the Sandwell's data with more reliable bathymetric data in the northern Kamchatka region has revealed significant (in some places) mismatch of that data with real depths. Moreover the trackline data in some coastal regions is not well correlates with bathymetry obtained on the base of the analysis of a gravimetry. In Figure 1 the fragment of the Sandwell's digital bathymetry that covers the region of central Japan and surrounding water areas is presented. The traces of vessel cruises (when the measurements of depths were made) can be

clearly seen on the bottom surface (almost all of them are converging in region of the Tokyo bay). In deep-ocean areas Sandwell's digital bathymetry is sufficient for modeling ocean processes.
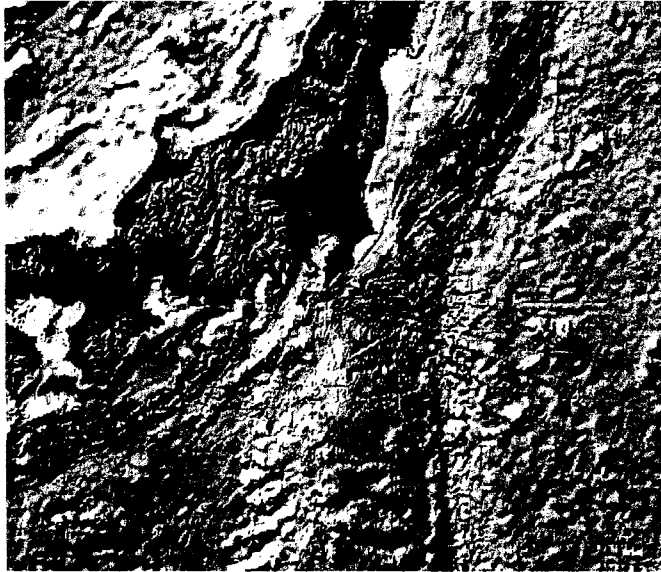
Figure 1. 3D shaded image of the Sandwell's relief around central Japan area

RECALCULATING RANDOMLY DISTRIBUTED DEPTH SOUNDINGS TO THE REGULAR GRID

Let's describe the technology of creating of the gridded digital bathymetry in case, when the points of depth sounding enough densely cover regarded area. On the first step it is necessary to choose from the whole database "Marine Trackline Data" a subset of points that are located in considered area. That will be the file, each string (line) of which consists of three numbers: longitude, latitude and measured depth. Then we must decide, what there will be a length of a step between grid points, where the depth values will be found. The last stage of the creating process will be execution of the program of recalculation of the randomly distributed depth data (depth soundings) to regular rectangular grid.

Firstly let's describe the recalculation algorithm, which uses the linear interpolation. The program considers one by one all our new grid-points. For every grid-point it is necessary to define it's geographical coordinates. Then we look through all points of the depth measurements finding distances from the considered grid-point up to each of them. If among them there is one or several points located closer, than one twentieth part of the new grid step length, then the value of depth in that grid-point is assumed to be equal to the depth value in the nearest point. If the Trackline database does not contain points, located to a new grid-point closer, than established distance, then let's take from it's (grid-point) nearest neighborhood three such points

171

from the database, that considered grid-point is located inside the triangle formed by these three points. Then, using known values of depth in these three points with the help of linear interpolation the value of depth in a considered grid-point can be defined. As the variation of this method it is possible to estimate the depth value in a grid-point using six nearest soundings, which are located in different sectors of Cartesian coordinate system with center in the regarded grid-point. So, considering one by one all points of a new regular grid, we shall find approximate values of depth in each of them. It is obvious, that the better densely coverage of the area by soundings provided the higher quality of the being created gridded digital bathymetry.

Another method is based on the more complicated interpolation method by radial functions. Proposed method uses up to nine points from data source. One point is the nearest one among all. The other eight points are chosen using two criterion's: the first - they must be situated in various sectors (between N, NE, E, SE, S, SW, W, NW directions) of Cartesian coordinate system with the center in regarded grid-point, and the second - they must be the nearest ones to this point in each sector. When the algorithm takes into account more that one point in each sector, the quality of gridded data will be better, but computations will take much more time and resources. In this case some procedures for optimizing calculation process are proposed.

The Green's function method, which is the special case of the radial functions method, is used for depth interpolation in grid-points. Let's notice that this method is exact on linear functions. The essence of method is in choosing of one dimensional radial functions $f(R)$. Then the linear combination

$$S(\vec{P}) = \sum_{i=1}^{k} \alpha(i) \cdot f\left(\left\|\vec{P} - \vec{P}(i)\right\|\right) + ax + by + c \tag{1}$$

represents two-dimensional function. Here $\vec{P} = (x,y)$ is an arbitrary point of the area, $\vec{P}(i) = (x(i),y(i))$ are interpolating points from different sectors. Coefficients $\alpha(i)$, a, b, and c are to be defined from interpolating conditions (the coincidence of the function $S(\vec{P})$ and sounding values $d(j)$ in points $\vec{P}(i)$ which are used for interpolation

$$S\left(\vec{P}(j)\right) = \sum_{i=1}^{k} \alpha(i) \cdot f\left(\left\|\vec{P}(j) - \vec{P}(i)\right\|\right) + ax + by + c = d(j), \; j=1,k \tag{2}$$

and orthogonality conditions:

$$\sum_{i=1}^{k} \alpha(i) = 0, \; \sum_{i=1}^{k} \alpha(i)x(i) = 0, \; \sum_{i=1}^{k} \alpha(i)y(i) = 0. \tag{3}$$

From system of equations (2) and (3) it is possible to find coefficients $\alpha(i)$, a, b, and c and then to define from the expression (1) the depth value in a new grid-point. Repeating this procedure for all grid-points of the area makes it possible to create the digital gridded bathymetry with arbitrary spatial grid-steps.

EXAMPLE OF APPLICATION

We shall illustrate application of such a technology of the gridded digital bathymetry creating on an example of obtaining the array of depths for small region in a northern part of Pacific around Kodiak Island. In this 5 x 5 degrees area (between 54th to 59th degrees North latitude and from 156th to 151st degrees West longitude) the detailed gridded bathymetry with resolution of 30 arc seconds in both directions was created. Available depth sounding data with the coastline from "Marine Trackline Data" and "Hydrographic Survey Data" sources are presented in the Figure 2. It is seen that in shelf zone the density of sounding measurements is rather higher than in deep ocean. In this area 600 x 600 points array of depth values was created using linear and spline interpolation methods. Both obtained digital arrays are visualized in Figure 3 as a 3-D shaded relief. This style of visualization makes all small-sized details of a bottom relief be very well visible (Fig. 3). Here the illumination vector is directed from the upper left corner of the area. In the bottom part of the left picture that is correspond to linear interpolation algorithm, some "star" structures around local depth extremums are visible. In this part of area depth soundings traces are located rather far from each other (Fig. 2).
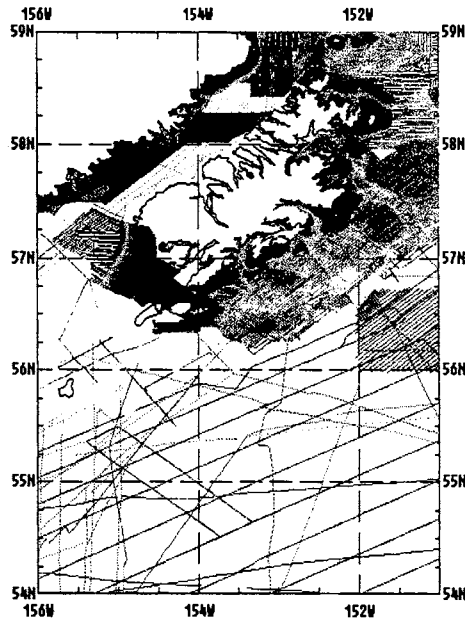
Figure 2. Marine Trackline data for the area around Kodiak Island in the North Pacific
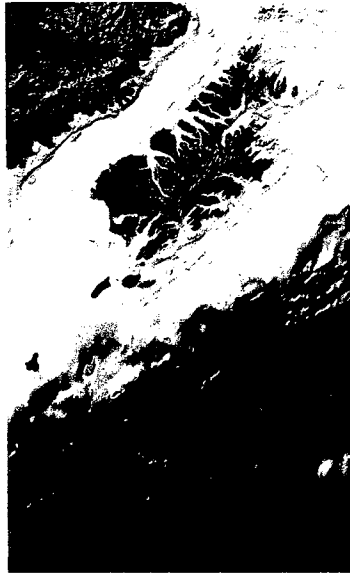
Figure 3. Three-dimensional shaded images of the bottom relief (gridded bathymetry) that had been created using linear interpolation (left) and spline interpolation (right) methods

For some areas of interest the information about depths from these global databases is insufficient for obtaining high quality gridded bathymetry. But if the paper bathymetry charts are available, it is possible to apply technologies for digitizing geographic information developed earlier by one author (Marchuk, 1996) and methods proposed in this paper. For example, the information about depths for Kuril-Kamchatka area in that both global data sets are insufficient for our purposes. So the set of four detailed bathymetry charts for this region were prepared in Kamchatka Institute of Volcanology. Figure 4 shows the coverage of these charts. In Figure 5 the GEBCO isolines of depth (left) and scanned image of one of this bathymetric chart (right) are shown. Using this data source (paper charts) makes it possible to create the new 1-min gridded digital bathymetry for that region. Comparison of several different gridded bathymetry sets (5-min ETOPO5, 2-min Sandwell's and the one developed by authors) can be found on our web site (http://omzg.sscc.ru/tsulab/ the item "Kuril-Kamchatka Bathymetry Project"). Now 1-minute gridded bathymetry was produced for areas 1-4 using linear interpolation method and 0.5-min bathymetry arrays, which were produced by spline interpolation, are ready for areas 2 and 3. Bathymetry arrays of this resolution for the last two areas will be completed in near future. As an example, the 3-D shaded relief of the area 2 is shown in Figure 6.
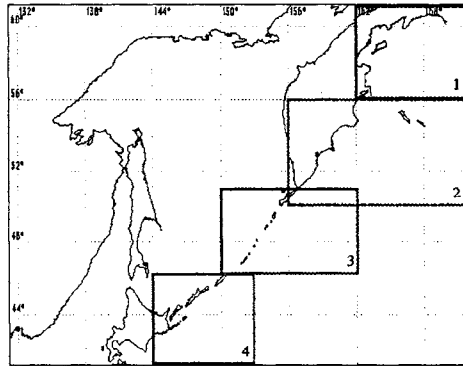
Figure 4. Geographic coverage of specially prepared bathymetric charts
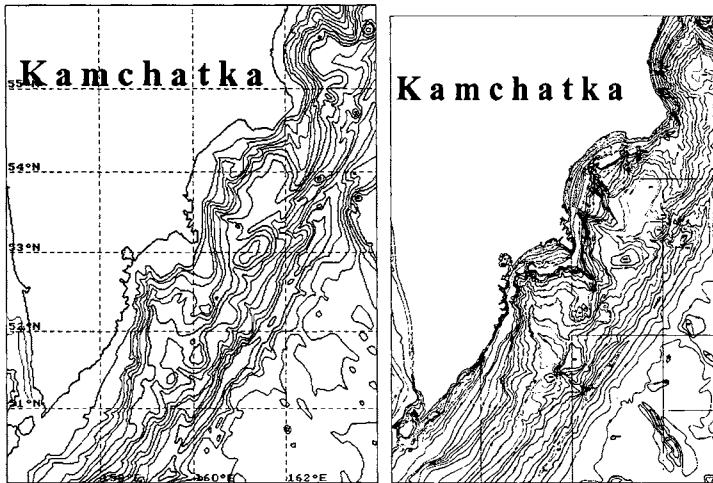
Figure 5. Comparison of the depths isolines sets from GEBCO database and specially prepared bathymetric chart.
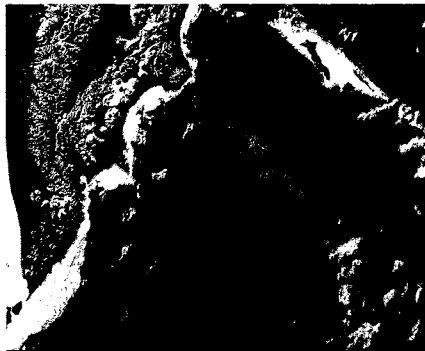
Figure 6. 3-D shaded bottom relief of the South Kamchatka area

175

CONCLUSION

For some regions of World ocean the quality of bathymetric data (on a random grid) that is contained in global databases allows to create rather detailed gridded digital bathymetry using proposed methods. If the number of depth measurements is insufficient, then additional sources of bathymetric information can be used. New digital bathymetry on a regular grid for the Kuril-Kamchatka region was created using the described in this paper technology and some numerical experiments of tsunami propagation was carried out.

ACKNOWLEDGMENTS

REFERENCES

GEBCO 97, Digital Atlas CD-ROM. 1997. *Intergovernmental Oceanographic Commission, International Hydrographic Organization. British Oceanographic Data Centre, Proudman Oceanographic Laboratory.* Bidston Observatory, Birkenhead Merseyside L43 7RA, United Kingdom.

Hydrographic Survey Data, CD-ROM data set, Ver. 3.2, *National Ocean Service, NGDC, NOAA*, E/GC3, 325 Broadway, Boulder, CO.

Marchuk, An. G. 1996. Interactive system for input digital geographic and bathymetric information. *Bulletin of the Novosibirsk Computing center. Series: Mathematical Modeling in Geophysics*, Issue: 2 (1996), NCC Publisher, Novosibirsk: 55-62.

Marine Geological and Geophysical Data from NGDC, Compact disc data set, *National Geophysical Data Center*, Boulder, Colorado, USA.

Smith, W.H.F. and Sandwell, D. 1997. Global seafloor topography from satellite altimetry and ship depth soundings. *Science.* 277: 1956-1962.

MAPPING TROPICAL SEAGRASS BEDS WITH AN UNDERWATER REMOTELY OPERATED VEHICLE (ROV)

Masumi Yamamuro[1], Kiyokazu Nishimura[1], Kiyoyuki Kishimoto[1], Ken Nozaki[1], Ken Kato[1], Akira Negishi[1], Kenji Otani[1], Hirofumi Shimizu[2], Takeshi Hayashibara[2], Motohiko Sano[2], Motoya Tamaki[2] and Kouki Fukuoka[2]

[1]National Institute of Advanced Industrial Science and Technology
Tsukuba, JAPAN
m-yamamuro@aist.go.jp

[2]Ishigaki Tropical Station
Seikai National Fisheries Research Institute Fisheries Research Agency
Ishigaki, Okinawa, JAPAN

ABSTRACT

The distributions of tropical and subtropical seagrass beds have not been properly monitored in many countries, owing to the limitations of observation methodologies. Conventional aerial photography fails to detect small-sized species and deep-water seagrass beds. We have developed a new mapping system that uses a remotely operated vehicle (ROV) equipped with an underwater digital camera to monitor seagrass beds. This system enables us to take digital photographs of seagrasses delimited by a quadrat frame. With semi-automatic processing of these photographs, seagrass leaf coverage can be calculated.

INTRODUCTION

Seagrasses are flowering plants that have evolved in seawater. There are about 60 species of seagrass in the world (Short et al., 2001). Of the 17 species found in Japan (Kuo et. al., 1995), 10 can be found in subtropical coastal areas. Seagrass beds are among the most productive ecosystems in the ocean, being a major food source for a number of aquatic grazing animals, such as dugong and turtles.

Many problems exist for the long-term survival and health of seagrass in the world's coastal zones. Anthropogenic pollutants have contributed most to the decline of seagrasses around the world, while careless land development has increased suspended sediments in runoff, which reduces light necessary for the growth of seagrass. Loss of seagrass habitat will result in loss of productivity in marine ecosystems as well as the extinction of species that depend on seagrass for survival. Such disturbances are expected to increase along the subtropical and tropical coasts of Asia, including Japan, owing to increased economic development.

In Japan, seagrass beds have been mapped with conventional aerial photography (e.g., Environment Agency, 1994). In the temperate coastal zone of Japan, seagrass beds are mostly composed of eelgrass (genera *Zostera*), and most of them are big enough to be mapped with aerial photography. For example, the leaf length of the most common eelgrass, *Zostera marina*, is greater than 1 meter. On the other hand, subtropical and tropical seagrass beds often consist of small sized species, such as *Halophila* spp., with leaf sizes of about 2–3 centimeters. It is

impossible to detect such small seagrasses with aerial photography. Because of such methodological limitations, the Japanese national seagrass-monitoring program reported the area of subtropical seagrass beds to be 1275 ha in 1978 and 6902 ha in 1989, although the decline of seagrass beds was obvious, owing to the development of coastal areas (Environment Agency, 1994). The report attributed the error to incorrect classification of the aerial photography.

In relatively shallow water (<10 m), divers have directly carried out underwater mapping of seagrass leaf coverage by putting down a quadrat of either 1 m^2 or 0.25 m^2 on seagrasses and estimating the percentage of coverage *in situ* (Duarte and Kirkman, 2001). To standardize the estimation of seagrass coverage, the divers carry photographs representing 1% to 100% coverage. If a submersible camera is available, diving time can be minimized by photographing the site vertically (including a scale) and estimating the seagrass coverage back in the laboratory (Duarte and Kirkman, 2001). Seagrass coverage is estimated by the naked eye.

For mapping deepwater seagrass meadows (>10 m), on the other hand, it has been recommended that an underwater video camera and GPS (Global Positioning System) receiver be used, because the working time of divers is restricted at such depths (McKenzie et al. 2001). Although using a digital video camera provides a great deal of picture-based information, it is difficult to estimate the seagrass leaf coverage with accuracy because of the low pixel resolution. Thus, the information for deep seagrass beds has not been of the same quality as that for shallow subtidal meadows (<10 m), where divers using quadrats can map seagrass coverage. Moreover, the position of the divers at the bottom cannot be exactly determined by GPS at the surface of the sea.

The aim of this research is to develop a new system of mapping seagrass beds growing in subtidal waters. We use a remotely operated vehicle (ROV) equipped with a submersible digital camera and a quadrat. The underwater position of the ROV is determined acoustically, and we are developing a computer system to analyze the digital photographs to evaluate the seagrass coverage.

SYSTEM SPECIFICATIONS

In coastal areas, position can be determined by GPS and acoustic navigation systems. We used DGPS (Differential GPS) to position the ROV on the water surface. When the ROV is under water, an acoustic navigation system is the only available positioning system. There are two types of acoustic navigation system, the LBL (Long Base Line) system and the SSBL (Super Short Base Line) system, both of which use frequencies of 19 and 20 kHz. In our system, the error of the LBL system and the SSBL system was 1 m and 10 m, respectively, when the distance between the transponder and transducer was 100 m. Thus, we found the LBL system (Fig. 1) to be better suited for shallow seagrass beds. We also invented a flexible, rising-and-falling buoy system on which to deploy the transponders to allow their positioning in shallow coastal waters under the influence of large tidal changes. This positioning system allows the ROV to move freely over the seagrass bed for monitoring. The position of the ROV is monitored with a video camera system attached to a moored balloon, and a real-time image is transmitted to a shipboard monitor. This enables us to avoid obstacles in the way of the ROV. A diver holding a digital camera on the other hand, has to swim along a fixed transect line whose position is measured beforehand.

178

Figure 1.   Schematic diagram of the LBL positioning system

A rectangular frame was fitted to the ROV to take underwater photographs of the seagrasses at the same camera angle as that used by scuba divers with a quadrat frame (Fig. 2, Photo 1). Because the photographs are taken with a digital camera, the digital images are easily transferred to a personal computer for further analysis.   The computer filters the image through the green light channel, and the seagrass coverage is calculated semi-automatically by using digital image processing based on the Otsu classification standard (Otsu 1979, Photo 2).

Figure 2.   Plan of the ROV (1) pressure-resistant box, (2) acrylic dome, (3) V-retainer clamp, (4) skid, (5) rear bumper, (6) side bumper, (7) horizontal thruster, (8) vertical thruster, (9) side thruster, (10) light, (11) plug, (12) cable connector, (13) Color TV camera, (14) tilting apparatus, (15) Vehicle bail, (16) quadrat frame and digital camera frame, (17) digital camera, (18) GPS

Photo 1. ROV equipped with a quadrat frame
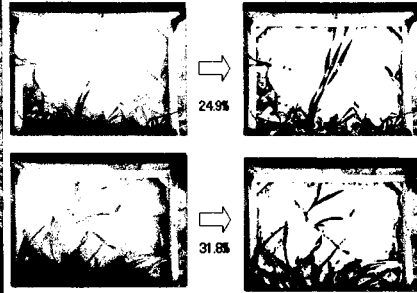
Photo 2. Semi-automated calculation of seagrass coverage (%)

FUTURE DIRECTION

Conventionally, underwater video camera systems have been used for ground truthing aerial photography for mapping seagrass beds (McKenzie et al., 2001). However, such systems cannot be successfully applied to deep subtidal areas, because relatively small sized-seagrasses are distributed there. For example, in Florida Bay, *Thalassia* and *Syringodium* were found at a maximum depth of 18.0 m, *Halodule* at 18.6 m, and *Halophila decipiens* at 26.5 m (Fourqurean et al., 2001). *Thalassia testudinum* was found even deeper in an area in Cuba (Buesa, 1975). Aerial photography cannot detect such species growing in deepwater areas. Also, the underwater video camera systems for ground truthing may easily fail to recognize such small species, or the video system may not operate at such depths. Because our ROV system uses an acoustic positioning system, a survey line does not need to be fixed beforehand, and the ROV can freely monitor any subtidal area.

There is a lack of information on the status and health of seagrasses worldwide, particularly in the less economically developed regions. Therefore, the UNEP World Conservation Monitoring Centre is presently conducting a global assessment of the status of seagrasses (Green and Short, in press). Local-scale monitoring programs are also ongoing worldwide; these include Seagrass Watch (Australia), Action Plan for Marine Vegetation in the Mediterranean, Caricomp (Caribbean), and SeagrassNet (USA). We would like to propose the development of a standard method for monitoring seagrass beds worldwide using remote sensing technology, including aerial photography, together with our system. Our system can semi-automatically record high-quality digital images, which can be used for later rough identification of seagrass species at sites facing sudden disturbance by human activity.

The present price of the whole system is ca$125,000 which is rather expensive for most developing countries. However, our monitoring system can dive to 140 m and can operate for longer than a diver, and the position of the ROV when taking pictures is automatically recorded on hard disk. The digital images may become a valuable testimony of the present status of coastlines, because rapid economic development can dramatically change it in a moment. These merits may offset the demerit of the cost of our monitoring system. International cooperative monitoring projects between developing and developed countries would also be a promising first step toward protecting the valuable seagrass bed ecosystems of the world.

180

ACKNOWLEDGEMENT

REFERENCES

Buesa, R.J. 1975. Population biomass and metabolic rates of marine angiosperms on the northwestern Cuban shelf. *Aquatic Botany* 1:11–23.

Duarte, C.M. and H. Kirkman. 2001. Methods for the measurement of seagrass abundance and depth distribution. In *Global Seagrass Research Methods*, edited by F.T. Short and R.G. Coles, 141–153. Elsevier Science B.V.

Environment Agency. 1994. Algal and seagrass beds. Tidal flats, algal and seagrass beds and coral reefs in Japan, Vol. 2. 400 pp.

Fourqurean, J.W., M.D. Durako, M.O. Hall and L.N. Hefty. 2001. Seagrass distribution in south Florida: a multi-agency coordinated monitoring program. In: Porter, J.W. and K.G. Porter, eds. The Everglades, Florida Bay, and the coral reefs of the Florida Keys. CRC Press LLC.

Green, E.P. and F.T. Short, 2003. World Atlas of Seagrasses. Prepared by the UNEP World Conservation Monitoring Centre. *University of California Press* (in press)

Kuo, J., Z. Kanamoto, T. Toma and M. Nishihira. 1995. Occurrence of *Halophila decipiens* Ostenfeld (Hydrocharitaceae) in Okinawa Island, Japan. *Aquatic Botany*. 51:329–334

McKenzie, L.J., M.A Finkbeiner and H. Lorlam. 2001. Methods for mapping seagrass distribution. In *Global Seagrass Research Methods*, edited by F.T. Short and R.G. Coles, 101-121. Elsevier Science B.V.

Otsu, N. 1979. A threshold selection method from gray-level histograms. IEEE Transactions on Systems, Man, and Cybernetics, 9: 62-66.

Short, F.T., R.G. Coles and P. Pergent-Mantini. 2001. Global seagrass distribution. In *Global Seagrass Research Methods*, edited by F.T. Short and R.G. Coles, 5–30. Elsevier Science B.V.

USING PREDICTIVE MONITORING TO MITIGATE CONSTRUCTION IMPACTS IN SENSITIVE MARINE ENVIRONMENTS

Riku W. Koskela[1], Petra Ringeltaube[1], Andrew R. Small[1], Thomas V. Koskela[1], Angus R. Fraser[1], Joanna D. Lee[1] and Paul Marshall[2]

[1]Aquatic Sciences Group, GHD Pty Ltd
Brisbane, Queensland, AUSTRALIA
rkoskela@ghd.com.au

[2]Monitoring and Assessment Unit, Great Barrier Reef Marine Park Authority
Townsville, Queensland, AUSTRALIA

ABSTRACT

A Predictive Monitoring Program (PMP) has been developed to mitigate construction related impacts in sensitive marine environments. The program aimed to intervene in the pollutant-generating process before the occurrence of environmental impacts. This has been achieved through compliance monitoring of the key pollutant processes using process specific trigger values. These trigger values were derived from a hydrodynamic model that incorporated habitat or biota tolerances to the pollutant. The Predictive Monitoring Program has been effectively implemented to mitigate the impacts of two common construction processes, these being de-watering discharge (Nelly Bay Safe Harbour Development, Magnetic Island, Townsville, Australia) and cutter-suction dredging (East Arm Port Stage 2A, Darwin, Australia) on nearby coral and mangrove communities (Great Barrier Reef Marine Park and Charles Darwin National Park respectively). This program differs substantially from the conventional Environmental Impact Monitoring Program, which requires the occurrence of measurable environmental harm prior to implementation of a management response.

INTRODUCTION

Substantial engineering works including port construction, dredging, coastal stabilisation, reclamation and wastewater discharge are occasionally undertaken within or in close proximity to marine protected areas. Authorities seek to moderate the impact of such works through various regulatory tools, management frameworks and environmental obligations (Craik, 1996; Puckette, 1998). As part of this mitigation process, many authorities require the design and implementation of an Impact Monitoring Program (IMP). The conventional IMP seeks to identify environmental impacts that result from a construction or pollutant-generating process. This includes routine monitoring of receiving water quality and benthic substrates (Jorgensen and Edelvang, 2000; Elander and Hammar, 1998; Ruffin, 1998; Wolanski and Gibbs, 1992), and in some instances, condition assessments of key habitats or biota (Healy et al., 1999; Quigley and Hall, 1999; Marques et al., 1993; Nichols et al., 1990; Lawing and Hanumara, 1989). However, using impact assessment of key habitats as the primary trigger for management response is a somewhat self-defeating approach to environmental protection. This is because measurable

environmental harm must be demonstrated before it can be recognised that mitigation measures are required.

Clearly, it is desirable to intervene in the construction or pollutant-generating process prior to the occurrence of a measurable impact in the receiving environment. Gray and Jensen (1993) identified the need for a marine monitoring system that integrated construction effects and ecosystem condition to allow for rapid management response. Bach et al. (1997) applied this concept in their Feedback Monitoring System. The system was developed to protect an eelgrass community from increased turbidity during dredging and reclamation works. The monitoring program was developed by integrating a mathematical model of turbidity with known turbidity tolerances of eelgrass to minimise physiological stress during construction. In this instance, eelgrass condition was the key performance indicator, however a lag time between impact and management response was in the order of 2 weeks (Bach et al., 1997).

More recently, Clarke and Wilbur (2000) have highlighted the need to integrate biological and engineering information to objectively evaluate potential environmental impacts. The ability to do this has been enhanced by ongoing advances in hydrodynamic modelling (Botev and Fryar, 2002) combined with improved understanding of biota and habitat tolerances to various pollutants. This approach has been integrated in a Predictive Monitoring Program (PMP) that has been designed for the protection of sensitive environments and implemented for the protection of a coral and a mangrove community during two major construction projects. These projects were undertaken in the Great Barrier Reef Marine Park (Nelly Bay, Magnetic Island, Queensland, Australia) and adjacent to the Charles Darwin National Park (East Arm Port, Darwin Harbour, Northern Territory, Australia).

This paper presents the overall philosophy of a PMP by discussing the outcomes of the two cases studies. In particular, it will describe how the program can substantially reduce the likelihood of construction impacts in sensitive marine environments. This has been achieved by focusing monitoring primarily on construction related pollutant-generating processes to instigate rapid management response. Condition assessment of the receiving habitats (sensitive environments) was used to validate the efficacy of the program.

MATERIALS & METHODS

Predictive Monitoring Program

Design and implementation of the PMPs required a staged process including pre-construction consultation, baseline data collection and hydrodynamic modelling. A schematic overview of this process is presented in Figure 1. The stages in this process include:
1. Identification of key habitats, biota and buffer zones through field assessment and consultation with stakeholders and regulatory authorities.
2. Identification of pollutant-generating construction processes and those pollutants that present a risk to the key habitats or biota. This enables the PMP to focus on the principal pollutants and the construction processes that generate them.

3. Conduct baseline studies on both key habitat or biota condition and natural variability of the principal pollutants with the system.
4. Determination of the tolerances of key habitats or biota to the principal pollutants through specialist review and baseline studies.
5. Development of a hydrodynamic model of the pollutant-generating process that integrates habitat tolerances, mixing and dispersion, tidal currents, sea state and buffer zones. The output of this model is a trigger value, which is the concentration of the pollutant that can be generated by the construction process without exceeding the key habitat tolerance.
6. Undertake validation studies of model outputs to allow for refinement of the trigger value.
7. Undertake compliance-monitoring of the construction process.
8. Instigate immediate pre-defined management actions in response to non-compliance.
9. Undertake routine biophysical monitoring of key habitats to validate the effectiveness of the PMP.
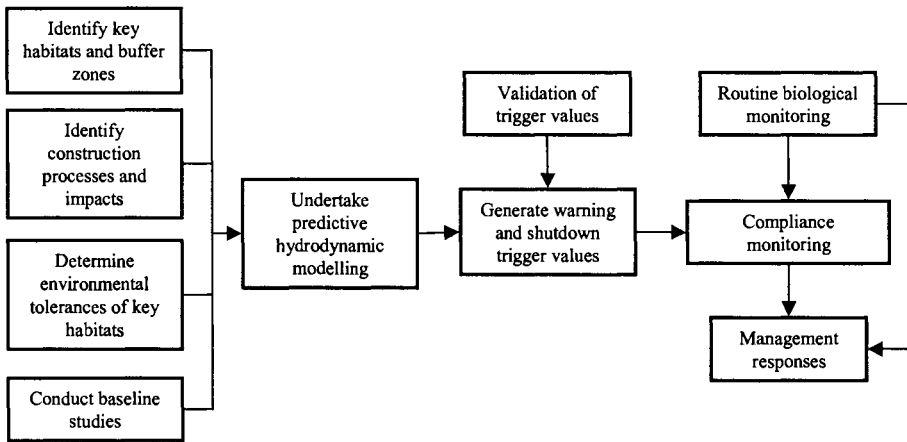
Figure 1. Schematic diagram showing the steps involved in the design of a Predictive Monitoring Program

Case studies

Predictive Monitoring Programs have been applied to two common pollutant-generating construction processes, these being de-watering discharge during construction of Nelly Bay Safe Harbour (Fig. 2a) and cutter-suction dredging during East Arm Port extensions (Fig. 2b). Detailed description of technical methods will be published elsewhere. The following represents an overview of these two monitoring programs.

Figure 2 (a). Aerial view of Nelly Bay Safe Harbour construction site, and (b) East Arm Port construction site.

Pre-discharge Monitoring - Nelly Bay Safe Harbour
Nelly Bay Safe Harbour is being constructed on Magnetic Island (19°08 S, 146°50 E), within the Great Barrier Reef Marine Park.

Key habitats: Protected habitats within the development area include fringing platform coral reefs located adjacent to the harbour breakwater and harbour entrance channel. These reef communities were selected as key habitats.

Pollutant-generating construction process: The harbour was sealed by a temporary semi-permeable breakwater and de-watering occurred at a discharge rate of ~5000 $m^3 \cdot hr^{-1}$. This water was pumped to a discharge point 100 m offshore. De-watering of sediment-laden waters from the harbour basin was a principal pollutant-generating construction process. As light attenuation and sediment deposition is known to substantially impact coral reef systems, suspended sediment was identified as the key pollutant (Loya, 1976; Hodgson, 1989; Rogers, 1990; Perry, 1996). For the purpose of this monitoring program, turbidity (ntu) was used as a surrogate measure of suspended sediment. The ability to monitor water quality prior to discharge enabled predictive monitoring for Nelly Bay to take the form of a pre-discharge monitoring program.

Baseline monitoring: To determine the natural variability of turbidity (ntu), baseline surveys were undertaken through the deployment of *in situ* turbidity loggers at various reef slope stations. Baseline monitoring enabled determination of fluctuations in turbidity of receiving waters associated with tidal phases (neap, spring), tidal cycles (flood, ebb) and sea states (calm, slight, moderate, rough, very rough). This information was also used to derive key habitat tolerances.

Modelling and trigger values: To predict the turbidity concentration that could be generated by the construction process to meet key habitat tolerances, the results from the baseline study were incorporated within a diffusion model of plume mixing and dispersion (Ridd et al., submitted). The outcome of this model was a set of warning and shutdown trigger values for pre-discharge and shutdown trigger levels for receiving waters.

186

Validation studies: The efficacy of the trigger values was validated by deployment of turbidity loggers at fixed locations on adjacent reef slopes.

Compliance monitoring: The model-derived trigger values (Tables 1 and 2) were applied in pre-discharge and receiving water quality compliance-monitoring programs. Compliance was determined by comparing turbidity to the appropriate warning and shutdown trigger values. Raw turbidity data (n=10 per station) were transformed and the 95% confidence interval of the mean was used to determine compliance with trigger values.

Table 1. Warning and shutdown turbidity trigger values (ntu) for pre-discharge waters

Tidal Cycle	Tidal Phase	Trigger	Sea state				
			Calm	Slight	Moderate	Rough	Very Rough
Flood	Neap	Warning	4	11	21	43	85
Ebb	Neap	Warning	6	14	28	56	113
Flood	Spring	Warning	13	32	64	128	255
Ebb	Spring	Warning	17	42	84	169	338
Flood	Neap	Shutdown	17	43	85	170	340
Ebb	Neap	Shutdown	23	56	113	225	450
Flood	Spring	Shutdown	51	128	255	510	750
Ebb	Spring	Shutdown	68	169	338	675	750

Table 2. Shutdown trigger values (turbidity, ntu) for receiving waters

Location	Trigger	Sea state				
		Calm	Slight	Moderate	Rough	Very Rough
Receiving Waters	Shutdown	6	15	30	60	120

Routine biological monitoring - Coral Condition Monitoring Program: A Coral Condition Monitoring Program was implemented to provide validation of the PMP. A detailed description of this program will be published elsewhere (R.J. Jones, pers. com.). In summary, monitoring commenced with a pre-construction baseline survey of coral condition and was conducted routinely for the duration of the de-watering process. Transects were located at impact and control stations to monitor 700 tagged coral colonies from four species: *Acropora latistella, A. subulate, Montipora aequituberculata* and *Turbinaria mesenterina*. Each coral colony was routinely assessed for changes in % bleaching and % partial mortality to ensure warning or shutdown habitat trigger values were not exceeded. To determine compliance with warning and shutdown trigger values, data were analysed using a Cumulative Frequency Analysis and Decision Curve Analysis (Stafford-Smith et al., 1994).

Management responses: When the pre-discharge warning trigger values were exceeded, receiving waters were monitored. If the trigger values for receiving waters were exceeded,

discharge was shutdown. In the instance that pre-discharge shutdown trigger values were exceeded discharge ceased immediately and receiving waters were monitored.

Dredge Plume Monitoring - East Arm Port
Dredging was conducted to remove ~1.15M m^3 of soft marine sediment as part of Stage 2 extensions for Port of Darwin (12° 30'E, 130° 50'S).

Key habitats: The development was undertaken adjacent to the Charles Darwin National Park, a coastal mangrove and estuarine habitat of regional importance. The mangrove communities were selected as the key habitat.

Pollutant-generating construction process: Dredging was undertaken via cutter-suction dredge, a process known to create substantial sediment-laden surface and sub-surface plumes. Therefore, dredging was regarded as the principal pollutant-generating process within the marine environment. As excessive sediment deposition is recognised to substantially impact on mangrove condition (eg Ellison, 1998; Clarke and Myerscough, 1993; Fairweather, 1990), excessive sediment suspension was identified as the key pollutant. For the purpose of this monitoring program, turbidity was used as a surrogate measure of suspended sediment. As pre-discharge monitoring was not possible for dredging, predictive monitoring of East Arm Port focused on a dredge plume-monitoring program.

Baseline monitoring: Background data on suspended sediment concentrations and turbidity was available from previous projects undertaken for the Stage 1 development of East Arm Port. These data were supplemented with a baseline-monitoring program for water quality at key habitat and control monitoring stations. This series of data enabled determination of fluctuations in turbidity of receiving waters associated with tidal phases (neap, spring). Baseline information was combined with known physiological tolerances of mangrove habitats (i.e., Frusher et al., 1994) to derive key habitat tolerances for neap and spring tidal phases (Table 3).

Table 3. Key Habitat Trigger Values

Tidal phase	Trigger value
Spring	27 ntu
Neap	14 ntu

Modelling and trigger values: To predict the turbidity concentration that could be generated by the construction process to meet key habitat tolerances, the results from the baseline study were incorporated within a far-field hydrodynamic model of dredge head sediment mobilisation (RMA-2; Fig. 3). The outcome of this model was a set of warning and shutdown trigger values at the post-mixing boundary of the plume (40 m from the dredge head) for multiple dredge locations (Table 4).
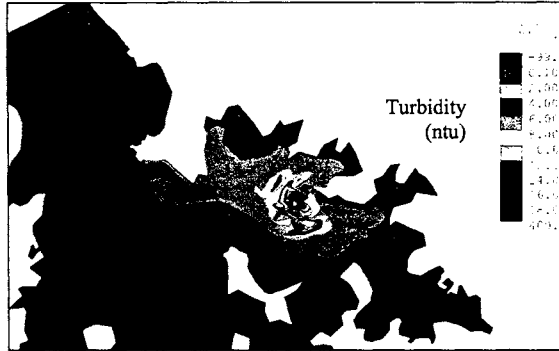
Figure 3. RMA-2 model output used to determine warning and shutdown trigger values at the post-mixing boundary of the dredge plume

Table 4. Dredge plume trigger values for the post-mixing boundary
located 40 m from the dredge head

Dredge location	Trigger values	
	Shutdown	Warning
Inside the port	457 ntu	190 ntu
At the tip of the port	30 ntu	16 ntu

Validation studies: The efficacy of the dredge plume trigger values was validated by a 10-day pilot study undertaken at the commencement of works.

Compliance monitoring: The dredge plume and key habitat trigger values were applied in a compliance-monitoring program. Compliance was determined by comparing turbidity to the appropriate warning and critical trigger values. Raw turbidity data (n=10 per station) were transformed and the 95% confidence interval of the mean was used to determine compliance with trigger values.

Routine biological monitoring - Mangrove Condition Monitoring Program: A Mangrove Condition Monitoring Program was implemented to validate the effectiveness of the PMP. A full description of this program and its findings will be published elsewhere by the authors. In brief, the program was conducted across a range of mangrove zones in two separate communities, these being *Sonneratia alba* and *Rhizophora* sp.. Condition indicators such as pneumatophore status, seedling recruitment, active crab burrow counts, active crab counts and mangrove snail counts were measured during each survey. Various stress indicators, including yellowing of leaves, aborting of fertile material, fragility and loss of turgidity in pneumatophores, excessive/unusual predation and disease were also recorded.

Management responses: When dredge plume warning trigger values were exceeded, receiving waters were monitored. If the trigger values for the receiving waters were exceeded, dredging was shutdown. In the instance that the dredge plume shutdown trigger values were exceeded, dredging operations ceased immediately and receiving waters were monitored.

189

RESULTS

De-watering – Nelly Bay Safe Harbour Development

Water Quality Compliance Monitoring
Turbidity of de-watering discharges varied markedly during construction (Fig. 4) and water quality trigger values were exceeded on 113 occasions during pre-discharge compliance monitoring (Table 5). On each of these occasions, a variety of management responses were implemented, including shut down of discharge activities and implementation of receiving water monitoring. On two occasions only receiving waters were found to be non-compliant to key habitat trigger values during the de-watering process.
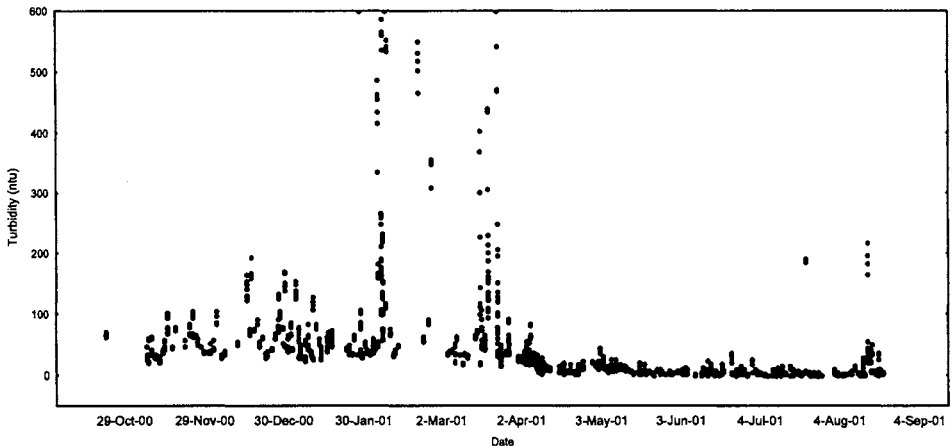
Figure 4. Turbidity (ntu) of the discharge waters as measured in the discharge pipe from October 2000 to August 2001

Table 5. Discharge and receiving water compliance monitoring results

Trigger values	Number of exceedances	
	Discharge non-compliance	Receiving water non-compliance
Warning	77	2
Shutdown	36	0

Coral Condition Monitoring Program
During 11 months of de-watering, all coral colonies exhibited less than 15% partial bleaching or partial mortality (Fig. 5). Coral condition surveys did not identify exceedance of warning (Level 1) or shutdown (Level 2) habitat trigger values for the percentage of partial bleaching or percentage of partial mortality (e.g., Fig. 6; partial mortality). Thus no construction related impacts could be identified.

190
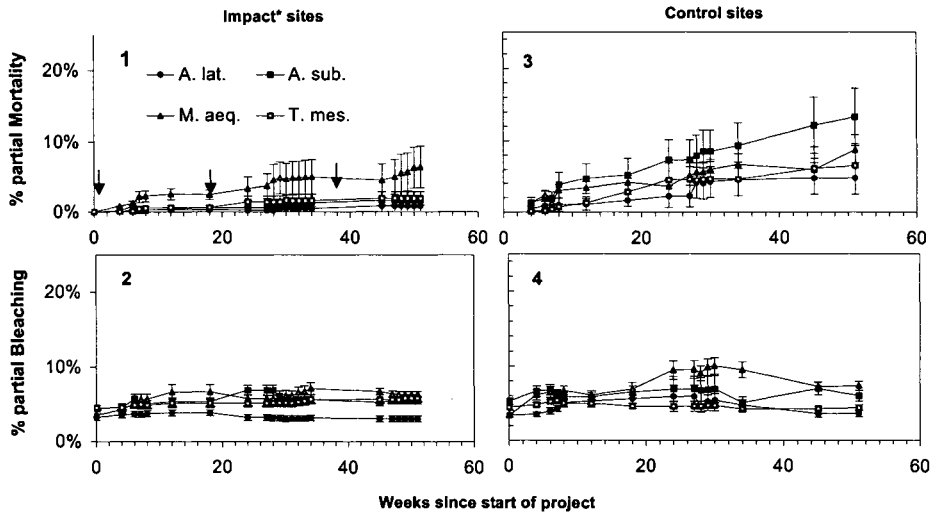
Figure 5. Mean percentage partial mortality and bleaching in *Acropora latistella*, *A. subulata*, *Montipora aequituberculata* and *Turbinaria mesenterina*. Data are expressed as mean ± SD (standard deviation)
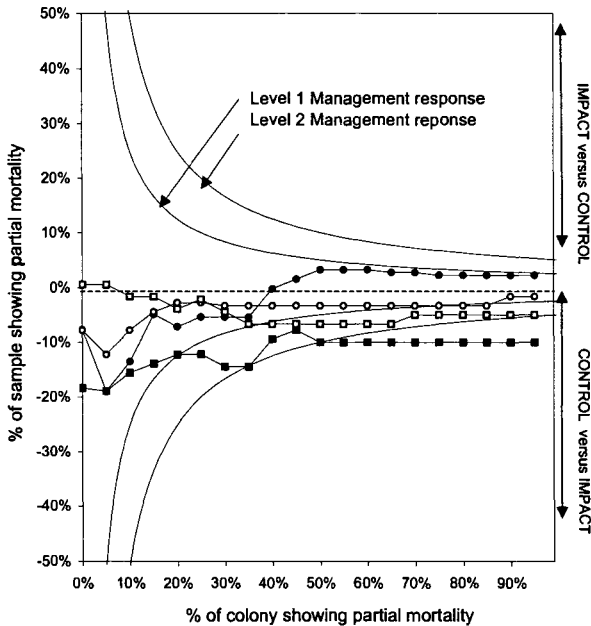
Figure 6. Decision curve analysis for partial mortality as measured by the Coral Condition Monitoring Program after 51 weeks ● = *Montipora aequituberculata*, ■ = *Acropora subulata*, O= *Acropora latistella*, □= *Turbinaria mesenterina*

191

Dredge plume monitoring – East Arm Port

Water quality compliance monitoring
Water quality remained compliant to warning and shutdown trigger values for the duration of dredging. On one occasion however, a substantial turbidity increase was observed within the receiving environment. This was due to the release of turbid dredge decant waters following the failure of a bund wall. Non-compliance with key habitat trigger values was recorded on the day following the bund failure.

Mangrove Condition Monitoring Program
According to the physiological indicators of mangrove stress, including pneumatophore turgidity and leaf yellowing, no difference in mangrove condition was identified between impact and control stations. Also, indicators of habitat condition, including active crab burrow count (sesarmid crabs are known to leave areas which are smothered by deep sediments) did not indicate an impact associated with increased sedimentation (Fig. 7).
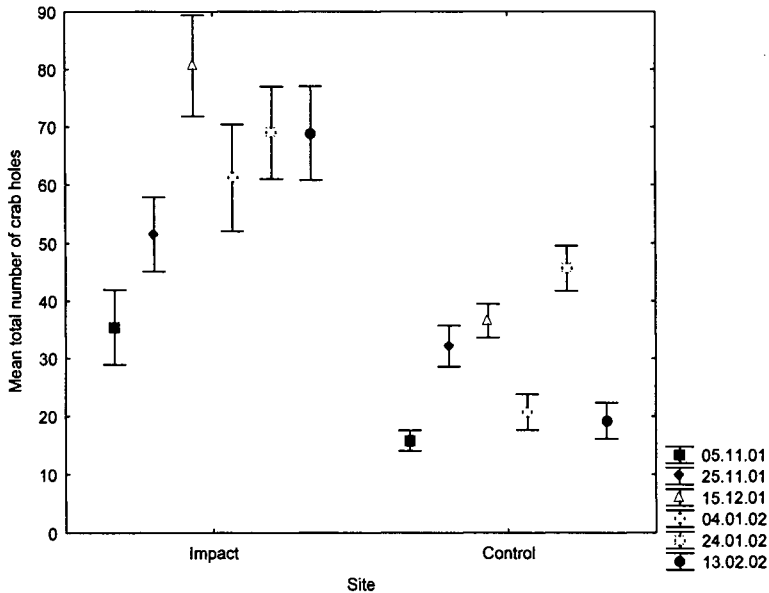
Figure 7. Mean total number of crab burrow counts for the duration of the project

DISCUSSION

Implementation

A Predictive Monitoring Program (PMP) has been developed to protect sensitive marine environments from the impacts of construction. The primary goal of the program is to predict the environmental impacts of key pollutant-generating processes in order to trigger intervention

before a measurable impact occurs. To do this, a PMP directs compliance monitoring primarily towards pollutant-generating activities, using model-derived pollutant trigger values that incorporate construction and hydrodynamic processes and known habitat tolerances. Non-compliance with these trigger values instigates immediate pre-defined management responses. To maximise protection, compliance monitoring of discharge activities is undertaken during the pre-discharge phase to allow intervention prior to discharge. For dredging activities, compliance monitoring is undertaken at the post-mixing boundary of the plume. Routine habitat condition monitoring is employed in a supporting role to validate the efficacy of the program for protecting key habitats.

The generic concept of the PMP has been implemented for two case studies to mitigate the impacts of sediment-laden water discharge and cutter-suction dredging in marine national parks. Increased sediment suspension was identified as the key pollutant generated by each construction process. Accordingly, programs were specifically developed to protect fringing coral reef and mangrove habitats from the impacts of light attenuation and sedimentation. Results indicated that the PMP was highly successful in protecting sediment-intolerant coral communities in the Great Barrier Reef Marine Park. This was largely due to the rapid and repetitive intervention that the program triggered. Intervention in the dredging process to protect mangrove communities in Charles Darwin National Park was not required.

Construction processes and habitat requirements

The success of the PMP can be attributed to the incorporation of important emerging philosophies in impact management within marine systems. Principal among these is the recognition that monitoring and management programs must integrate knowledge of construction processes and ecological requirements (Bach et al., 1997; Clarke & Wilbur, 2000). The PMP achieved this by integrating knowledge of habitat tolerances with hydrodynamic modelling of specific construction processes to produce pollutant trigger values that considered mixing and dispersion dynamics as well as environmental requirements. In the instance of the case study on dredging, trigger values were set at relatively high levels in consideration of substantial capacity for dispersion and the substantial sediment tolerance displayed by mangrove communities. As a result, dredge activities proceeded with a minimal requirement for intervention. In contrast, discharge of sediment-laden water in close proximity to fringing coral reef communities require substantial intervention because trigger values took into account limited dispersion characteristics and low sediment tolerances of key biota.

Rapid intervention

It was also recognised that management responses to unsustainable pollutant generation would need to be very rapid if highly sensitive habitats were to be protected. While the need for rapid response has been highlighted (Gray and Jensen, 1993; Bach et al., 1997), methods to achieve this have not proved to be as rapid as may be required. In addressing the impacts of substantial dredge works on eelgrass communities, Bach et al. (1997) implemented a feedback monitoring system that utilised physiological indicators of eelgrass condition as the trigger for management response. However, the use of biota as the trigger mechanism resulted in inherent delays in management response, due to the time required for stress to manifest itself. For eelgrass, this

was expressed as an approximate two-week delay (Bach et al., 1997). The PMP addressed this problem by focusing compliance monitoring on actual pollutant-generating processes, allowing non-compliance with trigger immediate intervention. In the case of wastewater discharge adjacent to coral reefs, lag-times did not exceed one hour. This rapid response was regarded as a key element in the success of the program.

Biological monitoring

The necessity to examine biological condition is well recognised (Thomas, 1993) and is usually incorporated within an impact monitoring program (i.e., Bach et al., 1997). In such cases, the detection of measurable environmental harm is used to trigger a management response. Although not used to trigger intervention, biological monitoring remained an integral component of the PMP, being used to validate trigger values, management responses and the effectiveness of the program for protecting key habitats. Specifically, biological assessment of coral communities, when integrated with water quality monitoring, proved useful to delineate construction impacts from natural variability. Given that dredging works did not trigger management responses, assessment of mangrove communities was used to validate the relatively high trigger values adopted by this program (Table 3).

Biological monitoring also plays a substantial role in the determination of habitat tolerances. While the tolerance of coral and mangrove communities to sedimentation is relatively well understood, the need for substantial baseline and other assessments may be required to adapt this approach to other habitat types. Such baseline studies may also prove useful to delineate the natural variability in condition that may exist in many habitats. It should be recognised that habitat condition assessment may be expensive. The PMP addressed this limitation by confining condition assessment to designated key habitats only.

Recommendations

1. Each case study would have benefited from more intensive baseline data collection to allow accurate determination of natural variability of pollutants and key habitat condition. This would enable construction monitoring to be more targeted and efficient and would have increased the cost-effectiveness of both programs. Therefore rigorous baseline studies are recommended.
2. The effectiveness of the PMP would be enhanced by incorporation of trigger values and pre-defined management responses within development approvals prior to the commencement of construction.
3. The case studies clearly identified that the generic PMP concept can successfully be implemented to protect sensitive environments from construction related impacts. A PMP needs to be designed according to specific environmental settings and proposed construction activities.

SUMMARY

The PMP philosophy has been developed to incorporate a preventative approach to environmental management. The two case studies presented indicate that the implementation of a PMP has been successful in mitigating construction related impacts in sensitive marine

environments. Furthermore, it is suggested that PMPs are sufficiently flexible to be implemented for a variety of construction processes and over a range of habitats. Advances in modeling technology will allow improved consideration of pollutant-generating processes, near-field mixing and far-field pollutant behavior (Fryar, et al., 2002). This is likely to substantially improve the performance of the PMP. The project team intends to continue the refinement of the PMP as a tool to protect sensitive marine environments.

ACKNOWLEDGEMENTS

REFERENCES

Bach, H.K. K. Jensen and J.E. Lyngby. 1997. Management of marine construction works using ecological monitoring. *Estuarine Coastal and Shelf Science*. 44(Supp A):3-14.

Botev, I. and R. Fryar. 2002. Application of 3D models in the coastal environment. *Australian Journal of Water Resources*. 6(1):1-9.

Clarke, D.J. and D.H. Wilbur. 2000. *Assessment of potential impacts of dredging operations due to sediment resuspension*. DOER Technical Notes Collection (EDRC TN-DOER-E9), US Army Engineering Research and Development Centre, Vicksburg MS. Available from US Army Corps of Engineers DOER Technical Notes via the Internet (http://www.wes.army.mil/el/dots/doer).

Clarke, P.J. and P.J. Myerscough. 1993. The intertidal distribution of the grey mangrove (*Avicennia marina*) in southeastern Australia: The effects of physical conditions, interspecific competition, and predation on propagule establishment and survival. *Australian Journal of Ecology*. 18:307-315.

Craik, W. 1996. The Great Barrier Reef Marine Park, Australia: A model for regional management. *Natural Areas Journal*. 16(4):344-353.

Elander, P. and T. Hammar. 1998. The remediation of Lake Järnsjön: Project Implementation. *Ambio*. 27(5):393-398.

Ellison, J.C. 1998. Impacts of sediment burial on mangroves. *Marine Pollution Bulletin*. 37:420-426.

Fairweather, P.G. 1990. Ecological changes due to our use of the coast: research needs versus effort. *Proceedings of the Ecological Society of Australia.* 16:71-77.

Frusher, S.D., F.L. Giddins and T.J. Smith III. 1994. Distribution and abundance of grapsid crabs (Grapsidae) in a mangrove estuary: effects of sediment characteristics, salinity tolerances, and osmoregulatory ability. *Estuaries.* 17:647–654.

Fryar, R.M., I.B. Botev and B.L. Regan. 2002. Using three dimensional models to Manage Outfalls and Minimise Environmental Impacts - Modelling Moreton Bay and The Brisbane River. Managing Water to Protect the Coastal Zone, AWA 2002 Weekend Regional Conference, Mooloolaba, QLD, 8-10 November 2002.

Gray, J.S. and K. Jensen. 1993. Feedback monitoring: A new way of protecting the environment. *Trends in Ecology and Evolution.* 8:267-305.

Healy, T., A. Mehta, H. Rodriguez and F. Tian. 1999. Bypassing of dredged littoral muddy sediments using a thin layer dispersal technique. *Journal of Coastal Research.* 15(4):1119-1131.

Hodgson, G. 1989. *The effects of sedimentation on Indo-Pacific reef corals.* PhD Thesis. University of Hawaii.

Jones, R.J., J.K. Oliver and R. Berkelmans. 1997. The recurrent bleaching of corals at Magnetic Island (Australia) relative to air and seawater temperature. *Marine Ecology Progress Series.* 158:289-292.

Jörgensen, P.V. and K. Edelvang. 2000. CASI data utilized for mapping suspended matter concentrations in sediment plumes and verification of 2-D hydrodynamic modelling. *International Journal of Remote Sensing.* 21(11):2247-2258.

Lawing, W.D. and R.C. Hanumara. 1989. Use of log-linear modelling to assess environmental changes. *Environmental Monitoring and Assessment.* 11(2):115-126.

Loya, Y. 1976. Effects of water turbidity and sedimentation on the community structure of Puerto Rican reefs. *Bulletin of Marine Science.* 26:450-466.

Marques, J.C., P. Maranhao and M.A. Pardal. 1993. Human impact assessment on the subtidal macrobenthic community structure in the Mondego Estuary (Western Portugal). *Estuarine Coastal and Shelf Science.* 37(4):403-419.

Nichols, M., R.J. Diaz and L.C. Schaffner. 1990. Effects of hopper dredging and sediment dispersion, Chesapeake Bay. *Environmental Geology and Water Science.* 15(1):31-43.

Rogers, C.S. 1990. Responses of coral reefs and reef organisms to sedimentation. *Marine Ecology Progress Series.* 62:185-202.

Perry, C.T. 1996. The rapid response of reef sediments to changes in community composition: Implications for time averaging and sediment accumulation. *Journal of Sediment Research.* 66:459-467.

Puckette, T.P. 1998. *Evaluation of dredge material plumes – Physical monitoring techniques.* DOER Technical Notes Collection (TN DOER-E5) US Army Engineer Research and Development Centre, Vicksburg MS. Available from US Army Corps of Engineers DOER Technical Notes via the Internet (http://www.wes.army.mil/el/dots/doer).

Quigley, M.P. and J.A. Hall. 1999. Recovery of macrobenthic communities after maintenance dredging in the Blyth Estuary, north-east England. *Aquatic Conservation.* 9(1):63-73.

Ridd, P.V., A. Orpin, P. Marshall and J. Oliver. Natural variability in turbidity close to coral reefs. Submitted to Estuarine Coastal and Shelf Science 2000.

Ruffin, K.K. 1998. The persistence of anthropogenic turbidity plumes in a shallow waste estuary. *Estuarine Coastal and Shelf Science.* 47(5):579-592.

Stafford-Smith, M.G., U.L Kaly and J.H. Choat. 1994. Reactive Monitoring (short term responses) of coral species. In: Benson L.J., P.M. Goldsworthy, I.R. Butler and J.K. Oliver (eds) *Townsville Port Authority Capital Dredging Works. 1993: Environmental Monitoring Program. Townsville Port Authority, No.1 The Strand, Townsville Qld 4810.*

Thomas, J.D. 1993. Biological monitoring and tropical biodiversity in marine environments: a critique with recommendations, and comments on the use of amphipods as bioindicators. *Journal of Natural History.* 27:795-806.

Wolanski, E. and R. Gibbs. 1992. Resuspension and clearing of dredge spoils after dredging, Cleveland Bay, Australia. *Water Environment Research.* 64(7):910-914.

REAL-TIME COASTAL MONITORING SYSTEM
USING WIRELESS INTERNET AND LIGHT TOWER

K. S. Park[1], J. K. Lee[2], S. W. Kang[1] and S. I. Kim[1]

[1]Coastal and Harbor Engineering Research Laboratory, KORDI
Seoul, KOREA
kspark@kordi.re.kr

[2]DATAPCS, Co., Kyungki-Do, KOREA

ABSTRACT

Kyboncho and Sokcho station was successfully launched as a real-time coastal monitoring station in comply with the national coastal monitoring plan. Real-time coastal monitoring system using light tower and wireless Internet will produce valuable information to reduce natural disaster damages by tracking typhoons or measuring high waves or reporting strong northwesterly winds in winter season. Types of real-time information include wind speed, wind direction, air temperature, relative humidity, atmospheric pressure, wave, tide, water temperature and salinity. Data are collected regularly and transmitted to the main server using CDMA wireless Internet connection. After post-processing on the server, data are distributed to the users on the wired and wireless Internet same time.

INTRODUCTION

Korea has great demands for the efficient uses of her coastal space. Currently, several coastal projects are in progress along the coast of Korea such as harbor constructions, coastal industrial complex developments, land reclamations, artificial islands, and other coastal constructions. Also, marine transportations, fisheries, coastal recreations, and naval operations have been far increased due to the growth of the Korean society and economy. Therefore, coastal information is needed to support these activities more than ever.

KORDI has been carrying out a research project of the development of an Integrated Coastal Monitoring Network, which is aimed for building an integrated coastal monitoring network of Korea (Lee et al., 2000a, 2000b). The primary goal of the system is to obtain enough coastal data sets in real-time by optimal utilization of the existing coastal structures and the latest communication breakthrough. Several real-time coastal monitoring stations are currently in operation and few are being constructed now.

This paper focuses on the setups of real-time coastal monitoring network using light towers and wireless Internet. The experiences of running the systems will be discussed. Especially, the elegant uses of wireless Internet based telemetering network and its superiority will be emphasized.

MONITORING SYSTEM SETUP

Data logging system (TCP-RT300) installed on a coastal light tower collects waves, tides, atmospheric and environmental data and transmits the data in real-time using wireless Internet at a preset interval. The uploaded data are then processed in different formats such as HTML or WAP (Wireless Application Protocol) and distributed to the users in real-time. The custom made data logging system, TCP-RT300 by DATAPCS, Korea, is a data acquisition device for the real-time data logging based on the CDMA (Code Division Multiple Access) wireless Internet technology. Besides the basic data logging functions, it is also capable of controlling systems and also providing multiple I/O. This system has been optimized for system power savings and easy maintenance. But the real-time capability anywhere and anytime in Korea makes it carry out the most functions wanted by researchers. The overall configuration of this system is given in Figure 1.
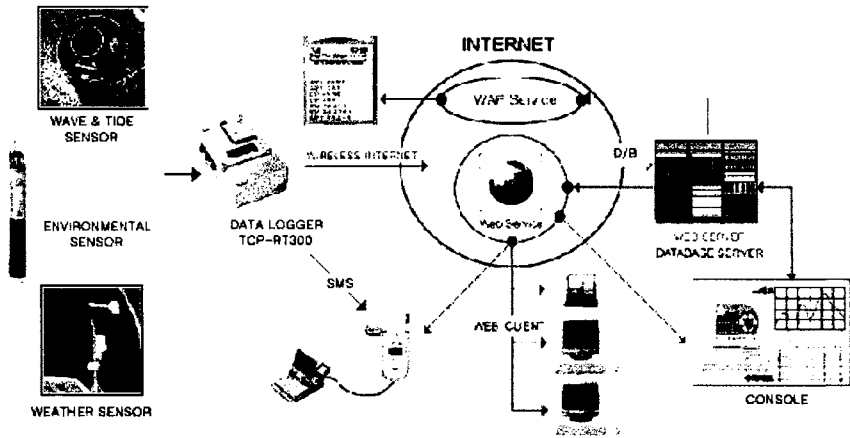
Figure 1. Monitoring network based on TCP-RT300 data logging system

The data controller has two independent processors. One is for the data logging and the other is for the watchdog purpose. These two processors really help each other to prevent the system from unexpected system holdings, which are frequent in coastal weather conditions and no serviceability in bad weather. The main controller is equipped with the 64 k program buffer, 32 k RAM for system memory, 32 k EPROM storage, a real-time clock automatically synchronized with GPS, a 16-bit pulse input, three relay contacts, 16 channel 12 bit A/D ports, a RS422 serial bus line, four software controlled RS232 lines, one hardware RS232 line, three digital I/O, and a digital GPS interface. By supporting many RS232 lines, the interfaces with YSI™ environmental multi-pack sensors, Aquatrak™ acoustic tide level sensor, Agronaut™ ultrasonic velocity meter, and Coastal system's AWS devices are supported simultaneously.

Though all the above interfaces are possible in other similar systems, but the interfaces of the TCP-RT300 were designed for the multiple connections in wireless mode. Therefore, the connection is more handy and effective compared with other systems in market. For example, SMS (Short Message Service) and MTOM (Mobile to Mobile) and Multiple Internet Connection

(MIC) are fully supported in the default setup and thus the user can reach the system easily anytime and anywhere when they need (Park et. al., 2000).

TELEMETERING METHODOLOGIES

The common method of telemetering in coastal environment is a wireless connection. It can be VHF or UHF radio modem connection or it can be a satellite connection such as Inmarsat™ or Orbcomm™. But these two have their pros and cons in real use. The former is handy and less expensive, but it usually reaches only short distance with civil permission and less reliable. The latter can reach the globe but it is slow and very expensive to operate.

The recent development of land based CDMA wireless networks in Korea is quite impressive and gives lots of possibilities for the setup of real-time coastal monitoring purpose. Because these networks provide more than 64 k bi-directional data link and the full digital connection, the quality of data transmission surpasses any previous wireless methods. More than that, this network covers more than 20 km outside from the coastal line, thus most of coastal monitoring stations can be hooked up to the monitoring net.

The advantage of the new system is clear in budgeting, maintenance, system integration, speed, reliability, etc. For the simple comparison of this network to a satellite network shows eight times faster speed and 100 times in operating cost. And the power requirement of the system has decreased two or three times less. But the most promising feature is the do-it-yourself real-time wireless network design capability because all the devices are now available to public without license obligation.

Software of this system is divided into three parts. Field part is written with PICBASIC language from Compile Technology, Co. of Korea. Server part is written with JAVA for Unix environment and Visual Basic for Windows environment. Mobile part is written with WAP (Wireless Application Protocol). The software are tested and optimized under wireless conditions especially with LG 019 PCS (Personal Communication Service) network.

From the data acquisition to the final data distribution the total process takes less than 25 seconds. Five seconds are to connect a system to the network and another five to ten seconds for the data uploading process and ten seconds in the data processing and distribution. Thus 25 seconds later from the starting of data acquisition process, a user really can see field data on the Internet environment.

TYPES AND FUNCTIONS OF SENSORS

Sokcho and Kyoboncho coastal monitoring stations were successfully constructed and launched. The locations are drawn in Figure 2. Three more stations including Ulungdo station will be in service near future. Enabled by the real-time wireless Internet, these stations collect all kinds of coastal data and provide current status of coastal environments.
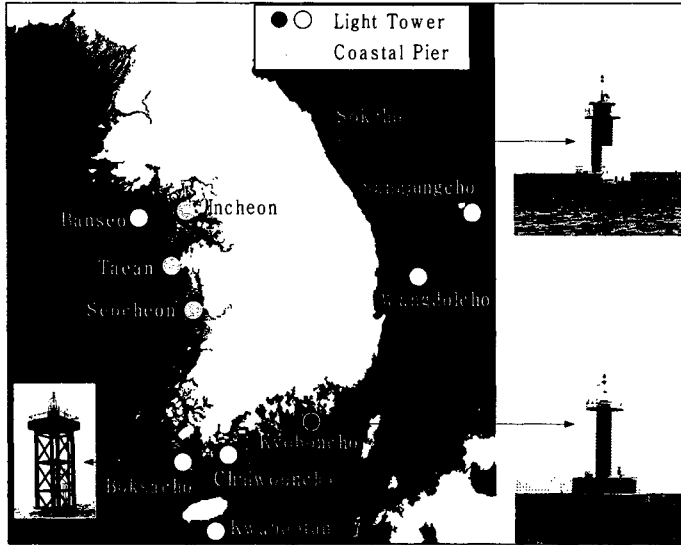
Figure 2. Locations of Kyoboncho and Sokcho station

The number of sensors in a station is typically five and observing parameters are eleven. Wave height, wave period and tide information comes from an ultrasonic surface level sensor. Wind speed, wind gust and wind direction information comes from a wind sensor. Temperature and humidity comes from a temperature sensor and a humidity sensor. The atmospheric pressure sensor gives the air pressure reading. In some cases, an environmental sensor obtains water temperature and salinity information. Usual parameters collected from this system are listed in Tables 1 and 2.

Table 1. Sensors installed at Sokcho station

Sensor	Parameter	Range	Model	Maker
Anemometer	Wind speed ·Wind direction	0 to 60 m/s	05106	R. M. Young
Thermometer	Air Temperature	-40~ +60°C	HMP45A	VAISALA
	Humidity	0~100%		
Barometer	Air pressure	600~1060 hPa	PTB101	VAISALA
UDM 200	Wave ·Tide	0.5~60m	UDM 200	DATAPCS
YSI 600R	Water Temperature	-5~ +45°C	YSI600R-C.T	YSI
	Salinity	0~70 PPT		

Table 2. Sensors installed at Kyoboncho station

Sensor	Parameter	Range	Maker/Model
Wind Direction Sensor	Wind direction		AANDERAA/MODEL 3560
Wind Speed sensor	Wind speed	0-79m/s	AANDERAA/MODEL 2740
Air Pressure Sensor	Air pressure	920~1080hPa	AANDERAA/MODEL 2810
Air Temperature Sensor	Air temperature	-43~+48°C	AANDERAA/MODEL 3455
Relative Humidity Sensor	Humidity	0~100%	AANDERAA/MODEL 3455
Salinity/Temperature Sensor	Water temperature, salinity	0~40ppt -7.5~+41°C	AANDERAA/MODEL 3210
AQUATRAK	Tide	0-15m	AQUATRAK

REAL-TIME ALARM FUNCTION

The new coastal monitoring network is designed to meet the basic needs of researchers and government officials and also civilians. But to the system manager independent anytime access to the system is anxiously needed and even "the must have option" for good maintenance. If Internet stops operations for hours, manager needs an access tool for checking field systems. In addition, if manager is away from Internet line, there must be a way to get information whenever some serious field conditions happen. If this kind of a handy alarm function exists, it will be very valuable to the system manager. Fortunately, this function is already built in this system through SMS service. Thus manager always can monitor the system status and happenings resulting in better system maintenance.

MOBILE DATA SERVICE

After sampling and transmitting to the server, raw data are stored in D/B and then processed in two viewable formats; HTML and WAP. Still, HTML format is more informative and fast to the Internet users, but it has a limitation of "go and check" philosophy. Thus when a user needs information on the road, he has to go to an Internet ready place to check information. In this sense, the value of real-time information is lowered. But the mobile format WAP can fill this gap between the out of office user and the real-time use. If someone has WAP ready compatible mobile phone, information goes anytime and anywhere. In Korea, the high-tech mobile phone uses are exploding and thus the service through this mobile phone is much practical. It's a very clear trend now.

For example, WAP service of Sokcho station is illustrated in Figure 3. If a WAP user enters keys of the mobile Internet address, he can get the real-time coastal data on his phone. He can browse the information in text and graphic formats. Already five coastal monitoring stations are in service.
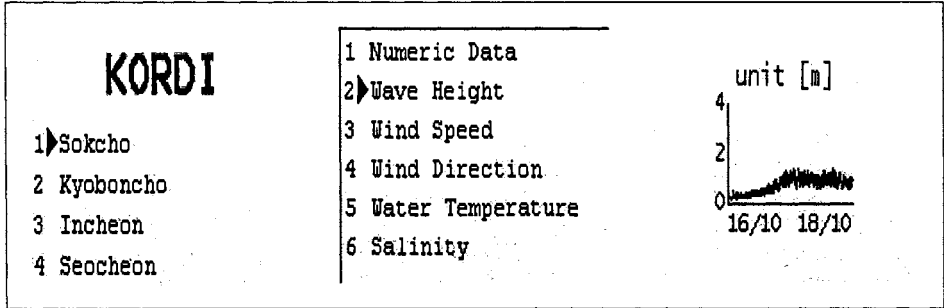
Figure 3. Mobile data service through WAP ready phone (http://m.aws.co.kr)

RECENT SYSTEM PERFORMANCE

A tropical depression developed in the southwest pacific region on June 29 2002 and became a category 3 typhoon (named Rammasun) three days later. After passing through the Yellow Sea, it penetrated the Korean peninsula and then disappeared seven days later. The approach and landing of the typhoon on the Korean peninsula was monitored at the Sokcho and Kyoboncho stations. Figure 4 shows the typhoon track obtained from the U.S. Navy FMOC site and Figure 5 shows wind speed and air pressure fluctuations recorded at each station.

Figure 4. Typhoon Rammasun track report on July 4, 2002

204

Wind Speed and Air Pressure Fluctuations due to the Typhoon Rammasun

Figure 5. Example of real-time data from the monitoring stations

It can be seen in Figure 5, the air pressure at Kyoboncho station (500 km eastside of typhoon center) dropped to 970 hPa and the wind speed was reaching up to 20 m/s. As a matter of fact, after five hours of peak detection of wind speed, the Kyoboncho system got a little maintenance problem, but it was repaired in two ways for its full function again.

CONCLUSION

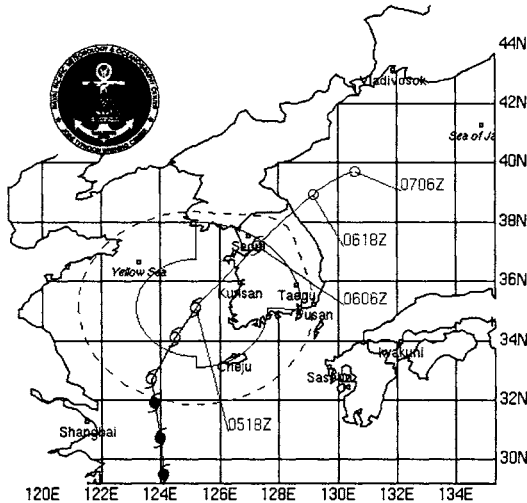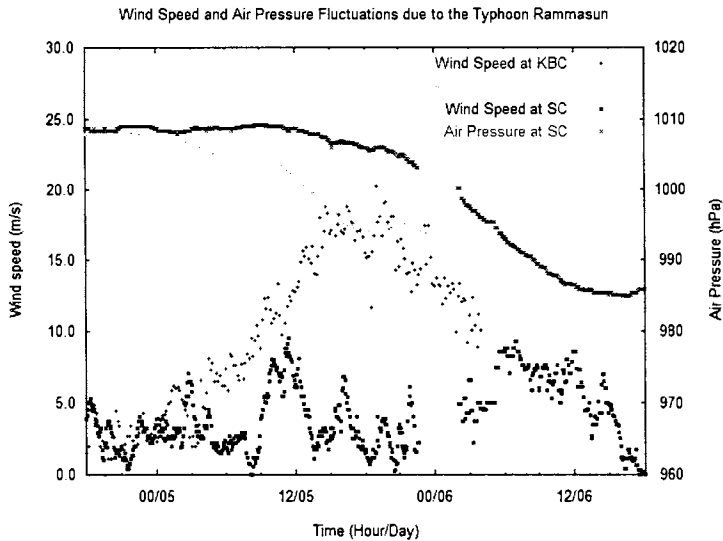Kyoboncho and Sokcho coastal monitoring stations were successfully launched a year ago according to the 10 year long national plan for the Korea coastal observation program. Compared with the old system, this new system is more efficient in real-time communication, maintenance cost, reliability, and user satisfaction. The exact time synchronization, two ways communication capability, and SMS function make the maintenance job much easier and thus result in overall system performance higher. Most of all, the most important feature of this new system is that it is Internet-ready at the field level.

This monitoring system will serve as following purposes. Firstly, valuable coastal data will be collected for the people who need real-time coastal information. Distributed over the Internet, data will be available to everyone who has access to the Internet. Secondly, these systems will provide more accurate scientific data sets to research community. Thirdly, Korea's coastal engineering standard will be updated and changed based on new statistics measured by this network. Fourthly, the experiences learned from this project will be used to the other areas such as real-time environmental monitoring, disaster prevention network and real-time weather monitoring. The remarkable wireless Internet network can really change and upgrade the real-time coastal information services to the public from the field data logger to the final data users.

205

ACKNOWLEDGEMENTS

REFERENCES

Lee, D.Y. and K.S. Park. 2000a. Integrated Coastal Observing System. Technical Report, BSPM 99043-00-1259-2, Korea Ocean Research and Development Institute. p. 617 (in Korean).

Lee, D.Y. and K.S. Park. 2000b. Integrated Coastal Observing System and Operational Korea Ocean Prediction System. Technical Report, BSPM 00050-00-1291-1. Korea Ocean Research and Development Institute. p. 237 (in Korean).

Park, K.S. and D.Y. Lee. 2000. An Implementation Plan for National Ocean Monitoring Network: Real-time Coastal and Ocean Monitoring Network. Technical Report, PK00035. p. 194. (in Korean).

Park, K.S., S.I. Kim, S.W. Kang, J.K. Lee and S.D. Kim. 2001. Real-time Tide and Storm Surge Monitoring System using Internet Wireless Modem. Proceeding of the Workshop on Meteorological Disaster of Natural Hazard Prevention Research. pp. 51-59. (in Korean).

A NEW MONITORING TOOL:
AUTOMATIC MEASUREMENTS FROM FERRY BOATS

Friedhelm Schroeder, Wilhelm Petersen, Michail Petschatnikov and Franciscus Colijn

GKSS Research Centre, Institute for Coastal Research
Geesthacht, GERMANY
friedhelm.schroeder@gkss.de

ABSTRACT

A new operational tool which uses ferry boats as carrier system for automated monitoring equipment has been developed. Such systems can be operated with much less costs than automatic buoys and have better performance with regard to bio-fouling. The "German FerryBox" consists of a fully automated flow-through system with sensors and automatic analysers for the measurement of oceanographic and chemical parameters, among which are nutrients and algal properties. It provides the possibility of automatic cleaning cycles and position-controlled sampling (GPS). Data can be transferred to shore and the system can be remotely operated by mobile phone. The system has been installed on the ferry Hamburg-Harwich (U.K.) and is under test since November 2001. Results from recent measurements demonstrate the function and applicability of the ferry system.

INTRODUCTION

General Monitoring Aspects

Since some decades the contamination of coastal waters with nutrients and toxic substances is of growing concern in European countries. For an assessment of the water quality of these regions operational monitoring programs had been implemented. In this context the main aims of water quality monitoring are:
- Preventing the potential danger to human health.
- Assessing the impact of anthropogenic substances on aquatic ecosystems.
- Documenting the present state of water pollution.
- Showing the efficiency of water protection measures by means of emission values.

In order to achieve these objectives mainly three different categories of monitoring are defined [EEA]:
- Statutory monitoring by which a state meets its legal obligations arising from EC and national legislation and international agreements.
- Surveillance monitoring through which a broad view and comparison of water resource quality and quantity can be obtained across a State (or across Europe). This type of monitoring is usually used to make spatial and temporal comparisons.

- Operational monitoring which is undertaken to meet the specific business and operational needs of the regulators or users of water. Examples might be the monitoring of specific discharges, clean-up campaigns on specific catchments or monitoring after pollution incidents.

Whereas in the last decades different approaches were used for monitoring of rivers and coastal areas the "European Water Framework Directive" which had been implemented in 2001 now points to an integrated assessment of whole watersheds [EEA]. This aspect is also followed in some running EU projects (e.g., the EUROCAT project: European catchments: Catchments changes and their impact on the coast).

There are three aspects of "integrated monitoring strategies" which are new in comparison to "conventional" monitoring:

1. Different physical, chemical and biological parameters have to be measured simultaneously in order to assess important processes which may influence the water quality,
2. Monitoring, i.e., sampling and in situ measurements, have to be carried out in a dense spatial and temporal grid. This implies that continuous (automatic) measuring stations have to be applied at strategic positions, e.g., river mouths, in order to monitor important short-term events, e.g., fresh water discharges (temporal dense time series). In order to assess spatial distributions (patchiness) remote sensing has to be taken into account, e.g., for algal distributions.
3. Due to high operational costs only few automatic stations can be operated. Therefore, numerical models (physical and ecological models) can be used for spatial and temporal "interpolations".

Another objective of monitoring is to use this as the basis for long-term ecological observations, which can be used as input for ecological models and to understand effects of global change on marine ecosystems.

Automatic Monitoring from buoys

Looking at the practical aspects of physical, chemical and biological monitoring of rivers, coastal areas and shelf seas it is evident that operational monitoring is mainly carried out by manual sampling during ship cruises and following analyses in the laboratory. In the "official" monitoring programs for the North Sea this is carried out three to six times per year, which is not enough to observe the spatial extensions of phenomena such as algal blooms, which have a typical random short time distribution. Information about spatial distributions therefore is strongly hampered by a fixed station strategy. (Althuis et al., 1994). Whereas sampling is the only feasible method for counting biological species and the analysis of trace contaminants, e.g., heavy metals or organic micro-pollutants, there are other, complementing methods for the automatic unattended measurement of standard oceanographic parameters, e.g., temperature, salinity, currents and in some cases other parameters, e.g., turbidity, oxygen, nutrients and chlorophyll fluorescence. Mainly these automated measurements are carried out from different types of moored buoys or other fixed marine stations (Hydes et al., 1998; Knauth et al., 1996, 1997; Nies et al., 1999; Sanders et al., 2001).

Despite the many advantages of these operational systems from buoys among which are
- The assessment of short-term events (storms, fresh water discharge etc.).
- Production of consistent long-term time series with high temporal density.

There are also some serious disadvantages:
- Only point measurements.
- Often data gaps due to bio-fouling of sensors and maintenance difficulties due to difficult accessibility of stations during bad weather.
- High operational costs due to maintenance by ship cruises.

Based on all these problems and limitations, it seems logical to investigate which role ships of opportunity could play (Tziavos and Flemming 1998; Fleming et al., 2002)

Automatic Monitoring from ships (Ferry Boats or Ships-of-opportunity)

There are many routes for ferryboats and "ships-of-opportunity" which run quite frequently. Already 60 years ago the "Continuous Plankton Recorder (CPR)" (Reid et al., 1998) followed the idea of using scientific equipment on such ships for continuous recording of environmental data. This method is now improved and shows an impressive data set of semi-quantitative phytoplankton data over the world oceans (SAHFOS). Within the last years some more sophisticated systems had been implemented on ferryboats, which allow more precise measurements of temperature, salinity and chlorophyll (Althuis et al., 1994; Harashima et al., 1997; Harashima and Kunugi, 2000; Koske, 2002; Rantajärvi et al., 1998; Ridderinkhof et al., 1999; Swertz et al., 1999) and even continuously measurements of some nutrients (Holley and Hydes, 2000).

Applying such measuring systems on ferry boats or ships-of-opportunity has several advantages:
- The measuring system is protected against harsh environment, e.g., waves & currents etc.
- Bio-fouling can be more easily prevented due to inline sensors).
- No energy restrictions in contrast to buoys.
- Easier maintenance when ferry comes back "on one's doorstep".
- Much smaller running costs since the operation costs of the ship have not to be calculated.
- Instead of point measurements (buoys) transects yield much more information a sea area.

Within the GOOS (Global Ocean Observing System) and EuroGOOS Framework we have started initiatives to develop automatic measuring systems for bio-oceanographic parameters. As a measuring platform ferries on regular routes offer a cheap and reliable possibility to obtain regular observations on near surface water parameters. Present activities are both nationally and internationally EU funded.

MATERIAL AND METHODS

German FerryBox project

The "German FerryBox" consists of a fully automated flow-through system with different sensors and automatic analysers. Figure 1 shows a schematic drawing of the German FerryBox system. Water is pumped into the ship from an inlet in front of the ships cooling system. A debubbling unit removes bubbles, which may enter the system during heavy seas. At the same time coarse sand particles which may be introduced in shallow harbours and which settle and tend to block the tubes are removed as well. Coupled to the debubbler is an internal water loop in which the seawater is circulated with a constant velocity of about 1 m/s. This already decreases the tendency for building bacterial slimes on sensors and tube surfaces. A small part of the water is filtered by a ribbon-type filter for automatic nutrient analysis. This type of filter has the advantage of regularly providing new filter material, therefore avoiding bacterial processes which may influence the measured concentration of nutrients (trace analysis). The system contains motor valves and control sensors, e.g., pressure and flow, for automatic operation. For a reliable unmanned operation the system is supervised by an industrial programmable logic control which can shut-off the system in case of very severe errors and operates automatic cleaning cycles, e.g., in harbour. Data acquisition, data storage and data transfer to shore is controlled by an industrial standard PC (Pentium II). Data can be transferred to shore and the system can be remotely operated by GSM (mobile phone).

Bio-fouling is prevented by cleaning of the sensors with tap water and rinsing with acidified water or under severe conditions (tropics) by chlorination. Sometimes clogging of the water inlet in the ship interface by debris or fish causes problems. Since all flow rates are supervised by the system in such cases an automatic pressure back-flushing cycle is initiated which clears the inlet.
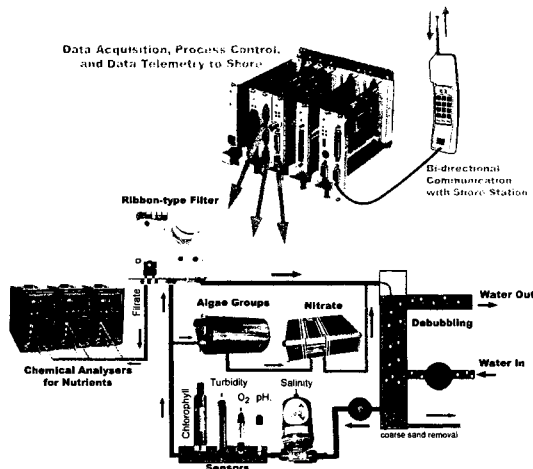

Figure 1. Schematic drawing of the German FerryBox system

At the time being, the FerryBox has sensors and analysers for the following parameters:

- water temperature (Endress & Hauser),
- salinity (ECELL from FSI),
- turbidity (Endress & Hauser),
- turbidity (Turner design),
- dissolved oxygen (Endress & Hauser),
- pH (Endress & Hauser),
- chlorophyll fluorescence (Turner design),

- nutrients: ammonium, nitrate/nitrite, phosphate, silicate(Grisard GmbH),
- main algal groups (special analyser to discriminate between different algal classes based on different fluorescence patterns) (bbe moldaenke).

- Housekeeping parameters: Position (GPS), pressures, flow velocities, position of valves etc.

From these sensors especially the analysers for nutrients and the sensor for algal groups should be mentioned:

Nutrient analysis is carried out by chemical analysers which automatically carry out the same procedures which are applied in standard marine chemistry manually in the laboratory:
1) Nitrate analysis is carried out by reduction of nitrate to nitrite (Cd-reductor) and formation of an azo dye (Grasshoff, 1983).
2) o-phosphate is determined by formation of a blue phosphomolybdate complex according to the method of Koroleff (Grasshoff, 1983).
3) Silicate analysis is carried out according to the method of Grasshoff (Grasshoff, 1983).
4) For ammonium the sensitive fluorometric method of Kerouel is used (Kerouel and Aminot, 1997).

The analysers are automated batch analysers with variable optical path length, manufactured by ME Grisard, Trappenkamp, Germany. In addition a new optical method for nitrate determination is under test: By measuring the spectrum of sea water from 200 nm to 400 nm and applying a multi-component analysis to the known spectra of nitrate, bromide and humic substances nitrate can be measured quantitatively in the range from about 1 μmol/l to 100 μmol/l (automatic change of path length) (Petschatnikov et al., 2003)

Algal groups are measured by sequential fluorometric excitation with five LED's (blue, green, yellow, orange & red) and measurement of the emitted fluorescence signal. By careful calibration phytoplankton with distinctive different pigment patterns can be distinguished, e.g., green algae, blue-green algae and diatoms. The instrument is now under test during the cruises. In regular intervals samples are taken and plankton is counted and chlorophyll measured by HPLC for comparison.

Table 1 gives an overview of the specification of the different sensors/analysers. The stated accuracies in the table are derived from data of the manufacturers and from experience on similar test systems. At the time being, a quality assurance program for qualifying all ferry modules is under way.

The first installation of the system has been taken place on the ferry between Hamburg (Cuxhaven) and Harwich and is under test since November 2001. Figure 2 shows the DFDS ferry route and a photo of the ferry. As shown the ferry route covers the southerly part of the North Sea and crosses the waters flowing from the English Channel to the North. Unfortunately, in March 2002 the ferry route has been shortened, it now starts from Cuxhaven missing the inner Elbe estuary. Figure 3a shows a detailed line diagram of the water system

with all main components. In Figure 3b a photo of the water system on board the ferry is shown.

Table 1: Accuracies of sensors resp. analysers

Parameter	Range	Accuracy	Resolution	Uncertainties or bias due to flow system
water temperature	-10 to 50 °C	0.1 °C	0.01	due to water inlet
salinity	0 to 50	0.02	0.001	due to very small bubbles
turbidity -E&H	0 to 9999 FNU	10 %	0.001 FNU	due to very small bubbles [2]
turbidity -Turner	0 to 50 NTU	to be tested	0.05 NTU	due to very small bubbles [2]
dissolved oxygen	0 to 20 mg/l	0.2 % F.S.	0.01	[3]
pH	0 to 15	0.1	0.01	
chlorophyll-Turner	0 to 200 µg/l	10%	0.5	uncertainties due to changing fluorescence yield, influenced by high turbidity
ammonia	0.1 to 30µmol/l	15%	0.001	
nitrate	0.5 to 500 µmol/l [1]	15%	0.01	
o-phosphate	0.2 to 50 µmol/l [1]	15%	0.05	
silicate	0.1 to 100 µmol/l [1]	15%	0.01	
algal groups	1 to 200 µg/l chloroph.	to be tested	5 µg/l	accuracy depending on calibration and algal group [4]

[1] With two different optical path lengths and dilution at larger concentrations.
[2] Normally only bubbles > 2 mm are occurring in the system; they are removed by the debubbling unit. It has to be tested if under certain conditions much smaller bubbles can occur which would mainly disturb the turbidity measurement.
[3] In similar system it could be proven that the pumping system does not distort the measurement of oxygen under normal conditions in the sea. However, it has to be tested what will be the error at situations with extreme under- or over-saturation.
[4] The method can only measure algal groups that have been calibrated. If another group appears it will be sorted into a wrong group. Algal groups with similar pigments may have a large error (Ruser, 2001).
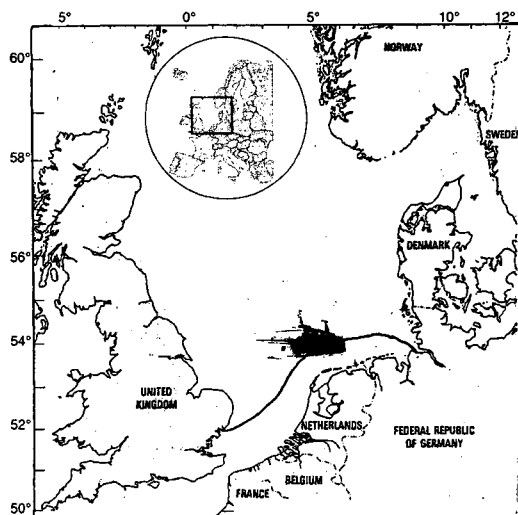

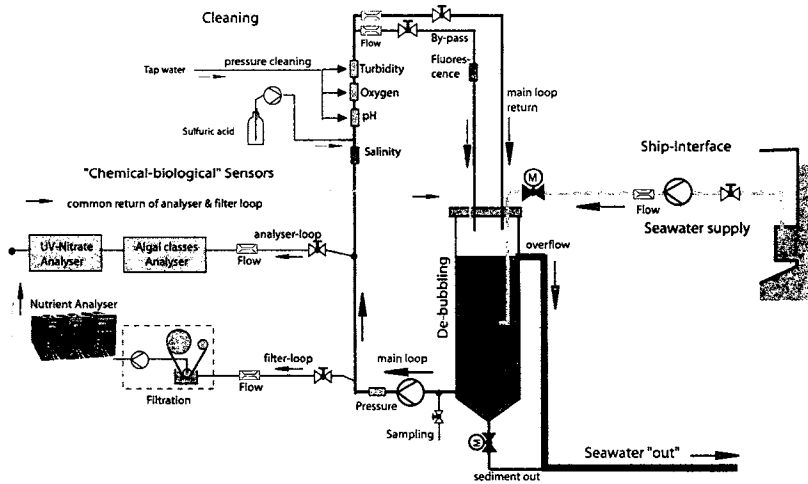Figure 2. Ferry route with photo of the ferry "Admiral of Scandinavia"

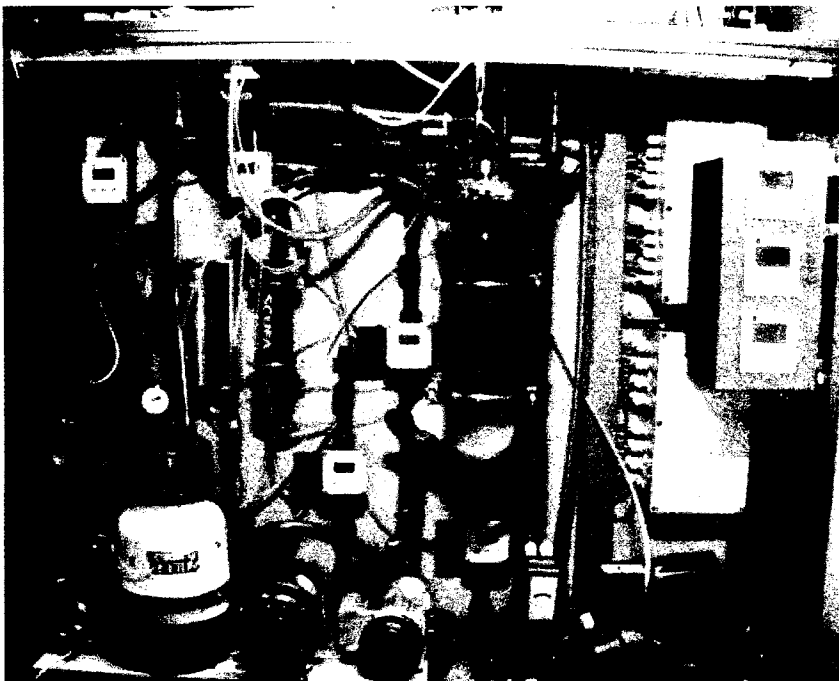Figure 3a. Line diagram of the water system

Figure 3b. Photo of the water system on board the ferry

As can be seen from the photo, the system consists of many components, many of them enabling a save automatic operation (the chemical analysers are not shown; they are located in a compartment above the flow unit together with cooled reagent reservoirs).

RESULTS AND DISCUSSION

Since November 2001 measurements were obtained regularly (one day Hamburg to Harwich, second day Harwich to Hamburg).

Results from one cruise in May 2002
In Figure 4 results from a cruise in May 2002 are shown.

In the following section some typical patterns of the measurements during springtime will be discussed:

Part A of Figure 4: Temperature, salinity & turbidity
In the temperature curve, the higher temperatures at the coastal waters (Cuxhaven and English coast) can be seen. The salinity curve near Cuxhaven shows the fresh water outflow of the river Elbe, whereas the decrease near Harwich is only marginal. It is also evident that along the Dutch coast lower salinities are observed than in the English Channel. This is due to fresh water influence of the Ijsselmeer and the river Rhine. Near Harwich a high turbidity is measured which is characteristic of the coastal areas at the English coast. Despite the low salinities off Cuxhaven the turbidity is not too high since the turbidity zone of the Elbe estuary is located in the inner estuary near Brunsbüttel.

Part B of Figure 4: Total chlorophyll concentration & algal groups
The total chlorophyll concentration shows two maxima, one near Cuxhaven and one between the English Channel and the Dutch coast. The maximum near Cuxhaven is typical for the first spring bloom in front of the Elbe estuary. The main reason for this could be the high nutrient concentrations (see Part D) in combination with the relatively moderate turbidity (light availability). In this peak diatoms are dominant, however also green algae exist. The second chlorophyll peak at the Dutch coast is the first mass occurrence of algae in this area in spring. Here, green algae and diatoms are both prevailing. We will see later that this algal bloom is not stationary over time (see below).

Part C of Figure 4: pH and oxygen concentration
The pH varies between 7.9 and 8.4 pH units. Near the Elbe estuary (Cuxhaven) the values are lower due to the fresh water input. However, other low values can be found near Harwich where the freshwater influence is negligible. Since here the oxygen concentrations are low, turbidity is high and ammonium is high as well, one could guess that oxygen consumption processes of re-suspended sediments will contribute to these lower pH values. As expected, pH and oxygen also show maxima at the chlorophyll peaks, thereby reflecting the higher primary productivity of these areas.

Part D of Figure 4: Ammonium and nitrate concentrations
Within the ferry profile the nitrate concentrations are varying between 0.1 and 90 µmol/l (1.5-1400 µg-N/l) and the ammonium concentrations vary between 0.1 and 1.3 µmol/l (1.5 - 18 µg-N/l). The largest nitrate concentrations are measured near Cuxhaven due to high nitrate input from the river Elbe. Near the English coast the largest ammonium concentrations are found whereas nitrate is slightly enhanced. One astonishing result is the broad maximum

between km 300 and km 430 which can be found during most ferry cruises in spring and summer. At the time being its origin is unclear.

Chlorophyll results from cruises January to October 2002
After presenting a transect at one time it will be interesting to observe the development of the algal bloom from the beginning in March. In Figure 5 a contour plot of the chlorophyll concentrations from Harwich to Cuxhaven is depicted for the time interval between January and October 2002. On the vertical axis the time is depicted; the horizontal axis shows the distance from Harwich (compare the map in Fig. 4). The chlorophyll concentrations are colour-coded from small values (light gray; 2-7 µg/l) to large values (dark gray to black; 14-22 µg/l). As can be seen, until the end of February no algal growth exists. This starts between 180 km and 220 km in early March. Later in April plankton growth occurs along the whole Dutch and German coast. In early May this bloom breaks down, leaving only the patches at 150 km and 560 km - as already shown in Figure 4. Then again in June some patches occur between 250 and 500 km. From mid of August only very small chlorophyll concentrations occur.

Figure 5 only reflects measurements along the ferry transect. It cannot decided if the decrease of chlorophyll concentrations along the Dutch and German coast reflects a break down of algal populations or if the large "algae patch" was drifting out of this transect.

DISCUSSION

From the chlorophyll data it is evident that due to the patchiness taking samples from research ships would only be successful if the cruise had been carried out at the "right" times and at the "right" locations. On the other hand, stationary (fixed) buoys would only by chance detect these algal blooms if they had been anchored within the area of the bloom. Contrary to this, transects with ferries have a greater chance for the assessment of algal blooms. If these measurements are combined with satellite measurements-as we plan to do in the very near future with ENVISAT- the "fate" of algal patches even can be followed. In the case of Figure 5 this means that one can decide if the algal bloom broke down or was drifting out of the region. Simultaneously the ferry data can be used for calibration of satellite data (*in situ* truth). Since in the North Sea the satellite coverage is poor due to clouds, a numerical model could be used for further improvement of the assessment of algal blooms.

CONCLUSIONS

It could be shown that ferry boats or ships-of-opportunity equipped with automated systems for water quality measurements are a suitable tool which can supplement existing "conventional" monitoring in coastal areas and shelf seas. However, integrated monitoring strategies which are carried out by combining sampling from ships, automatic fixed stations, automated ferry systems, remote sensing and numerical models do not only require good concepts and strategies in order to achieve the maximum of information with the minimum of resources, but also requires suitable tools to merge the different types of data (different spatial and temporal scales).

At the time being, some of these tools and methods are now developed and tested in EU projects, among which is the "FerryBox" project, in which eight ferry routes will be used for an comparison of different European ferry "boxes". After completion of the different EU

projects strategies should be developed which demonstrate how future integrated monitoring systems can be operated and show the benefits of enhanced coverage and information density.
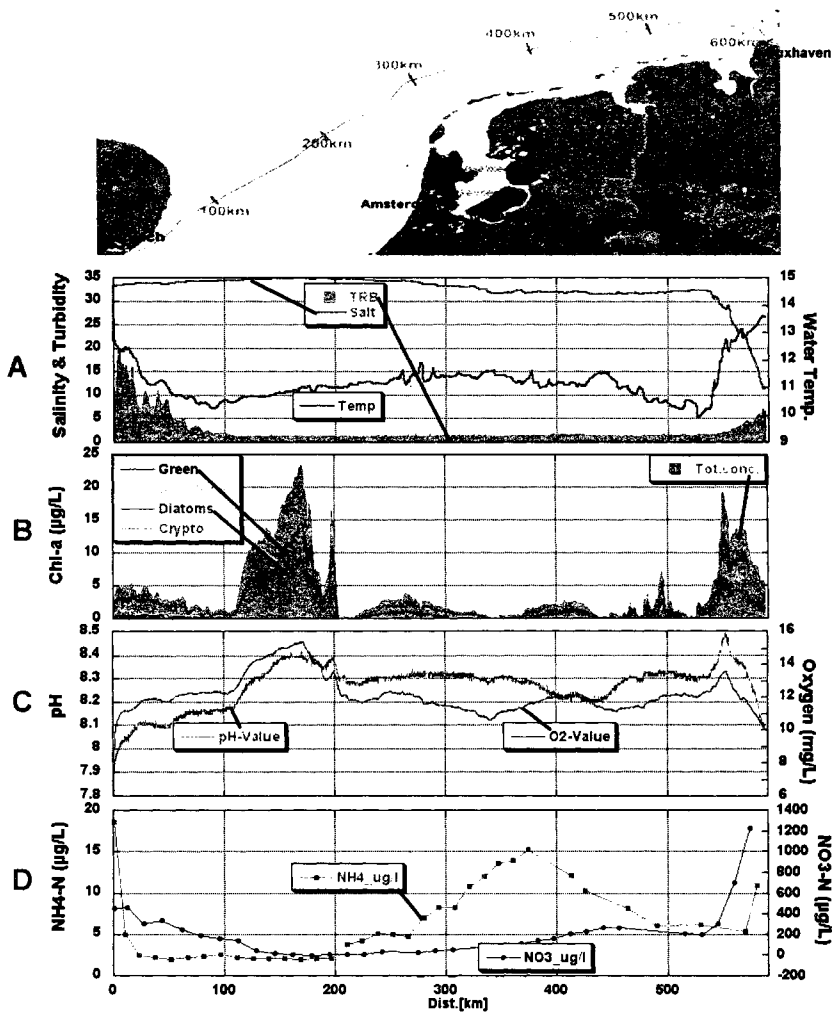

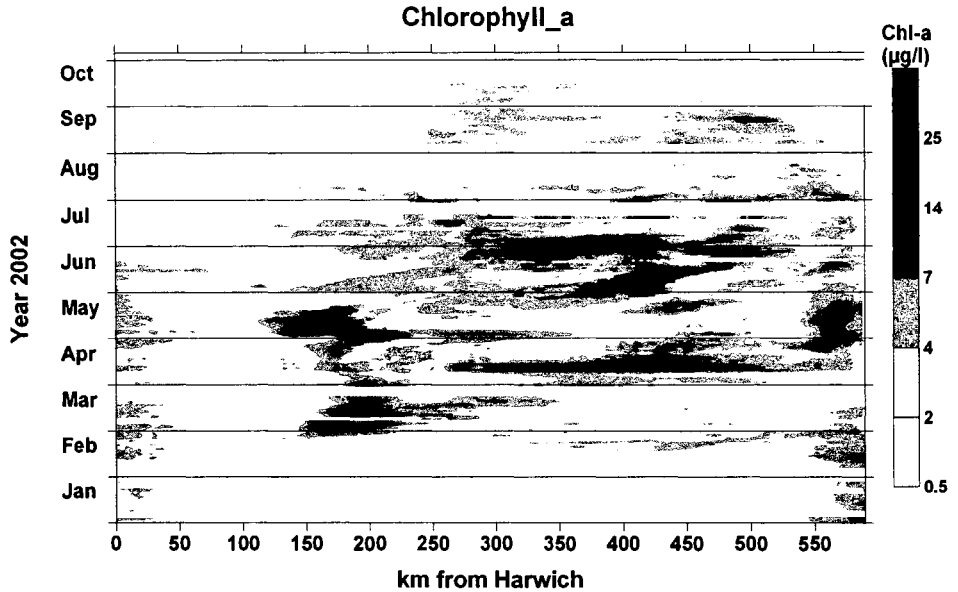Figure 4. Results from a ferry cruise Harwich to Cuxhaven 13.5.2002

Figure 5. Chlorophyll concentrations between January and October 2002

REFERENCES

Althuis, B.A., Gieskes, W.W.C., Villerius, L. and Colijn, F. 1994: Interpretation of fluorometric chlorophyll registrations with algal pigment analysis along a ferry transect in the Southern North Sea. Neth. *J. Sea Res.* 33 (1): 37-46.

EEA: Reports, recommendations and concepts by European Environment Agency, Internet address: http://themes.eea.eu.int/Specific_media/water.

Flemming, N.C.S., Vallerga, N., Pinardi, H.W.A., Behrens, G., Manzella, D. and Prandle, J.H. 2002. Operational Oceanography: implementation at the European and regional seas. Proc. Second International Conference on EuroGOOS, Elsevier Oceanography Series Publication series 17.

Grasshof, K., Ehrhardt, M. and K. Kremling (eds.) 1983. Methods of Seawater Analysis. Verlag Chemie, Weinheim, ISBN 0-89573-070-9.

Harashima, Akira and Masayuki Kunugi. 2000. Comprehensive Report on Marine Environmental Monitoring and Related Studies Using Ferry Boats. CGER-Report, National institute for Environmental Studies, Environmental Agency of Japan, CGER-M007-2000, ISSN 1341-4356.

Harashima, A., Tsuda, R., Tanaka, Y., Kimdo, T., Tatsuta, H. and Furusawa, K. 1997. Monitoring algal blooms and related biogeochemical changes with a flow through system deployed on ferries on the adjacent seas of Japan. pp 85-112 *In* Monitoring Algal Blooms; New techniques for detecting large scale environmental change (eds M. Kahru & C.W. Brown) Springer Verlag, Berlin.

Holley, S.E. and D.J. Hydes. 2000. Ferry-boxes" and data stations for the improved monitoring and resolution of eutrophication related processes. Conference Proceedings - Oceanography International 2000, Brighton, U.K. 7-10 March 2000. pp 521-529

Hydes, D.J., Wright, P.N., Waddington, I. and Rawlinson M.B. 1998. Real-time monitoring of eutrophication processes using adata buoy. Conference Proceedings Vol. I. Oceanography International 98, 10-13 March 1998 Brighton, U.K. ISBN 0900254203, pp 59-67.

Kerouel, R. and Alain Aminot. 1997. Fluorometric determination of ammonia in sea and estaurine waters by direct segmented flow analysis. *Mar. Chem.* 57 (1997) 265-275.

Knauth, H.-D., Schroeder, F., Kohnke, D. and Holzkamm, F. 1996. Coastal Monitoring Network- remotely controlled German system alerts operators to METOC events; provides monitoring and analysis data- New Technologies. Sea Technology, 1996, Vol. 37, No. 12, pp. 33-43.

Knauth, H.-D., Schroeder, F., Menzel, R., Gebhart, E., Marx, S., Kohnke, D., Holzkamm, F. , Nies, H. and Theobald, N. 1997. Marine Pollution Network EUROMAR-MERMAID: Results of the Experimental Operation. Dt. Hydr. Zt., Vol. 49 (1997), No. 2/3.

Knauth, H.-D., Schroeder, F., Menzel, R., Thurow, S., Marx, S., Kohnke, D. and Holzkamm, F. 1996. The German Operational Monitoring Network: Present State and New Technologie 1996. Oceanology 96, Brighton, Conference Proceedings. Spearhead Exhibition Ltd., New Malden, Vol. 3, pp.21-43 1996, ISBN 0-900254-13-0.

Koske, P. 2002. Ferries in operational oceanography – the German Ferry Box Project. In: Flemming, N.C., S.; Vallerga, N.; Pinardi, H.W.A.; Behrens, G.; Manzella, D.; Prandle, J.H. 2002. Operational Oceanography: implementation at the European and regional seas. Proc. Second International Conference on EuroGOOS, Elsevier Oceanography Series Publication series 17, 317-324.

Leppänen, J.-M. and E. Rantajärvi. 1995. Unattended recording of phytoplankton and supplemental parameters on board merchant ships- an alternative to the conventional algal monitorings programmes in the Baltic Sea. In: Lassus, P., Arzul, G., Erard-Le Denn, E., Gentien, P. and Marcaillore-Le Baut, C. (eds.), Harmful marine algal blooms. - Lavoisier. - Paris: 719-724.

Nies, H., Brügge, B., Sterzenbach, D., Theobald, N., Dick, S., Knauth, H.-D. and Schroeder, F. 1999. Erste Ergebnisse des Projektes CANVAS (Contaminants and Nutrients in Variable Sea Areas). Deutsche Hydrographische Zeitschrift. Supplement 10, 1999.

Petschatnikov, M., Schroeder, F. and Menzel, R. 2003. Determination of Nitrate in Natural Waters by evaluation of the UV Spectrum with Multiple Linear Regression (in publication).

Rantajärvi, E., Olsonen, R., Hällfors, S., Lepännen, J.H. and Raateoja, M. 1998. Effect of sampling frequency on the detection of natural variability in phytoplankton. Experiences based on unattended high-frequency measurements on bord ferries in the Baltic Sea. *ICES Journal of Marine Science.* 55;pp.697-704.

Reid, P.C., Edwards M., Hunt H.G. and Warner, A.J. 1998. Phytoplankton change in the North Atlantic. *Nature, London.* 391. 546

Ridderinkhof, H., van Haren, H., Eijgenraam, F. and Hillebrand, T. 1999. Ferry observations on temperature, salinity and currents in the Marsdiep tidal inlet between the North Sea and Wadden Sea. in: Second Eurogoos conference, Rome, 1999 (published by Elsevier).

Ruser, Andreas. 2001. Untersuchung der Erkennung von Algengruppen und deren photosynthetischer Aktivität im marinen Bereich. Dissertation at University Kiel. Berichte, Forschungs- und Technologiezentrum Westküste d. Univ. Kiel, Nr. 25, 206S, ISSN 0940-9475.

SAHFOS: Sir Alister Hardy Foundation for Ocean Science. Reports for 1999-2001. Internet address: www.sahfos.org

Sanders, R., Jickells, T. and Mills, D. 2001. Nutrients and chlorophyll at two sites in the Thames plume and southern North Sea. *J. Sea Res.* 46 (2001) 13-18.

Swertz, O.C., Colijn, F., Hofstraat, H.W. and Althuis, B.A. 1999. Temperature, salinity and fluorescence in the Southern North Sea: high resolution data sampled from a ferry. Environmental Management, 23(4): 527-538.

Tziavos, C. and Flemming, N.C. (eds). 1998. The EuroGOOS Technology Plan Working Group Report. EuroGOOS Publication No.13, Southampton Oceanography Centre, Southampton. ISBN 0-904175-37-5.

INTERMITTENT UPWELLING IN THE WESTERN EQUATORIAL PACIFIC OCEAN REVEALED BY SEAWIFS

Katsutoshi Kozai[1], Kunimitsu Ishida[2], Takuhei Shiozaki[3] and Yasuhiko Okada[4]

[1]Kobe University of Mercantile Marine
Kobe, JAPAN
kouzai@cc.kshosen.ac.jp

[2]Toba National College of Maritime Technology, Toba, Mie, JAPAN
[3]Osaka Prefecture University, Sakai, Osaka, JAPAN
[4]Kinki University, Higashiosaka, Osaka, JAPAN

ABSTRACT

During the research cruise of R/V MIRAI (MR01-K05 Leg3) from November 9 to December 9, 2001, at the point of 2°N and 138°E in the western equatorial Pacific Ocean, SeaWiFS local area coverage (LAC) scenes are received by the station onboard R/V MIRAI while in situ atmospheric and oceanographic observations including the parameter of sea surface temperature, salinity, chlorophyll- a and current velocity profile to the depth of 300 m are carried out. The observed surface salinity and chlorophyll- a concentration increase from 34.1 to 34.37 and from 0.05 to 0.14 mg/m^3 respectively while sea surface temperature decreases from 30 to 29.3 degrees after the week-long prevailing northwest monsoon wind with the maximum gust more than 20 m/s. The increase of chlorophyll- a in this region is also shown in the multi-date SeaWiFS chlorophyll-a concentration products. During the period of the week-long northwest monsoon wind the current velocity of upper 70 m reaches more than 60 cm/sec in the southeastward direction while the current velocity at the depth from 80 to 120 m indicates 50 cm/sec in the northwestward direction. The current of upper 70 m corresponds to the Northwest Monsoon Current (NMC) and the intrusion of NMC enhanced by the strong northwest monsoon winds (westerly wind bursts) causes a reversal in the sub-surface current (New Guinea Coastal Undercurrent (NGCUC)) which creates a temporal upwelling in this region.

INTRODUCTION

Equatorial upwelling in the Pacific Ocean is known to occur east of the date line (Wyrtki, 1981). However the estimates of equatorial upwelling in the western equatorial Pacific Ocean is reported based on the moored current measurements (Halpern et al., 1989; Helber and Weisberg, 2001). Furthermore the presence of upwelling produced by the predominantly easterly winds in the western equatorial Pacific Ocean is indicated (Richards and Pollard, 1991). Although the importance of monsoonal wind forcing on the surface circulation has been discussed (Lindstrom et al., 1987), the wind-induced upwelling in the western equatorial Pacific Ocean is little observed because of its intermittent characteristics in temporal and spatial scales. The purpose of this study is to not only describe the upwelling event observed by SeaWiFS and in situ samplings during the research cruise of R/V MIRAI (MR01-K05 Leg3) but also investigate the conditions of upwelling in temporal and spatial scales for contributing to better understanding of air-sea interaction in the western equatorial Pacific Ocean.

DATA AND METHOD

Figure 1 shows the study area with the stationary observation at 2°N, 138°E from November 9 to December 9, 2001. During this period the ship was moving around the stationary point except the CTD (Conductivity-Temperature-Depth) profiler observations four times a day. Details of the cruise log and summary of observations are listed in the R/V MIRAI Cruise Report (MR01-K05 Leg-3/4) (JAMSTEC, 2001). Methods of *in situ* atmospheric and oceanographic observation including the parameter of sea surface temperature, salinity, chlorophyll-a concentration and current velocity profile are summarized as follows. The surface meteorological parameters such as wind speeds and directions are observed during the cruise by the R/V MIRAI meteorological observation system. An anemometer is located at the foremast 24 m above sea surface and the 10-minute averaged true wind speeds and directions are recorded. Near-surface water at the depth of 4.5 m is continuously pumped up at the rate of 200 liter per minute from the intake to the sea surface-monitoring laboratory for measuring temperature and salinity. Surface seawater samples are taken four times a day and the concentration of chlorophyll-a is determined onboard. CTD (Conductivity-Temperature-Depth) profiler observations are carried out four times a day to the depth of 500 meters. Salinity is calculated from the observed pressure, conductivity and temperature. The specifications of CTD are listed in Table 1. Current velocity profiles are measured by the shipboard Acoustic Doppler Current Profiler (ADCP) from November 9 to December 9, 2001. The zonal (east-west) and meridional (north-south) velocity components of 40 depth cells are observed every five minutes. Major parameters for the measurement configuration of ADCP are listed in Table 2.
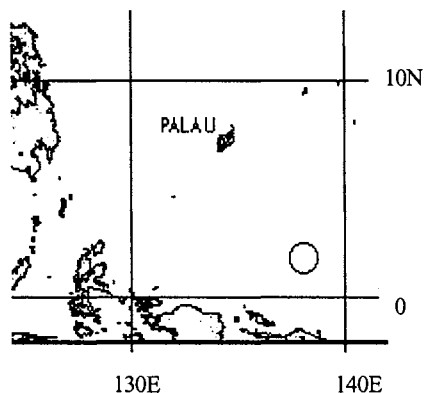

Figure 1. Study area with the stationary observation at 2N, 138E from November 9-December 9, 2001
(Circle represents the stationary observation area)

Table 1.   Specifications of CTD (Conductivity –Temperature -Depth) profiler

Underwater unit	CTD 9plus (Sea-bird Electronics, Inc.)
Temperature	Range:-5 to +35°C, Accuracy: 0.001°C
Conductivity	Range: 0 - 7 S/m, Accuracy: 0.0003 S/m
Pressure	Range: Up to 10500m, Accuracy: 0.015%

SeaWiFS is an abbreviation of Sea-viewing Wide Field-of-view Sensor onboard the SeaStar launched in 1998. The sensor has eight bands in the visible and near infrared wavelengths and the tilt mechanism to avoid sun glitter as shown in Table 3.

Table 2.   Measurement configurations of shipboard ADCP

Frequency	75kHz
Average	every 300 sec
Depth cell length	1600cm
Number of depth cells	40
First depth cell position	30.9m
Last depth cell position	654.9m
Ping per ADCP raw data	32

Table 3.   Specification of SeaWiFS

Band No.	Center wavelength (nm)
1~8	412, 443, 490, 510, 555, 670, 765, 865
Equator Crossing	Local Noon (±20min), descending
Orbit type	Sun Synchronous at 705km
Spatial resolution	1.13km(LAC), 4.5km(GAC)
Swath width	2801km(LAC), 1502km(GAC)
Scan Plane Tilt	+20°, 0°, -20°

During the research cruise from November 14 to December 10 SeaWiFS LAC (Local Area Coverage) scenes are received by the station onboard R/V MIRAI once a day under the authorization of NASA SeaWiFS project as the temporary real-time agreement.   All SeaWiFS raw data are decrypted by using the OGP software provided by NASA GSFC.   Higher-level products such as chlorophyll-a concentration are generated by using SeaDAS software.

RESULTS AND DISCUSSIONS

Throughout the period of research cruise there are two typical weather conditions.   One is characterized by the strong northwest monsoon winds (or westerly wind bursts) during the periods from November 18-24 and from December 1-9.   The westerly wind burst is one of the characteristic wind variability in the tropics with a period of 40-50 days (Madden-Julian Oscillation, (Madden and Julian, 1971, 1972)).   The other is characterized by the strong insolation with weak monsoon winds during the periods from November 12-17 and from November 25-30.   Since the SeaWiFS LAC scenes acquired during the former periods show the high cloud coverage, the SeaWiFS LAC scenes available for analysis are limited to those acquired during the latter periods.   From now on the observation period is divided into three periods, namely the period of (November 18-24), before (November 12-17) and after the strong northwest monsoon winds (or westerly wind bursts) (November 25-30).

Period before the strong northwest monsoon winds (from November 12-17)

Figures 2(a)-(e) show the temporal variability of wind speeds and directions, sea surface temperature and salinity at the depth of 4.5 meters, temperature and salinity overlaid with velocity vectors, temperature-salinity diagram with depth respectively.   Wind speeds are ranging from 0 to 10 m/sec and the wind directions are mostly northwest.   One of the typical features in the upper ocean can be seen in the sea surface temperature changes of 1.5°C during the local daytime of November 13 and 14, which are caused by the strong isolation with weak monsoon winds.
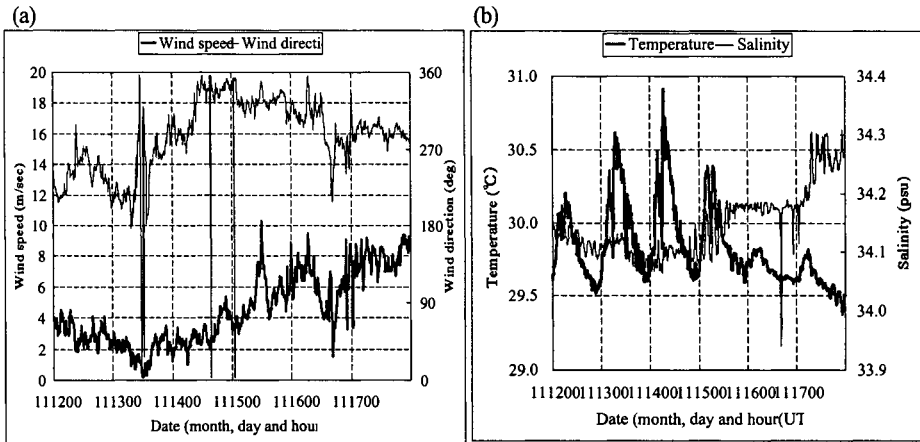
(a)

(b)

Figure 2. Temporal variability of wind speeds and directions (a) and the one of sea surface temperature and salinity (b) from November 12 -17

A sharp decrease of salinity in November 16 may be attributable to 3 mm/h precipitation observed by the shipboard rain gauge. As far as the temporal variability of temperature and salinity overlaid with ADCP data is concerned, three distinctive layered current structures are shown in Figures 2(c) and (d). The first one from the surface to the depth of 50 m corresponds to the Northwest Monsoon Current (NMC) (Masuzawa, 1968) which can be characterized by the weak flow (less than 30 cm/sec) toward southeast directions. The temperature and salinity are ranging from 29.2 to 29.8°C and from 34.1 to 34.4 psu respectively. The second one from the depth of 80 m to 120 m corresponds to the New Guinea Coastal Undercurrent (NGCUC) (Lindstrom et al., 1987). Although the NGCUC is originally defined as the sub-surface equatorward velocity maximum centered at the depth of 200 m adjacent to the coast at 2°S, it is indicated that the Northwest Monsoon Current overlies the northwestward flow of the NGCUC (Fine et al., 1994). The temperature and salinity are ranging from 25 to 29°C and from 34.6 to 35.2 psu respectively. The third one from the depth of 200 m to 250 m corresponds to the Equatorial Undercurrent (EUC) which can be characterized by the strong southeastward flow reaching about 70 cm/sec. The temperature and salinity are ranging from 13 to 20°C and from 34.6 to 35.2 psu respectively. Figure 2(e) shows the temperature-salinity diagram with four different depth ranges. The salinity maximum of 35.45 with the temperature of 22°C can be seen at the depth range of 100-199 m which is located between the NGCUC and the EUC. Figure 3 shows the SeaWiFS-derived chlorophyll-a concentration composite during this period. Around the stationary observation point (2N, 138E) the concentration is below 0.1 mg/m^3. On the other hand high concentration areas are found in the northwest of the stationary point (3N, 135E) and the northern coast of New Guinea Island.

224

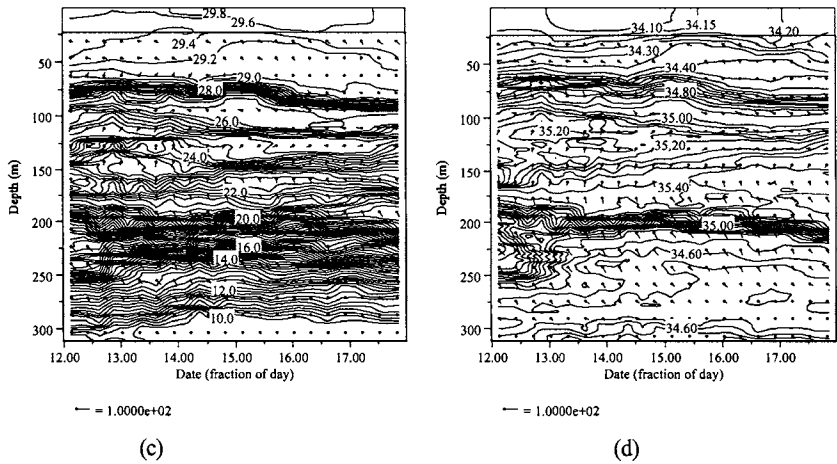(c)   (d)

Figure 2. Temporal variability of temperature (c) and salinity (d) overlaid with velocity vectors from Nov. 12 to 17 (Units of temperature, salinity and velocity are degree Celsius, psu and cm/sec respectively.)
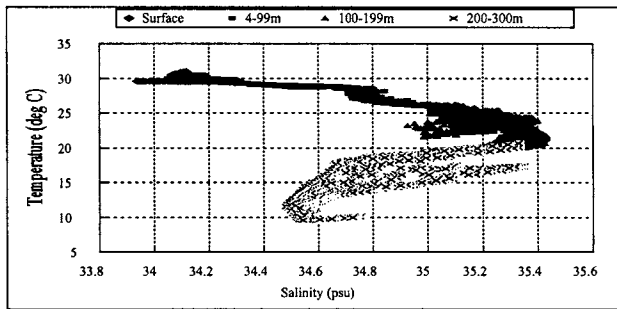

Figure 2(e).   Temperature-Salinity diagram with depth from November 12-17
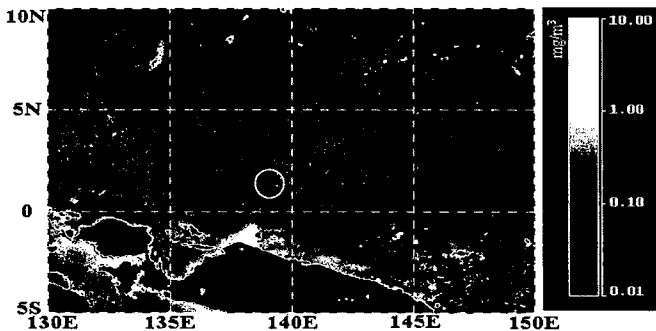

Figure 3. Chlorophyll-a concentration composite derived from SeaWiFS data. (November 12-17) (Circle represents the stationary observation area indicating low chlorophyll-a concentration below 0.1mg/m^3 (before the wind-induced upwelling))

225

Period of the strong northwest monsoon winds (from November 18 to 24)

Figures 4(a)-(e) shows the same parameters as shown in Figures 2(a)-(e) during the period from November 18-24. This period is characterized by the strong northwest monsoon wind (westerly wind burst) reaching more than 20 m/sec of instantaneous wind speed at November 20. Responses of the sea surface temperature and salinity are shown in Figure 4(b). Sea surface temperatures decrease from 29.5 to 29.3°C while salinity increases from 34.24 to 34.37 at November 22. The temporal distributions of temperature and salinity overlaid with ADCP data also illustrate the characteristic responses to the westerly wind burst. Figures 4(c) and (d) indicate that the Northwest Monsoon Current (NMC) reaches more than 60 cm/sec at the surface and extends to the depth of 70 m from November 20-21. The temperature and salinity contours of 29.2°C and 34.3 to 34.35 psu are sharply uprising respectively. The accelerated NMC caused by the westerly wind burst is called the Pacific Equatorial Monsoon Jet (PEMJ) (Lindstrom et al., 1987). The strong equatorial eastward jet in December, 1986 with the velocity more than 110 cm/sec are also observed (Delcroix et al., 1992). At the same time the northwestward flowing New Guinea Coastal Undercurrent (NGCUC) at the depth from 80 m to 120 m is seem to be decelerated and partly deviated clockwise because of the enhanced NMC or the PEMJ from November 20-21. These aspects of upper oceanographic response lead to a temporal upwelling which is revealed by the sharp increase of in situ chlorophyll-a concentration from November 19-22 expressed in Figure 5. SeaWiFS-derived chlorophyll-a concentrations are also shown in the same figure for comparison. It is found that in situ and SeaWiFS-derived chlorophyll-a concentrations are agreed well each other. It is indicated that the equatorial Pacific upwelling is defined at the surface by a salinity front (Rodier et al., 2000) and the close relationship between chlorophyll-a and salinity distribution has been discussed (Radenac and Rodier, 1996). Three distinctive layered current structures with the Pacific Equatorial Monsoon Jet caused by westerly wind bursts are illustrated in Figure 6.
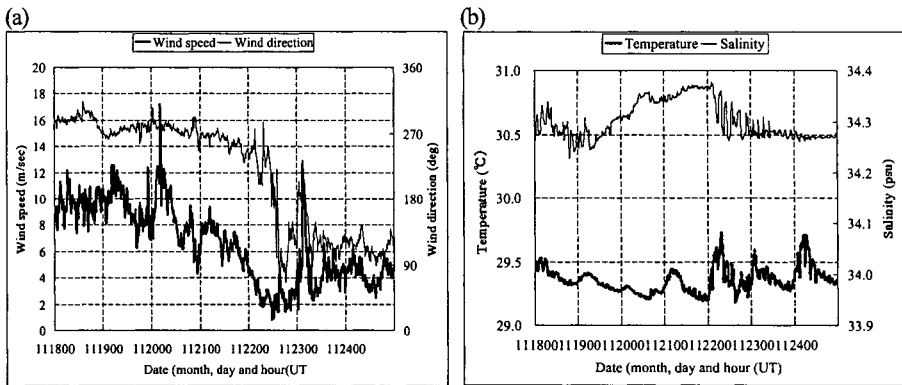
(a) (b)

Figure 4. Temporal variability of wind speeds and directions (a) and the one of sea surface temperature and salinity (b) from November 18 - 24
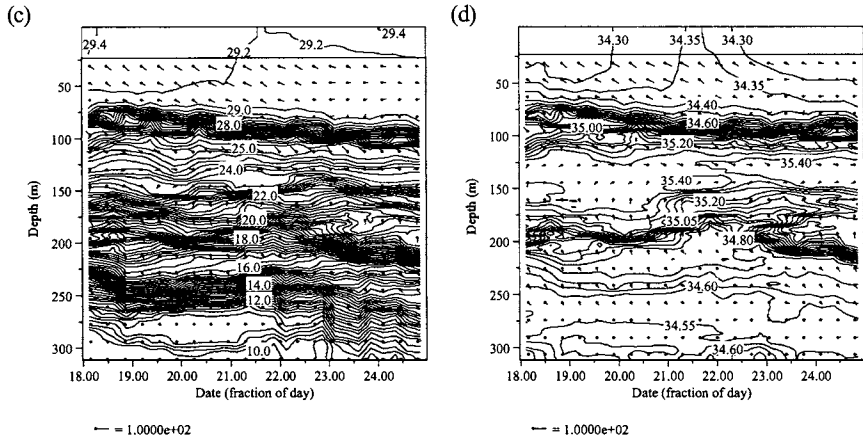
(c)

(d)

⌐ = 1.0000e+02   ⌐ = 1.0000e+02

Figure 4. Temporal variability of temperature (c) and salinity (d) overlaid with velocity vectors from November 18 to 24 (Units of temperature, salinity and velocity are degree Celsius, psu and cm/sec respectively.)
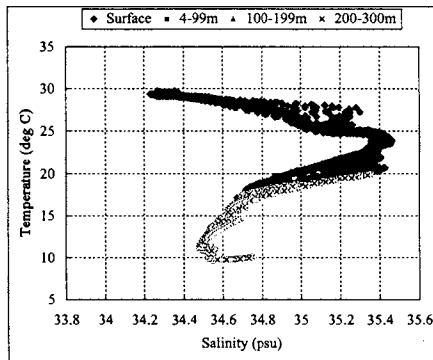

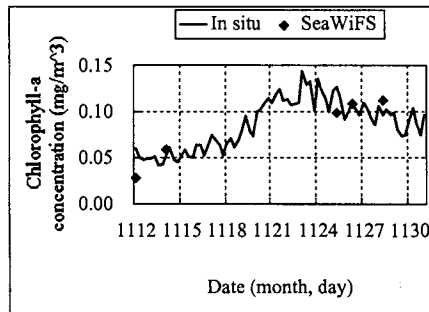Figure 4(e).   Temperature-Salinity diagram with depth from November 18 to 24

Figure 5. Comparison of in situ and SeaWiFS-derived chlorophyll-a concentration from November 12-to 30

Period after the strong northwest monsoon winds (from November 25-30)

Figures 7(a)-(e) show the same parameters as shown in Figures 2(a)-(c) during the period from November 25-30. This period is characterized by the moderate insolation with the weak monsoon winds shown in Figure 7 (a). During the period average wind speed is 5.2 m/sec. The wind directions are mostly east until November 27 and changing to the west afterwards. Because of the moderate insolation sea surface temperature shows small diurnal variability of 0.5° Celsius. Surface salinity shows a stable value of 34.28 shown in Figure 7(b). Since the wind directions are east until November 27, the Northwest Monsoon Current (NMC) at the surface becomes very weak indicated in Figures 7(c) and (d). On the other hand the New Guinea Coastal Undercurrent (NGCUC) at the depth from 80 m to 120 m shows the stable westward flow of about 50 cm/sec and the Equatorial Undercurrent (EUC) at the depth from 200 m to 250 m is strengthened especially after November 28. Since the northwest monsoon wind and the corresponding NMC are weak, the cause of the strengthened EUC is unknown. However, after comparing with the velocity vectors of the NGCUC during the previous period it is found out that the total transport of the NGCUC is getting increased toward the latter half of this period and the part of NGCUC may contribute to the enhancement of the EUC. Figure 7(e) shows the temperature-salinity diagram with four different depth ranges. Comparing Figure 2(e) and Figure 4(e) salinity maximums appeared not only at the temperature of 22-24°C but also at 27°C in Figure 7(e) which corresponds to the NGCUC at the depth of 100 meters.
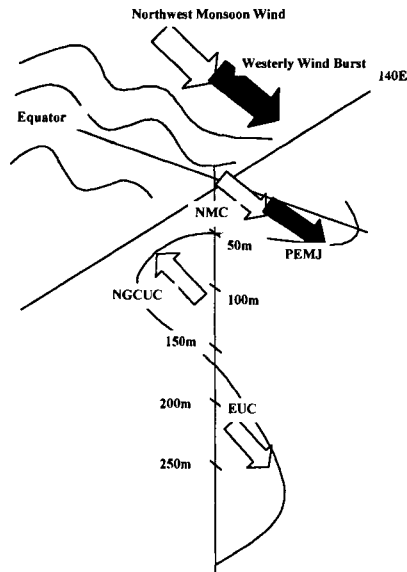

Figure 6. Layered current structure with the Pacific Equatorial Monsoon Jet (PEMJ) triggered by the westerly wind burst. (NMC: the Northwest Monsoon Current, NGCUC: the New Guinea Coastal Undercurrent, EUC: the Equatorial Undercurrent)

Figure 8 illustrates the chlorophyll-a concentration composite derived from SeaWiFS data during this period. The concentration around the stationary observation point (2N, 138E) indicates the values higher than 0.1 mg/m^3 which are agreed well with the in situ concentration values shown in Figure 5. The high concentration area extends to 4°N and the northern coast of New Guinea Island. However,

the low concentration areas are found east of 140 degrees meridian, which may indicate the temporal and spatial extent of the upwelling in this region.

(a)

(b)
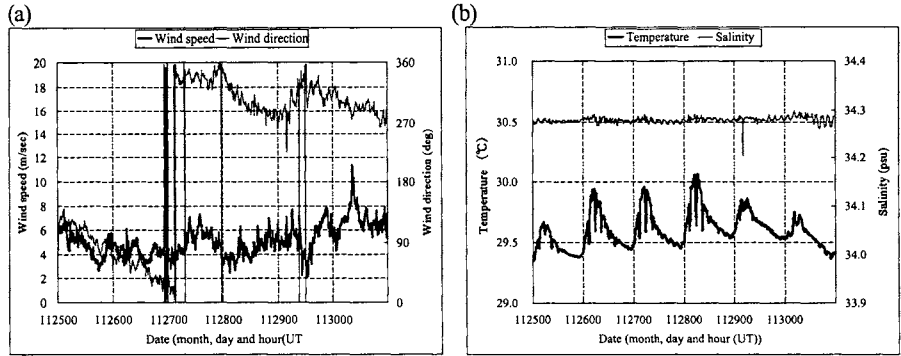
Figure 7. Temporal variability of wind speeds and directions (a) and the one of sea surface temperature and salinity (b) from November 25-30
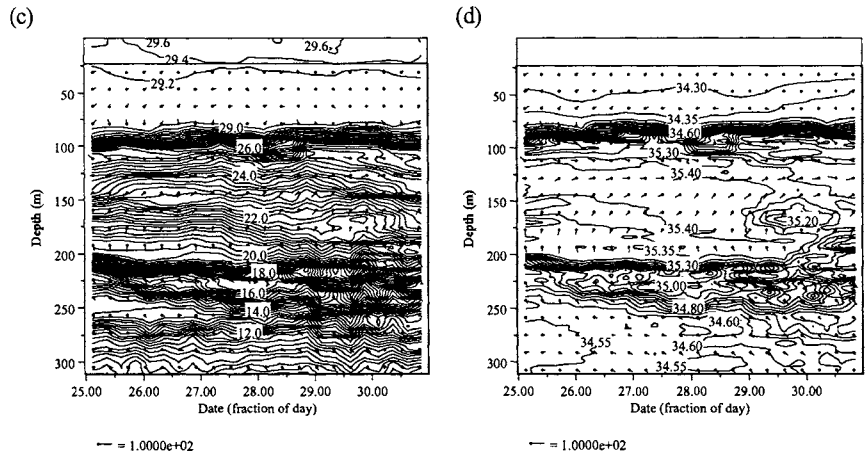
(c)

(d)

Figure 7. Temporal variability of temperature (c) and salinity (d) overlaid with velocity vectors from November 25-30 (Units of temperature, salinity and velocity are degree Celsius, psu and cm/sec respectively.)
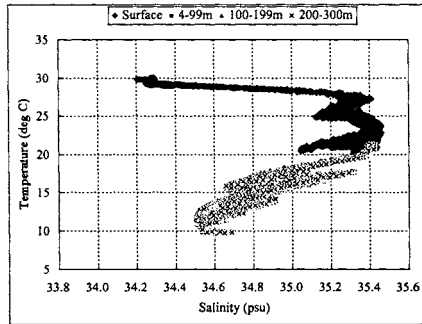
229

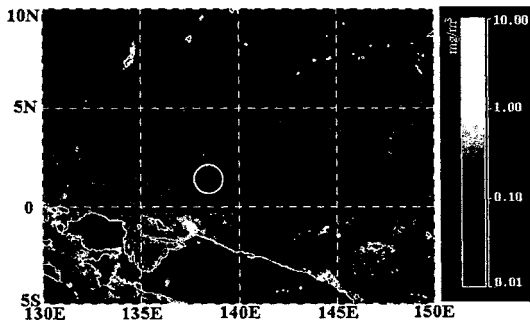Figure 7(e). Temperature-Salinity diagram with depth from November 25-30

Figure 8. Chlorophyll-a concentration composite derived from SeaWiFS data (November 25-30) (Circle represents the stationary observation area indicating high chlorophyll-a concentration above 0.1mg/m³ (after the wind-induced upwelling))

SUMMARY

The results of the study above are summarized as follows.

(1) Three distinctive layered current structures in the western equatorial Pacific Ocean namely the Northwest Monsoon Current (NMC) with high temperature (29.2 to 29.8°C) and low salinity (34.1 to 34.4 psu), the New Guinea Coastal Undercurrent (NGCUC) with moderate temperature (25 to 29°C) and high salinity (34.6 to 35.4 psu), the Equatorial Undercurrent (EUC) with low temperature (13 to 20°C) and high salinity (34.6 to 35.2 psu) are identified based on the temporal distribution of temperature and salinity from CTD and the velocity vectors from ADCP.

(2) The characteristics response of the upper oceanographic structure to the westerly wind bursts (instantaneous wind speed more than 20 m/sec) is found out as the Pacific Equatorial Monsoon Jet (PEMJ) reaching more than 60 cm/sec at the surface and extends to the depth of 70 m from November 20-21.

(3) The intrusion of the Northwest Monsoon Current (NMC) enhanced by the strong northwest monsoon winds (westerly wind bursts) causes a reversal in the sub-surface current (New Guinea Coastal Undercurrent (NGCUC)) which creates a temporal upwelling in this region.

(4) A temporal upwelling is revealed by the sharp increase of in situ chlorophyll-a concentration, salinity and the decrease of sea surface temperature from November 19-22.

230

(5) The upwelling event above is supported by the multi-date SeaWiFS chlorophyll-a concentration composites. The high concentration area extends to 4°N and the northern coast of New Guinea Island.

Though the SeaWiFS-derived chlorophyll-a concentration products revealed the average spatial extent of the wind-induced upwelling, the investigation for the temporal characteristics of upwelling is still hindered by the high cloud coverage of SeaWiFS data. A synthetic use with a passive microwave sensor like AMSR-E onboard the Aqua satellite is recommended for sea surface temperature analysis. Furthermore the SeaWiFS-derived chlorophyll-a concentration products showed an interleaving pattern east of the stationary observation point (2N, 138E), which may indicate the anomalous pattern of wind vectors like westerly wind bursts and associated air-sea interactions in this region. Combined uses of satellite scatterometer and altimeter for detecting sea surface winds and sea surface currents such as SeaWinds on QuikSCAT and Jason-1, a follow-on altimeter of TOPEX/Poseidon are recommended.

ACKNOWLEDGEMENTS

REFERENCES

Delcroix, T., G. Eldin, M. Radenac, J. Toole and E. Firing. 1992. Variation of the Western Equatorial Pacific Ocean 1986-1988. *Journal of Geophysics Research.* 97(C4): 5423-5445.

Fine, R.A., R. Lukas, F. M. Bingham, M.J. Warner and R.H. Gammon. 1994. The western equatorial Pacific: A water mass crossroads. *Journal of Geophysics Research.* 99(C12): 25063-25080.

Halpern, D., R.A. Knox, D.S. Luther, S.G.H. Philander. 1989. Estimates of Equatorial Upwelling Between 140° and 110° W During 1984. *Journal of Geophysics Research.* 94(C6): 8018-8020.

Helber, R.W. and R.H. Weisberg. 2001. Equatorial upwelling in the western Pacific warm pool. *Journal of Geophysics Research.* 106(C5): 8989-9003.

JAMSTEC. 2001. R/V MIRAI Cruise Report (MR01-K05 Leg-3/4). various pages.

Lindstrom, E., R. Lukas, R. Fine, E. Firing, S. Godfrey, G. Meyers and M. Tsuchiya. 1987. The Western Equatorial Pacific Ocean Circulation Study. *Nature.* 330: 533-537.

Madden, R.A. and P.R. Julian. 1971. Detection of a 40-50 Day Oscillation in the Zonal Wind in the Tropical Pacific. *Journal of Atmospheric Science.* 28: 702-708.

Madden, R.A. and P.R. Julian. 1972. Description of Global-Scale Circulation Cells in the Tropics with a 40-50 Day Period. *Journal of Atmospheric Science.* 29: 1109-1123.

Masuzawa, J. 1968. Second cruise for CSK, Ryofu Maru, January to March 1968. *Oceanogr. Mag.* 20: 173-185.

Radenac, M.H. and M. Rodier. 1996. Nitrate and chlorophyll distributions in relation to thermohaline and current structures in the western tropical Pacific during 1985-1989. Deep-Sea Research II. 43(4-6): 725-752.

Richards, K.J. and R.T. Pollard. 1991. Structure of the upper ocean in the western equatorial Pacific. *Nature.* 350: 48-50.

Rodier, M., G. Eldin and R.L. Borgne. 2000. The Western Boundary of the Equatorial Pacific Upwelling: Some Consequences of Climate Variability on Hydrological and Planktonic Properties. *J. Oceanography.* 56: 463-471.

Wyrtki, K. 1981. An Estimate of Equatorial Upwelling in the Pacific. *Journal of Physical Oceanography.* 11: 1205-1214.

THE DEVELOPMENT OF A NEW TECHNIQUE AS INDICES OF ACTIVITY IN FREE-RANGING FLATFISH

Ryo Kawabe[1], Yasuhiko Naito[2] and Katsuaki Nashimoto[3]

[1]Laboratory of Marine Ecosystem Change Analysis
Field Science Center for the Northern Biosphere, Hokkaido University
Hakodate, JAPAN
kawabe@fish.hokudai.ac.jp

[2]National Institute of Polar Research, Tokyo, JAPAN
[3]Hokkaido University, Hakodate, JAPAN

ABSTRACT

The tail beat and swimming behavior of four captive Japanese flounder (*Paralichthys olivaceus*) were monitored while swimming in an aquarium using acceleration data-loggers. Depth, swimming speeds and two-axis acceleration data were collected continuously for ca. 20 hours per fish. Simultaneously, the swimming behaviors of the fish were filmed at different angles. Using the specific characteristic of the acceleration profiles, in tandem with other types of data (e.g., speed and depth), four behavioral patterns could be recognized; (1) 'active' swimming, and (2) burying patterns, (3) 'inactive' gliding, and (4) lying on the bottom. Tail beat frequency ranged from 1.65±0.47 to 2.04±0.25 Hz (mean±S.D., N=4). Using the relationship between tail beat frequency and swimming speed, their 'preferred' swimming speed was estimated to be between 0.6 and 1.2 Body length (BL)/sec. Additionally, fish rarely swam faster than 1.2 BL/sec. This study shows that the acceleration data-logger is a useful and reliable system for accurate recording of the tail beat of free-ranging fish and estimating flatfish behavior.

INTRODUCTION

In order to understand fish ecology, further more the underwater behavior of free-ranging fish must be monitored precisely. However, since the difficulty of direct assessments of swimming speed and the proportion of time spent swimming by free-ranging fish (Hinch and Collins, 1991) a reliable methodology that would provide accurate information on the behavior and energetics of free-ranging fish have been required. Behavioral studies using water speed-sensing transmitters (Block et al., 1992) have allowed researchers to investigate the actual underwater behavior of free-ranging fish. Unfortunately, speed sensors are known to overestimate swimming speed. Moreover, water-current speed and direction may influence the energy expenditures of gliding fish (Carey and Scharold, 1990; Holland et al., 1990). Therefore fish swimming energy expenditures cannot be estimated using speed transmitters. Facilitated by recent advances in micro device technology, data-loggers that record body movements through two accelerometer signals were developed and deployed on a variety of free-ranging aquatic animals. This enabled researchers to monitor various activities, such as the porpoising behavior and postures of penguins (Yoda et al., 1999, 2001) or the fin-beating activity of free-ranging

migrating chum salmon, in tandem with records of swimming speed, diving angle and diving depth (Tanaka et al., 2001).

So far, few behavioral data are available for demersal fish such as flatfish. Flatfish do not have an gas bladder and are therefore negatively buoyant in their medium. This forces them to lie on one side on the seabed, which may be advantageous for camouflage and cryptic behavior (Norman, 1969). To measure the energetic costs of an active behavior, it is important to observe all of the activities of free-ranging flatfish for a long time and establish behavioral time budgets. However, time allocation and/or precise energy budgets cannot be estimated using only visual observation of captive fish. Only the data-logger is considered to be possible to measure the energy budgets of free-ranging flatfish.

In this regard, in seawater aquarium, acceleration data-loggers were attached to freely swimming Japanese flounders, (*Paralichthys olivaceus* – a key species in stock enhancement and marine ranching activities in Japan) and simultaneous measurement of their tail beat activity and swimming speed was conducted. The behavior of instrumented fish was also filmed by video cameras of multiple angles.

MATERIALS & METHODS

Four Japanese flounders (body length 52.0-54.0 cm, body weight 2.7-3.1 kg; Fish 1, 2, 3 and 4) were captured by commercial fishermen off the coast of Kashima, Ibaraki prefecture, Japan and transported to the Fish Behavior Laboratory of the National Research Institute of Fisheries Engineering (NRIFE). Fishes were kept in a circular tank of 2.5 m in diameter and 0.9 m deep (5,000 L) with a constant flow-through of seawater. The water temperature in the tank was maintained at ambient ocean temperatures (approximately 14°C) and natural light cycles were also simulated.

The behaviors of the flatfish were monitored with a 12-bit resolution, 16 MB memory, four channel ('acceleration') data-loggers with two acceleration sensors (UWE-200PD2G, Little Leonardo, Tokyo). These cylindrical-shaped, 20 mm diameter 120 mm long loggers weigh 64.0 g in air and 22.0 g in seawater. The devices include a depth recorder, speed meter and two piezo-resistive accelerometers (Model 3031, IC Sensors). These accelerometers record the 'surging acceleration' in the direction of the main axis of the flatfish (forward and backward) and the 'heaving acceleration' along the axis crossing the fish's body from the eyed (upward facing) side to the blind (downward facing) side (Fig. 1).
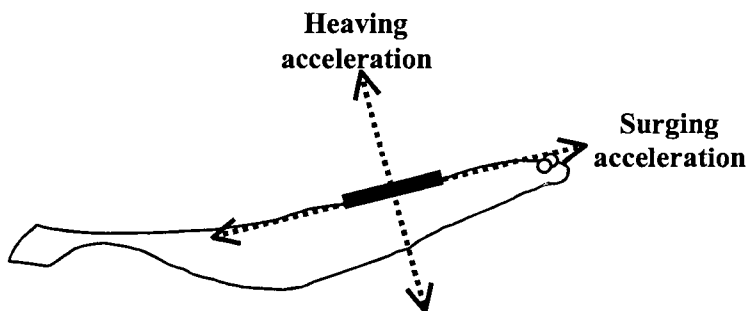
Figure 1. Schematic diagram showing the direction of surging and heaving accelerations recorded by an acceleration data-logger on the surface of the body of Japanese flounder.

The measuring ranges of both accelerometers were between -39.2 and 39.2 m/sec² (-4 and 4G, parallel and orthogonal to the main axis of the data-logger, respectively). The amplitude of acceleration was sampled at 16 Hz and filtered using an analogue sensor signal in the band pass filter between 0.5 and 8.0 Hz. Depth and swimming speed were sampled every second, with the resolution of 5 cm and 5 cm/sec, respectively. Swimming speed was measured by counting the number of revolutions per second (RPS) of an anterior-mounted propeller. The stall speed of the speed sensor was determined experimentally to be 25 cm/sec. Speeds below these values were considered to be indistinguishable from zero. A regression line was used to relate RPS to swimming speed. To calibrate the speed sensor, we examined the relationship between RPS and flow velocity (cm/sec) in NRIFE. The relationship was linear from 25.0 to 120.0 cm/sec and the regression coefficient was greater than 0.98.

Fish were transferred from the holding tank into individuals, where they were anesthetized by briefly submerging into well-oxygenated seawater containing 0.125 g/l of MS-222 (Ethyl m-Amino benzoate Methanesulfonate; NACALAI TESQUE, INC., USA). The acceleration data-logger was attached to each fish with two nylon straps, inserted through the dorsal musculature and aliened along the body axis. The fish were then allowed to recover for at least 12 hours before being released into an experimental rectangular seawater aquarium (13.0 m×7.5 m, 2.5-2.3 m deep). The water temperature in the aquarium was maintained between 15.5 and 18.5°C. The fish were also observed from three different angles using video cameras. One video camera was hand-held and two others were placed on the bottom of aquarium. Once the experiments ended, the fish were removed from the experimental aquarium and the acceleration data-loggers were retrieved.

After retrieval of the acceleration data-logger, data were downloaded into a laptop computer and analyzed with Igor Pro 3.1.4 software (WaveMetrics, USA). Statistical analysis was conducted significance using Stat View 4.5 software (SAS institute, USA) and mean ± standard deviation (S.D) were provided. Swimming movements off the bottom to depths of at least twice the depth resolution (±0.05 m) of the acceleration data-loggers were considered to be vertical and horizontal movements and were analyzed for swimming duration (sec) and swimming speed

(cm/sec and BL/sec). 'BL' stands for 'Body length', BL/sec being a common unit of measure for swimming speed in fish. The acceleration profiles were compared frame by frame with a visual analysis of the videotapes (30 frames/sec), and synchronized using a dubbed time interval (0.033sec) of the data-logger. Dynamic behaviors (i.e. swimming and burying) were categorized by usually examining the acceleration profiles. The periodic properties of the acceleration signals obtained from the dynamic behavior of the flatfish allowed us to apply an auto-correlation and fast Fourier Transform (FFT) analysis to determine the frequency of swimming and burying.

RESULTS

Approximately 20 hours of continuous behavior of the four individuals were recorded both by the video cameras and the acceleration data-logger. A visual analysis of videotapes revealed that all four fish spent most of the time lying on one side of their body on the bottom of the aquarium, also observed that they occasionally swam for a few minutes, either horizontally or vertically. While swimming, the fishes' entire body oscillated with an undulatory wave of vertical bending, progressing from the tip of the head to the end of caudal fin. While steadily swimming, the profiles of heaving acceleration, as recorded by acceleration data-logger, showed a cyclic and sinusoidal waveform (Fig. 2A). When compared with the data from the video camera, the frequency of heaving acceleration was synchronized with the sequences of swimming activity (Fig. 2B).
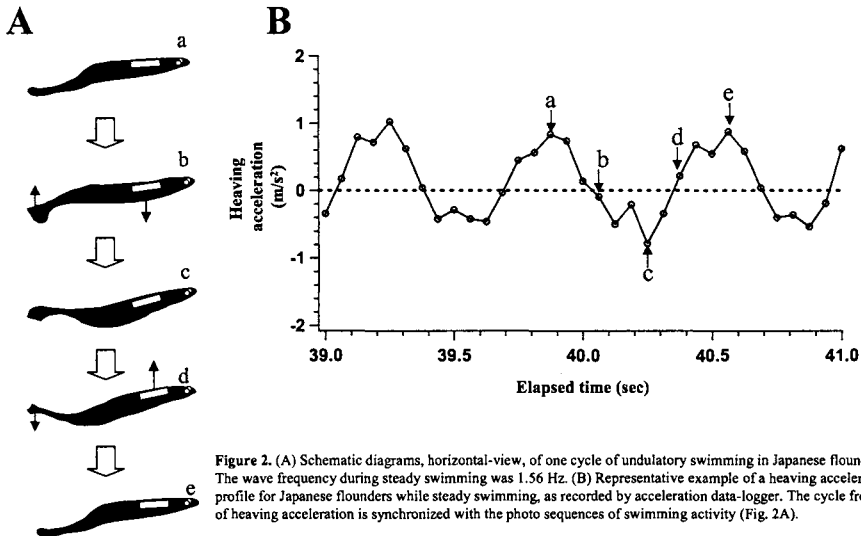
Figure 2. (A) Schematic diagrams, horizontal-view, of one cycle of undulatory swimming in Japanese flounder. The wave frequency during steady swimming was 1.56 Hz. (B) Representative example of a heaving acceleration profile for Japanese flounders while steady swimming, as recorded by acceleration data-logger. The cycle frequency of heaving acceleration is synchronized with the photo sequences of swimming activity (Fig. 2A).

In addition, the fishes tail beat frequency could be visually identified within the cycle of heaving acceleration during steady swimming phases.

The activities of the instrumented flounder were divided into four major categories; lying on the bottom, swimming, gliding and burying, based on differences within the acceleration profiles. Four distinct behaviors of the Japanese flounder were categorized using the data recorded by the acceleration data-loggers:

(a) **Lying on the bottom** (Fig. 3A). When lying on the bottom, each fish kept a rigid posture and its head, caudal fin and body laid flat on the bottom. Depth values remained constant around 2.3-2.5 m, and the swimming speed sensor recorded the 'stall speed' (<25 cm/sec.). Additionally, the acceleration remained constant at $0m/sec^2$. Thus, low and stable acceleration profiles indicate when the fish was lying on the bottom of the aquarium.

(b) **Swimming** (Fig. 3B). Fish were able to start swimming from any lying position. After taking-off from the bottom of the aquarium, they moved their head upwards and downwards, while the body musculature expanded and contracted. Depth values and swimming speed ranged from 1.1-2.5 m and 25-153 cm/sec, respectively. The heaving acceleration profile showed a series of rhythmical waveform with amplitude ranging from 0.29 to 16.83 m/sec^2 (mean±S.D.; 1.10±0.76). An example of typical heaving acceleration spectrum, whose frequency ranged from 0 to 6 Hz, is shown in Figure 4A. Heaving acceleration profiles of steady swimming had one or two marked peak in spectrum.
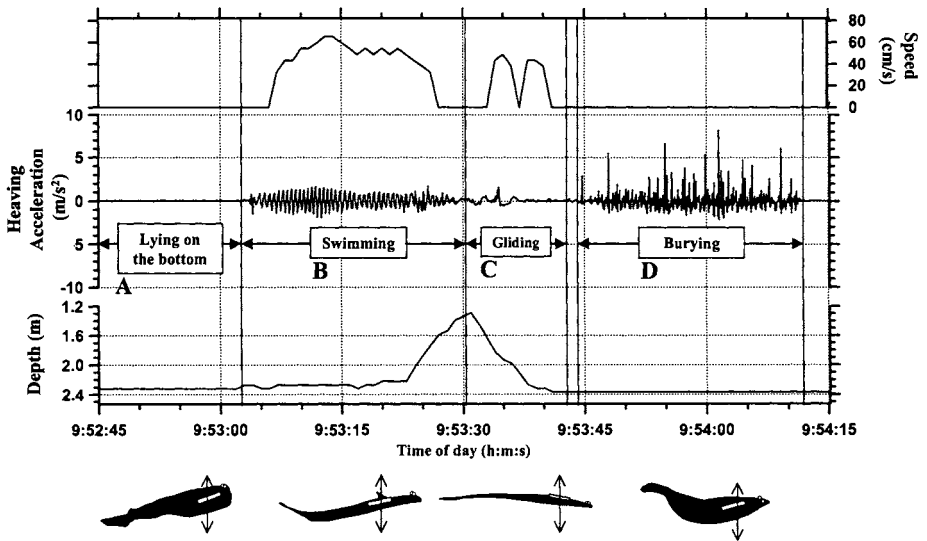
Figure 3. Depth, speed and heaving acceleration profiles for Japanese flounders, showing (a) lying on the bottom, (b) swimming, (c) gliding and (d) burying.

(c) **Gliding** (Fig. 3C). Prior to gliding, the fish would swim upward in the water column, and then, by positioning the head downward and flattering the body, glide downward to the bottom of the aquarium. When gliding, the heaving acceleration value was ca. $0m/sec^2$ or occasionally $±1m/sec^2$ and unchanging. Depth values decreased gradually as the fish descended towards the bottom of the aquarium.

237

(d) **Burying** (Fig. 3D). Soon after landing on the bottom of the aquarium, the fish would bury themselves by alternately beating their head and tail against the bottom. When the fish were engaged in burying activity, the depth value was that of bottom of the aquarium, swimming speed was <25cm/sec. An example of typical spectrum of heaving acceleration while burying, is shown in Figure 4B (note: the frequency ranged from 0 to 6 Hz). Heaving acceleration profiles while burying, had multiple peaks.

Data for each of the behavioral categories, based on depth, swimming speed and heaving acceleration data recorded by acceleration data-loggers, are shown in Table 1. The duration of recorded behaviors for each fish ranged from 16.8 to 19.5h, (N=4). They spent most of their time (Fish 1; 89.5%, Fish 2; 94.1%, Fish 3; 92.2%, Fish 4; 94.5%) on the bottom of the aquarium. The sum of the swimming periods lasted from 55.9 to 122.6min (mean±S.D.; 83.1±29.8min, N=4), representing 5.5-10.5 % of the duration of the experiments. The sum of the gliding periods lasted from 5.9 to 16.2min (mean±S.D.; 9.9±4.8min, N=4), representing 0.5-1.4 % of the duration of the experiments. The sum of the burying periods lasted from 0.9 to 14.8min (mean±S.D.; 6.0±6.5min, N=4), representing 0.08-1.5 % of the duration of the experiments (Table 1).

Of the total 451 swimming periods recorded, the four fish swam at speeds ranging from 0.4 to 2.8 BL/sec, with a mean swimming speed ranging from 0.8 to 0.9 BL/sec. While steadily swimming, undulatory cycles in the recorded heaving acceleration (indicating tail beat frequency) occurred between 1.00 and 2.67Hz. Tail beat frequency increased linearly with increasing swimming speed (n=1508, r^2=0.70, p<0.0001) according to the equation:

$$F = 1.08 \cdot V + 0.87$$

where V represents the swimming speed (BL/sec) and F is the tail beat frequency (Hz). During most of the time spent while swimming (88.1%), the frequency range of tail beating was between 1.45 and 2.29 Hz, with a mean frequency of 1.65±0.47 to 2.04±0.25 Hz depending on the individual. The fish rarely (0.75%) exceeded frequencies of 2.29 Hz, the highest frequency being 8 Hz.
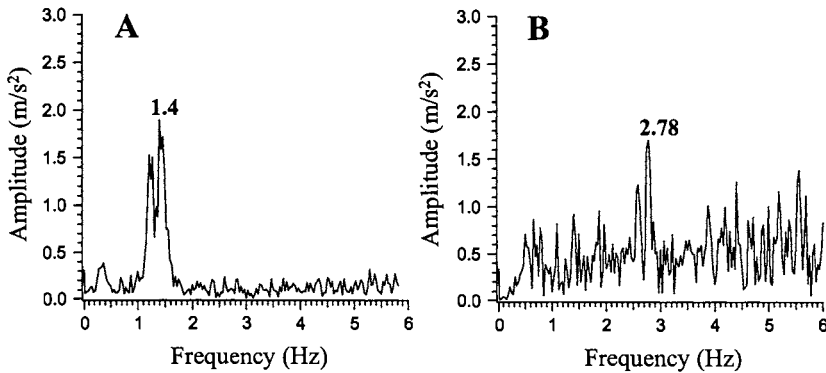
Figure 4. Amplitude spectrum of heaving acceleration while swimming (A) and burying (B).

238

Table 1. Summary statistics of swimming, gliding and burying behaviors for the four Japanese flounders instrumented for this study.

Fish No.	Fish 1	Fish 2	Fish 3	Fish 4
Record duration (hour)	19.5	18.2	19.2	16.8
Total number of taking off the bottom	132	129	104	39
Total swimming duration (min)	122.6	64.8	89.2	55.9
Mean duration of one swimming event (sec±S.D.)	53.0±52.8	25.1±12.3	42.1±24.1	76.3±54.4
Maximum duration of one swimming event (sec)	325	69	148	321
Total gliding duration (min)	5.9	11.0	16.2	6.3
Mean duration of one gliding (sec±S.D.)	2.7±2.9	5.1±3.3	9.3±5.5	9.6±10.3
Maximum duration of one gliding event (sec)	17.1	15.3	28.4	47.2
Total number of burying events	52	10	14	85
Total burying duration (min)	7.0	0.9	1.1	14.8
Mean duration of one burying event (sec±S.D.)	8.0±5.0	5.2±4.4	4.8±2.9	10.4±9.0
Tailbeat frequency (Hz) (range)	1.84±0.31 (1.14-5.33)	2.04±0.25 (1.33-2.67)	1.65±0.47 (1.10-8.00)	1.73±0.68 (1.00-8.00)
Mean swimming speed (cm/s)	43±9	58±12	42±12	46±17

DISCUSSION

Flatfish have been thought as a laterally compressed, benthic fishes that spend their adult lives lying on one side of their bodies on the seabed. However very little quantitative information of duration of a flatfish spends lying on the bottom is available. In the present study, four types of behaviors of the flatfish were recognized using acceleration profiles simultaneously with speed and depth data that was agreeable with the result of Olla et al. (1972). The acceleration data-loggers allowed us to distinguish between 'active' (swimming and burying) and 'inactive' phases (gliding and lying on the bottom of the aquarium). The burying behavior displayed by most flatfishes has been thought to be a way to both reduce the risk of predation and enhance the ability of the fish to catch prey (Ansell and Gibson, 1993). Our results also indicate that flatfish seem to rely on a swim-glide strategy (Fig. 3). In the case of negatively buoyant, fish this behavior has been suggested to be an efficient way to save energy for swimming long-distances (Weihs, 1973).

The effects of captivity and instrumentation appeared to have little influences on the behavior of flatfish. Previous investigations of the swimming abilities of captive Japanese flounders showed that the maximum sustainable swimming speed was 1.0 and 1.2 BL/sec at 18.5 and 19.4°C, respectively (Hashimoto et al., 1996). These values are similar to the maximum swimming speeds recorded in other flatfish species e.g. 0.95 and 1.50 BL/sec at 15°C (Duthie, 1982). Previous studies have demonstrated that tail beat frequency is related to swimming speed (Bainbridge, 1958; Nashimoto, 1980). Taking the equation, we could estimate the swimming speed using the tail beat frequency. The preferred tail beat frequency of captive Japanese flounders (1.45-2.29 Hz), corresponded to a 'preferred' swimming speed of 0.6-1.2 BL/sec. However, when compared with the range of values obtained by Duthie, the Japanese flounders in our experiments rarely swam in excess of 1.2 BL/sec. Thus, it might be inferred from these results that we could find no clear differences in swimming speed and tail beat frequency between instrumented and non-instrumented fish.

Most telemetry studies have estimated a rate of fish activities or 'rate of movement' (speed over-ground) by measuring the distance traveled over certain duration of time intervals (Greer-Walker et al., 1978; Kakimoto et al., 1979). However, such methodology does not take into consideration fine-scale movements, and therefore, the actual rate of activity may be underestimated. Indeed, 'rate of movement' measured from instantaneous swimming speeds, using speed meters and from tail beat frequency using acceleration data-loggers (mean, 0.79-1.10 BL/sec, N=4), are 1.8-15.7 times faster than those estimated by methods using the 'rate of movement' (mean, 0.07-0.43 BL/sec, N=3, Kakimoto et al., 1979). The instantaneous swimming speed, according to the acceleration data-logger, is consisted to be more similar to the 'rate of movement' if a fish only swims in straight lines because of its direct measurement nature. Similar observations were made by Gruber et al. (1988) using water speed sensors to determine the instantaneous swimming speeds of free-swimming lemon sharks. However, water speed sensors could not indicate whether an animal was continually swimming or gliding in order to save energy (Weihs, 1973). Thus, to estimate energy expenditure precisely, one needs monitoring of both the swimming speed and tailbeat activity of free-swimming fish simultaneously. Acceleration data-loggers appear to be a useful and reliable tool for accurate recording of the tail beat frequency of freely swimming flatfish and for estimating their activity.

Future improvements in the miniaturization of the logger would allow experiments on smaller fish.

REFERENCES

Ansell, A.D. and R.N. Gibson. 1993. The effect of sand and light on predation of juvenile plaice, *Pleuronectes platessa*, by fishes and crustaceans. *J. Fish Biol*. 43: 837-845.

Bainbridge, R. 1958. The speed of swimming of fish as related to size and to the frequency and amplitude of the tail beat. *J. Exp. Biol*. 35: 109-133.

Block, B.A., D.T. Booth and F.G. Carey. 1992. Direct measurement of swimming speeds and depth of blue marlin. *J. Exp. Biol*. 166: 267-284.

Carey, F.G. and J.V. Scharold. 1990. Movements of blue sharks, *Prionace glauca*, in depth and course. *Mar. Biol*. 106: 329-342.

Duthie, G.G. 1982. The respiratory metabolism of temperature-adapted flatfish at rest and during swimming activity and the use of anaerobic metabolism at moderate swimming speeds. *J. Exp. Biol*. 97: 359-373.

Greer-Walker, M., F.R. Harden Jones and G.P. Arnold. 1978. The movements of plaice, *Pleuronectes platessa L*, tracked in the open sea. *J. Cons. Int. Explor. Mer*. 38: 58-86.

Gruber, S.H., D.R. Nelson and J.F. Morrissey. 1988. Patterns of activity and space utilization of lemon sharks, *Negaprion brevirosris*, in a shallow Bahamian lagoon. *Bull. Mar. Sci*. 43(1): 61-76.

Hashimoto, S., T. Hiraishi, K. Suzuki, K. Yamamoto and K. Nashimoto, K. 1996. Swimming ability of Bastard Halibut *Paralichthys olivaceus* at the bottom of net cage. *Nippon Suisan Gakkaishi* 62: 12-16.

Hinch, S.G. and N.C. Collins. 1991. Importance of diurnal and nocturnal nest defense in the energy budget of male Smallmouth Bass: insights from direct video observations. *Trans. Am. Fish. Soc*. 120: 657-663.

Holland, K.N., R.W. Brill and R.K.C. Chang. 1990. Horizontal and vertical movements of yellowfin and bigeye tuna associated with fish aggregating devices. *Fish. Bull. US,* 88: 493-507.

Kakimoto, A., H. Ohkubo and H. Itano. 1979. Hirame seigyo no idouseitai –teremetori niyoru sokutei-. *Bull. Niigata Pref. Fish. Exp. Sta.* 8: 13-46.

Nashimoto, K. 1980. The swimming speed of fish in relation to fish size and frequency of tail beating. *Nippon Suisan Gakkaishi* 46: 307-312.

Norman, J.R. 1969. A systematic monograph of the flatfishes (Heterosomata) *Johnson Reprint Corp.,* London, 459.

Olla, B.L., C.E. Samet and A.L. Studholme. 1972. Activity and feeding behavior of the summer flounder (*Paralichthys dentatus*) under controlled laboratory conditions. *Fish. Bull. (Wash. D.C.)* 70: 1127-1136.

Tanaka, H., Y. Takagi and Y. Naito. 2001. Swimming speeds and buoyancy compensation of migrating adult chum salmon, *Oncorhynchus keta*, revealed by speed-depth-acceleration data logger. *J. Exp. Biol.* 204: 3895-3904.

Weihs, D. 1973. Mechanically efficient swimming techniques for fish with negative buoyancy. *J. Mar. Res.* 31: 194-209.

Yoda, K., K. Sato, Y. Niizuma, M. Kurita, C.A. Bost, Y. Le Maho and Y. Naito. 1999. Precise monitoring of porpoising behaviour of Adelie penguins determined using acceleration data loggers. *J. Exp. Biol.* 202: 3121-3126.

Yoda, K., Y. Naito, K. Sato, A. Takahashi, J. Nishikawa, Y. Ropert-Couder, M. Kurita and Y. Le Maho. 2001. A new technique for monitoring the behaviour of free-ranging Adelie penguins. *J. Exp. Biol.* 204: 685-690.

EFFECTS OF SHIP MOTIONS ON ECHOGRAMS IN FISHERIES

Adam Zielinski[1], Shuya Xiao[1] and Robert Kieser[2]

[1]University of Victoria, Department of Electrical and Computer Engineering
Victoria, B.C., CANADA
adam@ece.uvic.ca

[2]Pacific Biological Station
Nanaimo, B.C., CANADA

ABSTRACT

A typical echo sounder used in fisheries applications consists of a single, narrow beam transducer mounted on the hull of a vessel. Acoustic pulses (pings) are transmitted at a fixed rate and the echoes from various targets in the water column and from the bottom are conveniently displayed as an echogram. The horizontal axis of the echogram displays time or distance steamed while its vertical axis displays range or depth. Different colour indicates the intensity of the received echo after adjustments for absorption and spreading losses are made. The echogram provides information on single or multiple targets in the water column, such as individual fish or fish schools, and on the bottom. Vessel heave, roll, pitch and yaw have adverse effects on echograms. Heave will appear as a vertical offset on the features shown in the echogram and roll and pitch will affect both the intensity and the target traces. The degree of these distortions depends on vessel speed and motions, target structure and trajectory, ping rate and beam-pattern. We will evaluate these effects by synthesising echograms for different situations including simulated and actual vessel motion data. Methods to minimise these effects will be discussed.

INTRODUCTION

Fisheries acoustics has received a good deal of attention over the past years. A variety of procedures have been developed for the use of acoustics in fisheries. Currently, research vessels are the primary platforms for acoustic surveys in fisheries. Vessel motion will affect the observations made with a vessel-mounted transducer. In heavy weather, observations may be impossible or severely distorted. Here, we distinguish between primary and secondary vessel motion. The former describes the steady movement of the vessel along its path while the latter describes wind and sea induced vessel translations (surge, sway and heave) and rotations (roll, pitch and yaw).

Split-beam measurements can provide accurate estimates of the location of a target or single fish in the beam (MacLennan and Simmonds, 1992; Stephens, 1970). Additional knowledge of primary and secondary vessel motion is required to determine target location in a fixed reference frame. The processing of received sonar echoes must, therefore, include compensation for transducer motion when meaningful and accurate estimates of target position are required. This

paper presents a review and discussion of the effect of vessel motion on single fish echoes and provides a model to visualise and compensate for them.

EFFECT OF VESSEL MOTION ON ACOUSTIC MEASUREMENTS

Surveys and acoustic measurements that use hull mounted transducers will be affected by adverse weather conditions. The transducer will follow all vessel motions including surge, sway, heave, roll, pitch and yaw. When these motions are severe a transducer may transmit in one direction and look in another when the echo arrives. This misalignment results in errors in target strength estimates and has been well studied for fish biomass estimation from echo integration surveys (Furusawa and Sawada, 1991; Dunford, 2002; Stanton, 1982; Williamson, 2000). Vessel motions affect many other acoustic techniques. A list of acoustic techniques in order from least to most affected includes echo integration, echo counting, target strength (TS) measurement, near bottom detection, target tracking and, finally, calibration with a standard target. Adverse effects of vessel motion on the detection and tracking of single fish targets discussed here include not only the signal fluctuations mentioned above, but also the distortion of the target's trace on the echogram, the possible premature loss of the target from the acoustic detection volume and the difficulty of converting the observed target location in the beam to a fixed earth reference frame.

MODEL AND ASSUMPTIONS

To analyse the effect of vessel motion on acoustic measurements, a model for single target detection and location with a downward-looking, single-beam echosounder has been developed. Generally, an object in space has six degrees of freedom which here are: surge, sway, heave, roll, pitch, and yaw. Let us assume that vessel motion can be described by the primary and secondary vessel motions that were introduced above, that the transducer is rigidly mounted to the vessel, that its location may not coincide with the vessel's center of motion and that a single stationary target is observed. The acoustic size of the target is measured by its backscatter cross-section or TS. Accordingly, target tracks will be simulated and plotted for assumed echo sounder and vessel motion parameters, and for real vessel motion data. To generate echograms accurately, we make the following assumptions:
1. A fixed TS is used and effects of fish orientation and motion on TS are ignored.
2. Targets are located in the midwater layer; thus, unwanted echoes that may come from bottom, propeller wake, and surface bubble plumes are removed.
3. A circular piston transducer with an axially symmetric directivity pattern is used.
4. All measurements are made in the far-field of the transducer.

Typical single fish echoes from survey data

A single beam echo sounder provides amplitude and time (depth) information from each echo. The information from successive sound transmissions (pings) can be displayed in a depth *versus* ping count, time or distance diagram (echogram). A typical echogram from an acoustic survey is shown in Figure 1. Given a vertically aligned transducer and calm seas, single fish echoes

(traces) will be displayed as inverted Vs. Irregularities in target trace shape and intensity reflect wind and wave induced vessel motion.
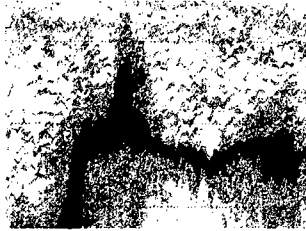

Figure 1. Widow rockfish aggregation observed off Vancouver Island, B.C. from the W.E. Ricker, January 1998. Depth ranges from 125 to 210 m, distance is 1.0 km.
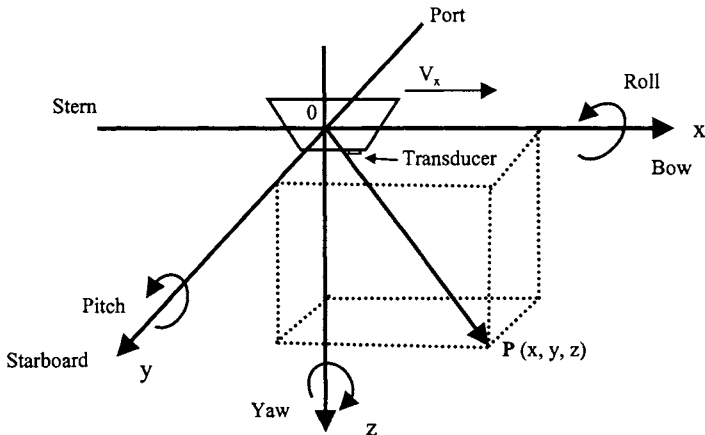
Co-ordinate Systems

Figure 2. Vessel transducer and target location in the LVCS. The positive roll, pitch and yaw rotations are indicated by the curved arrows.

The roll, pitch and yaw part of the vessel's secondary motion is observed in the right handed level vessel co-ordinate system (LVCS) shown in Figure 2. Its origin is at the vessel's centre of motion and its x and y-axes are in a horizontal plane. The x-axis points in the direction of the vessel's forward motion. Vessel roll, pitch and yaw correspond to rotations about the x, y and z-axes, respectively. The direction of positive rotation is given by the curved arrows and is defined by the right hand rule. In calm weather, the LVCS coincides with the vessel co-ordinate system (VCS) which has its axes aligned with the vessel's stern to bow, port to starboard and vertical axes, respectively.

The level transducer co-ordinate system (LTCS) is obtained by translating the origin of the LVCS to the rotated transducer location. In calm weather, the LTCS coincides with the transducer co-ordinate system (TCS).

245

Target Range Function (TRF)

For a single target, the target range function (TRF) is observed on the echogram as target range or depth *versus* time or distance. Given target position P(x, y, z) (Fig. 2) and assuming that the transducer is at the origin, the TRF is given by the range r between the transducer and the target:

$$r = \sqrt{x^2 + y^2 + z^2} \tag{1}$$

The TRF for arbitrary transducer location is given in the Appendix.

Echo Level and Target Strength Error (TSE)

The echo level from a single target is a function of its TS and position in the transducer beam. The echo sounder output level EL is given by:

$$EL = SL + RG + TVG - 40\log(r) - 2\alpha r + BP_t(\theta_t, \phi_t) + BP_r(\theta_r, \phi_r) + TS \tag{2}$$

where SL is the source level, RG and TVG are fixed and time varied receiver gains, BP_t and BP_r are the transmit and receive beam pattern at the respective angular directions, TS is target strength and the two negative terms account for the spreading and absorption loss. The range between transducer and target is r and α is the absorption coefficient. The target location in the beam is given by the spherical co-ordinates θ and ϕ. Subscripts t and r refer to transmit and receive, respectively. All quantities except r, θ and ϕ are in dB. SL and RG are determined by calibration with a reference hydrophone or a standard target. The TVG compensates for the spreading and absorption loss and range r is determined from the time between transmit and echo reception (Traynor and Ehrenberg, 1990). Combining known terms into a constant, CO, and cancelling the TVG terms against the spreading and absorption loss yields:

$$EL = CO + BP_t(\theta_t, \phi_t) + BP_r(\theta_r, \phi_r) + TS \; . \tag{3}$$

To eliminate the constant, we introduce the target strength error TSE. It is given by $-(BP_t + BP_r)$. The axis of the beam pattern may change between transmit and receive instances particularly if the target is at a large range (long echo travel time) and when vessel angular motion is rapid. For split-beam measurements that provide target position as seen by the receive beam and hence estimates of BP_r it would be appropriate to define a split-beam TS error TSE_{split} as: TSEsplit = $-(BP_t - BP_r)$. However, in this paper we have chosen to illustrate the target strength error, TSE that occurs when no beam pattern corrections are made. We also assume that BP_t is equal to BP_r, as our simulation will be for moderate target range and vessel motion.

Effect of Vessel Roll, Pitch and Yaw on Target Position in the Beam

The rotation of a point in a fixed co-ordinate system or the rotation of a co-ordinate system is described by well-known rotation matrices and matrix equations (Hare et al., 1995; Harrington, 1987; Hearn and Baker, 1986; Wolfram, 2002). A brief account is given below and further details appear in the Appendix. The effect of these motions on target position in the beam is

readily described when we assume that the transducer location coincides with the co-ordinate origin or equivalently with the vessel's centre of motion. In this case, the target position seen by the rotated transducer is given by:

$$P_{31} = R_x^{-1} R_y^{-1} R_z^{-1} P_{11} \tag{4}$$

where P_{11} and P_{31} are column vectors that give the target position as seen from a level and from a rotated transducer, respectively. The inverse rotation matrices R_x^{-1}, R_y^{-1} and R_z^{-1} are given in the Appendix. The Appendix also describes the general situation for a transducer that is not located at the origin and the transformation from Cartesian to spherical coordinates required for beam-pattern calculations (Clay and Medwin, 1987).

ANALYSIS AND RESULTS

Table 1. The parameters assumed for simulation

Vessel speed	5 m/s (approx. 10 knots)
Roll, pitch and heave period	10 s
Roll, pitch peak-to-peak amplitude	20°
Heave peak-to-peak amplitude	2 m
Echosounder frequency	38 kHz
-3 dB full beamwidth	7°
Ping period	1 s

In this section, simulation results for TRF, TSE and EL will be presented. The appearance of target traces and echo intensity is controlled by such factors as transducer beam pattern, relative speed between vessel and target, vessel motions and target range. Sinusoidal vessel roll, pitch, yaw and heave functions will be used to illustrate these effects. The parameters assumed to illustrate these effects are given in Table 1.

Effects of Vessel Motion on TRF and TSE

The TRF (Target Range Function) and TSE (Target Strength Error) for a stationary target observed from a vessel moving in calm seas are shown in Figure 3. TRF has an "inverted V" shape because the minimum target range will occur for the smallest horizontal distance between target and vessel. TSE is zero dB when the target is on the acoustic axis, which occurs at zero horizontal vessel to target distance. TSE increases with increasing distance from the center or, equivalently, with increasing angle from the acoustic axis. The transducer and target locations are A_{11} (0,0,0) and P_{11} (0,0,100), respectively. This implies that the transducer passes directly over the target at zero distance. TRF and TSE are continuous functions. The dots on the TRF and TSE diagrams represent the samples of these functions obtained by the acoustic pings. The pinging frequency may not be sufficient to reconstruct these functions (as postulated by the Nyquist sampling theorem). Actual echograms use a threshold that is set to eliminate ambient and other noise. For the sake of exposition we have assumed zero threshold and zero noise condition.
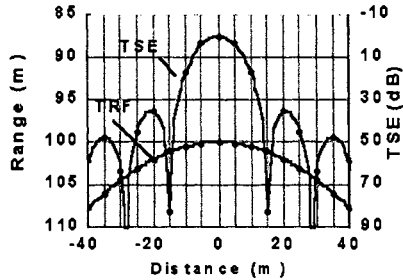
Figure 3. TRF and TSE for a stationary target observed from a moving vessel with no roll, pitch, yaw or heave. The x-axis represents distance travelled by the vessel with respect to target position.

More irregular patterns are observed when vessel roll and pitch are introduced, as shown in Figure 4. A sine function that is zero at zero distance simulates roll and pitch. The asymmetry in the sine function is reflected in the asymmetry in TRF and TSE. Additional asymmetry is added by locating the transducer at A_{11} (4,0,2), a position which is no longer at the centre of the rotation.
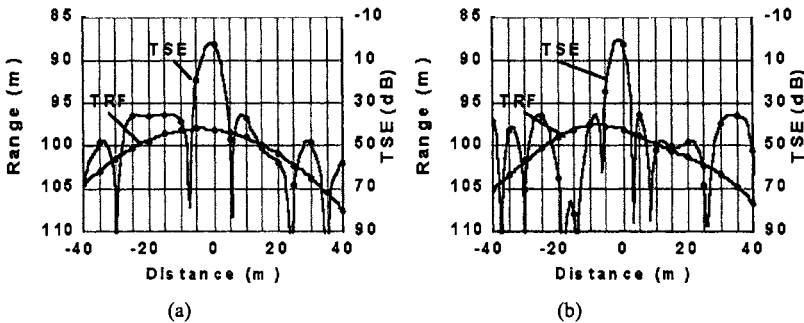

(a)   (b)

Figure 4. TRF and TSE for a stationary point target observed from a moving vessel (a) with vessel roll only, (b) with vessel pitch only.

Larger irregularities are seen in Figure 4b than in Figure 4a as pitch effects will add to or subtract from the vessel's forward motion while roll effects are perpendicular to that motion. Although not shown, yaw rotation will have relatively little effect on TRF and TSE, because yaw rotation is about the z-axis and is at least approximately aligned with the symmetric beam pattern of the circular piston transducer used here.
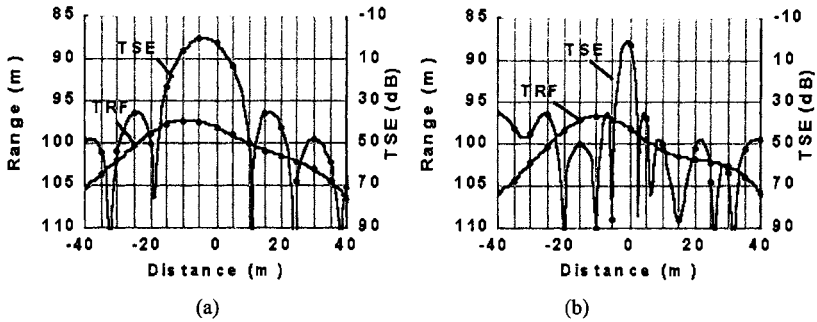
248

Figure 5. (a) TRF and TSE from a stationary point target (a) with vessel heave, (b) with vessel roll, pitch, yaw and heave.

Figure 5(a) shows the effect of vessel heave. Both TRF and TSE are similar to those in Figure 3 but heave effects are clearly stronger on TRF than TSE since heave adds to target range and has relatively little effect on the off axis target angle. The TRF and TSE functions shown in Figure 5(b) include roll, pitch, yaw and heave effects. Among the four motions, the effect of roll and pitch rotations are significant in TSE and heave plays an important role in TRF. Figures 4 and 5 use the same asymmetric transducer location. The resulting shift in TRF and TSE relative to distance is apparent in both figures.
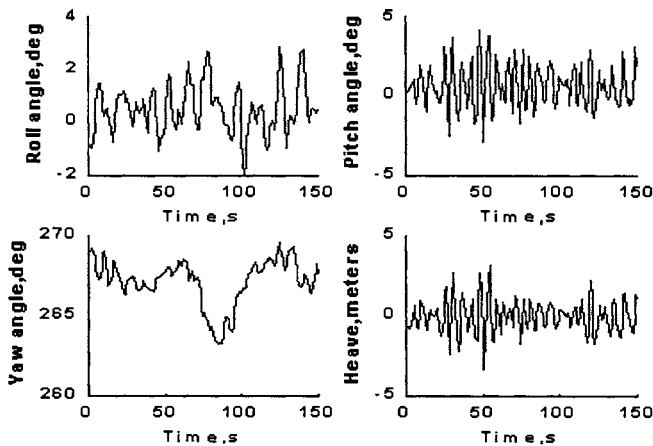
TRF and EL Based on Real Vessel Motion Data

Figure 6. Typical 150-second time series of roll, pitch, yaw and heave from Miller Freeman motion history.

249

In this section, we will demonstrate the effects of measured vessel motion data on TRF and EL. Figure 6 shows a brief sample from the motion that was experienced by the NOAA research vessel Miller Freeman 2-3 March 2001. Target traces based on real vessel motion data and sonar parameters as given in Table 1 are synthesized and presented in Figure 7. The figure shows the relative echo level from seven simulated targets at 10 and 2-knot vessel speed. The traces were terminated for EL below −90dB.
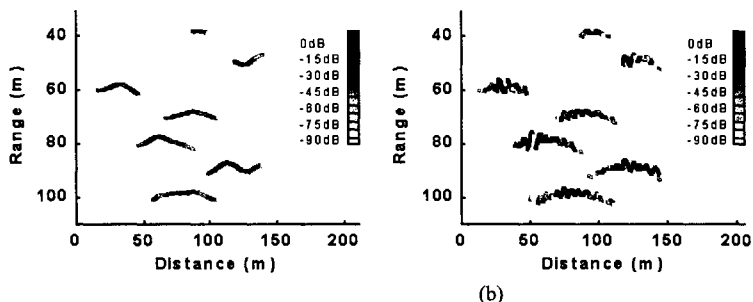

(b)

Figure 7. Seven target tracks based on measured vessel motion data and synthetic target information. (a) Vessel speed 10 knots (b) Vessel speed 2 knots

COMPENSATION FOR VESSEL MOTION EFFECTS

Our work suggests two new options to compensate and minimise the adverse effects of vessel motion on the acoustic detection of single fish targets:

1. An inverse form of our simulation model can be used to correct acoustically measured target positions; and
2. Echosounder transmissions may be synchronised with vessel motion.

Both methods require that vessel motion measurements are available. The former method also requires target position information that may be obtained from split-beam measurements. Given accurate vessel motion measurements the model and rotation matrices used for our simulation could, for example, be applied to vessel based, split-beam target position measurements to obtain estimates of target position and movement in a fixed reference frame. This information is essential for fish tracking and fish flux measurements that provide new insights into fish behaviour and migration. Fixed, split-beam installations, now used in many rivers, provide this kind of information (Enzenhofer et al., 1998). The second approach only depends on the availability of real-time vessel motion measurements that can be used to trigger echosounder transmissions at specific times rather than at constant time intervals. An obvious time for synchronised transmissions occurs when the vessel is in a near level position. Difficulties are that near levelled positions may occur too infrequently and that the rate of change for angular position will tend to be largest at that time. The method may, however, be useful in specialised situations.

Alternate methods for minimising the adverse effects of vessel motion include the use of a hull mounted and stabilised transducer or of a towed body that travels behind the vessel. Our model and simulation will be useful to explore the effectiveness and feasibility of these and other procedures designed to improve acoustic observations from a moving platform.

CONCLUSIONS

This paper presents a model and simulation results that demonstrate the adverse effects of vessel motion on single target detection and on the echogram. These effects are illustrated in a series of figures based on synthetic and real vessel motion data.

We come to the following conclusions:
1) In fisheries acoustics, measurements, such as echo integration, echo counting and TS measurement, are affected and degraded to an often-unknown degree by vessel motion.
2) For a vertically aimed transducer, the secondary vessel motions have different effects on TRFs and TSEs. Yaw by itself has little effect, while roll, pitch and heave might cause significant distortion. Superposition of all four motions can cause significant distortions on both TRF and TSE.
3) Analytical compensation is possible when secondary vessel motions are measured. Compensation will be limited when vessel motions are large enough that targets are prematurely lost from the beam.
4) Additional methods transducer stabilisation, variable ping rate and beaming steering should be considered, as the potential for correction appears to be limited.
5) Our model and simulations can provide an effective tool to assess the adverse effects of vessel motion and the effectiveness of actual and proposed compensation procedures. And it can provide a warning when a specified level of vessel motion and hence echogram distortion is exceeded.

ACKNOWLEDGEMENT

REFERENCES

Clay, C.S., and Medwin, H. 1977. Acoustical oceanography: principles and applications. John Wiley & Sons. New York.

Cushing, D.H. 1973. The detection of fish. Pergamon Press, Oxford.

Dunford, A.J. 2002. Correcting acoustic data for transducer motion. ICES Symposium on Acoustics in Fisheries and Aquatic Ecology, Montpellier, France, June 10-14, 2002. Paper # 68.

Enzenhofer, H.J., Olsen, N., and Mulligan, T.J. 1998. Fixed-location riverine hydroacoustics as a method of enumerating migrating adult Pacific salmon: Comparison of split-beam acoustics versus visual counting. *Aquatic Living Resources*, 11(2): 61-74.

Furusawa, M. and Sawada, K., 1991. Effect of transducer motion error on quantifying single fish echoes. Nippon Suisan Gakkaishi. 57:857-864.

Hare, R., Godin, A., and Mayer, L. 1995. Accuracy estimation of Canadian Swath (multibeam) and Sweep (multi-transducer) sounding systems. Canadian Hydrographic Service, Sydney, BC.

Harrington, S. 1987. Computer graphics: A programming approach. McGraw-Hill, New York.

Hearn, D., and Baker, M.P. 1986. Computer graphics. Prentice-Hall, New York.

Maclennan, D.N., and Simmonds, E.J. 1992. Fisheries acoustics. Chapman & Hall.

Stanton, T.K. 1982. Effects of transducer motion on echo-integration techniques. *J. Acoust. Soc. Am.*, 72(3): 947-949.

Stephens, R.W.B. 1970. Underwater Acoustics. John Wiley & Sons Ltd.

Traynor, J.J. and Ehrenberg, J.E. 1990. Fish and standard-sphere target-strength measurements obtained with a dual-beam and split-beam echo-sounding system. Rapp. P.-v. Reun. Cons. int. Explor. Mer, 89: 325-335.

Williamson, N. 2000. Impact of Transducer Motion on Echo Integration. Alaska Fisheries Science Centre. http://www.afsc.noaa.gov/Quarterly/ond2000/midwater.

Wolfram. 2002. Rotation matrices. http://mathworld.wolfram.com/RotationMatrix.html.

APPENDIX

Observation of a fixed target from a moving vessel

Co-ordinate system

The vessel roll, pitch and yaw motions are observed in the right-handed level vessel co-ordinate system (LVCS) shown in Figure A1. Its origin is at the vessel's centre of motion and its x and y-axes are in a horizontal plane. The x-axis points in the direction of the vessel's forward motion. Vessel roll, pitch and yaw correspond to rotations about the x, y and z-axes, respectively. The direction of positive rotation is given by the curved arrows and is defined by the right hand rule. In calm weather, the LVCS coincides with the vessel co-ordinate system (VCS) which has its axes aligned with the vessel's stern to bow, port to starboard and vertical axes, respectively. We

252

define roll, pitch and yaw in the LVCS as shown in Figure A1. However, roll, pitch and yaw are often defined in the VCS and may include sign conventions for the rotation directions based on naval traditions (Hare et al., 1995). We have chosen to develop our model in the LVCS for simplicity and as average results will be very similar.

Rotation of a point in a fixed co-ordinate system

In the LVCS, the effect of roll, pitch and yaw on the location of an object that is fixed to the vessel (e.g., a transducer) is described by the three rotation matrices (Hare et al., 1995; Harrington, 1987; Hearn and Baker, 1986; Wolfram, 2002):

$$\text{Roll: } R_x = \begin{pmatrix} 1 & 0 & 0 \\ 0 & \cos\varphi_x & -\sin\varphi_x \\ 0 & \sin\varphi_x & \cos\varphi_x \end{pmatrix} \tag{A1a}$$

$$\text{Pitch: } R_y = \begin{pmatrix} \cos\varphi_y & 0 & \sin\varphi_y \\ 0 & 1 & 0 \\ -\sin\varphi_y & 0 & \cos\varphi_y \end{pmatrix} \tag{A1b}$$

$$\text{Yaw: } R_z = \begin{pmatrix} \cos\varphi_z & -\sin\varphi_z & 0 \\ \sin\varphi_z & \cos\varphi_z & 0 \\ 0 & 0 & 1 \end{pmatrix} \tag{A1c}$$

where φ_x, φ_y and φ_z are the roll, pitch and yaw angles. Following a roll, pitch and yaw rotation the location of a transducer fixed to the vessel is given by,

$$A_{12} = R_z R_y R_x A_{11} \tag{A2}$$

where A_{11} gives the location of the transducer on the vessel before rotation (Fig. A1) and A_{12} is the new location (Fig. A2) and A_{11}, A_{12} and P_{11} are column vectors. The first 1 in the subscript indicates that we are using the LVCS. The position of the target remains unchanged at P_{11}.

Observation of a fixed point from a rotating co-ordinate system

To find the changed transducer view angle we now introduce the level transducer co-ordinate system (LTCS) that is obtained by translating the origin of the LVCS to the rotated transducer location A_{12}. The target position in the LTCS co-ordinate system is:

$$P_{21} = P_{11} - A_{12} \, . \tag{A3}$$

To account for the changed transducer view angle we now rotate the LTCS. This rotation differs from the previous one as we now rotate the co-ordinate system rather than a point in a fixed co-

ordinate system. This is accomplished by the use of the inverse rotation matrices in the following equation:

$$P_{31} = R_x^{-1} R_y^{-1} R_z^{-1} P_{21}$$

(A4)

where P_{31} is the position of the target in the transducer co-ordinate system (TCS) shown in Figure A3, and R_x^{-1}, R_y^{-1} and R_z^{-1} are the inverse rotation matrices obtained by using the

negative rotation angles $-\varphi_x$, $-\varphi_y$ and $-\varphi_z$ in equation A1.

To calculate the beampattern for the observed target we require the angular position of the target as seen in the TCS. It is obtained by using the (x, y, z) co-ordinates of P_{31} in the following conversions.

Conversion from Cartesian to Spherical co-ordinates

Spherical co-ordinates are shown in Figure A4. The transformation of vector (x, y, z) from Cartesian to spherical co-ordinates is provided by:

$$r = \sqrt{x^2 + y^2 + z^2}$$

(A5a)

$$\tan\theta = \frac{\sqrt{x^2 + y^2}}{z}$$

(A5b)

$$\tan\phi = \frac{y}{x} .$$

(A5c)

Conversion from Cartesian to Split-beam co-ordinates

Split-beam co-ordinates are shown in Figure A5. The transformation of vector (x, y, z) from Cartesian to split-beam co-ordinates is:

$$r = \sqrt{x^2 + y^2 + z^2}$$

(A6a)

$$\tan\alpha = \frac{x}{z}$$

(A6b)

$$\tan\beta = \frac{y}{z} .$$

(A6c)

Target position in the LVCS

Although the target is fixed in an earth co-ordinate system, it will appear to move relative to the vessel. In the LVCS, the target position will be given by:

$$\mathbf{P}_{11} = \begin{pmatrix} x_t - x_v - v_x t - s(t) \\ y_t + y_v + v_y t + w(t) \\ z_t + z_v + v_z t + h(t) \end{pmatrix} \tag{A7}$$

where (x_t, y_t, z_t) is the initial target position, (x_v, y_v, z_v) and (v_x, v_y, v_z) are the vessel's initial position and velocity and s, w and h are vessel surge, sway and heave, respectively. All are measured in the right handed earth co-ordinate system that, at t=0, coincides with the LVCS, but with inverted y and z-axes. Thus, vessel heave will be positive when the vessel is on a wave crest. Generally x_t, y_t, x_v, y_v, z_v and v_z will be zero.
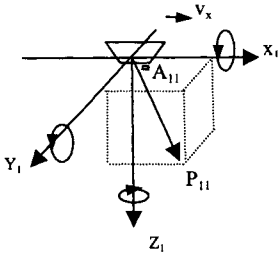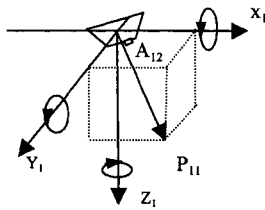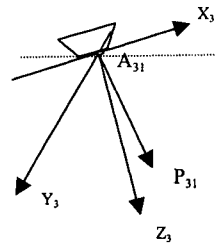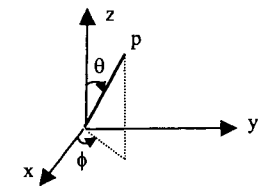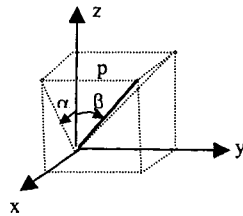

Figure A1   Figure A2   Figure A3

Figure A4

Figure A5

POSSIBILITY OF ISOLATION CO_2 IN THE HIGH LATITUDE OF THE PACIFIC OCEAN

Kazuyuki Hasegawa[1], Akira Wada[1], Seiichiro Nagoya[2], Kenji Takano[3] and Ryosuke Nishimura[1]

[1]Nihon University, College of Industrial Technology
Narashino, Chiba, JAPAN
c03810@cit.nihon-u.ac.jp

[2]Ark Information System, Tokyo, JAPAN
[3]Columbia University, Lamont-Doherty Earth Observatory, New York, USA

ABSTRACT

As one of measures for controlling the emission of carbon dioxide (CO_2) into the atmosphere, attention is focused on making effective use of the ability of the ocean to absorb CO_2, and an evaluation is performed on the ability to isolate CO_2 from the atmosphere by emitting CO_2 into areas deeper than the middle layer of the ocean. The subarctic region of the northern Pacific Ocean has recently been recognized as a sea area, which has the potential to absorb CO_2 although oceanographical data of this region are comparatively scarce except for sea areas adjacent to Japan, the Aleutian Islands and the Canadian coast. As this sea region is thought to play decisive roles in the climate fluctuations of the world in the time-scale of decade's years, it is indispensable to correctly evaluate effects of the ocean sequestration of CO_2 when this technique would actually be undertaken. Based on the flow fields of the whole Pacific Ocean, which were calculated by the data assimilation system, the authors examined changes in CO_2 concentration of the ocean, which may result from CO_2 introduction into the subarctic zone of the northern Pacific Ocean.

INTRODUCTION

The global warming, ascribed to increase in greenhouse gas emission by human activities, has become one of the most serious environmental problems on our planet. The Third Conference of the Parties (COP3) to the U.N. Framework Convention on Climate Change, which was held in 1997 in Kyoto, Japan, adopted targets of the cut of greenhouse gas emission form the 1990 level for major industrial countries. The target for Japan was a 6% cut by 2008. Under these circumstances, a greater amount of attention has recently been given to the technique of ocean sequestration of carbon dioxide (CO_2), one of the main greenhouse gases. The CO_2 ocean sequestration technique consists in directly introducing the man-made CO_2 and dissolving it in seawater of the deeper layers of ocean. As CO_2 injected into seawater of the deeper layers of ocean may eventually be dispersed into wider regions of the sea owing to current and diffusion, so it is necessary to examine the flow field of the ocean. Numerical simulation techniques using ocean circulation models have been widely employed in complementing for shortcomings of actual observation. Bryan (1969a) was the first to introduce for this purpose the Primitive

Equation Systems, which has influenced almost all Ocean General Circulation Models (OGCM) until now (Hasumi, 2001). Accuracy of numerical simulation results is an important factor in estimating the effectiveness of CO_2 ocean sequestration. We used the method of Sarmiento and Bryan (1982), in which differences between observed and calculated values are corrected at each time step of calculation, thus enabling to simulate a realistic flow field based upon observation results. Instead of using the wind stress at sea surface calculated from buoy and shipboard data by the method of Hellerman et al. (1983), which has been adopted in many of OGCM, we utilized the satellite observation data of wind speed (Special Sensor Microwave/Imager: SSN/I) that were converted to wind stress by the Bulk equation. Finally, we examined the feasibility of ocean sequestration technique for a case in which the CO_2 in surplus of the emission cut targeted for Japan in COP3 was introduced into the Pacific Ocean, and discussed a proper regions of water into which CO_2 should be introduced if the object of CO_2 sequestration is to be attained.

PACIFIC OCEAN CIRCULATION MODEL

Model Description

Calculation covered the entire Pacific Ocean. The calculation mesh in the horizontal direction was longitude-latitude $2° \times 2°$(110E~70W, 60N~74S). We assumed eleven vertical layers as shown in Table 1. The coordinate system is spherical coordinate to horizontal direction. The equations used are equation of motion (1), hydrostatic approximation equation (2), continuity equation (3), equation of heat conservation (4), salinity conservation equation (5) and condition equation (6).

$$\frac{\partial \vec{u}}{\partial t} + (\vec{u} \cdot \vec{\nabla})\vec{u} + w\frac{\partial \vec{u}}{\partial z} + f\vec{k} \times \vec{u} = -\frac{1}{\rho_0}\vec{\nabla}p + A_H\vec{\nabla}^2\vec{u} + A_V\frac{\partial^2 \vec{u}}{\partial z^2} \tag{1}$$

$$\frac{\partial p}{\partial z} = -\rho g \tag{2}$$

$$\vec{\nabla} \cdot \vec{u} + \frac{\partial w}{\partial z} = 0 \tag{3}$$

$$\frac{\partial \theta}{\partial t} + (\vec{u} \cdot \vec{\nabla})\theta + w\frac{\partial \theta}{\partial z} = K_H\vec{\nabla}^2\theta + K_V\frac{\partial^2 \theta}{\partial z^2} + \gamma(\theta^* - \theta) \tag{4}$$

$$\frac{\partial S}{\partial t} + (\vec{u} \cdot \vec{\nabla})S + w\frac{\partial S}{\partial z} = K_H\vec{\nabla}^2 S + K_V\frac{\partial^2 S}{\partial z^2} + \gamma(S^* - S) \tag{5}$$

$$\rho = F(\theta, S, p) \tag{6}$$

$\vec{u}$ the horizontal flow velocity, $\vec{\nabla}$ the horizontal gradient operator and $\vec{\nabla}^2$ the horizontal Laplacian operator of spherical coordinate, $\vec{k}$ u nit vector of triaxial reference system, w the vertical flow velocity, p is pressure, ρ is density, θ, θ^* the calculated value of potential water temperature and observed value of potential water temperature, respectively, S, S^* the calculated value of salinity and observed value of salinity respectively, f the Coriolis parameter, g the acceleration of gravity, γ the corrected term, A_H the coefficient of horizontal eddy viscosity $(1.0 \times 10^7 \text{cm}^2/\text{s})$, A_v the coefficient of vertical eddy viscosity $(1.0 \times 10^2 \text{ cm}^2/\text{s})$, K_H the coefficient

of horizontal eddy diffusion ($1.0 \times 10^6 \text{cm}^2/\text{s}$) and K_V the coefficient of vertical eddy diffusion ($1.0 \times 10 \text{ cm}^2/\text{s}$), its value is set up based on the value that Wada et al. (1996) used for calculation.

Table 1. Depths and Thickness of Model Levels

Level	Midpoint Depth(m)	Thickness(m)
1	10	0 ∟ 20
2	35	20 ∟ 50
3	75	50 ∟ 100
4	150	100 ∟ 200
5	300	200 ∟ 400
6	600	400 ∟ 800
7	1150	800 ∟ 1500
8	2000	1500 ∟ 2500
9	3000	2500 ∟ 3500
10	4000	3500 ∟ 4500
11	5000	4500 ∟ 5500

Data assimilation method

We introduced a term that assimilates calculated value and observed value in the salinity conservation equation and heat conservation equation after Sarmiento and Bryan (1982).

$$\gamma = \gamma_D + (\gamma_S - \gamma_D)e^{-z/h} \tag{7}$$

γ_S the sea surface value (1/50 days=$2.31 \times 10^{-7} \text{ sec}^{-1}$), γ_D the value in deep water (1/250 day=$4.6 \times 10^{-8} \text{ sec}^{-1}$), z the calculated depth, h the influenced depth of assimilation terms (=500 m).

By equation (7), observed data are assimilated continuously to a model through the assimilated term. When a calculated value deviates from an observed value, the assimilated term becomes bigger and works to return the calculated value to observed value (Fujio et al., 1992a, 1992b).

Data used

Wind stress was calculated from satellite observed data sets (SSM/I: (1988 ~ 1998)) (Atlas et al., 1996) and the data were applied to a model. For calculation of wind stress, a bulk method was adopted (Garratt, 1997). This method evaluates the flux using the observation values at optional height on water surface. The flux calculation formula is given below:

$$\tau_x = \rho_a C_D |V| u_a \quad : \text{ East-West component of wind stress} \tag{8}$$

$$\tau_y = \rho_a C_D |V| v_a \quad : \text{ South-North component of wind stress} \tag{9}$$

ρ_a the air density, $|V|$ the absolute value of wind speed, u_a and v_a are East-West and South-North components of wind speed (wind speed value measured at 10m high is used). C_D the Bulk coefficient (conversion coefficient for kinetic momentum) estimated by Kondo (1975). Generally, the value of C_D is determined by wind speed or by a function of wind speed and stability. As there are areas where tropical ($10°S$ $120°E$, $120°E$ $170°E$) and sub-tropical ($30°N$, $35°S$) area winds converge and have small value, it was necessary to meticulously define a bulk coefficient at breeze. As for water temperature and salinity data, we used data in the area between $100°E \sim 60°W$, during about 80 years (1906~1988), stored by JODC. For sea bottom

topography are used the General Bathymetric Chart of the Oceans (GEBCO) published by the Canadian Hydrographic Service.

FLOW ANALYSIS RESULT

Surface layer circulation

Figure 1 shows the calculated horizontal current field (water depth 10 m) after 30 years. The Northern Equatorial Current, the Kuroshio, California Current and the clockwise North Pacific sub-tropical circulation are reproduced. In the southern hemisphere, the South Equatorial Current, the Antarctic Circumpolar Current, the East Australia Current and the counter-clockwise South Pacific sub-tropical belt circulation are reproduced. In addition, detailed examination of the numerical results shows that the Equatorial Countercurrent, the Oyashio and the Subtropical Counter current are also well reproduced.
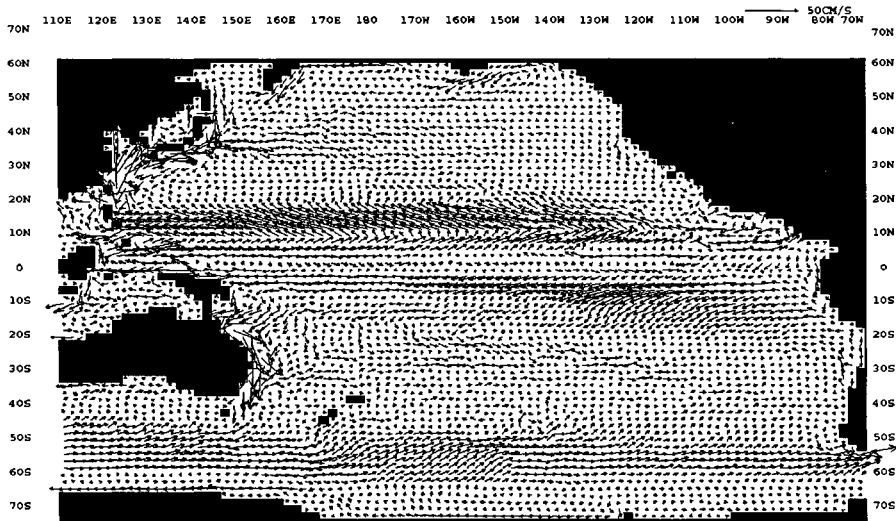

Figure 1. The calculated horizontal current field (water depth 10 m) after 30 years

OCEAN SEQUESTRATION OF CARBON DIOXIDE

Ocean sequestration technique of CO_2 may not be able to replace the cut of CO_2 emission itself, but can be one of quick-effect measures against the climate warming, elevation of sea level, and other influences of the global climate changes due to greenhouse gas accumulation in the atmosphere. Environmental effects of CO_2 ocean sequestration on surrounding sea areas must be properly assessed. One of the proposed methods consists in releasing CO_2 from onshore plants through pipeline at pre-determined depth in the ocean. In another, CO_2 may be continuously released into the middle depth from a ship cruising at a slow speed (Ozaki, 2001). In alternative

methods, CO_2 may be deposited on the deepest sea bottom where no current and turbulence are considered to exist. In order to examine the feasibility of CO_2 sequestration technique, we followed the behavior of CO_2 released into the Pacific Ocean using the flow field discussed in the chapters above. We analyzed a case in which CO_2 generated by electric power plants is released through a pipeline at a fixed point in the ocean.

Amount of CO_2 to be sequestrated

Total CO_2 emission of Japan in 1999 was billion tons (as CO_2), according to a report published by Environment Ministry in 2001. This amount exceeds by about 0.046 Gt (as C) the targeted cut of emission stated in COP3 (6% cut from the reference year of 1990). We examined by numerical simulation the behavior of this excess CO_2 that might be continually introduced in a single cell of the Pacific Ocean for 50 years. Whole calculated sea area was 0 (µmol/kg) at the initial state. The site of introduction was supposed to be under the stratification layer (in this study we assume the 7th layer) at the subarctic region of the Northern Pacific Ocean, where has the potential to absorb CO_2.

Calculation of Predicted Behavior of Sequestrated CO_2

Behaviors of sequestrated CO_2 are calculated by the following equation:

$$\frac{\partial C}{\partial t} + \vec{u} \cdot \vec{\nabla} C = K_H \vec{\nabla}^2 C + K_V \frac{\partial^2 C}{\partial z^2} + \beta(\lambda, \phi, Z) \tag{10}$$

Where C the total carbonate concentration (µmol/kg), t is time (s), K_H the horizontal diffusion coefficient $1.0 \times 10^6 \text{cm}^2/\text{s}$, K_V the vertical diffusion coefficient ($1.0 \times 10 \text{cm}^2/\text{s}$) and $\beta(\lambda, \varphi, t)$ the annual input concentration of CO_2, 1.26×10^2 (µmol/kg/yr). The value of C was calculated from the surplus over the targeted emission cut (0.046 Gt).

Predicted behavior of sequestrated CO_2

To consider the CO_2 sequestration, most important problem is even if the injected CO_2 can be saved in the ocean for a long time. From the viewpoint of marine ecology, an abnormally high CO_2 concentration in specific sea areas must be avoided. Effects on meiobenthos, small bottom-living creatures less than 1 mm with little mobility, such as nematodes and foraminiferans, have also to be taken into consideration. Table 2 shows that calculation results of the total amount of CO_2 reaching for the surface, maximum CO_2 concentration at the surface and ratio of CO_2 reaching for the surface layer after the 50 years continual discharging in the North Pacific Subarctic region, is well known to the CO_2 absorption areas. The different sites of injection cause the variation of the total amount of CO_2 reaching for the surface and maximum CO_2 concentration at the surface. In case of zonal sites variation, further eastern sequestration can suppress the amount of reaching the CO_2 in the sea surface layer. On the other hand, meridional sites changes do not influence the CO_2 concentration. These trends are same in the all test case of injection CO_2. Figure 2 shows vertical distribution of CO_2 concentration at latitude 170°E and longitude 52°N in case of injection at 7th layer and Figure 3 shows vertical distribution of CO_2 concentration (µmol/kg) at latitude 160°W and longitude 52°N in case of injection at 7th layer.

261

Table 2. Evaluation of the CO_2 injection at the 7th layer using the CO_2 diffusion model in the North Pacific Subarctic region

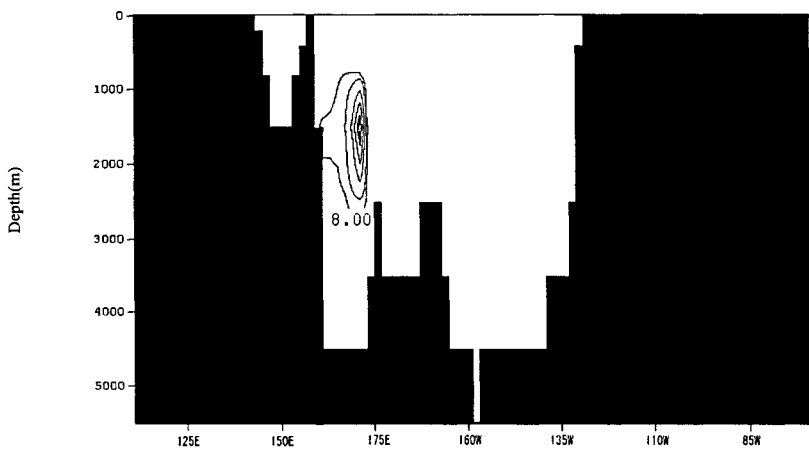| Injection Point	Total amount of CO_2 reaching for the surface ($\times 10^{-3}$ Gt)	Maximum CO_2 concentration at the surface (μ mol/kg)	Ratio of CO_2 reaching for the surface layer (%)
50°North, 160°East	14.20	3.50	30.87
170°East	10.90	3.87	23.70
180°	9.84	3.67	21.39
170°West	10.40	3.79	22.61
160°West	8.11	3.26	19.22
150°West	7.51	3.02	17.63
140°West	6.68	2.66	16.33
52°North, 160°East	13.90	3.37	30.22
170°East	11.60	3.58	25.22
180°	11.30	3.67	24.57
170°West	10.90	3.68	23..70
160°West	9.78	3.46	21.26
150°West	8.71	3.21	18.93
140°West	7.21	2.65	15.67
54°North, 160°East	14.50	3.74	31.52
170°East	12.10	3.74	26.30
180°	11.80	3.83	25.65
170°West	11.40	3.59	24.78
160°West	9.17	3.22	19.93
150°West	9.19	3.31	19.98
140°West	6.82	2.50	14.83

Figure 2. Vertical distribution of CO_2 concentration (μmol/kg) at latitude 170°E and longitude 52°N in case of injection at 7th layer
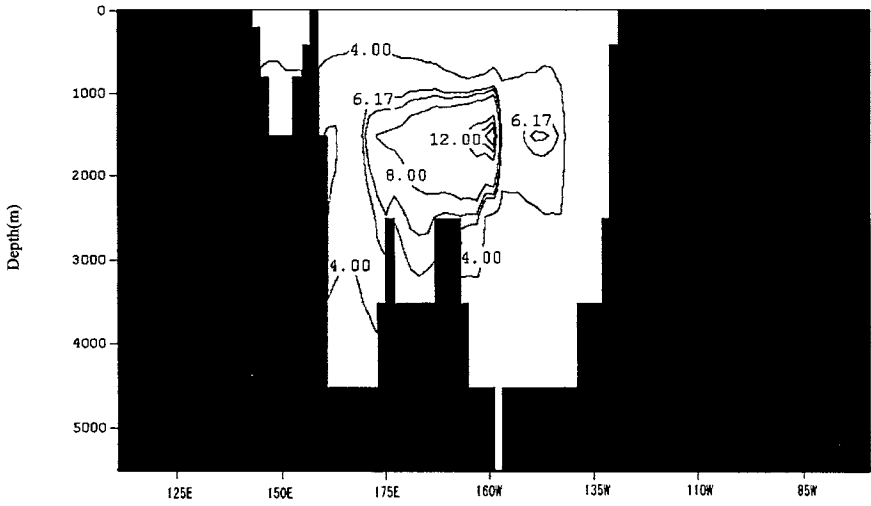
Figure 3. Vertical distribution of CO_2 concentration (μmol/kg) at latitude 160°W and longitude 52°N in case of injection at 7th layer
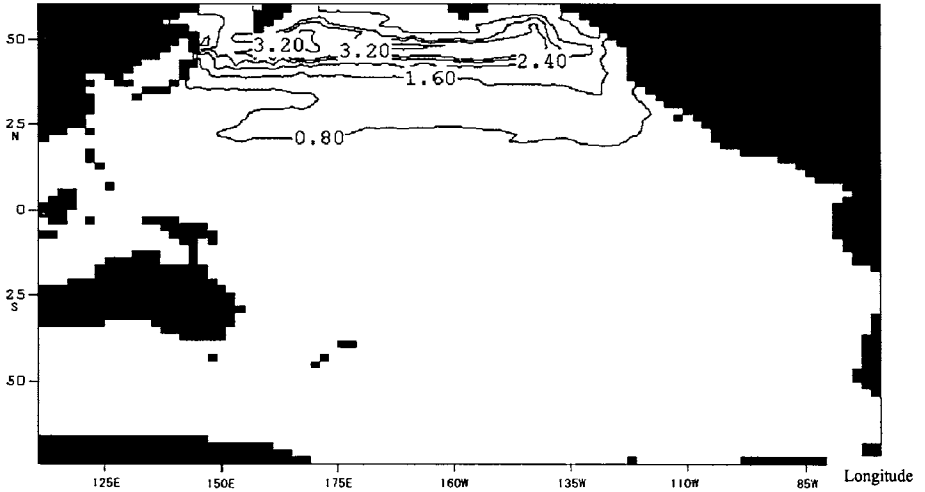

Figure 4. Surface distribution of CO_2 concentration (at 10 m depth) in case of injection at latitude 160°W and longitude 52°N, 7th layer

Figure 4 shows the surface distribution of CO_2 concentration when CO_2 was released at 7th layer. CO_2 reaching the surface is advected and diffused westwards from the release point under the influence of North Pacific Current. It was confirmed that CO_2 hardly crossed the equator into the southern hemisphere although it dispersed extensively in Subtropical Circulation System.

DISCUSSION AND CONCLUSION

(1) Flow fields of the Pacific Ocean were reproduced by using the data assimilation system; in which differences between observed and calculated values of water temperature and salinity were corrected at each time step of calculation (Fig. 1). Reproducibility was verified separately for the surface layers where an ample amount of observation data exits and for the middle and deeper layers where such data are scarcely available. The good fitness of the calculation is considered to be owing to the fact that we had estimated the wind stress by utilizing the satellite observation data of SSM/I. Since flow field of the surface layer strongly influenced by wind, determination of the wind stress will be an important factor in OGCM calculations in the future.

(2) We examined feasibility of the CO_2 ocean sequestration, using the flow fields obtained by Pacific circulation model. CO_2 was supposed to be released in subarctic region of the Northern Pacific Ocean, where has the potential to absorb CO_2. Injected CO_2 was confined into seawater that was the primary criteria. But biological effects of CO_2 on benthos living on sea bottom were also taken into consideration. CO_2 injected into 7th layer, which is placed under the thermocline, we could obtain the effective results as follows. Calculation results shows that further eastern sequestration can suppress the reaching of the CO_2 in the sea surface layer at the subarctic Northern Pacific region (Table 2). The site differences attain the results, which are shown in Figures 2 and 3. As shown in Figure 4, most of CO_2 injected in subarctic region of the northern Pacific Ocean remained in this area although some part might disperse into southern regions. If the CO_2 sequestration technique is to be realized in the future, not only the isolation of adverse effects on marine biota should be taken into consideration.

REFERENCES

Atlas, R., R. Hoffman, S. Bloom, J. Jusem and J. Ardizzone. 1996. A multi-year Global surface wind velocity data set using SSM/I wind observations. *Bull. Amer. Meteor. Soc.* 77(5). 869-882.

Bryan, K. 1969a. A numerical method for the study of the circulation of the world ocean. *J. Comput. Phus..* 4. 347-376.

Fujio, S., T. Kadowaki and N. Imasato. 1992a. World ocean circulation diagnostically derived from hydrographic and wind stress fields 1, The velocity Field. *J. Geophys.Res..* 97. 11163-11176.

Fujio, S., T. Kadowaki and N. Imasato. 1992b. World ocean circulation diagnostically derived from hydrographic and wind stress fields 2, The water movement. *J. Geophys. Res.*. 97. 14439-14452.

Garratt, J.R. 1997. Review of drag coefficients over oceans and continents, *Monthly Weather Review*. 105. 915-929.

Hasumi, H. 2001. Present state and significant challenge of ocean general circulation model. *Oceanography in Japan*. 10(1). 25-39. (In Japanese).

Hellerman, S. and M. Rosenstein. 1983. Normal Monthly Wind Stress Over the World Ocean with Error Estimates. *Journal of Physical Oceanography*. 13. 1093-1104.

Kondo, J. 1975. Air-sea bulk transfer coefficients in diabatic conditions. *Bound.-Layer Meteor.*. 9. 91-112.

Ozaki, M. 2001. Dilution discharge technique of released CO_2. *Kaiyo Monthly*. 33(11). 767-774. (In Japanese)

Sarmiento, J.L. and K. Bryan. 1982. An Ocean Transport Model for the North Atlantic. *J. Geophys. Res*. 87. 349-408.

Wada, A. and S. Nagoya. 1996. Pacific Ocean flow simulation using the data assimilation system. *Flow Modeling and Turbulence Measurements VI*. 631-637.

TIDAL SIMULATION IN ARIAKE SEA
BY PARALLELIZED OCEAN MODEL

Kyeong Ok Kim[1] and Takao Yamashita[2]

[1]Department of Civil Engineering, Kyoto University
Uji, Kyoto, JAPAN
kokim@rcde.dpri.kyoto-u.ac.jp

[2]Research Center for Disaster Environment, Disaster Prevention Research Institute
Uji, Kyoto, JAPAN

ABSTRACT

The tide of the Ariake Sea is characterized by very large difference of tidal height and strong tidal current. In recent years, the Ariake Sea has encountered serious environmental problems, typified by the seaweed damage, which may be caused by serious proliferation of phytoplankton due to environmental changes, such as tidal transformation by coastal development. In this study, characteristics of the tide and tidal current in the Ariake Sea were investigated with the numerical experiment by a parallel three-dimensional primitive σ-coordinate model for seawater circulation. The parallel linux system was used to calculate and predict the Ariake Sea tide. The computed results were compared with the existing charts and coastal tidal observations. The influence of Isahaya Dike on the changes in tidal environment in the Ariake Sea was also examined.

INTRODUCTION

The Ariake Sea is a large bay and macro-tidal estuary located in the western part of Kyushu Island, the southwestern part of Japan (Fig. 1). This sea is the main production area of "Nori"(seaweed) in Japan, providing nearly half of the nations supply. In the recent years, environmental factors have changed in the Ariake Sea; turbid sea water, increased sea water level, changed fish species, risen sea water temperature, etc. The Ariake Sea has suffered a general deterioration of its environment, impacting the general economy of the region and especially leading to dramatic seaweed crop failures caused by unusual red tides. Lots of aggravation factors can be included on this issue; decrease of tideland area, development of coastal industrial area, water pollution, etc. But it is still not clear in detail because of its complexity. In 1952, looking at ways to boost rice production after the War and to solve food shortage problems, decided to drain parts of Isahaya Bay. The construction of Isahaya Dike was started in 1988 and the bay was closed by a 7 km-seawall constructed by the Ministry of Agriculture, Forestry and Fishery on April 14, 1997. A possibility of a negative effect of this reclamation project on seaweed harvests in the Ariake Sea becomes the target of debate of physical-biological relation.

In this research, characteristics tide and tidal current, one of the most important physical factors, in the Ariake Sea and the effect of seawall construction in Isahaya Bay were investigated by numerical experiment using the parallel three-dimensional primitive σ-coordinate model in the Linux-based parallel clustering computer system which connected four clients together via 100M based Ethernet (Fig. 2). This code came from the TOPAZ project at the University of Minnesota. TOPAZ is a compiler tool that helps in the conversion of serial codes to parallel form. TOPAZ was used to help create a parallel version of the POM97 code. (Oberpriller et. al., 1998)
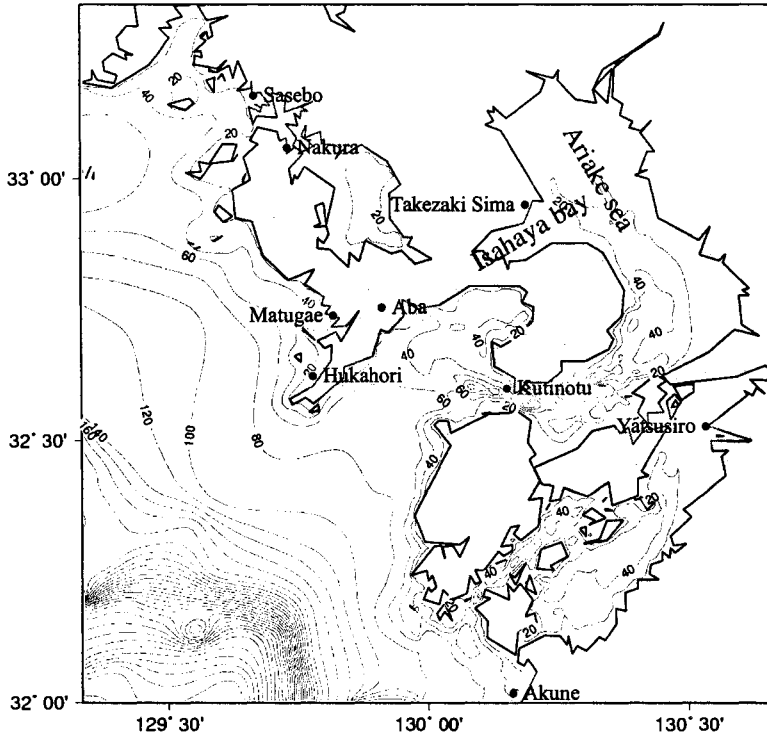

Figure 1. The water depth chart of the computational domain and the location of the Ariake Sea, Isahaya Bay and the tidal observation stations
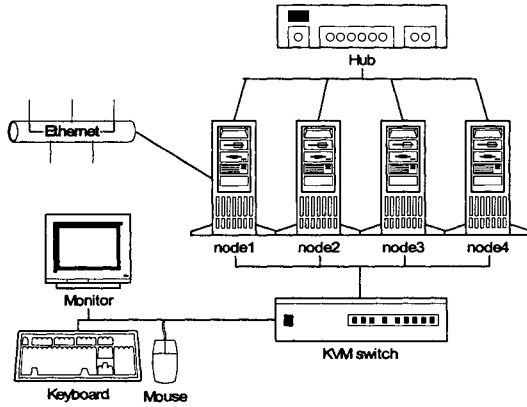
Figure 2. Linux-based parallel clustering computer system

NUMERICAL MODEL

The basic equations consisting of the continuity, momentum, hydrostatic, temperature, salinity and density equations of the three-dimensional primitive σ-coordinate model are given by

$$u_x + v_y + w_z = 0 \tag{1}$$

$$u_t + uu_x + vu_y + wu_z - fv = -\rho_0^{-1} p_x + (K_M u_z)_z + F^u \tag{2}$$

$$v_t + uv_x + vv_y + wv_z + fu = -\rho_0^{-1} p_y + (K_M v_z)_z + F^v \tag{3}$$

$$\rho g = -p_z \tag{4}$$

$$\theta_t + u\theta_x + v\theta_y + w\theta_z = (K_H \theta_z) + F^T \tag{5}$$

$$\rho = \rho(\theta) \tag{6}$$

where (u, v, w) are the velocity components in the (x, y, z) directions, respectively, p the pressure, θ the temperature or the salinity, ρ *in situ* density, ρ_0 (=const.) the reference density, f the Coriolis parameter, g the acceleration due to gravity, K_M the vertical eddy viscosity, K_H the vertical eddy diffusivity, $F^{(u,v)}$ the horizontal eddy friction terms, and $F^{(T,S)}$ the horizontal eddy diffusion terms. The K_M and K_H are determined by Mellor and Yamada level 2.5 turbulence closure model (Mellor and Yamada, 1982). The horizontal friction and diffusion terms are given by Smagorinsky nonlinear viscosity. The model first transforms (1)-(6) into the sigma coordinate system defined by $\sigma = (z - \eta)/(H - \eta)$ where η and H are the surface elevation and the water depth, respectively. The resulting equations are splitted into the external (vertically averaged) and the internal (3-D) modes, and they are solved by the mode splitting method, an idea originally developed by Simons (1980). The Asselin filter is used every time step to prevent a split in the solution associated with the leapfrog scheme. The hybrid friction is hired for calculation of bottom friction. (Luettich and Westerink, 2000)

269

$$C_f = C_{f\min}\left[1+\left(\frac{H_{break}}{H}\right)^{\theta}\right]^{-\frac{\gamma}{\theta}}$$ (8)

In the hybrid friction relationship C_f approaches $C_{f\min}$ in deep water $(H > H_{break})$ and approaches $C_{f\min}\left(H_{break}/H\right)^{\gamma}$ in shallow water $(H < H_{break})$. The value of $C_{f\min}$ is 0.0025, H_{break} is 20, θ is 1/3, γ is 1. In this study area, C_f is distributed in 0.0025~0.0045.

The model computed by the horizontal grid size of 30 arc-second (about 900 m) and the external and internal time step of 0.5 and 15 seconds. The water depth data was composed by digitized numerical data from sea maps and 1-minute grid digital East Asia topographic data from Sungkyunkwan University (Choi et. al., 2002). The tidal elevation in open boundary was interpolated by the observed data at Sasebo and Akune, and modified to improve the reappearance of tide in the Ariake Sea.

MODEL RESULTS

Tidal computation of the Ariake Sea

The model was integrated for 12 tidal periods (six days in M_2 constituent). The model results are shown in Figure 3 from the final period. The amplitude and phase of the tidal elevation were calculated by the harmonic decomposition from the elevation results of each constituent case run. Figure 3 is the co-amplitude and the co-phase tidal chart of the M_2 constituent. Tidal harmonic constants at nine stations (Sasebo, Nakura, Hukahori, Matugae, Aba, Akune, Kutinotu, Takezaki Sima and Yatsusiro) from the table of the tidal harmonic constant published by the Japan Coast Guard were compared with computed data (Table 1, Fig. 4). The RMS (root mean square error) of the amplitude was 9.249 cm, and the RMS of phase is 3.838 degrees. The result of tidal computation shows the similar result with observed data, but the over-amplitude in inner bay of the Ariake Sea estimated. It seems that this model cannot estimate the variable tideland topography clearly.
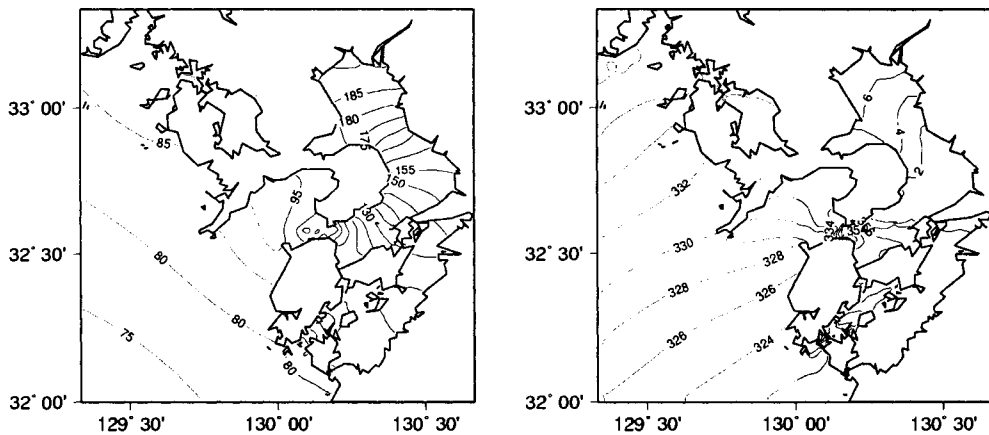
Figure 3. The amplitude (in unit of cm) and the phase (in unit of degree referred Greenwitch) of the M_2 tidal chart computed by the model

Table 1. Observed and computed tide data of M_2 constituent

| Location	Observed amplitude (cm)	Observed phase (degree)	Computed amplitude (cm)	Computed phase (degree)
Sasebo	85.0	340.043	84.592	341.255
Nakura	68.6	347.743	65.441	348.904
Aba	94.9	333.143	93.098	334.724
Matugae	83.5	328.943	84.417	331.579
Hukahori	83.8	329.543	83.525	330.939
Takezaki Sima	155.1	358.343	180.025	5.864
Kutinotu	101.4	350.143	107.680	356.000
Yatsusiro	112.4	351.843	122.112	357.085
Akune	79.7	320.243	80.406	320.224

271
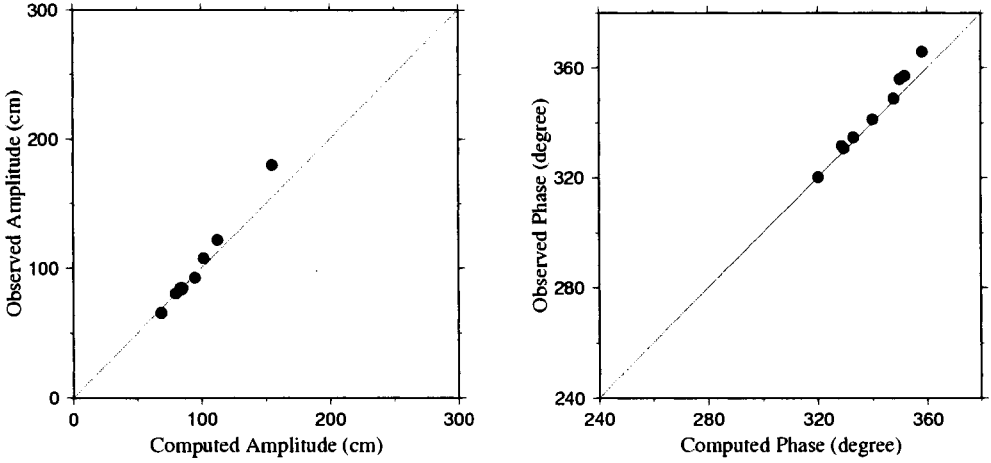
Figure 4. The comparison chart between observed and computed M2 tidal constituent
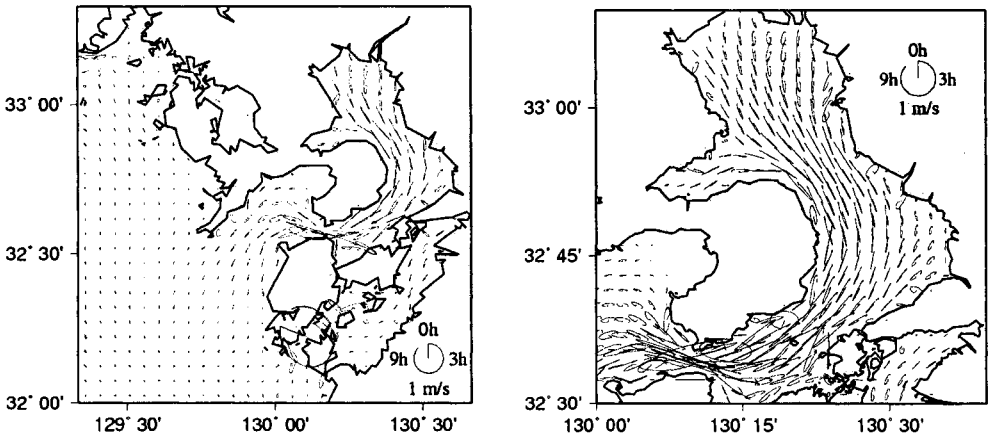

Figure 5. The computed tidal ellipses chart at the surface layer of M_2 constituent

Figure 5 shows the surface tidal current of M_2 constituent. The mouth of the Ariake Sea shows strong current, and the current of the inner Ariake Sea shows the strong currents at 3 hr and 9 hr (lunar time) and clockwise current pattern.

The mean current vectors averaged over one tidal period are shown in Figure 6. There are two strong mean current pattern; one is a northwestward current in inner Ariake Sea by anticyclonic eddies on the onshore side, and the other is a southward flow near the eastern boundary. The southward mean flow over the eastern coastline was recently suggested from the results of the drifter track observations made in July 1992. Figure 7 shows the mean flow pattern inferred from this observation undertook by Ariake Fishery Institute and Sanyo Techno Marin Inc. From Figure 7 we can see a northwestward flow in the offshore region and a southward flow

272

along the east coast.   These features agree well with that in Figure 6.   The similar result is
shown in the study of inner Ariake Bay (Hukuda et al., 1994).
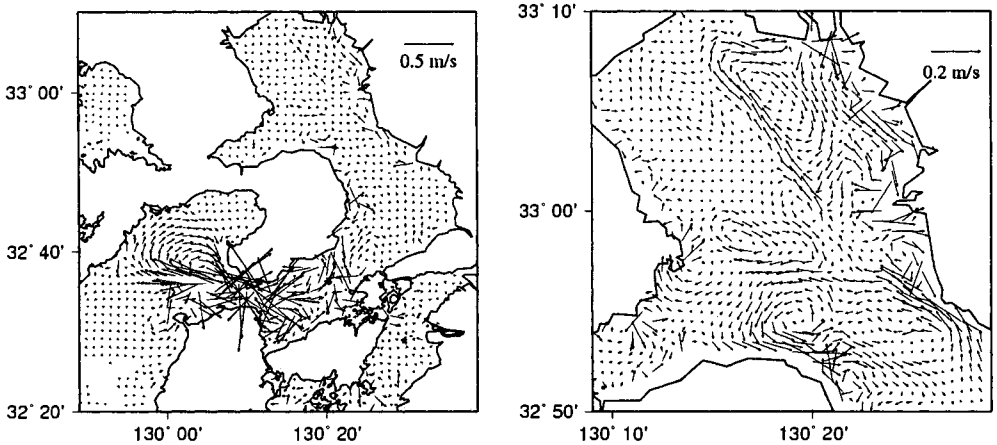

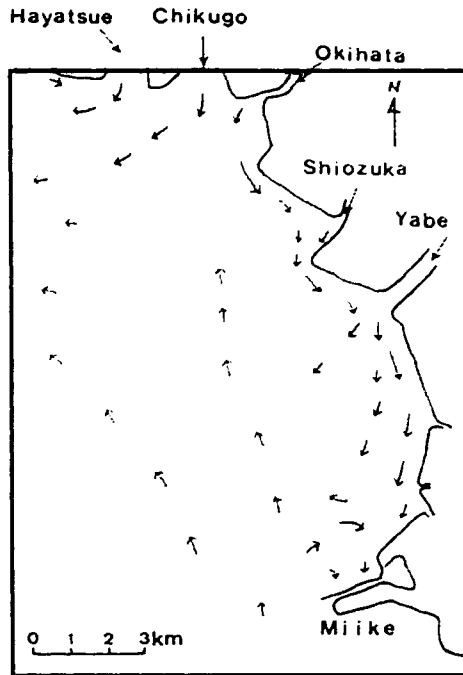Figure 6. The depth-averaged residual current vectors

Figure 7. The surface mean current pattern inferred from the results of drifter track observations
made in July 1992. Cited from "A report on tidal analysis in Ariake Kai fishing grounds" by
Sanyo Techno Marine Inc. (1993)

The effects after the construction of Isahaya Dike

The Ariake Sea is the top "Nori" growing region in Japan, accounting for nearly 40% of total production. However, this year the area suffered a poor harvest and may decrease output by 50 percent. The unusually red tide which used up all the nutrients in the water turning the seaweed from a healthy black to a sickly yellow was often occurred. The red tide in the Ariake Sea seems to be connected with the government's reclamation project in Isahaya Bay. The construction of Isahaya Dike was started in 1988 and completed in 1997. The part of Isahaya Bay was closed to reclaim 3,550 hectares of land, and the contaminated water is regularly discharged from a reservoir inside the gates. Therefore the mean sea level in West Japan was increased by 10 cm during 1985-1999 and tidal amplitude was decreased. The observed tidal amplitude decreased by 3 cm (Kuchinotsu) and 6 cm (Oura) during 1974-1999 in the Ariake Sea, and the tidal amplitude in Isahaya Bay has decreased over 10 cm after the construction of Isahaya Dike. These changes are about 2-3% effects of total tide. Observed data was effective from Isahaya Dike and other reclamations, but this study is considering only the effect of Isahaya Dike. The decrease of the tidal amplitude, in the major eight tidal constituents, was computed to be 1.84 cm at Kuchino station and 9.83 cm at Oura station (Fig. 8).

The difference of maximum current magnitude is increased at the north part of the entrance of Isahaya Bay, and decreased at the around of Shimabara peninsula (Fig. 9). This computational result is similar to the result of Nadaoka (2002) and Unoki (2001). Figure 10 shows the change of eddy with the reduced current, specially, in the middle of Isahaya Bay. Isahaya Bay seems a cavity, so the eddy forms in Isahaya Bay was changed by the construction of Isahaya Dike.

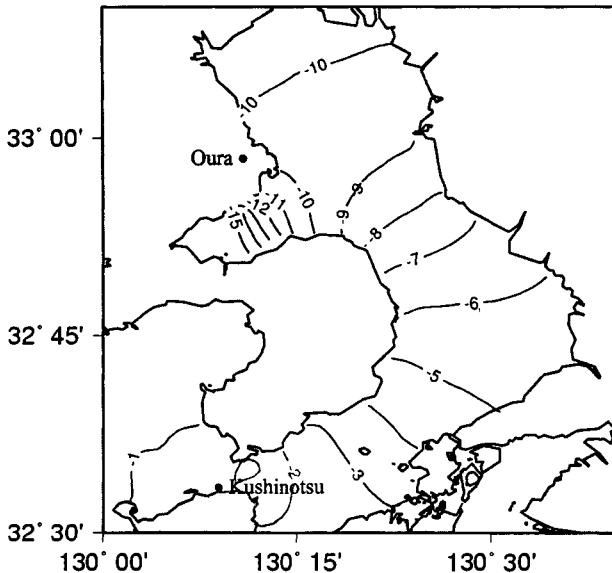Figure 8. The difference of tidal amplitude before and after the construction of Isahaya Dike (in unit of cm)
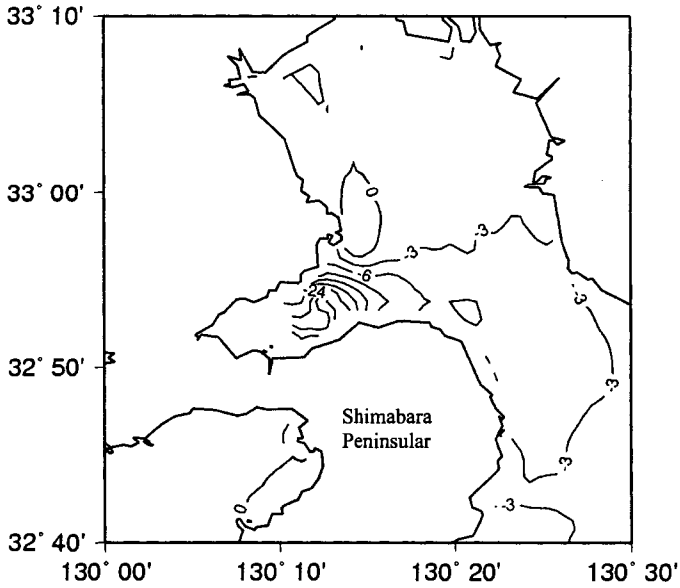
Figure 9. The difference of maximum current magnitude of M_2 constituent before and after the construction of Isahaya Dike (in unit of cm/s, the gray part shows increasing)
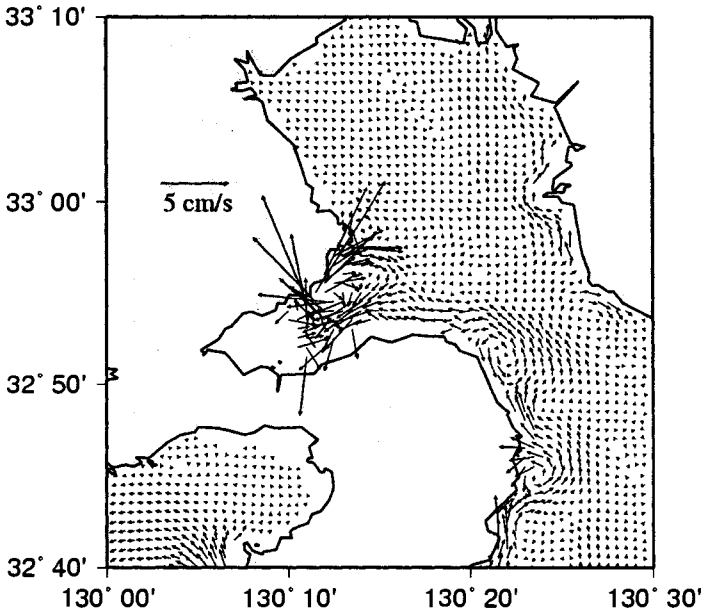

Figure 10. Difference of tidal residual flow (8 constituents) before and after the construction of Isahaya Dike

SUMMARY

The parallel version of a three-dimensional primitive equation model was set up to study the tidal current in the Ariake Sea. The tidal simulation computed effectively in the parallel Linux system, and compared observed tidal harmonic constants and residual currents in the inner Ariake Sea. But, exact bathymetric data for computation are not enough, especially for the tidal flat area. This model does not include the tidal flat solving computation with moving boundaries. It seems to cause overestimation of the tidal elevation in the inner Ariake Sea. For examining the effects of the construction of the sea dike in Isahaya Bay on the changes in tide and current in the Ariake Sea, an attempt has been made to perform the tide simulation. Tidal amplitude in Isahaya Bay has decreased over 10 cm, these changes are about 2-3% effects of total tide, and tidal current has decreased after the construction.

This study about tidal simulation by parallel POM is in the first stage of establishing the comprehensive model for mesoscale air-sea circulation by coupling the third-generation ocean wave model, the three-dimensional ocean circulation model and mesoscale atmospheric model. Seawater circulation is the basis of predictions of pollutant diffusion, sediment transport from the rivers, sea bottom changes as well as seawater exchange. Dominant external forces for water circulation are winds, waves and tides that generate wind-driven and wave-driven currents with three-dimensional structure. Future work will make progress in coupling of water circulation, waves and winds.

REFERENCES

Choi, B.H., K.O. Kim and H.M. Eum. 2002. Digital bathymetric and topographic data for neighboring seas of Korea (in Korean) *J. KSCOE*. 14(1):41-50.

Hukuda, H., J.H. Yoon and T. Yamagata. 1994. A tidal simulation of ariake bay – a tideland model, *Journal of Oceanography* 50:141-163.

Japan Coast Guard. 1992. *Tidal harmonic constituents tables – Japanese coast*. Japan Coast Guard.

Luettich, R. and J. Westerink. 2000. *A Advanced circulation model for oceanic, coastal and estuarine waters*. http://www.marine.unc.edu/C_CATS/adcirc.

Mellor, G.L. and T. Yamada. 1982. Development of a turbulence closure model for geophysical fluid problems. *Reviews of Geophysics and Space Physics*. 20(4):851-875.

Nadaoka, K. 2002. Influence of the Isahaya Bay sea-dyke on the changes in tide, currents and water quality in Ariake Sea. In *The 51th National Congress of Theoretical & Applied Mechanics 2002*. PD1-8.

Oberpriller, W, A. Sawdey, M. O'Keefe, S. Gao and S. Piascsek. 1998. Parallelizing the Princeton Ocean Model Using TOPAZ. *http://topaz.lcse.umn.edu*.

Sanyo Techno Marine Inc. 1993. *A report on tidal analysis in Ariake Kai fishing grounds* (in Japanese) Sanyo Techno Marine Inc.

Simons, T.J. 1980. Circulation models of lakes and inland seas. *Can. Bull. Fish. Aquat. Sci.* 203:146.

Unoki, S. 2001. The change of water elevation and current in the Ariake Sea. In *Kyushu-Okinawa Joint Symposium – the oceanic environment in the Ariake Sea.*

THE FLOW PARAMETERS ESTIMATION ABOVE DRY LAND IN THE TSUNAMI RUN-UP MODELING

Andrey G. Marchuk and Alexandr A. Anisimov

Institute of Computational Mathematics and Mathematical Geophysics
Siberian Division of the Russian Academy of Sciences, Novosibirsk, RUSSIA
mag@omzg.sscc.ru

ABSTRACT

The most important question in the prognostic tsunami modeling is estimation of tsunami run-up heights at different points along the coastline. Also, it is of great importance to know the water flow velocity in submerging areas, because a high-speed flow during tsunami run-up is the main destructive factor of a tsunami attack. In the paper the new method for numerical simulation of the long wave run-up process is proposed. Nonlinear shallow water equations are used for description of the wave propagation up to the water-edge point. Then the special algorithm used for estimation of the flow parameters and location of the moving water edge. It is based on the energy and mass conservation laws. Several series of one-dimensional computations were carried out. Shore profile, which gives the maximum run-up height for the fixed initial wave parameters have been found. Results of modeling of the tsunami run-up on the real shore in the Akita prefecture (Japan) are presented.

INTRODUCTION

One of the most important questions in prognostic tsunami modeling is estimation of tsunami run-up heights in different points along the coastline. Methods for numerical simulation of tsunami waves propagation in deep and shallow sea are well developed and are widely used by a great number of scientists. Some of them, in order to find possible submerged areas use the simplifying assumptions about the ratio between the tsunami wave height near the shore and wave's run-up height. But this ratio strongly depends on the shore profile above mean sea level.

STATEMENT OF THE PROBLEM

In this paper the method for numerical calculation of tsunami waves run-up on a shore of arbitrary profile will be described. Numerical modeling of this process was carried out based on the one-dimensional nonlinear shallow-water model

$$u_t + uu_x + g\eta_x = 0,$$
$$\eta_t + (u(\eta + H))_x = 0, \tag{1}$$

where u - velocity, η - surface elevation, H - the value of depth. The problem statement is as follows: there is one-dimensional nearcostal area with an arbitrary bottom relief. From the left

boundary of computational area tsunami wave is coming toward the shore. Above the mean sea level the coast have arbitrary profile (Fig. 1).
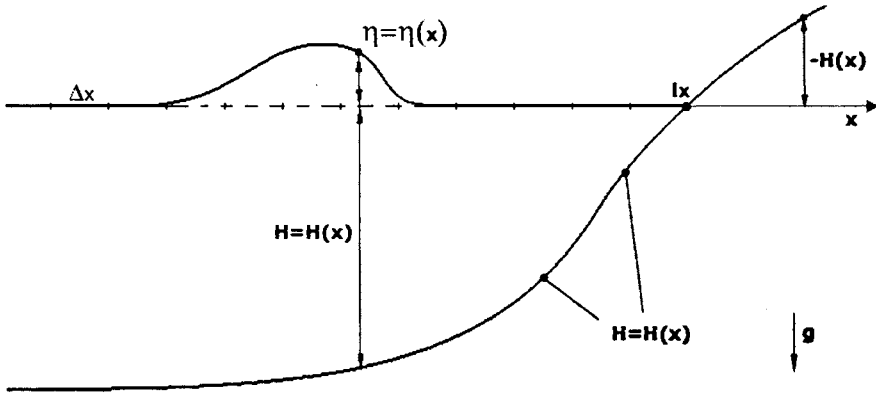

Figure 1. The statement of the run-up problem

The shore surface above the mean sea level has an arbitrary profile. In numerical computations it is given as an array of elevation values in grid-points. Bottom relief can have any form. In the beginning, the water in the area is still, so the initial conditions can be written as

$$u(x,0) = \eta(x,0) = 0 \tag{2}$$

The incident tsunami wave is generated by water motion and moving of a free surface on the left boundary of computational area

$$\eta(t) = 1 + \sin(b \cdot t - \pi/2),$$

$$u(t) = \eta(t) \cdot \sqrt{g/H}, \qquad t \in \left(0, \ \frac{2\pi}{b}\right). \tag{3}$$

After the wave is formed completely (it will happen, when the time value t will become equal to $2\pi/b$), the "free" boundary conditions will be assigned to this boundary

$$\frac{\partial \eta}{\partial x} = 0, \ \frac{\partial u}{\partial x} = 0. \tag{4}$$

NUMERICAL ALGORITHM

The differential problem (1)-(4) is solved numerically with the help of method of finite differences. So all the variables are defined in the grid-points and the values of the depth and topography elevation is given as the array H_i (i=1, M). The explicit finite difference equations with central differences

$$\frac{u_i^{n+1} - u_i^n}{\Delta t} + u_i^n \frac{\left(u_{i+1}^n - u_{i-1}^n\right)}{2\Delta x} + g\frac{\left(\eta_{i+1}^n - \eta_{i-1}^n\right)}{2\Delta x} = 0 \qquad (5)$$

$$\frac{\eta_i^{n+1} - \eta_i^n}{\Delta t} + \left(H_i + \eta_i^n\right)\frac{u_{i+1}^{n+1} - u_{i-1}^{n+1}}{2\Delta x} + u_i^{n+1}\frac{H_{i+1} + \eta_{i+1}^n - H_{i-1} - \eta_{i-1}^n}{2\Delta x} = 0$$

are used for computations in the inner points of the area. Values of the velocity u_i^{n+1} (i=1, M) are preliminary defined from the first equation (5) in whole computational area. Then from the second equation (5) one can define the values of the surface elevation η_i^{n+1} on the higher time level in all inner grid-points.

On the right boundary (the coast) where the depth value is equal to zero or is very close to this value (~0.01m) the "free" boundary conditions (4) are used until the moment, when the surface disturbance will reach this boundary grid-point. From this moment the special algorithm for computation of the flow parameters is used.

Let introduce the new computation point B, which shows the location of the water-edge point in every discrete time moment (time step). The position of this point is determined by calculating the volume of water, which comes through the cross-section MC during every time interval (Fig. 2). We assume that the surface profile between points A and B represents a straight segment. The location of the point B can be calculated from the total water volume rightwards the cross-section MC.

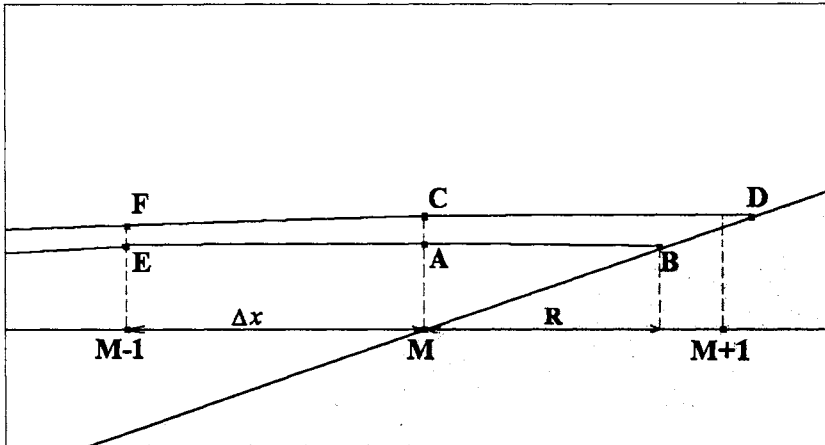Figure 2. Definition of the water edge-point location

The distance between a projection of a point A and projection of a water edge point B cannot exceed one computational step on space. The change of a volume at each step is summarized and based on the full volume (square of a triangle MCD) the new position of a point of a water edge is determined. The scheme of the given algorithm is drawn in Figure 2.

281

Let at some time moment the points E and A show positions of the free surface at computational grid-points with numbers M-1 and M accordingly and point B - position of the point of a water edge at this moment. Elevation of the free surface and water velocity in the grid-point M-1 are calculated by difference scheme (2). And in the grid-point M this can be done using the following procedure: at first we define new values of velocity and elevation ($u_{M-1/2}^{n+1}$ and $\eta_{M-1/2}^{n+1}$) in a midpoint between grid-points with numbers M-1 and M using difference equations

$$\frac{u_{M-1/2}^{n+1} - u_{M-1/2}^{n}}{\Delta t} + \frac{\left(u_{M-1}^{n} + u_{M}^{n}\right)}{2} \cdot \frac{u_{M}^{n} - u_{M-1}^{n}}{\Delta x} + g\frac{\eta_{M}^{n} + \eta_{M-1}^{n}}{\Delta x} = 0$$,

$$\frac{\eta_{M-1/2}^{n+1} - \eta_{M-1/2}^{n}}{\Delta t} + \frac{\left(H_M + \eta_M^n + H_{M-1} + \eta_{M-1}^n\right)}{2} \cdot \frac{u_M^{n+1} - u_{M-1}^{n+1}}{\Delta x} +$$

$$+u_{M-1/2}^{n+1}\frac{H_M + \eta_M^n - H_{M-1} - \eta_{M-1}^n}{\Delta x} = 0$$ (6)

And in a midpoint between points M and B (values $u_{M+1/2}^{n+1}$ and $\eta_{M+1/2}^{n+1}$):

$$\frac{u_{M+1/2}^{n+1} - u_{M+1/2}^{n}}{\Delta t} + \frac{\left(u_{M}^{n} + u_{M+1}^{n}\right)}{2} \cdot \frac{u_{M+1}^{n} - u_{M}^{n}}{R} + g\frac{\eta_{M+1}^{n} + \eta_{M}^{n}}{R} = 0$$

$$\frac{\eta_{M+1/2}^{n+1} - \eta_{M+1/2}^{n}}{\Delta t} + \frac{\left(H_M + \eta_M^n + H_{M+1} + \eta_{M+1}^n\right)}{2} \cdot \frac{u_{M+1}^{n+1} - u_{M}^{n+1}}{R} +$$ (7)

$$+u_{M+1/2}^{n+1}\frac{H_{M+1} + \eta_{M+1}^n - H_M - \eta_M^n}{R} = 0$$

Then with the help of a linear interpolation values of velocity and elevation on the new time level are define in the grid-point with number M.

$$u_M^{n+1} = \frac{\left(\frac{\Delta x}{2} \cdot u_{M+1/2}^{n+1} + \frac{R}{2} \cdot u_{M-1/2}^{n+1}\right)}{(R + \Delta x)/2}$$, (8)

$$\eta_M^{n+1} = \frac{\left(\frac{\Delta x}{2} \cdot \eta_{M+1/2}^{n+1} + \frac{R}{2} \cdot \eta_{M-1/2}^{n+1}\right)}{(R + \Delta x)/2}$$

Here the value R represents distance along the horizontal axis from the most right computational grid-point up to a current position of the water edge point, and the gridded variables with index

282

M+1- are values of flow parameters in the mobile point of a water edge. The water-edge velocity is determined from the mass and energy conservation laws.

$$u_{M+1}^{n+1} = u_0 - \Delta u = u_0 - \frac{g \cdot \Delta x \cdot tg(\alpha)}{u_0} = u_0 - g \cdot \Delta t \cdot tg(\alpha),$$

where u_0 is the preliminary water edge velocity, estimated from the one time-step increment of the triangle MAB square value (Fig. 2) and $tg(\alpha)$ is the shore inclination between M and M+1 grid-points. If the distance between projections of points C and D becomes greater than step of spatial computational grid then we introduce the new grid-point with number M+1 and the computational algorithm moves to this new grid-point.

RESULTS OF NUMERICAL EXPERIMENTS

Using this computational method a number of computational experiments of tsunami run-up on a shore of an arbitrary profile are carried out. The main goal of these computations was testing of this algorithm using results of other methods and investigation of the run-up height dependence from the shore profile.

The first series of test experiments was carried out for the uniformly sloping shore with following parameters:

Spatial step of the grid:	dx = 10 meters.
Initial number of computational grid-points:	M = 400
Time step :	dt = 0.2 seconds
Length of an incident wave (expression 3)	B = 0.05
Initial wave height	h = 2 meters

The wave was generated at the distance of 4 kilometers off the shore. The bottom profile was as following: from the water-edge point the bottom has the constant inclination angle (tg α =0.1) and increase linearly till the depth 100 m. Then, the depth is not varying until the left boundary. Table 1 shows the run-up heights of generated waves at different beach slopes:

Table 1. Calculated wave run-up height according to the beach slope angle.

Beach slope angle $tg(\alpha)$	0.1	0.2	0.3	0.4	0.5	0.6	0.7	0.8	0.9	1
Run-up height	19.5	19.3	18.9	18.5	18.1	17.8	17.5	17.3	17.1	16.9

During the way to the coast the wave height increases up to 8 meters. From the table it is visible, that increasing of declination of a shore causes decreasing of the wave run-up height, which corresponds to the results obtained earlier with the help of analytical (Pelinovsky, 1982, 1985) and numerical methods (Marchuk, 1982). In Figure 3 the wave profile at the moment of maximum run-up is shown.
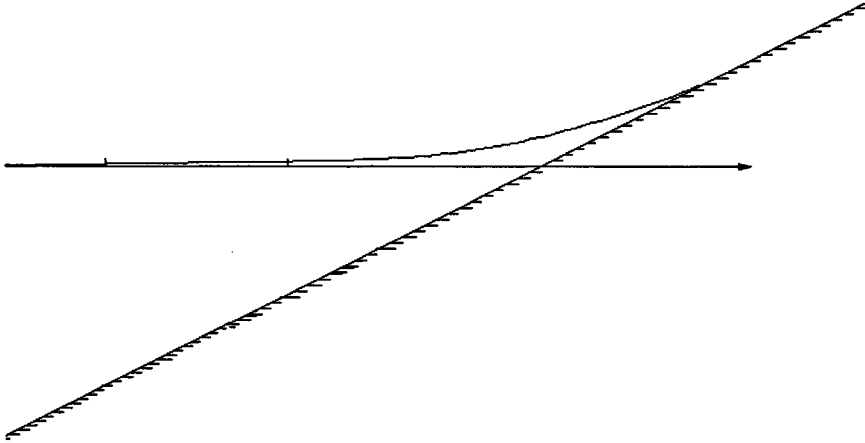
Figure 3. The moment of highest run-up of a wave to the uniform slope

Now we shall consider tsunami wave run-up on a shore with a more complicated profile. The second series of numerical experiments is carried out in order to investigate correlations between wave run-up height and shore profiles of submerging area. In this case the submerging area of the shore (up to 25 meters above mean sea level) has the profile, which is defined by the following expression:

$$H(r) = r \cdot tg(\alpha) - C \cdot \sin\left(\frac{\pi \cdot r}{r_0}\right), \ 0 \le r \le r_0$$

Here the distance r measured from the initial water-edge point to the right, and r_0 - is the width of a shore area with varied declination (in this series of calculations it was equal to 250 meters). All remaining parameters were the same, as in the previous case. In this series of computations the wave height near the shore was equal to 7.6 m. As the result of computations with the positive values of parameter C the following table was obtained:

Table 2. Run-up heights for positive curvature parameter values

Curvature parameter C	0.0	1.0	2.0	3.0	4.0	5.0	6.0	7.0
Run-up height	23.067	23.086	23.132	23.73	23.86	23.54	23.68	23.63

The shore and the water surface profile when the curvature parameter value is equal to 4 are shown in the Figure 4.
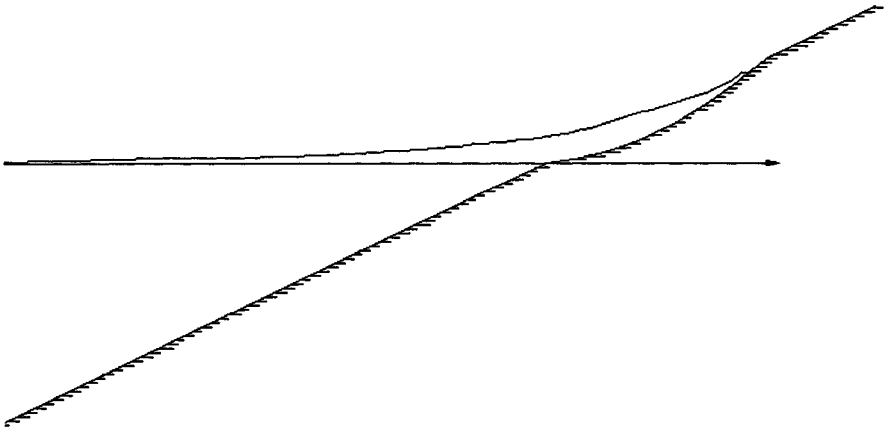
284

Figure 4. Wave run-up on a shore with the positive curvature parameter ($C = 4$)

Results of computations with the negative values of the curvature parameter C are shown in the Table 3.

Table 3. Run-up heights for negative curvature parameter values

Curvature parameter C	-1.0	-2.0	-3.0	-4.0	-5.0	-6.0
Run-up height	22.58	22.82	22.40	22.37	21.88	20.86

The shore and the water surface profile when the curvature parameter value is equal to -6, are shown in Figure 5.
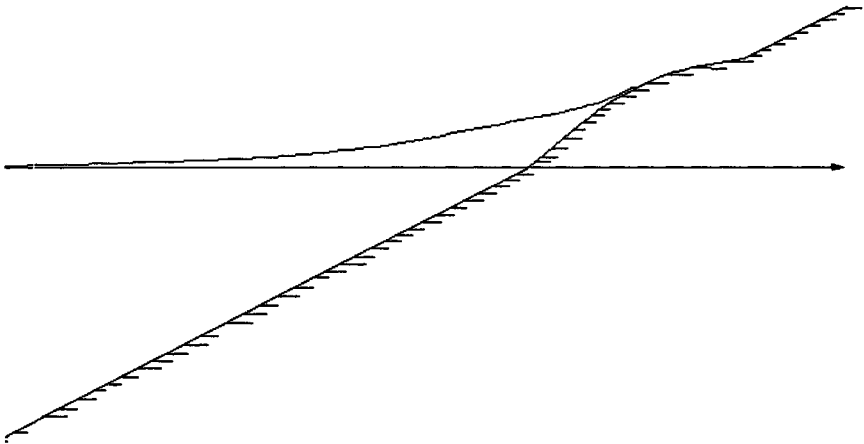

Figure 5. Wave run-up on a shore with the negative curvature parameter ($C = -6$)

From Tables 2 and 3 it is seen that the maximum run-up height of the wave with given initial parameters is observed when parameter C is equal to +4.

FLOW PARAMETERS BEHAVIOR DURING WAVE RUN-UP AND DRAWN-DOWN

Proposed method makes it possible to calculate and watch all flow parameters during whole process (tsunami wave run-up and drawn down). For example the flow velocity is one of the most important parameters of the wave during inundation process. It determines the force of the wave impact to the shore structures. Potential force of the flow per unit shore width is proportional to the water layer thickness and the squared flow velocity $(\eta+H) \cdot V^2$. In Table 4 the values of flow parameters, which are written in the second column, are given for almost all coastal grid-points. Their numbers are given in the first row of this table. In the first column the initial tsunami wave period (parameter b in formula (3)) and amplitude (η_0) are given. In these computations the shore slope was constant and equal to 0.1 (tg α). After the analysis of flow parameters, given in Table 4, we may conclude that during the wave run-up the maximum flow velocity is registered in grid-points which are located at a quarter of the final run-up length from the initial water edge point. For instance the maximum of the water flow rate during the 6 m high wave run-up is detected in the 6th grid-point of the total 20 inundated grid-points. In the same numerical experiment the flow velocity during the wave drawn-down was much greater in all coastal grid-points with maximum of 24 m/sec near the initial water edge point. The integrated parameters $\eta \cdot V$ and $\eta \cdot V^2$ reach their maximums near the initial water-edge point because of big water-layer thickness during inundation process in these points.

MODELING OF TSUNAMI RUN-UP ON A REAL SHORE

Numerical modeling of the long wave run-up on the real shore was carried out. The profile of the Japan coast (Fig. 6) was taken from Survey Report of Tsunami of May 26 1983 Along the Coasts of Akita Prefecture (Akita Prefecture Office Report, 1984). In this place (near Minehama village) run-up height was recorded as 14.08 m. To reach such a height the incident tsunami wave with the period 65 sec must be about 8 meters high near the coastline. The wave profile in this case is shown in the Figures 7-8.

CONCLUSIONS

The new algorithm of tsunami wave run-up computation a on a shore of an arbitrary profile is developed. The results of the wave run-up on a sloping shore are in good agreement with the results obtained earlier with the help of analytical and numerical methods. The computational experiments of a tsunami impact on a shore of an arbitrary profile have revealed such type of shore relief, which gives the highest climb of the water on the shores of various profiles with identical initial wave. The destructive tsunami effect due to the water-flow force is bigger when the affected structure is closer to the initial water edge. The wash-away force is much greater than water flow force during run-up. The described model reasonably simulates tsunami wave run-up on a beach with arbitrary profile and can be used in simulation of real tsunami waves. Two-dimensional description of the flow near the moving water edge point is the main advantage of this method

Table 4. Flow parameters during tsunami wave run-up and drawn-down

| Wave parameters	Measured value	2	3	4	5	6	7	8	9	10	11	12	13	14	15	16	17	18	19
b=0.05 η_0=4	V_{max}	4.67	4.50	4.26	3.93	3.60	3.44	3.02	2.80	2.25	1.79	1.54	0.09						
	V_{min}	-15.3	-13.9	-13.1	-12.0	-11.2	-10.1	-9.23	-8.15	-6.97	-5.54	-3.66	-0.52						
b=0.05 η_0=5	V_{max}	4.69	4.71	4.80	4.77	4.69	4.60	4.48	4.38	4.22	4.00	3.76	3.43	2.95	2.23	1.35			
	V_{min}	-16.4	-15.5	-14.9	-13.9	-13.3	-12.4	-11.8	-10.9	-10.1	-9.21	-8.24	-7.14	-5.90	-4.36	-1.95			
b=0.05 η_0=6	V_{max}	4.80	5.04	5.45	5.63	5.72	5.76	5.74	5.73	5.66	5.52	5.31	5.19	4.96	4.63	4.26	3.73	3.12	2.30
	V_{min}	-24.3	-22.3	-20.0	-19.0	-17.7	-16.5	-15.6	-14.5	-13.7	-12.8	-12.0	-11.1	-10.2	-9.31	-8.28	-7.25	-5.81	-4.13
b=0.03 η_0=5	V_{max}	2.11	2.09	2.62	2.71	2.54	2.20	2.17	2.06	1.53	1.32	1.04	0.25						
	V_{min}	-14.9	-13.9	-13.2	-12.4	-11.4	-10.4	-9.31	-8.21	-6.99	-5.61	-3.84	-1.05						
b=0.05 η_0=5	$(\eta \times V)_{max}$	31.8	28.9	26.1	23.1	20.6	17.9	15.2	12.9	10.2	8.12	6.15	4.40	2.91	1.56	0.47			
	$(\eta \times V)_{min}$	-47.1	-42.3	-38.6	-34.3	-30.6	-26.8	-23.2	-19.8	-16.4	-13.2	-10.2	-7.31	-4.63	-2.28	-0.43			
	$\eta \times (V_{max})^2$	144	127	115	101	88	76.8	63.4	52.0	41.8	31.6	24.5	17.5	11.6	6.8	3.0	0.5		
	$\eta \times (V_{min})^2$	603	543	461	407	341	292	240	197	156	120	88.0	60.9	37.5	19.5	7.0			
b=0.05 η_0=6	$(\eta \times V)_{max}$	45.4	43.7	38.9	36.1	33.3	30.0	26.7	23.4	21.4	17.8	15.2	12.7	10.4	8.07	6.01	4.16	2.58	1.17
	$(\eta \times V)_{min}$	-60.2	-55.7	-51.7	-47.3	-43.6	-39.3	-35.7	-31.9	-28.2	-24.9	-21.3	18.2	-14.9	-12.0	-9.07	-6.39	-3.89	-1.73
	$\eta \times (V_{max})^2$	245	227	215	184	183	160	139	122	107	93.9	72.6	63.2	50.6	39.1	27.8	19.3	12.0	6.4
	$\eta \times (V_{min})^2$	877	788	702	627	552	490	423	371	314	267	221	179	144	108	80.0	53.5	32.7	16.1
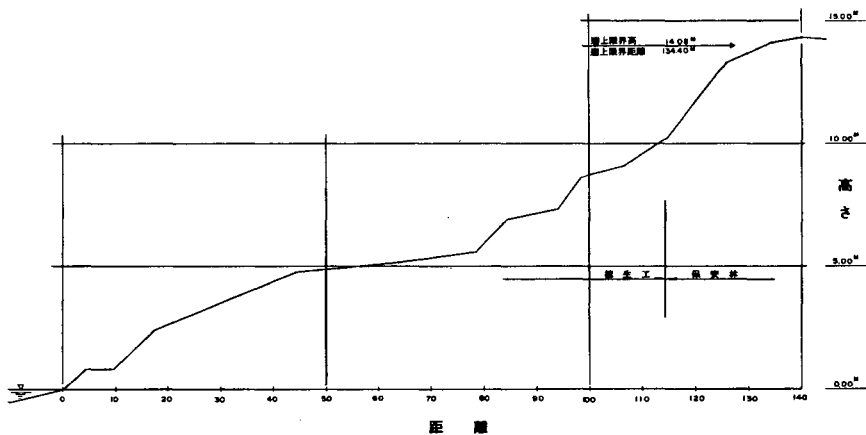
Figure 6. Shore profile near Minehama village in Akita prefecture (Japan)
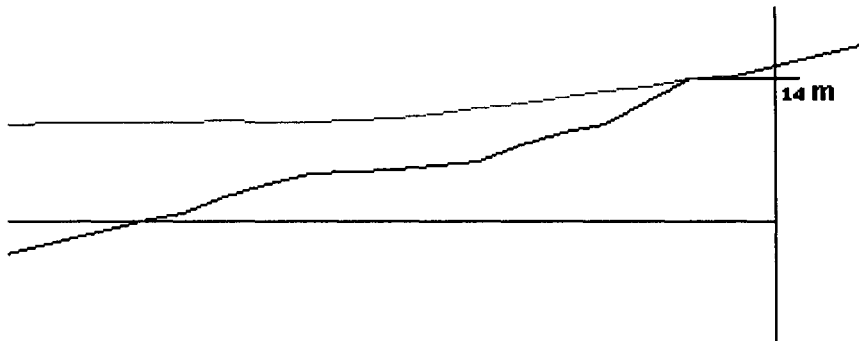

14 m

Figure 7. Modeling of Japan Sea Tsunami 26.05.1983 at the Akita coast. Tsunami wave profiles at the moment of highest run-up

REFERENCES

Akita Prefecture Office Report. 1984. *Survey Report of Tsunami of May 26 1983 Along the Coasts of Akita Prefecture* (in Japanese) Japan: Akita Prefecture Office.

Marchuk An. G. 1982. Method for computations of long gravity waves run-up on sloping shore (in Russian). *Tsunami evolution from the source up to run-up on a shore* Moscow: Radio i Sviaz.

Pelinovsky E.N. 1982. *Nonlinear dynamics of tsunami waves* (in Russian) Gorky: Institute of Applied Physics RAS.

Pelinovsky E.N. 1985. *Tsunami Run-up on a shore* (in Russian) Gorky: Institute of Applied Physics RAS.

EFFECT OF THE TSUNAMI BREAKWATER UNDER CONSTRUCTION AGAINST TSUNAMI DISASTERS

Hiroaki Sato[1], Hitoshi Murakami[2], Yasunori Kozuki[2] and Kengo Kurata[2]

[1]Coastal Engineering Division, River and Coastal Engineering Department
NEWJEC Inc., Osaka, JAPAN
satohr@osaka.newjec.co.jp

[2]Department of Ecosystem Engineering, University of Tokushima
Tokushima, Tokushima, JAPAN

ABSTRACT

Usually, the tsunami breakwater is designed based on the historical tsunami height. However, if the tsunami occurs at the some other place, tsunami height in the bay may be over allowable height. It is important to consider the various locations and magnitudes of seabed displacement. In this study, the Monte Carlo method was used for prediction of tsunami height in the bay. In the tsunami calculation it was considered the random tidal height, latitude, longitude, vertical fault deformation and calculative accuracy. They were defined as the Normal or Weibull distribution. Six cases of the different tsunami breakwater length were set, and the iterative calculations were carried out at 5,000 times for one case. The number of tsunami that is over allowable height in the bay was counted, and "the tsunami suffering probability" was defined by using them. The tsunami suffering probability enabled to estimate the length of tsunami breakwater against various tsunamis. For instance, the tsunami breakwater under construction will have no effect for decay of the tsunami. When the allowable tsunami suffering probability is fixed, the best length of the tsunami breakwater can be decided simply.

INTRODUCTION

In Japan, Nankai Trough runs from east to west of offshore Shikoku Island and Kii peninsula (here in Nankaido), and this is an area experienced many big earthquakes. The quake registers a magnitude of near or over 8.0. Each time, residents living near the Nankaido suffered a damage from tsunami disasters. All these areas will be dangerous for next tsunami, because of the tsunami attacks within about 20 minutes after the seabed displacement (Murakami et al., 1996). It means that the residents have hardly any time to evacuate. Thus, the government has constructed the tsunami breakwater at these districts. The common breakwater or the seawall was designed based on the encounter probability, for example, the wave with a return period of 50 years. The tsunami breakwater, however, was designed based on the most dangerous tsunami in the past, because the large tsunamis rarely occur at Nankaido. Therefore, we cannot assume the encounter probability against tsunami. Tsunami height will change with the fault location. Supposing the same fault model of Ansei earthquake in 1854 is utilized in the theoretical calculation, the result values maybe change according to the different set-up of the model (Kawata et al., 1994; Murakami et al., 1997; Hiraishi et al., 1999; Tohiki et al., 2000). In this study, to propose an optimum design method of tsunami breakwater the suffering probability acquired by launching multiple is used. In order to install the probability, the Monte Carlo method was used for the prediction of tsunami height in the bay. It was considered random tidal height, latitude, longitude, vertical fault deformation and calculative accuracy in the tsunami calculation.

BASIC EQUATIONS AND CALCULATION DOMAIN

Basic equations

Basic numerical equations of tsunami propagation are equation (1) ~ equation (3). The second and third terms in the left side of equations (1) and (2) can be neglected when the water depth is over 50 meters.

$$\frac{\partial M}{\partial t} + gH \frac{\partial \zeta}{\partial x} + f \frac{MQ}{H^2} + \frac{1}{H}\left(M \cdot \frac{\partial M}{\partial x} + N \cdot \frac{\partial M}{\partial y} \right) = 0 \tag{1}$$

$$\frac{\partial N}{\partial t} + gH \frac{\partial \zeta}{\partial y} + f \frac{NQ}{H^2} + \frac{1}{H}\left(M \cdot \frac{\partial N}{\partial x} + N \cdot \frac{\partial N}{\partial y} \right) = 0 \tag{2}$$

$$\frac{\partial \zeta}{\partial t} + \frac{\partial M}{\partial x} + \frac{\partial N}{\partial y} = 0 \tag{3}$$

where, t denotes time; g is the gravity accelerator; ζ is water level lift from still water level; h is water depth; f is friction coefficient of ocean bottom; M and N represents the discharge flux in x and y direction, respectively; ξ is the vertical amount of seabed displacement, which can be estimated by Manshinha-Smylie theory (1971) by fault model. Here, ξ is the water surface change by the wave. In the above equations, H and Q can be yielded as

$$H = h + \zeta - \xi \tag{4}$$

$$Q = \sqrt{M^2 + N^2} \tag{5}$$

For the boundary conditions, full reflection is assumed at the landward side, while non-reflection is used at the other sides. Linear long propagating wave is assumed which fulfills equation (6).

$$M^2 + N^2 = gH \cdot \zeta^2 \tag{6}$$

Calculation domain and conditions

Figure 1 shows the computation domain of the present study, which covers an area 515.00km×168.75km. The coordinate system is also illustrated in Figure 1 where the symbol "•" indicates the historical earthquake epicenters at the Nankaido offshore. In history, at the Nankaido, all serious earthquakes occurred within this area. The grid size for the numerical scheme is 12.5 m; the minimum water depth is 1.0 m; time step is chosen as 0.5 second for stability. In addition, offshore tsunami waves are calculated for three hours after the seabed displacement using a two-dimensional leapfrog method.
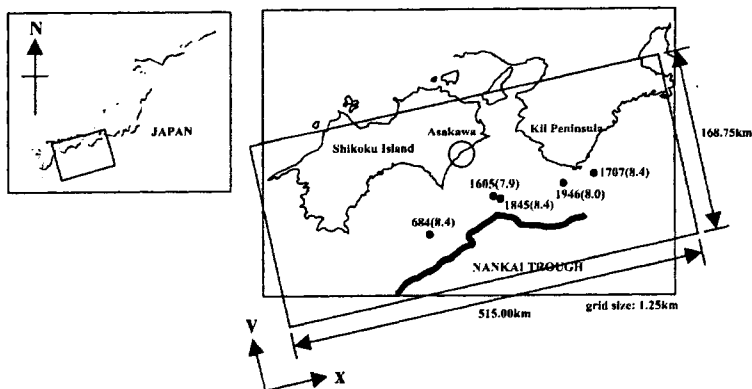
Figure 1.   Calculation domain

Present situation of Asakawa town, Japan

We considered the tsunami suffering probability at Asakawa town (Fig. 1).   Historically,
Asakawa town frequently suffers from tsunamis; immediately, the loss of residents is very large.
For instance, the Showa earthquake and tsunami in 1946 caused 66 deaths in Asakawa.   While
in a coastal community of Shikoku Island, the average numbers of deaths were about ten.   The
main reason lies in the fast arrival time (10 minutes) and high tsunami wave (5-6 m).   Now, two
tsunami breakwaters are under construction at the bay mouth. South side is completed, but north
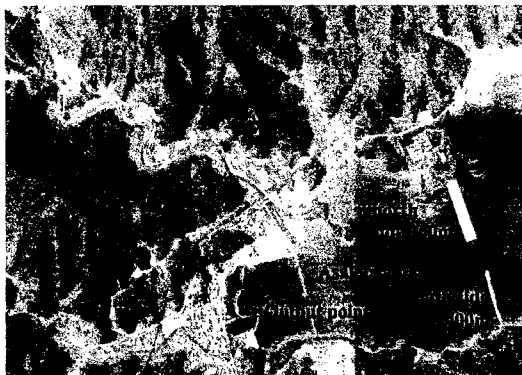side is not finished yet (Fig. 2).

Figure 2.   Asakawa bay

CALCULATION OF THE TSUNAMI SUFFERING PROBABILITY

Monte Carlo method

Figure 3 shows the flow of the Monte Carlo method for the calculation of the tsunami suffering probability. The tsunami calculation was considered random tidal height, latitude, longitude, vertical fault deformation and calculative accuracy. The iterative calculations were carried out at 5,000 times. The random data were changed on every cycle.
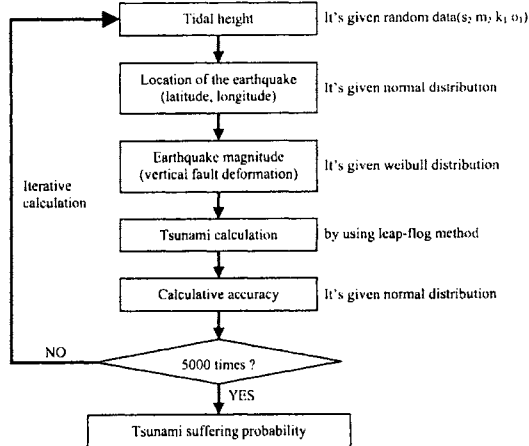

Tidal height	It's given random data(s_2 m_2 k_1 o_1)
Location of the earthquake (latitude, longitude)	It's given normal distribution
Earthquake magnitude (vertical fault deformation)	It's given weibull distribution
Tsunami calculation	by using leap-flog method
Calculative accuracy	It's given normal distribution
5000 times ?	
Tsunami suffering probability	

Iterative calculation

NO

YES

Figure 3. Flow of the Monte Carlo method

1) Tidal height
Only the astronomical tide was considered. Main four tidal waves (M_2, S_2, K_1, O_1) were used for tidal height. The random date was chosen every cycle of iterative calculation. The sea level discrepancy from normal at the Muroto-misaki cape were picked up.

2) Location (longitude and latitude)
At Nankaido, 34 historical earthquakes are recorded. The maximum magnitude is 8.4. The location of seabed displacement is distributed around Nankai trough. Figure 4 shows the distributions of longitude and latitude. The shapes both of them were nearly a normal distribution. We assumed the distributions as below Table 1.

Table 1. Distribution of the historical earthquake locations

	Distribution	Average	Standard deviation
Longitude	Normal	East 135.54	1.37
Latitude	Normal	North 33.72	0.52

292

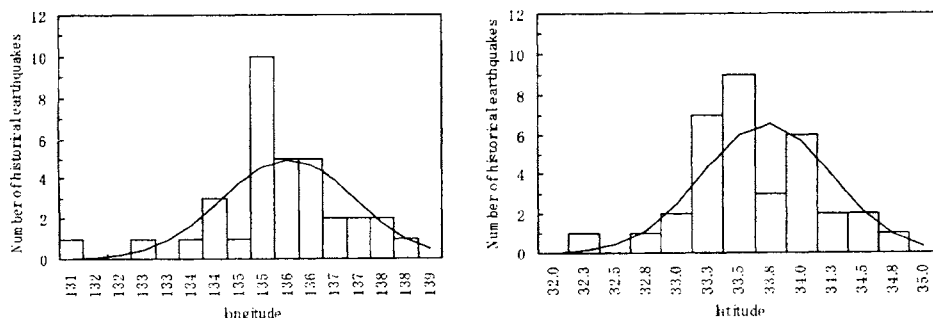Figure 4.   Distributions of historical earthquake epicenters

3) Earthquake magnitude
An extreme statistics analysis was carried out on the 34 earthquakes that occurred in the offshore Nankaido.   The earthquake magnitude fits well with a Weibull distribution (k=2.0).   As a result, we presumed the probability of the occurrence of an earthquake of M8.0 to be 100 years, and M8.4 to be 180 years.   This presumption is very close to the occurrence interval of huge tsunamis at Nankaido (Table 2).

Table 2. Historical earthquakes at Nankaido
(The earthquake magnitude is near or over 8.0)

Historical earthquake	Earthquake Magnitude	Occurrence year (BC)	Interval
Shohei	M8.4	1361	-
Meio	M8.6	1498	137
Keicho	M7.9	1605	107
Hoei	M8.4	1707	102
Ansei	M8.4	1854	147
Showa	M8.0	1946	92

We introduced various magnitudes into the tsunami calculation in the Monte Carlo simulation in the following way.   First, the fault model is used for tsunami calculation.   Second, the fault Area is fixed, and only the vertical fault deformation is changed.   Third, the vertical fault deformation corresponding to each of the randomly chosen earthquake magnitude is acquired by complementing the vertical fault deformation of Showa earthquake (M8.0) and Ansei earthquake (M8.4).

4) Calculative accuracy
Figure 5 shows the comparison of height between trace data to calculation result at around Nankaido.   It is impossible to reproduce perfectly the traces of tsunami height by calculation. We must consider that the tsunami calculation is certain to include these errors.   The calculation error of the tsunami propagation calculation is readjusted by "trace height / calculation height". Figure 6 shows them.   The ratio of trace height to calculation height becomes close to a normal distribution with a mean value of 1.04, and its standard deviation is 0.26.
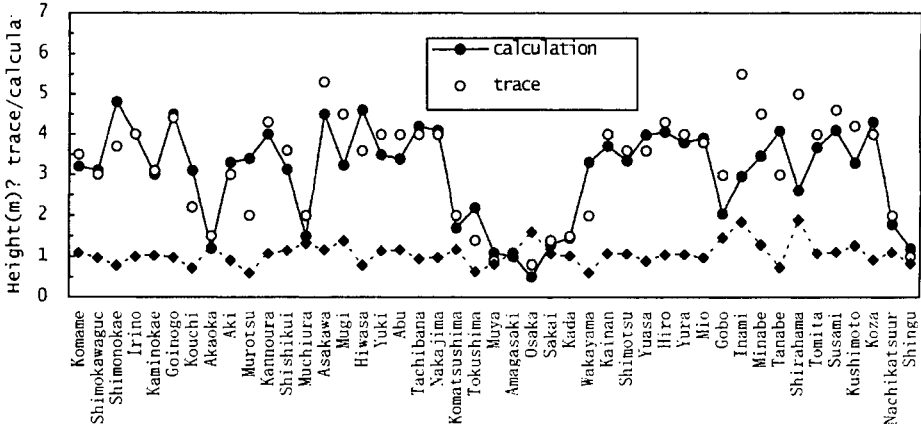
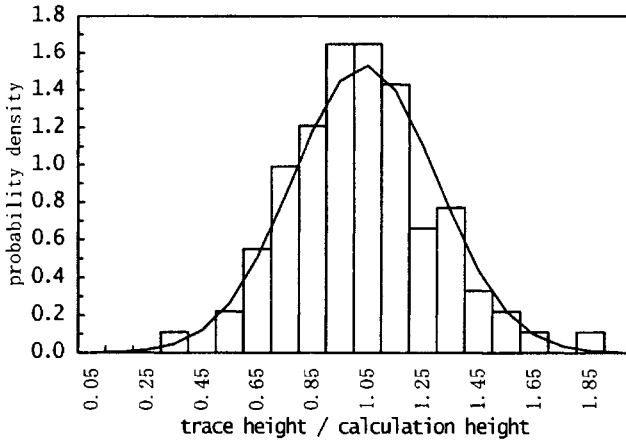Figure 5. Comparison of height between trace data to calculation result

Figure 6. Distribution of the calculative accuracy

Cases of the consideration

We will examine on the case of the tsunami breakwater under construction at Asakawa bay. The tsunami propagation calculation was carried out on the six cases below each with different opening widths (Table 3). Case-1 (width=100) is a condition within both the south and north tsunami breakwaters have been completed. Case-5 (width=500) is a present condition. Only the tsunami breakwater on the south side has been completed. Case-6 (width=860) is a non-breakwater condition.

294

Table 3. Cases of the consideration

Case	Width of bay mouth	Tsunami breakwater length at north side	Tsunami breakwater length at south side
Case 1	100 m	360 m (completed)	400 m (completed)
Case 2	200 m	260 m (under construction)	400 m (completed)
Case 3	300 m	160 m (under construction)	400 m (completed)
Case 4	400 m	60 m (under construction)	400 m (completed)
Case 5	500 m	0 m (non breakwater)	400 m (completed)
Case 6	860 m	0 m (non breakwater)	0 m (non breakwater)

Distribution of the tsunami height in the Asakawa bay

The output points of the tsunami calculation must be in front of the existing breakwater (Fig. 3). Figure 7 shows a distribution of tsunami height which is composed of 5,000 times iterative calculation. Case-1 is the narrowest width of the bay mouth. Over half of the 5,000 calculation results are under 50 cm. While in case-6 that is non-breakwater condition, a lot of tsunamis become 1.0 to 3.0 in the bay. When the earthquake magnitude is over 8.0, the tsunami height becomes more than 5.0 meters. Compared Case-1, peak of the distribution shift more high risk.
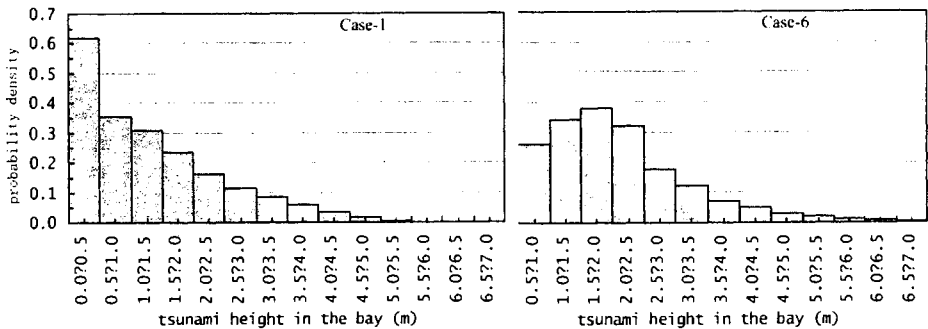

Figure 7. Distribution of tsunami height in the Asakawa bay

Tsunami suffering probability

In this study, "the tsunami suffering probability" is defined as the tsunamis it overtopping the crown height (=5.0 m) of the existing seawall at Asakawa bay divided by the times of repetition (=5000).

Figure 8 shows the tsunami suffering probability each case. At the present tsunami breakwater condition, we cannot expect the effect to decrease tsunami energy. Thus, the risk of tsunami disaster will be underestimated. At the districts where the tsunami breakwater is under construction, the government should reconsider the hazard map and evacuation plan. When the allowable tsunami suffering probability is fixed, the best length of the tsunami breakwater can be decided simply.
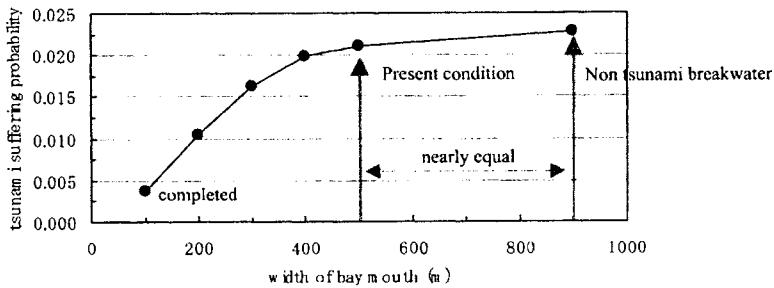
295

Figure 8. Tsunami suffering probability

CONCLUSIONS

In this study, to propose an optimum design method of tsunami breakwater using the suffering probability acquired by launching multiple is used. In order to install the probability, the Monte Carlo method was used for the prediction of tsunami height in the bay. The tsunami calculation was considered random tidal height, latitude, longitude, vertical fault deformation and calculative accuracy.

At the Nankaido, both the location of the earthquake and calculation accuracy distributes nearly normal distribution. And the magnitude fits the weibull distribution. "The tsunami suffering probability" is defined by 5,000 times iterative calculation in the Monte Carlo simulation.

At the districts where the tsunami breakwater is under construction, the risk of tsunami disaster will be underestimated. Therefore, the government should reconsider the hazard map and evacuation plan. When the allowable tsunami suffering probability is fixed, the best length of the tsunami breakwater can be decided simply.

ACKNOWLWDGEMENTS

REFERENCES

Hiraishi, T., H. Shibaki, K. Harasaki and S. Tanaka. 1999. Probabilities of Nankai-earthquake tsunamis occurrence, *Proceedings of Coastal Engineering, JSCE.* 46, pp. 366-370, in Japanese.

Kawata, Y. and N. Koike. 1994. Emergency Management and Evacuation Manual for Tsunami Disaster, *Annuals, Disas. Prev. Res. Inst. Kyoto Univ.* 38 B-2, pp. 157-211.

Manshinha, L. and. D.E. Smylie. 1971.   The Displacement Fields of inclined Faults, *Bulletin of the Seismological Society of America* 61-5, pp. 1433-1440.

Murakami, H., N. Yamamoto, S. Itoh, Y. Kozuki and H. Sato. 1996.   Study on the tsunami risk assessment for Shikoku island and Kii peninsula, *Proceedings of Coastal Engineering, JSCE.* 46, pp. 361-365, in Japanese.

Murakami, H., N. Yamamoto, S. Itoh, Y. Kozuki and H. Sato. 1997.   Tsunami risk assessment for Shikoku island and Kii peninsula, *Recent Advances in Marine Science and Technology, 96,* PACON International, pp. 55-64.

Tohiki, I., K. Oshida, T. Gakuta and H. Shibaki. 2000.   The database of tsunami wave height with the incidence in Japan and simple prediction of flooded area, *Proceedings of Coastal Engineering, JSCE.* 47, pp. 386-390, in Japanese.

EFFECT OF TIDE AND FLOOD GATES
ON TSUNAMI INUNDATION

Takuji Sugimoto, Hitoshi Murakami, Yasunori Kozuki,
Kengo Kurata and Takemi Shikata

Department of Ecosystem Engineering, University of Tokushima
Tokushima, JAPAN
sugimotot@nita.co.jp

ABSTRACT

In September 2001, the Japanese government evaluated the probability of occurrence of the next Nankaido earthquake in the Pacific Ocean to be 80% within the next 50 years. It is therefore necessary that countermeasures against this disaster should be improved as soon as possible. In this study, a tsunami numerical simulation taking into account the effect of tide and flood gates on inundation was first developed. The effect of tsunami inundation from these gates was estimated for Usa town in Kochi prefecture, Shikoku Island. The gates were investigated so as to ascertain if they would be able to be closed when a tsunami comes. It was found that tsunami inundation decreased when the gaps of the gates decreased, in Usa town. In particular, these structures, which shut out the first and second tsunami waves, can serve to delay inundation time. Therefore, it is necessary to close such gates so as to allow longer evacuation time for inhabitants as a preventative measure against tsunamis. However, it was confirmed from investigation of gate control, that some gates could not be closed because of either poor maintenance or taking too long to close. In some cases, the manager who closed the gate would not be able to seek refuge in time, for gates located far from the evacuation place for gates, which take a long time to close. To be effectively useful as a regional tsunami countermeasure, some of these gates need improvement of the closing method and evacuation routes need regular maintenance so as to be kept in good condition.

INTRODUCTION

A number of earthquakes have occurred at intervals of 100-150 years along the Nankai Trough. In the past, the coastal area of Shikoku Island in Japan has suffered great tsunami damage caused by these earthquakes.

In September 2001, the Japanese government evaluated the probability of occurrence of the next Nankai earthquake to be 80% within the following 50 years. With this in mind, it is therefore necessary that countermeasures against such a disaster be improved urgently. Shimada et al. (1999) showed the change in distribution of tsunami inundation with time, clarified the process of human damage occurrence with evacuation activities of inhabitants, and proposed detailed tsunami countermeasures. Their disaster mitigation measures software is useful for predicting areas at risk of inundation due to a tsunami.

Large-scale hardware measures, such as the construction of tsunami breakwaters and rising of embankments and seawalls, require much time and money. But with a probable Nankai earthquake tsunami looming and the Japanese economy being somewhat depressed, the above-mentioned measures are unrealistic. Thus, both cost effective and substantial measures are required. More effective measures using existing structures will reduce the cost and can be completed in a relatively short time period.

In many existing structures, tide and flood gates are the focus of our attention. In Japan, coastal areas are more often struck by typhoons than by tsunamis. So, most gates have been constructed to prevent inflow of seawater to protect against storm surges. Tide gates are located as a part of seawalls to protect traffic and to prevent inflow of seawater. Flood gates are located along rivers, and prevent seawater inflow to the river. But, Kawata (2001) pointed out existing problems with the present tide and flood gates for tsunami countermeasures as follows: 1) It takes much time to close a gate and 2) Many gates are closed manually.

In this study, the purpose is to clarify the effect of tide and flood gates related to tsunami inundation. Also, countermeasures necessary for the effective use of these gates are proposed for the case of tsunamis.

TSUNAMI NUMERICAL CALCULATION

Tsunami numerical calculation is applied to an existing method, which provides substantiation of repeatability of tsunami numerical calculation around an object area (Murakami et al., 1996(a), 1997). Usa town in Kochi prefecture was selected as the study area (Fig. 1). This town has been damaged periodically by Nankai earthquake tsunamis. The 1854 Ansei Nankai earthquake tsunami (Magnitude 8.4) was used as a case study.
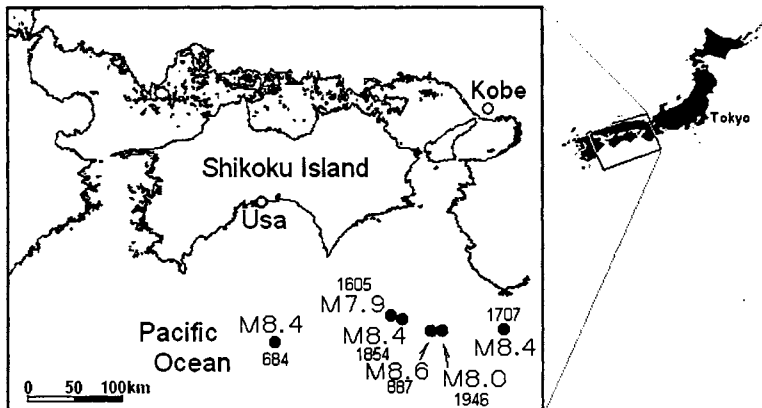

Figure 1. Location of Usa town, Kochi prefecture, Japan

This tsunami was estimated to be the highest risk tsunami for this town in previous studies (Murakami et al., 1996(b)). Even the width of seawalls and gates, which are smaller than a grid interval, are considered in the calculation.

Consideration of gate open-close situation

In the tsunami numerical calculation presented here, breakwaters, sea embankments and seawalls that are in calculation areas, are given in the boundary condition.   When water surface elevation is higher than their crest elevations, flood volume is calculated by Honma's function (1940).   If the widths of flood and tide gates are smaller than the grid interval, a traditional difference method can be used to calculate gates, walls and embankments within grid interval units, but this method cannot be used to calculate actual width.   Therefore, in this study, gate open situations, which are smaller than the grid interval, are dealt with as follows.

a) When gate is closed
When tide and flood gates are closed and when tsunami height is greater than crest elevation, flood volume (Q) is calculated by Honma's function, for breakwaters, sea embankments and seawalls that are in calculation areas.

b) When gate is open
Flood volume (Q) is calculated using formula (1) or (2) depending on the relationship between water surface elevation in front of and behind gate and crest elevation.
When water surface is below crest elevation ($H<BY$).

$$Q = \frac{BX}{\Delta S} Q_0 \tag{1}$$

When water surface is higher than crest elevation ($H>=BY$).

$$Q = \left\{ 1 - \frac{BY(\Delta S - BX)}{H \cdot \Delta S} \right\} Q_0 \tag{2}$$

where, BX represents gate width, BY is gate height, H is inundation depth, ΔS is grid interval, and Q_0 is the flow volume which is not a given boundary condition. When flood gates are open, flow volume is given by forward and backward ground levels.

EFFECT OF GATE ON TSUNAMI INUNDATION

Effect of tide gate

The effect of closed tide gates on tsunami inundation was evaluated by numerical calculation. The northern area of Usa town was focused upon, because there were many tide gates in this area.

Figure 2 shows the distribution of tsunami inundation for a 30-minute period after an earthquake. In this figure, the unfilled circles indicate the location of opened gates.   If the gates are open, inundation flows in through the gates, and spreads out into the outside area of tide embankment, which are gray areas in this figure.   On the other side of the figure, it can be seen that if all tide gates are closed, tide wall and closed gates are able to block tsunami inundation.

Figure 3 shows the relationship between water elevation and time at inland points of tide gates. The gray line shows water elevation when the tide gate is open, and the black line shows it when the gates are closed.   When the 1st wave arrives, a closed tide gate reduces inundation

significantly. But, 76 minutes after an earthquake when a tsunami flows over the top of the gate, the inundated seawater does not drain away.
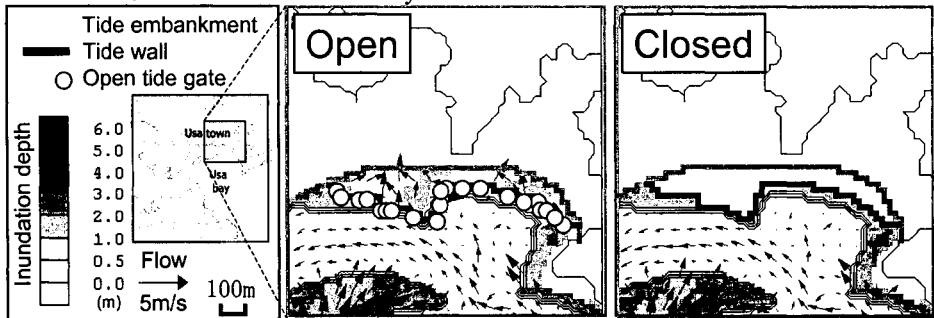

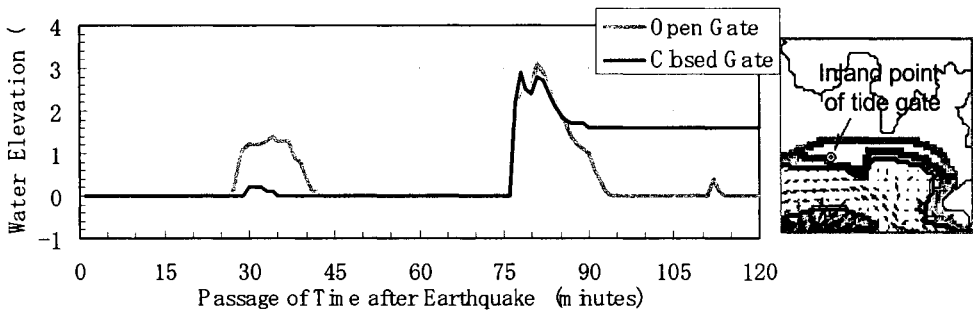Figure 2.   Distribution of tsunami inundation for 30 minutes following an earthquake

Figure 3.   Relationship between water elevation and time

Effect of flood gate

The effect of closed flood gates on tsunami inundation was evaluated from numerical calculations.   Figure 4 shows the distribution of tsunami inundation for 87 minutes after an earthquake. 87 minutes after an earthquake is the time that the third wave arrives at Usa.   If the floodgate is open, tsunami runs up along the river, and the inundated area spreads out over land. On the other hand, if the floodgate is closed, the gate stops the inflow along the river and protects from inundation on land.
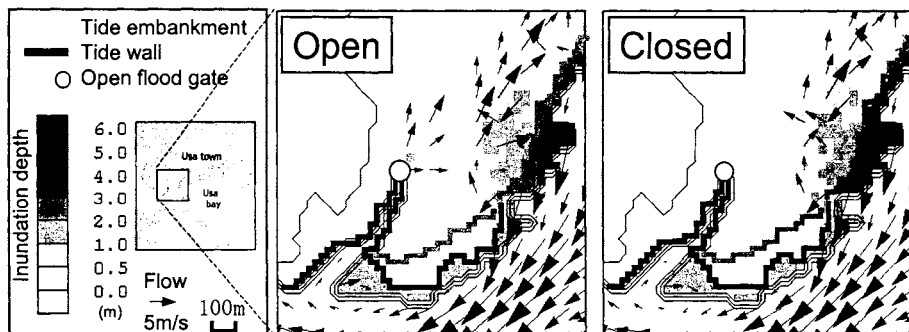
Figure 4.   Distribution of tsunami inundation for 87 minutes following an earthquake

Figure 5 shows water elevation with time at an inland point of a floodgate.   The gray line shows the water elevation when the floodgate is open, and the black line shows it when the gate is closed.   When the floodgate is open, a tsunami runs up to the river since the 1st wave came. On the other hand, when the floodgate is closed, the gate stops inundation until the third wave came. But, inflowed water has not drained away completely and remains pooled inside of gates and walls.
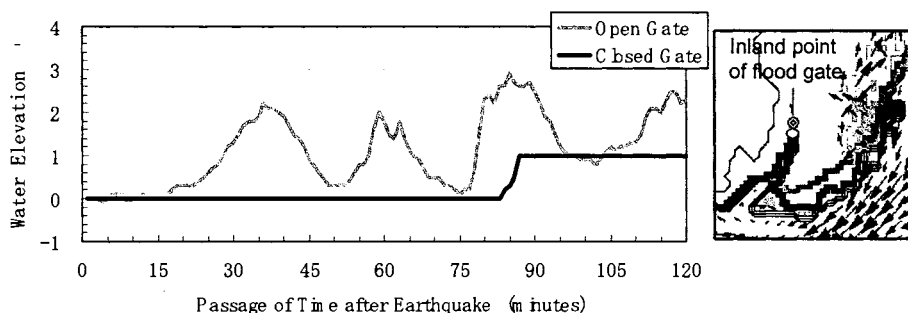
Figure 5.   Relationship between water elevation and time

Here, the results of tsunami numerical calculations are integrated.   Most tide and flood gates are always open.   As a result of closing these gates, tsunami run-up and inundation are delayed and reduced in Usa town.   In other words, these gates are effective against blocking tsunamis. They extend inhabitants evacuation time and decrease damage due to inundation.

USE OF GATES AGAINST TSUNAMI DISASTER

In this section, the probability of whether gates can be closed in the event of a Nankai tsunami coming is examined.

Condition of gate management

To begin with, the condition of gate management was researched. Figure 6 shows the results from this. According to these results, 14% of gates cannot be closed due to corrosion and other factors. 25% of gates had some troubles to close. For example, they are too heavy to close, cannot be closed quickly, are hindered by deposits of sand, and so on. Thus, in Usa town, 40% of gates may not be able to be closed in the event of a tsunami approaching.
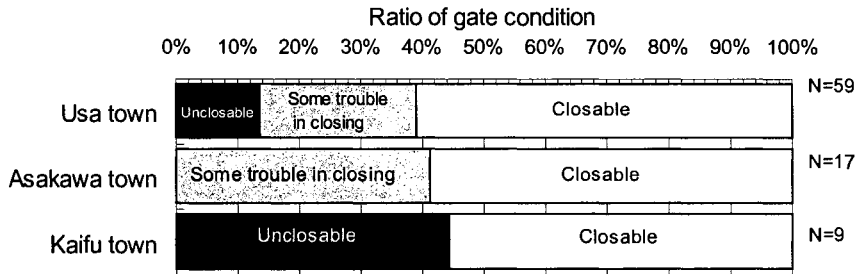
Ratio of gate condition

	0%	10%	20%	30%	40%	50%	60%	70%	80%	90%	100%	
Usa town	Unclosable	Some trouble in closing			Closable							N=59
Asakawa town	Some trouble in closing				Closable							N=17
Kaifu town	Unclosable					Closable						N=9

Figure 6. Condition of gate management

In addition, in some other regions, the condition of gate management was researched. It was found that about 40% of gates have some troubles to be closed, as in Usa town. Therefore, present gate management is inadequate to close them when a tsunami comes, and it must be stressed that present gate condition and gate management must be improved.

Judgment of gate management from gate operator's schedule

It was ascertained whether or not gate operators could close a gate and evacuate to a safe place before a tsunami came. The assumed conditions in this judgment are explained as follows.

After an earthquake occurs, earthquake motion continues for two minutes. A gate operator comes to the gate within five minutes, and closes the gate. The time required to close a gate depends on the gate type. The relationship between gate type and time to close gate is shown in Table 1. A gate operator's refuge time from the gate to an evacuation place is given as the distance divided by a walking speed of 1 meter per second.

304

Table 1. Relationship between gate type and time to close

	Gate type	Basis of time to close gate	Time to close
Flood gate	Flap type	No time required to close.	0.0 min
	Other types	Management ledger & interview (lifting height) / (closing gate speed)	0.3 m/min*
Tide gate	Sliding door type	Time to close in disaster prevention training	2.0 min
	Hinged door type	Time to close in disaster prevention training	1.5 min
	Rotating handle type	Interview	3.0 min

* ; In case of emergency, 1.0m/min

The judgment is based on whether or not these tasks can be completed before tsunami arrival. When a gate operator cannot finish these tasks before tsunami arrival, it is estimated not only that the gate operator would suffer from injury or death, but also an unclosed gate would increase tsunami damage.

Tide gate
At first, Figure 7 shows the time schedule of a tide gate operator. Tsunami arrival time was calculated to be 20 minutes after earthquake occurrence. The solid gray area in Figure 7 shows the time after tsunami arrival. All tide gates in Usa can be closed before a tsunami comes. But some of them cannot be closed leaving a sufficient safety margin before a tsunami comes. So, some additional measures are needed (i.e., to upgrade the evacuation routes, etc.).
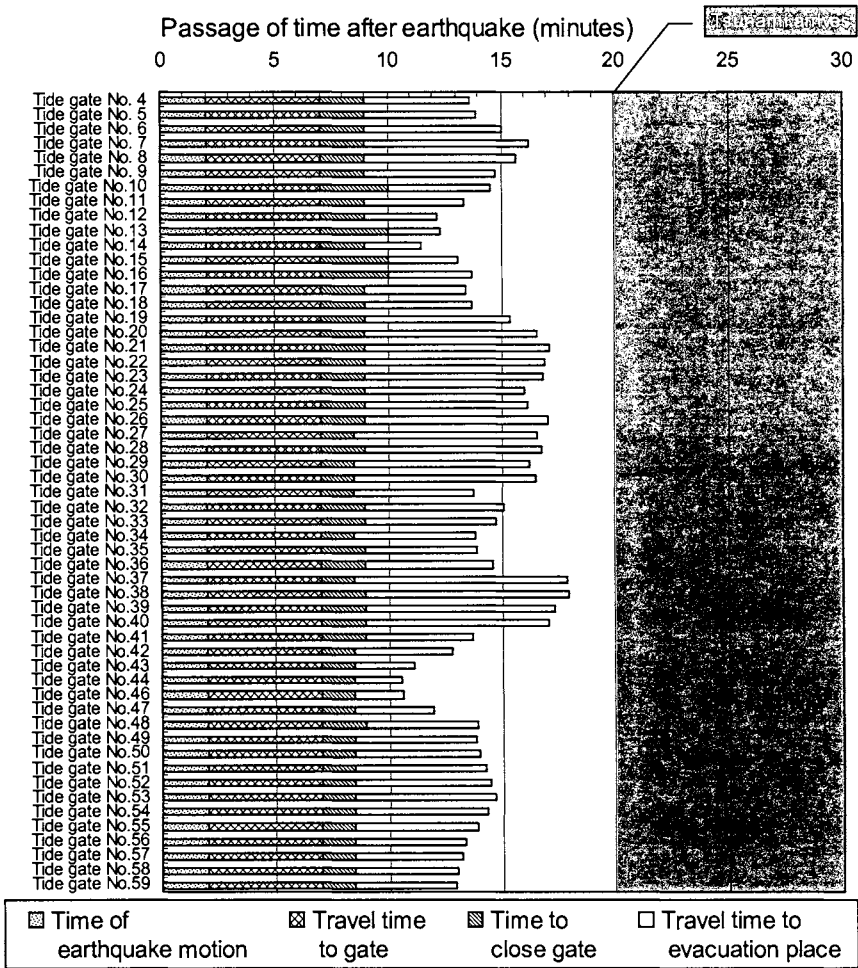
Figure 7.   Time schedule of tide gate operators

Flood gate
Next, the time schedule of a floodgate operator is shown.   Figure 8 shows the total time needed for closing gate No. 2 and No. 3 exceeds tsunami arrival time.   This means that if a gate operator closes the gate, he will be at high risk of injury or death due to the tsunami.   Therefore, these flood gates require some countermeasures to rectify this situation.
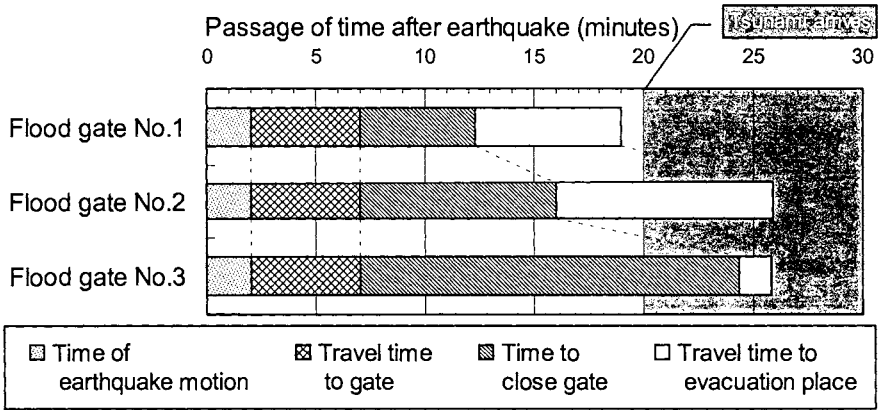
Figure 8.   Time schedule of flood gate operators

In the next section, the effect of both attaching an emergency closing system and remote control system are estimated.

Attaching an emergency downward closing system
In case of attaching an emergency downward closing system, gate closing speed increases from 0.3 m/min to 1.0 m/min.   As a result, in Figure 9, the total time to close gate No. 3 is reduced and, as a result, the operator can close it before a tsunami arrives.   But, the total time for No. 1 and No. 2 gates does not decrease as much as that for No. 3 gate.
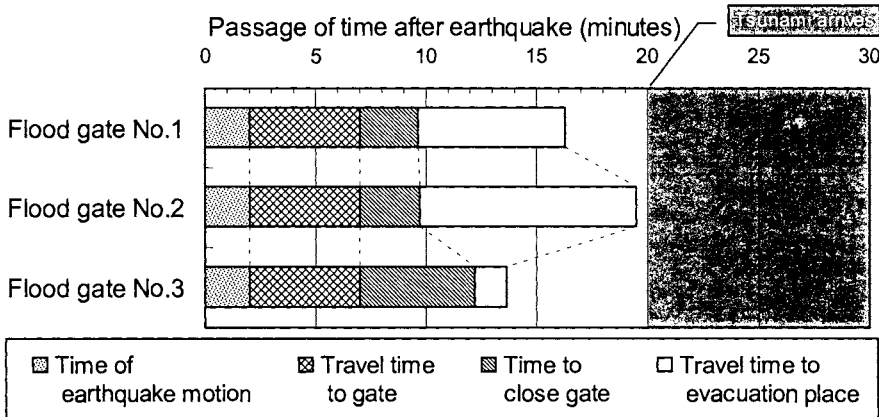
Figure 9.   Time schedule of flood gate operators with an emergency downward closing system attached

Installation of a remote control system
In case of introducing a remote control system, gate operators do not need to go to a gate after an earthquake.   As a result, gate closing time for gates No. 1 and No. 2 was reduced, and it made closing the gate both safe and fast.   But, in a case of power failure or disconnection due to an

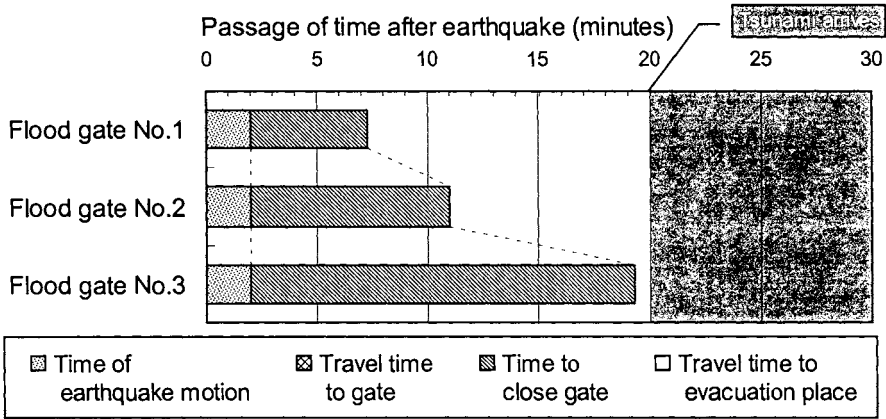earthquake, there is some risk of system malfunction due to its reliance on an external power source.

Figure 10.   Time schedule of flood gate operators after installation of remote control system

CONCLUSION

1. The influence of tide and flood gates on tsunami inundation can be shown when the effect of such gates is taken into account.
2. Closing gates is effective for decreasing tsunami inundation and delaying the inundation onset.
3. Present day gate management is inadequate to close gates when a tsunami comes, and it is stressed that improvement of gate management is necessary.
4. The above considerations provide effective countermeasures to decrease tsunami damage.

ACKNOWLEDGMENT

REFERENCES

Honma, H. 1940. Coefficient of flow volume on low overflow weir, *Japan Society of Civil Engineers Journal*, Vol. 26-6, 635-645. (In Japanese)

Kawata, Y. 2001. New Concept for Storm Surge and Tsunami Disaster Reduction Based on the Lessons for Flood Disaster, *Proceeding of Coastal Engineering*, Vol. 48, Japan Society of Civil Engineers, 1361-1365. (In Japanese)

Murakami, H., Itoh S. and Yamamoto, N. 1996(a). Consideration on tsunami simulation using proposed fault models in Shikoku Island, *Bulletin of Faculty of Engineering, The University of Tokushima*, No. 41, 39-53. (In Japanese)

Murakami, H., Itoh S., Yamamoto, N. and Sato, H. 1996(b). Study on the tsunami risk assessment for Shikoku Island and Kii peninsula, *Proceeding of Coastal Engineering*, Vol.43, Japan Society of Civil Engineers, 316-320. (In Japanese)

Murakami, H., Kozuki, Y., Yamamoto, N. and Gotoda, T. 1997. Fundamental study of tsunami numerical calculation in Usa, Kochi prefecture, *Technical Research Presentation summary*, Vol.3, Shikoku -based affiliate Japan Society of Civil Engineers, 166-167. (In Japanese)

Regional Data for Disaster Prevention, Regional Evacuation Edition. 1987. *Institute for Fire Safety & Disaster Preparedness*, 91-96. (In Japanese)

Shimada, T., Murakami, H., Kozuki, Y., Sugimoto, T. and Nishikawa, K. 1999.   Estimation of loss of lives due to tsunami disasters, *Proceeding of Coastal Engineering*, Vol. 46, Japan Society of Civil Engineers, 361-365. (In Japanese)

TSUNAMI PROPAGATION CHARACTERISTICS IN CHANNELS LEADING INTO THE SETO INLAND SEA

Kazuo Yoshida[1], Tomio Shimada[2], Hitoshi Murakami[3],
Yasunori Kozuki[3] and Hiroshi Ichishima[3]

[1]Coastal Engineering Division, River and Coastal Engineering Department, NEWJEC Inc.
Osaka, JAPAN
yoshidakz@osaka.newjec.co.jp

[2]Department of Construction Systems Engineering, Anan National College of Technology
Tokushima, JAPAN

[3]Department of Ecosystem Engineering, University of Tokushima
Tokushima, JAPAN

ABSTRACT

It is predicted that, in the near future, a big earthquake and subsequent tsunami may occur along the Nankai Trough off the coast of Shikoku Island in the south west of Japan. In this study, characteristics of tsunami propagation in the Kii and Bungo channels leading into the Seto Inland Sea are clarified in the first stage of investigating tsunami characteristics in the Seto Inland Sea. Consequently, it was shown that the propagation characteristics of a tsunami propagating into the Kii and Bungo channels is influenced by the relationship between locations of submarine canyons, a continental shelf and wave source, that both Kii and Bungo channels have a specific resonant period of 50 minutes, and 22-25 minutes, and that the tsunami heights in the Kii channel are easy to amplify irrespective of the period of incident waves.

INTRODUCTION

Shikoku Island is located in the southeast part of Japan and offshore of Shikoku Island to the Pacific Ocean side is the Nankai Trough. At the Nankai Trough, a huge earthquake and an accompanying tsunami is expected in the near future. This earthquake tsunami is called the Nankai earthquake tsunami.

The Japanese government has been seriously carrying out research and exploring countermeasures since 2001 for such a Nankai earthquake tsunami. The reasons for the Japanese government's moves are as follows. First is the fact that historically, Nankai earthquakes have occurred at intervals of 100 to 150 years. Second, is that the two most recent quakes occurred in 1944 and 1946 and since then fifty years has already passed. From those facts, it has been speculated that in the first half of this century, a huge earthquake and tsunami will occur. In addition, in October of 2001, the Japanese government estimated the probability of the Nankai earthquake occurring in the next thirty years to be 40%, in the next fifty years to be 80 percent. Also, stated that the magnitude of the earthquake will be around 8.4. From these

movements, we must modify the countermeasures for the Nankai earthquake tsunami along the pacific coast of Japan.

Many researchers have investigated Nankai earthquake tsunamis. However, almost all the research has been on the pacific coast. Figure 1 shows the focus position of Nankai earthquakes, which occurred in the past and a map around Shikoku Island. A calm inland sea called the 'Setonaikai' exists between the Mainland and Shikoku Island. Although damage by tsunamis in the Seto inland sea have been reported in past research, the 1946 Showa Nankai earthquake tsunami did not cause much damage. Thus, the characteristics of a tsunami in Seto inland sea have not been researched in much detail. In order for a tsunami to advance into the Seto inland sea, it will have to go through the Kii and Bungo channels. Moreover, it will have to go through narrow straits called 'Kitan, Naruto and Hyoyo straits'. Therefore, interest in tsunamis is very low in the coastal region of the Seto inland sea. Although it is hard for a tsunami to advance into the Seto inland sea, the water particle velocity and it's traveling distance will be large. As a result, there may be serious damage to cultivation rafts and berthing facilities for small ships.
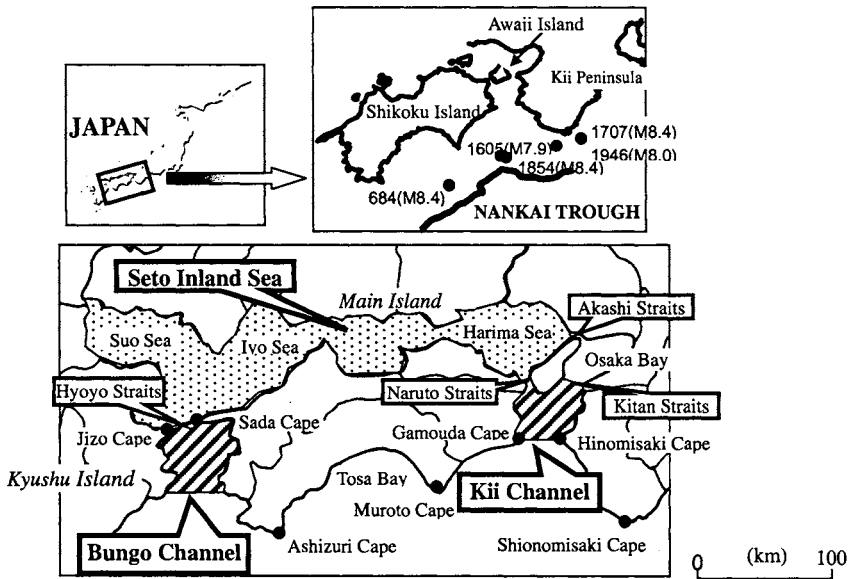

Figure 1. The focus position of the Nankai earthquakes, which occurred in the past and a map around Shikoku Island

With, the above in mind, the main purpose of this study is to clarify the propagation characteristics of tsunamis, and the degree of risk of tsunamis in the Seto inland sea coast. For the first stage of this study, we carried out research on the tsunami's propagation characteristics in the Kii and Bungo channels located at the entrance of the Seto inland sea and the period response characteristics in both channels.

PROPAGATION CHARACTERISTICS OF A TSUNAMI IN THE KII AND BUNGO CHANNELS

Tsunami numerical simulation method

First, we carried out research on the propagation characteristics of tsunamis in the Kii and Bungo channels. For the numerical simulation of a tsunami, we analyze the wave rays by the wave front method and wave ray method from the tsunami source area. In addition, we calculate the space distribution of concentration and concentration emission of a tsunami. There's no guarantee that the next Nankai earthquake tsunami's source area will be the same as the source area of previous ones. In addition, characteristics of the tsunami will change with the scale of the earthquake, location of the fault plane and the tsunami source area. As shown in Figure 2, referring to the focus positions of the past Nankai earthquakes, we placed eight focus positions and the accompanying tsunami sources along the Nankai Trough and on each focus position tracked down the propagation characteristics of the tsunami into the two channels. Here, we looked at the Ansei Nankai earthquake tsunami, which occurred in 1854 and was the largest earthquake of the Nankai earthquakes. As the tsunami source area model for the 1854 Ansei Nankai earthquake tsunami, referring to past research, we adopted an ellipse of 126km in major axis and 70km in minor axis. No.⑤ is the case of the 1854 Ansei Nankai earthquake tsunami.
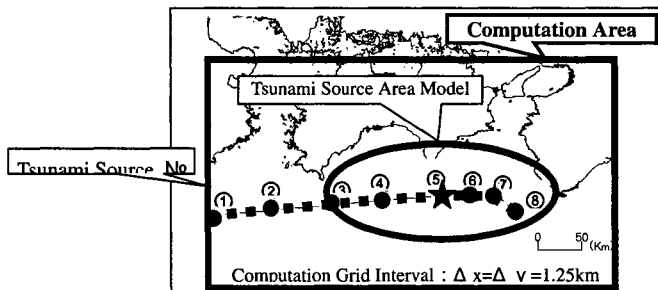

Figure 2. Location of the eight-tsunami source area models

Propagation characteristics of the tsunami of the 1854 Ansei Nankai earthquake tsunami scale

Figure 3 shows the distribution of wave rays when moving the tsunami source area east from the 1854 Ansei Nankai earthquake tsunami source area. Wave rays, which go to the Kii channel, are divided into the coast in Muroto cape to Gamouda cape, and the coast in Shionomisaki cape to Hinomisaki cape. We can see that for this reason the energy of a tsunami going into the Kii channel disperses and spreads. In the case of the Bungo channel, the western tip of the tsunami source area does not reach the channel. Therefore, the wave rays are refracted and concentrated along the coast from Ashizuri cape to Oki Island. From this, we can see that the energy of the tsunami doesn't go into the Bungo channel easily. This is thought to be due to the effect of the continental shelf which exists offshore of Ashizuri cape. However, when the wave rays are looked at carefully, it reaches the coasts inside of the channels, such as Yura and Yuasa of Wakayama prefecture, which are located north of Hinomisaki cape, and Shukumo in Kochi

313

prefecture. As can be seen, it can be explained why these areas were damaged by the 1854 Ansei Nankai earthquake tsunami from this method, too.

Propagation characteristics of the tsunami in the Kii channel

The next research is a case where the tsunami occurred east of where the 1854 Ansei Nankai earthquake tsunami occurred. Here we focus on No.⑦ (Fig. 3).   In this case, since the tsunami source becomes closer to the inlet of the Kii channel than No.⑤, the wave rays reach the Kitan straits located at the inner part of the Kii channel.   It is thought that the difference between No. ⑤ and No. ⑦ is dependant on the influence of the tsunami source area and the sea bottom topography of the inlet of the Kii channel.
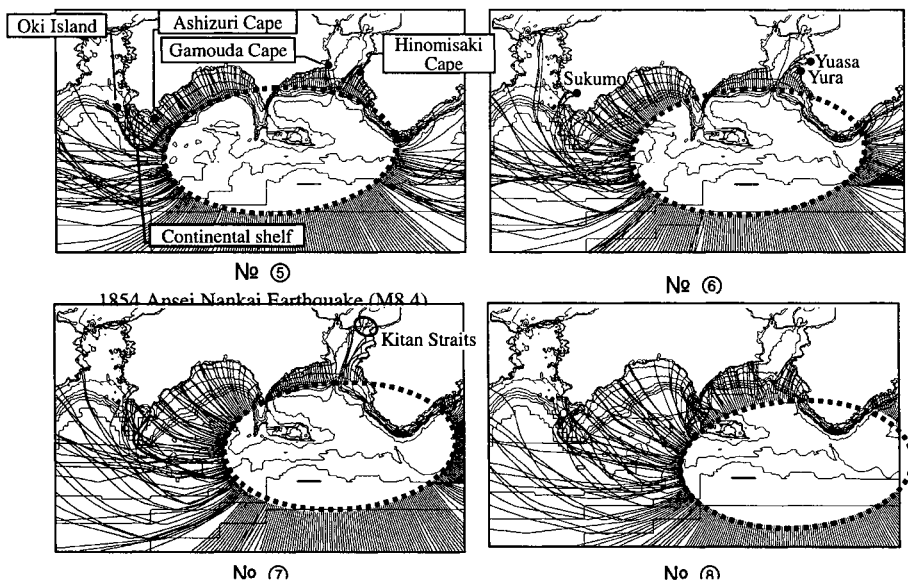
Figure 3. Spatial distributions of the wave rays (No.⑤-No.⑧)
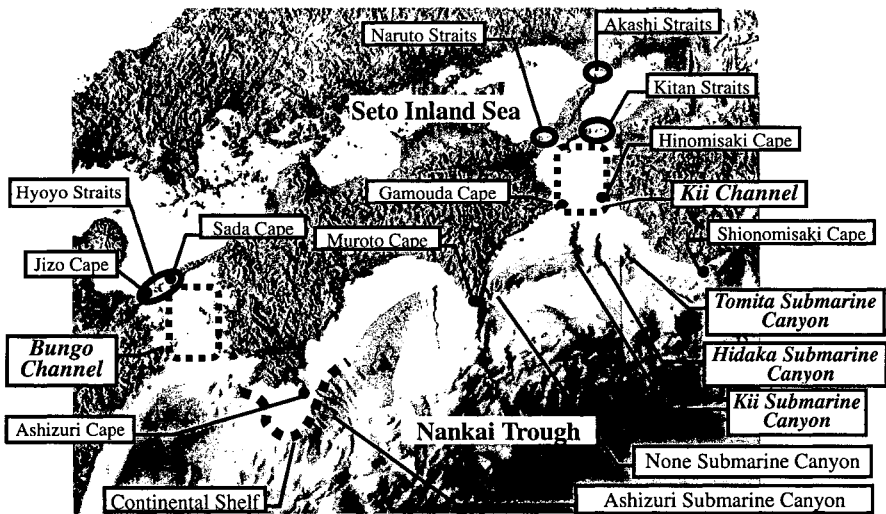
Figure 4. Sea bottom topography around Shikoku Island

Figure 4 shows the sea bottom topography around Shikoku Island. At the inlet of the Kii channel, there are three V-shaped submarine canyons. They are called, from west to east, Kii, Hidaka and Tomita. Moreover, these three submarine canyons are thought to affect the propagation of tsunamis into the Kii channel.

In order to verify the influence of submarine canyons, we studied the wave rays of tsunami supposing eight tsunami sources, which are changed, by the position related between three submarine canyons and the tsunami source (Fig. 5). In the cases of lines ③ to ⑧ of which the tsunami sources are located to the south of the three submarine canyons, the wave rays will be bent towards the coasts south of Gamouda and Hinomisaki capes and therefore will not enter the Kii channel. On the other hand, in the cases of lines ① and ② of which the tsunami source is located to the north of the three submarine canyons, the wave rays enter the Kii channel. This shows the propagation characteristics of tsunamis on the coastal areas of the Kii channel will be affected greatly by whether the tsunami source is located to the north of the three submarine canyons or not.
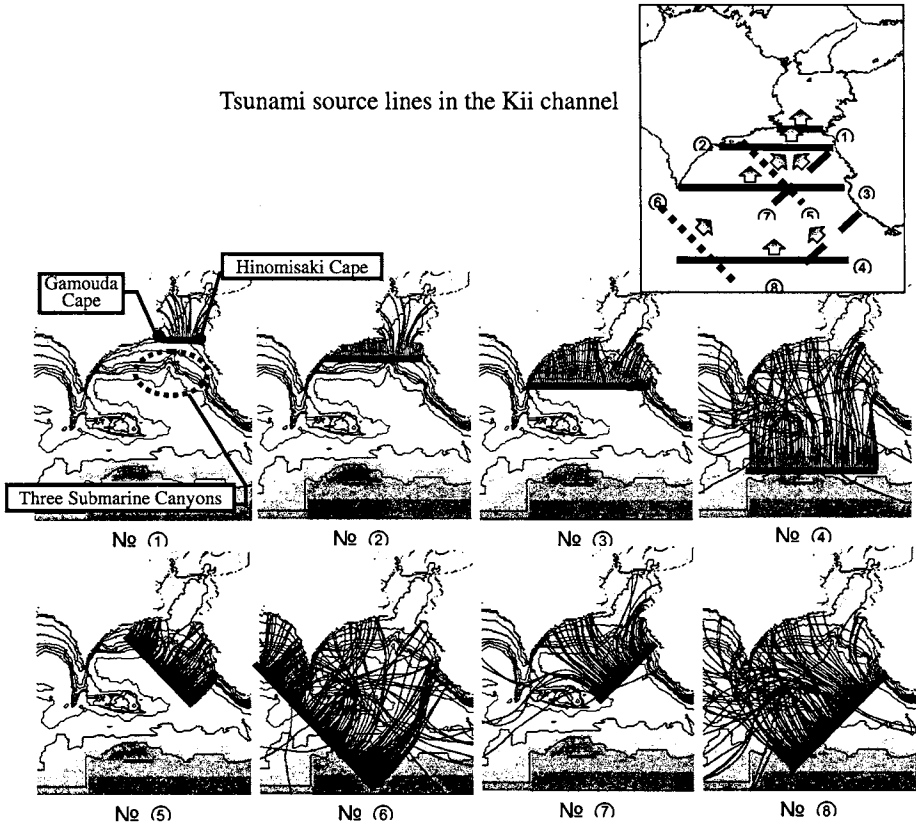
315

Figure 5. Wave propagation characteristics from tsunami sources in the Kii channel

Propagation characteristics of a tsunami in the Bungo channel

Our next research focused on the case in which a tsunami occurred on the southern side of where the 1854 Ansei Nankai earthquake occurred (Fig. 6). Here we focus on the No.②. In this case, the wave rays enter the Bungo channel easily and reach the Sada cape peninsula located in the inner part of the Bungo channel. This is because, unlike the Kii channel, the sea bottom topography doesn't change drastically and thus the tsunami propagates into the inner parts of the Bungo channel without being strongly refracted.
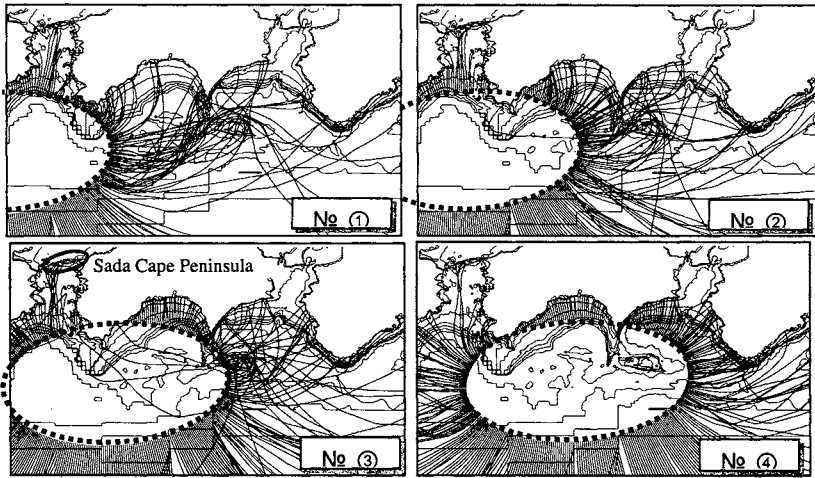
Figure 6. Spatial distributions of the wave rays（No.①-No.④）

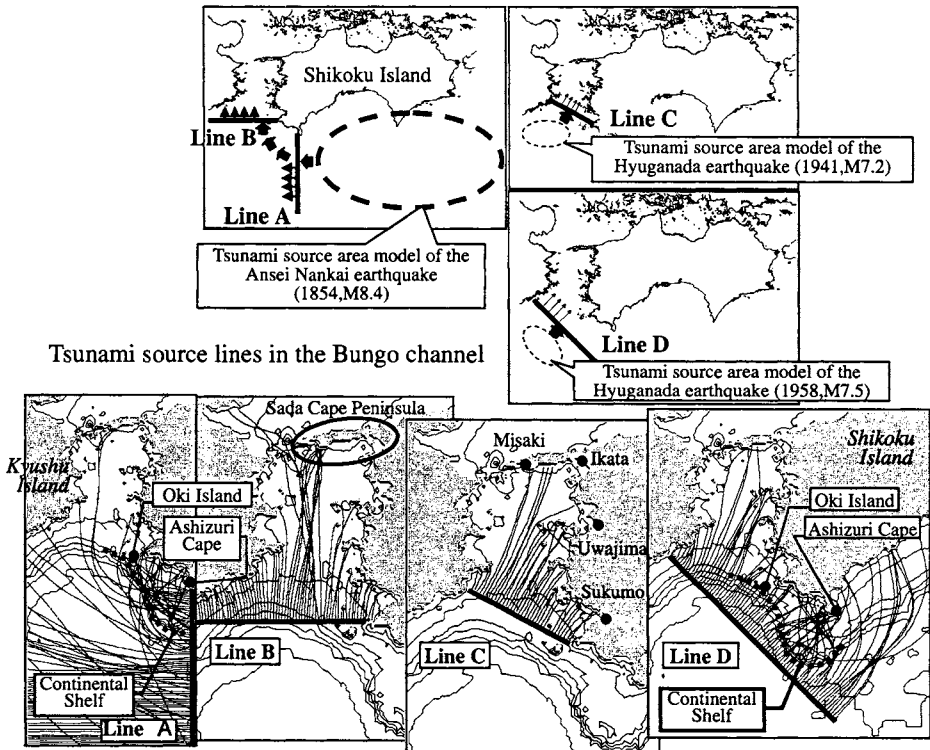Tsunami source lines in the Bungo channel

Figure 7. Wave propagation characteristics from tsunami sources in the Bungo channel

Just like in the case of the Kii channel, we installed four tsunami sources near the inlet of the Bungo channel, in order to understand the relationship between the location of the tsunami source and sea bottom topography (Fig. 7). In this case, as the model for the tsunami source, we installed the source of the Hyuganada earthquake tsunamis, which occurred in 1941 and 1958 as well as the Nankai earthquakes.

In the case of line A (Fig. 7) where a tsunami goes west at first, we can see that the wave rays will bend towards the coast from Ashizuri cape to Oki Island influenced, by the continental shelf which extends from Ashizuri cape to Oki Island, and that it is difficult for it to enter the Bungo channel. In the case of line B in which tsunamis go north, tsunamis go straight on toward the Sada cape peninsula, therefore very little will reach the west coast of Shikoku island and the east coast of Kyushu island. Also, in the case of line C and D in which the tsunami will propagate north east like the 1941 and 1958 Hyuganada earthquake tsunami, the tsunami will propagate north east, straight to the west coast of Shikoku island and will propagate very little to the east coast of Kyushu island. We think that this is due to the drastic difference in the sea bottom topography between the Bungo and Kii channels. It should be noted that the wave rays did not reach the west coast of Shikoku Island or the east coast of Kyushu Island in the inner parts of the Bungo channel because the numerical simulation was stopped when the wave rays reached the many islands along the coast. In reality, a tsunami with a long wavelength will pass easily through the small islands and peninsulas and propagate deeper into the channel. This is the reason why there are records of damages by tsunamis in such places as Uwajima, Ikata and Misaki of Ehime Prefecture and Sukumo of Kochi Prefecture.

RESPONSE CHARACTERISTICS OF TSUNAMIS IN THE KII AND BUNGO CHANNELS

Method of the tsunami numerical simulation

Next, research was done on how a tsunami, which propagated into both channels changes in a channel. A tsunami that propagates into channels, it is deformed through refraction, wave shoaling and reflection. Also, through the relationship with the natural period of the bay or the sea area, resonance or decay will occur, sometimes causing huge tsunamis at localized areas. Therefore, we carried out research on the period response characteristics of a tsunami in both channels. First, the tsunami profiles at the points shown in Figure 8 were acquired by numerical simulation. Then we analyzed the spectrum of the acquired tsunami profile and acquired the amplification rate (①/②), where ① is the spectrum at each point and ② is the spectrum at the tsunami source. In addition, from this we examined the response characteristics of each periodic wave. The numerical simulation of the tsunami was done by analyzing nonlinear long waves theory equation using the Leap-Frog difference method, with complete reflection at the land area. The calculation-grating interval was 600 m, calculation time was 6 hours and the calculation time interval was 1 second. The wave profiles of the tsunamis that we used are represented as sine waves of 2 m in wave height and 1 m in wave amplitude. The range of wave period is from 10 to 60 minutes with a 5-minute interval.

Response characteristics of a tsunami in the Kii channel

Figure 9 shows the distribution of the amplification rate of periodic waves in the Kii channel. From this figure, it can be seen that in K2, K4, K5, the peak of amplification appears at the time of 25 and 50 minutes, and that these are the natural period of the Kii channel. In K2, the rate of amplification for 25 minutes becomes larger than the rate of amplification for 50 minutes. In the Naruto straits where it is located in the inner part of a bay, and width is narrower than the Kitan straits, the rate of amplification for 50 minutes becomes larger than the rate of amplification for 25 minutes. We have done spectral analysis on the observation record of Kamchatka earthquake tsunami observed at K8: Nasa bay in 1977 and found that the resonant period at Nasa bay is around 21 and 11 minutes. This verifies the tendency that outside of the K2: inlet of the channel, periodic waves of 20-25 minutes is amplified.
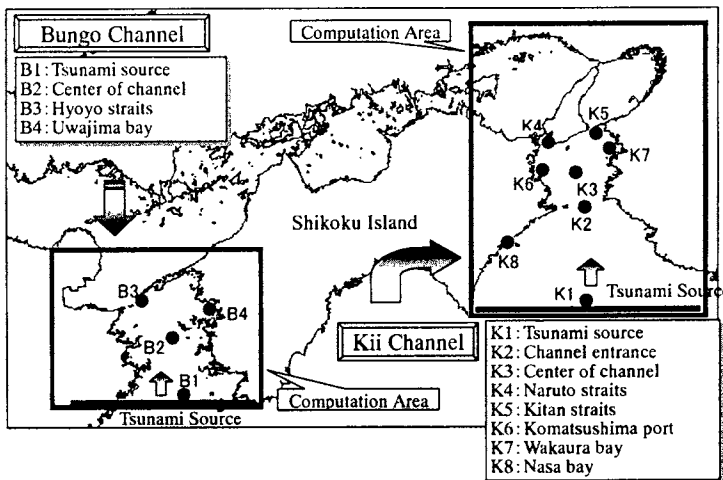

Figure 8. Computation area and output point positions of a tsunami profile

In Figure 9, in order to examine the response characteristics of the tsunami at coastal areas of the Kii channel, we showed the amplification rates of each periodic wave at K6 and K7. The amplification characteristics of K6 and K7 are similar to that of the Naruto and Kitan straits. But the amplification rate of periodic waves for 10 to 25 minutes is about twice as large as that of the Naruto and Kitan straits. Here, we have analyzed the spectra of the secondary undulation of tides at Komatsushima port in1979 and found that the natural period of Komatsushima port is about 14 minutes. When the results are compared, it is clear see that resonance occurs at this period. Moreover, a larger resonance occurs at period of 50 minutes, which is the natural period of the Kii channel, and the amplification rate is larger. From this we found that even in each of the bays along the coast of the Kii channel, the characteristic that the amplification rate of periodic waves of 25 and 50 minutes are large does not change. In addition, the amplification rate is larger at the natural period of the Kii channel, 50 minutes, than the natural period of the bay. This means that the resonance of the whole Kii channel contributes more to the amplification of the tsunami height than the natural period of the bays. It was found that the

319

amplification characteristics in the Kii channel and outside of the channel is different and that while outside of the channel the natural period of 25 minutes is predominant, inside of the channel the natural period of the Kii channel, 50 minutes, is predominant, even though amplification is also seen at 25 minutes, which is the natural period of the bays, and also the natural period of the Kii channel. In addition, here it should be emphasized that when a tsunami propagates into the Kii channel the amplification rate is larger than one, even at periods other than resonance periods.   This means that if a tsunami propagates into the Kii channel it will inevitably amplify and the tsunami height will become higher as a result.
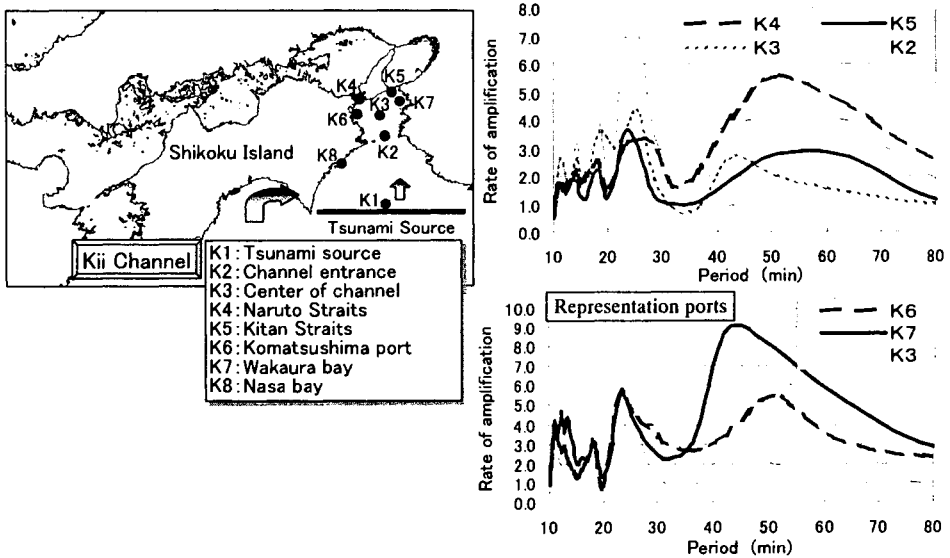
Figure 9. Response characteristics of each periodic wave in the Kii channel

Response characteristics of tsunamis in the Bungo channel

Figure 10 shows the distribution of the amplification rate of each periodic wave in the Bungo channel and in this figure, in order to see the affection of the shape of the bay, we picked out B4 as an example and showed the variance of the amplification rate.   When we look at B3 located at the deep inner part of the channel, it can be seen that even though the amplification rates at 25 and 50 minutes are at the extreme value, it is only as large as the incident wave, and that other periodic waves have decreased.   However, since in B4, which is located at the deep inner part of the channel, amplification rates at 50 and 22 minutes are at the extreme values, it appears that this is the natural period of the Bungo channel.
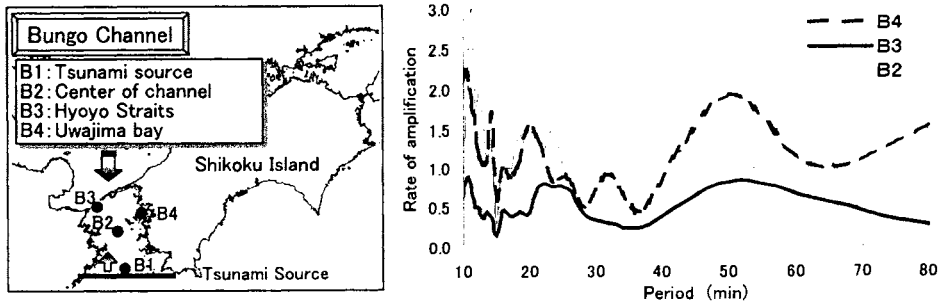
320

Figure 10. Response characteristics of each periodic wave in the Bungo channel

These results were examined and it was concluded that the Hyoyo straits have a wider opening width compared to the Kitan and Naruto straits and thus the energy of a tsunami may propagate more easily to the Seto inland sea. There may be an affection of this fact. In addition, if we obtain the natural period of Uwajima bay using the Merian wave period, the results are 55 and 19 minutes respectively. This period is almost the same as the natural period of the Bungo channel seen in the figure. However, related to this point, we feel that it is necessary to analyze it in more detail oscillation mode and we intend to carry with such research in the future.

CONCLUSION

The results from this research are summarized as follows. First, the Kii, Hidaka and Tomita submarine canyons affect tsunami propagation when a tsunami enters the Kii channel, and if the tsunami source is located to the north of the submarine canyons, the wave rays of tsunamis more easily propagate into the Kii channel. Secondly, in the Bungo channel, the wave rays of a tsunami more easily propagate into the Bungo channel if the center of the tsunami source is located to the west of Ashizuri cape or a tsunami occurs in the same tsunami source as the Hyuganada earthquake tsunami. Thirdly, tsunami heights in the Kii channel are easily amplified irrespective of the period of incident waves and the Kii channel has resonant periods of 25 and 50 minutes. Fourthly, tsunami heights along the coast of the Kii channel are strongly influenced by the natural period of 50 minutes of the Kii channel rather than the natural period of the bay. Fifthly, in the Bungo channel, tsunami heights are not easily amplified for all periodic waves, but resonate by the specific periodic waves for 22 and 50 minutes.

REFFERENCES

Murakami, H. and H. Takatani. 1977. "Harbor oscillation characteristic of Nasa bay", *Proc. Annual Conference, JSCE*, Vol. 32, pp.63-64. (In Japanese)

Murakami, H. and T. Shimada. 1979. "Study on the characteristic of the secondary undulation of tides based on field data and survey", *Proc. Coastal Eng., JSCE*, Vol. 26, pp. 129-133. (In Japanese)

Murakami, H., Y. Ito, N. Yamamoto and H. Sato. 1995. "Study on the tsunami risk in the coast of Shikoku island", *Proc. Coastal Eng., JSCE*, Vol. 42, pp. 361-365. (In Japanese)

Murakami, H., T. Shimada, Y. Ito, N. Yamamoto and J. Ishizuka. 1996a. "Review of the height of historical tsunami (1605 Keityo, 1707 Houei, 1854 Ansei) in Shikoku island", *J. JSNDS,* 15-1, pp. 39-52. (In Japanese)

Murakami, H., Y. Kozuki, K. Kurata, T. Sugimoto and K. Yoshida. 2001. "Propagation characteristics of the 1854 Ansei Nankai earthquake tsunami in the Kii and Bungo channels", *Historical Earthquake*, Vol.17, pp.110-116. (In Japanese)

Shimada, T., Y. Mori and T. Sakai. 1984. "Development of the numerical analysis model of deformation of tsunamis in Osaka Bay", *Proc. Annual Conference, JSCE*, Vol. 38, pp. 351-352. (In Japanese)

ARMOR STABILITY OF RUBBLE MOUND FOUNDATION FOR HIGH MOUND COMPOSITE SEAWALL

Masaya Mori[1], Yasuji Yamamoto[1], Nobutoshi Umezawa[1] and Katsutoshi Kimura[2]

[1]Civil Engineering Research Institute of Hokkaido
Sapporo, JAPAN
99258@ceri.go.jp

[2]Muroran Institute of Technology, Muroran, JAPAN

ABSTRACT

High mound composite seawall with slit crown wall is currently under development as a new type of seawall, which is aimed at cost reduction and environmental enhancement. The structure of this seawall allows a high rubble mound, whose mound slope negates the force of most waves by its wave-breaking action. Employment of the slit structure in the superstructure of this seawall enables reduction of wave forces acting on the seawall. The mound slope provides a living environment for seaweed where sunlight abounds.

To clarify the hydraulic characteristics of the high mound composite seawall with slit crown wall, wave forces characteristics and wave-overtopping characteristics have been studied. These studies revealed that the hydraulic characteristics are superior to the conventional seawall. However, sufficient examination has not been conducted on the stability of the armor units of the rubble mound foundation. Therefore, it is not possible to calculate the stable mass of the armor units. We report the results of two-dimensional and three-dimensional hydraulic model experiments on the stability of the armor units for high mound composite seawall with slit crown wall.

INTRODUCTION

At present, the high mound composite seawall with slit crown wall (Fig. 1) is being developed as a new type of high mound composite seawall. This structure's rubble mound foundation is high and rubble mound attenuates the energy of breaking waves. The structure's upright section is designed with a slit structure to absorb the wave force and dissipate the overtopping waves. The water above the shallow rubble mound offers an ideal photo environment for seaweed growth.

Several studies have focused on the hydraulic characteristics of the high mound composite seawall with slit crown wall. Shimosako et al. (1996) reported on their hydraulic model experiment. They clarified the characteristics of wave forces acting on the upright section. Kimura et al. (1999) and Schuttrumpf et al. (1999) performed an experiment using a large hydraulic model structure and proposed a calculation method for wave overtopping rate. They also studied the characteristics of wave run-up height.

However, the method of designing a mound armor unit has not been examined, and some of its aspects remain unknown. Therefore, we made two-dimensional and three-dimensional hydraulic model experiments on the stability of the armor units and foot protection blocks for high mound composite seawall with slit crown wall.
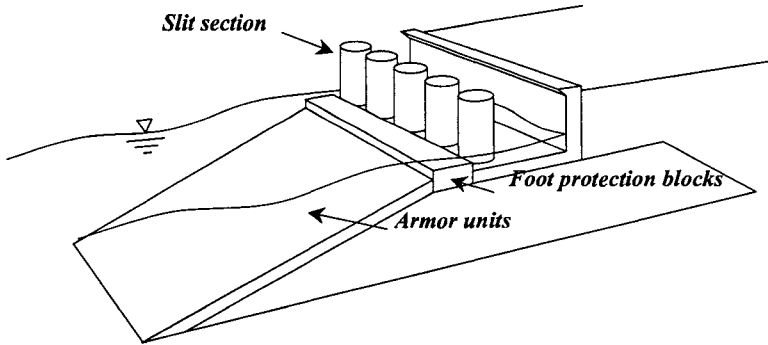

Figure 1. High mound composite seawall with slit crown wall

CALCULATION METHOD OF STABILITY NUMBER

The stable mass of the mound armor units M is usually calculated using the Hudson's formula:

$$M = \frac{\gamma_r H_{1/3}^3}{N_S^3 (S_r - 1)^3} \tag{1}$$

Where $H_{1/3}$ is the significant wave height, S_r is the specific gravity of the armor units to seawater, γ_r is the unit mass of concrete, and N_S is the stability number of armor units, which is a function of wave conditions, water depth, structural body shape and armor unit shape.

Tanimoto et al. (1982) reported on their hydraulic model experiment using irregular waves on the mound armor units of a composite breakwater. They also proposed a calculation method for the stability number of armor units N_S, using the dimensionless flow velocity near the mound κ. Fujiike et al. (1999) examined the stability number of mound armor units on the front wall of breakwater covered with wave-absorbing blocks. Those researchers introduced a coefficient of breakwater body shape C_R into the calculation method of dimensionless flow velocity κ, to include the effects of the wave-absorbing effect. Also, they extracted the standard stability number N_{S0}, which is peculiar for every armor units, from the Tanimoto's formula, to formulate the following equation.

$$N_S = N_{S0} \max\left\{1.0, 0.525\frac{(1-\kappa)}{\kappa^{1/2}}\frac{h'}{H_{1/3}} + \exp\left[-0.9\frac{(1-\kappa)^2}{\kappa^{1/2}}\frac{h'}{H_{1/3}}\right]\right\} \tag{2}$$

Where h' is the mound depth of the seawall, $H_{1/3}$ is the significant wave height.

324

Matsuda et al. (2000) reported on the stability of mound armor units of a high mound composite breakwater. They clarified the relationship between the impulsive wave pressure coefficient α_I proposed by Takahashi et al. (1992) and the stability number N_S, and calibrated the dimensionless flow velocity κ. Here, we modify the method of Matsuda et al. (2000) to calculate the stability number of mound armor units at high mound composite seawall with slit crown wall. We incorporate the wave-absorbing effects of the slit structure by employing the coefficient of breakwater body shape C_R. In other words, the equation for dimensionless flow velocity κ is transformed into the following equation, which uses the C_R and α_I.

$$\kappa = \begin{cases} C_R \cdot \kappa_1(\kappa_2)_B & (\alpha_I \leq 0.05) \\ C_R \cdot \max\{\kappa_1(\kappa_2)_B, \kappa_m\} & (\alpha_I > 0.05) \end{cases} \tag{3}$$

$$\kappa_1(\kappa_2)_B = \frac{4\pi h'/L'}{\sinh 4\pi h'/L'} \max\{\alpha_S \sin^2 \beta \cos^2(kB_m \cos\beta), \cos^2 \beta \sin^2(kB_m \cos\beta)\} \tag{4}$$

$$\kappa_m = \begin{cases} 0.2 & (0.05 < \alpha_I \leq 0.2 \ (\\ 0.3 & (0.2 < \alpha_I \leq 0.4 \ (3 \\ 0.4 & (0.4 < \alpha_I \ (3 \end{cases} \tag{5}$$

Where L' is the wavelength at a mound depth of h', k is wave number ($2\pi/L'$), B_m is berm width, β is wave incident angle, and α_S is correction coefficient, α_I is the impulsive wave pressure coefficient.

EXPERIMENTAL METHOD

2-D test

The two-dimensional wave flume was used in the cross-sectional experiment. The flume length, height, and width were 28.0 m, 1.0 m, and 0.8 m, respectively. The model structure (Fig. 2) was placed horizontally and connected to a sea bottom slope whose gradient 1: 30. The model structure was set at the water depth h of 26.0 cm. The water depth of mound crown h' was varied 0cm, 4.0 cm, and 8.0 cm. Two types of upright section were used: a wave-absorbing section with slit crown wall and a vertical section with conventional upright wall. This allowed comparison of the armor unit stability between different structures. The width of wave chamber for the wave-absorbing section was 22.0 cm, and the opening ratio of the cylindrical slit section was 15% based on a frontal view. The experimental waves were all irregular. The wave height $H_{1/3}$ ranged from 5.0 to 15.0 cm. The period $T_{1/3}$ was 1.4s, 2.0s, and 2.6s. The cross-sectional experiment was performed for two wave conditions. In one condition, 3,000 waves were continuously generated and progress of damage was measured. In the other condition, 500 waves were generated in separate groups, and the wave height was raised gradually to enable calculation of the stability limit wave height. During the experiment, armor units were not fixed, even if the damage was generated. The experiment employed flat armor units weighing 66 g, 100 g, and 140 g. The stability number N_S was calculated for the damage level of 1%. Damage was defined as movement by more than half the length of the armor unit.
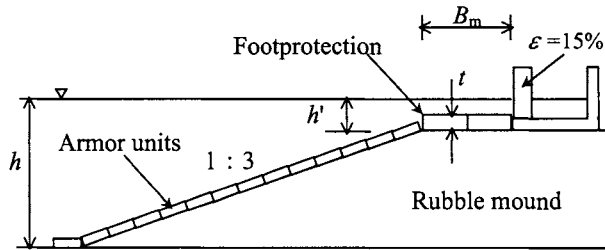
Figure 2. Cross section

3-D test

A three-dimensional experiment was made with a wave basin of length 23.3 m, width 28.2 m, and depth 1.0 meter. A 6.8-m-wide detached structure was installed. The incident angle was set at 0° and 45 degrees. The relative mound depth h'/h was 0.2. The other conditions were the same as those of the two-dimensional experiments. The experiment employed foot protection blocks, whose length and width were set constant at 10.0 cm and 5.0 cm, respectively, and whose thickness t was alternated between 1.0 cm and 2.4 cm. Horizontal movements of 10.0 mm by the foot protection blocks were set as the critical value of stability.

Figure 3 shows the relationship between the number of waves N and the damage level of armor units D. Here, the wave height and the period were set at 11.2 cm and 1.4s, respectively, and there were three relative mound depth h'/h. For each of the three ratios, the damage does not progress after the application of the first 500 waves. The damage ratio is greatest when h'/h is 0.15. Even when the mound depth decreases, the damage does not necessarily increase. Photo 1 depicts the damage after 3,000 waves. The photo at left shows the damage when $h'/h = 0$. The photo at right shows the damage when $h'/h = 0.15$. At these two ratios, armor unit displacement occurred at almost the same location on the mound slope.
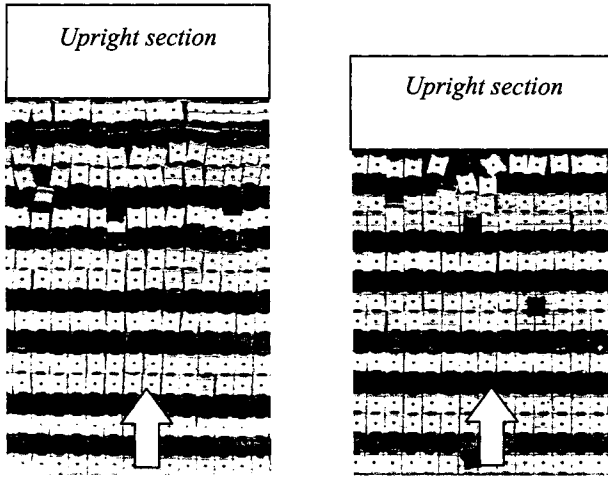

Figure 3. Progress of damage
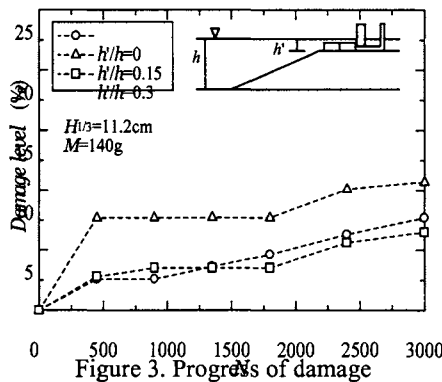
Photo 1. Damage location

STABILITY OF ARMOR UNITS

Damage location of armor units

To clarify the location of damage to armor units for a high mound, the relationship between wave steepness and damage location was examined by arranging armor units on a uniform slope of 1:3 slope. The wave steepness of experimental wave was 0.045 and 0.025, and the ratio of wave height to water depth was 0.3 and 0.5. In Figure 4, the horizontal axis represents $x/L_{1/3}$, the ratio of slope length to wavelength. The slope length x is measured from the still water surface along the slope. The vertical axis represents the relative frequency distribution of the damage rate. The damage is concentrated just below the still water surface level. The peak damage location is constant with wave steepness and not with wave height.

In Figure 3, under the condition of $h'/h = 0.15$, the damage is significant. This is because the shoulder of the slope is located at the damage peak location on the mound slope.
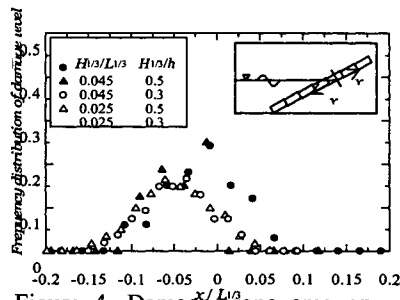

Figure 4. Damage-prone area on

Comparison between wave-absorbing wall and vertical wall

Figure 5 shows the relationship between the ratio of mound depth to wave height $h'/H_{1/3}$ and the stability number of armor units N_S. The dotted line represents the N_S values of the high mound composite seawall calculated according to Matsuda et al. (2000). It agrees well with the measurement results of our experiment on the vertical wall. The solid line represents the values calculated by our proposed method. When the coefficient of structural body shape C_R is 0.4, it agrees well with experimental values.

Oblique incident waves

Figure 6 shows the relationship between the stability number N_S and the dimensionless berm width $B_m/L_{1/3}$ for vertical seawalls and wave-absorbing seawalls, where the relative mound depth h'/h is set constant at 0.2 and the incident wave angle is alternated between 0° and 45°. The stability number is roughly the same when the incident wave angle β is 0° and 45°. The dotted line represents the values calculated using the proposed method. These correspond closely to agree well with the measured values.
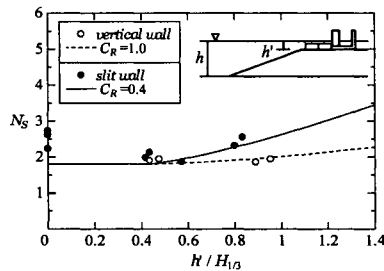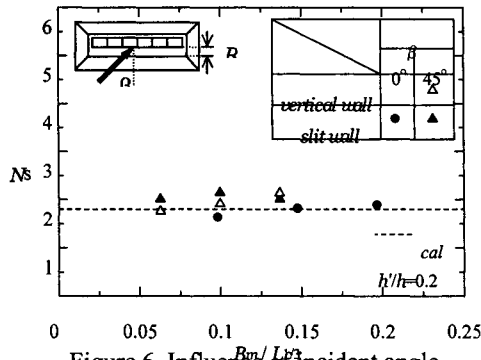

Figure 5. Vertical wall and slit

Figure 6. Influence of incident angle

STABILITY OF THE FOOT PROTECTION BLOCKS

Figure 7 shows the relationship between dimensionless value of the thickness of foot protection blocks $t/H_{1/3}$ and $h/L_{1/3}$, where the relative mound depth h'/h is 0.2 and the incident wave angle β is 0° and 45 degrees. When β is 0°, noticeable differences in stability are not observed between slit wall and vertical wall because wave-breaking on the rubble mound exerts large affects. When β is 45°, the required thickness increases for the vertical wall type. When the mound is high and incident waves are oblique, flows above the foot protection blocks are generated in the normal direction of the structural body as shown in Figure 7. These flows cause the foot protection blocks to slide in the normal direction. Unlike for the vertical wall, the required thickness does not increase for the slit wall type, even when β is 45 degrees. This is because, under this condition, strong flows are generated inside the wave chamber.

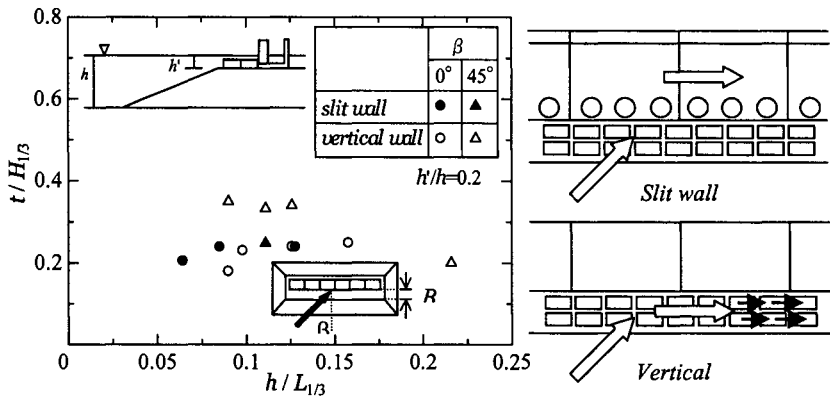Figure 7. Stability of foot protection blocks

CONCLUSION

The present paper can be summarized as in the following:

1) Stable mass of mound armor units decreases, when the upright section is wave-absorbing structure. However, when the $h'/H_{1/3}$ is 0.4 or below, the difference between slit wall and vertical wall is small, due to the effects of wave-breaking on the rubble mound.

2) We proposed a calculation method for evaluation of the stable mass of armor units at a wave-absorbing high mound composite seawall, and it was validated by hydraulic model test.

3) For the vertical-type high mound composite seawall, the required thickness of foot protection block is greater in the case of $\beta = 45°$ than in the case of $\beta = 0°$, because under oblique waves there are flows in the normal direction of the structural body. However, for the wave absorbing structure, the required thickness is not considerably greater in the case of oblique waves, because flow takes place only inside the wave chamber.

REFERENCES

Fujiike, T. K. Kimura, T. Hayashi and Y. Doi. 1999. Armor stability of rubble mound foundation for composite breakwater. *Proceedings of Coastal Engineering* (in Japanese), Vol. 46:881-885.

Kimura, K., T. Hayakawa, S. Takahashi, K. Simosako and H. Oumeraci. 1999. Large scale experiment on wave overtopping of high mound composite seawall. *Proceedings of Coastal Engineering* (in Japanese), Vol. 46:756-760.

Matsuda, S., K. Nishikiori, T. Matsumoto and M. Saitoh. 2000. Experimental study on the stability of armor blocks covering the rubble mound of composite breakwaters under impulsive wave action. *Proceedings of Coastal Engineering* (in Japanese), Vol. 47:896-900.

Muttray, M., H. Oumeraci, K. Simosako and S. Takahashi. 1998. Hydraulic performance of a high mound composite breakwater. *International Conference on Coastal Engineering*, Vol. 26:2207-2220.

Schuttrumpf, H. Oumeraci, H. Moller, J. Kimura, K. and T. Hayakawa. 1999. Wave overtopping on a high mound composite type breakwater. *Proceedings of coastal structures 99*:397-404.

Takahashi, S. K. Kimura and K. Tanimoto. 1991. Stability of armor units of composite breakwater mound against oblique waves. *Proceedings of Coastal Engineering* (in Japanese), Vol. 33:596-600.

Takahashi, S. K. Tanimoto, K. Simosako and T. Hosoyamada. 1992. The proposal of impulsive wave pressure coefficient by the mound shape of composite breakwater. *Proceedings of Coastal Engineering* (in Japanese), Vol. 39:676-680.

Tanimoto, K. T. Tagyuu, T. Muranaga, K. Shibata and Y. Goda. 1982. Stability of armor units for foundation mounds of composite breakwaters by irregular wave tests. *Report of the port and harbor research institute* (in Japanese), Vol. 21 No 3:3-42.

INFLUENCE OF SUBMERGED BREAKWATER TO WAVE RUNUP ON STEP DIKE

Jea-Tzyy Juang[1], Chao-Fu Lin[2] and Chi-Da Huang[2]

[1]Department of Environmental Engineering, Fooyin University
Taliao, Kaohsiung County, TAIWAN
jtjuang@mail.fy.edu.tw

[2]Department of Hydraulic Engineering, Fonchia University
Taichung City, TAIWAN

ABSTRACT

Submerged breakwater was the structures that normally constructed with rubblemound and it has a submerged crest depth below the sea water level. It was well suited to maintain a moderate degree of energy transfer from the offshore to the shoreline region. In this study, the wave runup theorem which proposed by Cross and Sollitt (1972) was quoted for analysis first. After that, based on the results of the wave runup test by the incident irregular wave, the coefficients in the wave runup equation of the runup profile can be estimated. At the second, the computation method for the calculate of the wave energy loss coefficient in wave runup on sea dike as well as the energy loss of the incident wave pass over the submerged breakwater was proposed. At last, by advantage the result of the experiment of wave runup, a prediction model for the wave runup height was proposed too. Comparison of the result of the predicted wave runup height that obtained by the proposed calculation model and the wave runup height that measured from the experiments was coinciding each other very well.

INTRODUCTION

The offshore structure likes the submerged breakwater was used to reduce the incident wave energy as well as the incident wave height then can achieve the purpose of coastal protection work. Meanwhile, in order to reduce the wave runup height, a series of study work on decrease down the wave runup height on sloping dike was completed at the past time. One of the ways was to construct the step dike to increase the roughness on the sloping dike surface. Based on the above-mentioned reason, the combination of the submerged breakwater and the step dike to reduce the wave runup height for protect the coastline was conducted in this study.

LITERATURE REVIEW

Seabrook and Hall (1998) proposed a calculation formula for calculate the transmitted coefficient Kt) of the waves pass over a submerged breakwater as follows.

$$K_t = 1 - (e^{-0.65(\frac{D_2}{H_i})-1.09(\frac{H_i}{b})} + 0.047(\frac{bD_2}{LD_{50a}}) - 0.067(\frac{D_2 H_i}{bD_{50a}})) \tag{1}$$

where D_2 : the submerged depth of the crest of submerged breakwater

H_i : incident wave height

L : incident wave length

b : crest width of the submerged breakwater

D_{50a}: medium diameter of the armor layer

Van der Meer and Stem (1992) according the experiment data of the wave runup on smooth surface dike that completed by Ahren in 1981 and their own experiment data of the run up experiment on a rubble mound dike to regress out the correlation equation between the relative wave run-up height and the surf parameter as follows:

$$\frac{Ru_{2\%}}{H_s} = 1.5\xi_p \quad \text{如} \ 0.5 < \xi_p < 2 \quad \text{(smooth surface dike)} \tag{2}$$

$$\frac{Ru_{2\%}}{H_s} = 0.83\xi_p \quad \text{如} \ 0.5 < \xi_p < 2 \quad \text{(rubble mound surface dike)} \tag{3}$$

$$\xi_p = \tan\theta / (2\pi H_s / gT_p^2)^{0.5}$$

in which ξ_p called the surf parameter and T_p was the peak period. $R_{u2\%}$ was the averaged value of the largest 2% runup wave height.

For the calculation formula of the runup wave height, if the peak wave period (T_p) was instead by the mean wave period (T_m) for analysis then the correlation equations will be changed as follows

$$\frac{Ru_{2\%}}{H_s} = 0.96\xi_m \quad \text{如} \ \xi_m \leq 1.5 \tag{4}$$

$$\frac{Ru_{2\%}}{H_s} = 1.17\xi_m^{0.46} \quad \text{如} \ \xi_m \geq 1.5 \tag{5}$$

THEORETICAL ANALYSIS

The calculation of the runup wave profile

Cross and Sollitt (1972) proposed a calculation formula to compute the wave runup profile (Fig.1) on a sloping dike as follow

$$Y = MX^N - A \tag{6}$$

In which X, Y was the two-dimensional coordinate. A was the wave amplitude at the trough of the runup wave that in front of the smooth sloping dike.

$$A = A_i + A_r = A_i(1+K_r) \tag{7}$$

where A_i was the incident wave amplitude and K_r was the refraction coefficient. Yamamoto et. al. (1994) proposed a correlation formula of A_i and the incident significant wave height H_{si} as $A_i = 0.471 H_{si}$. Therefore, the above equation becomes

$$A = 0.471 H_{si} \cdot (1+K_r) \tag{8}$$

In advance, divide both sides by A in equation (6) can obtained

$$\frac{Y}{A} = \frac{ML_R^N}{A} (\frac{X}{L_R})^N - 1 \tag{9}$$

Let y, $r = Y/A$, R/A, and x, $x_1 = X/L_R$, X_1/L_R, then Figure 1 can changed to the dimensionless equation as shown in Figure 2. Meanwhile, the above equation becomes

$$y = (r+1)x^N - 1 \tag{10}$$
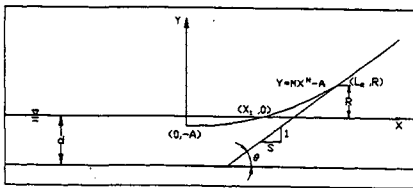
Fig. 1 Wave runup
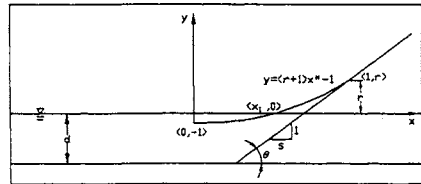
Fig. 2 Wave runup(dimensionless)

From Figure 2 we can understand

$$\int_0^1 y dx - \frac{sr^2}{2} = 0 \tag{11}$$

Substitute equation (10) into (11) can obtained

$$N = \frac{2r - sr^2}{2 + sr^2} \tag{12}$$

$$M = \frac{R + A}{L_R^N} \tag{13}$$

There have two boundary conditions. The first one was when $X = X_1$ then $Y = 0$. After substitute it into equation (6) can obtained

$$M = \frac{A}{X_1^N} \tag{14}$$

The second one was when $X = L_R$ then $Y = R$, In this case, equation (6) becomes

$$L_R = X_1.(r+1)^{1/N}$$ (15)

Substitute equation (14) into (15), we can obtain

$$L_R = X_1(r+1)^{1/N}$$ (16)

Again, substitute equation (16) into (12) can obtained the following equation

$$(N+1)[\frac{ASr^2}{2X_1(r+1)^{1/N}}]+N-r=0$$ (17)

Use the above equation and the experimental data, due to A, X_1, R can be measured from the experiment, so that we can compute the N value.   After that, use equation (14), the value of M can be calculated out also.

Energy loss in the runup waves

By advantage of the concept of control volume to analysis the wave runup phenomenon.   In general, the wave energy will changed after the wave runup on a sloping dike (Fig. 3) and the correlation formula of the wave runup can to formulate as follows (Cross and Solitt, 1972)

$$E_iC_g - E_rC_g - \frac{E_0}{T} = \frac{PE-E_0}{T}K_l$$ (18)

where E_i ○incident wave energy ($= \frac{1}{2}\rho g A_i^2$)

E_r ○reflected wave energy ($= \frac{1}{2}\rho g A_r^2 = \frac{1}{2}\rho g A_i^2 K_r^2$)

E_0 ○wave energy of overtopping

PE ○potential energy of the runup wave

K_l ○energy loss coefficient

C_g ○group wave velocity

T ○wave period

If the waves only runup and without overtopping, the above equation can to simplified as

$$E_iC_g - E_rC_g = \frac{PE}{T}K_l$$ (19)

Let $pe = PE/\rho g A^2 L_R$ and substitute it into the above equation then

$$pe = n \cdot \frac{L}{L_R} \cdot \frac{1}{2K_t} \cdot \frac{(1 - K_r{}^2)}{(1 + K_r)^2} \tag{20}$$

$$n = \frac{C_g}{C} = \frac{1}{2}\left[1 + \frac{2\,kh}{\sinh(\,2\,kh\,)}\right] \tag{21}$$

where k was the wave number.

Besides, from Figure 2, we can understand that the dimensionless runup wave energy (*pe*) can to calculated by the following equation

$$pe = \int_{x_1}^{1} \frac{y^2}{2}\,dx - \frac{sr^3}{6} \tag{22}$$

After integration, we have

$$pe = \frac{1}{2}\left\{\frac{(r+1)^2}{2N+1}\left[1 - \frac{1}{(r+1)^{2+\frac{1}{N}}}\right] - \frac{2(r+1)}{N+1}\left[1 - \frac{1}{(r+1)^{1+\frac{1}{N}}}\right] + \left[1 - \frac{1}{(r+1)^{\frac{1}{N}}}\right] - \frac{sr^3}{3}\right\} \tag{23}$$

At last, use this equation and equation (20) then the value of the relative wave runup height can be predicted.

Wave transmission and interaction

Seabrook and Hall (1998) proposed a calculation formula for compute the wave transmission coefficient over a submerged breakwater as shown in equation (1). If the submerged breakwater was impermeable and the surface of the submerged breakwater was smooth (that means frictionless) then equation (1) can to simplified as

$$K_t{}' = 1 - e^{-0.65(\frac{D_2}{H_i}) - 1.09(\frac{H_i}{b})} \tag{24}$$

When the incident wave pass over the submerged breakwater and reflected from the sloping dike as shown in Figure 4. The wave energy of the transmitted wave will change at the place where between the submerged breakwater and the sloping dike. That is, $E_S = E_t + E_r$. So that

$$H_S = \sqrt{(H_1 \cdot K_t{}')^2 + (H_1 \cdot K_t{}' K_r)^2} = H_1 \cdot K_t{}'\sqrt{1 + K_r{}^2} \tag{25}$$
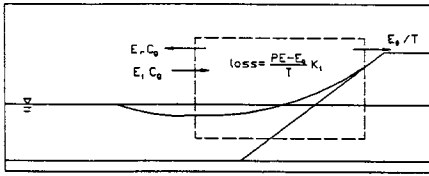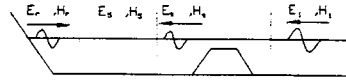
Fig. 3 Control volume of wave runup

Fig. 4 Wavw transmission and reflection

EXPERIMENT ARRANGEMENT

The experiment study was carry out in the wave flume of the Institute of Harbor and Marine Technology. The length of the channel equals 100 meters, the height 2 meters and the width 1.5 meters. The distance of the test model to the wave generator was 80 meters. Inside the test channel, a thin wood plate dividing the channel cross section into two portion was made. The width of both portion equal 0.75 m so that the wave runup height can be measured at the different dike style (for example the smooth and the step dike) simultaneously in the same incident wave condition. In front of the sea dike, there have a submerged breakwater was build up so that the influence of the submerged breakwater to the wave runup on the smooth and the step dike can be measured for analysis and comparison. The layout of the experiment was shown as in Figure 5. The incident wave height (Hs) is 4, 6, 8, 10, 12, 14, and 16 cm. The wave period that set on wave generator was fixed on 1.8 second. The side slope of the submerged breakwater was 1 to 1.5 (height to length) on both sides.
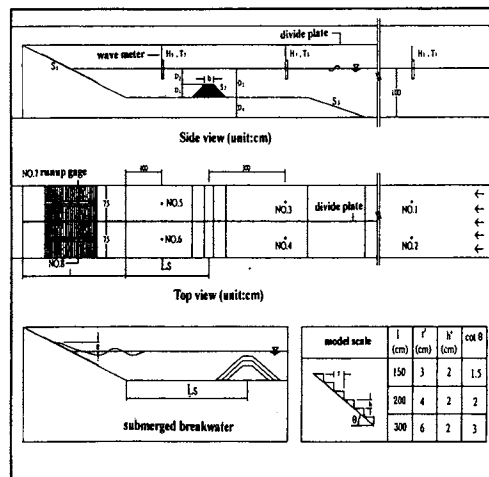

Fig. 5 Layout of experiment

RESULT AND DISCUSSION

Correlation of reflection coefficient to surf parameter

In the condition of the submerged breakwater was removed, the correlation of the reflection coefficient to the surf parameter by the test result was obtained as shown in Figures 6 and 7.
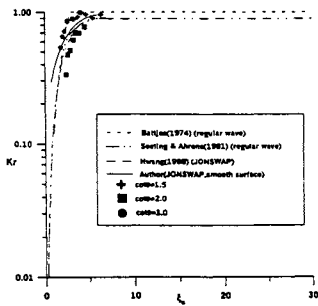

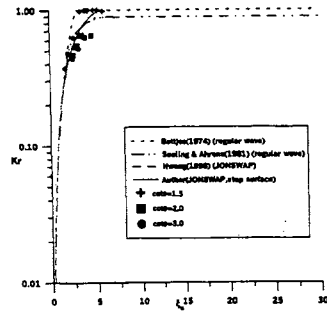Fig. 6 Correlation between κ, and ζ_s (smooth)

Fig. 7 Correlation between κ, and ζ_s (step)

From the figures, we can see the steeper the dike slope, the bigger the reflection coefficient. Its relation equation can be obtained.

$$K_r = 0.110 + 0.269\xi_s - 0.021\xi_s^2; \text{ for smooth dike surface} \qquad (26)$$

$$K_r = 0.268 + 0.390\xi_s - 0.029\xi_s^2 ; \text{ for step dike surface} \qquad (27)$$

where $\xi_s = \tan\theta / \sqrt{H_0 / L}$

Due to the wave runup profile will changed on different incident wave steepness and the dike slope. Therefore, the correlation between the coefficients N and M to the surf parameter at different dike slope can be obtained as shown in Figures 8-11.
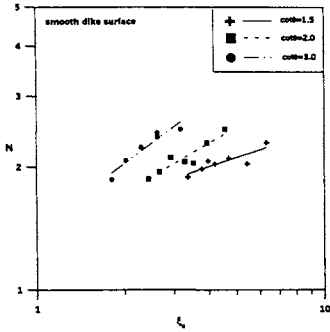
337

Fig. 8 Correlation between N and ξ_s (smooth)

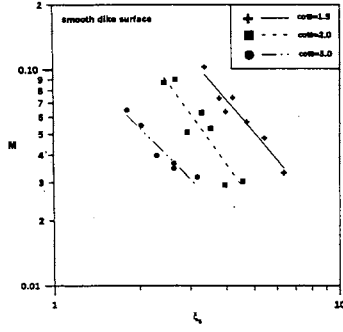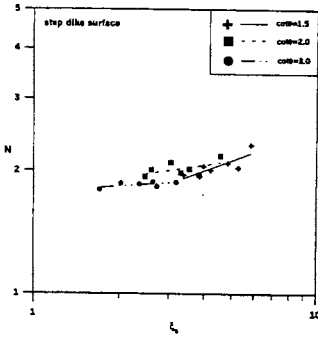

Fig. 9 Correlation between M and ξ_s (smooth)
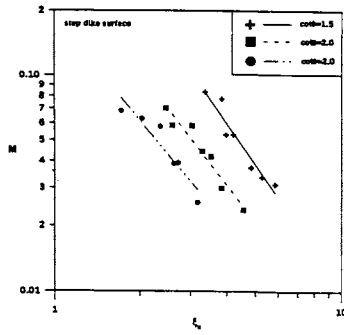

Fig. 10 Correlation between N and ξ_s (step)

Fig. 11 Correlation between M and ξ_s (step)

After the regression analysis, the correlation formula between N or M and the surf parameter can be obtained as follows.

For smooth dike surface

$$N = 1.447(\xi_s)^{0.23} , M = 0.661(\xi_s)^{-1.59}; \cot\theta = 1.5 \tag{28}$$

$$N = 1.30(\xi_s)^{0.41}, M = 0.486(\xi_s)^{-1.87}; \cot\theta = 2.0 \tag{29}$$

$$N = 1.423(\xi_s)^{0.52} , M = 0.134(\xi_s)^{-1.33}; \cot\theta = 3.0 \tag{30}$$

For step dike surface

$$N = 1.388(\xi_s)^{0.26} , M = 0.914(\xi_s)^{-1.97}; \cot\theta = 1.5 \tag{31}$$

$$N = 1.772(\xi_s)^{0.11} , M = 0.348(\xi_s)^{-1.75}; \cot\theta = 2.0 \tag{32}$$

$$N = 1.761(\xi_s)^{0.05} , M = 0.184(\xi_s)^{-1.59}; \cot\theta = 3.0 \tag{33}$$

Correlation between energy loss and the surf parameter

When the incident wave assails the dike, the wave runup on the dike slope and the wave reflection from the sloping dike will to happened simultaneously. Meanwhile, the wave runup

338

height as well as the wave energy loss will to changed at different incident wave and the dike condition. In this study, the correlation between the wave energy loss and the surf parameter was obtained as shown in Figures 12 and 13. From the figures, we can see the wave energy loss was bigger in big incident wave. Besides, we can see the bigger the wave energy loss, the milder the dike slope too. The reason was the milder the dike slope; the longer distance the wave to climbed. So that the bigger the wave energy loss will to generated. In addition, from these two figures, we also can find the wave energy loss was bigger at the step dike surface than the smooth dike surface in the same incident wave condition.

After the K_l value can to estimated then use the above mentioned formula, the values of N, M, K_r as well as the runup wave height can to computed. The comparison of the computed wave runup height with the measured wave runup height was shown in Figures 14 and 15 (without submerged breakwater). The correlation coefficient (R^2) for the smooth surface dike and the step dike are equal to 0.9195 and 0.9484 respectively. It indicates that this wave runup height prediction model was quite reliable.
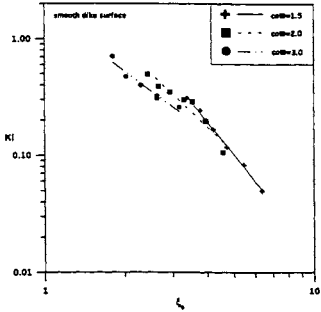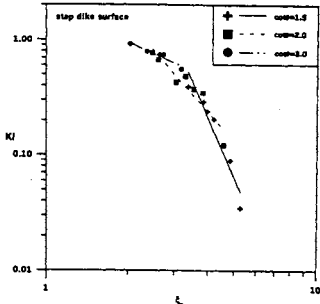

Fig. 12 Correlation between κ_l and ς (smooth)

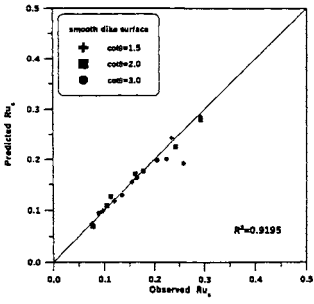Fig. 13 Correlation between κ_l and ς (step)
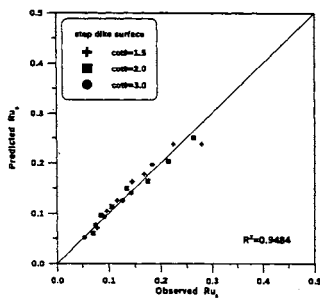

Fig. 14 Comparison of wave runup (smooth)

Fig. 15 Comparison of wave runup (step)

339

Influence of submerged breakwater to wave runup height

The main function effect of the submerged breakwater was to reduce the wave energy of the incident wave. After the incident wave passes over the submerged breakwater, its energy was break down, so that the runup height on the sloping dike decreases down also. In this study, the submerged breakwater was impermeable and the surface of submerged breakwater was smooth, so that the frictionless assumption was made. Due to the wave reflection coefficient (Kr) can to obtained and the transmission coefficient (Kt') can to computed also. Therefore, using equation (25), the wave height at the place where between the submerged breakwater and the sloping dike can be calculated. The comparison of the computed wave height and the measured wave height was shown in Figure 16 (smooth dike surface). The correlation coefficient $R^2 = 0.8940$. This result can say acceptable.

At last, in advantage of equations (20) and (23), the wave runup height on the sloping dike can to computed. The comparison of the computed wave runup height to the measured wave runup height was shown in Figure 17 (smooth dike surface). The correlation $R^2 = 0.8614$. This result can say acceptable also.
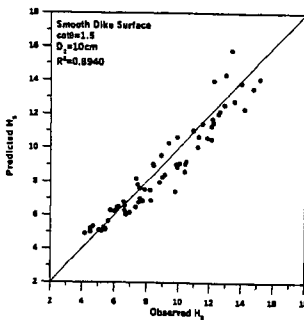

Fig. 16 Comparison of wave height after transmission (smooth)
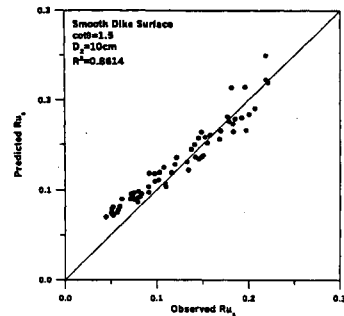
Fig. 17 Comparison of wave height after transmission (smooth)

CONCLUSIONS

1. The correlation equation between the reflection coefficient from the sloping dike and the surf parameter (ξ_r) was obtained as shown in equations (26) and (27).
2. The runup wave profile coefficients N and M are function of the surf parameter and can be obtained by use equations (28) to (33). It can to computed by use equations (17) and (14).
3. The correlation between the coefficient of energy loss in wave runup and the surf parameter was obtained as shown from Figures 12 to 15.
4. The wave energy loss was bigger at the step dike than at the smooth surface dike in the same incident wave and dike slope conditions.
5. Although the wave height will reduced after it pass over the submerged breakwater. But due to the reflection effect from the sloping dike. Sometime the wave height will grow up again at

340

the place where between the submerged breakwater and the sloping dike. The reason may be the wave-wave interaction can to induced in this place.

6. The prediction model of wave runup under the influence of submerged breakwater was conduct in this study. Although the primary result can says acceptable. However, the advance study on the effect of wave transmission over rough and permeable submerged breakwater as well as the influence of the wave runup on step dike were suggest.

ACKNOWLEDGEMENT

REFERENCES

Ahrens, J.P. 1981. Irregular wave runup on smooth slopes. *Tech.* Report No. 81-17. Coastal Engineering Research Center. Waterways Experiment Station. Vicksburg. Mississippi.

Cross, R.H. and C.K. Sollitt 1972. Wave Transmission By Overtopping. *Journal of Waterways, Port, Coastal and Ocean Eng. ASCE.* Vol.98. pp. 295 -309.

Seabrook, S.R. and K.R. Hall. 1998. Wave Transmission at Submerged Rubblemound Breakwaters. *Coastal Eng..* pp. 2000-2013.

Van der Meer, J.W. and C.J.M. Stam 1992. Wave Runup on Smooth and Rock Slope of Coastal Structures, *Journal of Waterway, Port, Coastal and Ocean Eng.. ASCE.* No.5.

Yamamoto, Y., K. Tanimoto and K.G. Harshinie. 1994. Run-up of Irregular Wave on Gentle Sloping Beach. *Coastal Eng..* pp. 689-703.

EVALUATION OF WORKING ENVIRONMENTS IN FISHING PORTS BY USING OVAKO WORKING POSTURES ANALYSIS SYSTEM

Mio Anai[1], Heon Chol Park[1], Takeo Kondo[1], Masaharu Kimoto[1], Kazukiyo Yamamoto[1], Kimiyasu Saeki[2], Sadamitsu Akeda[2] and Nobuo Takaki[2]

[1]Nihon University
Funabashi, Chiba, JAPAN
k04004@ocean.cst.nihon-u.ac.jp

[2]National Fisheries Research Institute Fisheries Research Agency
Kashima, Ibaraki, JAPAN
kysaeki@fra.affrc.go.jp

ABSTRACT

An alternative to relieving the burden of both skilled fishers and beginners is considered clarifying the cause of the burden in the fishery and removing it. Among methodologies, this paper describes the characteristics of on four fishing practices and introduces OWAS-Ovako Working Posture Analysis System in order to clarify unproven working postures and physical burdens on a landside of the fishing ports. The analysis shows that most physical burdens are concentrated on the back and legs and identifies required action categories for working postures, which should be improved. The burdens may result from the vertical distance between the pier and the fishing boat, the weight of freights, and long working hours. Also, questionnaire and interview researches support the results.

INTRODUCTION

Since the 1990s, the fishery industry in Japan has faced the decrease of fishermen because of the advent of the aged society, the lack of new young fishermen, and the dramatic social and industrial change. Under these situations, many older fishermen have to continue working until they find a follower, and women should fill in the lack of the workforce. Among many difficulties of working environments in a fishing port, physical burdens seem to cause a possible accident and increase the physical fatigue. Unfortunately, the research on these parts had not been done until those problems came to reality because the concept of working environment and efficiency had been discussed in the industry, which is dependent on the natural environment. Considering these circumstances, a paper (Yamashita, 2000) showed the methodological approach in order to illustrate the characteristics of the fishing on offshore and measure the burden of each work. However, the paper did not cover the several types of fishing practices on a landside of fishing ports where the types of works are complicated and workers have diverse physical abilities. Therefore, this paper focuses on several types of fishing practices on the landside of fishing ports.

PURPOSES

The purpose of this paper is to describe the characteristics of four types of fishing practices: trawl fishery, purse seine fishery, fixed gill net fishery, and shell dredge net fishery, and mainly clarify the undesirable working postures on the landside of fishing ports and action categories that indicate the degree of the requirement for measured the postures. Also, it focuses on the causes of physical burdens and the facilities that should be improved

METHODOLOGIES

Five fishing ports in Chiba prefecture (Fig. 1) are selected as research sites, considering fishing activities during the summer season, the scale of the port facilities and the fishing practice. Table 1 shows the outline of the research. Fifty copies of questionnaire are distributed to each fishing port and are collected by post. Also video recordings as well as interviews are conducted at four among five fishing ports except for Katsu-ura, during working hours on each fishing practice. "Class" in Table 1 shows size of fishing port. The largest port among the fishing ports in Japan is Special Class Third. Class Four is an emergency fishing port.
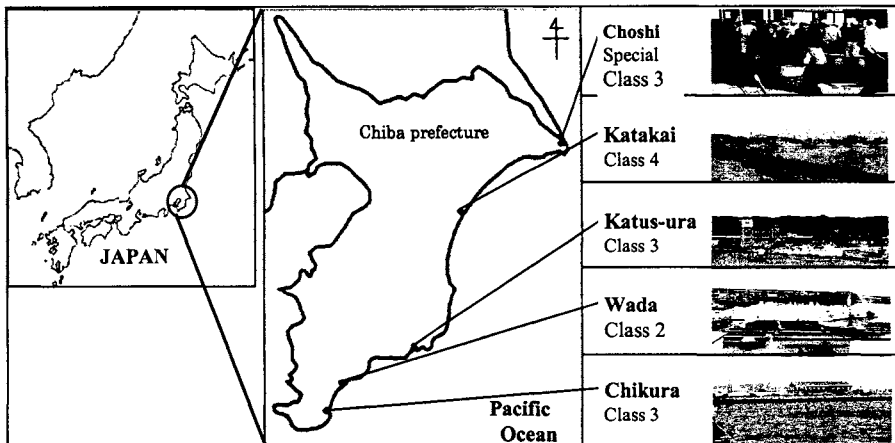
Figure 1. Survey sites

EXPLANATION OF OVAKO WORKING POSTURE ANALYSIS

The working postures of fishermen are measured by using OWAS, Ovako Working Posture Analysis System, which can determine the level of burden posed by a specific posture at a given time and the degree of required correction. The OWAS method is based on a simple and systematic classification of work postures combined with observations of work tasks. Working together, specialists and workers can apply the method to find measures for reducing the harmful load caused by poor work postures. OWAS assesses the posture of a worker in terms of the back, arms, legs and burden (Louhevaara, 1992). A posture can be classified into one of four

344

action categories (AC) depending on the level of burden and the degree of required correction. The posture evaluation based on the AC score, shown in Table 2. The particular posture for a specific type of work can be assessed based on the frequency of the AC scores for the following two aspects. One is "physical burden" from the viewpoint of the entire work postures. The other is "burden on a particular part of the body", such as the back, arms or legs, from the viewpoint of the frequency of a specific posture (bending the back or raising (an) arm(s), etc.). The result of the former identifies the degree of required correction and work processes in need of correction while the result of the latter identifies the specific body part subject to a particularly heavy burden in a specific type of work. The classification of working postures on body parts is shown in Table 3. In the case of work posture combination is determined (Fig. 2). The crossing point shows the AC score.

Table 1. Outline of the research

Study Site / Classification of port / Fishing practice	Date of Survey (Year 2001)	Present Condition
Wada / Class 2 / Fixed gill netting	14th September	Number of fishermen: 98, Number of fishing boats: 74 Average age of fishermen: 65.5 Landing fishery product: 2,042 tons
Chikura / Class 3 / Fixed gill netting	18th September	Number of fishermen: 73, Number of fishing boats: 50 Average age of fishermen: 64 Landing fishery product: 7,876 tons
Katsu-ura / Class 3 /	19th September	Number of fishermen: 71, Number of fishing boats: 56 Average age of fishermen: 57.4 Landing fishery product: 21,280 tons
Choshi / Special Class 3 / Trawling, Round haul netting (single boats)	25th, 26th and 27th September	Number of fishermen: 651, Number of fishing boats: 50 Average age of fishermen: 64 Landing fishery product: 252,177 tons
Katagai / Class 4 / Shell dredge netting, Round haul netting (two boat)	27th and 28th September	Number of fishermen: 74, Number of fishing boats: 41; Average age of fishermen: 53 Landing fishery product: 18,041 tons

Methods	Research Contents
Questionnaire	Types of work, evaluation of facilities, physical burdens and causes
Interview	Problems associated with facilities, details of physical burden
Video recording/ photography	Physical burden inflicted on working (by OWAS and AC method)

Table 2. Evaluation of working posture based on AC score

AC1	No action required.
AC2	Corrective measures should be taken in the near future.
AC3	Corrective measures should be taken as soon as possible.
AC4	Corrective measures should be taken immediately.

Table 3. Classification of working postures

Back	1. Straight 2. Bent 3. Twisted 4. Bent and twisted
Arms	1. Both arms below the shoulder 2. One arm above the shoulder 3. Both arms above the shoulder
Legs	1. Sitting 2. Standing on both legs 3. Standing on one leg 4. Standing with both knees bent 5. Standing with one knee bent 6. Kneeling 7. Walking
Load	1. W ≤ 10 kg 2. 10kg < W ≤ 20 kg 3. W > 20 kg

back	arm	1 123	2 123	3 123	4 123	5 123	6 123	7 123	leg weight
1	1	111	111	111	222	222	111	111	
	2	111	111	111	222	222	111	111	
	3	111	111	111	223	223	111	112	
2	1	223	223	223	333	333	222	233	
	2	223	223	233	344	344	334	234	
	3	334	223	333	344	444	444	234	
3	1	111	111	112	333	444	111	111	
	2	223	111	112	444	444	333	111	
	3	223	111	233	444	444	444	111	
4	1	233	223	223	444	444	444	234	
	2	334	234	334	444	444	444	234	
	3	444	234	334	444	444	444	234	

Figure 2. Action categories for work posture

STUDY RESULTS AND FURTHER ANALISIS

Evaluation of Physical Burden Caused by Fishery Work

Quantitative evaluation of physical burdens
Burdens of working postures are analyzed by using the OWAS, which are associated with each fishing practice on the landside of fishing ports such as unloading of fish catches, loadings of supplies and equipments, and repairs of nets. All of them seem to involve hard work because they accompany the lifting of heavy items and long working hours. Results of the analysis are shown in Table 4.

Table 4. Fishing practice and AC

Fishing practice	Characteristics	Working Postures to be Improved	AC Score	Body Part Subject to be burden	Causes of burden
Trawling	Boat size is: 70 tons (large) with 8 crew members Landing volume is approx. 35 tons per operation Fishing activity takes approx. one day Temporary sorting work is conducted on boat A crane is used for both landing and preparatory	unloading 40 minutes	AC2 AC3 AC4	Back Legs	Vertical distance between landing pier and bottom of boat (1 – 2 m) Weight of fish (approx. 40 kg/box)
		Loading supplies and equipment 15 minutes	AC2 AC3	Back Legs	Distance between pier and bottom of boat
Round Haul Netting	Boat size is 300 tons with 8 – 10 crew members Landing volume is approx. 45 tons per operation Temporary sorting work is conducted on the boat Landing and preparatory work are fairly mechanised	unloading 50 minutes	AC2	Back	Location of machine to conduct landing work
		Ice loading 50 minutes	AC2	Back Legs	Machine operation
Fixed Gill Netting (Prawns)	Boat sizes is 0.6 tons with single crew member Landing volume is approx. 25 kg per operation Work at port is entirely conducted manually Net and litter removal is conducted by more than one person A long time is required for net repair	Loading supplies and equipment 3 minutes	AC2 AC3	Back Legs	Distance between pier and bottom of boat (0.3 – 1.5 m) Weight of equipment (approx. 30
		unloading 3 minutes	AC2 AC3	Back Legs	Distance between pier and bottom of boat (0.3 – 1.5 m) Weight of fish (approx. 35 kg/box)
		Removing of shrimps from net 70 minutes	AC2	Back Legs	Sitting work on the ground
		Removing of garbage 50 minutes	AC2	Back Legs	Height of working arms
		Repairs of nets. 450 minutes	AC2	Back Legs	Sitting work on the ground
Shell Dredge Netting	Boat size is 5 tons with 4 crew members Landing volume: approx. 500 kg per operation Work at port is entirely conducted manually Sorting is conducted on boat	unloading 7 minutes	AC2 AC3	Back Legs	Distance between pier and bottom of boat (1 – 1.3 m) Weight of equipment (approx. 35 kg/box)

Unloading	Loading supplies and equipment	Unloading	Ice loading	Unloading
Trawling		Round haul netting		Shell dredge netting

Loading supplies and equipment	Unloading	Removing of shrimps from net	Removing of garbage	Repairs of nets
Fixed gill netting				

AC2 (shown as Table 2) for every type of work is frequently observed among high AC scores that indicate the need for correction of the working posture. AC3 and AC4, which require the instant correction of the postures, are observed at the unloading of fish catches in trawling practice (evaluation result are AC3 and AC4), fixed gill netting (evaluation result is AC3), and shell dredge netting (evaluation result is AC3). In short, these results indicate that uploading pasture is the most difficult posture in the landside among evaluated postures except for round haul netting. It seems that evaluating the burden on each body part can identify causes of such

a high level of burden. The body parts on which heavy loads are concentrated are the back and legs. The parts are equivalent to AC2 or higher action categories, AC3 or AC4. Especially, the back in many types of work is imposed with a burden. According to human engineering of a UNESCO report in 1999, the hazard factors for backache are "heavy work (lifting, cargo handling, work demand physical strength, bending of the body and twisting of the body, etc.) and long work hours under crouched postures". Fishermen also work under these types of hazard factors. In case of the legs, the physical burden is particularly increased when the center of gravity is placed on the bent knees. In the case of landing for round haul netting, the impact of the vertical distance between the pier and the floor of the boat on the back and legs is not particularly large because a machine is used for unloading large amount of fish catches. However, in case of large-scale trawling, even though a machine is used for unloading like round haul netting, the horizontal distance between the fishing boat and the pier and the vertical distance between the pier and the floor of the fishing boat causes the bending or crouch of the back and legs because a fisherman manually hangs the bucket on a rope in order to unloading the catches (Fig. 3).
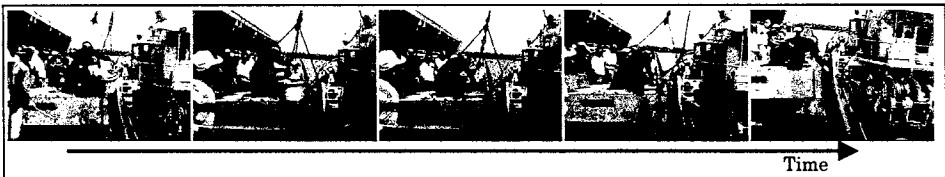
Figure 3. Working postures of trawling (unloading)

Particularly, in case of the fixed gill netting of prawns and shell dredge netting, the vertical distance from 0.3 m to 1 m between the pier and the floor of the fishing boat, the horizontal distance between the pier and the fishing, and especially 35 kg of the fish catches per box influences the physical burden because all work is done by the manpower (Fig. 4).
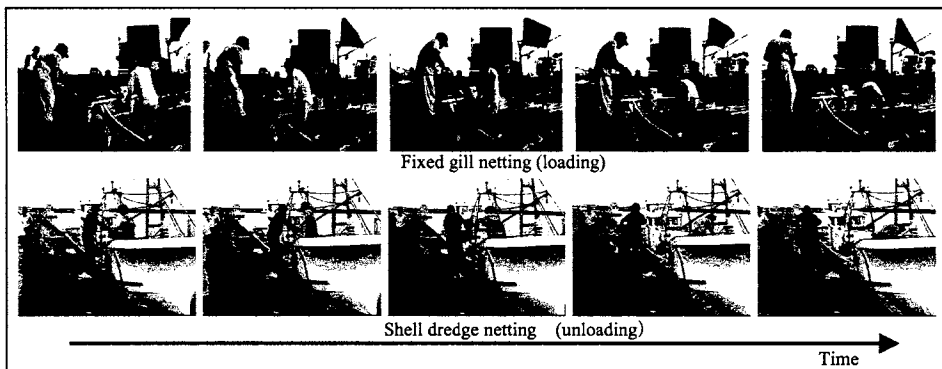
Figure 4. Working postures of fixed gill netting and shell dredge netting

Self-evaluation of physical burden by fishery workers
Questionnaire surveys on whole fishery work are conducted on fishery workers, and results of self-evaluation on the physical burden associated with different fishing methods are shown in

Figure 5.   In this Figure, the question of "the body part most burdened in fishery work" allows multiple answers while the question of "evaluation of the burden on each body part" is based on five-grade evaluation ranging from very hard (-2) to very easy (+2).   The results show that a heavy burden on the back is commonly identified for all fishing practices.   The indicated causes of the burden on the back in trawling are "bending work, heavy muscle work such as transportation of the product by hand, and chilling of the body due to early morning work".
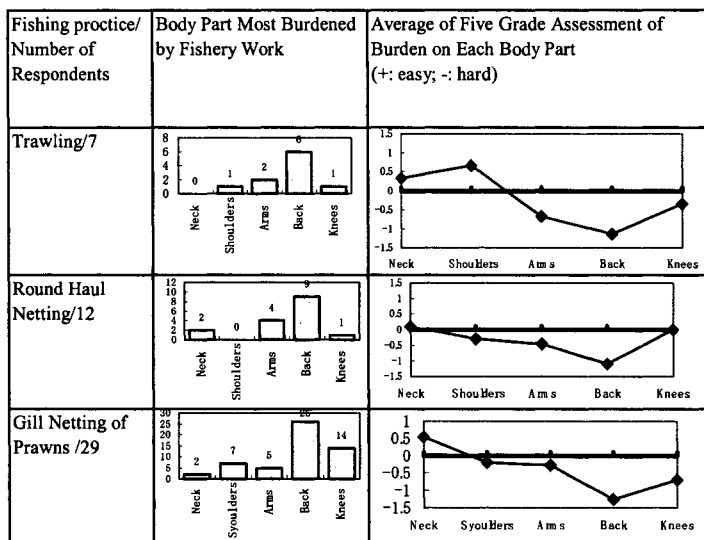
Figure 5. Self-evaluation of burden by fishery workers

Meanwhile, the types of heavy work indicated include "loading of the net and ice, replacement of the net, landing, sorting of fish and shellfish".   In case of round haul netting, the indicated causes of the heavy burden are "net repair sitting on asphalt surface and unloading".   In case of the fixed gill netting of prawns, the indicated causes of the heavy burden are "poor footing, bending work, and long sitting work" while "loading of the net and net repair" are considered particularly heavy work.   These results confirm results of OWAS analysis except for factors such as chilling of the body due to early morning work and work on asphalt, which cannot be evaluated by the OWAS.   In case of trawling and round haul netting, the back comes first and arms come second.   The indicated cause is work on offshore like net lifting. Unlike fishing practices, the results in fixed gill netting of prawns are similar to those of the results by OWAS. This similarity may originate from longer working hours on landside than those on offshore because the OWAS in this paper is done on the landside of fishing ports.   Also, questions about the experiences of the injury and their causes are mainly related to work on the fishing boat such as falling during net lifting, being caught by the machine, fishing in rough weather, and striking rocks.   Injuries on landside are the sprain by falling on a slippery surface and light wounds during the work to remove fish from the net and by fishhooks.   The findings above suggest that work on landside of the fishing port involves a heavy burden on the back and legs such as

bending and the transportation of heavy items although it is much less dangerous than offshore work.

PROBLEMS AND CAUSES IN WORK SPACE

Table 5 shows facilities, which should be improved soon.   At those fishing ports where there are a number of workers, the evaluation on the volume of space is low.   Danger and the difficult in mobility are high at ports with the large amount of fish catches because of the high level of vehicle traffic.   Especially, the cars of pleasure boat users have an effect on the traffic too. Among facilities in need of improvement or new establishment, a rest room is the most urgent. The rest room is still in lack, and the current rest room is full with bad smell.   Therefore, many women workers go home to use the rest room.   The bad smell of the toilet results from the traditional toilets without flush. Resting places are mostly "homes".   The reason for the frequent use of the home for toilet and resting purposes is a little way from fishing ports.

Table 5. Facilities in need of improvement in fishing ports

Fishing Port	Wada	Chikura	Katsu-ura	Choshi	Katagai
Narrow space	• Piers • Fishing gear repair yard	None	• Fishing gear repair yard	• Anchorage • Piers • Sorting yard • Fishing gear repair yard	• Sorting yard • Fishing gear repair yard
Danger	None	None	• Piers • Sorting yard • Fishing gear repair yard	• Piers • Sorting yard	• Piers • Sorting yard • Fishing gear repair yard
Difficulty in mobility	None	None	• Sorting yard	None	• Piers • Fishing gear repair yard

CONCLUSIONS

In this paper, the characteristics of each fishing practice are discussed.   Also, the working postures are analyzed by the OWAS and the action categories are presented to identify the postures, which should be improved soon.   With the questionnaire and interviews, the facilities in fishing ports are evaluated.   Each fishing practice shows the different action categories to improve the burden from different working characteristics and postures.   The working postures with high action categories which should be improve are the preparatory work such as unloading and ice loading in trawling and round haul netting, unloading in shell dredge netting, and net repair and unloading in gill netting of prawns.   The back is the most part of bodies, which supports most burdens.   The causes of the burden are the weight of the fish bucket, and the vertical and horizontal distance between the pier and the floor of the fishing boat.   The facilities especially for the sanitation are necessary.   The high level of the physical burden occurring at the moment of unloading of the fishing practices except for round haul netting results from the several causes such as the vertical distance between the pier and the floor of the fishing boat and the weight of fish catches.

350

REFFERENCES

Takaki, N. and K. Saeki. 2001. *Researching and evaluation method of working environment at the fishing ports.* Research report of National Fisheries Research Institute Fisheries Research Agency

Yamashita, S. 2000. *Study on Improvement of Fishing Ports and Fishing Boat Functions Based on Analysis of Work Processes and Work Burden in Coastal Fishery.* Research Institute for Construction Technology for Fishing Ports and Fishing Villages.

UNESCO Report. 1999. *Human Engineering: Its Impacts.* Japan Publication Service.

Louhevaard, V. and T. Suurnakki. 1992.*OWAS: a method for the evaluation of postural load during work.* Health Centre for Occupational Safety.

EVALUATION AND IMPROVEMENT OF WORKING ENVIRONMENT AT FISHING PORTS

Kimiyasu Saeki, Nobuo Takaki and Sadamitsu Akeda

National Research Institute of Fisheries Engineering, Fisheries Research Agency
Hasaki, Ibaraki, JAPAN
kysaeki@fra.affrc.go.jp

ABSTRACT

The work at fishing ports consists of various tasks. Workers are often forced to have a bad posture under severe climatic conditions when they undertaking tasks. Such a working environment needs to be improved. In this paper, various tasks at fishing ports are broken down into three categories, then a checklist for evaluating the working environment is suggested, and moreover, some information for actual evaluation is shown. To build safe, comfortable and functional work spaces at each fishing port, it is necessary to evaluate the quality of the work space comprehensively.

INTRODUCTION

There are about 2,900 fishing ports throughout Japan. In the past 50 years, improvements have been made to many of these ports. In particular, many breakwaters and quay walls necessary for mooring the fishing boats have been built.

For example, Figure 1 shows the Choshi fishing port in Chiba Prefecture. These improvements have been undertaken at places where waves from the open sea hit against the water flowing out of the river. In the past many fishing boats have capsized here. More than 1,000 people have died in these accidents, and a memorial stone has been built nearby the fishing port to mourn the victims. However, since 1960, a train of walls separating waterway from the river has been built to ensure the safety of the port and there has been a dramatic decrease in the danger of accidents. Figure 2 shows a sand beach in Chiba Prefecture as another example. In the past, there was nowhere to moor the boats. Up until the 1970s, the fishing boats were manually pulled up onto the beach. Many women had to undertake this heavy physical labor (Karaki, 1993). But as a result of building the breakwaters and quay walls, the boats can now be easily moored, as shown in the photo.

Figure 1. Construction of Choshi fishing port in Chiba prefecture

Figure 2. Loading a fishing boat on a sand beach in the past and the present fishing port

THE FISHING PORT AS A WORK SPACE

Some new problems

As shown in the previous section, great improvements in navigation and mooring safety have been made at Japanese fishing ports in the past 50 years. However, the Japanese fishing industry is now facing some new problems. These include the decrease in the number of fishermen and the ageing of fishing village societies. There is a need to support the fishery production with this drop in labor. Furthermore, many women are working at fishing ports, and up to now, not enough consideration has been given to the labor burden of women working at fishing ports. In order to improve the appeal of the fishing industry, it is also necessary to create an environment in which it is easy for women to work.

These are the areas we will be addressing, to improve the quality of fishing ports as workspaces. There is a need to build safe, comfortable and functional work spaces at each fishing port (Takaki and Saeki, 2001).

Characteristics of fishing port work

There is a difference in the work carried out at fishing ports, depending on the type of fisheries (fixed netting, purse seine, aquaculture, etc.). Usually, the work does not involve a clear process like factory work. However, the work can be broken down into the three categories as shown in Figure 3.

354
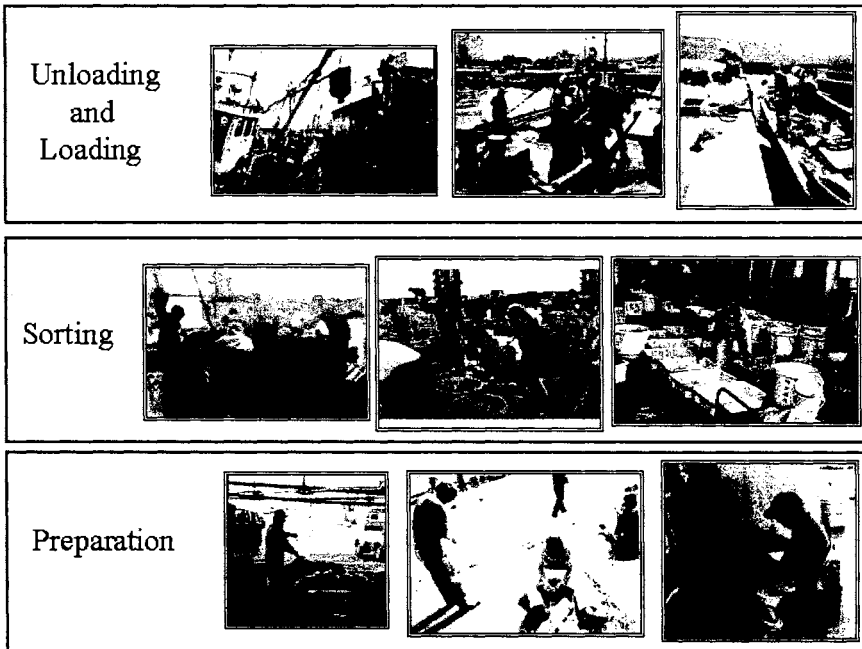
Figure 3. The three categories of the work at the fishing ports

First, there is unloading and loading work. This includes unloading the fish from the boats, and loading ice and fishing nets onto the boats.

Second, there is sorting. This involves sorting the fish that has been caught into type and size before selling. With trawling, for example, many different species of fish are caught, and sorting them tends to require heavy physical labor.

Third, there is preparation work. This involves repairing nets that have been damaged, attaching bait to the longlines and other work in preparation for the next fishing. Quite often this work is carried out while sitting on the ground of the fishing port. Furthermore, quite often it tends to require lengthy physical work.

Then, before and after all this work is done, the task of transporting the fish and the fishing implements remains. Trucks, forklifts and handbarrows are often used for this work.

Recently, some machines have begun to be introduced to fishing ports. However, even now, many manual tasks need to be done. With the unloading work, in the case of large boats, ordinarily the crane installed on the boat is used. However, small boats are not equipped with these cranes, so the work usually has to be done manually. With the sorting work, if the sorting task is simple, belt conveyors and other equipment can be used to reduce the burden on the working women. However, when many different types of fish are caught together, this

equipment cannot help the workers. An example of preparation work, the workers at the fishing ports use their own eyes and hands to stitch the nets that have been damaged. Rocks and the tide often damage these nets, which can be several hundred meters long.

Much of the work at fishing ports is not repetitive, and involves many different irregular tasks as shown in Figure 4. Furthermore, the work and the time required are greatly influenced by the season, the weather and the size of the catch. Therefore, it is difficult for researchers to recognize and analyze the content of the work of fishermen. Nevertheless, in order to clarify problems with the working environment, the actual working conditions, such as the movement of the workers, the work posture and the muscular load of the workers must be studied and understood. It is then desirable to sort thus data into figures and tables. This could be used as the base data for clarifying areas that need to be improved.

Figure 4. Different irregular tasks at fishing ports

EVALUATION OF THE WORKING ENVIRONMENT

A prototype of a checklist

For factory labor, a working environment evaluation checklist is already established (Joint Industrial Safety Council, Sweden/ILO, 1987). In Japan, evaluation and improvement of the working environment in the agricultural industry is being undertaken (BRAIN, 2000). Examples of these improvements are shown in Figure 5. On the left, an example of a reduction in lifting workload is shown, where the amount of vegetables put into a single cardboard box has been reduced and a conveyor belt has been introduced (MAFF, 1996). On the right, there is an example of a table used to sort the vegetables. The table is round, and turns easily. This means it is possible for the farmers to sort most of the vegetables in the photo while seated (JRISA, 2001).
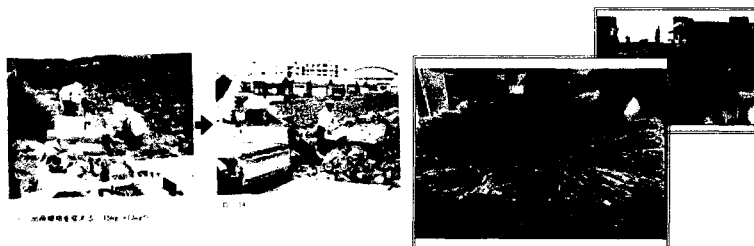

Figure 5. Improvements of the working environment in the agricultural industry

356

There is a need for a system for evaluating the present condition and making improvements at fishing ports. Table 1 is a prototype of a checklist for evaluating the safety, comfort and convenience levels of fishing ports as workspaces. Evaluation is made for three types of work: loading and unloading, sorting and preparation. These are shown in the top cells. The left cells show the items, which make the working environment better or worse. These include working posture, muscular load, avoidance of danger, the size of the workspace, protection from wind, snow and direct sunlight, and work movement. Also, the existence of toilets is an important item. Toilets should be located near the workplace.

Table 1. Checklist for evaluating the working environment at fishing ports

	Loading and unloading	Sorting	Preparation
1. Working posture	L-1	S-1	P-1
2. Muscular load	L-2	S-2	P-2
3. Avoidance of danger	L-3	S-3	P-3
4. Size of work space	L-4	S-4	P-4
5. Protection from wind, snow and direct sunlight	L-5	S-5	P-5
6. Distance to toilets	L-6	S-6	P-6
7. Work movement	L-7	S-7	P-7

The cells in Table 1 are named, such as L-1 and S-2. These cells become the items that are used for the actual evaluation. In reality, the causes of the hard work and discomfort involve many different interwoven elements. However, we believe evaluating each of the cells in the table, and ranking the present situation can make a relatively suitable evaluation.
For example, using the following four ranks can make the evaluation:
Rank D: serious problems; improvements should be made immediately
Rank C: moderate problems; improvements should be made quickly
Rank B: slight problems: improvements are desirable

Rank A: no problems

We believe this type of evaluation should be made on each fishing port.

The specific standards for the ranking should be decided after studying the actual work conditions and using ergonomic evaluation methods. As will be discussed below, some information has already been obtained for the ranking in several areas.

Evaluation of the work posture

Most workers at fishing ports complain of back or other pains. Their work posture is considered to be the main cause of these pains. Fishing industry work often requires the workers to bend their knees and backs and lean forward. This posture puts a heavy burden on the body. The work posture is affected by workers environment, such as the size of the work space, equipment being used, or desks and chairs. Workers are forced to have a bad posture when they undertaking tasks.

357

In recent years, methods for evaluating good or bad work postures have been developed, such as the OWAS, the Ovako Working Posture Analysis System method (Stoffert, 1985). It is a practical method for identifying and evaluating working postures. In OWAS procedure, upper limb position, knee angle, torso angle and the amount of load are classified with a digit code. Given a posture code, an action category can be determined and is used as the criteria to evaluate if the working method or workplace needs to be redesigned.

Typical work postures at fishing ports are classified as damaging, and something must be done to improve it (Yamashita, 2000; Saeki et al., 2002). Examples are shown in Figure 6. In the future, there is a need to make improvements to equipment and facilities at fishing ports so that the workers no longer need to have bad postures. For example, the situation shown in the photo could be improved if the worker had a desk and chair that was suitable for the task.
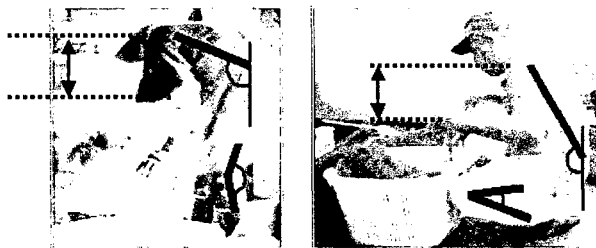
Figure 6. Evaluation of work postures at fishing ports

Problems with heat and cold

Characteristic fishing industry business is carried out in northern and southern Japan, according to the different hydrographic conditions. The left section of Figure 7 shows the operation being undertaken in Hokkaido, in northern Japan. The workers have to take the cultivated scallops out of the baskets at the fishing ports even in snow and while cold winds are blowing. The right section of the figure shows the unloading work for seaweed in Okinawa, in southern Japan. The workers have to do this work in direct sunlight. Workers in the fishing industry often have to work outside under severe climatic conditions such as these. This has a bad effect on the mental and physical health of the workers.
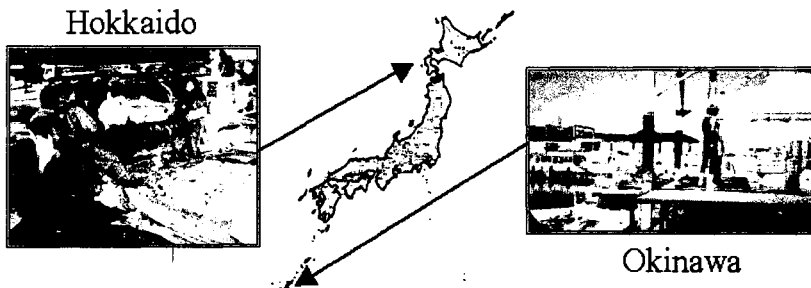
Figure 7. Fishing industry work in hot and cold regions

Several methods for evaluating the influence of cold and heat have been proposed. The Hokkaido Development Bureau has actually tried to evaluate the effect of the cold on workers at fishing ports (Sekiguchi et al., 1997). They used the wind chill index (WCI), as shown in Figure 8. This is a commonly used method for expressing the degree of cold felt by the body, taking into account the outside temperature and wind speed. Subjective data has also been collected regarding the degree of cold that fishermen can withstand. By comparing these two sets of data, improvement objectives for the WCI values have been set. In order to achieve these improvements, windbreak walls with roofs were designed and built, as shown in Figure 9. These insulate the workers from the snow and wind, and contribute to making the work more comfortable.

The evaluation of heat is also an important topic. This is because high temperatures not only affect the working environment, but also affect the freshness of the fish catch. Recently, paving the top surface of quay walls is being promoted. However, direct sunlight greatly increases the temperature of concrete and asphalt, up to as high as 57° Celsius. Therefore, the workers have to cope with these high temperatures. There is a need to evaluate and make improvements in this area.

Figure 8. WCI values and awareness of workers

Figure 9. Windbreak walls built at the fishing port in Hokkaido

RELATIONSHIP TO THE QUALITY OF LIFE

In this section, fishing work is discussed from different viewpoints.
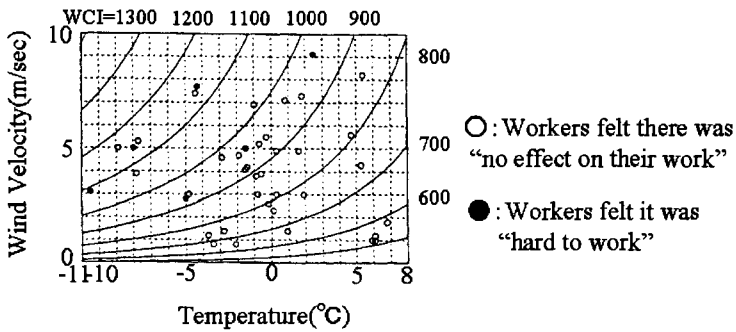
In Japan, most office and factory workers spend over an hour traveling between their home and workplace. Their working hours are rigid, and it is almost impossible for them to return home during working hours. However, as shown in Figure 10, most Japanese fishing ports are located near villages. There is no clear borderline between the living space and workplace. Therefore, the workers are able to return home briefly during their working hours, and do some housework, such as preparing meals, or doing the laundry. In other words, it is easy for them to carry out their work and domestic life.

Also, husbands and wives often work together, and sometimes friends living nearby can drop in to the fishing port. They can exchange information about their life, or share jokes while working. In this way, the workers are able to carry out even monotonous tasks in a relaxed frame of mind.

When evaluating the working environment in the fishing industry, there is a need to make suitable consideration of the relationship with this type of lifestyle. This actual evaluation is a topic for future consideration.

Figure 10. Relationship between workplace and living space

CONCLUSION

There is a need to implement improvements in the working environment at fishing ports. Therefore, there is a need for a suitable evaluation system, and the setting of objectives that need to be achieved. Also, a management system is required to make sure the improvements are made, according to the evaluation. Government departments and researchers should set up this system, evaluate the quality of the workspace at fishing ports, and assist with the introduction of improvements. This system must reflect the characteristics of the fishing industry labor. The relationship with labor and overall lifestyles is a topic that should be addressed in the future.

ACKNOWLEDGEMENTS

REFERENCES

Bio-oriented Technology Research Advancement Institution (BRAIN). 2000. The improvement of farm work: A check list (in Japanese). Saitama: BRAIN.

Japan Rural Information System Association. 2001. Safe and comfortable farm work (Videotape). Tokyo: Rural Culture Association.

Joint Industrial Safety Council, Sweden/ILO. 1987. Safety, Health and Working Conditions: A training manual. Stockholm: Prevent.

Ministry of Agriculture, Forestry and Fisheries. 1996. A guidebook for comfortable farmwork-2 (In Japanese).

Karaki, S. 1993. Umi-to-jinsei (The sea and people's lives) (in Japanese) Chiba: Ron-shobo.

Saeki, K., H.C. Park, M. Anai, S. Akeda, N. Takaki and T. Kondo. 2002. Study on fishermen's posture in sorting and repairing work. *Proceedings of Annual Conference of the Japanese Society of Fisheries Engineering* (in Japanese), 169-172.

Sekiguchi, K., S. Akeda, N. Umezawa, S. Hashimoto and T. Tanaka. 1997. Study on design of wind barrier for fishing ports, *Proceedings of Cold Region Technology Conference'97* (in Japanese), 93-100.

Stoffert, G. 1985. Analyse und Einstufung von Korperhaltungen bei der Arbeit nach der OWAS-Methode. *Zeitschrift fur Arbeitwissenschaft*, 1, 31-38.

Takaki, N. and K. Saeki. 2001. Researching and evaluation methods of working environment at the fishing ports. *Bulletin of Fisheries Research Agency* (in Japanese), No.1, 39-57.

Yamashita, N. 2000. Research on the improvement of fishing port and vessels by the analysis of work process and work load in a coastal fishery. *Report of The Japanese Institute of Technology on Fishing Ports and Communities* (in Japanese).

361

DESIGN OF TRAPS FOR SEDIMENT MANAGEMENT IN HARBORS AND NAVIGATION CHANNELS

Trimbak Parchure, Robert McAdory, Allen Teeter, and Ben Brown

US Army Engineer Research and Development Center
Vicksburg, Mississippi, USA
parchut@wes.army.mil

ABSTRACT

Most of the harbors and navigation channels in the world experience at least occasional shoaling problems, which result in loss of water depth needed for safe navigation of vessels. The major sources of shoaling include littoral transport, deposition of suspended sediment, sliding down of soft top layer along the slope of channel bank, sediment transport originating from adjacent areas, and slope instability. Catching sediment before it enters the project area is one of the effective methods for management of sediment deposition. Under favorable site and climatic conditions this can be achieved by providing a sediment trap at a carefully selected location.

Sediment traps do not catch all the sediment moving in the area. Hence dredging cannot be completely avoided, but the frequency and quantity of dredging can be significantly reduced. This increases harbor facility efficiency and results in significant cost savings on maintenance dredging. The sediment trap itself must be emptied periodically to keep it functional. Sediment traps cannot provide a general solution to channel sedimentation, however, they can be very effective in selected locations. Physical or numerical model studies are very useful in designing sediment traps. This paper describes the circumstances under which sediment traps can be effectively designed and operated for maximum benefit. Examples of sediment traps at Rollover Pass, Texas; Channel Islands Harbor, California, USA; Carolina Beach Inlet, North Carolina; and Visakhapatnam Port, India, are described. It is concluded that effective sediment traps can be designed at select sites for achieving reduction in maintenance dredging cost. Numerical and physical model studies, collection and analysis of field data on site parameters (particle size distribution of bed sediment, suspended sediment concentration, direction and magnitude of currents, bathymetry) and analysis of historical dredging records, are essential for a successful design and operation of sediment traps.

INTRODUCTION

Most of the major estuarine, coastal and inland harbors in the world are connected to the sea. Ships from the sea access the berthing areas of these harbors through navigation channels. For the prevailing drafts of commercial vessels the depth of navigation channel varies from about 10 m to 15 m. Large oil tankers require greater depths of up to 20 m. After initial navigation channel dredging, most projects require periodic maintenance dredging, which is quite expensive. Port operating agencies all over the world have continually tried adopting various ways to reduce the amount, frequency, and cost of dredging.

Catching sediment before it enters the sensitive area is one of the effective methods for management of sediment deposition. Under favorable conditions of site and climate this can be achieved by providing a sediment trap at a carefully selected location. Sediment traps do not catch all the sediment moving in the area. Hence navigation channel maintenance dredging cannot be completely avoided, but the frequency and quantity of channel dredging can be significantly reduced. This increases the efficiency of harbor facilities and results in significant cost savings on maintenance dredging. The sediment trap must be emptied periodically through dredging to keep it functional. Although the volume to be dredged from the trap may sometimes offset any reduction in project shoaling, there can still be benefits. These include a) navigation is not disrupted by shoaling in the project, b) less frequent dredging usually reduces overall dredging costs, c) the trap can be intentionally located close to dredged material disposal areas, which results in reduced transportation time and cost. Sediment traps are not very common because they can be effective only at selected locations and cannot be provided as a general solution to channel sedimentation problems. Physical or numerical model studies are very useful in designing sediment traps.

LITERATURE REVIEW

Literature on the subject of trapping sediments is found under three main categories:
Type 1: Portable traps for collecting sediment samples at project locations.
> These are used for collecting bed material samples for environmental studies or for determining the sediment transport rates in rivers or for estimation of littoral transport rates in coastal zones. Rosati and Kraus (1989) have given an exhaustive review of literature available on portable sand traps used at a large number of projects and have also given a description of a trap developed by them. Data obtained from these portable traps are useful in estimation of littoral transport rates and for designing large sediment traps.

Type 2: Estimation of sediment trapped in lakes and reservoirs.
> While lakes and reservoirs are mainly considered as storage of water for agriculture and drinking, they often collect large amounts of sediment from their catchment areas. Studies need to be conducted to determine their shoaling rates. For instance, Herb (1980) of U.S. Geological Survey studied sediment-trap efficiency for the years 1967 to 1976 for Lake Bernard Frank, a multiple – purpose reservoir in Montgomery County, MD. Total sediment outflow from Lake Frank during these years was estimated to be 5,910 tons. The entire outflow was considered to consist of suspended load with no bed load contribution. Computations based upon total estimated sediment inflow and measured total sediment outflow indicated a trap efficiency of as high as 96 percent. Studies like these help in estimating the useful life of reservoirs.

Type 3: Large traps dredged for sediment management of harbors and navigation channels.
> This is the subject of the present paper. Such traps are designed with coastal jetties at tidal inlets or elsewhere inside estuaries and rivers. Parchure and Teeter (2002a) have documented lessons learned from existing projects on shoaling in harbors and navigation channels, which also includes dredged sediment traps.

Five case studies along with details of sediment traps designed by the authors at two other projects are described in this paper.

SEDIMENT TRAP ANALYSIS

When sediment-carrying currents flow normal or near normal to a navigation channel, the channel acts like a trap in collecting a part of the sediment crossing the channel and the remaining is bypassed. Larson and Kraus (2001) have given an analysis of the sediment-trapping phenomenon and a method to work out the trapping efficiency. The parameters that affect the efficiency of sediment trap are: depth of water inside and outside of trap, type and particle size of sediment, plan area of trap, alignment of trap relative to the predominant current direction, magnitude and distribution of current velocity, and mode of transport of sediment (bed load or suspended load). Sand traps are more efficient in catching bed load transport consisting of sand than in catching suspended sediment. Larger and deeper sediment traps may be required for trapping suspended sediment.

REVIEW OF SELECT CASE STUDIES

Parchure and Teeter (2002b) have conducted a review of potential methods adopted at several projects for reducing shoaling in harbors and navigation channels. The following case studies will illustrate the effective use of sand traps at a few projects. It is interesting to note that in the case of Delaware City Channel project, studies indicated that sand traps would have an adverse effect on shoaling.

1. Delaware River Channel, Marcus Hook – Schuylkill River reach, Bobb (1967)

A fixed-bed hydraulic model was used to qualitatively assess the relative merits of several shoaling-reduction proposals consisting of seventeen plans. One of the conclusions of the study was that a combination of three sediment traps and a deepened portion of Marcus Hook anchorage would materially reduce navigation channel maintenance from the Philadelphia Navy Yard to Marcus Hook.

2. Channel Islands Harbor, California, Hobson (1982)

Sediment traps are sometimes used in conjunction with jetties to intercept and collect littoral sand, which might otherwise cause shoaling in a navigation channel. The trap is positioned to interrupt the natural flow of sand transported along a coastline before it reaches the channel. This sand is periodically dredged and placed down coast where it is reintroduced back into the natural transport system. A single updrift trap is used where longshore transport is dominantly unidirectional whereas twin traps may be employed to protect a channel where major transport reversals occur. The Channel Islands sediment trap has functioned well as designed by trapping the bulk of littoral drift sediment.

3. Carolina Beach, North Carolina, Jarrett (1988)

The sediment trap in Carolina Beach Inlet has functioned fairly well but was located too close to the main flow through the inlet to be completely effective. Studies showed that relocation of the sediment trap seaward of and away from the main channel should greatly enhance its overall sand trapping ability. Jarrett (1988) has made the following recommendations. "Sediment traps in tidal inlets should be located in areas removed from the concentrated tidal flows. For example, an ideal location for a sediment trap would be in the area of an existing interior shoal that is fed with littoral material moving off the inlet shoulders. In the case of Carolina Beach

Inlet, much of the trap was located in the area of concentrated tidal flows and, as a result, the trap only filled to about 66 percent of its dredged capacity. The trap should also be dredged as deep as possible, but not deep enough to create problem with sloughing of the adjacent shorelines into the trap."

4. Savannah Harbor, Georgia
Various plans to reduce heavy siltation in the harbor area of Front River were examined in a physical model (US Army Engineer Waterways Experiment Station, 1963). The recommended plan consisted of a sediment trap in the lower portion of Back River, and a tide gate structure in Back River upstream of the trap. The gates would be closed during ebb tide, forcing more flow down through Front River. This would flush sediments downstream in the navigation channel. The gates would be opened during flood tide, allowing normal flow up through Back River. This would divert sediments from the navigation channel into the Back River sediment trap. Relocation of the sediment deposition area not only reduced shoaling in the harbor area but also resulted in dredging operations closer to available disposal areas. Navigation channel shoaling was reduced by about 30 percent. The trap functioned very well for several years. The gates had to be removed later for environmental reasons.

5. Delaware City Channel, Bobb (1965)
The Tidewater Oil Company, Delaware Refinery, at Delaware City explored the possibility of reducing shoaling at their facility. Six plans were developed consisting of dikes and two locations of a sand trap. The results of investigations were interesting. They showed that all the plans tested had an adverse effect on total shoaling in the company channels. If the plans were implemented, total shoaling was expected to increase by amounts varying between 4% and 42% per year depending upon the plan.

DESIGN OF SEDIMENT TRAP AT ROLLOVER PASS, TEXAS

Rollover Pass is a narrow man-made channel, which connects the Gulf of Mexico and Rollover Bay. The Gulf Intracoastal Water Way (GIWW) crosses the Rollover Bay on the north side of Rollover Pass. The U.S. Army Corps of Engineer District, Galveston, maintains a navigation channel, 40 m wide and 3.6 m deep within the GIWW for commercial barge traffic. Over the past several years considerable siltation has been taking place within the GIWW in the vicinity of Rollover Pass area and periodic dredging is required for maintaining navigable depths. The U.S. Army Engineer Research and Development Center (ERDC), Vicksburg examined ways to reduce siltation of the channel. The objective of the study was to construct a working numerical model of the Rollover Pass area and to use the model for design of a sediment trap, which would be feasible and effective in reducing the frequency of dredging in GIWW. Parchure et al (2000) have described the design of a sediment trap at this location. The hydrodynamic model code RMA2, available at ERDC, was used to calculate the hydrodynamics of the system with this two-dimensional numerical model. The model was verified using hydrodynamic field data. Velocity patterns under selected tidal conditions were generated.

Sediment data collected from site included bed samples, water samples and past dredging records. Results of analysis of bed samples are given in Figure 1. It was seen that the reach of

channel directly in the path of flood currents through the inlet consisted of sand whereas on both sides of this reach the bed material consisted of fine sediments. It was noticed that the average composition of the bed samples consisted of 30% sand, 50% silt, and 20% clay. Coarse sediment appeared to be traveling from the sea all the way to the GIWW whereas East Bay has been the source of finer sediment. Analysis of dredging records showed (Fig. 2) that a length of GIWW between sections 2136 and 2166 had a much higher rate of sediment deposition. Typical flow patterns in the vicinity of the proposed sediment trap for the flood and ebb currents obtained on the numerical model are shown in Figures 3 and 4 respectively. Computation and analysis of bed shear stress patterns were used along with the velocity data to estimate where and by how much sediment deposition is expected to occur. Several alternative sediment trap layouts in terms of location, shape, size and depth were used for evaluation. The recommended layout is shown in Figure 5.

The recommended sediment trap layout has a length of 915 m and a width of 120 m and it is separated from GIWW by a distance of 60 m. The 120 m width would be needed not only for obtaining better trapping efficiency but also for providing adequate room for maneuvering a dredge inside the trap. Recommended design depth in the trap is 2.75 m, which is expected to be adequate for safe dredging operation. The width and depth of the trap may varied in the future, if found necessary and advantageous.

It is recommended that the new sediment trap be dredged over a smaller area. Its effectiveness should be monitored over the next two years after construction. Expansion of the trap over larger areas in the next two phases should be done later, if experience shows that the first phase is having the desired effect. The proposed trap is expected to catch the excessive sediment accumulating between sections 2136 and 2166 and prevent formation of a local hump, which at present necessitates more frequent dredging. Hence the sediment trap is expected to reduce the frequency between consecutive dredging operations and the average annual cost of dredging.

The recommended trap configuration has the following features. It is not connected to the GIWW over its entire length. It does not include construction of any structures. It provides one connection with GIWW for a dredge to enter. The trap does not permit a "flow-through" hydraulic condition. Phasing of dredging work for future expansion is easy and feasible. The sediment removed for making the trap should be deposited on the eroding beach, provided it is suitable for beach nourishment. Environmental impacts of the sediment trap were not examined in the study. The Galveston District has accepted the recommendation and is proceeding with plans for construction. Field data on its functioning will be available after the trap is constructed.

DESIGN OF SAND TRAP AT VISAKHAPATNAM

The ancient Visakhapatnam Port located on the east coast of India was an inland port connected to the sea by a long navigation channel. It was well protected from waves by a natural geographical configuration. Presence of bedrock at shallow depths below sea level precluded economical expansion of the port for modern deep-draft vessels up to 150,000 DWT having drafts up to 15 m. It was therefore decided to construct a new outer harbor enclosed by long breakwaters for wave protection. While littoral transport occurs in both directions at this site, the

predominant direction is northward. Hence construction of a shore-connected breakwater would result in large accumulation on the south side, eventually resulting in sand bypassing into the navigation channel after a few years. It was proposed to provide a gap between the shoreline and south breakwater and locate a sand trap within the gap (Fig. 6) for trapping littoral drift.

Parchure (1978) has described the studies conducted at the Central Water and Power Research Station, Pune, India for a new sand trap designed for the Visakhapatnam Outer Harbor. Quantitative estimation of littoral drift was a major component of this study. Wind data for the past several years were obtained from the India Meteorological Department. These were analyzed and wind rose diagrams were plotted. Wave rose diagrams were constructed using wind and fetch data in the hindcasting techniques. Wave data reported for ships from offshore locations were used for validation. Wave-induced sediment transport was computed by adopting methods recommended in the Shore Protection Manual (1984) and site-specific correlations were established between the wave energy and littoral drift rates. It was estimated that for an average annual wave climate, the net northward littoral drift would be 700,000 cu m.

Movable bed model studies were conducted on a wave-current physical model having horizontal and vertical scales of 1:240 and 1:80 respectively. Crushed walnut shells having a specific gravity of 1.36 and a median diameter of 0.6 mm were used as bed material. Field data on shoreline changes and quantities of sediment collected in the existing sand trap were used for model validation. After testing several layouts for a sand trap, the final layout shown in Figure 6 was recommended. It had a volumetric capacity of 600,000 cu m, and a bed level of 17.5 m below sea level. It was estimated that the south breakwater would arrest 21 percent of littoral drift, while the new sand trap will catch 66% and the remaining 13% would bypass the system. The new sand trap has been functioning successfully since its construction in the late 1970s.

ACKNOWLEDGMENT

REFERENCES

Bobb, W.H. 1965. Effects of proposed dikes and sediment traps on shoaling and currents in tidewater's Delaware city channels, Miscellaneous Paper No. 2-723, U.S. Army Engineer Waterways Experiment Station, Vicksburg, MS.

Bobb, W.H. 1967. Results of Hydraulic and Shoaling Studies in Marcus Hook – Schuylkill Reach of Delaware River, Miscellaneous Paper No. 2-887, U.S. Army Engineer Waterways Experiment Station, Vicksburg, MS.

Herb, W.J. 1980. Sediment–trap efficiency of a multiple–purpose impoundment, Report, North Branch Rock Creek Basin, Montgomery County, Maryland, 1968-76.

Hobson, R.D. 1982. Performance of a sand trap structure and effects of impounded sediments, Channel Islands Harbor, California,

Jarrett, J.T. 1988. Beach fill and sediment trap at Carolina Beach, North Carolina, Technical Report CERC-88-7, U.S. Army Engineer Waterways Experiment Station, Vicksburg, MS.

Larson, M. and N.C, Kraus. 2001. Estimation of suspended sediment trapping ratio for channel infilling and bypassing, ERDC/CHL CHETN-IV-34, U. S. Army Engineer Research and Development Center, Vicksburg, MS.

Parchure T. M. 1978. Movable Bed Model Studies for Visakhapatnam Outer Harbour Project. Proceedings of 47th Annual Research Session of Central Board of Irrigation and Power, India.

Parchure, T.M., B. Brown, and R.T. McAdory. 2000. Design of sediment trap at Rollover Pass, Texas, ERDC/CHL TR-00-23, Coastal and Hydraulics Laboratory, U. S. Army Engineer Research and Development Center, Vicksburg, MS.

Parchure, T.M. and A.M. Teeter. 2002a. Lessons Learned from Existing Projects on Shoaling in Harbors and Navigation Channels, Technical Note (in preparation), Coastal and Hydraulics Laboratory, U. S. Army Engineer Research and Development Center, Vicksburg, MS.

Parchure, T.M. and A.M. Teeter. 2002b. Potential Methods for Reducing Shoaling in Harbors and Navigation Channels, Technical Note (in preparation), Coastal and Hydraulics Laboratory, U. S. Army Engineer Research and Development Center, Vicksburg, MS.

Rosati, J.D. and N.C. Kraus. 1989. Development of a portable sand trap for use in the nearshore, Technical Report CERC-89-11, U.S. Army Engineer Waterways Experiment Station, Vicksburg, MS.

Shore Protection Manual. 1984. U.S. Army Engineer Waterways Experiment Station, Government Printing Office, Washington, DC.

U.S. Army Engineer Waterways Experiment Station, 1963, Savannah Harbor Investigation and Model Study: Vol. III, Results of model Investigations, Section 3, Results of Supplemental Tests. Technical Report No. 2-580, Vicksburg, MS.
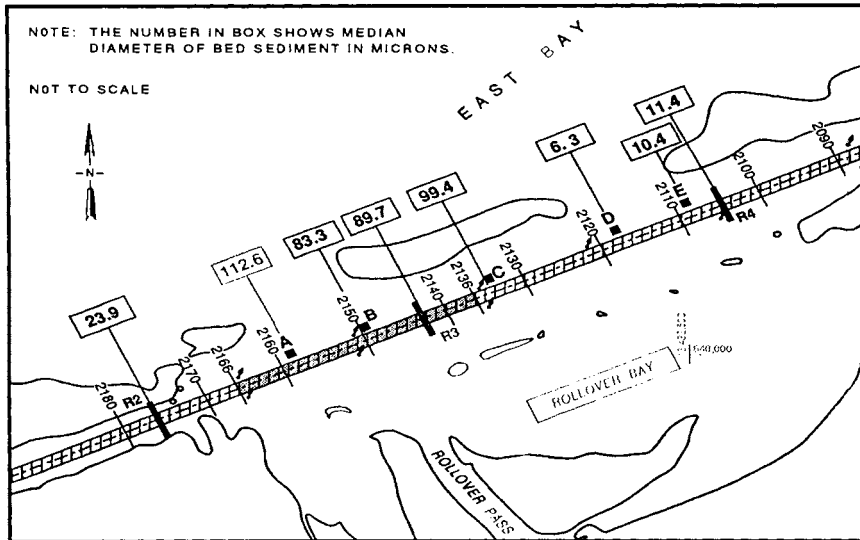
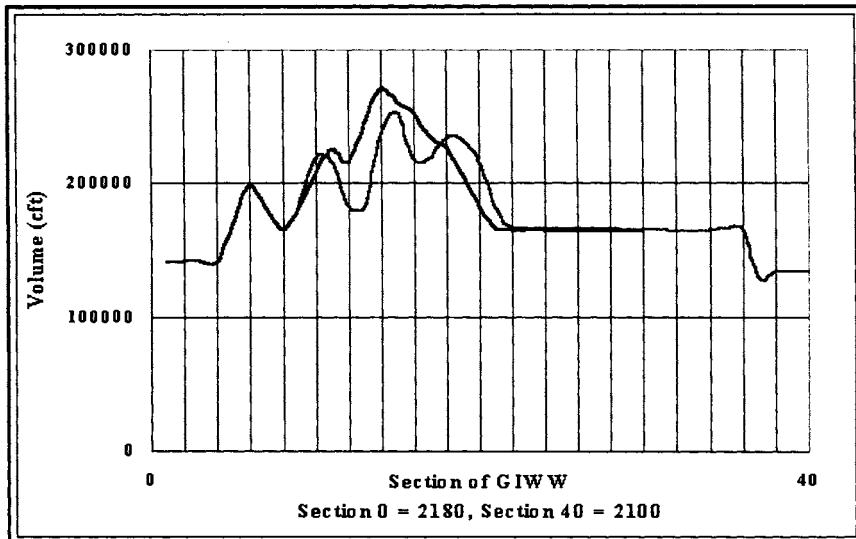Figure 1. Bed material size in GIWW at Rollover Pass

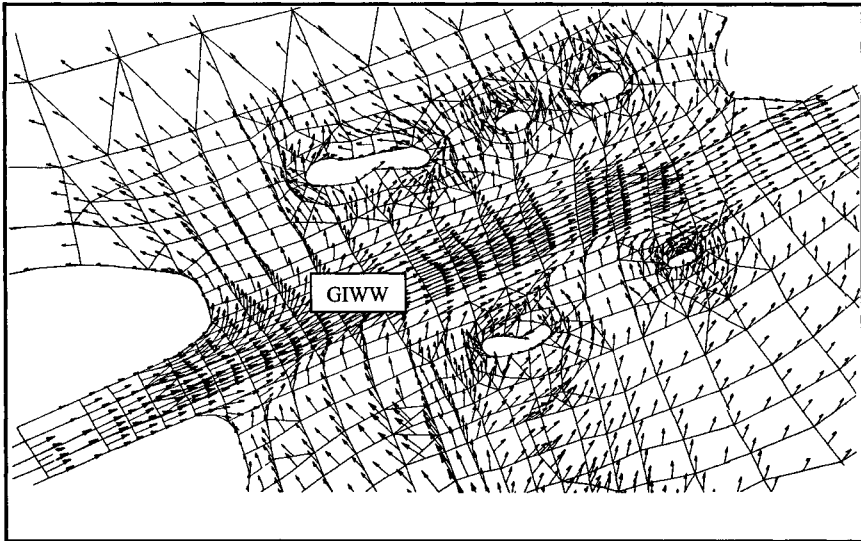Figure 2. Historical dredging quantities in GIWW
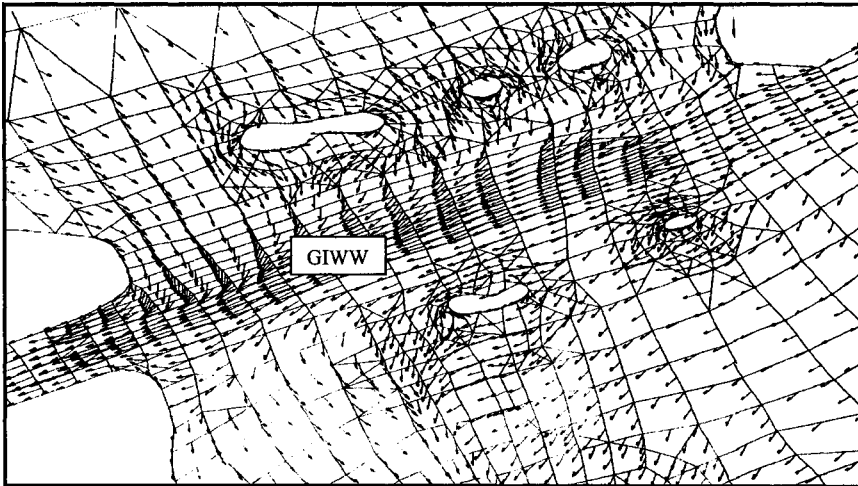
Figure 3. Flow pattern during flood tide
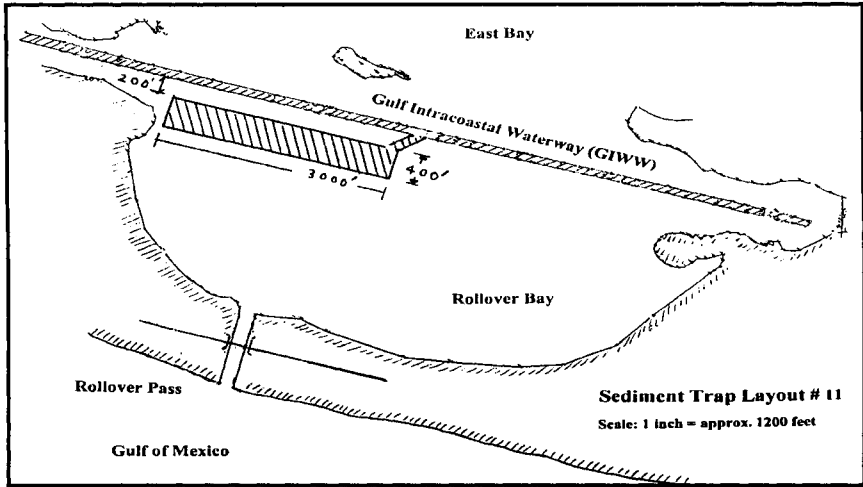

Figure 4. Flow pattern during ebb tide

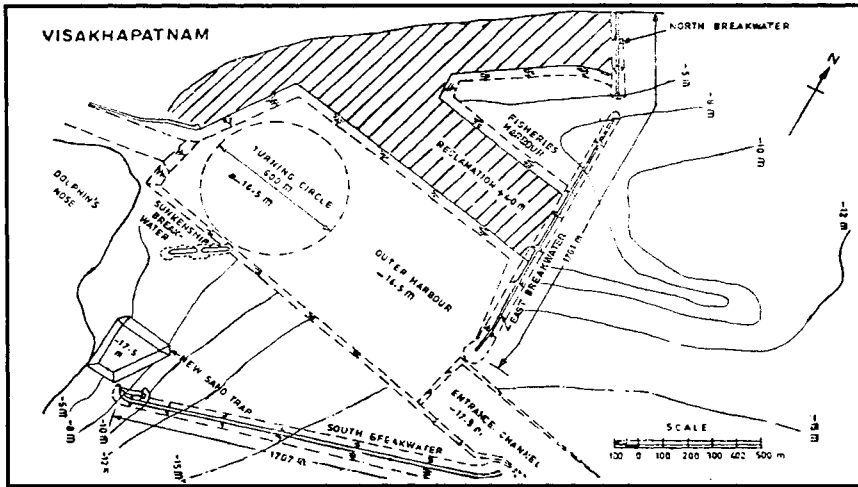Figure 5. Sediment trap recommended at Rollover Pass

Figure 6. Sediment trap at Visakhapatnam Port

372

LISST/ADCP OBSERVATION OF SUSPENDED SEDIMENT PROFILES IN THE SURF ZONE

Shigeru Kato[1], Takao Yamashita[1] and Abbas Yeganeh Bakhtiary[2]

[1]Disaster Prevention Research Institute, Kyoto University
Gokasho, Uji, Kyoto, JAPAN
katou@rcde.dpri.kyoto-u.ac.jp

[2]Department of Civil Engineering, Iran University of Science & Technology
Tehran, IRAN

ABSTRACT

Undertow (offshore-going current under the strong wind and wave conditions) may be the main cause of severe beach erosion. In the surf zone, undertow induced by the mean sea level set-up due to wind and waves, will be strong enough to transport sediment offshore through the surf zone. It is very important to measure offshore-going sediment transport rate, particularly suspended load, which is directly related to the current. The field observations of (1) the vertical mean current profile by the ADCP, (2) concentration of suspended sediment and its mean diameter by the LISST-25 and (3) wave conditions by ultrasonic-type wave gauges in the nearshore zone, were conducted using the observation pier in the Ogata Coast. A scheme for separation of air bubble and suspension in the LISST-25 data was developed. The vertical profile of suspended sediment and the flux of offshore-going suspended load were estimated with observed profile data of current and sediment concentration under the condition including storm events.

INTRODUCTION

A bursting of undertow (sudden occurrence of strong offshore-going near-bottom currents) has often been observed in the surf zone under winter storm conditions in the Ogata Coast facing the Japan Sea (Yamashita et al., 1998; Kato et al., 2000). This phenomenon should be generated by mean water set-up due to wind and breaker-induced cross-shore currents and the velocity frequently exceeds 0.5 m/s. Moreover, they can be observed even in a region of 10-15 m in depth (near the closure depth for sediment movement). Net volume of cross-shore sediment transport and sediment sorting may be determined by the power relationship between suspended load and bed load and the current fields combined wave motion with undertow. Suspended load in the surf zone can be generated with combined current fields of undertow and pick-up forces due to wave motion. Bed load can be determined from the shear stress field caused by asymmetry of wave motion and the near-bottom mean current of undertow. When the shear stress caused by asymmetry of wave motion is stronger than that of undertow, the net volume of bed load moves onshore in the surf zone, the shear stress by undertow is stronger, direction of the bed load is offshore. However, the suspended load in the surf zone is always in the direction offshore because of the existence of offshore-going near-bottom mean current (undertow). We

may have a lot of general knowledge about dynamics of suspended sediment generated by fluid motion of waves, turbulence and mean currents. However, very limited knowledge is available for suspended sediment in the real coast under storm conditions. Many studies that include measurement of suspended sediment have been carried out; e.g. Williams et al. (1999a) and Rijn (1984) in a laboratory; Williams et al. (1999b) and Rose et al. (2001) in a uniform current condition of river or tide; Katayama et al. (1999), Izumiya et al. (1999) and Beach et al. (1996) in the calm sea conditions. There are very few measurements of active suspended sediment in the storm conditions (Williams et al. 1996; Miller, 1999).

Recent development of measuring equipment in the coastal ocean, such as acoustic Doppler current profiler (ADCP) and Laser turbidimeter, makes it possible even under the storm condition to measure suspended load directly in the surf zone if we can make use of observational coastal structure, such as a pier or tower in the nearshore zone. In this study, using the observation pier in the surf zone, we carried out the observation of suspended load and sea states under the storm condition with the following measurements: (1) vertical profile of suspended sediment by the LISST-25 (Laser In-Situ Scattering and Transmissiometry), (2) vertical profiles of mean currents by the ADCP, (3) wave conditions by ultrasonic wave gauges, and (4) wind velocities by the 3-components ultrasonic anemometer.

The scheme of separation of air bubble and suspension in the LISST-25 data, which contains air bubbles entrained by wave breaking, was developed. The vertical profile of suspended sediment and the flux of offshore-going suspended load are estimated with observed profile data of current and sediment concentration under winter sea condition including storm events. Finally, the relationship between the net sediment transport toward offshore from the surf zone and the incident wave energy flux was discussed.

OBSERVATION

We conducted an observation of suspended load profiles by using the T-shaped Observation Pier (TOP), Disaster Prevention Research Institute (DPRI), Kyoto University, in the Ogata Coast facing the Japan Sea, in winter 2002. Seven ultrasonic wave gauges and a propeller-type anemometer are installed to measure wave and wind conditions for a 20-minute period every hour throughout the year along this pier. A 3-component ultrasonic anemometer was installed to measure wind shear and mean velocity. An ADCP was also installed on the sea bottom at the offshore end of TOP to measure the vertical profiles of nearshore currents. As the ADCP was connected with a cable, it was possible to supply its power and to send data to the observation room on the pier, where a personal computer saved the ADCP data. The standard deviation of ADCP measurements is about 2.0 cm/s in this observation. Wave gauges record sea surface elevation during 20 minutes every hour with 10 Hz sampling frequency. The ADCP measures the vertical profile of mean current (30 seconds average). The observation for suspended sediment by LISST-25 was carried out at the same measuring points as the ADCP during 28 hours, from 8:00 on February 9 to 12:00 on February 10, 2002, every two or three hours. The LISST-25 can measure the mean diameter (μm), particle volume concentration (μl/l) and optical transmission. Its range of particle size is from 1.25 to 250 μm. The output of LISST-25 data is recorded by averaging over ten seconds (30 sampling data). The vertical profile of LISST data

was measured by manually moving from the bottom to the surface along the messenger wire rope, and data were obtained during each 5 minutes at the five heights as shown in Figure 1. Then, we obtained thirteen datasets by the LISST-25, the ADCP and wave gauges (Table-1).

Figure 1.   Set up of field observations at the pier

Figure 2 shows the observed data of wave, wind and current in February and the observation period. $H_{1/3}$ is the significant wave height, W is the wind velocity averaged over 20 minutes and U_b is the current velocity averaged over 10 minutes near the sea bottom.   The maximum wave height was 4.5 m at the top of the pier, and the maximum instantaneous wind speed was 15 m/s. Most of waves broke off the pier, and broke again around the horizontal bridge of the pier. Therefore, this observation was conducted in the surf zone and in the storm conditions.

The volume concentration and mean diameter measured by LISST-25 are shown in Figure-3, in which dots indicate the ensemble averaged values and error bars indicate the maximum and minimum values of each 5-minute measurement.   Figure 3(a) shows the data of the volume concentration, and (b) shows the data of mean diameter.   The concentration near the sea surface and the bottom represent two peaks.   Judging from the wave conditions under storm condition, the peak near the sea surface may be caused with air bubbles generated by wave breaking.   The vertical profiles of the mean diameter are similar to those of the concentration. Near the sea surface, particles are large, and at the middle layer, the diameters become smaller. Measurements by Farmer et al. (1998) in the Gulf of Mexico showed that the size of entrained air bubble generated by wave breaking at 0.7 m below the sea surface was in the range of 80 - 200 μm, and the size became smaller with increasing depth.   In our observations, the size of the mean diameters near the sea surface is in the range of 40 - 120 μm, and the size becomes smaller with

375

increasing depth too. Consequently, these vertical profiles of volume concentration can be regarded as mixture of suspended sediment and air bubble entrained by surface wave breaking.

[020908]

z(m)	time(hh:mm:ss)
0.0	7:48:45- 7:53:45
0.5	54:00- 59:00
1.5	59:10- 8:04:10
3.0	8:04:20- 09:20
4.0	09:40- 14:40

[020915]

z(m)	time(hh:mm:ss)
0.0	14:55:30-15:00:30
0.5	15:00:40- 05:40
1.5	05:50- 10:50
3.0	11:00- 16:00
4.0	21:10- 26:10

[021001]

z(m)	time(hh:mm:ss)
0.0	0:58:10- 1:03:10
0.5	1:03:20- 08:20
1.5	08:40- 13:40
3.0	13:50- 18:50
4.0	19:10- 24:10

[021012]

z(m)	time(hh:mm:ss)
0.0	11:57:00-12:02:00
0.5	12:02:10- 07:10
1.5	07:20- 12:20
3.0	13:00- 18:00
4.0	18:10- 23:10

[020909]

z(m)	time(hh:mm:ss)
0.0	9:04:50- 9:09:50
0.5	10:20- 15:20
1.5	19:00- 24:00
3.0	24:40- 29:40
4.0	29:50- 34:50

[020917]

z(m)	time(hh:mm:ss)
0.0	17:04:50-17:09:50
0.5	10:00- 15:00
1.5	15:10- 20:10
3.0	20:20- 25:20
4.0	25:30- 30:30

[021004]

z(m)	time(hh:mm:ss)
0.0	4:06:00- 4:11:00
0.5	11:10- 16:10
1.5	16:20- 21:20
3.0	21:40- 26:40
4.0	26:50- 31:50

[020911]

z(m)	time(hh:mm:ss)
0.0	10:57:30-11:02:00
0.5	11:02:10- 07:10
1.5	07:20- 12:20
3.0	12:30- 17:30
4.0	17:40- 22:40

[020919]

z(m)	time(hh:mm:ss)
0.0	18:55:30-19:00:30
0.5	19:00:40- 05:40
1.5	05:50- 10:50
3.0	11:00- 16:00
4.0	16:10- 21:10

[021007]

z(m)	time(hh:mm:ss)
0.0	7:05:00- 7:10:00
0.5	10:10- 15:10
1.5	15:20- 20:20
3.0	20:40- 25:40
4.0	25:50- 30:50

[020913]

z(m)	time(hh:mm:ss)
0.0	12:57:00-13:02:00
0.5	13:02:10- 07:10
1.5	07:20- 12:20
3.0	12:30- 17:30
4.0	17:40- 22:40

[020922]

z(m)	time(hh:mm:ss)
0.0	21:58:20-22:03:20
0.5	22:03:30- 08:30
1.5	08:50- 13:50
3.0	14:00- 19:00
4.0	19:20- 24:20

[021010]

z(m)	time(hh:mm:ss)
0.0	10:03:20-10:08:20
0.5	08:30- 13:30
1.5	13:40- 18:40
3.0	19:00- 24:00
4.0	24:10- 29:10

Table 1.   Lists of datasets obtained by LISST-25, wave gauges and ADCP
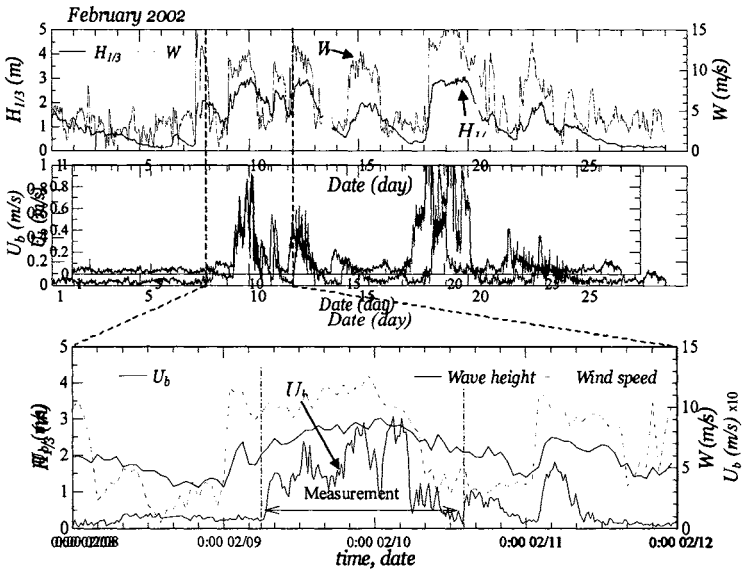
Figure 2.   Observed data of wind, wave and current in February 2002

376

(a) Concentration
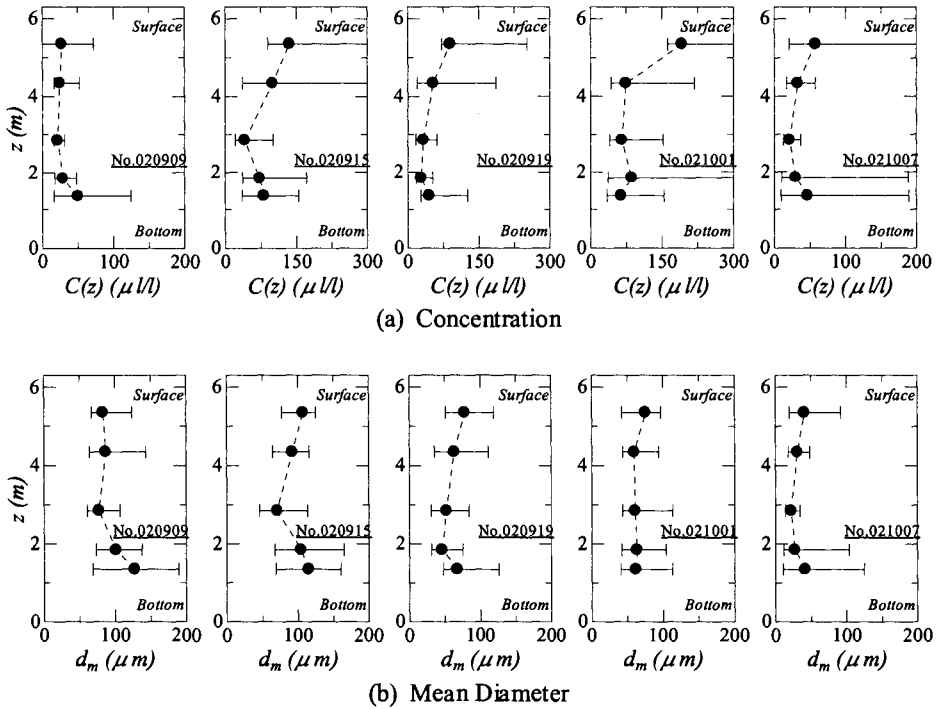
(b) Mean Diameter

Figure 3. Vertical profiles of the volume concentration and its mean diameter obtained by LISST-25

ESTIMATION OF VERTICAL PROFILES OF SUSPENDED SEDIMENT AND ENTRAINED AIR BUBBLE

The vertical profile of suspended sediment concentration is estimated by the following Vanoni Distribution, Equation (1) (Vanoni, 1975).

$$C(z) = C_b \left(\frac{D-z}{z} \frac{b}{D-b} \right)^\alpha \tag{1}$$

$$\alpha = \frac{w_s}{\kappa U_{fc}} \tag{2}$$

$$w_s = \left(\frac{\gamma_s}{\gamma} - 1 \right) \frac{g \, d_m^2}{18\nu} \tag{3}$$

where, $C(z)$ is the vertical profile of suspended sediment concentration, C_b is sediment concentration at the reference height, b (m), z is the height from bottom (m), D is the depth (m), w_s is the fall velocity of particle (m/s), κ is von Karman's constant (=0.4), U_{fc} is the critical friction velocity due to current and wave (m/s), γ, γ_s is the density of water and sediment (kg/m^3),

377

respectively, g is the acceleration of gravity (m/s^2), d_m is the mean diameter of sediment particle (m) and ν is the kinematic viscosity (m^2/s). As this distribution was originally proposed by Rouse (1937), α is called as Rouse number. U_{fc} is estimated using by the logarithmic current profile analysis by Rose et al. (2001), Soulsby et al. (1987), and using the turbulent kinetic energy method with the approximation of quasi-steady flow condition and turbulence data of Soulsby (1983) and Rose et al. (2001). Equation (1) was proposed for steady currents. In this study, the following equations are employed to estimate U_{fc} (Fredsoe et al., 1992) taken into account the critical friction velocity in wave and current condition,

$$U_{fc} = \sqrt{\frac{2}{\pi} f_w U_{1m} U_\delta} \tag{4}$$

$$U_{1m} = \frac{\pi H_s}{T_s \sinh(kD)} \tag{5}$$

$$a = \frac{U_{1m}}{\omega} = U_{1m} \frac{T_s}{2\pi} \tag{6}$$

$$f_w = 0.04 \left(\frac{a}{k_N} \right)^{-0.25} \quad ; \quad \frac{a}{k_N} > 50$$

$$= 0.4 \left(\frac{a}{k_N} \right)^{-0.75} \quad ; \quad \frac{a}{k_N} \leq 50 \tag{7}$$

where, f_w is the friction coefficient, U_δ is the mean current (m/s), U_{1m} is the current due to wave (m/s), H_s is the wave height (m), T_s is the wave period (s), ω is the angular frequency of waves, k is the wave number and k_N is the bottom roughness length (m). The ADCP data near the sea bottom are used as U_δ, H_s and T_s are given by wave gauges' data.

As mentioned before, the LISST-25 data contain both sediment particles and entrained air bubbles caused by surface wave breaking. It is necessary to separate suspended sediment and bubbles in the data. First, the vertical profile of sediment concentration is estimated by above equations with two measurements near the bottom, $C(z_1)$ and $C(z_2)$, which are indicated in Figure-4. The reference concentration, C_b, and its height, b, are determined as an average of $C(z_1)$ and $C(z_2)$, and that of z_1 and z_2. Then, the entrained air bubble concentration near the sea surface is estimated by subtracting sediment concentration from the observed concentration. Finally, the vertical profile of bubble concentration, $C_{bubble}(z)$ is estimated by the least squares method with the exponential function, Equation (8).

$$C_{bubble}(z) = A e^{Bz} \tag{8}$$

where, A and B are fitting parameters.

Figure 5 shows the estimated vertical profiles of suspended sediment, the entrained air bubble and the total concentration together with the raw data measured by LISST-25. The entrained air bubble concentration increases in proportion to the wave heights, which indicate the possibility of wave breaking.

In the separation scheme developed in this study, we assumed the zero concentration of the entrained air bubble at the sea bottom (actually, 1 µl/l was assumed instead of the zero concentration). However, the entrained bubbles of wind wave breaking can be measured even at the point of five times of the significant wave height (Yoshioka et al., 1998). Since the observation in this study was carried out inside the surf zone in the storm condition, the assumption of zero-concentration at the sea bottom is not always valid. There is some possibility of overestimation of suspended sediment concentration near the bottom.
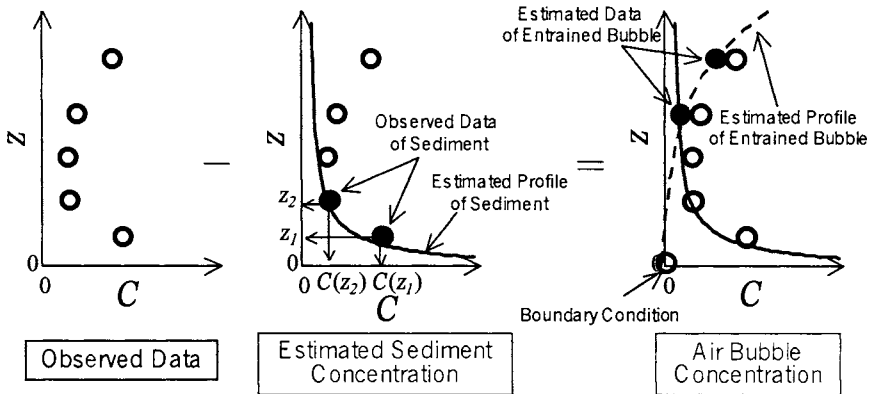
Figure 4. The separation scheme of suspended sediment and air bubbles in the vertical profile of concentration data measured by LISST-25
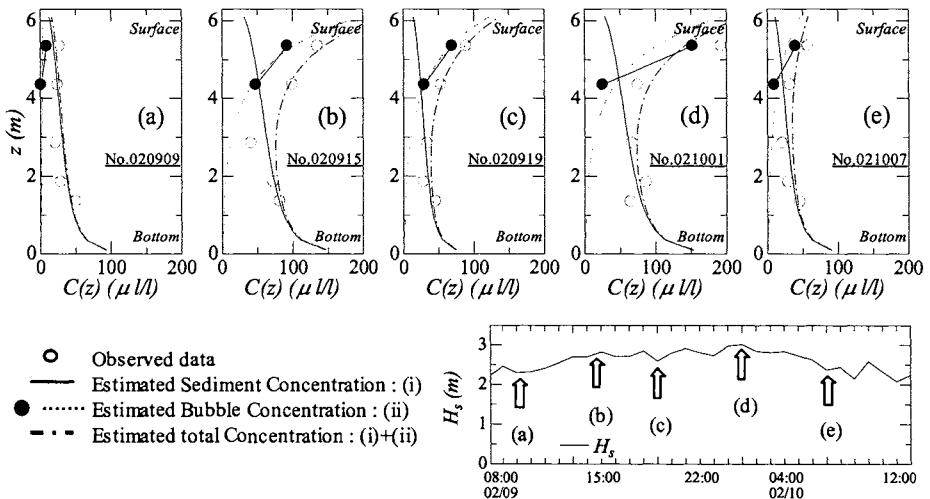
Figure 5. Estimated profiles of suspended sediment and air bubble concentrations

NET FLUX OF CROSS-SHORE SUSPENDED SEDIMENT

Net flux of cross-shore suspended sediment per unit width, Q_s, is calculated by multiplying the estimated sediment concentration, $C(z)$, by the mean current, $U(z)$, as shown in Figure 6. The successive results of the net flux of suspended sediment is shown in Figure 7. The sediment flux becomes larger when strong offshore-going current U_{off} occurs. Then, the volume of the sediment flux corresponds to the magnitude of the mean current $U(z)$. The total sediment flux during this storm, $Q_s|_{Total}$ is also calculated with Equations (9) and (10), resulting in the approximation of 10 m^3/m/storm.

$$Q_s = \sum_z C(z)U(z)\,dz \tag{9}$$

$$Q_s|_{Total} = \sum_T Q_s \Delta T \tag{10}$$

where, $z = 1.35$ m to 5.1 m, $dz = 0.25$ m, $T = 29$ hours and $\Delta T = 2$ or 3 hours.

As a representative parameter of wave energy flux, the following F is defined based on the significant wave height and period:

$$F = H_s^2 T_s \tag{11}$$

The linear relationship between the estimated sediment flux, Q_s and the wave energy flux, F, is shown in Figure 8. It is revealed that offshore-going sediment occurs when wave energy flux exceeds a critical value, F_c. Thus, it will be possible to estimate offshore-going sediment flux based on the wave conditions in the surf zone.
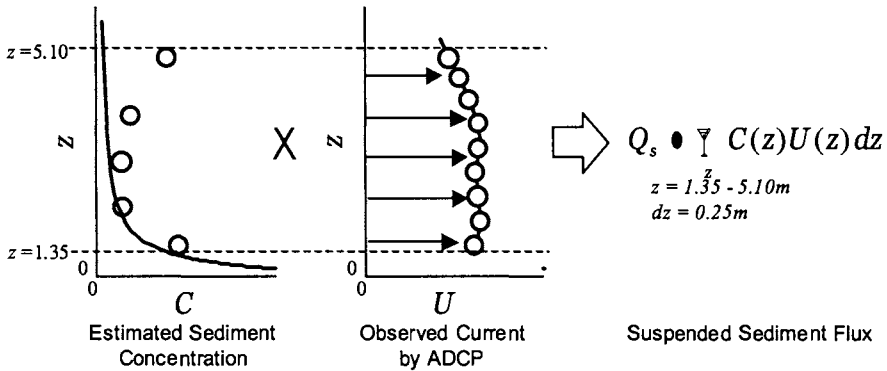
Figure 6.   Calculation of suspended sediment flux using the estimated and observed data
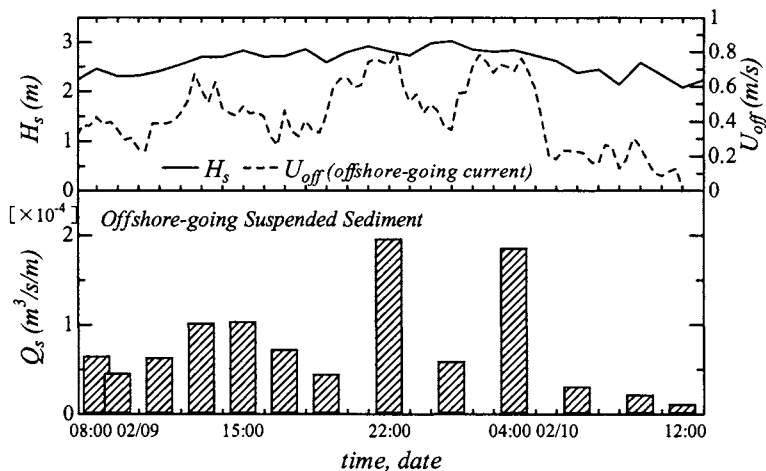
Figure 7. Time series of estimated offshore-going sediment flux during the storm condition
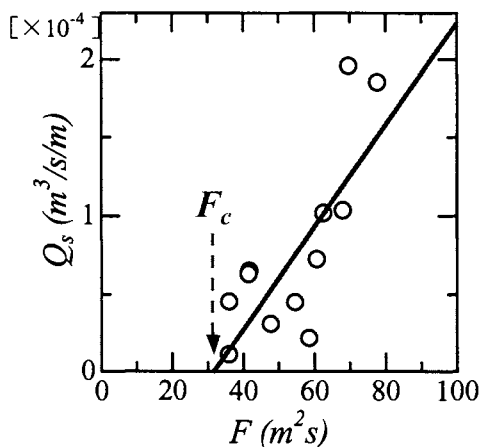
Figure 8. Relationship between wave energy flux and cross-shore flux of suspended sediment

IMPROVEMENT OF LISST-25 OBSERVATION

The data obtained in these observations will be useful for the estimation of an amount of sediment transport in the surf zone, and for the prediction of the sea bottom changes in coastal regions. However, there still exist some uncertainties about the accuracy of the LISST-25 in field observations. Therefore, it will be necessary (i) to calibrate the accuracy of LISST-25 in a laboratory and field site, (ii) to confirm the applicability of LISST-25 in field observations, and (iii) to obtain a large amount of data under the various sea conditions.

CONCLUSIONS

Filed observations of the vertical profiles of suspended sediment concentration, coastal currents and waves by employing LISST-25, ADCP and wave gauges were conducted in the surf zone under storm conditions using the T-shaped Observation Pier in the Ogata Coast. The main conclusions are summarized below.

(1) The vertical profiles of suspended sediment concentration and air bubble concentration, which may be entrained by wave breaking, were estimated using observed data by the LISST-25, the ADCP and wave gauges and employing Vanoni distribution.

(2) The offshore-going suspended loads in the surf zone under the storm conditions are estimated based on the derived suspended sediment concentration.

(3) The linear relationship between offshore-going suspended sediment flux and wave energy are shown. It will be possible to estimate offshore-going sediment flux based on wave conditions.

ACKNOWLEDGEMENT

REFERENCES

Beach, R.A. and R.W. Sternberg. 1996. Suspended-sediment transport in the surf zone: response to breaking waves, *Continental Shelf Research*, Vol.16, No.15, pp. 1989-2003.

Farmer, D.M., S. Vagle and A.D. Booth. 1998. A free-flooding acoustical resonator for measurement of bubble size distributions, *J. Atmospheric and Ocean Tech.*, pp. 1132-1146.

Fredsoe, J. and R. Deigaard. 1992. *Mechanics of coastal sediment transport*, World Scientific, 369p.

Izumiya, T., T. Kunita, M. Izumi, H. Nagamatsu and K. Ishibashi. 1999. Field observation of temporal and spatial variation of concentration of silty fine sand estimated from ADCP data, *Proc. of Coastal Eng., JSCE*, Vol.46, pp. 576-580. (in Japanese)

Katayama, H., A. Okayasu and T. Nagata. 1999. Field measurements of suspended sediment concentration and grain size distribution by high speed water sampling system, *Proc. of Coastal Eng., JSCE*, Vol.46, pp. 571-575. (in Japanese)

Miller, H.C. 1999. Field measurements of longshore sediment transport during storms, *Coastal Eng.*, Vol. 36, pp. 301-321.

Rijn, L.C. 1984. Sediment transport, Part II: suspended load transport, *J. Hydraulic Eng.* Vol.110, No.11, pp. 1613-1641.

Rose, C.P. and P.D. Thorne. 2001. Measurements of suspended sediment transport parameters in a tidal estuary, *Continental Shelf Research*, Vol.21, pp. 1551-1575.

Soulsby, R.L. 1983. The bottom boundary layer of shelf seas. In: Johns, B. (Ed.), *Physical Oceanography of Coastal and Shelf Seas*, pp. 189-266.

Soulsby, R.L. and B.L.S.A. Wainwright. 1987. A criterion for the effect of suspended sediment on near-bottom velocity profiles, *J. Hydraulic Res.*, 25(3) pp. 341-356.

Vanoni, V.A. 1975. *Sedimentation Engineering*, ASCE Manuals and Reports of Engineering Practice No.54, New York, p. 76.

Yamashita, T., H. Yoshioka, M. Lu and S. Kato. 1997. ADCP observation of nearshore current structure in the surf zone, *Proc. of Coastal Eng., JSCE*, Vol.44, pp. 361-365. (in Japanese)

Yoshioka, H., S. Serizawa and T. Takayama. 1998. Acoustic observation of sea surface boundary layer (bubble entrainment at wind wave breaking), *Proc. of Coastal Eng., JSCE*, Vol.45, pp. 71-75. (in Japanese)

Williams, J.J., C.P. Rose and L.C. Rijn. 1999a. Suspended sediment concentration profiles in wave-current flows, *J. Hydraulic Eng.*, Vol.125, No.9, pp. 906-911.

Williams, J.J., C.P. Rose, P.D. Thorne, B.A. O'Connor, J.D. Humphery, P.J. Hardcastle, S.P. Moores, J.A. Cooke and D.J. Wilson. 1999b. Field observations and predictions of bed shear stresses and vertical suspended sediment concentration profiles in wave-current conditions, *Continental Shelf Research*, Vol.19, pp. 507-536.

Williams, J.J., C.P. Rose, P.D. Thorne, L.E. Coates, J.R. West, P.J. Hardcastle, J.D. Humphery, S.P. Moores and D.J. Wilson. 1996. Observed suspended sediments in storm conditions, *Proc. 25th ICCE*, pp. 3257-3296.

SHORELINE CHANGE DUE TO CONSTRUCTION OF INTAKE BREAKWATERS OF WOLSUNG NUCLEAR POWER PLANT

Kyung-Duck Suh[1] and Yong-Taek Oh[2]

[1]School of Civil, Urban, and Geosystem Engineering
Seoul National University
Seoul, KOREA
kdsuh@snu.ac.kr

[2]Korea Port Engineering Corp.
Seoul, KOREA
dragon5@korea.com

ABSTRACT

The Naari beach located at the southern part of the east coast of Korean Peninsula has experienced severe shoreline change during the first several years after the construction of the intake breakwaters of the Wolsung Nuclear Power Plant. The beach was largely accreted at the northern part, while severe erosion occurred at the southern part, eventually causing damage of the seawall behind the beach. In the present study, we analyze the shoreline change using aerial photographs taken before and after the construction of the nuclear power plant. Also a curvilinear-coordinate shoreline evolution model combined with a Cartesian-coordinate wave model is used to calculate the shoreline change, which is compared with the observed shoreline change through the analysis of the aerial photographs.

INTRODUCTION

The Wolsung nuclear power plant is located at the southern part of the east coast of Korean peninsula as shown in Figure 1. It has intake breakwaters in the south, and outfall breakwaters in the north. The Naari beach is located to the south of the nuclear power plant. The intake breakwaters were completed on September 24, 1979. After the intake breakwaters were constructed, severe erosion occurred at the southern part of the Naari beach, whereas severe accretion occurred at its northern part. Figure 2 shows several photographs of the beach. The upper left photo is the view from the center of the beach to the north. The power plant buildings are shown in the middle, and the intake breakwaters extended to the right. The upper right is the view from the center of the beach to the south. The lower right shows the southern end of the beach, where the beach is very narrow because severe erosion occurred there. The beach material consists of gravel and coarse sand on the beach as shown in the lower left photo, but it changes to fine sand in deeper water.

The purpose of the present study is to calculate the shoreline change using a numerical model and to compare the results with the measurement. Because there is no direct measurement data of the shoreline change, we used the aerial photographs taken by the National Geography

Institute, Ministry of Construction and Transportation, Korea, before and after the construction of the nuclear power plant. A curvilinear-coordinate shoreline evolution model combined with the RCPWAVE model (Ebersole et al., 1986) is used to calculate the shoreline change. The wave hindcasting data of the Korea Ocean Research and Development Institute are used to provide the RCPWAVE model with the offshore boundary wave conditions.
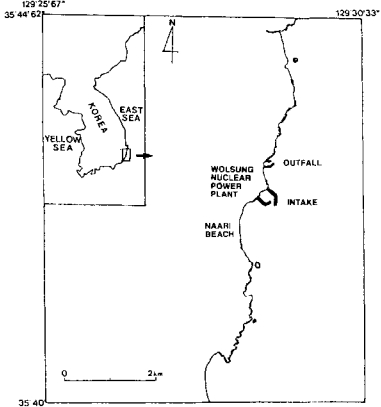
Figure 1. Site map of Wolsung nuclear power plant and Naari beach
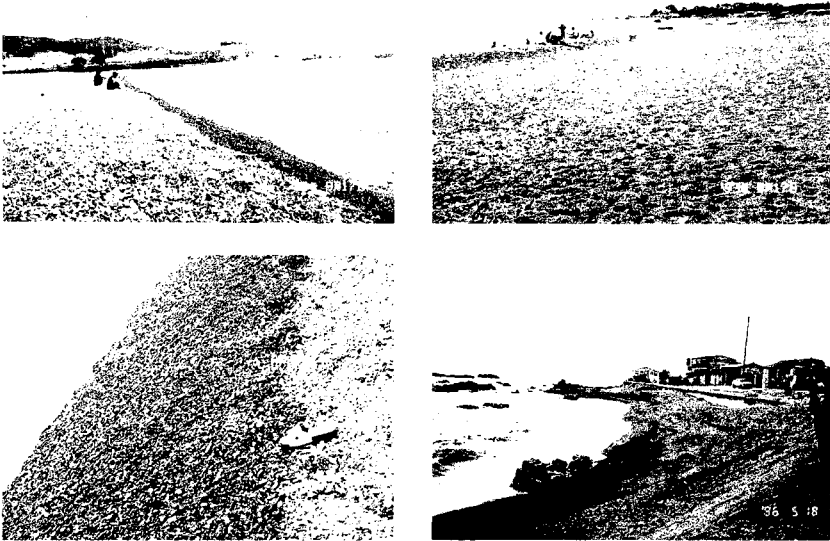
Figure 2. Photographs of Naari beach

ANALYSIS OF SHORELINE CHANGE USING AERIAL PHOTOGRAPHS

Figure 3 shows the aerial photographs taken by the National Geography Institute almost every five years.   We can see that the intake breakwaters were expanded between 1993 and 1996.   In the photographs taken in 1993 and 1996, it is very hard to read the shoreline data because of severe wave breaking.   Therefore, these were not included in the analysis of shoreline change.

| Sep. 1977 | Sep. 1982 | Oct. 1987 |

| Apr. 1993 | Sep. 1996 | Nov. 2001 |
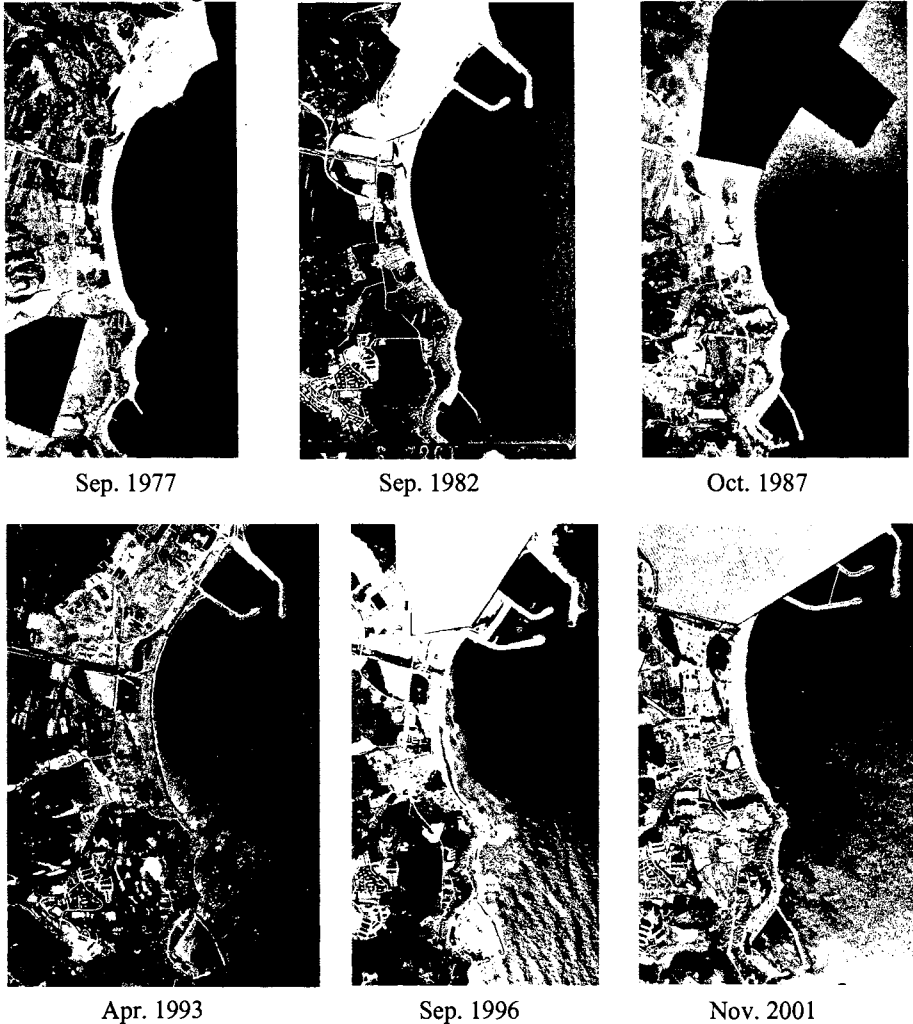
Figure 3.   Aerial photographs

We cannot immediately use the aerial photographs as shown in Figure 3 because each of them was taken from a different altitude and at a different angle.   In order to make use of the aerial

photographs, first we have to make the geometric correction of the original photographs such that the image of the photograph and the real topography become similar figures. This correction process is called rectification. We used the image-processing program, Imagine version 8.4 of ERDAS, digital maps, and topographical maps of 1:5,000 scale for the rectification. Figure 4 shows examples of the rectified image of the photographs. As one can see, between 1977 and 1982, severe erosion occurred at the southern part, whereas severe accretion occurred at the northern part.

Sep. 1977   Sep. 1982
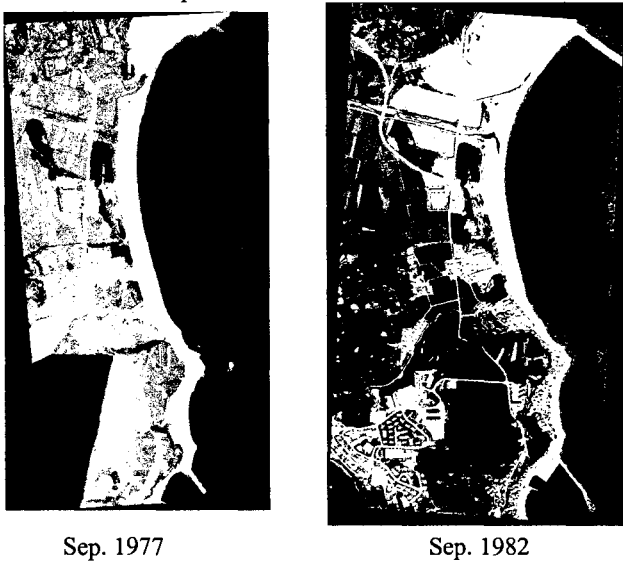
Figure 4. Rectified images of aerial photographs
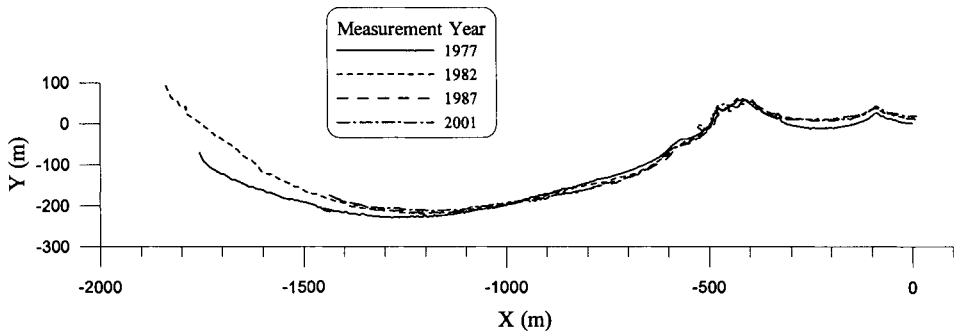
Figure 5. Shoreline change between 1977 and 2001

Figure 5 shows the shoreline change between 1977 and 2001. The shoreline changed significantly between 1977 and 1982, but only minor change occurred after 1982. Since the

388

intake breakwaters of the nuclear power plant were completed in 1979, we could say that the significant shoreline change was caused by the construction of the intake breakwaters. Therefore, in this study, we calculate the shoreline change for the three years from September 1979, when the intake breakwaters were completed, to October 1982 when the first aerial photograph was taken after the construction of the breakwaters.

NUMERICAL MODELS

Shoreline Evolution Model

We used the shoreline evolution model using the curvilinear coordinate system of Suh and Hardaway (1994). The curvilinear coordinate system of the model is shown in Figure 6 along with some other notations. The symbol s denotes the coordinate following the shoreline. The coordinate pair (x_s, y_s) gives the location of an arbitrary point on the curved shoreline in terms of a Cartesian coordinate system.

$$\vec{m} = \left(\frac{\partial x_s}{\partial s}, \frac{\partial y_s}{\partial s} \right) = (\cos\theta, \sin\theta) \tag{1}$$

is the unit tangential vector to the shoreline in the direction of increasing s,

$$\vec{n} = \left(-\frac{\partial y_s}{\partial s}, \frac{\partial x_s}{\partial s} \right) = (-\sin\theta, \cos\theta) \tag{2}$$

is the seaward unit normal vector to the shoreline, and θ is the angle between $\vec{m}$ and the x-axis which is measured counterclockwise from the positive x-direction. In the figure, Q is the volumetric sediment transport rate, and α_b is the breaking wave angle between the wave crest and the x-axis, which is measured counterclockwise from the positive x-direction. Assuming that the point, (x_s, y_s), moves perpendicular to the shoreline, so that

$$\left(\frac{\partial x_s}{\partial t}, \frac{\partial y_s}{\partial t} \right) = e\vec{n} \tag{3}$$

in which $e = -(1/D)\partial Q/\partial s$ ($D =$ depth of profile closure) is the rate of shore-normal movement of shoreline, and introducing $z_s = x_s + iy_s$, in which $i = \sqrt{-1}$, the preceding equation can be written as

389
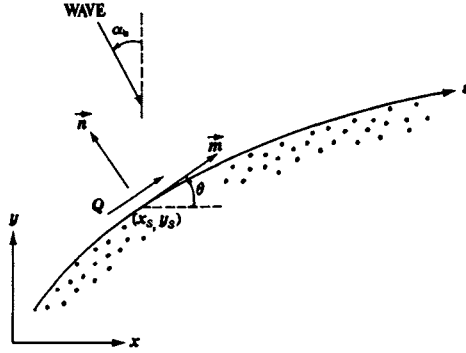
Figure 6. Curvilinear coordinate system and definition of model variables

$$\frac{\partial z_s}{\partial t} = -\frac{1}{D}\frac{\partial Q}{\partial s}\exp\left\{i\left(\theta + \frac{\pi}{2}\right)\right\} \tag{4}$$

The longshore sediment transport rate formula proposed by Ozasa and Brampton (1980) is used, which includes the effect of wave diffraction on longshore sediment transport:

$$Q = \Gamma H_b^{5/2}\left[K_1\sin(2\delta_b) - K_2\frac{\partial H_b}{\partial s}\cot\beta\cos\delta_b\right] \tag{5}$$

in which

$$\Gamma = \frac{\sqrt{g}}{16(s_s - 1)(1 - p)\sqrt{\kappa}} \tag{6}$$

and

$$\delta_b = \alpha_b - \theta \tag{7}$$

is the breaking wave angle relative to the shoreline under the assumption that the breaker line and the shoreline are locally parallel, and $g =$ gravitational acceleration; $s_s =$ specific gravity of sediment relative to fluid; $p =$ porosity of sediment; $\kappa =$ ratio of wave height to water depth at breaking; $H_b =$ breaking wave height; $\tan\beta =$ beach slope; and $K_1, K_2 =$ empirical longshore sediment transport coefficients. An explicit finite-difference method is used to solve Equations (4), (5) and (7) numerically for the wave condition computed along the shoreline. See Suh and Hardaway (1994) for the finite-difference equations.

Wave Model

The sediment continuity equation (4), can be solved for the shoreline position, z_s, if the wave heights and angles along the breaker line are given. To calculate these, the RCPWAVE model developed by Ebersole et al. (1986) was used, which computes the wave transformation due to shoaling, refraction, and diffraction over an arbitrary bathymetry. For the offshore boundary condition of the wave model, we used the wave hindcasting data provided on the homepage of the Korea Ocean Research and Development Institute (http://www.kordi.re.kr). The deepwater wave hindcasting was made every three hours for 20 years (from 1979 till 1998) using the HYPA (HYbrid PArametrical) model and the ECMWF (European Center for Medium-range Weather Forecasts) wind data. The site provides statistical data including significant wave height and period, principal wave direction, and directional wave spectrum at 67 locations around South Korea as shown in Figure 7. We used the data at Location 50 for three years from September 1979 to October 1982.

Figure 8 shows the distribution of heights and directions of the waves at Location 50. In the simulation, we used wave data in the sector between 45° and 152.5° clockwise from the north. Also we used only the waves of significant period greater than 4.0 s. The largest significant wave height is almost 5 m. The waves in the sector between NE and ENE are dominant.
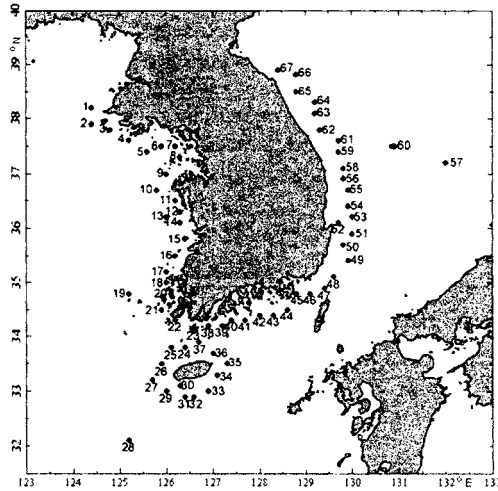
Figure 7. Location of wave hindcasting (from http://www.kordi.re.kr)

391
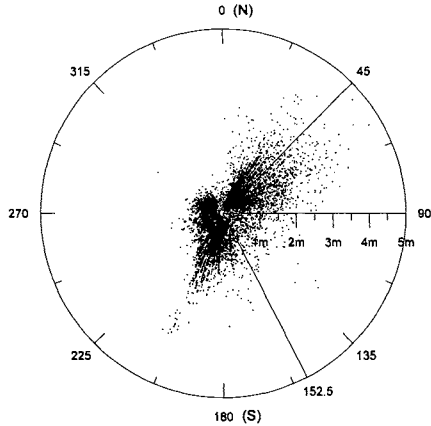
Figure 8. Distribution of wave heights and directions at Location 50

The wave model uses Cartesian coordinate system with fixed grid spacing in both x and y directions. But the shoreline evolution model uses a curvilinear coordinate system in which the shoreline points move in both x and y directions, so that the spacing between shoreline points in x-direction is not constant even though we have a constant spacing at the beginning of the simulation. In order to calculate the breaking wave height and angle of a shoreline point, we took the weighting average of the values calculated at the neighboring points of the wave model. The detailed procedure can be found in Oh (2002).

SIMULATION

Figure 9 shows the bathymetry of Naari beach. We took the computation area of the wave model up to the water depth of about 40 m where the bottom contour line is almost straight in the north-south direction. Both Δx and Δy were 30 m so that 110 and 113 grid points were used in x- and y-direction, respectively. Constant (but changing with time) wave heights and directions were assumed along the offshore boundary. Figure 10 shows an example of the distribution of wave heights normalized with respect to the incident wave height and the wave direction vectors computed by the wave model. In the lee of the intake breakwaters where wave diffraction is dominant, the wave heights are small and the wave directions change significantly.

392
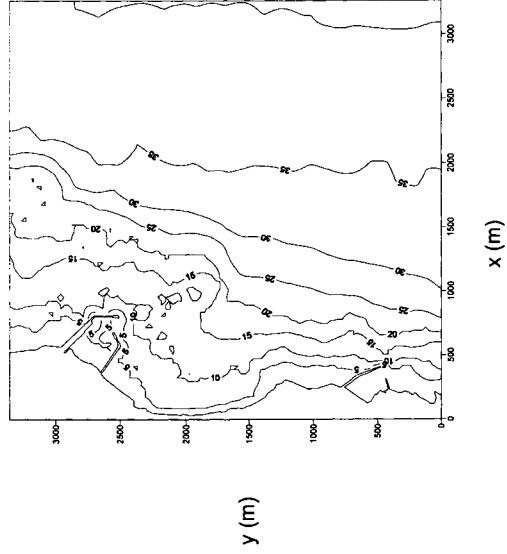
Figure 9.   Bathymetry of Naari beach

x (m)

y (m)

Height=2m Period=5s (Angle=30)

Height=2m Period=5s (Angle=30)
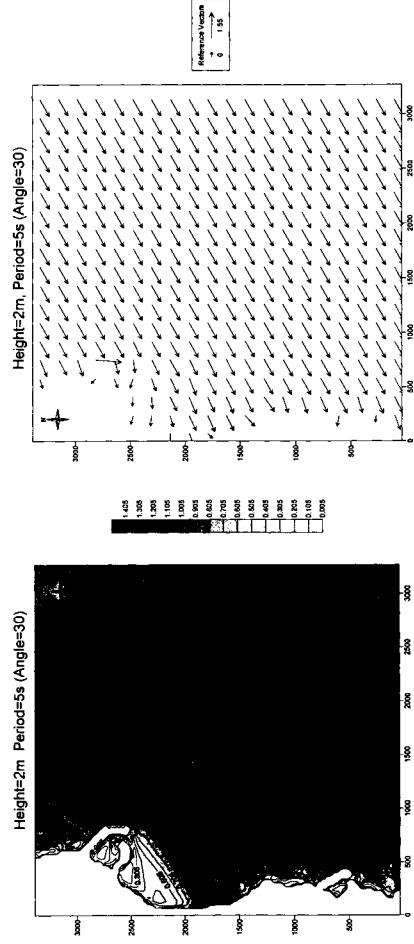
Figure 10. Example of computational results of wave model
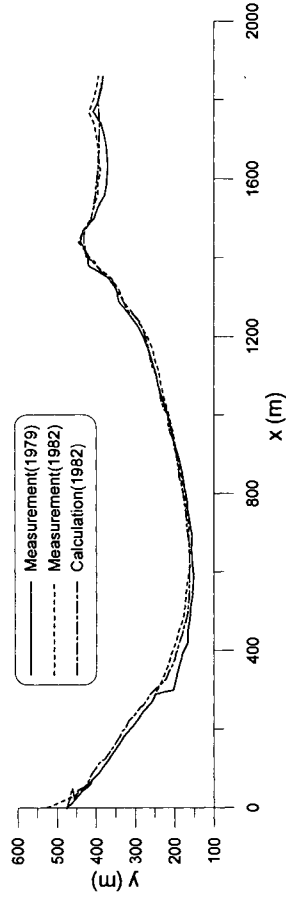
Figure 11. Comparison of measurement and calculation of shoreline change

x (m)

y (m)

Measurement(1979)
Measurement(1982)
Calculation(1982)

The initial shoreline was discretized by 10 m in x-direction. The north end of the beach is blocked by the intake breakwater of the nuclear power plant and the south end is blocked by the breakwater of a fishery port (Fig. 9). Therefore, the boundary conditions of no flux of sediment were imposed at both ends of the shoreline. The mean diameter of the bottom sediment was 1.71 mm (Korea Electric Power Company, 1994), indicating coarse sand. The depth of profile closure is calculated to be 11.3 m using the formula proposed by Hallermeier (1983):

$$D = \frac{2.9(H_s)_{max}}{\sqrt{s_s - 1}} \qquad (8)$$

where $(H_s)_{max}$ is the maximum significant wave height during the simulation period and s_s is the specific gravity of sediment relative to fluid. $K_1 = 0.6$ and $K_2 = 0.1$ were used.

Figure 11 shows the comparison between measurement (using aerial photographs) and calculation of the shoreline change during the first three years after the construction of the intake breakwaters. A good agreement is observed between measurement and calculation, even though there are small deviations in several places.

CONCLUSIONS

We analyzed the shoreline change of Naari beach due to the construction of intake breakwaters of the Wolsung Nuclear Power Plant using aerial photographs taken almost every five years before and after the construction of the nuclear power plant. It was found that significant shoreline change occurred during the first several years after the construction of the intake breakwaters whereas only minor change occurred afterwards, indicating that the shoreline change was caused by the construction of the intake breakwaters.

A curvilinear-coordinate shoreline evolution model combined with the Cartesian-coordinate RCPWAVE model was used to simulate the shoreline change during the first three years after the construction of intake breakwaters. A reasonable agreement was observed between the calculated shoreline change and the measured one by the aerial photographs.

Finally we could conclude that the aerial photographs could be used for the long-term monitoring of the shoreline change and the numerical shoreline evolution model as a fairly accurate tool for the prediction of the shoreline change due to the construction of coastal structures.

REFERENCES

Ebersole, B.A., M.A. Cialone and M.D. Prater. 1986. Regional coastal processes numerical modeling system Report 1 RCPWAVE – A linear wave propagation model for engineering use. *Technical Report CERC-86-4*. Coastal Engineering Research Center, Waterways Experiment Station, Corps of Engineers, Vicksburg, Mississippi, USA.

Hallermeier, R.J. 1983. Sand transport limits in coastal structure designs. In *Conference on Coastal Structures '83*. 703-716.

Korea Electric Power Company. 1994. A study on the reduction of thermal discharge effects around nuclear power plants – Wolsung. *Report No. 92-802* (in Korean).

Oh, Y.T. 2002. Curvilinear coordinate shoreline change model combined with finite-difference wave transformation model. Master's thesis. Seoul National University, Seoul, Korea.

Ozasa, H. and A.H. Brampton. 1980. Mathematical modelling of beaches backed by seawalls, *Coastal Engineering*. 4:47-63.

Suh, K.D. and S.C. Hardaway. 1994. Calculation of tombolo in shoreline numerical model, In *24th International Conference on Coastal Engineering,* edited by B. Edge, 2653-2667. Kobe, Japan.

.

ADVANTAGES OF FERTILIZER FOR ALGAE ENHANCEMENT TECHNOLOGY

Kyoichi Okamoto[1], Kenji Hotta[1] and Tetsuo Suzuki[2]

[1]Dept. of Oceanic Architecture and Engineering, Nihon University
Funabashi, Chiba, JAPAN
okamoto@ocean.cst.nihon-u.ac.jp

[2]CELLS Coastal Environmental Lab.
Numazu, Shizuoka, JAPAN

ABSTRACT

Fishery resources in the world are decreasing year by year. The reasons are over-catching, change of habitable environments caused by pollution, and global environmental change. As a result, seaweed communities that support marine ecosystems are especially decreasing in the ocean. Algae enhancement technology is, therefore, the most important thing to improve the living environment of the seaweed communities. Ferrous sulfate is the micronutrient element considered essential to all algae. Ferrous sulfate is used is an industrial waste, which comes from processing titanium ore, and it is very expensive. Slag, used as a core material, is also a waste material for steel works. Our point is to use ocean fertilizer technology, especially a throwing type of iron fertilizer. It becomes harmless that this type of iron fertilizer had transferred the basic behavior of the slag with ferrous sulfate. Our object is to apply algae enhancement technology to real ocean zone by using this throwing type of iron fertilizer. In this paper, the application used by this fertilizer will be introduced and discussed.

INTRODUCTION

We have so many coastal zone developments now. Faster these developments, especially in Japan have executed, considered not ocean environment but mainly the economy and the efficiency. We also have problems with ocean pollution caused by too much of land-living draining from rivers in Japan. As a result of these problems seaweed communities have been decreasing yearly. The seaweed community in Japan had lost 6,500(ha) for fifteen years. Here, seaweed communities have a function, which supports marine ecosystems, and have a water purification quality. Therefore, creating or improving seaweed communities is very important.

Moreover, problems on industrial waste, at the present time in Japan, are caused by very few final-disposal facilities, high cost and high environmental load by not appropriate disposal of waste including toxic substances, so that re-usage of industrial waste is needed. For the purpose of re-usage of industrial waste, ferrous sulfate and also steel slag were selected. These are produced as a waste by titanium oxide or iron manufacture. The main components of this iron fertilizer are ferrous sulfate and slag.

Here, iron is micronutrient element for all seaweeds and also plankton (Takeda, 1996). For improving or creating seaweed communities, we have to check the effects. That is, if the iron fertilizer accelerates the growth of seaweed. Our object of this research is to apply algae enhancement technology by using iron fertilizer in the real ocean.
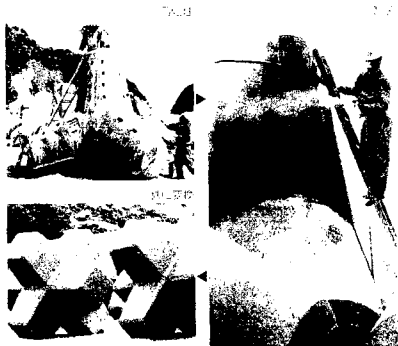
Photo 1. Usual Type of Iron Fertilizer

The usual type of iron fertilizer, including ferrous sulfate is almost paint type, which had already been developed by two of the authors (Hotta, Suzuki et al., 2000), and shown in Photo 1. We used a new type of iron fertilizer in this research. Since this new type is solid and small it is easy to use. We put it on or threw it to use (Photo 2).

Photo 2. Iron Fertilizer Used by Ferrous Sulfate

The iron fertilizer on the right side of Photo 2 consists of ferrous sulfate, sea salt and calcium carbonate (Hotta and Suzuki, 2000), and the left side of Photo 2 consists of ferrous sulfate, slag and diatomaceous. We had carried out two experiments. In experiment 1 in the test tank, the effects had been checked on growth of spore of seaweed. In experiment 2 in the real ocean, the effects had been also checked on the growth of the organism of seaweed.

EXPERIMENT IN TANK TEST

The object of experiment 1 was to check the difference of growth on a spore of seaweed (*Ecklonia cava*) in the culture tank with or without iron fertilizer. Before executing this

experiment we had to get the algae and then dry it in the shade.   After extracting seedlings we had put it in the culture tank (Photo 3).
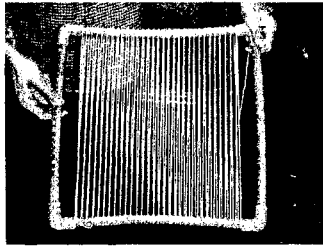
Photo 3.   Prepared seedling

The experimental date was from October 25 to November 11, 2001 and the place was at building No. 5, Department of Oceanic Architecture and Engineering at Nihon University in Japan.   We set two tanks; one with iron fertilizer and the other without iron fertilizer.   The size of the tanks was 800 x 400 x 500 mm and the volume of seawater was 100 liters.   The culture tanks are shown in Photo 4.   The iron fertilizer used in this experiment included salt (right side in Photo 2).

Figure 1 shows a diagram of the culture tank.   Slide glasses were set at the center of the tanks for checking spores by use of a microscope.   The weight of iron fertilizer used in this experiment was 40 g, which had been referred to by Hotta and Suzuki (2000), so that the concentration of iron is 0.07(g/L).   The other experimental conditions were referred by Sudo, 1948 (Table 1).
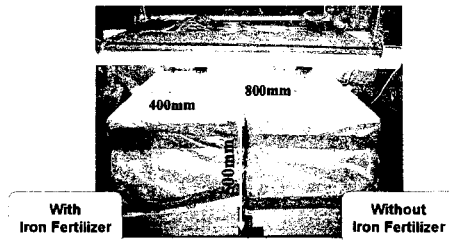
Photo 4.   Culture Tanks.
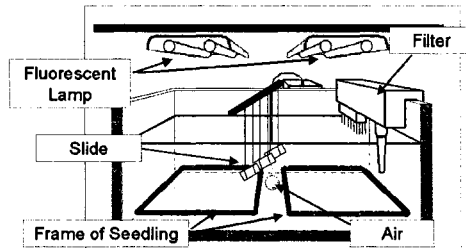
Figure 1.   Diagram of Test Tank

399

Table 1.　Experimental Conditions

Intensity of Illumination	2500-3500(Lux)
Time of Illumination	09:00-19:00
Duration Time	10(hours)
Air Temperature (Controlled)	20(degree Centigrade)
Water Temperature	19-20(degree Centigrade)
PH	7.9-8.3
Salinity	34-37(PSU)
Concentration of Iron	0.07(g/L)

Results

Photo 5 is the result after three days using a microscope.　The average number of spores in this case, used with iron fertilizer, was thirty-two, and the number of spores used without iron fertilizer was eighteen.　The germination of spores used with the iron fertilizer was much better than the germination of spores without using the iron fertilizer.

With Iron Fertilizer　　　　Without
Photo 5.　Results after three days
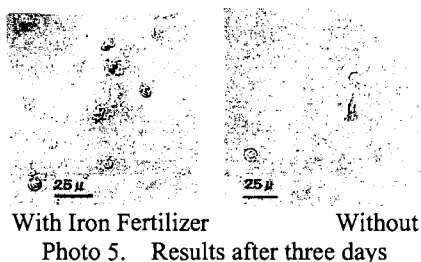
Photo 6 is the result after five days.　The average number of spores used with iron fertilizer was twenty-nine, and the number of spores used without the iron fertilizer was sixteen.　In the case of including iron fertilizer, distinguishable male and female were found out, but we could not see these in the other case.

With Iron Fertilizer　　　　Without
Photo 6.　Results after five days
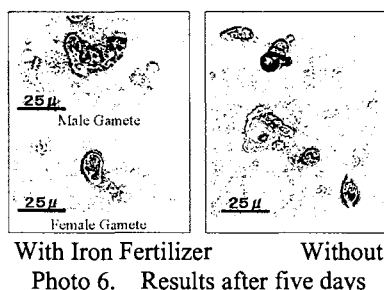
Photo 7 is the result after eight days.　The growth of female gametophytes with the iron fertilizer was much better than those used without it in that the gametophytes were longer, bigger, and had some egg cells.
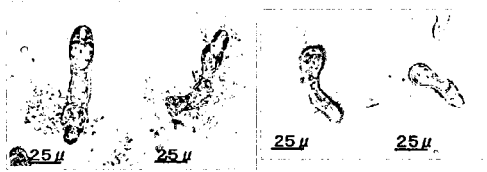
With Iron Fertilizer   Without
Photo 7.   Results on female gamete after eight days

Photo 8 is the result after twelve days. All of them in case to use with iron fertilizer were inseminated, but only one-third in case not to use iron fertilizer was inseminated. The average cell division per spore used with the iron fertilizer was ten, but without the fertilizer was four.

With Iron Fertilizer   Without
Photo 8.   Results after twelve days

Photos 9 and 10 are the results after 16 days using the iron fertilizer. The average cell division per spore using iron fertilizer was forty-four (Photo 9), but those without was fourteen (Photo 10).
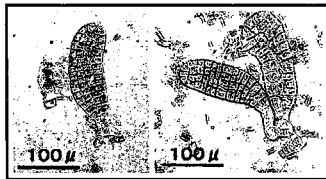
Photo 9.   Results after 16 days with iron fertilizer
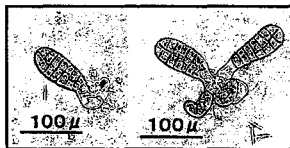
Photo 10.   Results after 16 days without iron fertilizer

Figure 2 shows the average number of cell per spore. The number of cells of a spore using the iron fertilizer was larger than the cells not using the fertilizer. We can see that cell division of cells using the iron fertilizer is faster than without.

401

Figure 2.   Average number of cell per a spore of seaweed

Consideration

The number of germination on a spore of seaweed using iron fertilizer was much better than without.   The growth on spore of seaweed using the iron fertilizer was much better than without. Cell division on spore of seaweed using iron fertilizer was active and much better than without. Therefore, it was actually pointed out that iron fertilizer accelerates germination, growth and cell division on spore of seaweed by the tank test.

EXPERIMENT IN REAL OCEAN

The object of experiment 2 was to check the effect on the growth of the seaweed organism (*Unidaria peterseniana*), in the real ocean to use with or without iron fertilizer.   Iron fertilizer in this experiment included slag (left side, Photo 2).   The experimental place is a section in the Chikura fishing port (Chiba, Japan), (Fig. 3) and the date was from December 9, 2001 to February 16, 2002.   The measurements had been carried out seven times on December 15, 27, January 11, 29, February 6, 11, and 16.

Figure 3.   Experimental place

As an arrangement of this experiment, a rope was set from one side to the other side on a raft, (Photo 11, Fig. 4).   Seaweeds were hung on the rope (Photo 12).

402

Photo 11. Raft used for experiment
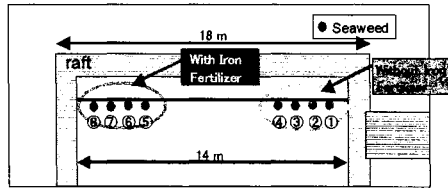
Figure 4. Arrangement of this experiment

Photo 12. Position of seaweed hung by rope

The iron fertilizer was set at the same location and in an upper level with seaweed on only one side of the raft. This setting used three bags including iron fertilizer and each weight was 3 kg. At the other side of the raft, iron fertilizer was not set. We measured the wet weight after removing the seaweed from the rope, to check growth.
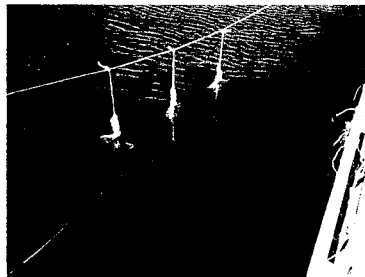
Photo 13. Position of iron fertilizer in upper level with seaweed

Results

Figure 5 shows the results in change of wet weight of the seaweed. After February 11, we can see obviously wet weight on the side used with iron fertilizer is much better than the other side. It supposedly had no effects on the results before February 11 but we decided to indicate wet weight between measured days (Fig. 6). Now, we could see the wet weight between measured days using the iron fertilizer was almost increasing, compared with the other side.

We had re-set up this experiment on February 6, so we had two terms of this experiment in Figure 6. We got final results from Figure 6 that the growth rates using iron fertilizer were about 1.3 and 1.35 times compared with not using it.
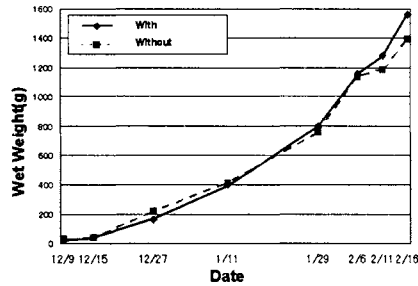
Figure 5.   Results of change of wet weight
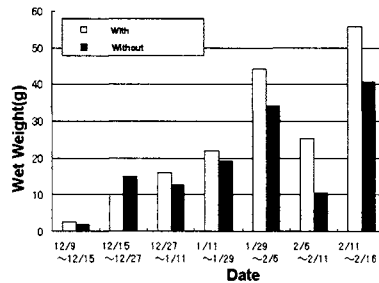
Figure 6.   Results of wet weight between measured days

Consideration

As a result from experiment 2, rate of increase on wet weight using iron fertilizer according to measured terms was good, compared with not using it. The wet weight between measured days using iron fertilizer was increasing. Therefore, we concluded that the iron fertilizer made the organism of seaweed have very good growth.

CONCLUSIONS AND REMARKS

Iron fertilizer including ferrous sulfate made the spore of seaweed have good germination. Existence and growth on spores of seaweed, by culture tank test, was noted in experiment 1. Iron fertilizer makes acceleration of growth on organism of seaweed in real ocean test as experiment 2. Therefore, it was shown that the iron fertilizer gave spore and organism of seaweed good growth effects. Basic results on algae enhancement technology were also obtained.

Here, we had considered the difference of number of germination of spore and organism of seaweed in case to use with iron fertilizer or without one in this research, but did not consider the comparison of the quantity of iron fertilizer. Our future work is to discuss about the quantity of the iron fertilizer by experiment, and to obtain quantitative results of iron fertilizer, so that we can apply this technology to create or improve seaweed communities.

ACKNOWLEDGEMENT

REFERENCES

Hotta, K., T. Suzuki, N.T. An , B.H. Long, N.H. Dai and P.H. Tri. 2000. An Experimental Study on Artificial Reef for Algae Enhancement Technology: Effects of Iron Ion, *Abstract of the Ninth Pacific Congress on Marine Science and Technology*, pp.112.

Hotta, K. and T. Suzuki. 2000. A Study on Practical Experiment of Ocean Fertilizing Technology Using Nutrient Salts for Restoration of Marine Resource Production, *Abstract of the Ninth Pacific Congress on Marine Science and Technology*, pp.110.

Izawa, Y. 2002. An Experimental Study of Algae Enhancement Technology by Use of Iron Fertilizing, Master's Thesis, Nihon University.

Sudo, S. 1948. Shedding, Swimming and Fixing of the Zoospores in Some Species of Laminariaceae, *Proceedings of Japan Society of Fishery Science*, Vol.13(4):123-128.

Takeda, S. 1996. Micronutrient and Plant Plankton, KAIYO MONTHLY, Ex.Vol.10: 69-77.

A STUDY OF THE RELATIONSHIP BETWEEN HUMAN AND NATURE ON BANZU TIDELAND

Shibagaki Taro[1] and Kuroyanagi Akio[2]

[1]Graduate School of Science and Technology, Nihon University
Funabashi, Chiba, JAPAN
K15003@ocean.cst.nihon-u.ac.jp

[2]College of Science and Technology, Nihon University
Funabashi, Chiba, JAPAN

ABSTRACT

Exploring the relationship between people and a tideland, this research attempted to understand the differences in the concepts of the residents and the citizens toward the tideland, in order to clarify the local structure surrounding the tideland. Also, the location of the tideland selected for this study was in Kisarazu-city, Chiba, and the results are shown below.

1. Environmental changes of the fishing industry have brought about changes in the people's concept of the tideland.
2. In order to improve their living environment, the residents have changed the existential value of the tideland from a place of livelihood to a place of capital gain.
3. The residents request the tideland have economical value. On the other hand, the citizens request the tideland have intellectual value.

INTRODUCTION

The tideland not only gives people a sense of peacefulness and grace, but also provides an environment for a highly diverse range of creatures, which play very important roles in water quality purification and high productivity.

However, it also has many unpleasant elements, such as bad odor generated from piled up soil, sand, nutritive salts and organic matter that is carried away from the land and transported to the ocean nearby, etc. Therefore, although the significance of the tideland is acknowledged, people still consider the tideland as an area they do not wish to live by (NMBY=Not In My Backyard), and which they want to be reproduced at a location that maintains physical distance from their residences. In such a situation, and taking the characteristics of the tideland into account, it seems necessary to consider the reproduction of a tideland based on the agreement of the people. In order to accomplish this, as is evident, it is extremely crucial to understand the structure of the "people – tideland – and other creatures" system.

RESEARCH CONCEPT AND PURPOSE

This research is paying attention to the relationship between the people and the tideland, this study attempted to clarify the local structure surrounding the tideland as its center, by understanding the people's concepts of the tideland right at the spot long associated with people's livelihoods and by understanding other inhabitants living in the area around the tideland and the tideland itself. An attempt was made to acquire the knowledge and experiences to proceed with improvements of the tideland environment.

It is to be noted that, during this research, people were divided into two groups, the residents and the citizens, during the interview survey study, in order to clearly grasp the concepts of the people living around the tideland. The definition of "resident" refers to those who directly relate to BANZU Tideland in daily business and personal life. On the other hand, "citizens" here refers to those who do not directly relate to BANZU Tideland in their daily business and personal life.

RESEARCH METHOD

Selection of the Subject Location

Figure 1 indicates the site map for the research subject location. In this research, in order to obtain ideas about the relationships between people and the tideland, people and other inhabitants, and the relationship between the inhabitants and the tideland, an area where the agricultural/fishing industry has been established by utilizing the surrounding natural environment was selected as the study subject. The region selected was the BANZU Tideland in Kisarazu-city, Chiba, where only remnants of a wild tideland can be found on the shore.
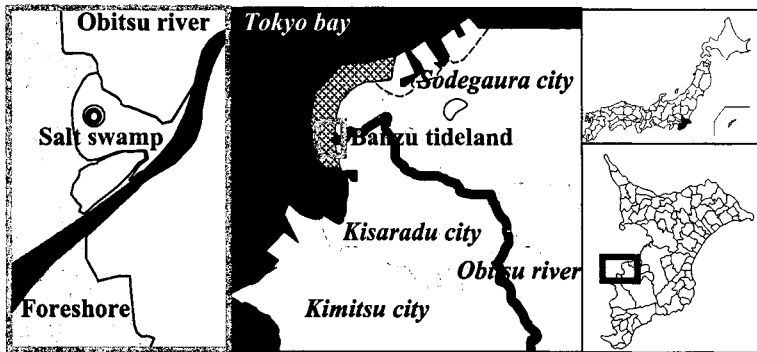
Figure 1. Map of the Banzu Tideland

Research Outline

The research outline is shown in Table 1. In this research, a reference study (Japan Ministry of the Environment, 1994; Chiba prefecture, 1996; Touhei et al., 1998) was first conducted to learn

about the influence on the tideland and the situation of its inhabitants in BANZU Tideland, and community development, along with the influence of development projects at BANZU Tideland, etc. Subsequently, an interview survey was then conducted with the residents and the citizens. The survey subjects were selected from the residents and citizens living around the BANZU Tideland, who were involved in BANZU Tideland preservation activities relating to BANZU Tideland. While the subject numbers were few, many hours were spent on individual interviews and listening to their stories. The contents of each subject's story were mutually evaluated in order to confirm and adjust the consistency of the information that was gathered. The contents of the interview survey involved asking each research item shown in Table 1, which was tape-recorded to be categorized and reviewed later per each question.

Table 1. The Research Outline

item		outline of research	
period		August~November.2001	
method		Literature and Hearing Investigation	
contents	Literature	Thriving state of fauna and flora	
		Act of developments, etc	
	Hearing	Play	Region
		Nature	Work
target of hearing		Total 16 persons	Living at surrounding of BANZU tideland
			Ecoactivist in BANZU tideland
brief of BANZU tideland	location	Kisaradu City, Chiba. JAPAN	
	demension	Salt Swamp	43hectare
		Foreshore	780hectare
	depth	Less than 1 meter	
	incline	1/800	

RESULT

Current Status of Inhabitation

The habitation conditions in the BANZU Tideland are as follows:

1. Many species protected by Chiba Prefecture live and grow there.
2. The number of types and the quantity of species in the BANZU Tideland exceeds the number of species and types in other tidelands in Chiba.
3. Although various types of species still live and breed there today, this trend is declining. In fact, more species types existed in the Showa 40s than in the present day.

From these facts, it seems that BANZU Tideland has more and varied possibilities for developing relationships between people and other inhabitants compared to other tidal shores because it has more numbers and types of species than those in other distinguished tidelands in Chiba such as SANBANZE or YATSU Tideland.

Relationship between the Residents /the Citizens and Nature

Based on the interview surveys, Figures 2 and 3 indicate the way the residents and citizens in BANZU Tideland relate to the nature around the tideland in their daily lives. Figure 2 indicates

the ways nature and people surrounding BANZU Tideland relate to one another. Figure 3 shows how BANZU Tideland relates to the surrounding nature and area. These figures were developed based on each inter-relationship after analyzing the behavior and thinking patterns of the residents and the citizens by evaluating these factors according to the reference study and interview survey information. From here, this paper will demonstrate the inter-relationship between the residents/citizens and nature, and the community and nature surrounding the tideland as their center.
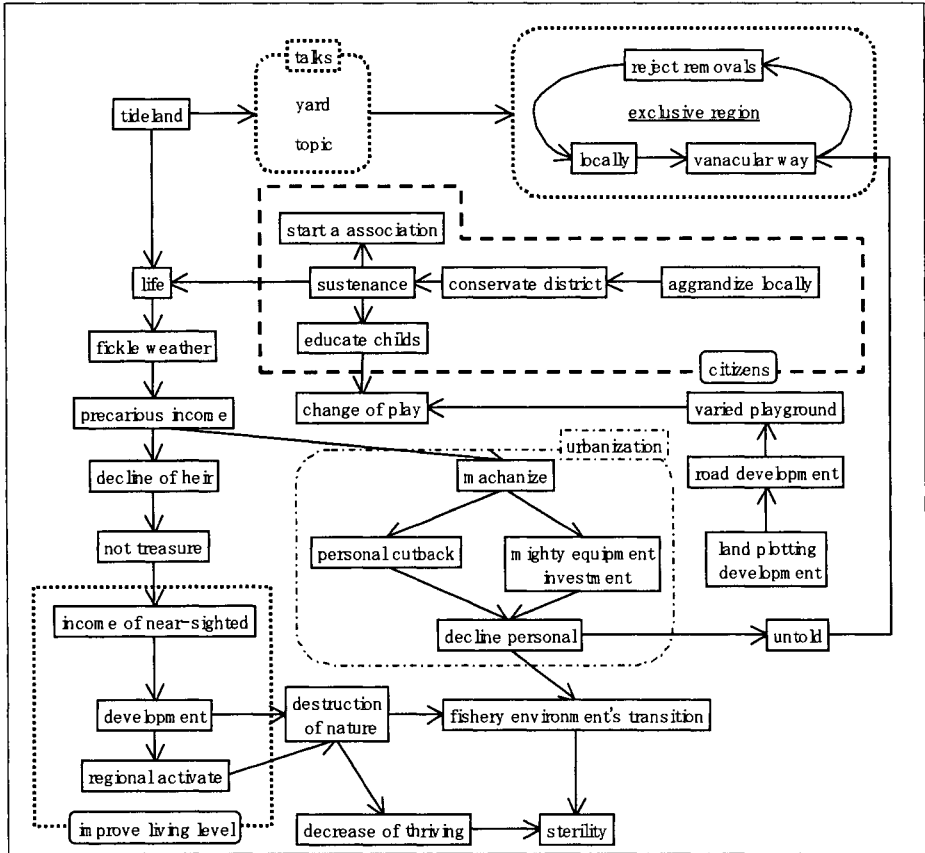
Figure 2. The ways nature and people surrounding BANZU Tideland

form ing com m un ity

common topics | cooperative operation | cooperative place

fishery lver weather area | *be tanagashi am hari* drainage cleaning | tide land fishery union road

sect of preservate tide land

aggrandize locally

belong to resident

get into living environment

preservation of locality

environment maintenance

preservation of tide land

m ine of em pirical inform ation ← depend on tide land

development

land trade

importance of tide land

affluent scholarly ideas

change of brink environm ent

aggravation of creature's habitat
water polution
tidal carrent change
bottom polution
decrease of vegetation

change of biota
decrease of fishry product
decrease of avifauna

change of fishry environm ent

change of relation

environment aggravate look to weather for income m achanize

consc iousness about tide land

deecrease of production deprec iate of tide land

econom ical value decrease

decrease of subsistence activity

sect of develop tide land

short of scholarly ideas

looking at scholarly angle

subsistence don't belong to tide land

citizen

urban ization industrialization

com m un ity breakdown ← disappear of com m on topics cooperativi place

resident

Figure 3. BANZU Tideland relates to the surrounding nature and area

Relationship between Residents and Nature
In this community, most people have depended on the semi-agricultural and semi-fishing industry for their living since long ago. Also, because many residents have lived there all their lives, they have chosen a life style that is dependent on nature.

"To create a place of recreation/relaxation is the same as making a place of recreation through fishing in the case of Kaneda Community. This is after all, a place where we all weaved bamboo screens on which to dry the seaweed, you may have seen it. Then, we all put the seaweed on the nets. After doing all these things together, the process then went like this: when making a net, only men from the neighborhood got together and weaved all day while drinking cups of tea together. Women likewise worked on something while chatting all day. So, work had become a place of recreation."

In the past, children used to play outside in places such as Obitsu River, BANZU Tideland, in fields and on vacant land. It was simply the gathering of neighborhood children. And when their play involved something to do with nature, they actually ate what they caught or sold it to get some pocket money. From these activities, it is very easy to understand how children in the past could nurture a rich knowledge of nature because their playground and playthings were deeply

411

related to nature. Knowledge gained in such a manner was not the intellectual kind gained from books and school classes, but was that gained from their own experience and routines.

"Also, it is prohibited now, but we had this stuff, (Japanese) mist net. Friends from the elementary school used to play with this a lot. We went to Kisarazu-town to buy the stuff, then took it to the tideland to hunt birds: Japanese white-eye, also amadavat. There was a middle-aged guy in our neighborhood who wanted to buy them. We sold them to get some pocket money ourselves. That was how we played."

As you heard, the life style itself depended on and had affinity with nature; team work for livelihood and playing with neighborhood children created interactions. Also, customs and neighborhood relationships borne from this livelihood (marriage courtship,"Koyasu-Koh"(that is an association of wives. It originated from their belief in the"Koyasu god"to whom they pray for easy delivery and fertility, etc.), Shut-in day building a Bonnden and funeral custom still remains in the community. With this in mind, it seems clear that the relationship among residents with similar life styles brings them closer to one another, increasing the opportunities for interaction because of the customs and neighborhood connections, resulting in a deepening of their relationships.

"Now, it has become something of a treat, but "Koyasu-Koh" used to take place during childbirth and involved carrying something resembling a hook to help a mother have an easier delivery. But such occasions have become less, so it seems true that now it's like, "let's get together and just have a cup of tea" type of thing, don't you think? In the past, they seemed to do "Koyasu-Koh" a lot."

"I heard a story from the Edo (Tokugawa) period. A Tokugawa government's ship was sunk. So, to show that it was not their fault, they built a Bonnden (a guardian idol). This is not really an old story. Anyhow, a ship was sunk and they were blamed for it. That kind of thing happened sometimes. I really do not know much about the details."

As is evident, this community has active residential interactions among those sharing a similar life style through livelihood; nevertheless, the fishing industry environment surrounding BANZU Tideland has changed. Based on the reference study and interview survey, an obvious change in the fishing industry environment is shown in Figure 4. According to this figure, the differences are clearly distinguishable among the pre-1960s, the golden age of the fishing industry, the 1960s when the pollution of the fishing field became extremely bad and the present day in which the fishing style has greatly changed. Factory industry began to coexist polluting the fishing fields, resulting in many occurrences of fish deformity or fish with bad odor. Then, the fishing industry was prevented from conducting their businesses in the market. As a result, the residents changed the target of their livelihood from fish to dry seaweed production and shellfish farming selling shellfish such as clams, which were less susceptible to the effects of pollution. Consequently, many residents have been on the verge of giving up on the fishing industry because of the income decrease.
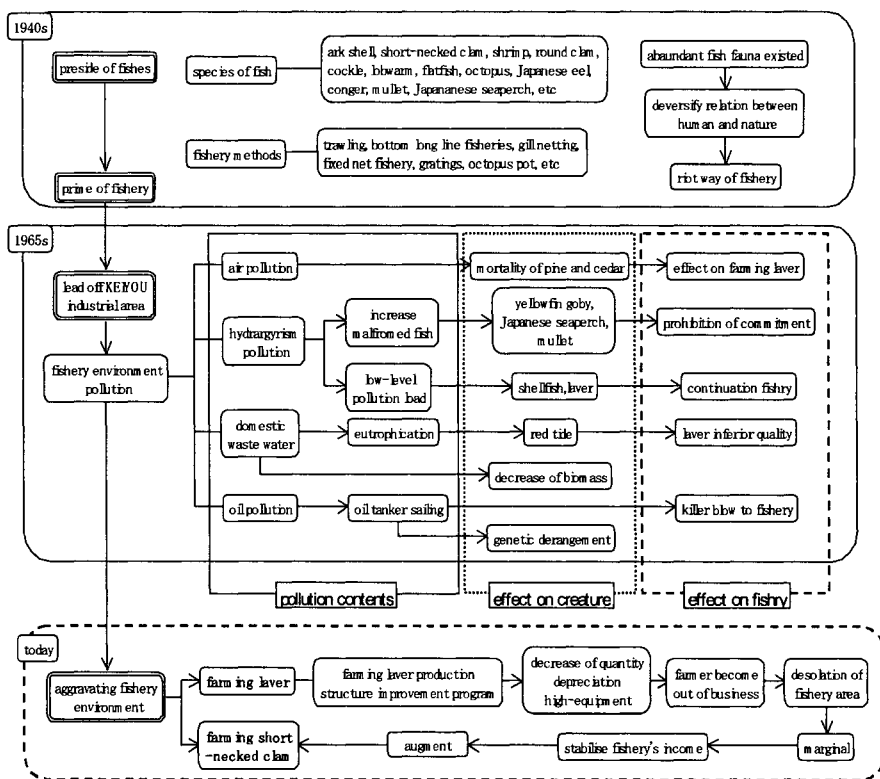
Figure 4. Change of fishing industry environment

"It is not that fishing productivity has changed but rather that there has been no pay back for what we catch. Thirty years ago, there was a time when dry seaweed cost 100 yen, but it is still sold at 100 yen. Only the cost of living has gone up, forcing us to use machines that cost hundreds of millions of yen. In the past, of the many things we did, the highest price we could get was only 100 yen. Anyhow, we did not have to dip into our savings much, so we could save more. But now, we have to use machines." "In an extreme sense, if they cannot find big clams then, they compromise by picking small clams. If they waited a little while longer, they could sell them at 3,000 yen, but the actual price is 1,000 yen because they feel like they have to sell them right a way. Because they gather clams that are worth 3,000 yen and then sell them for only 1,000 yen, there are no 2,000 yen clams left for the next time."

In this way, the deterioration of the fishing industry has caused the decrease of its volume, resulting in lower income from the fishing business and the lack of a next generation to take over the businesses. All these have created such disadvantages for the continuation of the fishing industry that many residents are gradually beginning to leave this type of business. Because of this, many residents have lost their connection to fishing along with their interest in BANZU Tideland that was closely related to the fishing industry. As a result, the existential value of

413

BANZU Tideland has changed from a necessary existence to an unnecessary existence, changing the concepts of people toward BANZU Tideland. On the other hand, there are a few residents who are eager to take over the fishing industry in spite of such deterioration, most of them being involved in the clam business. These people have an intimate relationship with the fishing industry even now, and express a stronger interest in BANZU Tideland. BANZU Tideland, for them, is a necessary existence in their lives. Accordingly, it is obvious that the existential value of BANZU Tideland is regarded as a necessary factor of life.

"You cannot take clams from places other than at full tide on the tideland. See, 'clam' in Japanese means 'shallow.' They are only found on a shallow surface. It's 'clam'. So, the tideland is our work place. After all, dry seaweed is too. We can make dry seaweed without having to split lines only on the tideland. In other words, we are making our living on the tideland. I cannot live if the tideland disappears. So, it's like protecting myself, in my case."

"The tideland is important. It is important for filtering water. But, it seems like we do not have a life style that goes with it."

"No, we do not need it. Just do the reclamation and get money from that. I bet the fishermen are also hoping that someone will do reclamation of the whole of Tokyo Bay."

"For a local community, there seems no benefit in keeping it. Even us! We would protect the tideland if we could make a living out of it, but there is no profit whatsoever."

Since the existential value of BANZU Tideland has changed in such a way, those residents who have given up or are willing to give up are hoping for any improvement that would revive their community life, such as the development of the surrounding area of the tideland, reclamation of the tideland, building projects, etc. From this fact, many residents are considering utilizing the tideland for practical life;, not for the purpose of livelihood, but using it as a development site hoping to utilize this place for people's lives in practical ways. This has resulted from the following: People used to be able to maintain a high living standard because the tideland and the natural environment around it were fertile generating high fish hauls. And for those people depending on it for their living, BANZU Tideland's existence was highly valuable in an economical sense. However, along with the change of the fishing environment, BANZU Tideland's existence was turned into one of low economical value leading to the degradation of the living standard of the residents. For this reason, they are hoping for a way to utilize the tideland that would revitalize the economical value to the community. From these facts, paradoxically it could be said that the existence of BANZU Tideland has provided economical benefits throughout the ages.

On the contrary, those residents who are currently still involved in the fishing industry still depend on BANZU Tideland for their living and highly evaluate BANZU Tideland; thus, they are opposed to the development or reclamation plans for BANZU Tideland. Based on the above information, the understandings of the residents toward BANZU Tideland are divided into two: progress of tideland development and preservation of the tideland. Such a difference in understanding seems to be rooted in whether their living relates to BANZU Tideland or not. And for both sides, one common denominator is the goal, "for their livelihood."

414

Relationship between the Citizens and the Tideland
Since 1970's when development surrounding BANZU Tideland started, the citizens have campaigned for the preservation of the tideland, for instance, by creating an environmental study program in school. Below is a list of characteristics of people who belong to civic organizations:

1. Citizens do not live around the tideland.
2. In the BANZU Tideland area, people are not involved in the fishing industry except for those who live around the tideland; in other words, their living is not associated with the tideland. From the above factors, it is clear that many citizens living far from BANZU Tideland are dependent on something other than the fishing industry for their living. Also, the citizens view the tideland from a perspective other than that for living. It could be concluded that the residents' perspective on the tideland is experiential and existential; whereas, the citizens, on the other hand, see the tideland from an intellectual perspective.

"For example, I pick up garbage, treat the participants to clam miso-soup and so on. 'Tideland Clean-up Strategy' has been an on-going activity up until now."

"I have been teaching children about the tideland in school for the last 17 years since Showa 53. So, the community is beginning to realize that the tideland is very important for the community."

Additionally, with the leadership of the civil organization, events for the "Tideland Clean-up Strategy" have been held and an appeal for the tideland within and outside of the community has been made, clean-up actions have been promoted and also tideland field trips have been incorporated into elementary school curricula, etc. Recently, the citizens have been making an effort to preserve the tideland for the next generation by an informational campaign about the significance of the tideland.

Relationship between the Residents and the Citizens
In this area, where most residents share a similar life style, association among the residents is often found through conversations on common topics relating to their livelihood such as fishing and weather, cooperative tasks such as net casting, bamboo bind weaving, dry seaweed net making and ethnical (rural) beliefs such as "Koyasu-Koh" and Net-setting (This is a religious festival to pray for great hauls and harvests. Then, they hang objects (shrimp, octopus etc) at the city limits or village limits praying for a "Rich Harvest of Staple Grains"), and other topics related to their local customs.

"Even around here, when the subject 'tideland' comes up, for some reason, people create something like the 'Wild Bird Association.' We are not getting food to live out of the 'Wild Bird Association.' Still, the 'Wild Bird Association' opposes anything against it. Whatever it is, even if it is something to do with my own personal life, they are going to oppose if it does not generate any profit. That is fine for them. They can just spend the day watching birds. I wonder how they are making a living."

"If you have a gathering around here, what you hear and talk about are only, how the seaweed drying is going, or whether the seaweed drying has been completed. Or, people ask, 'How is your seaweed?' 'Aren't there a lot of clams in that place?' So, when a new resident who lives on

a salary moves here, he just can't get into the society because he has nothing in common to talk about."

When new residents attempt to start a new fishing business, many times, they end up leaving the area because getting a fishing license is made difficult for them, thus preventing them from sharing a similar life style to that of the residents, or having daily association with the residents. Yet, those who have turned their backs on the fishing work can still maintain and develop associations with the residents by participating in neighborhood relationships and various social gatherings, just because they are familiar with the life style. Consequently, new people who move into this area usually end up leaving if they do not make their living through fishing because they are unable to get into the rural culture.

Another aspect is that there is little association between the citizens and the residents whose lives solely depend on an affinity with aqua-nature. Especially, the difference in concepts of the tideland makes association unfeasible between the residents who are pro-development of the tideland and the citizens who aim at preserving the tideland.

CONCLUSIONS

As a result, the following items have become clear:
1. After the living environment was polluted because of developmental projects around BANZU Tideland, creatures that could not adapt to such an environment became extinct. This resulted in the creation of different daily associations between people creating diverse perspectives on the tideland.
2. The change of the fishing environment caused a decrease of income in the fishing industry for the residents. Since then, people seemed to have lost their consideration/interests in the tideland changing the existential value of the tideland to one that looks for an improvement in their living environment.
3. Although the concepts of the tideland between the residents and the citizens differ due to their different life styles, their goal in utilizing BANZU Tideland for the good of the community is the same. Yet, the residents request that it has economical value; whereas, the citizens request it has a more intellectual value.

REFERENCES

Chiba prefecture. 1996. Chiba natural environmental preservation academic investigation report.

Ministry of the Environment, JAPAN. 1994. Ocean space living thing environmental investigation report -The 1st volume Tideland -.

R. Touhei, T. Fukushima and T. Iwase. 1998. OBITU river region natural environmental academic investigation report.

ANALYSIS OF DISSOLVED OXYGEN AND TRANSPORT OF FISH EGGS IN A BAY

Yoshihiro Suenaga[1], Koichi Masuda[2], Takashi Sasaki[1], Hee-Do Ahn[3],
Tetsuro Kobayashi[1], Takashi Hoshino[4] and Kaori Yasuoka[4]

[1]Faculty of Engineering, Kagawa University
Takamatsu, Kagawa Pref., JAPAN
suenaga@eng.kagawa-u.ac.jp

[2]College of Science and Technology, Nihon University
Chiba, JAPAN

[3]Korea Ocean Research and Development Institute
Seoul, KOREA

[4]Kuroshio Marine Technology, Co, LTD
JAPAN

ABSTRACT

Coastal aquaculture has been increased and developed in a semi-enclosed bay. In Seto inland Sea, Japan could produce marine aquaculture productions to supply the population demands. While the feeding rate of fish farming in Sido-Bay, Kagawa Pref., Japan is approximately 12,378 tons a year, with the highest rate in summer. Therefore, the pollution from floating aquaculture cage can affect the environment via fecal waste, dissolved waste and excess feed settles. After the field experiments, it was found the tidal current, bottom topography and DO consumption rate by sediment are important factors to evaluate the carrying capacity of aquaculture grounds. The authors proposed a more appropriate evaluation method for DO by using three-dimensional numerical model taking the effect of oxygen consumption by the fish in the aquaculture cage and bottom sediment into consideration. In this study has revealed that transportation of fish eggs and larvae from spawning ground to the nursery ground in and around the semi-enclosed bay by using numerical simulation model. Then, it is necessary to take the system for creating fishery ground and to estimate the carrying capacity of aquaculture grounds.

INTRODUCTION

Sido Bay is a small coastal aquaculture system that located 34° 20'N and 134° 11'E. The climate in this region is influence by the tidal current, the Seto Inland Sea Japan. The bay is about 6 km in length and approximately 4 km in width at the mouth with a surface area of *ca.* 20 km^2, average depth of 8.3 m and the total water volume of *ca.* 140 m^3 (Fig.1). Recently variable environmental problems have been caused by red tide, such as poor oxygen concentration at the bottom, exploitation of sand resources for construction materials and many kinds of coastal developments. Although aquaculture habitats in the Sido bay have been

decreased, the impact of aquaculture on environment could be manifest in a wide variety of ways (i.e. waste feed setting and oxygen deplete). We have conducted field research to confirm the oxygen consumption by the fish in the aquaculture cage and bottom sediment by using undisturbed core method. In this paper, we described a more appropriate evaluation method for the carrying capacity of aquaculture grounds by using three-dimensional numerical simulation models (Suenaga et al., 1996; Fujihara et al., 1997) taking the effect of oxygen consumption rate at each area in Sido bay into consideration. Also, the authors calculated the transport of fish eggs and larvae in and around the Bisan-Seto area to clarify the nursery ground by using Euler-Lagrangian method. This method is useful in estimating the carrying capacity for aquaculture grounds in a semi-enclosed bay.
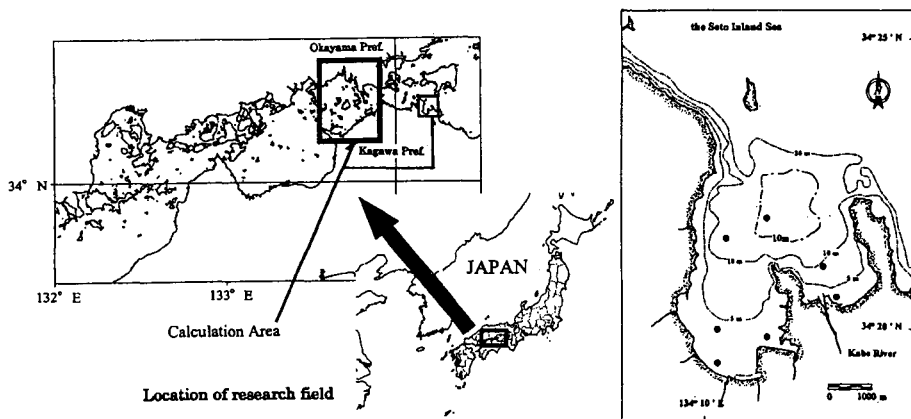
Figure 1. Bottom topography of Sido bay
●Collection of water and sediment samples

MATERIALS & METHODS

Governing equations

The current in the Sido bay is under the influence of tidal current and west and east component of current is predominant along the both shores of Okayama Prefecture and Kagawa Prefecture. A multi-level model (Suenaga et al., 1996; Fujihara et al., 1997; Suenaga et al., 1999; Sakuta et al., 1993) presently employed is represented by the momentum equation on the rotating earth accepting f-plane and hydrostatic approximations, the continuity equation, equation of free surface, the diffusion equations of water temperature and salinity and DO and state equation, as follows (Eqs. (1)-(8));

$$
\begin{aligned}
&\frac{\partial u}{\partial t} + u \frac{\partial u}{\partial x} + v \frac{\partial u}{\partial y} + w \frac{\partial u}{\partial z} \\
&= f_0 v - \frac{1}{\rho} \frac{\partial P_0}{\partial x} + N_x \frac{\partial^2 u}{\partial x^2} + N_y \frac{\partial^2 u}{\partial y^2} + N_z \frac{\partial^2 u}{\partial z^2}
\end{aligned}
\tag{1}
$$

418

$$\frac{\partial v}{\partial t} + u \frac{\partial v}{\partial x} + v \frac{\partial v}{\partial y} + w \frac{\partial v}{\partial z}$$
$$= - f_0 u - \frac{1}{\rho}\frac{\partial P_0}{\partial y} + N_x \frac{\partial^2 v}{\partial x^2} + N_y \frac{\partial^2 v}{\partial y^2} + N_z \frac{\partial^2 v}{\partial z^2} \tag{2}$$

$$- g - \frac{1}{\rho}\frac{\partial P_0}{\partial z} = 0 \tag{3}$$

$$\frac{\partial u}{\partial x} + \frac{\partial v}{\partial y} + \frac{\partial w}{\partial z} = 0 \tag{4}$$

$$\frac{\partial \eta}{\partial t} = - \frac{\partial}{\partial x}\left(\int_{-H}^{\eta} u dz \right) - \frac{\partial}{\partial y}\left(\int_{-H}^{\eta} v dz \right) \tag{5}$$

For T

$$\frac{\partial T}{\partial t} = - \frac{\partial}{\partial x}(u \cdot T) - \frac{\partial}{\partial y}(v \cdot T) - \frac{\partial}{\partial z}(w \cdot T)$$
$$+ \frac{\partial}{\partial x}\left(k_x \cdot \frac{\partial T}{\partial x} \right) + \frac{\partial}{\partial y}\left(k_y \cdot \frac{\partial T}{\partial y} \right) + \frac{\partial}{\partial z}\left(k_z \cdot \frac{\partial T}{\partial z} \right) \tag{6}$$

For S and DO

$$\frac{\partial C}{\partial t} = - \frac{\partial}{\partial x}(u \cdot C) - \frac{\partial}{\partial y}(v \cdot C) - \frac{\partial}{\partial z}(w \cdot C)$$
$$+ \frac{\partial}{\partial x}\left(K_x \cdot \frac{\partial C}{\partial x} \right) + \frac{\partial}{\partial y}\left(K_y \cdot \frac{\partial C}{\partial y} \right) + \frac{\partial}{\partial z}\left(K_z \cdot \frac{\partial C}{\partial z} \right) + R \tag{7}$$

$$\rho = (T, C) \tag{8}$$

where u and v are the horizontal current vectors, w the vertical current velocity, T the water temperature, C is the state variables (the salinity, S and DO), ρ the density of water, g the acceleration due to gravity, f ($=8.15 \times 10^{-5}$ /s: at $34°$ N) the Coliolis parameter, η the elevation from the mean sea level (positive upward), H the water depth, N_x, N_y ($=0.01$ m^2/s) and N_z {friction coefficient at surface ($=0.0013$): bottom ($=0.0026$): internal ($=0.0001$)} the horizontal and vertical eddy viscosity coefficients, k_x ($=10^4$cm/s) and k_y ($=1$ cm^2/s) the horizontal and vertical turbulent diffusion coefficients of water temperature, K_x, K_y ($=10^4$ cm^2/s) and K_z ($=1$ cm^2/s) the horizontal and vertical diffusion coefficients of salinity and k the unit vector(positive upward), respectively (Sasaki and Inoue, 1984).

In the diffusion equation of DO, the last term "R" in equation (7) includes the DO flux by water surface (Sasaki and Inoue, 1984). Re-aeration, consumption rate (A:0.003, B:0.004, C:0.005, D:0.008, ml/sec/m^2) by the respiration of fish (yellowtail fish), consumption by suspended matters (0.068ml/l/hr) and sediment. Also, the consumption rate by sediment (A:0.017, B:0.017, C:0.018, D:0.018, ml/sec/m^2) was measured by undisturbed core method.

Euler-Lagrangian Method

The eggs and larvae treated as particles were traced in the computed flow field for their planktonic period (27 days) using the Euler-Lagrangian Method. The governing equations are as follows:

$$d X /dt = V \tag{9}$$
$$X (0) = X_0 \tag{10}$$

$$X^{(n+1)*} = X^{(n)} + F^{(n)}\Delta t \tag{11}$$
$$X^{(n+1)} = X^{(n)} + (F^{(n)} + F^{(n+1)*})/2 * \Delta t \tag{12}$$
$$F^{(n)} = V^{(n)} + \{(V^{(n)} \cdot \nabla)V^{(n)}\}\Delta t \tag{13}$$

where X is the position, V the velocity, ∇ the horizontal differential operation, Δt (=20s) the time increment; superscript means the time level and * is temporary value at the time level. Initial value problem of the differential equations expressed in equations (9) and (10) is solved using two-step Runge-Kutta integration method expressed in equations (11)-(13). The velocity and shear at the egg/larva position are calculated by interpolation using surrounding values. Particles are located the depth of 10 m and transported only by water movement for the first 3 days and then gradually swim up to the depth of 3 m for 12 hours (Nakata et. al., 1999). After that they gradually swim down to depth of 10 m for 12 hours, and they repeat that movement during 27 days.

Computed domain

Figure 2 shows the computed domain of this study area. The bottom topography in and around the Western Bisan-Seto area and computational domain are shown in Figure 2. The whole body of water is described into 500 m × 500 m square meshes horizontally and three levels vertically (1st level:0-6m, 2nd level:6-15 m, 3rd level:15 m-bottom) for the computation. Tidal flow (tidal level: half amplitude=1 m) is given at the each entrance of Bisan-Seto area as a boundary condition. The flow fields were first reproduced using a multi-level density flow model with observed velocities as boundary tidal conditions. In Sido-Bay, the whole body of water is described into 100 m × 100 m square meshes horizontally and six levels vertically (1st:0-1.5 m, 2nd:1.5-3.5 m, 3rd:3.5-6.5 m, 4th:6.5-9.5 m, 5th:9.5-25.5 m, 6th:25.5 m-bottom) for the computation. Tidal flow is given at the each entrance of Sido bay as boundary conditions shown in Table 1. Also, river discharge was added from Kabe-river (3.9 × 10^4 m^3/day) to the sea (Fig.1).

Table 1.   The boundary conditions for calculation

Area	Amplitude (m)	Period (hr)	Phase lag (deg)
A	0.563	12.42	324.5
A'	0.563	12.42	324.5
B	0.456	12.42	331.9
B'	0.456	12.42	331.9
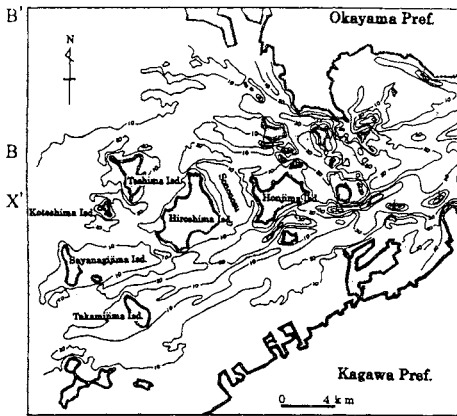
Western Bisan-Seto area
Sido Bay
Figure shows water depth (m)
Figure 2. Computed domain of each study fields
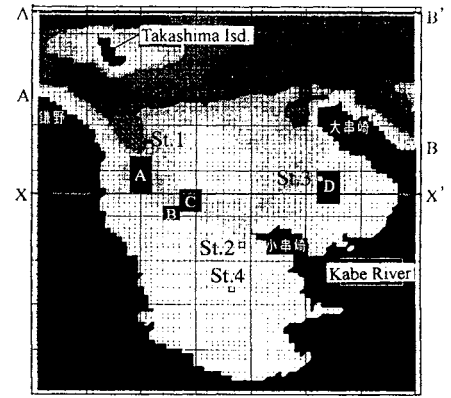
RESULTS AND DISCUSSION

Figures 3 and 4 show the observed and computed tidal residual flow of the surface layer. The results of computed tidal residual current showed flows from the north to the south in the northwestern part of the bay entrance. Also, computed results has good agreement with the results of field experiment conducted in 1983 (Sasaki and Inoue, 1984) and August 1998 (Kagawa Pref., unpubl.). Westward current is predominant on the flood tide; on the other hand, eastward current is predominant on the ebb tide in and around the Bisan-Seto area. The current speed in the area at the mouth of bay is 15-20 cm/s much larger than near the inner part of bay. Particularly, northward current less than 10 cm/s appear at-offshore area. Figures 5-8 show the results (August, 2000) of the distribution of DO from field experiment and computed by numerical model. These results were taken into the DO consumption rate by fish and sediment at each area in Sido bay. The comparison shows it is necessary to calculate the distribution of DO taking into the changes in DO consumption rate at each area in a semi-enclosed bay. Figures 9 (at Stn. 4) and 10 show the computed vertical profile of DO (X-X section, Fig. 2). The lowest values of DO occurred at lower layers between 8 m depth and the bottom. The concentration is over 3.0 ml/l all over the bay and this condition is not bat for fish in an aquaculture grounds. Also, the results have good agreement with field experiments.
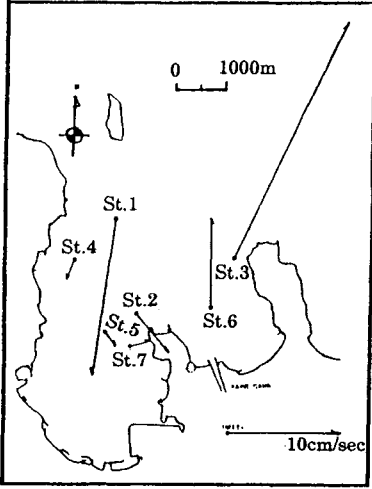
Figure 3. Observed tidal residual current (surface)
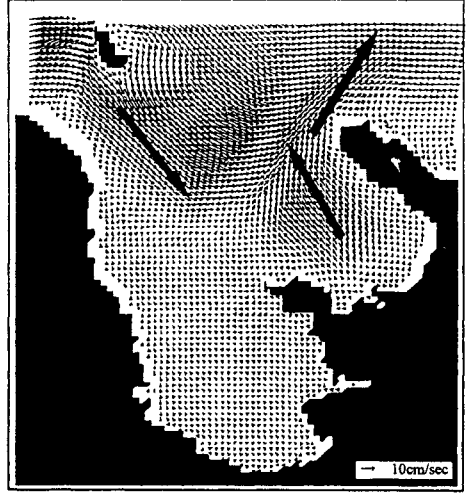
Figure 4. Computed tidal residual current (0-1.5m)
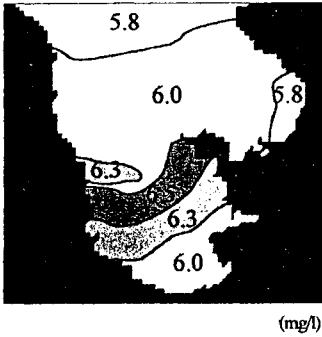
Figure 5. Observed distribution of DO (surface layer)
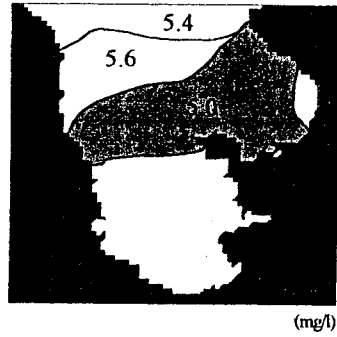
Figure 6. Observed distribution of DO (lower layer)
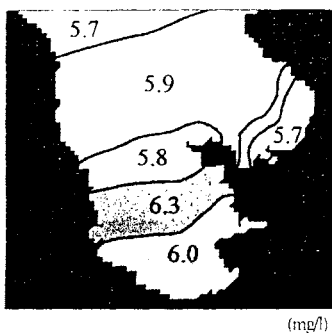
Figure 7. Computed distribution of DO
(0-1.5m)
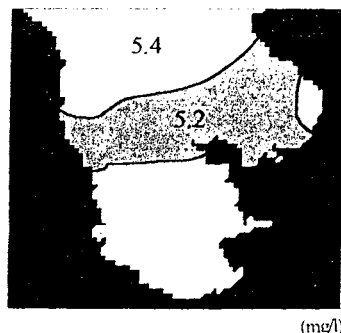
Figure 8. Computed distribution of DO
(6.5-9.5 m)
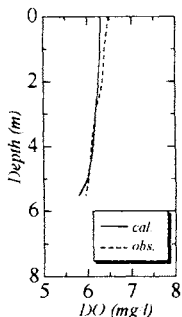
Figure 9. Vertical profiles of DO
(Stn. 4)
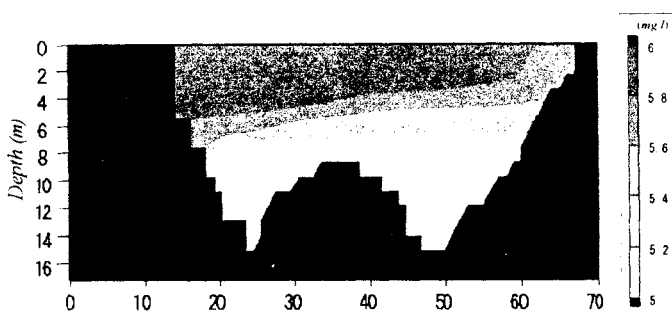
Figure 10. Vertical Distributions of DO
(X-X' section)

Figure 11 depicts the velocity field of the surface layer. The computed flow fields are verified by results of field experiment conducted in 1998 (Kagawa Pref., unpubl.). Westward current is predominant on the flood tide; on the other hand, eastward current is predominant on the ebb tide around the Bisan-Seto area. The current speed in the area among the islands is 1.0-1.5 m/s much larger than near the shore area. Particularly, northward current less than 0.1 m/s appears between Koteshima Island and Teshima Island. We hear from fishermen working and fishing in the area around the Koteshima Island, Teshima Island, Hiroshima Island and Takamishima Island is one of good fishing ground in Bisan-Seto area. The area between Koteshima Island and Teshima Island is considered for main spawning ground.
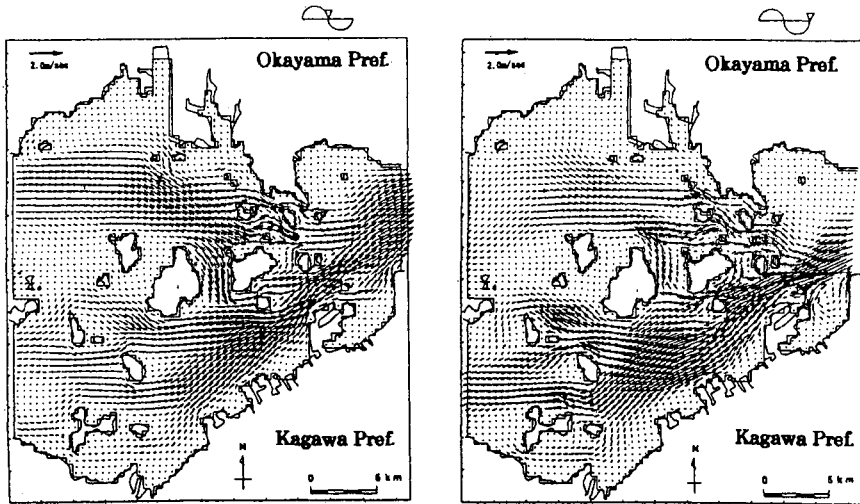
Figure 11. Computed flow field (depth:0-6 m)

Figure 12 depicts computed trajectories of 400 particles supposed to eggs/larvae during 30 days from the spawning ground. From the results of numerical simulation, about 65% particles are transported toward the shelf region area shallower than 10 m around the four islands. It is suggested from this results, that region would be become a good habitats or nursery grounds for marine resources. It is further necessary to look at how the seasonal wind condition affect on the recruitment in the future.
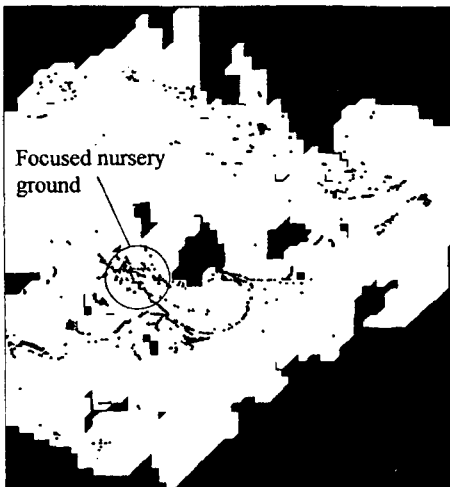
Figure 12. Computed trajectories of 4,000 particles for 30 days after they were released from spawning ground where locate the near shore of islands (heard from fishermen who work in the Bisan-Seto area)

424

CONCLUSIONS

A numerical model of distributions of DO in an aquaculture grounds has been made. The model was applied to the aquaculture grounds in a semi-enclosed bay that utilizes wave energy for water exchange by itself. Tidal current coming from the north and south generally created a recirculating flow pattern influenced by geographic effect at mouth of the bay. About 60% of the whole bay respiration is due to organisms and chemicals suspended in the water, about 25% is due to the fish in the aquaculture cage, and 15% is due to the sediment. A useful evaluation method to estimate the DO distribution of aquaculture grounds was proposed by using numerical model taking the effect of oxygen consumption rate at each area in semi-enclosed bay into consideration. Also, this study has revealed that transportation of fish eggs and larvae from spawning ground to the nursery ground in and around the Bisan-Seto by using numerical simulation model. Then, it is necessary to take the system for creating fishery ground and to estimate the carrying capacity of aquaculture grounds. It is the most important to do continuous field experiment and that results are applied to numerical simulation model again and again to evaluate of changes marine environment.

ACKNOWLEDGEMENTS

REFERENCES

Fujihara, M., Y. Suenaga, H. Nakata, T. Nagasawa and H. Yamada. 1997. Numerical Simulation on the Transport of Brown Sole Eggs and Larvae Using an Euler-Lagrangian Method (in Japanese with English abstract). *Fisheries Engineering,* 34(2): 147-154.

Nakata, H., Y. Suenaga and M. Fujihara. 1999. Wind-induced drift of brown sole eggs and larvae in the shelf region near Sado Strait in relation to the recruitment mechanism. In the *Bulletin of Tohoku National Fisheries Research Institute,* No. 62:51-60.

Suenaga, Y., H. Nakata, M. Fujihara and T. Nagasawa. 1996. Numerical Simulation of the Wind Effect on the Transport of Brown Sole Eggs and Larvae in and around the Sado Strait (in Japanese with English abstract). *Fisheries Engineering,* 32(3): 219-228.

Suenaga, Y., M. Fujihara, T. Sasaki and K. Masuda K. 1999. Development of Evaluation Method for Constructing Aquaculture Habitats. In *Recent Advances Marine Science and Technology 98,* pp. 93-99.

Suenaga, Y., H. Nakata, M. Fujihara and T. Nagasawa. 1996. Numerical Simulation of the Wind Effect on the Transport of Brown Sole Eggs and Larvae in and around the Sado Strait (in Japanese with English abstract). *Fisheries Engineering,* 32(3): 219-228.

Suenaga, Y., M. Fujihara, T. Sasaki and K. Masuda K. 1999. Development of Evaluation Method for Constructing Aquaculture Habitats. In *Recent Advances Marine Science and Technology 98,* pp. 93-99.

A STUDY ON KELP FOREST REGENERATION USING POROUS CONCRETE

Munehisa Yoshida[1] and Motoharu Tamai[2]

[1]Technical Center, Okumura Engineering Corporation
Minatoku, Osaka, JAPAN
munehisa.yoshida@okumuradbk.co.jp

[2]Department of Civil Engineering, Kinki University
Higashi Osaka, Osaka, JAPAN
tamai@civileng.kindai.ac.jp

ABSTRACT

Porous concrete contains many cavities and it is effective as an adherent basis for marine organisms. This paper presents the results of an investigation undertaken to develop additional data on the properties of porous concrete mixed with granulated fertilizer. Granulated fertilizer is composed of dissolved nutrients, which are useful for the growth of algae in the long term. Test plates were installed in the SETO Island Sea, Japan, in order to evaluate the effectiveness of porous concrete with fertilizer. The size of the test plates for experiment was 2m in height and 1m in width. Properties of three types of mixture proportion were evaluated experimentally, namely, porous concrete, porous concrete with fertilizer and normal concrete. The experimental term was two years from September 1999 to March 2002, and adherence of algae on the test plates was observed. As a result, compressive strength was stabilized over 18 MPa. The algae succession was observed on all test plates, and biota of circumference was formed on test plates. The quantity of large algae on porous concrete was more abundant than on normal concrete. However, the greatest abundance of large algae was found on porous concrete with fertilizer. Seaweed adhesion to porous concrete was found to be greater than with normal concrete. As a result of using a mixture of granulated fertilizer and converter slag, there tended to be a high degree of seaweed cover. It is concluded that porous concrete with fertilizer is effective as an adherent basis of algae.

INTRODUCTION

In Japan, the harvest of seafood has gradually decreased in sea coastal areas. The main cause of this is the disappearance of kelp forests. Based on recently published public statistical data, reclamation and the construction of artificial revetments constitute the greatest cause of this disappearance. Another reason is the emergence of coralline flats in sea coastal areas brought about by changes in hydrographic conditions. Also, there are some reports that the mineral supply through rivers from inland areas has decreased due to artificial development.

The Fisheries Agency in Japan has advocated the recovery of diverse organisms through advances in environmental preservation and improvements to nearby sea areas. This is a change from the previous policy of gaining fisheries simply to forming fishery. According to the guidelines of the Fisheries Agency, regulations for fishing port construction should consider not only the effects of ocean waves and weather, but also the revitalization and the mitigation of aquatic resources. In this way, the environment of organisms which inhabit port facilities can be restored, and aquatic resources can be recovered and increased.

427

Although much research has been done on kelp forest creation, the goal here is to increase the production of aquatic resources. There is a considerable body of research work showing that seaweed can be made to effectively adhere to concrete surfaces through the addition of acute-angled roughness (Hasegawa et al., 1992). In addition, there have been some positive tests in which an effective nutrient composition was dissolved within the ions of a hard materials for the purpose of seaweed growth. However, the elution of the nutrient composition comes only from the surface of a hardened material, and there are some problems with the amount of elution and the elution persistence. Porous concrete is advantageous for the adhesion of algae (Tamai and Nishiwaki 1992), and it has been proven to function as a habitat for microorganisms and small animals (Tamai et al., 1997).

The purpose of this study is to establish a method for the urgent recovery of biodiversity in coastal areas. The basis for this biodiversity of the ocean is kelp forest creation. Therefore, enriched porous concrete was developed as a base material into which seaweed was efficiently inserted. This paper describes the physical properties of enriched porous concrete and the effect of adherent seaweed.

ENRICHED POROUS CONCRETE (EPOC)

The composition of enriched porous concrete is shown in Figure 1. Porous concrete is a construction material which is less damaging to the environment than normal concrete. The continuous voids of porous concrete become spaces which can be inhabited by organisms, and the coarse surface shape is effective for seaweed adherence. Granulated fertilizer and minerals employed for the growth of seaweed, are mixed into the porous concrete. In sea areas where the oligtrophy or nutrient balance has collapsed, it is possible to supplement a moderate nutrient composition by installing this basic material. Also, it is possible to adjust the fertilizer components and the amount of elution according to the hydrographic conditions of the different sea areas. Enriched porous concrete is a type of technology which can assist in the rapid and natural revegetation of coralline flat sea areas. This technology restores a natural environment to sea areas which have been artificially destroyed.
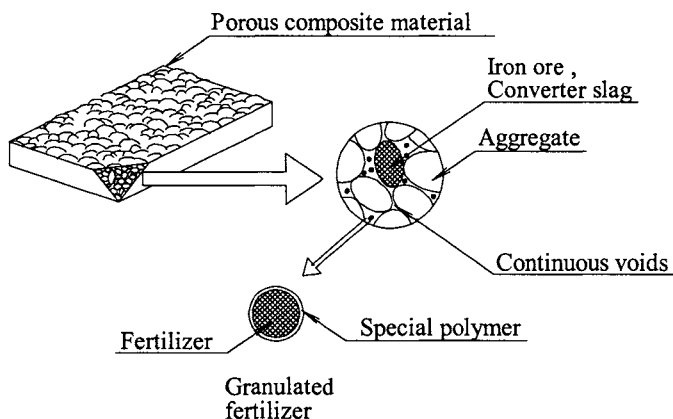
Figure 1. Composition of enriched porous concrete

MATERIALS AND MIXTURE PROPORTIONS

The only stipulation is that the crushed stone contain particles of equal size. Cement paste is used as the binding material. However, when aggregate No.6 (Size 5-13 mm) crushed stone is chosen, mortar is used for the binding material in order to reduce material separation and contraction from drying. Blast furnace slag cement is used for the cement.

It is possible for blast furnace slag cement to reduce adverse effects on flora and fauna caused by the elution of free lime, and to counteract the decrease in durability of the concrete. This is because it has a small, silicic acid-free lime content. High-range water-reducing admixtures are used in an attempt to attain high viscosity and the densification of the binding materials.

The granulated fertilizer consists of urea (a nitrogen component) and phosphoric acid (a phosphorus component), which are sealed in a special polymer in two layers. The reason for the seal is to prevent the destruction of the granulated fertilizer when it is mixed with concrete, and to control the amount of elution of the fertilizer component to sea areas. Using a polymer is very safe for the environment.

The mixture proportions of test plates are shown in Table 1. The voids of the porous concrete are filled up to 40% with an aggregate containing a binding material. In such a case, the free volume of the porous concrete constitutes 24 percent. The granulated fertilizer makes up 20% of the total cement content by mass. This is considered the ideal mixture for strength and permeability. By changing the mixture, it is also possible to alter the strength. When iron ore and converter slag (a heavy material containing Fe) are used, 20% of the aggregate is replaced with this mixture. Converter slag is used to supply Fe supplement.

Table 1. Mixture proportions

Mixture type	Materials	W/C (%)	Unit product weight (kg/m^3)						
			W	C	SS	G	Sp	GF	G2
POC	Porous concrete	24	62	261	0	1489	2.6	0	0
EPOC	Porous concrete With fertilizer	24	62	261	0	1043	2.6	52.2	612
NC	Normal concrete	63	161	256	822	1019	0.6	0	0

C: Cement (Blast furnace slag cement), W: Water, G: Gravel (5-13mm),
GF: Granulated fertilizer, SS:Silca sand, Sp: Super plasticizer,
G2: Converter slag

PROPERTY OF ENRICHED POROUS CONCRETE

Continuous percentage voids and compressive strength

Test results on the void ratio and the compressive strength of the hardened porous concrete are shown in Table 2. In general, when the aggregate grain diameter increases, the voids increasingly represent a structural defect and the compressive strength of the concrete decreases. The strength of the concrete is inversely proportional to the void ratio when the void ratio of the aggregate is different, even if the diameter range is identical. Using a hard aggregate, like iron ore, it is possible to increase the compressive strength without changing

429

the void ratio. The addition of fertilizer lowers the void ratio by only a minute amount. However, the mixture of fertilizer hardly influences the compressive strength at an age of 28 days.

Table 2. Properties of hardened porous concrete

Mixture type	Void ratio (%)	Compressive strength (N/mm^2)
POC	25.7	18.3
EPOC	21.8	18.0

Dissolution performance of the nutrient composition

Results of the dissolution tests on nitrogen and phosphorus are shown in Table 3. They confirm that ammonia and phosphoric acid dissolve in the EPOC type mixture containing the granulated fertilizer after 90 days in the sea. The cumulative leaching of ammonia was 2.3%, and the cumulative leaching of phosphoric acid was 0.025 percent. It is confirmed that the elution function of the fertilizer component works effectively even if the enriched porous concrete is immersed in seawater.

Table 3. Cumulative leaching rate from EPOC in sea

Mixture type	Nitrogen (%)		Phosphorus (%)	
	30 days	90 days	30 days	90 days
EPOC	0.8	2.3	0.008	0.025

METHODS

Some test plates were sunk in the experimental sea area, and the adherent condition of the seaweed was observed. For this experiment, seaweed was naturally inserted into the test blocks. Therefore, a moderate seaweed community existed around the test plates, and an experimental site was now required which would provide hydrographic conditions suitable for the growth of seaweed. An experimental site satisfying the above conditions was selected, as shown in Figure 2. It is located in the SETO Inland Sea of Japan, and a community of *Ecklonia cava* exists within the circumference (Fig. 3).
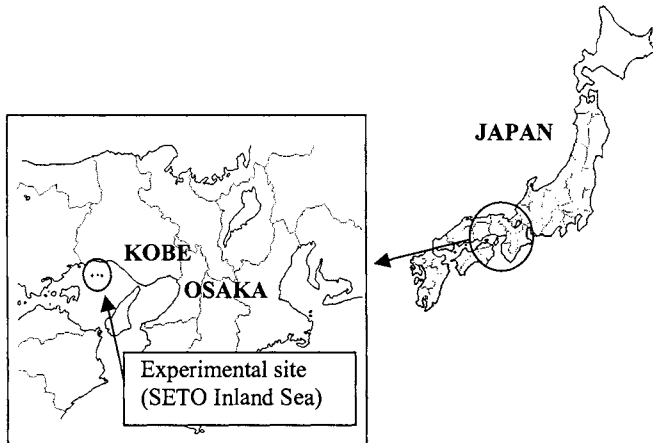
Figure 2. Experimental site

Figure 3. Condition of the *Ecklonia cava* community around experimental site

Three kinds of test plates were made with the mixtures shown in Table 1.   The shapes of the test plates used at experimental site were 2 m in height x 1 m in width x 20 cm in thickness. They were immersed in the water at the low water depth line -0.5 m - -2.5 m on a caisson wall. The condition of the test plates is shown in Figure 4.
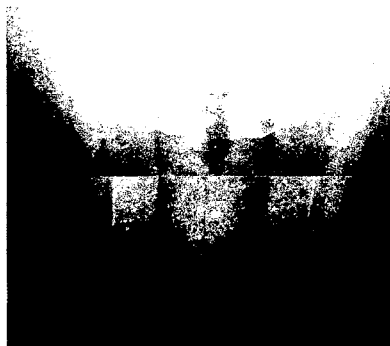
Figure 4. Condition of the test plates

A biological study was carried out two years after the installation of the test plates.   On the surface of the test plates, the type and the degree of cover of all the organisms which could be confirmed macroscopically were observed.

Table 4. Adherent seaweed on test plates

Mixture type	3 months	5 months	1 year
POC	BACILLARIOPHYCEAE (70) Total 7 types	BACILLARIOPHYCEAE (65) *Colpomenia sinuosa* (10) Total 15 types	*Ecklonia cava* (60) Total 5 types
EPOC	BACILLARIOPHYCEAE (65) Total 8 types	BACILLARIOPHYCEAE (45) *Colpomenia sinuosa* (5) Total 11 types	*Ecklonia cava* (70) Total 8 types
NC	BACILLARIOPHYCEAE (75) Total 8 types	BACILLARIOPHYCEAE (30) Total 12 types	*Ecklonia cava* (40) Total 3 types

(%): degree of seaweed

RESULT AND DISCUSSION

The degree of seaweed cover on the test plates is shown in Table 4.   After three months, the surfaces of the test plates were covered in *Bacillariophyceae,* and arthropod adhesion was confirmed.   The condition of the EPOC type plate after one month is shown in Figure 5. After five months, the adhesion of *Colpomenia sinuosa* was confirmed on porous concrete. After one year, the adhesion of *Ecklonia cava*, over 40 cm in length, was confirmed on the EPOC plates.   The dominant species after one year was *Ecklonia cava* of the brown alga plant.
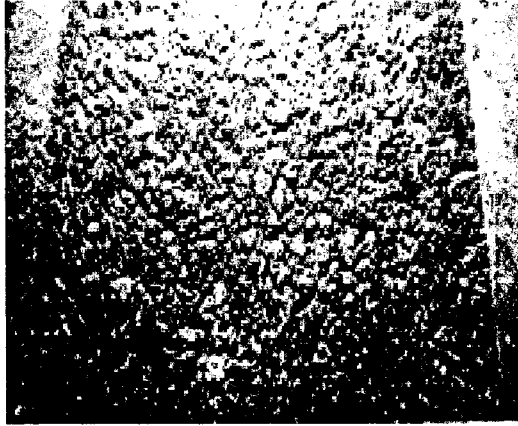
Figure 5. Condition of the test plate after one month (EPOC)

The degree of seaweed cover on the porous concrete was clearly higher than on normal concrete. The condition of seaweed adhesion on the EPOC plate is shown in Figure 6.
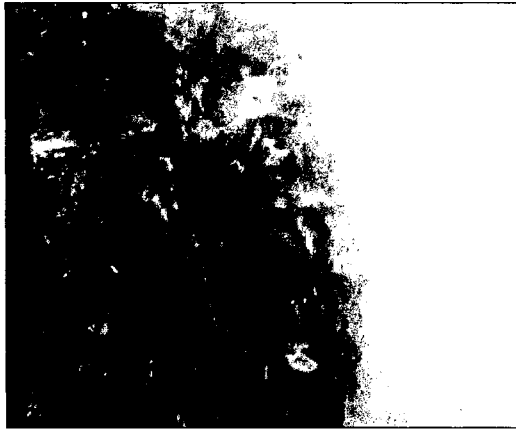
Figure 6. Condition of the test plate after one year (EPOC)

The population of *Ecklonia cava* on test plates is shown in Figure 7. After two years, the population increased. Also, the population *cava* on the EPOC plates was clearly higher than on other types.
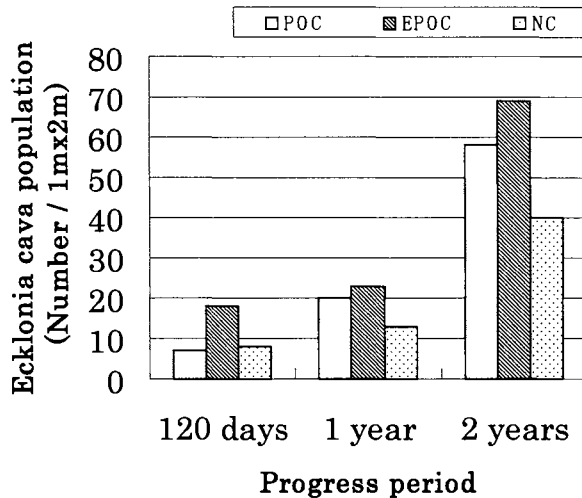
Figure 7. Relationship between seaweed population and progress period

EPOC has the strength and voids which are necessary as a base for seaweed bed creation. Seaweed rapidly adheres to porous concrete. Seaweed adhesion to porous concrete was found to be greater than was the case with normal concrete. Because of the mixture of granulated fertilizer and converter slag, there tended to be a high degree of seaweed cover. It is concluded that porous concrete with fertilizer is effective as an adherent basis for algae.

CONCLUSION

The following conclusions have been reached.

1. Employing a special method for treating fertilizer, using a special polymer in the seal, a granulated fertilizer for porous concrete has been developed. It has been confirmed that by using this granulated fertilizer, the elution of the rapid fertilizer component from porous concrete can be prevented and fertilizer elution can be maintained.

2. A mixture with converter slag also becomes a source of elution for ferrous ion.

3. Seaweed rapidly adheres to porous concrete. Seaweed adhesion to porous concrete was found to be greater than with normal concrete.

4. Because of the mixture of granulated fertilizer and converter slag, there tended to be a high degree of seaweed cover and wet weight.

REFERENCES

Hasegawa, H., H. Hirakuchi, Y. Terawaki and Y. Kawasaki. 1992. Structual design of artificial foundation for kelp bed. In *JCI Proceedings of Civil Engineering in the Ocean*, Vol. 8, 379-384. JAPAN

Tamai, M. and Y. Nishiwaki. 1992. Studies on marine epilithic organisms to no-fine concrete using slag cement and portland cement with silica fume. *ACI Journals.* SP-132-87, Vol. 2: 1621-1635.

Tamai, M., H. Mizuguchi. and T. Okamoto. 1997. Organism adaptable concrete. *Journal of Global Environment Engineering.* Vol. 3: pp.65-75.

ENVIRONMENTAL EVALUATION OF AN ARTIFICIAL LAGOON BASED ON THE SESSILE ORGANISM COMMUNITY

Naotaka Yoshimura[1], Yasunori Kozuki[1], Hitoshi Murakami[1], Kengo Kurata[1], Koji Otsuka[2] and Naoki Nakatani[2]

[1]Graduate School of Engineering, The University of Tokushima
Tokushima, Tokushima Pref., JAPAN
n-yoshi@sogokagaku.co.jp

[2]Graduate School of Engineering, Osaka Prefecture University
Sakai, Osaka Pref., JAPAN

ABSTRACT

Artificial lagoons have been constructed in enclosed sea areas in order to conduct restoration of water quality and to enhance floral and faunal settlement. Rinku Park Uchiumi, which formed an artificial lagoon, in Osaka Bay, Japan was constructed in 1996. Water exchange of the water body in Uchiumi periodically occurs through the permeable rubble-mound breakwater by the tide. The purpose of this study is to evaluate the environment of the artificial lagoon by examining the community structure of sessile organisms, and to optimize the management for the good condition, which keeps and improves the water purification functions, of the artificial lagoon.

Investigation of the sessile organisms was carried out in the permeable rubble-mound breakwater of the seaward (area A) and the shoreward side (area B), and on the rubble-mound inside the lagoon (area C) in summer and winter. The results showed that the sessile organism community depended on the area. The sessile organism community in area A was composed of diverse organisms in each trophic level, such as marine algae and some animals. There were also diverse organisms in area B with seawater flowing, but the number of species in area B was lower than in area A. The rubble-mound in area C were thickly overgrown with green algae, and the number of species in area C was low. This showed that green algae were dominant in such a calm environment as an artificial lagoon.

Generally speaking, the presence of green algae in the calm area is taken as a positive sign and as leading to an improvement of the water quality due to the assimilation of nutrients by algae. However, eutrophication occurred because of few herbivores and much green algae which decomposed on a seabed. As a result for better control of the environment of the artificial lagoon, the green algae must be regularly harvested.

INTRODUCTION

The water quality in enclosed sea areas encircled by big industrial cities, such as northwest part of Osaka Bay, is generally chronically bad since the pollution load is much higher than the natural purification capacities. In order to purify the seawater, several coastal eco-technologies have been proposed.

Artificial lagoons, which are calm water areas surrounded by permeable rubble-mound breakwaters, were proposed as one of the coastal eco-technologies applicable to the enclosed sea (Akai, 1984). It has been pointed out that artificial lagoons may have some water purification functions, such as wave breaking re-aeration, biological contact oxidation in the permeable rubble-mound breakwater, increased transparency due to the sinking of suspended matter, carbon and nutrient fixation and improved oxygen supply from algae, creation of the biological material cycle.

Some investigations on the water purification functions of permeable rubble-mound breakwaters have been carried out. The biological water purification mechanism of the artificial lagoon in Rinku Park in Osaka Bay was investigated (Otsuka and Nakatani, 2001). Their approach was according to an ecosystem modeling technique, which consists of field investigations and numerical analysis using an ecosystem model. The results of estimations showed that the carbon and nutrient fixation effects by marine algae was large and the total fixation effects decreased year by year because of the accumulation of the sedimentary organic matter. However, environmental evaluation of an artificial lagoon based on the sessile organism community has not been discussed from the viewpoint of ecology in these investigations.

The purpose of this study is to clarify the community structure of sessile organisms, based on the biota and biomass in the artificial lagoon, to evaluate the environment of the artificial lagoon by the sessile organism community, and to optimize the management for the good condition, which keeps and improves the water purification functions, of the artificial lagoon.

MATERIALS & METHODS

Investigation Site and Zoning

Rinku Park, the investigation site in this study, is located near the Kansai International Airport in Osaka Bay (Fig. 1). In this park, there is an artificial lagoon so-called Uchiumi which is surrounded by rubble-mound revetment including transmittable breakwater and sand beach (Fig. 2). Rinku Park Uchiumi, which is about 120 m long, 50 m wide, and 1.5 m deep in average, was constructed in 1996. The water area and volume of Uchiumi are about 6,600 m^2 and 10,000 m^3 in average, respectively, and over 40% of the seawater is exchanged between inner and outer lagoon areas at flood tide.

Uchiumi of the investigation site was divided into three areas (A, B and C) in this study. The wave dissipating concrete blocks on the permeable rubble-mound breakwater on the open sea side were designated as "area A", and the stones on the inner lagoon side as "area B" and the stones used in the rubble-mound surrounding the inner lagoon side as "area C" (Fig. 2).
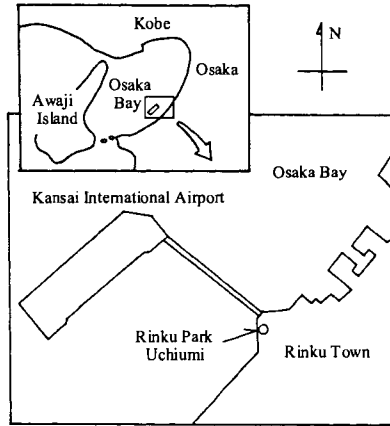
Figure 1.   Location of Rinku Park Uchiumi which has the investigation site
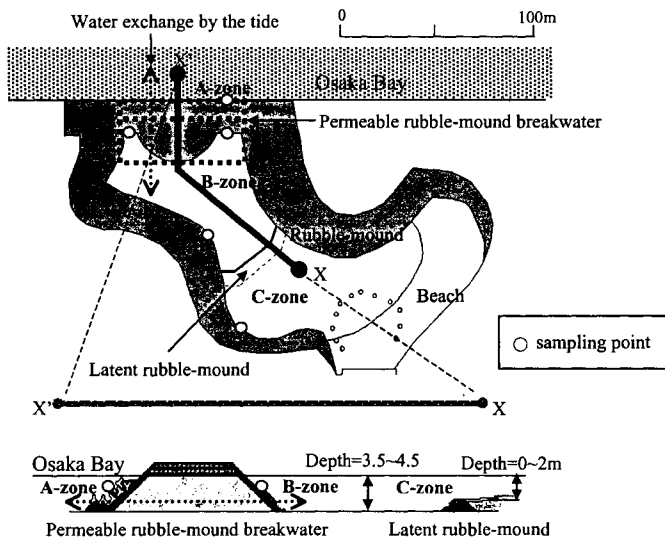
Figure 2. Location of sampling point, general arrangement and cross section of Rinku Park Uchiumi which formed an artificial lagoon

Methods of investigation

Field investigations were performed on August 6, 1998 in summer and February 17, 1999 in winter.   The sampling points of each area in the artificial lagoon were 1 point in area A, and 2 points in areas B and C (Fig. 2).   The mean of 2 points data was used in the sampling data in areas B and C. The sampling water level was about 1 m under the mean water level in Osaka Bay.

Quadrat samples (30 cm * 30 cm) of the sessile organisms in the artificial lagoon were taken from the sloping surface of the blocks and stones using a scraper, followed by checking for the organisms present.

The samples of the sessile organisms were identified, and the wet weight was measured for each species. For sessile animals which had a shell, the wet weight was measured including the shell. Data on wet weight were converted into 1 m * 1 m. Moreover, a part of dominant species measured for dry weight was examined for amounts of carbon by using a Carbon and Nitrogen Analyzer.

Methods of Analysis

Calculation of Biomass of the Sessile Organisms
The annual mean of biomass averaged wet weight of summer and winter was converted into the amount of carbon using the ratio of carbon to wet weight (= C/W ratio, see Table 1), and into the annual production using the ratio of annual production to annual mean biomass (= P/B ratio). The P/B ratio 2.19 of *Ulva pertusa* (Fuji and Kawamura, 1970) was used for marine algae because of much green algae. The P/B ratio 2.82 of *Mytilus galloprovincialis* of Osaka Bay (Yamochi et al., 1995) was used for sessile animals because of many suspension feeders which had a shell. In addition, the C/W ratio of three sessile animals, *Omphalius rusticus*, *Crassostrea gigas* and *Balanus* sp., was taking carbon weight including the shell into consideration.

Table 1. Contents of the C/W ratio of the dominant species of the sessile organisms

Taxon		Species	C/W	Average
Marine Algae	Green Algae	*Enteromorpha* spp.	0.0634	0.0630
		Ulva sp.	0.0626	
	Brown Algae	*Ectocarpus* sp.	0.0167	0.0167
	Red Algae	*Grateloupia lanceolata*	0.0333	0.0333
Sessile Animals	Mollusks	*Omphalius rusticus*	0.1040	0.1066
		Crassostrea gigas	0.1091	
	Arthropods	*Balanus* sp.	0.0865	0.0865
	Tunicates	*Ciona* sp.	0.0173	0.0173
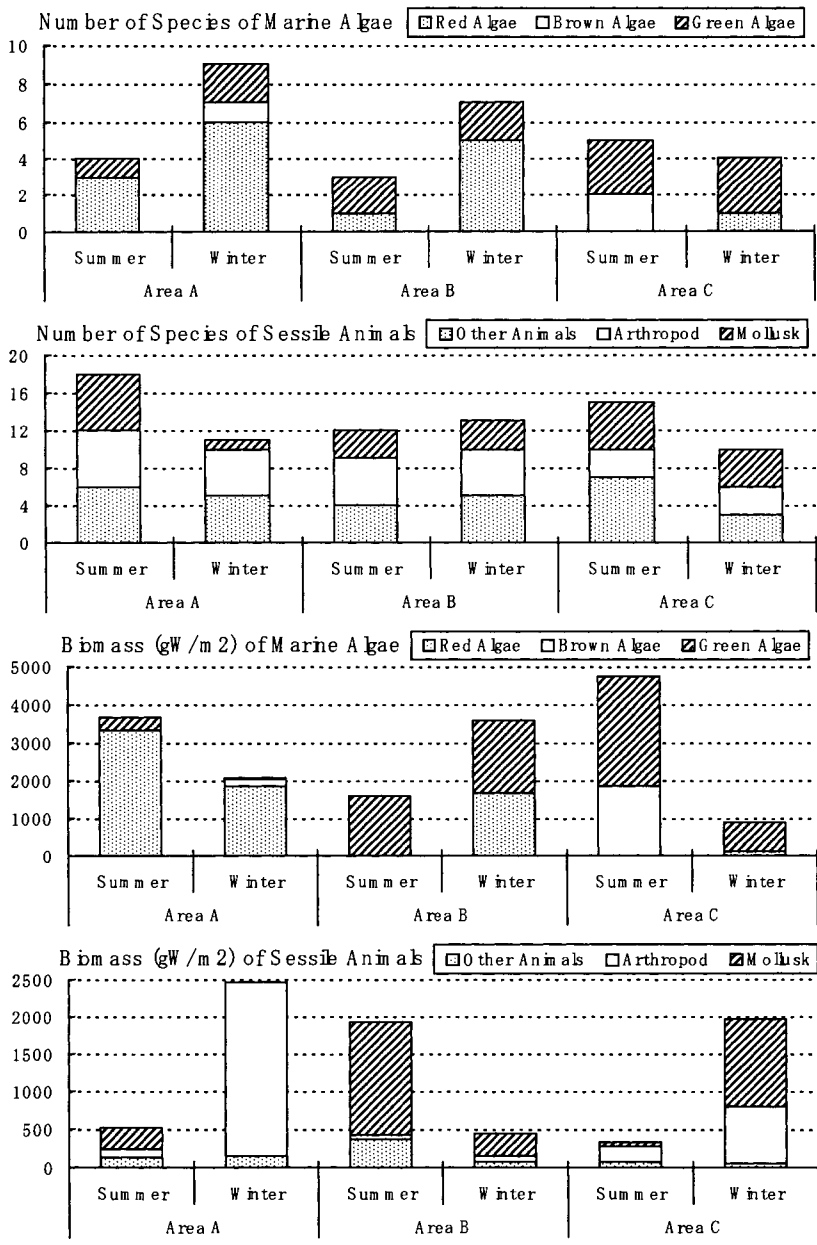
Figure 3. Seasonal changes of the number of species and biomass (gW/m²) in each taxa of marine algae and sessile animals.

Analysis of the Community Structure of Sessile Organisms
The classification of the trophic level of sessile organism commuity was as follows. (1) The first trophic level which was the producers was made of marine algae. (2) The second trophic level which was the primary consumers was made of herbivores (Polyplacophora, Gastropoda, Echinoidea, etc.) and suspension feeders (Porifera, Bivalvia, *Balanus* spp., Bryozoa, Tunicata, etc.). (3) The third trophic level which was the higher consumers was made of carnivores (Actiniaria, Gastropoda, Crustacea, Asteroidea, etc.).

In order to evaluate the trophic structure, the annual production of each trophic level on the basis of this investigation was compared to the expected value. The relation between the first and second trophic levels (only herbivore) and between the second and third trophic levels were examined in this study. The expected value was calculated from 15 % of the ecological efficiency (Ryther, 1969) of the coastal sea shore. It was considered that a smooth material cycle was formed if the measured value of annual production was close to the expected value. Since a smooth material cycle was the good condition of ecosystem in the artificial lagoon, it was regarded as good environment of the artificial lagoon.

RESULTS

Distribution of the Sessile Organisms

Number of Species (Table 2, Fig. 3)
The number of species of marine algae was 7-9 in each area, and the relation between the areas was C<B<A. The number of species of red algae increased in winter. The number of species of sessile animals was 17-22 in each area, and the relation between the areas was C<B<A. The number of species of sessile animals in this study did not show any seasonal changes.

Dominant Species (Table 2)
The dominant species of marine algae were red algae (*Chondrus* sp., *Gelidium elegans, Grateloupia lanceolata*, etc.) in area A, red algae (*Gracilaria textorii*, etc.) and green algae (*Enteromorpha* spp., *Ulva* sp., etc.) in area B, green algae (*Enteromorpha* spp., *Ulva* sp., etc.) and brown algae (*Ectocarpus* sp.) in area C. The dominant species of sessile animals were arthropods (*Balanus* spp., etc.) in area A, mollusks (*Omphalius rusticus*, etc.) and tunicates (*Ciona* sp., etc.) in area B, mollusks (*Crassostrea gigas*, etc.) and arthropods (*Balanus* spp., etc.) in area C.

Biomass (Table 2, Fig. 3)
The annual mean biomass of marine algae was 2,585-2,868 gW/m^2 and 99-138 gC/m^2, and the relation between the areas was B<C<A in wet weight, and A<C<B in carbon weight. This change is the reason that C/W ratio of green algae is much higher than it of other algae. The annual mean biomass of sessile animals was 1,152-1,496 gW/m^2 and 106-123 gC/m^2, and the relation between the areas was B<C<A. There was a high biomass of the sessile organisms in areas A and C in summer, and in area B in winter.

Production (Table 2)
The annual production of marine algae was 217-302 gC/m^2/y, and the relation between the areas was A<C<B. The annual production of sessile animals was 299-346 gC/m^2/y, and the relation between the areas was B<C<A.

Table 2. Comparisons of data on the sessile organism community in this study

	Area	Number of Species	Annual Mean Biomass		Annual Production	Dominant Species
			gW/m^2	gC/m^2	gC/m^2/y	
Marine Algae	A	9	2,868	99	217	*Chondrus* sp. *Gelidium elegans* *Grateloupia lanceolata*
	B	8	2,585	138	302	*Enteromorpha* spp. *Ulva* sp. *Gracilaria textorii*
	C	7	2,818	133	291	*Enteromorpha* spp. *Ectocarpus* sp. *Ulva* sp.
Sessile Animals	A	22	1,496	123	346	*Balanus* spp.
	B	18	1,191	106	299	*Omphalius rusticus* *Ciona* sp.
	C	17	1,152	107	303	*Crassostrea gigas* *Balanus* spp.

Community Structure of the Sessile Organisms

Biomass of Trophic Level (Fig. 4)
Biomass of the first trophic level was the highest of all the trophic levels at each area. There was a high biomass of suspension feeders at the second trophic level in areas A and C, and a high biomass of herbivores at the same level in area B.

Trophic Structure (Table 3)
The annual production of herbivores in the second trophic level in area A showed that the measured value was near the expected value. The annual production of herbivores in the second trophic level was markedly more than the expected value in area B, and markedly less than in area C. The annual production of the third trophic level in areas A and B showed that these measured values were near the expected values. The annual production of the third trophic level was less than the expected value in area C.

443
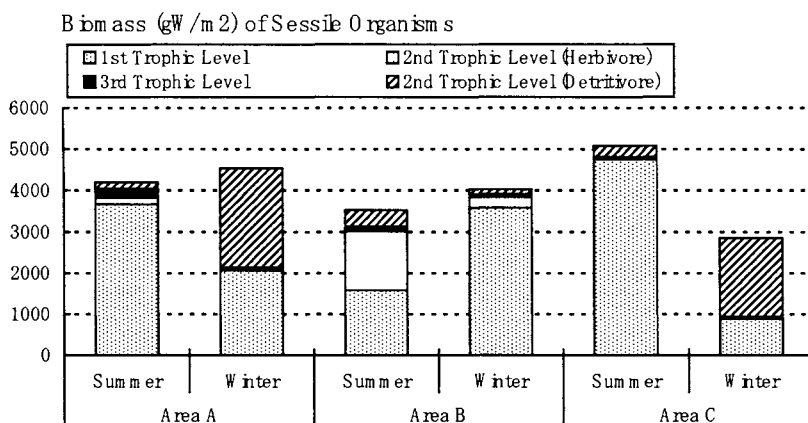
Figure 4. Seasonal changes of biomass (gW/m^2) in each trophic level of the sessile organisim community.

Table 3. Comparisons between the measured and expected value of annual production (gC/m^2/y) in trophic levels of the sessile organism community

Trophic Level	Value	area A	area B	area C	Remarks
The First Trophic Level	Measured	217	302	291	
The Second Trophic Level (Only Herbivore)	Measured	22	254	3	
	Expected	33	45	44	15% of the first trophic level
The Second Trophic Level	Measured	315	274	294	
The Third Trophic Level	Measured	31	25	9	
	Expected	47	41	44	15% of the second trophic level

DISCUSSION

Relation between the Sessile Organisms and Physical Environment

Suspended matter content of the seawater through the permeable rubble-mound breakwater in an artificial lagoon was less than of the outer seawater (Akai, 1984). It was considered that the water quality of Rinku Park Uchiumi, which has the investigation site, was almost homogeneous (Otsuka et al., 1998). In this study, the sessile organism community was examined in the response to flow and suspended matter content of seawater as physical environment.

The distribution of marine algae in area A, where red algae was dominant, was similar to the distribution in area B in winter because the seawater of the outer sea side flowed into the inner sea side. On the other hand, there was much thread-shaped brown algae, *Ectocarpus* sp., in area C in summer. Thin leaf-shaped, shell-shaped and thread-shaped algae were dominant in an area where the seawater flow was very low (Neushul, 1972). These show that the distribution of marine algae in area C is formed on the basis of the calm environment.

The distribution of sessile animals in area A, where cirripedes in the suspension feeders were dominant, was not similar to the distribution in area B, where *Omphalius rusticus* in herbivores was dominant. This suggests that suspended matter content of the seawater in the artificial lagoon is less than it of the outer seawater. These results show that the sessile organism community is formed according to the physical environment of each area in the artificial lagoon.

Evaluation of the Trophic Structure of Sessile Organisms

The annual production of the third trophic level in areas A and B was relatively similar to the expected value, but it in area C was less than the expected value. This indicates that a smooth material cycle was not formed in the calm area C because of few carnivores of the sessile organisms community in it.

The annual production of herbivores in the second trophic level in area A was relatively similar to the expected value, but it in area B was much more than the expected value. This means that marine algae used as the food of herbivores are insufficient, if the energy flow from marine algae to herbivores was appropriately formed, in area B. This is the reason that the annual production in the first trophic level in the sessile organism community does not contain it of microalgae. Therefore, it is thought that the production of microalgae is higher in area B and contributes to the water purification in the area with seawater flowing in the artificial lagoon.

On the other hand, the annual production of herbivores in the second trophic level in area C was much less than the expected value. It was shown that a smooth material cycle was not formed in the calm area C because of marine algae and few herbivores in the sessile organism community in it. The dominant species of this area were short-lived algae, *Enteromorpha* spp., *Ulva* sp. and *Ectocarpus* sp. Since these algae wither and die, and partly decompose on the seabed, these algae accumulate on the bottom of the artificial lagoon. Finally, it may be caused that the water quality and the quality of the bottom sediment become bad in the calm area of the artificial lagoon. These results indicate that some controls of the biomass of marine algae, e.g. harvesting, are required to keep and improve the water purification functions of the artificial lagoon.

CONCLUSIONS

The distribution and trophic structure of the sessile organisms in the artificial lagoon were different from each area corresponding to the physical environment. A smooth material cycle was formed in the area with seawater flowing, and contributed to the water purification in the artificial lagoon. However, the energy efficiency among the trophic levels of the sessile organism community was low in the calm area because of much green algae, and a smooth material cycle was not formed in it. It seems that the presence of green algae in the calm area is taken as a positive sign and as leading to an improvement of the water quality due to the

assimilation of nutrients by algae.   However, eutrophication occurred because of few herbivores and much green algae which decomposed on a seabed.   It was suggested that environmental deterioration was likely to be caused by much green algae in the calm area of the artificial lagoon. These results indicate that some controls of biomass of green algae, e.g. harvesting, are required to keep and improve the water purification functions of the artificial lagoon.

ACKNOWLEDGEMENTS

REFERENCES

Akai, K. 1984. A Water Purification System in Enclosed Sea Area. In *Proceedings of the 11th Architectural Technology Symposium*, 76-79. (In Japanese)

Fuji, A. and K. Kawamura. 1970. Studies on the biology of the sea urchin-Ⅶ. bio-economics of the population of *Strongylocentrotus intermedius* on a rocky shore of southern Hokkaido. *Bulletin of the Japanese Society of Scientific Fisheries*. 36(8):763-775.

Neushul, M. 1972. Functional Interpretation of Benthic Marine Algal Morphology. In *Contributions to the Systematics of Benthic Marine Algae of the North Pacific*, edited by I. A. Abbott and M. Kurogi, 47-73. Japan: Japanese Society of Phycology, Kobe.

Otsuka, K., N. Nakatani, M. Miyachi, T. Nakanishi, N. Yoshimura and M. Sawada. 1998. Water purification machanism of artificial lagoonin Rinku Park, 1st Report. Field investigations. *J Kansai Society of Naval Architects, Japan*. 229:211-219. (In Japanese)

Otsuka, K. and N. Nakatani. 2001. Estimation of Carbon and Nutrient Fixation Effects of an Artificial Lagoon in Osaka Bay. In *Proceedings of OMAE '01, 20th International Conference on Offshore Mechanics and Arctic Engineering*, OMAE-01-5036, 1-8.

Ryther, J.H. 1969. Photosynthesis and fish production in the sea. *Science*. 166:72-76.

Yamochi, S., H. Ariyama, T. Kusakabe, M. Sano, Y. Nabeshima, K. Mutsutani and T. Karasawa. 1995. Effects of a predominant sedentary organism of the coastal artificial structure on the eutrophiction of the coastal area of Osaka Bay, 1. Growth and elimination of *Mytilus edulis galloprovinciallis* on the vertical wall. *UMI-NO KENKYU*. 4(1):9-18. (In Japanese)

ON THE RESPONSE OF RESIDENTS
AROUND THE TOKYO BAY AQUALINE BRIDGE

Naohiro Takahashi, Yoshihiko Maeno and Mitsuo Takezawa

Nihon University
Tokyo, JAPAN
takezawa@civil.cst.nihon-u.ac.jp

ABSTRACT

Fifteen major bays exist along the 35,000-km shoreline of Japan, including seven closed bays and eight open bays. Recently, a number of large bay bridges have been planned in Japan. The bay bridge spanning Tokyo Bay between Kawasaki and Kisarazu entered service in 1997. The present study investigates the concerns of residents living near the Kisarazu side of the Tokyo Bay Aqualine to the opening of the bridge. Kisarazu had been a prosperous port town for several decades, but recently the prosperity of the area has declined. In the present study, one-thousand residents of Kisarazu were asked to respond to a questionnaire regarding the effects of the Tokyo Bay Aqualine on the local economy and communities. The conclusions are as follows:

    (1) Kisarazu was within easy access of metropolitan Tokyo, Yokohama and Haneda International Airport.

    (2) There was a lack of entertainment in and around Kisarazu Station and Kisarazu Harbor, although no major changes were made to Kisarazu after beginning service Tokyo Bay Aqualine.

    (3) Kisarazu is to be revitalized by attracting tourism, and vitalizing commerce and fishery.

    (4) Kisarazu will be developed with preserved nature and will have many opportunity of doing business in fishery.

    (5) In order to economically strengthen Kisarazu, the fundamental tourist attractions, such as marine life, seafood restaurants and fishing resources as well as shell gathering at low tide around Kisarazu Harbor and Banzu Tideland must be boosted.

INTRODUCTION

Bridges and tunnels can bring prosperity to cities and towns on either side of the bay, channel and river that they connect. A number of bridges and tunnels have been constructed in order to help connect neighbors. However, until recently, the length of such bridges and tunnels was 2-3 km at most. In 1964, the Chesapeake Bay Bridge-Tunnel (approximately 28 km long) connected Norfolk and Cape Charles at the entrance of the Chesapeake Bay in the U.S. (Heibonnsha, 1967). The construction of the Chesapeake Bay Bridge-Tunnel was an epoch-making achievement. In Japan, the Tokyo Bay Bridge-Tunnel (called the Tokyo Bay Aqualine, approximately 15 km long) was constructed to link the cities of Kawasaki and Kisarazu that border Tokyo Bay. How do residents on either side of the bridge-tunnel respond to the construction of the Tokyo Bay Aqualine? The purpose of the present study is to search for some revivals plan in and around Kisarazu from results of questionnaire.

TOKYO BAY AQUALINE

The toll highway across Tokyo Bay was proposed by Ministry of Construction in 1966, and the investigation was taken over by the Japan Highway Public Corporation in 1976. The Tokyo Bay Aqualine was opened to traffic between Kawasaki and Kisarazu on December 18, 1997. The Tokyo Bay Aqualine was constructed in order to vitalize cities and towns along Tokyo Bay.

The Tokyo Bay Aqualine is divided by an artificial island called the sea firefly into a 4.4 km bridge section from Kisarazu and a 9.5 km tunnel section from Kawasaki. Although the estimated traffic was 25,000 cars per day at the time, the bridge opened, at present only about 13,000 cars per day use the Tokyo Bay Aqualine due to the high toll. Figure 1 is the site map of Tokyo Bay. Photo 1 shows a scene of a declining Kisarazu and Photos 2, 3, and 4 are the Tokyo Bay Aqualine.

HISTORY OF KAWASAKI AND KISARAZU

The development of Kawasaki is a result of the Tama River, which flows between the Tokyo Metropolis and Kanagawa prefecture. Kawasaki was a post town on the Tokaido during the Edo period (1600-1889). A number of factories have been built along the coastal zone of Kawasaki since 1900. After World War II, Kawasaki has prospered as the center of the Keihin Industrial Area, which is one of three large industrial areas in Japan. Recently, Kawasaki has been developing into a region associated with highly advanced research and manufacturing and is becoming a world-class ultra-technology center. Kawasaki has a specially designated major port for which the annual gross tonnage of ships and boats putting into the harbor is approximately 91 million gross tons. The total cargo handled at the harbor was 92 million tons in 2000. At present, the population of Kawasaki is approximately 1,230,000, the land area is 142 km^2 and the number of households is 547,000 (Asahi newspaper, 2002). Figure 2 shows a map of the Kawasaki area and the junction of the Tokyo Bay Aqualine.

During the early Edo period, Kisarazu was under the direct control of the Tokugawa Shogunate and marine transportation between Edo and Kisarazu was restricted.
The harbor of Kisarazu has been a collection and distribution area for local goods. The Kisarazu harbor was constructed in 1908 and was designated as an important harbor nationally in 1945. At present, Kisarazu is a small city of the population 123,000 and the number of households 46,600 even though the land area is 138 km^2. Kisarazu is the center of a provincial city along Tokyo Bay in Chiba prefecture and has a major port for which the annual gross tonnage of ships and boats putting into the harbor is 41 million gross tons of ships and boats (Japan Harbor Association, 2002). The total cargo handled at the harbor was 69 million tons in 2000. Moreover, Kisarazu has two fishing harbors (Kaneda and Ushigome) that support 230 registered boats and handle 1100 tons of fish annually. The Banzu tideland fans out from the mouth of the Obitsu River in Kisarazu, and many people come to the tidelands to gather seashells at low tide. Figure 3 shows a map of the area around Kisarazu and the junction of the Tokyo Bay Aqualine.

The standard of living in Kisarazu is approximately ten times higher than that Kawasaki. In 2000, annual store sales in Kisarazu were 315 billion yen, compared to 2.78 trillion yen in Kawasaki, and annual expenditures in Kisarazu were 33 billion yen, compared to 548 billion yen in Kawasaki. Table 1 shows data of Kisarazu and Kawasaki in 2001.

QUESTIONNAIRE RESULTS

The Tokyo Bay Aqualine began service between Kawasaki and Kisarazu in December 1997. Whereas Kawasaki is adjacent to Tokyo, Kisarazu is located approximately 50 km the Tokyo region. Previously Kisarazu was a prosperous port town, supplying goods and labor from Chiba prefecture to the Keihin districts of Tokyo, Yokohama, and Kawasaki. New economic development and prosperity based on sightseeing, commerce, and resort industries was expected upon opening of the Tokyo Bay Aqualine. However, the expected economic development and prosperity did not materialize. In the present study, a questionnaire was concerning the effects of the Tokyo Bay Aqualine on the residents of Kisarazu was performed. Contents of the questionnaire are as follows:
  (1) Gender.
  (2) Occupation.
  (3) Age.
  (4) Do you hope to settle here in future?

(5) What are your feelings concerning the future of Kisarazu harbor?
(6) What is the pride of Kisarazu?
(7) What are the effects of the Tokyo Bay Aqualine?
(8) Which route do you take when traveling to Tokyo, Yokohama, Kawasaki?
(9) What is the direction in which Kisarazu is heading?
(10) What is the image of Kisarazu?
(11) Where are the sightseeing spots in the area?
(12) In what leisure activities do you engage in the area?
(13) How many times have you been to the Banzu Tideland?
(14) What are your feelings concerning the protection of the Banzu Tideland?
(15) Why did you visit the Banzu Tideland?
One thousand residents of Kisarazu were asked to respond to the questionnaire. The questionnaire was carried out in 2001 by the custody method through the mail using post cards. Out of 1,000 questionnaires, 316 were completed and returned. The responses are summarized as follows:
(1) Gender of respondents: male 57%, female 43%.
(2) Occupation of respondents: housewife 26%, no occupation 24%, office worker 22%, fishermen 7%, self-employed 5%, student 5%, other 7%.
(3) Age of respondents: 80~89 years 2%, 70~79 years 5%, 60~69 years 29%, 50~59 years 25%, 40~49 years 19%, 30~39 years 14%, 20~29; 4%, 13-19 years 2%.
(4) Respondents hoping to settle in Kisarazu in the future 68%, respondents displeased with living in Kisarazu were 24%.
(5) Maintain the status quo of Kisarazu harbor 46%, Kisarazu harbor should be expanded in future 30%, Kisarazu harbor should be eliminated or reduced in size 6%.
(6) Pride of Kisarazu: nothing 37%, sea products, such as the short-necked clam or sea-weed 15%, nature 8%, gathering sea shells 6%, weather 5%, Academia Park 4%, history 3%, inexpensive housing 3%, other 19%.
(7) Effect of Tokyo Bay Aqualine: good 70%, bad 16%.
(8) Traveled to Kawasaki and Yokohama via Tokyo Bay Aqualine 48%, traveled to Kawasaki and Tokyo via Tokyo Bay Aqualine 37%, traveled to Tokyo via Chiba along Tokyo Bay 31%.
(9) Future of Kisarazu: sightseeing 36%, commerce 28%, fishery 10%, industry 9%, agriculture 8%.
(10) Image of Kisarazu: abundant nature 50%, fishery town 20% .
(11) Sightseeing spot: nothing 48%, Sea firefly 20%, Ota mountain 8%, Banzu tideland 7%.
(12) Leisure activities: shell gathering 87%, golf 20%, fishing 20%, hot springs 3%.
(13) Trips to Banzu tideland per year: more than 10 trips 6%, four or five trips 2%, two or three trips 12%, one trip 17%, no trips 58%.
(14) Respondents that agreed to the protection of the Banzu tideland 88%.
(15) Reason for traveling to the Banzu tideland: gathering sea shells at low tide 52%, fishing 17%, wild bird watching 16%.
Cross-totaling results are as follows:
(1) Questions (1) and (4): 70% of male and female respondents answered "settle at present address".
(2) Questions (2) and (4): 80% of fishery, self-employed and no occupation respondents answered "continue present living situation".
(3) Questions (3) and (4): 80% of respondents in their sixties or older answered "continue present living situation" and 70% of respondents under sixty answered "live in a different situation in the future".
(4) Questions (2) and (5): Concerning the future of Kisarazu harbor, "Kisarazu harbor should be maintained in its present state" was the most prevalent response for all occupations, and the second most prevalent response was "expansion". Among the self-employed, 30% of respondents answered reduction or elimination of Kisarazu harbor.
(5) Questions (3) and (5): Several respondents in all age groups answered either that Kisarazu harbor should be maintained in its present state or expanded. However, a number of respondents in their thirties, forties and fifties answered that Kisarazu harbor should be reduced or eliminated.

(6) Questions (5) and (9): Respondents who stated that Kisarazu harbor should be maintained in its present state or expanded identified tourism and commerce are the future of Kisarazu.

(7) Questions (2) and (6): Over 30% of working respondents answered the Japanese pear, the short-necked shell and seaweed, in that order. A number of respondent answered nature and history.

(8) Questions (4) and (6): The pride of respondents hoping to remain in Kisarazu were reported as the short-necked shell, sea-weed and nature, respondents hoping to leave Kisarazu was the Japanese pear.

(9) Questions (9) and (6): Several people hoping that sightseeing, commerce and fishing would be developed answered the short-necked shell, seaweed, nature or gathering seashells at low tide, as the pride of Kisarazu.

(10) Questions (7) and (8): 70% of respondents who said the effect of the Tokyo Bay Aqualine was good used the Tokyo Bay Aqualine to travel to Kawasaki, Yokohama and Tokyo.

(11) Questions (7) and (9): Several respondents answered that the areas for development should be sightseeing and commerce.

(12) Questions (1) and (8): 62% of male and 75% of female respondents travel to Kawasaki, Yokohama or Tokyo.

(13) Questions (2) and (8): Housewives are the most users of the Tokyo Bay Aqualine. (80%)

(14) Questions (3) and (8): Over 50% of residents of all ages use the Tokyo Bay Aqualine as their usual route.

(15) Questions (4) and (8): 72% of respondents hoping to settle in Kisarazu use the Tokyo Bay Aqualine.

(16) Questions (1) and (9): 53% of male and 61% of female respondents expect development sightseeing and commerce to develop.

(17) Questions (2) and (9): Though several residents hoped for the development of sightseeing and commerce in general, public servants hoped for the development of agriculture.

(18) Questions (3) and (9): Respondents over eighty years of age hoped for the development of commerce and agriculture, whereas teen-age respondents hoped for the development of sightseeing. Respondents from twenty to seventy-nine years of age hoped for the development of sightseeing, commerce, agriculture or fishing.

(19) Questions (4) and (9): 33% of respondents hoping to settle in Kisarazu hoped for the development of sightseeing.

(20) Questions (1) and (10): 40% of males and 33% of females reported the image of Kisarazu to be that of abundant nature, and 10% of males and 22% of females reported the image of Kisarazu to be that of a fishing village.

(21) Questions (2) and (10): 40% of students reported the image of Kisarazu to be that of nature, and 60% of students reported the image of Kisarazu to be that of fishery. Other respondents reported the image of Kisarazu to be that of nature and fishery.

(22) Questions (3) and (10): Several residents over sixty years of age feel that the image of Kisarazu is that of nature. Respondents in their twenties, thirties, forties and fifties feel that the image of Kisarazu is that of nature and fishery.

(23) Questions (4) and (10): 40% of respondents hoping to settle in Kisarazu feel that the natural areas of Kisarazu are abundant. Respondents hoping to leave Kisarazu feel that Kisarazu is a town of odds and ends shops.

(24) Questions (2) and (11): The sightseeing spot was reported to be the sea firefly of the Tokyo Bay Aqualine by 40% of students, 25% of public workers, 20% of fishermen, 25% of housewives and 20% of office workers.

(25) Questions (3) and (11): Respondents in their eighties answered gathering sea shells at low tide. Several residents in their twenties, thirties or forties answered the sea firefly. However, teenage respondents answered that Kisarazu had no sightseeing spots.

(26) Questions (4) and (11): 15% or 25% of respondents hoping not to settle in Kisarazu reported that the sightseeing spot is the sea firefly, whereas respondents hoping to settle in Kisarazu reported that no sightseeing spot exists in the area.

(27) Questions (9) and (11): 40% of respondents who reported the direction of development in Kisarazu to be fisheries stated that the sightseeing spot is the sea firefly.

(28) Questions (2) and (12): Employed respondents of all types answered that the leisure activities in Kisarazu is gathering seashells at low tide.

(29) Questions (3) and (12): Respondents of almost all ages answered that the leisure activity in Kisarazu is gathering seashells at low tide. Secondly, residents in their twenties and older answered that leisure activities in Kisarazu are fishing and playing golf.

EFFECTS OF TOKYO BAY AQUALINE

The concrete opinions for effects of the Tokyo Bay Aqualine were as follows:

(1) Good access to Yokohama, Tokyo and Haneda Airport, has made shopping in Yokohama or Tokyo and foreign or domestic touring of these areas much easier. However, Kisarazu was not vitalized because the consuming public left Kisarazu for Yokohama or Tokyo.

(2) Local exchanges were progressing and the commuting range was larger everywhere in Chiba prefecture.

(3) An improvement in economical image was obtained by increasing the distribution of goods through Tokyo Bay Aqualine.

(4) Tourism in southern Chiba Prefecture was on the increase, but cars began to pass through Kisarazu without stopping.

(5) Automobiles from other districts have congested the roads of Kisarazu leading to the southern and eastern parts of Chiba prefecture, and the entire town has become a motorway.

(6) Natural habitats were destroyed, but residents of Kisarazu must preserve the remaining undamaged natural areas.

(7) Kisarazu will be vitalized by merging with surrounding cities, such as Sodegaura, Huttsu, and Kimitsu.

(8) Kisarazu harbor became a desolate place because due to disuse of the ferry between Kawasaki and Kisarazu. Therefore, Kisarazu harbor must be renewed as a sightseeing spot surrounded by fishing harbors, tidelands and sea-bathing places.

(9) Kisarazu is a traditional and historical town, and is well proportioned by three parts of the seasides, between the mountain and the farms, and so residents wish to maintain Kisarazu harbor in its present state.

(10) The construction of the Tokyo Bay Aqualine required a public investment of 130,000,000 yen. An appalling fact because no projects or enterprises will be developed to return the investment, not to mention the cost of construction and maintenance. An old proverb states, 'The foot of a bridge will not be prosperous' . The Tokyo Bay Aqualine has been used by sightseeing buses and private cars for traveling to fish, play golf, etc., whereas trucks rarely use the bridge. Several shoppers travel to Kawasaki, Yokohama and Tokyo via highway buses because large shopping centers have become rare in Kisarazu. Therefore, more money is flowing out of Kisarazu than is flowing into Kisarazu. Residents and visitors are passing by the area at the foot of bridge without stopping. The development of Kisarazu and the surrounding area requires a combined development plan for Huttsu, Kimitsu and Sodegaura early on, and a highly skilled administrative executive.

CONCLUSIONS

There are three routes by which to access the southern region of Chiba prefecture from Tokyo and Yokohama. These include the Keiyou route from the Capital Highway 7, the Higashikantou Highway along Tokyo Bay, and the Tokyo Bay Aqualine from Kawasaki. The tolls for the Keihin route and Higashikantou Highway are cheaper than Tokyo Bay Aqualine, but the Tokyo Bay Aqualine route is shorter. In the future, another bay bridge connecting Kannonnzaki of Kanagawa prefecture to Huttsu of Chiba prefecture at the entrance in Tokyo Bay is being planned. In Japan, bridges and tunnels across bays or

451

channels are necessary for the well-being of cities and towns on both sides of the bay. The results of questionnaires in this study will be helpful for the construction of future bay bridges. The conclusions of the present study are as follows:

(1) Several respondents answered that Kisarazu was within easy access of metropolitan Tokyo, Yokohama and Haneda International Airport.

(2) A number of respondents reported a lack of entertainment in and around Kisarazu Station and Kisarazu Harbor, although no major changes were made to Kisarazu after beginning service Tokyo Bay Aqualine.

(3) Several respondents stated that Kisarazu should be revitalized by attracting tourism, and vitalizing commerce and fishery.

(4) Several respondents expected that Kisarazu will be developed with preserved nature and will have many opportunity of doing business in fishery.

(5) In order to economically strengthen Kisarazu, the fundamental tourist attractions, such as marine life, seafood restaurants and fishing resources as well as shell gathering at low tide around Kisarazu Harbor and Banzu Tideland must be boosted.

REFERENCES

Asahi newspaper. 2002. The Living Standard in 2002.

Heibonsha. 1967. The World Encyclopedia.

Japan Harbor Association. 2002. Pocket Book of Harbor.

STATISTICS BUREAU. 2002. STATISTICAL OBSERVATIONS OF SHI, KU, MACHI, MURA

Teikoku Shoin. 2000. Complete Atlas of Japan.

Table 1. Comparison between Kisarazu and Kawasaki (STATISTICAL BUREAU, 2002)

	Population	>15 years old	15 – 64 years old	65 years old <
Kisarazu	122768	17558	86191	19018
Kawasaki	1249905	170670	923655	154704

	Daytime Population	Number of Households	Move in Population	Move out Population
Kisarazu	119995	43251	5489	6514
Kawasaki	1097090	543088	98342	106265

	Total Area	Inhabited Area	Taxable Income	No. of Taxpay
Kisarazu	138.65(km^2)	92.14(km^2)	¥189068(million)	49455
Kawasaki	142.70	134.78	¥2459855	572562

	Places of Bussiness	Workers	Agricultural Production Cost	Shipment of Production
Kisarazu	5714	52415	¥6930(million)	¥274449(million)
Kawasaki	46789	536614	¥3400	¥4346334

	Sale Price of Commerce	Number of Store	Value of Land (Residence)	Value of Land (Commerce)
Kisarazu	¥314938(million)	1531	¥58600/m^2	¥139800/m^2
Kawasaki	¥2784145	3168	¥2874000	¥617500

	Primary Industry Workers	Secondary Industry Workers	Tertiary Industry Workers
Kisarazu	3320	16718	41029
Kawasaki	2964	177773	457387

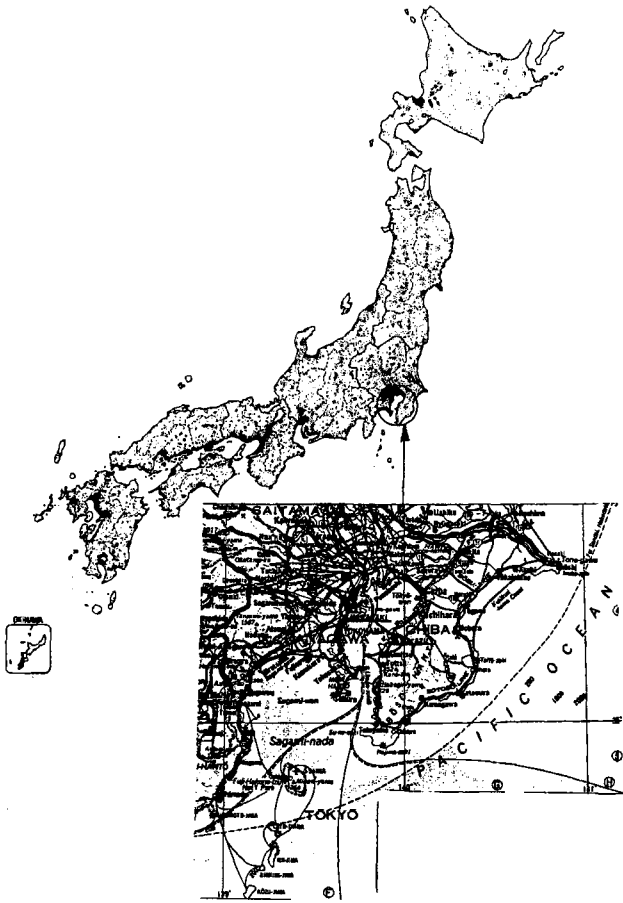|	Road Extension	Number of Park	Number of Hospital	Number of Old Age Home
Kisarazu	868.3(km)	109	11	5
Kawasaki	2455.3	810	39	22

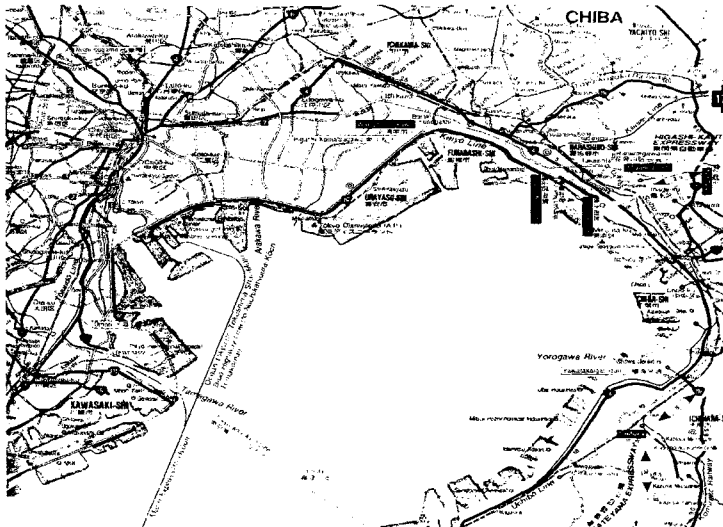Figure 1.   Site of Tokyo Bay (Teikoku Shoin,   2000)

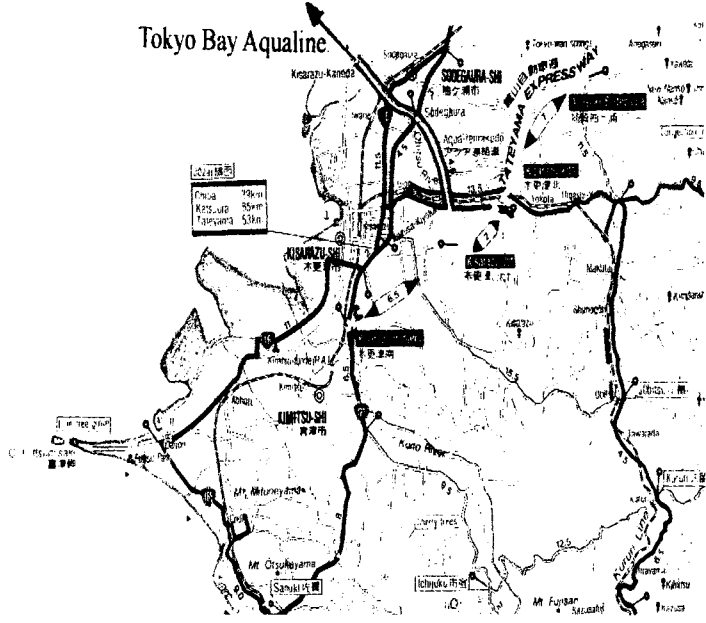Figure 2. Map of Kawasaki/Tokyo/Chiba district

Figure 3. Map of Kisarazu district

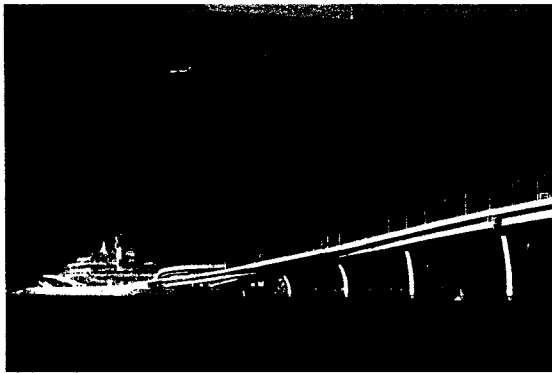Photo 1. A scene of a declining Kisarazu

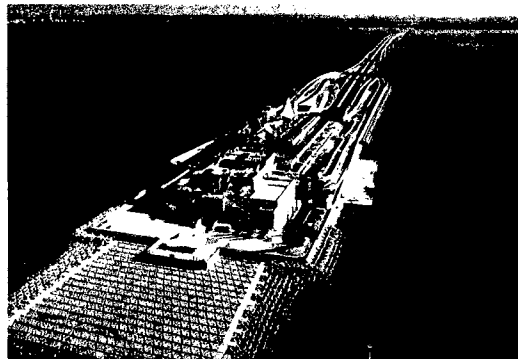Photo 2. Tokyo Bay Aqualine (from Kisarazu side)

Photo 3. Sea firefly and Tokyo Bay Aqualine (from Kawasaki side)
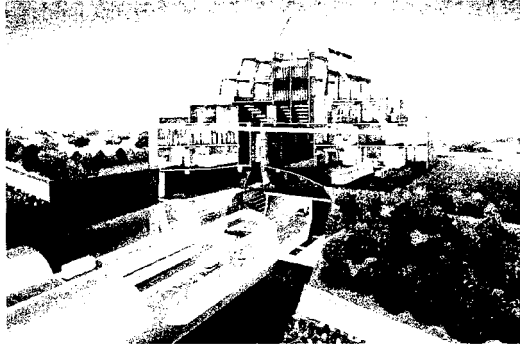
Photo 4. Tunnel part of Tokyo Bay Aqualine

THE GREAT IMPACT OF HUMAN ACTION ON THE DEVELOPMENT PROCESS OF COASTAL LANDFORM

Da-yuan Yang, Xu-sheng Li, Xiao-wei Jiang, Jiang-hua Wu

Department of Geography, Nanjing University
Nanjing, CHINA
yangdy@nju.edu.cn

ABSTRACT

Taking the Yangtze River delta and the old Yellow River delta of China as examples, this paper analyzes the impact of human action (building dykes along the river) on the delta coastal development. Constructing dykes along the rivers relieved flood overflowing and silt depositing on the flood plains along the valley. But, it not only increased the silt depositing in the bed of the rivers, but also increased the flood and sediment discharge into the sea, that speeded up the river delta development. Therefore, construction of artificial dykes played an important role on the coastline development.

INTRODUCTION

The human impact on coastal development has been a topical subject in academic circles for over years (Bird, 1976). With regard to the change of advance speed of the Yangtze Delta coastline, Tan Qixiang (1970) put forward that it related to northern war of China, population migration southward, sloping fields reclamation, and soil erosion increase. Actually, human impact on coastal landform process is more complicated than that was studied. Besides direct impact, long-distance human activity and lag influence should be considered. For example, annual sediment discharge of the Yellow River is considered as 16×10^8 t/a, and the Yangtze River is about 4.71×10^8 t/a. Actually, the sediment discharge of the Yellow River and the Yangtze River is changeable. The human activity exerts impact on annual sediment discharge in multiple ways, while the annual sediment discharge plays a decisive role on delta development.

Coastline change of the old Yellow River delta

From A.D. 1128 to 1855, the Yellow River had been entering the Yellow Sea through middle area of Jiangsu Province. During this time, the river from near Kaifeng city to the mouth is called the old course of the Huanghe River. One of delta plains was formed out of the ancient mouth there (Fig. 1). The delta coastline had advanced toward the sea with the average rate from 7 m/a to 24 m/a before A.D.1496, but it increased to 91 m/a on average from 1495 to 1855. The mentioned change was not related to the sea level changes in that period, and may be mainly related to the sediment discharge of the lower reaches of the ancient Yellow River (Fig.2, Yang, 1991). Before A.D. 1495, the inundation of the ancient Yellow River submerged the ancient Xuzhou city, Kaifeng city, and led to the construction of the ancient flood plain and the delta in the Weishanhu Lake (Zhang Zulu, 2002). The ancient Kaifeng City in Song Dynasty was

inundated to a depth of about 8m by sediment of the Yellow River. But when the artificial dyke was built along the ancient Yellow River in A.D. 1496, the riverbed aggradated rapidly by appreciable sediment trapping behind the dams and formed shoals along the banks. The surface of the shoals was higher about 8-9 m than that of the plain beside the dykes. In the same time, the flood and sediment discharge into the sea increased, which resulted in the rapid growth in area of the ancient Yellow delta. The coastline advanced approximate 33 km seaward during 360 years before A.D. 1855, when the Yellow River returned back into the Bohai Sea.
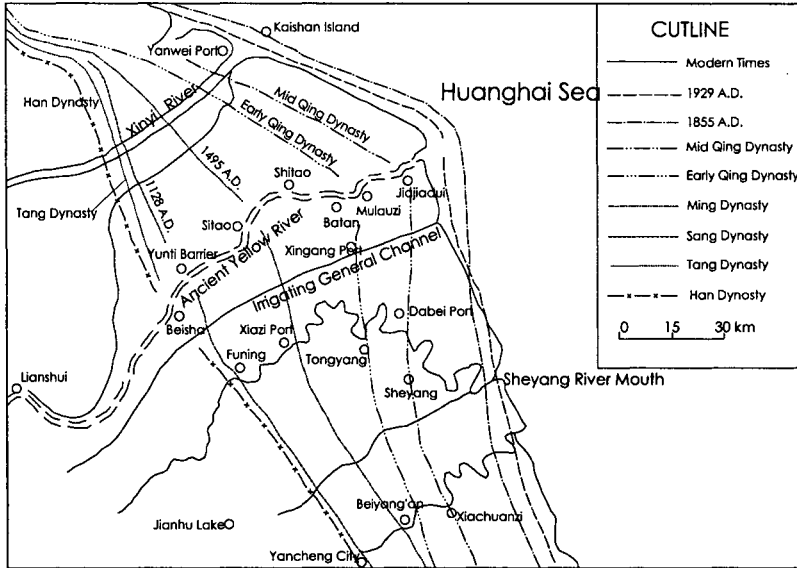
Figure 1. The development of the old Yellow River delta

In the last 50 years, there has been no great inundation occurred in the lower course of the Yellow River. Based on the comparison among maps from different ages simultaneously, from 1953 to 1982, the terrestrial land in the yellow River delta increased about 1100 km². Up until 1994, another 1100 km² was added to the delta due to the same reason (Chen Chao, 2002).
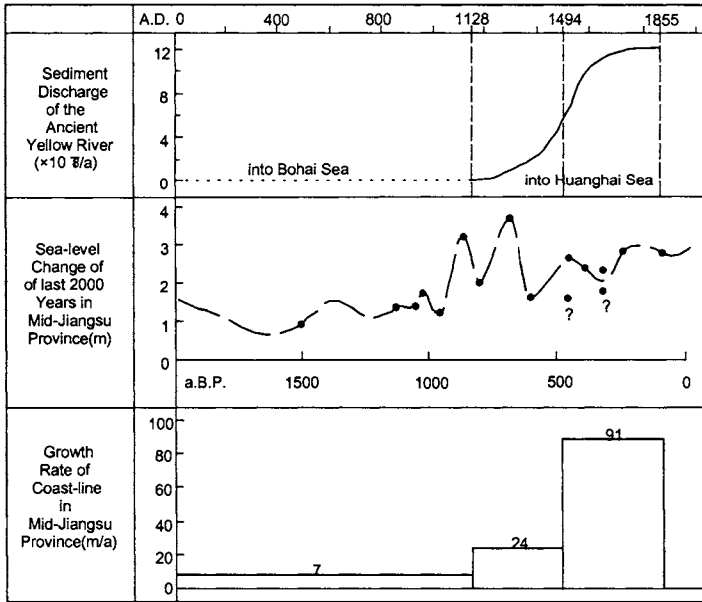
Figure 2. The main influencing factors on the development of the old Yellow River

Growing of the Yangtze River delta

The middle and lower reaches of the Yangtze River, which extend from Yichang to the river mouth, are about 1,800 km long. Collectively, a length of 3,600 km of dykes has been built along the river since A.D. 345. (Table 1)

Table 1. Some long dykes along the middle-lower reaches of the Yangtze River

Dyke	Length (km)	Construction time
Jingjiang Dyke	182.31	Originally constructed in AD 345 System formed in AD 1542
Honghu Dyke	130	
Wuhan Dyke	178.53	Originally constructed in AD 1635 System formed in Qing Dynasty
Huangguang Dyke	87.3	Originally constructed in AD 1404 System formed in AD 1932
Jiujiang Dyke	60	Originally constructed in AD 1954
Gandong Dyke	141.46	Originally constructed in Song Dynasty (A.D.960-1127)
Tongma Dyke	130	Originally constructed in Jin

		Dynasty (A.D.265-420)
Jiangsu Dyke (left bank) (right bank)	498.5 529.7	Originally constructed in Song Dynasty System formed in last century

Most dykes were originally constructed in the Song dynasty, and the river-dyke system was formed in the Ming-Qing Dynasties. Because of the dyke-system getting more and more mature, more and more sediment discharged to the river mouth. In the middle-late of last century, the sediment discharge reached to 4.71×10^8 t/a according to the data from Datong monitoring station, which is located in the lower reaches of Yangtze River. The development of the Yangtze River delta has also speeded up since the Song Dynasty (Xu et al., 1987). (Fig. 3)
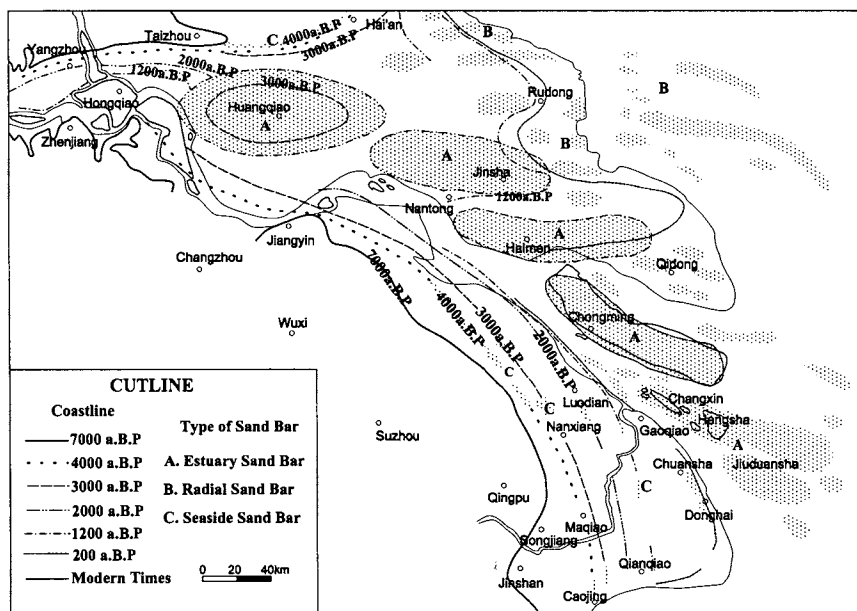
Figure 3. The development of the Yangtze River delta

In the last 50 years, there have been no great inundations in the Yangtze River and the great amount of sediment poured into the mouth reaches of the Yangtze River. It caused that the Zhengrunzhou flood plain near Zhenjiang city deposited about 6×10^8 t sediment based on the analyses of isobath lapse. The area of the Chongming Island of Shanghai city was increased rapidly from 600km^2 to 1200 km^2, and formed Changxing Island, Hengsha Island and Jiuduansha Island one by one.

462

CONCLUSION AND DISCUSSION

Based on the historical records reviewed here, we discovered that delta building by the rivers accelerated following completion of the artificial dyke system. Taking the Yangtze River delta and the old Yellow River delta as examples, flood overflowing from the channel supplied sediment to build wide flood plains along the rivers before the construction of artificial river-dyke. However, after the dyke construction, river sediments no longer build the flood plain but are deposited in the riverbed to build shoals and transferred downstream to build the delta plain at the mouth of the river. Therefore, the human activities have become the dominant agent for development of some delta plains and exerted important impact on the coastal landform development.

ACKNOWLEDGEMENT

REFERENCES

Bird, E.C.F. 1976. Shoreline changes during the past century. *Proceedings of the 23rd International Geographical Congress, Moscow*. Elmsford, N.Y. Pergamon. 54 pp.

Chen, Chao. 2002., Striking terraqueous change of the Chinese territory. *Xinhua Daily*. [In Chinese] Jan. 30, 2002, p. C2.

Tan, Qixiang. 1970. Sea-land change and exploitation process of the coast of Shanghai city. *Archaeology*. [In Chinese] 1. 28-35.

Xu, Shiyuan, Wang Jingtai, Li Ping, 1987, On the Developmental Periods of the Yangtze River Delta. In: Yan Qinshang, Xu Shiyuan eds. Recent Yangtze Delta Deposits. Shanghai, East China Normal University Press. [In Chinese] 264-277.

Yang, Dayuan. 1991. Sea level change of the middle Jiangsu province since 2000a B.P.. *Chinese Science Bulletin*. [In Chinese] 20: 1574-1577.

METAMORPHOSIS INDUCTION AND ITS POSSIBLE APPLICATION TO CORAL SEEDLINGS PRODUCTION

Masayuki Hatta[1] and Kenji Iwao[2]

[1]Department of Biology, Ochanomizu University
Bunkyo-ku, Tokyo, JAPAN
mhatta@cc.ocha.ac.jp

[2]Akajima Marine Science Laboratory
Zamami-son, Okinawa, JAPAN

ABSTRACT

Coral reefs are the bases of ecosystems and environments in tropical and sub-tropical shallow seas; however, despite their importance, coral reefs around the world are declining at an alarming pace. In Indo-Pacific reefs, the coral genus *Acropora* consists of major components, and coral communities are maintained in large part by recruitment of their larvae. Many acroporids participate in 'mass spawning' in which a large number of species spawn their gametes synchronously. Huge numbers of larvae are produced by mass spawning, but most of them are lost prior to metamorphosis and settlement. If the larvae were collected and grown into colonies under controlled conditions, they could be used as donors for transplantation without damaging existing coral communities. Previously we found that a hydra neuropeptides induced the metamorphosis and settlement of *Acropora* larvae with 100% efficiency. Using the peptide, we succeeded producing primary polyps from coral larvae collected in the field. The primary polyps could be used for transplantation with the aim of reconstructing denuded reefs. Here we propose 'coral seedlings production' by collecting larvae after mass spawning and controlling metamorphosis with the peptide.

INTRODUCTION

Coral reefs are the bases of ecosystems and environments in tropical and sub-tropical shallow seas. Despite their importance, coral reefs all over the world are declining at an alarming pace as a consequence of direct and indirect human activities even though preservation and management measures have been taken. The conspicuous reef decrease is due to coral bleaching, which is the loss of color in corals in appearance as corals' intracellular symbiotic algae are lost. Coral bleaching has increased in frequency, intensity and extent over the last two decades (Huppert and Stone, 1998). Most recently, in the summer of 1998, high sea surface temperatures (SSTs) resulted in massive mortality of reefs worldwide (Tsuchiya, 1999). Many shallow reefs that have been impacted are dominated by the genus *Acropora*, since this genus consists of major components of the reefs in Indo-Pacific oceans and acroporids are sensitive to high temperature. Some reefs are recovering; e.g. around Kerama Islands in Okinawa, Japan. Others, however, remain denuded such as those around Okinawa's main island. Active restoration is acquired in Okinawa and in many other areas. Since coral communities are maintained in large part by

recruitment of their larvae, increasing recruitment efficiency of acroporids through human intervention would be an effective contribution to reef restoration.

Many acroporids reproduce sexually in a unique manner termed 'mass spawning'; huge numbers of gametes are released into the water column synchronously within an hour by many colonies belonging to multiple species (Babcock et al., 1986; Hayashibara et al., 1993). The buoyant gametes form high-density patches called 'slicks' on the sea surface. The resultant larvae are dispersed by currents and settle on substrates to start their sedentary life. Despite a large number of larvae being produced by mass spawning, most of the larvae are lost during the drifting period and only a small fraction are recruited into reef communities. If such larvae that will be lost prior to settlement are collected and grown to colonies under controlled conditions, they could be used as donors for transplantation without damaging existing coral communities. The problem to date has been the lack of a method by which to control metamorphosis and settlement of *Acropora*. Recently, we found that one of hydra neuropeptides can induce metamorphosis of acroporids' larvae into polyps at high rates (Iwao et al., 2002). In this study, we tested the use of the peptide in 'coral seedlings production', which consists of collecting coral larvae after mass spawning events and producing primary polyps or infant colonies for the purpose of transplantation.

MATERIALS & METHODS

Preparation and maintenance of coral larvae
All experiments were done at Aka Island of Kerama Islands in Okinawa, Japan. Colonies of *Acropora tenuis* were collected two days before the predicted spawning date and kept in the Aka fishery harbor. When gamete bundles emerged at the mouth of the polyps, each colony was put in a separate bucket, and allowed to spawn in the laboratory. The egg-sperm bundles taken from five colonies were mixed in a bowl for two hours to allow fertilization, and then the eggs were transferred to new bowls filled with fresh 10-micron-filtered seawater. Larvae were transferred to new bowls with daily changes of filtered seawater, and maintained in densities of 1000-3000 per bowl (about 1.5 liter seawater, 25 cm diameter) at 26°Celsius.

Slicks of coral embryos/larvae were scooped in the Aka port in the morning at 9 – 10 a.m. after the mass spawning event in the night on May 25, 2000, and larvae were maintained as above.

Metamorphosis assay
Planula larvae were once washed with seawater filtered through a 0.2-micron nitrocellulose filter (filtered seawater, FSW), and 10 larvae were placed in each well of 24-well culture multiplates (SUMILON) with 1 ml of FSW. The peptide Hym-248 (EPLPIGLWamide, Takahashi et al., 1997) was added to the indicated final concentrations, and the number of metamorphosed animals, which formed mesenteries (Fig. 1B) was counted 12 hours after the beginning of the treatment. All experiments were done at 26° Celsius.

RESULTS

Morphological changes during metamorphosis induced with the peptide

Figure 1 shows a representative of morphological changes during metamorphosis of *Acropora tenuis*, induced with 1×10^{-6}M Hym-248. Panel A is the planula larva swimming to the aboral direction with cilia. The larva attached the aboral side to the culture dish and contracted subsequently, after 1hr of the peptide treatment. After four hours, the aboral side transformed to a stalk-like structure, which soon shortened, and septation of the tissues became visible. The mouth became obvious within six hours. The whole tissue flattened, and twelve mesenteries were clearly formed after 12 hours (panel B). Panel C represents a primary polyp three days after the peptide treatment. Tentacles and calcified septa were formed. The metamorphosis processes appeared normal, since no morphological differences were noted between animals induced with the peptide or calcareous algae and those metamorphosed incidentally in bulk cultures (data not shown).
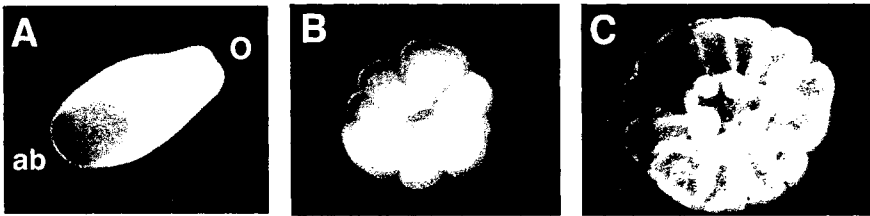
Figure 1. Morphological changes during metamorphosis
Panel A represents a side view of a planula larva of *A. tenuis*. The oral and aboral ends of the planula are indicated by 'o' and 'ab' respectively. Panel B and C show polyps after metamorphosis, viewed from the top.

Time requirement for metamorphosis commitment

To examine the minimal time required for the Hym-248 treatment to induce commitment to metamorphosis, the peptide-containing FSW was replaced by fresh FSW after various interval times, and the frequency of metamorphosis was counted at 12 hours after the onset of the peptide treatment. The results using *A. tenuis* larvae 10 days after fertilization are shown in Figure 2. The larvae rounded up after one hour, but regressed to normal planulae when the peptide-FSW was replaced by FSW within three hours. Significant rates of metamorphosis were observed when the larvae were incubated with the peptide for more than four hours. The relatively lower rates of metamorphosis were obtained in this particular experiment compared to simple induction experiments, which gave rise to mostly 100% metamorphosis (Iwao et al., 2002, also see below) probably due to extensive washing, which may have caused physiological stress. But the results clearly showed a gap between three and four hours. Thus, we conclude that a four hours' exposure to Hym-248 is the minimum required for irreversible commitment to the metamorphosis pathway at 26°C, hence the minimum treatment time for metamorphosis induction.
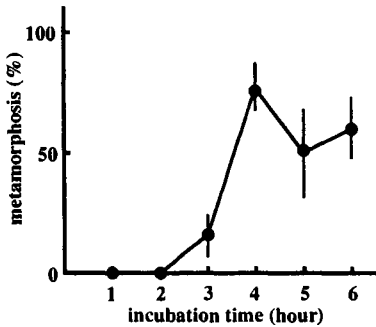
Figure 2. Time required for commitment to metamorphosis

Acropora tenuis planula larvae were treated with 1×10^{-6}M Hym-248 for different periods of time and transferred to FSW, and the metamorphosis frequency was counted 12 hours after the beginning of the peptide treatment. The values are the average percentages of triplicates of each experiment (SE values are shown by bars).

Maturation time course of slick larvae
All the larvae in the collected slick seemed to be acroporids judged by their appearance; size, color and the absence of symbiotic algae. In order to know the culture period required to obtain mature larvae, which are competent for metamorphosis, the larvae collected from slicks were subjected to the metamorphosis assay with 2×10^{-6}M Hym-248 along days of culture. The results are summarized in Figure 3. Larvae of the day 3 and 3.5 after fertilization did not respond to the peptide at all, whereas the metamorphosis frequency of the day 4 larvae exceeded 50 percent. The day 5.5 larvae revealed the 100% metamorphosis ability, and the high metamorphosis efficiency was kept till 6 days after fertilization. Further experiments were not done.
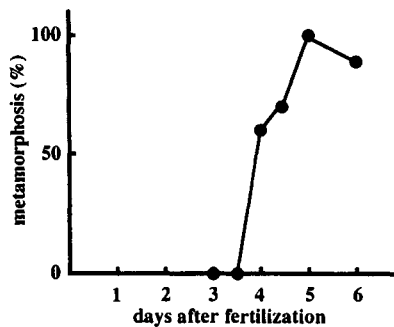
Figure 3. Metamorphosis ability of slick larvae during culture

Changes of the metamorphosis ability during culture were measured by treatment with 2×10^{-6}M Hym-248. The metamorphosis percentages are the average of duplicates.

468

DISCUSSION

Restoration of heavily denuded reefs is dependent on the recruitment of coral larvae from 'source' reefs where coral populations are capable of producing large numbers of drifting larvae by sexual reproduction. For example, reefs around Okinawa's main island have been seriously damaged in decades, especially in the mass-bleaching event in 1998, and signs of recovery have not been observed yet. Coral larvae are thought to be conveyed from Kerama Islands to Okinawa's main island by the strong current Kuroshio, and this flow pattern was recently confirmed by following slicks (Nadaoka et al., 2001). Reefs around Kerama Islands could act as the source of coral larvae for Okinawa's main island. Nonetheless, few larvae are likely to succeed in traveling 30 km distance through the ocean, even if enormous quantities of gametes were released in mass spawning events. Transportation of slicks through human intervention would be an effective way of enhancing restoration of reefs around Okinawa's main island. Further, if coral larvae collected from slicks were transformed to polyps under controlled conditions, greater successes at coral propagation would be expected than simple transportation of larvae accompanied by low frequencies of settlement and metamorphosis in natural conditions. Controlled induction of metamorphosis will also aid efforts to increase corals within specific reefs, since most of larvae are lost and only a very small fraction of them settle and accomplish metamorphosis in nature.

In this study, we demonstrated that the Hym-248 peptide induces metamorphosis in nearly 100% of larvae from slicks (Fig. 3). Although this peptide is only effective for acroporids (Iwao et al., 2002), it could be applied to produce polyps from slicks because major mass spawners are acroporids and their larvae dominate slicks (data not shown). Some calcareous algae and marine bacteria can also be used to induce metamorphosis in acroporids (Morse et al., 1996; Negri et al., 2001). However, the efficiency of metamorphosis induction by these organisms is lower and induction takes longer than with the peptide (Fig. 2). Another advantage of the peptide is its availability; anyone can obtain peptides by ordering them from reagent companies. In addition, we recently succeeded in culturing over 250,000 larvae from slicks collected in the field in a 1,000 liter-tank till they gain competence of metamorphosis (data not shown). We believe that these results pave the way for 'coral seedlings production', production of a large number of primary polyps as donors for transplantation without damaging existing coral colonies.

Coral bleaching events may be becoming more frequent, and it has been suggested that such events will become even more common if global warming persists and summer SSTs increase (Glynn, 1991). Active restoration efforts will become more and more desirable in the future. We hope that this study will be applied to restoration of coral reefs worldwide.

ACKNOWLEGMENTS

REFERENCES

Babcock, R. C., G.D. Bull, P. Harrison, A.J. Heyward, J.K. Oliver, C.C. Wallace, and B.L. Willis. 1986. Synchronous spawning of 105 scleractinian coral species on the Great Barrier Reef. *Mar. Biol.* 90:379-394.

Glynn, P.W. 1991. Coral reef bleaching in the 1980's and possible connections with global warming. Trend. Ecol. Evol. 6:175-179.

Hayashibara T., K. Shimoike, T. Kimura, S. Hosaka, A. Heyward, P.L. Harrison, K. Kudo and M. Omori. 1993. Patterns of coral spawning at Akajima Island, Okinawa, Japan. Mar. Ecol. Prog. Ser. 101: 253-262.

Huppert, A. and L. Stone. 1998. Chaos in the Pacific's coral reef bleaching cycle. *Am. Nat.* 152: 447-459.

Iwao, K., T. Fujisawa and M. Hatta. 2002. A cnidarian neuropeptide of the GLWamide family induces metamorphosis of reef-building corals of the genus *Acropora*. *Coral Reefs* 21:127-129.

Morse A.N.C., K. Iwao, M. Baba, K. Shimoike, T. Hayashibara and M. Omori. 1996. An ancient chemosensory mechanism brings new life to coral reefs. *Biol. Bull.* 191:149-154.

Nadaoka K., Y. Nihei, K. Wakaki, R. Kumano, S. Kakuma, S. Moromizato, T. Omija, K. Iwao, K. Shimoike, H. Taniguchi, Y. Nakano and T. Ikema. 2001. Regional variation of water temperature around Okinawa coasts and its relationship to offshore thermal environments and coral bleaching. *Coral Reefs* 20:373-384.

Negri A.P., N.S. Webster, R.T. Hill and A.J. Heyward. 2001. Metamorphosis of broadcast spawning corals in response to bacteria isolated from crustose algae. Mar. Ecol. Prog. Ser. 223:121-131.

Takahashi T., Muneoka Y., Lohmann J., Lopez de Halo M. S., Solleder G., Bosch T. C. G., David C. N., Bode H. R., Koizumi O., Shimizu H., Hatta M., Fujisawa T., and Sugiyama T. 1997. Systematic isolation of peptide signal molecules regulating development in hydra: LWamide and PW families. Proc. Natl. Acad. Sci. 94:1241-1246.

Tsuchiya, M. 1999. Warning from the coral reefs. Galaxia 1:27-29 (In Japanese and English).

COASTAL WAVE SOUNDS AS A RESOURCE OF COASTAL MARINE TOURISM

Jong-in Choi[1], Kenji Hotta[2] and Ken Yamazaki[3]

[1]Department of Oceanic Architecture and Engineering
College of Science and Technology, Nihon University
Chiba, JAPAN
k10001@ocean.cst.nihon-u.ac.jp

[2]Department of Oceanic Architecture and Engineering
College of Science and Technology, Nihon University
Chiba, JAPAN

[3]Department of Electric Engineering
College of Industrial Technology, Nihon University
Chiba, JAPAN

ABSTRACT

Coastal area is one of the most attractive places not only for recreation but also for educational purposes. Recently, it is reported from psychologist that coastal wave sounds make us relaxed. The reason has not been fully clarified yet, however, recently also it is reported that in audible sound which contains high frequency sound, so called ultra-sonic property of frequency, makes human brain waves vitalized. Most of related past research has been made based on the audible sound. The authors conducted several experiments using ultra-sonic wave, which was recorded from actual wave sound at the coast and examined its influences. In this paper, the method and obtained result of experiment will be introduced and finally from in the perspective of coastal marine tourism, sound resource management, as a new resource in the coastal area, will be discussed.

INTRODUCTION

Human beings can recognize outside environmental information through the five senses (sight, hearing, taste, touch and smell). Of these five senses, the sense of hearing, which makes us recognize sound, is always functioning, and sound is an important factor with regard to discerning whether or not we find something pleasant.

With environmental sounds that exist in the natural world, a large distinction can be made between audible sounds that can be heard through the ears of human beings, and ultrasonic waves that cannot be heard.

In recent years, there have been reports that in the field of music, high-frequency sound elements (ultrasonic waves) contained in music increase activity of the alpha waves of human brains

471

(Oohashi and Nishina, 1992). This suggests there is a possibility that these ultrasonic wave elements that cannot be heard have some effect on human beings.

With regard to the influence of ultrasonic waves at natural environment sounds on human beings, through the experiments using the sounds of waves that have a rich content of ultrasonic wave elements, changes on the physiological side and the psychological side of human beings were observed. Similarly, the purpose of study is to consider influence of natural ultrasonic wave elements on human beings and discuss sound resource management as a new tourism resource in the coastal area.

This paper consists of 1) the method of experiment, 2) the results of experiment and considerations.

METHOD OF EXPERIMENT

Test subjects and presentation sounds
The subjects were students (13 males and 13 females) with normal auditory sense between 18 to 22 years of age. The presentation sound was the wave sounds recorded on the seashore in Jamaica, and was given to the subjects for 90 seconds.

The breaking times for 15 minutes were repeated between the presentation sounds, as shown in Figure 1. Moreover, the questionnaire survey (POMS) was conducted in the breaking time.
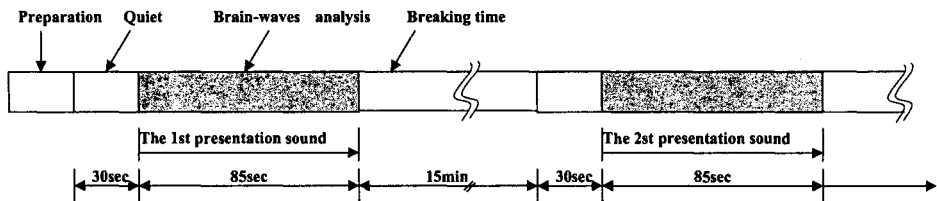
Figure 1. Time lag of the presentation sound

There were two types of presentation sounds used. One was only the audible sound which did not contain an ultrasonic ingredient (LPS), and the other sound contained the ultrasonic ingredient (FPS).

Figure 2 shows a 90-second WIGUNER distribution of LPS and FPS, and a 10-second 3-dimensional frequency for the characteristics of presentation sound. From this we can find that many ultrasonic ingredients are contained in the presentation sound of FPS.
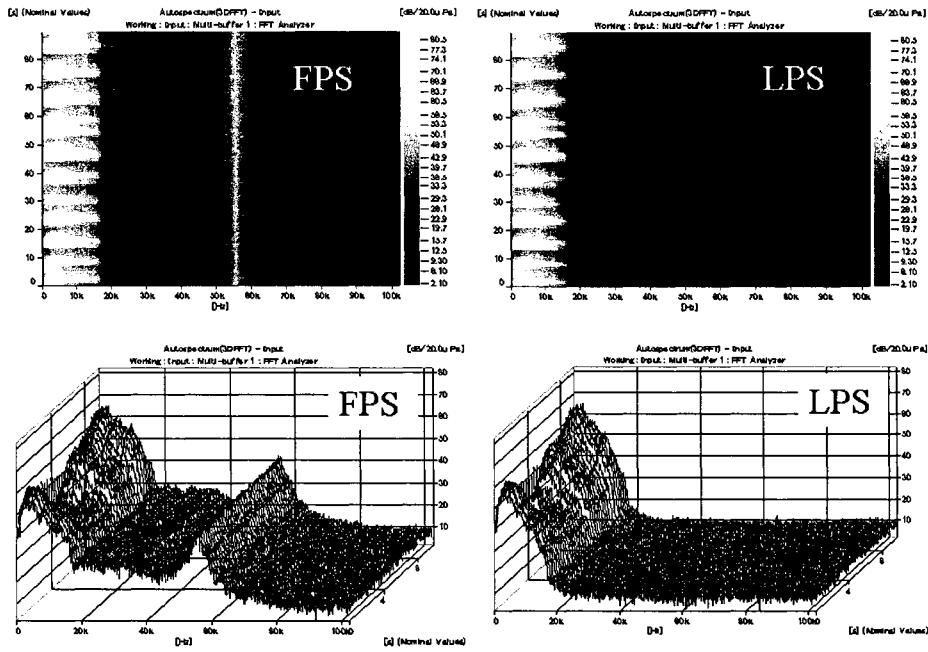
Figure 2. The characteristic of presentation sound

Polar zone place fixed
by the experiment

The place which fixed the
electrode by the experiment
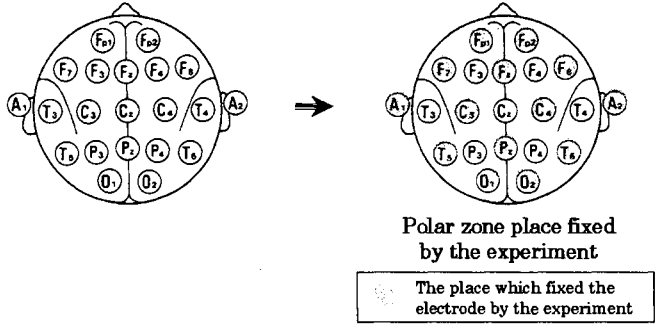
Figure 3. 10-20 Electrode layout method

Brainwaves
Brainwaves ware selected because they can be used as indices showing the physiological effects of environmental sounds on human beings. As shown in Figure 3, the 10-20 method was used for the positioning of the electrodes for measuring the brainwaves. The 10-20 method is the standardized method recommended by the International Brainwave and Clinical Physiology Society for the positioning of electrodes on the scalp.

473

POMS (Profile of Mood States)
In order to examine the mental situation after showing one presentation sound, a POMS questionnaire survey was conducted on every subject.

Experimental room
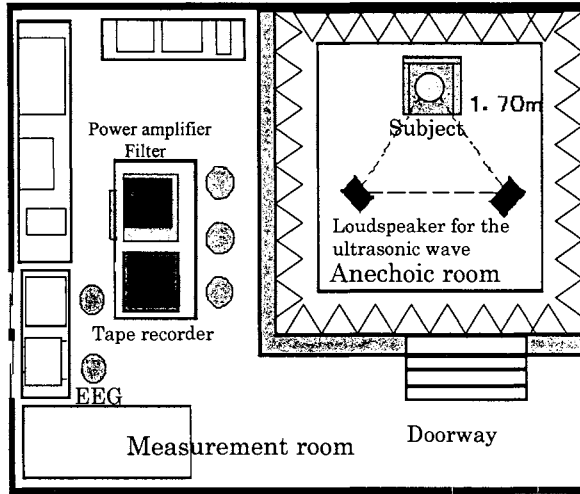
Figure 4. Experiment specification figure

As shown in Figure 4, the experiments were carried out in an anechoic room. The anechoic room was insulated from the outside sounds and absorbed the reflection of inside sounds so that there was no influence from any sounds apart from the sounds being used. Also, air-conditioning of the room was managed, maintaining the room temperature between 22°C to 25°C with the humidity between 55-75 percent. There were also no air currents in the room. The speakers were positioned, taking into consideration the direction of ultrasonic waves, with the front toward the test subject. The two speakers and the test subject made up a three point triangular shape.

Equipments Used for Releasing the Sounds and Measurement

Figure 5 shows the arrangement of the equipment and the testing set. With regard to releasing the sounds, special speakers that can reliably replay sounds in the high-frequency range were used to deliver the ultrasonic waves. The range of the replay frequencies was between 5,000 and 120,000 Hz, and there was no problem recreating the ultrasonic wave range used in the experiments. The brainwaves were measured from each of the 12 electrodes attached to the scalp conducted the level of electrical impulses produced by activity of the nerve cells in the brain, and these were recorded by the hard disc.

474
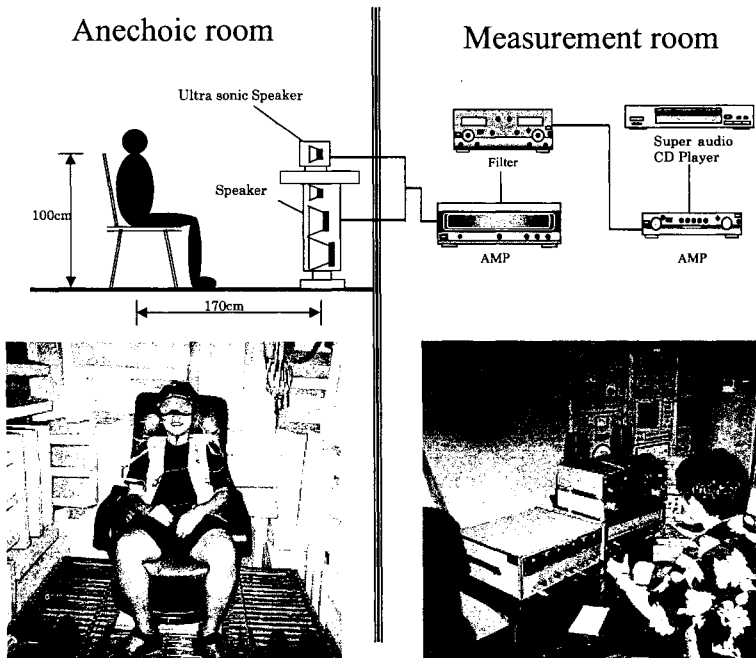
Figure 5. Composition of equipment and experimental photo

Method for the analysis of Brainwave

The brainwave data classified by frequency band were acquired every 5.12 seconds, and it was analyzed focusing on the quantitative change in each frequency band of brainwaves. From the brainwave of each subject's twelve electrodes by every presentation of LPS and FPS, frequency analysis was carried out and then classified into zone of δ, θ, α and β wave. Each amount of the brainwaves for every subject (from 5 to 90 seconds after sound presentation) was obtained and compared with the difference of the amount of LPS and FPS.

RESULTS OF EXPERIMENTS

Result of Brain Activity

Table 1 denotes the number of times when brainwaves became more active in case of release of FPS than only audible sound. In addition, other trouble states were not seen during this experiment. As shown in Table 1, alpha wave was activated in nine subjects among thirteen male subjects, and also in ten subjects among thirteen female subjects. Moreover, activation of alpha wave content classified by subjects was expressed in Figure 6. The alpha wave reaction and individual difference for the subjects can be seen in this figure.

475

Table 1. The quantitative increase number classified by frequency of brain waves

	δ wave	θ wave	α wave	β wave
Male(13)	3	5	9	5
Female(13)	6	6	10	6
TOTAL(26)	9	11	19	11
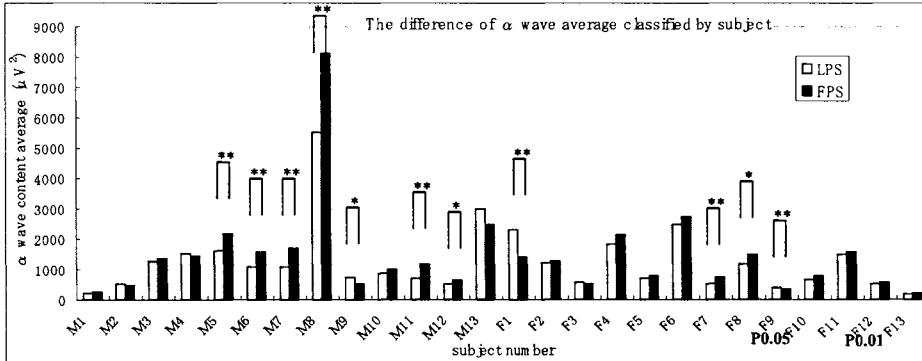
Figure 6. The difference of alpha wave average classified by each subject

Result of POMS Test

This experiment was the analysis of 25 subjects, except one female subject showing the halo effect. This POMS test was performed after each sound presentation, following POMS evaluation method, and answers which were obtained from 65 items of question were classified by six factors based on five stage consultations value and each factor was compared using T score. Six POMS factor items are "Tension-Anxiety", "Depression-Dejection", "Anger-Hostility", "Vigor", "Fatigue" and "Confusion" respectively.

Figure 7-1 shows average of T score on male subjects and Figure 7-2 on female subjects. In many factors presented at FPS presentation sound, T score became lower, showing good state, than at LPS presentation sound. In the case of the male subject, the significant difference was accepted by the factor of "anger-hostility (A-H)" * and "confusion (C)" *(*P<0.05). However, female subjects did not show significant difference. This shows that male subjects were quick to react by the components of ultrasonic wave including FPS presentation sound, but female subjects did not clearly show psychological reaction by those of ultrasonic wave.
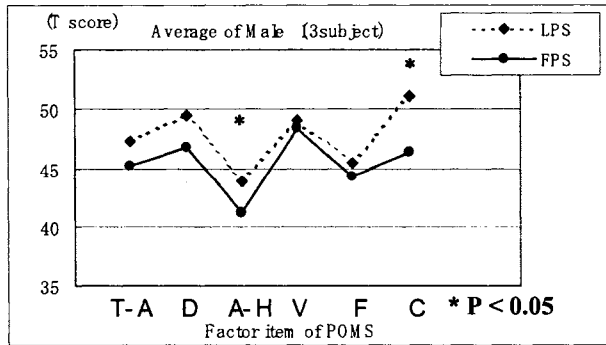
Figure 7-1.Average of male subjects
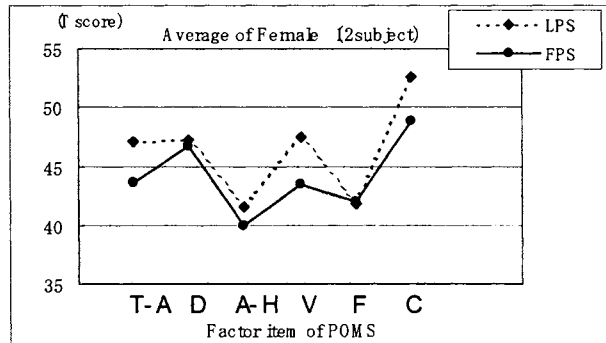
Figure 7-2. Average of female subjects

CONCLUSION

This research further verified existing research on activating effect of ultrasonic waves mainly in the field of music on human brainwaves by producing the same results using the ultrasonic waves contained in the sounds of sea waves. Currently, it is thought that we are only on the way to researching the influence of ultrasonic waves on human beings (Oohashi and Nishina, 1991; Choi and Hotta, 1998, 2001). Up to now, with regard to the influence of ultrasonic waves on brainwaves, there has mainly been quantitative analysis of brainwave activity, but in the future it is important that qualitative evaluation be tried. In the future, if a new evaluation is done of coastal regions from the side of the sound environment including ultrasonic waves, and if those results can be mapped out, it can be used for the development of coastal marine tourism and at the same time, research on the configuration of wave breakers to create comfortable wave sound as well as sound resource management.

REFERENCES

Choi, J-i., S-i. Kanzaki and K. Hotta. 1998. A study on the Physiological effects of ultra-sonic waves of coastal area on human brain waves, *Recent Advancement in Marine Science and Technology 1998*, PACON International, Honolulu Hawaii, USA

Choi, J-i and K. Hotta. 2001. The effects on the auditory evoked potential caused by ultra-sonic wave property including sound of coastal waves, *Proceedings of Japan Society of Acoustics, 2001*, Japan

Oohashi, T. and E. Nishina. 1991. High-frequency sound above the audible range affects brain electric activity and sound perception, 91st Convention of the Audio Engineering Society 3207 (W-1), New York.

Oohashi, T. and E. Nishina. 1992. Physiological Influences of Gamuran High-frequency Band-width, *Proceedings of Japan Society of Acoustics*, Japan.

A FEASIBILITY STUDY ON THE MARICULTURE
OF PUFFER FISH IN HONG KONG

Chun-fai Yu and Peter Hoi-fu Yu

Department of Applied Biology & Chemical Technology
The Hong Kong Polytechnic University
HONG KONG
95983046r@polyu.edu.hk

ABSTRACT

During the period 1996-2002, nine species of puffer fishes were identified by us in Hong Kong waters. Although a total of twenty-six marine fish culture zones have been established in Hong Kong since the 1980s, puffer fishes are not among the cultured species as they are toxic and so are banned from marketing and consumption by the Hong Kong Government. Nevertheless, in some local restaurants, the serving of puffer fish is allowed if the fish are shown to be imported directly from Japan with the required health certificates.

Among the nine local species of puffer fish, most of which were reported to be toxic, we confirmed three species to be toxic and only one was non-toxic with the standard mouse bioassay. Moreover, the annual toxicological profiles of two toxic species revealed that the toxicity of their flesh was less than 10 mouse units per gram throughout the whole year. With proper processing, screening and storage methods, the flesh of most puffer fish is able to meet the safety standards of Japan and China for human consumption.

To fully utilize the local marine resources in Hong Kong, puffer fishes should be potential candidates for aquaculture in the near future. Apart from the flesh being for human consumption, the toxic viscera of puffer fish (mainly ovaries and liver) can be explored to produce the valuable tetrodotoxin (a neurotoxin mainly found in puffer fishes), which is a potential anesthetic and neuropathic pain drug, a proposed formulation to treat heroin addiction and a known cancer cell suppressor.

Keywords: Puffer fish; Marine fish culture zones of Hong Kong; Tetrodotoxin

INTRODUCTION

The Hong Kong fishing industry used to be very important and support the livelihood of the local fishing communities before the 1960s. By then, the local marine fish catch was sufficient to meet the domestic demand and the surplus was usually for producing some side-business, such as sun-dried fish, salted fish, fish sauce, shrimp paste, etc. However, due to a number of factors, (1) the deterioration of seawater quality caused by pollution, rapid population growth and unmonitored industrial and domestic sewage, (2) a drastic decrease in coastal fish breeding grounds caused by large scale land development, (3) over-exploitation, etc., the fisheries resources in Hong Kong waters and the South China Sea as a whole has dramatically decreased

over the past several decades, especially for the high value fishes (Environmental Resources Management, 1998).

The introduction of the marine fish culture zones along the Hong Kong costal waters by the Hong Kong Agriculture and Fisheries Department (which becomes the Agriculture, Fisheries and Conservation Department in 2000) in the 1980s helped to alleviate the shortage problem of fisheries supply for a short while. The common cultured fishes were highly esteemed species such as the groupers, sea breams, snappers, etc. Unfortunately, the mariculture industry (mariculture) died down rapidly as a result of water pollution, aging of the culture zones, red-tides, epidemic fish diseases, etc.

To date, the local fisheries supply, live, chilled or frozen, is mainly imported from mainland China, some Southeast Asian countries and some other western countries. Hong Kong people used to consume a lot of live marine fish, apart from being very delicious but also very nutritious, which is one of the main sources of the human essential proteins.

With the recent decline in the local fisheries resources, puffer fishes can still be easily caught along the coastal waters. A total of nine species (belonging to five different genera) has been identified and reported by us (Yu and Yu, 2002a, 2002b) which coincided with the number of species in the reports of Chan (1968), but the species were different. However puffer fish are not among the cultured species as they are toxic and are banned from marketing and consumption by the Hong Kong Government except in some restaurants where puffer fishes were imported directly from Japan and which were accompanied with health certificates showing they are safe for human consumption.

The mariculture of puffer fish has long been practised in Japan since the 1960s (Pawar et al., 2002) as puffer fish have long been an expensive delicacy among the Japanese, especially the species *Takifugu rubripes* (Temminck & Schlegel) (Fig. 1) served in the restaurants. Moreover, processed frozen puffer fish fillets are commonly available on sale in the Japanese fish markets for household consumption (Fig. 2). Puffer fishes are also cultured in mainland China, Taiwan and Korea, for both local consumption and exportation. The two marine species, *T. rubripes* (Temminck & Schlegel) and *T. chinensis* (Abe), cultured in northern China are solely for exporting to Japan and the two anadromous species, *T. ocellatus* (Linnaeus) and *T. obscurus* (Abe), which migrated to the Yangtze estuary in eastern China during their spawning seasons in March to April every year, are mainly for local consumption (Jiang et al., 2000).

There was hardly any attempt which had ever been made to investigate the culture and growth rates of puffer fish in captivity in Hong Kong where they have never been considered as food fish, except for the non-toxic species (*Lagocephalus wheeleri*, Abe, Tabeta and Kitahama) among the minor fishing community (Yu and Yu, 1997, 1998). A feasibility study on the mariculture of puffer fish in Hong Kong is, therefore, being conducted with a view to explore the possibility of using local puffer fish resources as new cultured candidates. So some common local puffer fish juveniles were collected along the coastal waters and reared in cages in order to observe their growth rates, feeding habit and mortality during culture.

With proper processing, screening and storage methods, the toxicity of the flesh of most puffer fishes is less than ten mouse units per gram in mouse bioassay, which is actually safe for human consumption (Ministry of Health and Welfare, Japan, 1991; Yu and Yu, 2001, 2002a). Besides the skin of puffer fish is a potential source of collagen which is an essential human protein

protein (Nagai et al., 2002), the toxic viscera of puffer fish (mainly ovaries and liver) can be explored to produce the valuable tetrodotoxin (a non-protein neurotoxin mainly found in puffer fishes), which is also a potential anesthetic (Kohane et al., 1998), a promising neuropathic pain drug (Lyu et al., 2000), a proposed formulation to treat heroin addiction (Sellers et al., 2002) and a known cancer cell suppressor (Fraser et al., 1999).

Figure 1. *T. rubripes* (Temminck & Schlegel), the most popular puffer fish for consumption in Japan

Figure 2. Frozen puffer fish fillets on sale in Japanese fish markets

MATERIALS & METHODS

Puffer fish juveniles of *T. alboplumbeus* (Richardson), measuring from 4 to 6 cm in total length (Fig. 3), were found swimming and feeding in large numbers along the seashore from March every year immediately after their spawning season from December to February (Yu and Yu, 2002). This species is one of the most commonly found local puffer fish (common name is known as Hong Kong Puffer fish) and the fish juveniles were easily collected with fishing net in coastal waters.

A total of 100 healthy specimens of *T. alboplumbeus* (Richardson) were collected along the shores in March 2002. They were weighed and measured individually and the healthy juveniles were reared in a net cage suspended in floating wooden fish raft at one of the marine culture zones in Hong Kong.

With reference to the mariculture practices and techniques for fish floating cage farming recommended by the Hong Kong Agricultural, Fisheries and Conservation Department (Agriculture, Fisheries and Conservation Department, 2001), the size of the fish cages used in this experiment were about 2x2x2 m and the mesh size was adjusted as the fish grew up. The cage was covered with a net to prevent the fish from being caught or eaten by some flying birds.

New and clean cages would replace fouled cages regularly to maintain water current passing freely through the cages. The stocking density of the fish was kept at an optimal level (between 10 – 20 tails per cubic meter from juveniles to adults) to prevent overcrowding which would cause biting and coeval (sibling) cannibalism among themselves (Baras et al., 1999). The fish were fed daily with ground trash fish once in the morning until satiety. About 10% of the fish were weighed and measured (total length) every month to assess the growth rate. Dead and diseased fish were removed immediately from the cage everyday.

There were reports emphasizing that puffer fishes were instinctive biters which caused large-scale damages to fish cages and fishing gears (Naik, 1998). In order to prevent damage to the fish cage (hence escape and loss of fish), which was commonly made of polyethylene, by the sharp teeth and strong jaws of the fish when they grew up, the cage was replaced with metal cage when the fish approached about 50 g each.
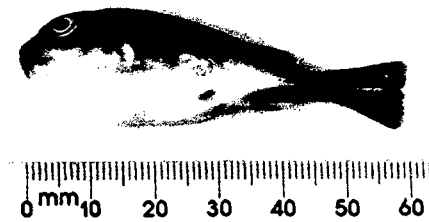
Figure 3. A juvenile specimen of *T. alboplumbeus*
(Richardson)

RESULTS AND DISCUSSION

The monthly mean weight and total length of *T. alboplumbeus* (Richardson) in the culture (March to September 2002) are shown in Table 1. The error bars in Figures 4 and 5 were the standard deviation of the weight and length measurements.

The growth rates of *T. alboplumbeus* (Richardson) from March to September 2002 were 3.1 g/month and 1.7 cm/month (calculated from the slopes of the best fit lines in Figures 4 and 5 respectively). The mortality rate within the same period was observed to be 52 percent.

Table 1. The mean weight and length of *T. alboplumbeus* (Richardson) specimens cultured in floating cage from March to September 2002

Month/year	Total number of fish survived in cage	Number of fish measured (n)	Weight [a] (g)	Total length [a] (cm)
Mar 2002	100	20	7.83±4.52	5.46±3.01
Apr 2002	81	15	10.26±6.93	6.92±4.85
May 2002	73	12	13.56±8.32	8.49±5.54
Jun 2002	66	11	18.79±10.17	10.83±7.18
Jul 2002	59	10	20.34±14.12	12.63±9.47

Aug 2002	53	13	23.96±19.71	14.27±12.87
Sept 2002	48	10	25.26±16.75	14.82±9.63

[a]mean ± standard deviation
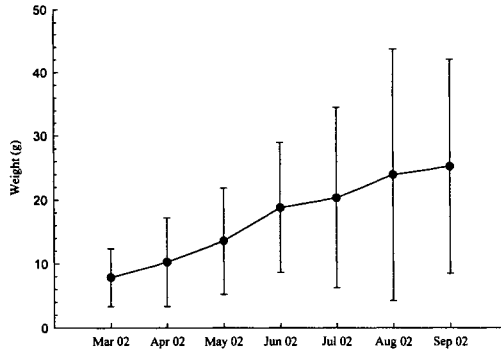
(error bars represent standard deviation)

Figure 4.   The mean weight of *T. alboplumbeus* (Richardson) specimens from March to September 2002
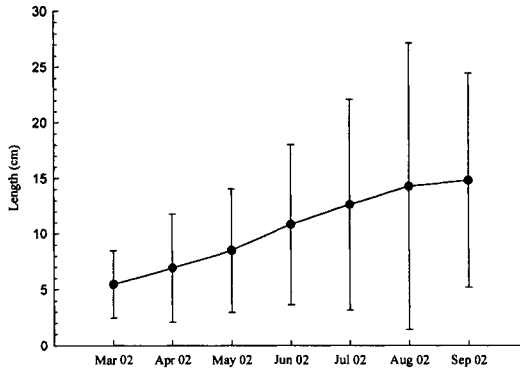
(error bars represent standard deviation)

Figure 5.   The mean length of *T. alboplumbeus* (Richardson) specimens from March to September 2002

According to the growth rates of *T. alboplumbeus* (Richardson) in the summer months (April to September in Hong Kong) obtained in this study, the projected weight and length of the fish at the end of 2003 (about 22 months of rearing in fish cage) would be 55.8 g and 30.6 cm respectively (Fig. 6). Typical grown-up and mature *T. alboplumbeus* (Richardson) specimens (Fig. 7) were, however, found to be within the ranges of 35 – 81 g and 15 – 20 cm (Yu and Yu, 2002). Therefore, the projected weight of the cultured specimens after 22 months of rearing in fish cage would be within the typical range but the projected length would not be, which might

483

be due to the slowing down of the growth rate in length when the fish grow up and increase in body weight.

The mortality rate (52%) was found to be more than half of the total number of fish in the first seven months of culture, which might be due to the following contributing factors: (1) the feed was not suitable for the juveniles in terms of nutrition and palatability, (2) cannibalism happened among the fish because of large size heterogeneity or overcrowding, and (3) epidemic diseases were frequent among the fish in a confined fish cage. It should be pointed out that the fairly high growth rates in weight and length observed in this period might partly due to the remaining stronger survivors left, which might not truly reflect the actual growth rates. The use of a suitable artificial feed for fish juveniles to start with and the monitoring of similar size of fish being reared in the same cage will certainly improve the survival rate in future experiments.

Jiang et al. (2000) reported that, among the 22 species of puffer fish belonging to the genus *Takifugu* found in Chinese waters, there were only about 4 species suitable for cultivation, and all of which took more than two years to grow up and mature. Moreover they also required special facilities for overwintering because they will die when the culture water fell below about 7 °C (Sun et al., 2000). As Hong Kong has a sub-tropical climate, the culture of *T. alboplumbeus* (Richardson) does not require any overwintering facility and it can mature and grow up within 2 years, which is shorter than the culture time of the northern species. However, *T. alboplumbeus* (Richardson) is a relatively small species and it seldom reaches more than 200 g each, whilst those northern species can normally reach over 500 g each.

In view of fully utilizing the local marine resources, the mariculture of puffer fish in Hong Kong is certainly feasible and will create more working opportunities among the fishing communities. The present study has preliminarily showed that *T. alboplumbeus* (Richardson) is another marine puffer fish species feasible for culture in fish cages. However, further studies are required to improve the survival rate of the fish and the introduction of artificial feed will improve the fish growth rate (Liang et al., 2001) and slow down the ageing of the culture zones (Pawer et al., 2002). Moreover, the exploration of natural or artificial spawning of puffer fish for the production of a steady supply of larval fish of high quality and homogenous size for culture (Dinis et al., 1999; Jiang et al., 2000), which would be much better than collecting the fish juveniles from the wild. This would be an important criterion for a cultured species to be successfully cultivated in future.

There were reports from China (Jiang et al., 2000), Japan (Saito et al., 1984) and Taiwan (Lin et al., 1998; Hwang et al., 2000) that cultured puffer fish were non-toxic or in reduced toxicity when compared with the same species caught from the wild. However there is still no information available about the toxicities of the cultured puffer fish in Hong Kong, which will require further studies to be undertaken by the authors when the fish grow up and mature. Therefore, the grown-up cultured puffer fish could be exported overseas either as live fish or processed as frozen fish fillets. The toxic viscera can be used for the extraction of the valuable neurotoxin, tetrodotoxin (TTX), which, to the best of our knowledge, is still the current practicing method to produce TTX for sale in the world market. At present, large-scale production of TTX from TTX-producing bacteria *in vitro* is still not well developed and successful.
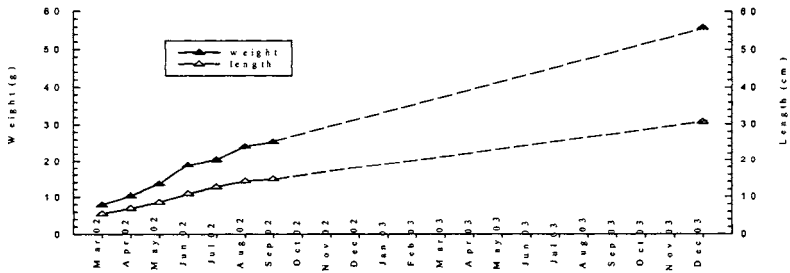
Figure 6.   Projected weight and length of *T. alboplumbeus* (Richardson) at the end of 2003

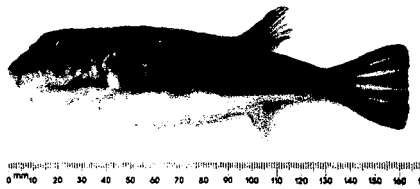Figure 7. A grown-up and mature *T. alboplumbeus* (Richardson) specimen

ACKNOWLEDGEMENTS

REFERENCES

Agriculture, Fisheries and Conservation Department. 2001. *Department Annual Report 2000 – 2001*. Hong Kong Printing Department, Hong Kong.

485

Baras, E., F. Tissier, J.C. Philippart and C. Mélard. 1999. Sibling cannibalism among juvenile vundu under controlled conditions. II. Effect of body weight and environmental variables on the periodicity and intensity of type II cannibalism. *Journal of Fish Biology.* 54:106-118.

Chan, W.L. 1968. *Marine Fishes in Hong Kong* (Part 1). Hong Kong: Hong Kong Government Press.

Dinis, M.T., L. Ribeiro, F. Soares and C. Sarasquete. 1999. A review on the cultivation potential of *Solea senegalensis* in Spain and in Portugal. *Aquaculture.* 176:27-38.

Environmental Resources Management. 1998. *Fisheries Resources and Fishing Operations in Hong Kong Waters (Final Executive Summary).* Hong Kong: Environmental Resources Management.

Fraser, S.P., Y. Ding, A. Liu, C.S. Foster and M.B.A. Djamgoz. 1999. Tetrodotoxin suppresses morphological enhancement of the metastatic MAT-LyLu rat prostate cancer cell line. *Cell and Tissue Research.* 295:505-512.

Jiang, R.L., C.W. Zhang, Y.K. Ding, C.B. Chen and M.F. Li. 2000. Artificial propagation of nontoxic *Takifugu obscurus* cultured in pond (in Chinese). *Journal of Fisheries of China.* 24(6):539-543.

Kohane, D.S., J. Yieh, N.T. Lu, R. Langer, G.R. Strichartz and C.B. Berde. 1998. A Re-examination of Tetrodotoxin for Prolonged Duration Local Anesthesia. *Anesthesiology.* 89(1):119-131.

Liang, M.Q., C.G. Wang, C. Chen, H. Yu, Q. Chang, J.H. Lian, Y.W. Yang, F. Shi, B.Y. Fang and H.B. Yu. 2001. Effect of five additives on promoting growth of *Fugu rubripes* and the relationship with RNA/DNA (in Chinese). *Marine Fisheries Research.* 22(2):38-41.

Lin, S.J., T.J. Chai, S.S. Jeng and D.F. Hwang. 1998. Toxicity of the puffer *Takifugu rubripes* cultured in northern Taiwan. *Fisheries Science.* 64(5):766-770.

Lyu, Y.S., S.K. Park, K. Chung and J.M. Chung. 2000. Low dose of tetrodotoxin reduces neuropathic pain behaviors in an animal model. *Brain Research.* 871:98-103.

Ministry of Health and Welfare, Japan. 1991. *Standard Methods of Analysis in Food Safety Regulation (Chemistry),* 296-300 (in Japanese). Japan: Japan Food Hygienic Association, Tokyo.

Nagai, T., Y. Araki and N. Suzuki. 2002. Collagen of the skin of ocellate puffer fish (*Takifugu rubripes*). *Food Chemistry.* 78:173-177.

Naik, S.D. 1998. Observations on large-scale destruction of fishing gear by the pufferfishes (family Tetraodontidae) along the south Konkan coast (west coast of India). *Indian Journal of Marine Sciences.* 27:421-425.

Pawar, V., O. Matsuda and N. Fujisaki. 2002. Relationship between input and sediment quality of the fish cage farms. *Fisheries Science.* 68:894-903.

Saito, T., S. Maruyama, S. Kanoh, J.K. Jeon, T. Noguchi, T. Harada, O. Murata and K. Hashimoto. 1984. Toxicity of cultured pufferfish *Fugu rubripes rubripes* along with their resistibility against tetrodotoxin (in Japanese). *Nippon Suisan Gakkaishi*. 50: pp.1573-1575.

Sellers, E.M., M.K. Romach, A.H. Ngoc, S. Lu, H.L. Kaplan, D.N. Juurlink and P. du Souich. 2002. Pharmacologic effects and safety of single and multiple doses of tetrodotoxin (TTX), *Clinical Pharmacology and Therapeutics*. 71(2):P16-P16.

Sun, Z.Z., S.G. Sun, H. Yu and C. Chen. 2000. On the overwintering experiment of *Fugu rubripes* (in Chinese). *Marine Fisheries Research*. 21(1):63-67.

Yu, C.F. and P.H.F. Yu. 1997. A preliminary study of puffer fishes and their toxins found in Hong Kong waters. *Journal of the Food Hygienic Society of Japan*. 38(6):460-463.

Yu, P.H.F. and C.F. Yu. 1998. The toxicological study of puffer fishes in Hong Kong (in Chinese). *Journal of Fisheries of China*. 22(4):382-384.

Yu, C.F. and P.H.F. Yu. 2001. Study on the edibility and resources of Hong Kong puffer fish (in Chinese). *In Fourth Anniversary Commemorative Publication of Hong Kong Food Science and Technology Association*, edited by W. Wong, 28-29. China: Hong Kong Food Science and Technology Association.

Yu, C.F. and P.H.F. Yu. 2002a. Are puffer fish more toxic in their spawning seasons? *Marine Biology*. 140:1053-1057.

Yu, C.F. and P.H.F. Yu. 2002b. The annual toxicological profiles of two common pufferfish, *Takifugu niphobles* (Jordan and Snyder) and *Takifugu alboplumbeus* (Richardson), collected along Hong Kong coastal waters. *Toxicon*. 40:313-316.

IMPLICATION OF N: P: SI RATIOS TO HARMFUL ALGAL BLOOMS IN HONG KONG WATERS

K.C. Ho[1], John Hodgkiss[2] and Ironside Lam[2]

[1]School of Science and Technology, The Open University of Hong Kong
Hong Kong, CHINA
kcho@ouhk.edu.hk

[2]Department of Ecology & Biodiversity, The University of Hong Kong
Hong Kong, CHINA

ABSTRACT

Since the 1980s, waters in Hong Kong and Southern China have suffered from occasional attacks of harmful algal blooms (HABs). An episode in 1998 resulted in a total loss of 350 million Hong Kong dollars in the aquacultural industry. While most HABs were triggered by special oceanographic and climatic conditions, microalgal biomass was closely related to nutrient supplies. Past research showed that dinoflagellate-caused HABs were associated with changes in N:P (atomic) ratio when the minimum concentration of 0.1 mg-N/L of TIN and 0.02 mg-P/L of DIP was reached. Recent findings indicate that interspecific competition between diatoms and dinoflagellates should not be overlooked. Silicate (Si), the limiting factor for diatom growth, has played a significant role in determining the dominant species and the magnitude of red tides. The Redfield Ratio should be critically reviewed in terms of its application to HABs dominated by dinoflagellates and the Si:N ratio should be considered in parallel with N:P ratios. Data from Tolo Harbour of Hong Kong show that dinoflagellate blooms are favored by N:P (atomic) ratio of 10-22 and Si:N (atomic) ratio <1; diatom blooms are favored by larger N:P and Si:N ratios; whereas micro-flagellate blooms often occur after collapse of diatom and dinoflagellate blooms. Therefore, besides discharges of domestic sewage and agricultural wastes, which contain a huge quantity of TIN and DIP, variation of Si input due to urbanization, soil erosion and river diversion should be considered.

INTRODUCTION

Harmful algal blooms (HABs), which used to be known as red tide, are a global concern. Like other temperate and subtropical waters, Hong Kong and indeed the whole southern portion of China have been frequently affected by HABs since the 1980s. A total of 644 HAB incidents were recorded in Hong Kong waters particularly Tolo Harbour from 1980 to 2001 (Hong Kong Red Tide Information Network, 2002). In addition, 69 HABs/red tides occurred in other South China waters (Hodgkiss et al., 2001).

Harmful algal blooms often result in extensive fishkills in aquacultural zones. For example, a prolonged HAB in April - May 1998 caused around a 350 million Hong Kong dollars (~42 million US dollars) loss in the local aquacultural industry (Lu and Hodgkiss, 1999). While a

great deal of resources have been deployed in forecasting as well as mitigating HABs, the major formation mechanism and limiting factors have yet to be clarified by scientists. This paper presents analysis of the observed characteristics of HABs in Hong Kong waters and this information is anticipated to be useful in understanding the principal ecological processes of HABs in the coastal marine environment.
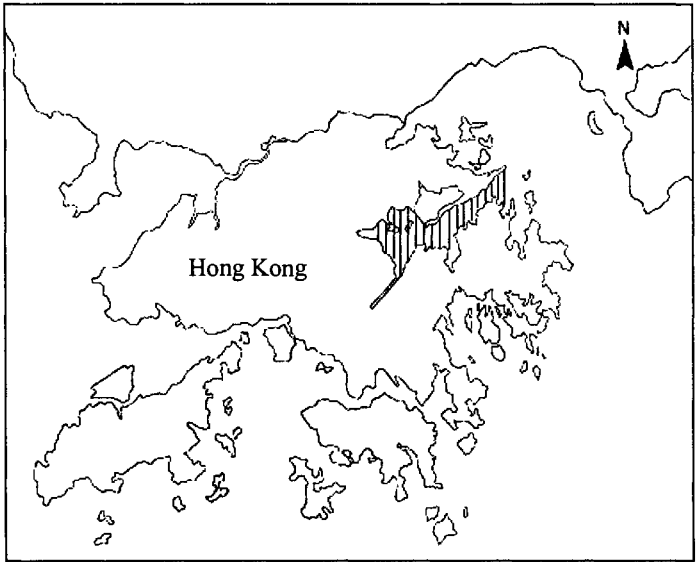
Figure 1. Hong Kong and the location of Tolo Harbour (hatched)

CHARACTERISTICS OF HABs IN TOLO HARBOUR

Of the various affected waters in Hong Kong, Tolo Harbour, a semi-enclosed embayment with a narrow outlet channel in the northeast of Hong Kong (Fig. 1), have been extensively studied in terms of the causes and impacts of HABs (Holmes and Lam, 1985; Hodgkiss and Chan, 1987; Lam and Ho, 1989a and 1989b; Wong, 1989; Lam and Yip, 1990; Hodgkiss and Ho, 1992; Ho and Hodgkiss, 1993a and 1993b; Hodgkiss and Ho, 1997). In addition to tidal force and oceanic intrusion of water which carried vegetative cells into Tolo Harbour, salinity shock and the uniform meteorological conditions (cool temperature, overcast skies and low rainfall) in March to early May every year were believed to allow favorable growth of causative dinoflagellates during HABs (Lam and Yip, 1990; Yung et al., 1997). While nutrients (N, P) and micro-nutrients (ferric ions, Vitamins) are considered the major triggering and supporting factors of HAB (Ho and Hodgkiss, 1991), interestingly, Holmes and Lam (1985) and Holmes (1988) showed the positive correlation between nitrogen loading increase in the watershed of Tolo Harbour and the increase in red tide incidents there. Extensive urban development, untreated domestic sewage and discharge of livestock wastes were considered the major contributors to increase nitrogenous compounds and phosphates in inner Tolo Harbour during the 1980s to early 1990s. Going one step further, Ho and Hodgkiss (1993b) and Hodgkiss and Ho (1997) reported

that when the minimum concentration of 0.1 mg-N/L of TIN and 0.02 mg-P/L of DIP was reached, red tide occurrence in Tolo Harbour was highly possible. Furthermore, Hodgkiss and Ho (1997) revealed that the decline in annual mean N:P (atomic) ratio 1982 - 1989 in the surface water of Inner Tolo Harbour was often associated with increase in red tide incidents in the same year (Fig. 2A). Their conclusions were generally agreed with the findings of Hodgkiss and Chan (1987), Chan and Hodgkiss (1987) and Huang et al. (1994) that a decline in N:P ratio in surface water usually resulted in dinoflagellates (the main red tide causative organisms) taking over dominance from the diatoms. Thus, the decline of annual mean N:P (atomic) ratios from around 20:1 in 1981 to 11:1 in 1990 reflected the change in phytoplankton community in Inner Tolo Harbour during the 1980s , when incidents of red tide peaked.
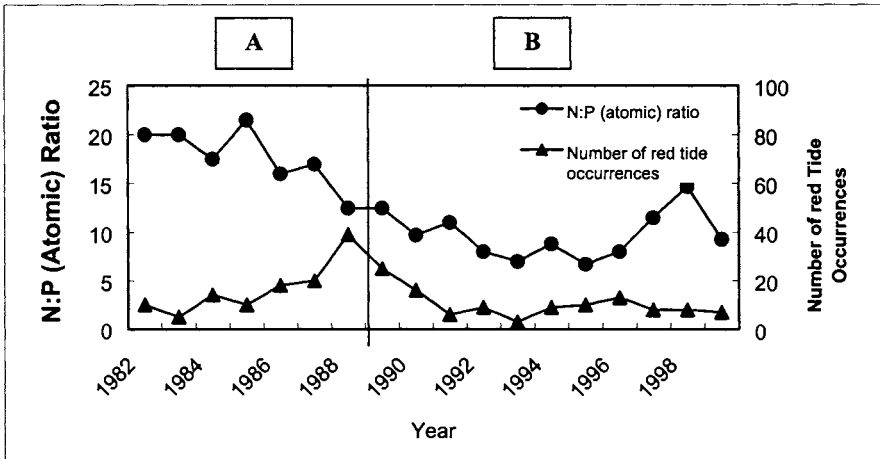
Figure 2. N:P ratios versus numbers of red tides in the surface waters of Inner Tolo Harbour during the period A:1982 - 1989 (after Hodgkiss and Ho, 1997) and B: 1990-1999 (updated by the present authors)

Table 1. Optimal N:P (atomic) ratios in cultivated medium for various red-tide causative dinoflagellates and diatoms in Tolo Harbour (After Hodgkiss and Ho, 1997)

Species	Optimal N:P (atomic) Ratio
Alexandrium catenella	(15-30) : 1
Ceratium furca	(12-22) : 1
Cryptomonas sp.	(12-20) : 1
Gonyaulax polygramma	(4-8) : 1
Karenia mikimotoi	(11-16) : 1
Noctiluca scintillans	(8-14) : 1
Olisthodiscus sp.	(6-15) : 1
Prorocentrum dentatum	(6-13) : 1
P. minimum	(4-13) : 1
P. sigmoides	(4-15) : 1
P. triestinum	(8-15) : 1
Prymnesium spp.	(6-12) : 1

491

Pseudonitzschia pungens	9 : 1
Scrippsiella trochoidea	(6-13) : 1
Skeletonema costatum	>24 : 1

During the 1990s, the levels of TIN and DIP in the surface water of Inner Tolo Harbour were significantly reduced due to enforcement actions under the Water Pollution Control Ordinance of Hong Kong (Environmental Protection Department 1991-2001). While the frequency of red tide have also been reduced since 1991, Figure 2B shows that the association between decreases in N:P (atomic) ratio and increases in red tide incidents as shown in Figure 2A is nearly no changed. This confirms that red tide formation, which is mainly due to rapid dinoflagellates growth in the surface water of Inner Tolo Harbour, demands minimum (critical) concentrations of TIN and DIP and specific N:P (atomic) ratios. This conclusion is supported by bottle algal bioassay experiments (Hodgkiss and Ho, 1997) which showed that out of the 15 red-tide causative organisms studied in Tolo Harbour, eleven dinoflagellates were favored by N:P (atomic) ratios of 4-16 and only four were favored by N:P (atomic) ratios from 12-30 in the initial culture medium (Table 1). For *Skeletonema costatum*, a red-tide causative diatom, was favored by an N:P (atomic) ratio >24. The optimal N:P ratios in coastal diatoms and dinoflagellates are found to be different from the Redfield Ratio of 16:1 which has been applied to phytoplankton of open water (Redfield et al., 1963). The discrepancy is probably due to the adapting ability of phytoplankton to strong land-based discharge and salinity stress in estuarine and coastal environment.

SIGNIFICANCE OF INTER-SPECIFIC COMPETITION

While the relationship between N:P (atomic) ratios and HAB occurrences has been widely discussed, the related inter-specific competition within the phytoplankton community has not yet been comprehensively elaborated (Ho and Hodgkiss, 1991). In fact, from the above conclusions regarding the relationship between N:P ratios and red tide occurrences at Tolo Harbour, it can be seen that diatoms and dinoflagellates are assumed to have a similar ecological niche in coastal marine waters and their strive for a nutrient supply similar too. Hence, it is not unexpected that strong biological competition occurs between diatoms, dinoflagellates and other small flagellates (including zooplankton) in the community. This hypothesis is supported by Figure 3, which records the population dynamics of diatoms, dinoflagellates and small flagellates during a red tide in Inner Tolo Harbour in March 2000. During most times of the year, diatoms are the dominant group within phytoplankton in Inner Tolo Harbour (Chan and Hodgkiss, 1987; Lam and Ho, 1989b). Nevertheless, as seen in Figure 3, when the seed population of *Noctiluca scintillans* began to bloom, the cell concentration of diatoms (dominated by *Skeletonema costatum*) was significantly reduced, with dominance taken over by dinoflagellates. While the population of *N. scintillans* changed occasionally due to diurnal migration between surface and middle layers (Blasco, 1979; Ho, 1994), after one to two days the red tide caused by *N. scintillans* dissipated, and then, diatoms (mainly *Skeletonema costatum*) resumed their dominance of the phytoplankton community. When both dinoflagellate and diatoms blooms were over small flagellates assumed dominance for a short period of time. A few days after this red tide event, diatoms resumed their normal dominance in Inner Tolo Harbour.

On the basis of observations and studies, HABs cannot be viewed solely as a chemical response by specific species of phytoplankton to supply of nutrients. Although nutrients are able to trigger

and support HABs, the fundamental changes in phytoplankton dynamics are closely related to biological processes and ecological competition. Therefore, it is likely that HABs are actually a succession process in the coastal marine environment, where the dominance by diatoms, dinoflagellates and small flagellates (including zooplankton) is gradually taken over by each in turn.
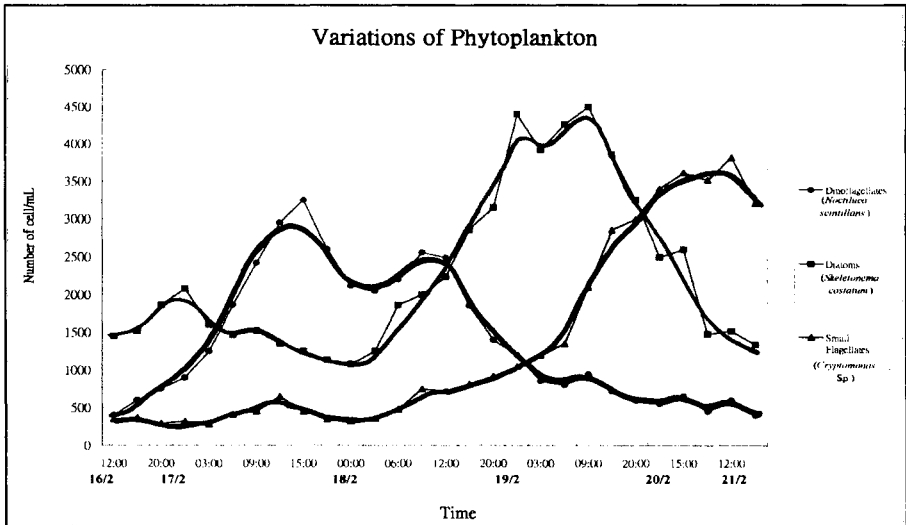

Figure 3. Changes in the diatom, dinoflagellate and small flagellate populations in Inner Tolo Harbour during a red tide in February 2000

It has been reported that dinoflagellates have a relatively slow growth rate, rarely exceeded one doubling per day (Karentz, 1983). Since diatoms are able to have 2-6 doublings per day, this can result in prolonged dominance of diatoms in marine and estuarine environments (Werner, 1977; Stoermer and Smol, 1999). As observed in Tolo Harbour, only when the available nutrients or environmental conditions changed, dinoflagellates take over the dominance (Lam and Ho 1989b). Thus, when the surface nutrient supply dwindled, diatoms receded in importance and dinoflagellates took up dominance because of their migrating ability between surface and middle layers and their different requirement for nutrients and N:P ratios (Ho and Hodgkiss, 1991; Ho, 1994). Further studies on phytoplankton dynamics in relation to competition at genus and species levels should be considered in future HAB research.

RELATIONSHIP BETWEEN Si : N RATIOS AND HAB

Silicon (Si) comprises around 5% dry weight of diatoms and so is an essential element for diatom growth (Werner, 1977). It has been suggested above that natural succession and biological competition are the major factors regulating phytoplankton composition and HAB outbreaks. Si supply is another factor regulating HAB occurrence, but unfortunately, there has been little research in this area. Long-term monitoring data collected by the Environmental Protection Department (EPD, 1991-2001) showed that chlorophyll-a peaks in the inner portion of Tolo Harbour were not necessarily matched with total number of red tide reports. This was

mainly because most of the chlorophyll-a was contributed by diatoms rather than the red tide causative dinoflagellates. Instead, on normal days the peaks of chlorophyll-a closely matched peaks of dissolved silicates in Inner Tolo Harbour (Fig. 4). During days of red tide occurrence, however, the level of silicates was usually low in the seawater, indicating that dinoflagellate growth was frequently promoted by the exhaustion of silicate supply and the resultant reduction of diatoms (Fig. 5). These conclusions were supported by the fact that in Outer Tolo Harbour and Mirs Bay Water Control Zone, Hong Kong, where diatoms are the dominant species and red tides rarely occur, the annual mean Si:N ratio was often greater than 1 or closely equivalent to 1. Furthermore, Liu et al. (2002) found that the Si:N and Si:P ratios in Tolo Harbour have been gradually increased since 1991, resulting in increased prominence and increased overall cell concentrations of diatoms.

Figure 4. Changes of surface chlorophyll-a (mg/L, shaped black) and silicates (mg/L, white lines) in the Inner Tolo Harbour (1982-2000) during normal sampling days
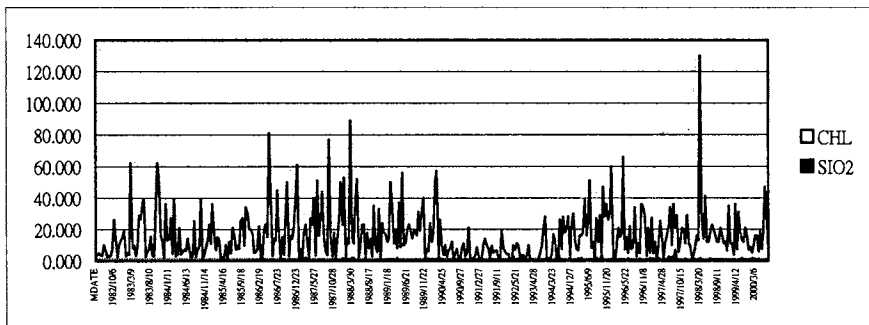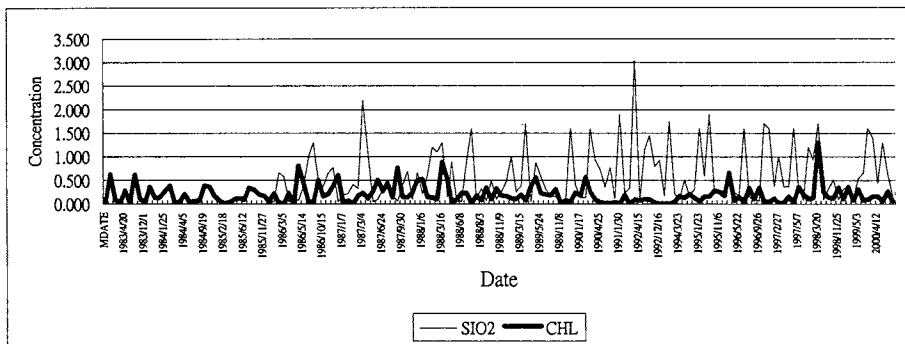

Figure 5. Changes of surface chlorophyll-a (g/L) and silicate (g/L) in the Inner Tolo Harbour (1982-2000) during red tides

If silicon plays an important role in regulating the growth of diatoms, which consequently affects the phytoplankton community structure and the possible outbreak of dinoflagellate blooms, the detailed ecological and physiological mechanisms need further research.

494

Several researchers proposed that allelopathy is involved in the succession of phytoplankton community. The phenomenon of allelopathy was defined as the harmful effect of one alga on a second alga by means of a chemical compound liberated into the environment (Darley, 1982). Kakisawa et al. (1988) showed that an allelopathic substance isolated from a brown alga, namely *Cladosiphon okamuranus*, affected 36 species of microalgae, including *Chaetoceros debile*, and destroyed their cell structure in 30 minutes. Recent studies by Hiromi (2002) also showed that the inhibition of *Heterosigma akashiwo* growth was due to allelo-chemicals produced by a diatom, namely *Cylindrotheca closterium*. Unfortunately, no comprehensive research on allelopathy has been conducted in Hong Kong. Liu and Wu (2002) however found that a strain of *Chattonella marina* isolated from the Hong Kong water was able to produce a significant concentration of reactive oxygen species (ROS), and the ROS might be responsible for gill damage and then kills of local cultured fishes (Tang and Au, 2002). Wu and Lee (2002) also reported that the growth of *Chattonella marina* was inhibited when the alga was exposed to 50 μW/cm^2 of UV-B and 40 μW/cm^2 of UV-A irradiance for 12 hours for several days. The growth inhibition might be due to photo-inhibition or inactivation of nitrogenase within *C. marina*. Hence, further research in the interactions between allelopathic chemicals, environmental factors and interspecific competition on phytoplankton community is a challenge to scientists who intends to clarify the formation mechanism of HABs in Hong Kong and the South China.

According to the present research findings, besides the discharge of domestic sewage and agricultural wastes, which contain a very large quantity of TIN and DIP, variation of Si input due to urbanization, soil erosion and river diversion could be an other cause of increased red tides in enclosed coastal waters. The relevant implications to control, management and mitigation of HABs worthy is to concern.

CONCLUSION

While most of the harmful algal blooms (HABs) in Hong Kong were triggered by special geographic, oceanographic and climatic conditions, dinoflagellate-caused HABs were closely associated with nutrient supplies. In particular, the variation of N:P (atomic) ratio plays an important role in supporting algal biomass. Based on review of the literature and analysis of long-term monitoring data in Hong Kong, it is proposed that dinoflagellate-related HABs are regulated by two major factors: (a) the threshold concentrations of TIN (generally 0.1 mg-N/L) and DIP (generally 0.02 mg-P/L) and, (b) the N:P (atomic) ratios (mostly 4-16). The Redfield Ratio should be critically reviewed in terms of its application to HABs dominated by dinoflagellates in coastal waters.

Recent research indicates that interspecific competition between diatoms and dinoflagellates, with particular reference to natural succession and the relevant demands for nutrients by diatom, dinoflagellate and micro-flagellate communities, also plays a regulating role in HAB occurrence.

Silicon (Si) concentration limits the optimal growth of diatoms, thus regulating the dominant species in the phytoplankton community. Generally speaking, diatom blooms are favored by larger N:P (atomic) ratios (often >22) and a Si:N (atomic) ratio close to or greater than one. The implications of this conclusion are worth further in-depth analysis.

ACKNOWLEDGEMENT

REFERENCES

Blasco, D. 1979. Changes on the surface distribution of a dinoflagellate bloom off the Pierce coast related to time of day. In *Toxic Dinoflagellate Blooms. Proceedings of the Second International Conference on Toxic Dinoflagellate Blooms*, edited by D.L. Taylor and H.H. Seliger, 209-14. Elsevier North Holland.

Chan, B.S.S. and I.J. Hodgkiss. 1987. Phytoplankton productivity in Tolo harbor. *Asian Marine Biology* 4: 79-90.

Darley, W.M. 1982. *Algal biology: a physiological approach*. Oxford: Blackwell Scientific Publications, p.168.

Environmental Protection Department (EPD) 1991-2001. *Marine water quality in Hong Kong, for the years 1990-2000* (11 volumes), Environmental Protection Department, Hong Kong Government. The Government of Hong Kong Special Administrative Region, China.

Hiromi, J., T. Kojima, K. Ara and N. Uchida, N. 2002. Utility of allelochemicals produced by marine diatoms for collapse of red tides. In *PACON 2002 The Ocean Century*. July 21-26, 2002, Chiba, Japan. (Abstract), p. 192.

Hong Kong Red Tide Information Network. 2002. http://www.hkredtide.org/first.htm. Agriculture, Fisheries and Conservation Department, Government of the Hong Kong Special Administration Region.

Ho, K.C. 1994. Several fish kills in Hong Kong and the South China Sea by *Noctiluca scintillans* blooms. In *Proceedings of the IOC-WESTPAC 3rd International Scientific Symposium*, Bali, Indonesia, November, 1994. pp. 73-78.

Ho, K.C. and I.J. Hodgkiss. 1991. Red Tides in subtropical waters: an overview of water occurrence. *Asian Marine Biology* 8:5-23.

Ho, K.C. and I.J. Hodgkiss. 1993a. Assessing the limiting factors of red tide by bottle bioassay. *Asian Marine Biology* 10:77-94.

Ho, K.C. and I.J. Hodgkiss. 1993b. Macronutrients in Tolo Harbour and their relations to red tides. *Environmental Management of Enclosed Coastal Sea (EMECS) Newsletter*, Vol. I (4): 10-11.

Ho, K.C. and I.J. Hodgkiss. 1995. A study of red tides caused by *Prorocentrum micans, P. sigmoides* and *P. triestinum* in Hong Kong. In *The Marine Biology of the South China Sea II - Proceedings of the 2nd International Conference, Guangzhou, China, 1993*, edited by B. Morton, G.Z. Xu, R.L. Zou, J.P. Pan and G.X. Cai, 111-118. Beijing, Shanghai, Xian and Guangzhou: World Publishing Corporation.

Hodgkiss, I.J and B.S.S. Chan. 1987. Phytoplankton dynamics in Tolo Harbour. *Asian Marine Biology* 4:103-112.

Hodgkiss, I.J. and K.C. Ho. 1992. Variations in macronutrients in relation to red tides – The Tolo Harbour experience. *Colloquium on Red Tides in Hong Kong and South China Sea, Hong Kong, September 1992.*

Hodgkiss, I.J. and K.C. Ho. 1997. Are changes in N:P ratios in coastal waters the key to increased red tide blooms? *Hydrobiologia* 352:141-147.

Hodgkiss, I. J., S. Lu and Y. Qi. 2001. Harmful algal blooms in Hong Kong waters – where are they from? In *Harmful Algal Blooms 2000*, edited by Hallegareff, G.M., S.I. Blackburn, C.J. Bloch and R.J. Lewis, 454-457. Intergovernmental oceanographic Commission of UNESCO.

Holmes, P.R. 1988. Tolo Harbour – the case for integrated water quality management in a coastal environment. *Journal of Institute of Water and Environmental Management* 2: 171-9.

Holmes, P.R. and C.W.Y. Lam. 1985. Red tides in Hong Kong Waters – Response to a growing problem. *Asian Marine Biology* 2: 1-10.

Huang, B., H. Hong and L. Chen. 1994. The physiological effects of different N/P ratios on algae in semicontinuous culture. *Asian Marine Biology* 11: 137-142.

Kakisawa, H., F. Asari, T. Kusumi, T. Toma, T. Sukurai, T. Oohusa, Y. Hara, and M. Chihara. 1988. An allelopathic fatty acid from the brown alga, *Cladosiphon okamuranus. Phytochemistry* 27: 731-735.

Karentz, D. 1983. Pattern of DNA synthesis and cell division in marine dinoflagellates. *Journal of Protozoology* 30: 581-8.

Lam, C.W.Y and K.C. Ho. 1989a. Red tides in Tolo Harbour, Hong Kong. .In *Red tides : Biology, Environmental Science and Toxicology,* edited by Okaichi, T., D. M. Anderson and T. Nemoto, 233-236. New York, Amsterdam, London: Elsevier.

Lam, C.W.Y. and K.C. Ho. 1989b. Phytoplankton Characteristics of Tolo Harbour. *Asian Marine Biology* 6: 5-18.

497

Lam, C.W.Y. and S.S.Y. Yip. 1990. A three-month red tide event in Hong Kong. In *Toxic marine Phytoplankton*, edited by Graneli, E., B. Sunddstrom, L. Edler, and D.M. Anderson, 481-486. New York: Elsevier.

Liu J.H., C.S.W. Kueh and M.J. Broom 2002. Phytoplankton population dynamics, nutrient changes and red tides in the southern waters of Hong Kong. *Asian Marine Biology* 17:137-147.

Liu, W. and R. Wu 2002. Production of reactive oxygen species by *Chattonella marina*: implications in fish kills. In *Book of Abstract, X^{th} international Conference on Harmful Algae, St. Pete Beach, Florida, USA, October 21-25, 2002.* p. 173.

Lu, S. and I.J. Hodgkiss. 1999. An unusual year for the occurrence of harmful algae. *Harmful Algal News* 18:1 & 3.

Redfield, A.C., B.A Ketchum and F.A. Richards (1963). The influence of organisms on the composition of seawater. In: Hill M. H. (ed) *The Sea*. Wiley, New York, 26-77.

Stoermer, E.F. and J.P. Smol. 1999. *The Diatoms: Applications for the Environmental and Earth Sciences*. Cambridge University Press: UK.

Tang, J.Y.M. and D.W.T. Au 2002. Morphometric changes in fish gill upon chronic exposure to *Chattonella marina*. In *Book of Abstract, X^{th} international Conference on Harmful Algae, St. Pete Beach, Florida, USA, October 21-25, 2002.* p. 275.

Werner, D. (ed.). 1977. *The Biology of Diatoms*. Botanical monographs Volume 13, Blackwell Scientific Publications: Oxford London Edinburgh Melbourne.

Wong, P.S. 1989. The occurrence and distribution of red tides in Hong Kong – Applications in red tide management. In *Red tides : Biology, Environmental Science and Toxicology,* edited by Okaichi T., D.M. Anderson and T. Nemoto, 125-128. New York, Amsterdam, London: Elsevier.

Wu, R. and W. Lee. 2002. Environmental realistic irradiance of UV-B inhibits growth of Chattonella marina. In *Book of Abstract, X^{th} international Conference on Harmful Algae, St. Pete Beach, Florida, USA, October 21-25, 2002.* p. 307.

Yung, Y.K, C.K. Wong, M.J. Broom, J.A. Ogden, S.C.M. Chan and Y. Leung. 1997. Long-term changes in hydrography, nutrient and phytoplankton in Tolo Harbour, Hong Kong. *Hydrobiologia* 352: 107-115.

INTEGRATING AN AUTO-NUTRIENT ANALYZER INTO A TELEMETRY SYSTEM FOR RED TIDE STUDIES

Ironside Lam[1], John Hodgkiss[1] and K.C. Ho[2]

[1]Department of Ecology & Biodiversity, The University of Hong Kong
Hong Kong, CHINA
lamhyi@hkusua.hku.hk

[2]School of Science and Technology, The Open University of Hong Kong
Hong Kong, CHINA

ABSTRACT

Nutrients, particularly total inorganic nitrogen (TIN) and dissolved inorganic phosphates (DIP), are generally considered to be the major triggering and limiting factors for harmful algal blooms. While some models have been developed on the basis of TIN:DIP ratios to interpret red tide occurrences in Hong Kong, collection of real time data by *in situ* measurement of nutrients has been constrained by limited research funds and available technology. A pilot test incorporating an auto-nutrient analyzer with a telemetry system was conducted to study the possibility of providing *in situ* and real time nutrient data for environmental models. A diurnal study of phytoplankton dynamics at Crooked Island, Hong Kong evaluating the effectiveness of the integrated analyzer-telemetry system is reported.

INTRODUCTION

Since the first scientific report of red tide in Hong Kong (Morton and Twentyman, 1971), there has been more three decades of red tide research in Hong Kong. However, it appears that no significant progress has been made in understanding the formation mechanisms of red tides. Some studies have indicated that eutrophication (Lam and Ho, 1989) and an increase in nutrient (N and P) loading (Hodgkiss and Ho, 1992) may be considered as the most important factors related to the frequent occurrence of red tides in Tolo Harbour, Hong Kong. Ho and Hodgkiss (1993), using bottle bioassay tests, showed that the growth of four dinoflagellates isolated from Tolo Harbour was optimum at N:P (atomic) ratios from 4-22, and further studies on *Prorocentrum micans, P. sigmoides* and *P. triestinum* suggested that increased red tide due to all three species in the late eighties might have been related to a reduced N:P ratio in the water of inner Tolo Harbour (Ho and Hodgkiss, 1995). Thereafter, nutrients, and total inorganic nitrogen (TIN) and dissolved inorganic phosphates (DIP) in particular, have been considered as the major triggering and limiting factors for harmful algal blooms in Hong Kong.

Hodgkiss and Ho (1997) reviewed evidence collected from Tolo Harbour together with data from Japan and North European coastal waters and indicated that both long term and relatively short-term changes in the N:P ratio are accompanied by increased blooms of non-siliceous phytoplankton groups and showed that nutrient ratios could be more informative than nutrient

concentration *per se*. Some models on the basis of TIN:DIP ratios have been developed to interpret red tide occurrences in Hong Kong and such a N:P ratio hypothesis seems to have been established validly both in Tolo Harbour and other areas of Hong Kong waters in recent studies (Yang, 2000; Lu, 2001).

However, it is unknown whether such N:P ratios are applicable at Crooked Island, where it is believed that the 1998 episode of large scale red tides was initiated (Anderson et al., 1998). Indeed, little is known concerning the effects of nutrient dynamics on the formation of red tides there. To better understand the relationship between N:P ratios and red tides, the collection of real time data by continuous *in situ* measurement of nutrients is important but has been constrained by limited research funding and the available technology. The traditional approach in red tide studies is based on periodic and discrete sampling, and such an approach can cause loss of data between sampling intervals. In view of this limitation and in order to provide more background information about nutrient dynamics during red tide formation, telemetry has been adopted to study and monitor red tides (Lee et al., 2000). However, the lack of real time *in situ* as well as continuous nutrient data prevented insight being gained into the role of nutrients in the period preceding red tides. A pilot test involving diurnal observations of marine microalgal dynamics, was conducted to test the feasibility of integrating an auto-nutrient analyzer into this telemetry system, providing *in situ* and real time nutrient data for environmental models, as well as to investigate the limitations and technical problems, if any. The telemetry system itself consists of a series of probes to monitor chlorophyll *a,* water temperature, dissolved oxygen, solar radiation, wind, tidal level and current. The data are logged in a micrologger and transmitted via modems to The University of Hong Kong (for data retrieval, analysis and storage) from the fish raft mounted system at Crooked Island (Lam and Hodgkiss, 2000, 2001).

MATERIALS AND METHODS

Site location

A fixed field research station at Crooked Island (latitude: 22°33'N, longitude 114°18'E), which is situated in the north-eastern waters of Hong Kong, located between latitude 22°9' and 22°37'N and longitude 113°52' and 114°30'E, in Mirs Bay (Fig. 1), was chosen for this pilot study. At the station, a telemetry system was deployed on a fish raft. This system consists of a membrane type dissolved oxygen probe, fluorimeter, Acoustic Doppler Current meter, a peristaltic pumping system, a micrologger, a 12V car battery, thermistor, anemometer and pyranometer, telecommunication software through modems for data retrieval. The more detailed configuration, operation and functioning of the telemetry have been given in the literature (Lee et al., 2000).
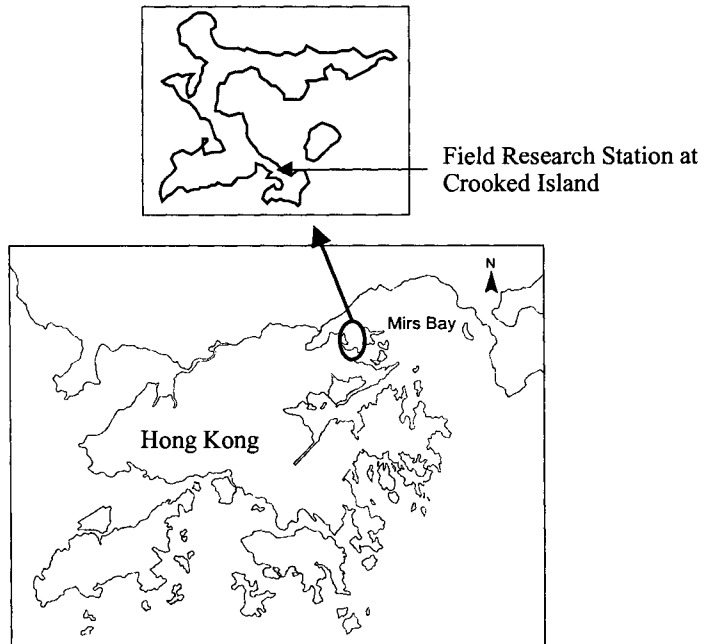
Figure 1. Outline of Hong Kong and the location of the Crooked Island field research station

Auto-nutrient analyzer

An auto-nutrient analyzer, AutoLAB Model ANA-1 developed and manufactured by W.S. Ocean System Ltd, was employed for this pilot testing. The analyzer measures the concentrations of nutrients in water using conventional wet chemistry and colourimetric analysis techniques and consists of several parts, including a nutrient analysis module, an electronics enclosure and bottles for the storage of chemicals. Each analysis module is comprised of three major components: an eight-way rotary valve; a motor driven syringe; and a colorimeter. Water samples and chemical reagents are taken by syringe plunger and mixed for reaction and then injected into the colourimeter for further development and measurement. Results of measurements can be stored in memory for data extraction, and the system can be used on-line or in telemetry applications (W.S. Ocean Systems, 2000).

The two analysis modules employed in the pilot test were nitrate and phosphate and the standard seawater methods of nitrate and phosphate analysis were based on the literature (Armstrong et al., 1967; Murphy and Riley, 1962 respectively) (W.S. Ocean Systems, 2000).

Water samples for testing the auto-nutrient analyzer

Water sampling for diurnally based nutrient analysis was carried out from 16:00h on 30 January 2002 to 13:00h on 31 January 2002. Two 300 ml water samples were taken simultaneously every four hours near the water surface (depth 1 m) and filtered on site through a membrane of

0.45μm pore size. One set of the filtrates was collected in a 100 ml polyethylene vial, stored in an ice container and then sent to the Agriculture, Fisheries and Conservation Department (AFCD) laboratory, Hong Kong Special Administrative Region (HKSAR) Government for analysis with a ChemLab Continuous Flow Analyser. The other set of filtrates was analyzed *in situ* with the auto-nutrient analyzer.

In addition, another set of water samples was taken hourly from the same water depth and analyzed *in situ* with the auto-nutrient analyzer in order to obtain finer resolution and to test the reliability of the analyzer's response to the changes of nutrient concentration within a short period.

Water samples for the diurnal observation of nutrient dynamics

Water samples, in addition to those from 1 m water depth referred to above, were collected from 3 m and 5 m every four hours, and sent to AFCD for analyzing dissolved inorganic nitrogen as ammonia, nitrate, nitrite; and dissolved inorganic phosphorus (DIP) as ortho-phosphate. The filtration procedure and storage of water samples for analysis was the same as above.

Calculation of nutrient ratios

N:P ratios (atomic weight) were calculated from the AFCD results by dividing the total inorganic nitrogen (TIN) value, which was the summation of ammonia, nitrate and nitrite, by the relevant ortho-phosphate value.

Water samples for studying diurnal microalgal dynamics

2L water samples were collected simultaneously with the samples for nutrient analysis from the same three water depths, that is, 1 m (surface: s), 3 m (middle: m) and 5 m (bottom: b) and concentrated by a special hand-made tube-shaped sieve of mesh size 20 μm, and then collected in a 100 ml polyethylene vial; preserved with 3 ml Lugol's solution immediately; stored in an ice container; and taken back to the laboratory for overnight settling in a refrigerator at 4°C to a final volume of 5 ml – 10 ml, after the supernatant was siphoned off. A thoroughly mixed aliquot of 1 ml from each sample was pipeted into a Sedgwick Rafter counting chamber and 10-20 minutes allowed for settling of the microalgae in the counting chamber. Under an Olympus IX50 inverted microscope with magnifying power ranging from 100 to 400 times, the algal species present were identified and the cell number of each enumerated. The total number of cells of each individual species in the original sample was finally calculated and the total microalgal "biomass" was expressed as the number of cells per litre.

Identification of microalgae was carried out using Jin et al (1965), Yamaji (1984), Larsen & Moestrup (1989), Fukuyo et al. (1990), Hallegraeff (1991), Hallegraeff et al (1995), Balech (1995) and Tomas (1997). Diatoms and dinoflagellates were the main focus of this research, but other microalgae were identified as far as possible.

RESULTS

Nutrient analysis

The two sets of data analyzed by AFCD and *in situ* are plotted in Figure 2. In the case of phosphate, the general trend of the data from the AFCD and the auto-nutrient analyzer are almost consistent, except for the reading (4 μgL^{-1}) from the AFCD at 04:00h on 31 January 2002. Results for phosphate concentration by the AFCD were within the range 13 - 16 μgL^{-1}, and within the range 10 to 17 μgL^{-1} from the auto-nutrient analyzer. However, for nitrate, they were totally different. The variation between the results from the AFCD and the auto-nutrient analyzer were widely inconsistent. A negative reading for nitrate was also recorded.
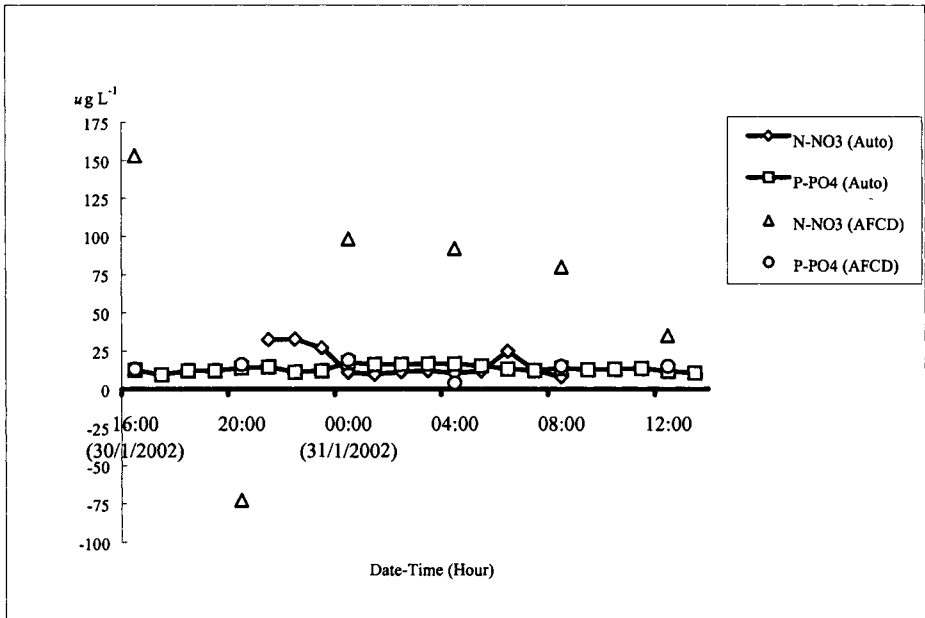
Figure 2. Time series of nutrient dynamics on 30 to 31 January 2002 (Auto: analyzed by *in situ* auto-nutrient analyzer; AFCD: analyzed with a ChemLab Continuous Flow Analyser)

Nutrient ratios of TIN:DIP

The general pattern of TIN:DIP ratios calculated from the AFCD results (Fig. 3.) were generally within the range 5 to 19, except for two readings below 5 at 08:00 and 12:00 on 31 January and a value of 37.7 at 04:00 on 31 January 2002, due to an 'unusual' reading as discussed above.

Figure 3. Time series with 4-hour intervals of TIN: DIP ratios on 30 to 31 January 2002
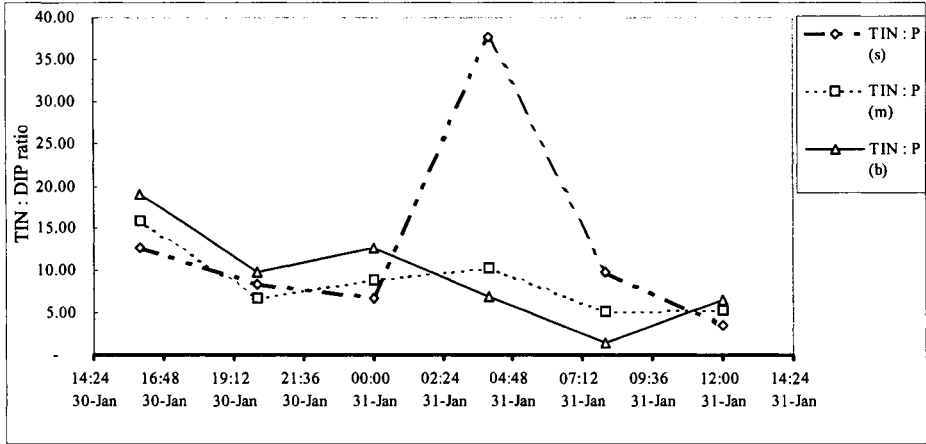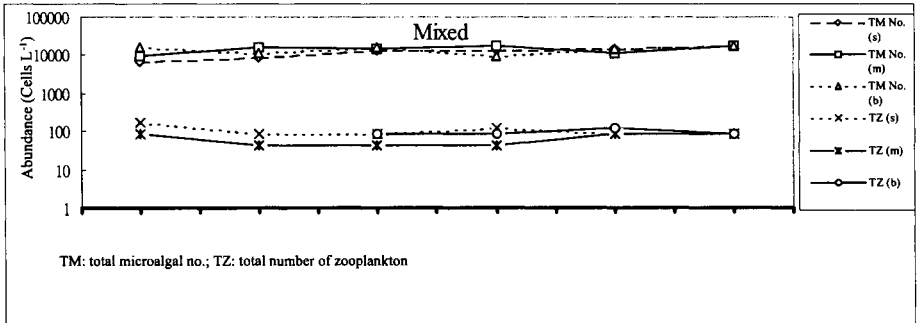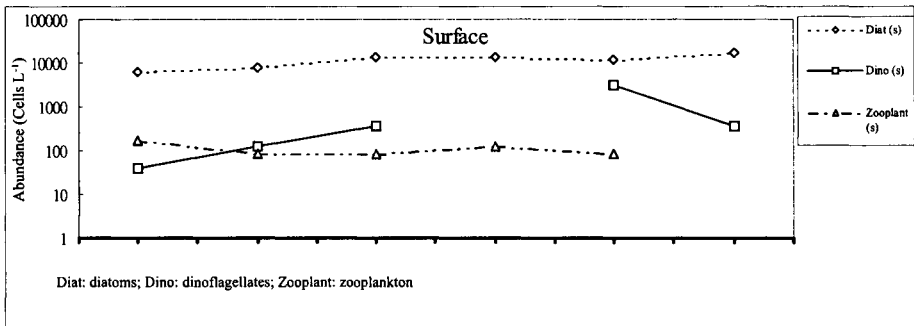

TM: total microalgal no.; TZ: total number of zooplankton

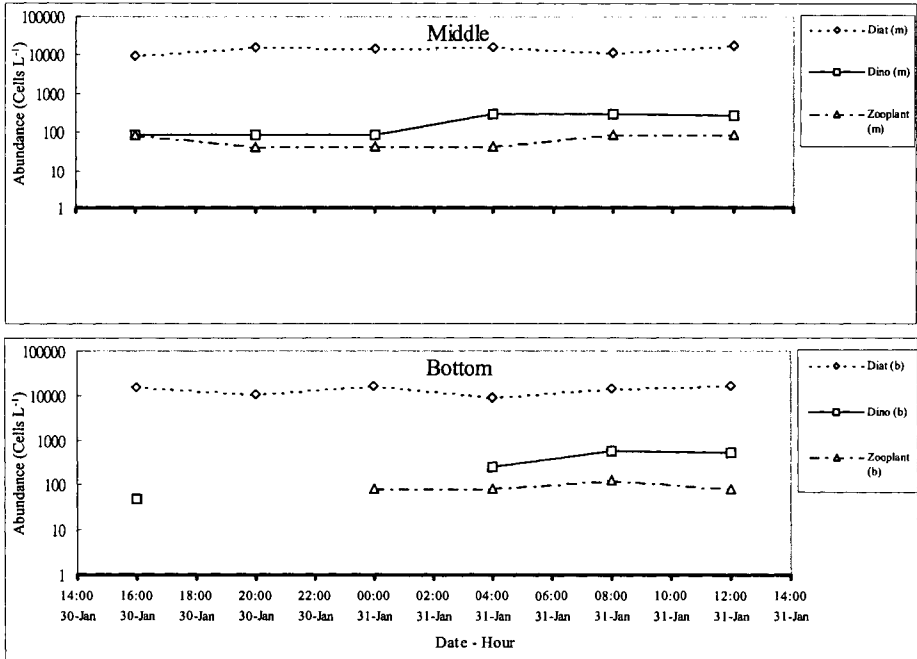Diat: diatoms; Dino: dinoflagellates; Zooplant: zooplankton

Figure 4. Diurnal dynamics of marine microalgae and abundance of zooplankton

Diurnal microalgal dynamics

The diurnal dynamics of marine microalgae and the abundance of zooplankton are shown in Figure 4, in which the plot at the top is for total microalgal and zooplankton abundance at the different water depths, and the other three plots labeled 'surface', 'middle' and 'bottom' are the results for the individual water depths 1 m, 3 m and 5 m respectively. Only two groups of microalgae (diatoms and dinoflagellates) were found in the water samples during the diurnal observation.

LIMITATIONS, DISCUSSION AND RECOMMENDATIONS

The two 'unusual' readings, one for phosphate and one for nitrate, in Figure 2 warned that sometimes, attention must be paid to the reliability of results from a benchtop continuous flow analyzer, even though it is commonly and routinely operated. Results may not always meet expectations. If the reading for phosphate at 04:00h on 31 January 2002 is reliable, it could be deduced that the variation in an interval of four hours was very rapid. Thus, Hiiro et al. (1989), who pioneered the development and application of telemetry for red tide studies, pointed out that concentration of nutrients could change rapidly (on a time scale of one hour). However, there seems to be little evidence to support this hypothesis, since neither the AFCD results, nor the results of the hourly series from the *in situ* auto-nutrient analyzer showed any obvious trend for such fluctuations and, furthermore, no noticeable variation could be seen from the corresponding

microalgal abundance. Thus, such a supposition is unlikely and the results should be treated as invalid. For the negative reading of nitrate in the AFCD data set, it probably implies that the concentration of nitrate at that particular moment was undetectable. Unfortunately, no corresponding data were available at this time from the auto-nutrient analyzer for comparison because of a fault which occurred in the programming of the auto-nutrient analyzer.

Since this was a pilot test, there are certain limitations and difficulties. The data lost due to the programming fault was a technical problem and underlined the need to make improvements to ensure the programming work is done properly. Furthermore, the chemicals used in the analyzer have to be disposed of and then replenished, and this demands human resources for routine maintenance and calibration. In addition, the traditional approach to using auto-nutrient analyzers in the laboratory requires a filtering procedure, and it is not known whether there would be any effect from the direct injection of water samples and their reaction with the chemicals in the *in situ* auto-nutrient analyzer. If a filtering procedure is needed, a sub-system needs to be required designed for such purpose in order to collect reliable data.

In order to perfect the sub-system and provide meaningful and comprehensive nutrient data, it is recommended that further analyzer modules such as silicate and ammonia, are integrated into the sub-system, so as to form part of the telemetry system. For ensuring data reliability, calibration tests still need to be carried out using standards to test and compare the results from the traditional method used in the laboratory and the auto-nutrient analyzer.

As pointed out in the Introduction, nutrient ratios played an important role in red tide occurrences in Tolo Harbour as well as other Hong Kong waters, and TIN:DIP ratios during this diurnal observation were also found to fall within the range 4-22 documented by Ho and Hodgkiss (1993). However, based on the corresponding results for microalgal abundance, there was no significant variation observed during these diurnal studies and diatoms dominated throughout the period of observation. The zooplankton abundance was far below the total microalgal abundance at each water depth and this suggests that zooplankton was dependant on the microalgae, but probably exerted no significant grazing pressure on the microalgal community. This result is consistent with the observation of Yang (2000) at Port Shelter.

As revealed in the review by Hodgkiss and Ho (1997), both long term and relatively short-term changes in the N:P ratio are accompanied by increased blooms of non-siliceous phytoplankton groups. Thus, diurnal observation should help to understand the moment by moment variation in nutrient dynamics. However, attempts to establish any relationship between red tide and nutrient ratios at Crooked Island were unsuccessful. More data and a longer observation period are needed to provide enough baseline data for analysis and to validate whether or not N:P ratios apply at Crooked Island.

Application of telemetry for studying marine microalgal dynamics and monitoring algal blooms has shown some success in terms of a surface bloom or a subsurface bloom at Crooked Island, Hong Kong (Lam and Hodgkiss, 2000, 2001). But, there is no real time *in situ* and continuous nutrient data for understanding the conditions preceding a red tide as well as the dynamics of the microalgae. However, it is well known that marine microalgal dynamics as well as red tides are subject to the influence of different environmental parameters, sometimes acting individually,

but in synergy at other times (Lam and Hodgkiss, 2000). One of these factors is nutrients. Undoubtedly, nutrients are an essential factor because there will be no dynamics and no algal blooms if there are no nutrients, even when other conditions are favorable. But, the conventional approach to studying the interaction between nutrients and marine microalgal dynamics is to take water samples alongside microalgal samples back to the laboratory for analysis and then try to establish any co-relationship. However, such discrete and periodic sampling results have the same limitations as conventional sampling for microalgae: any variation during the sampling interval is ignored.

CONCLUSION

Application of an auto-nutrient analyzer at the field station to provide real time, *in situ* and continuous data for studying nutrient dynamics and their interaction with marine microalgal dynamics in coastal waters is novel. Even though there are limitations to its application, this pilot test which attempted to integrate an auto-nutrient analyzer into a telemetric system, showed that it is feasible to obtain real-time *in situ* nutrient data as well as background information for nutrient dynamics in this way. It also showed that it is possible to minimize the uncertainty introduced because of the drawbacks in the conventional approach, in which discrete and periodic samples require time to be sent back to the laboratory for analysis and so time lags can cause unknown variation in the samples, as well as a decrease in accuracy. Furthermore, the auto-nutrient analyzer can provide hourly sampling and so give fine resolution in tracing the nutrient dynamics, and this, if coupled with a sub-system for automatic phytoplankton sampling, can synchronously provide the insight necessary for a true understanding of the interaction and mechanisms amongst all the factors involved in marine microalgal dynamics.

ACKNOWLEDGEMENTS

REFERENCES

Anderson, D., P. Anderson, M. Bricelj, J. Cullen, I.J. Hodgkiss, K.C. Ho, J.H.W. Lee and J.E. Rensel. 1998. *Study of red tide monitoring and management in Hong Kong: Technical Report No.1 – Literature review and background information.* Agriculture and Fisheries Department, Government of the Hong Kong Special Administrative Region.

Armstrong, F.A.J., C.R. Stearns and J.D.H. Strickland. 1967. The measurement of upwelling and subsequent biological process by means of the Technicon Autoanalyser and associated equipment. *Deep-Sea Research* 14:381-389.

Balech, E. 1995. *The Genus Alexandrium Halim (Dinoflagellata)*. Sherkin Island Marine Station, Ireland.

Red Tide Organisms in Japan – an Illustrated Taxonomic Guide, edited by Y. Fukuyo, H. Takano, M. Chihara and K. Matsuoka. 1990. Tokyo: Uchida Rokakuho.

Hallegraeff, G.M. 1991. *Aquaculturists Guide to Harmful Australian Microalgae*. Australia: Fishing Industry Training Board of Tasmania and CSIRO Division of Fisheries.

Manual on Harmful Marine Microalgae, edited by G.M. Hallegraeff, D.M. Anderson and A.D. Cembella. 1995. Intergovernmental Oceanographic Commission Manuals and Guides 33, UNESCO.

Hiiro, K., J. Nagao, and T. Kimoto. 1989. Development of continuous monitoring systems for environmental parameters related to red tides. In *Red Tides: Biology, Environmental Science and Toxicology*, edited by T. Okaichi, D. M. Anderson and T. Nemoto, 165-168. New York, Amsterdam, London: Elsevier.

Ho, K.C. and I.J. Hodgkiss. 1993. Assessing the limiting factors of red tide by bottle bioassay. *Asian Marine Biology* 10:77-94.

Ho, K.C. and Hodgkiss, I.J. 1995. A study of red tides caused by *Prorocentrum micans, P. sigmoides* and *P. triestinum* in Hong Kong. In *The Marine Biology of the South China Sea II - Proceedings of the 2nd International Conference, Guangzhou, China, 1993*, edited by B. Morton, G.Z. Xu, R.L. Zou, J.P. Pan and G.X. Cai, 111-118. Beijing, Shanghai, Xian and Guangzhou: World Publishing Corporation.

Hodgkiss, I.J. and K.C. Ho. 1992. Variations in macronutrients in relation to red tides – The Tolo Harbour experience. *Colloquium on Red Tides in Hong Kong and South China Sea, Hong Kong, September 1992*.

Hodgkiss, I.J. and K.C. Ho, 1997. Are changes in N:P ratios in coastal waters the key to increased red tide blooms? *Hydrobiologia* 352:141-147.

Jin, T.C., G.H. Chen and K.G. Huang. 1965. *Marine Planktonic Diatoms in China*. Shanghai Science and Technology Press. China. (in Chinese).

Lam, C.W.Y. and K.C. Ho. 1989. Phytoplankton characteristics of Tolo Harbour. *Asian Marine Biology* 6:5-18.

Lam, I.H.Y. and I.J. Hodgkiss. 2000. Application of a telemetry system to studying microalgal dynamics and red tides in Hong Kong. In *Algae and their biotechnological potential*, edited by F. Chen and Y. Jiang, 279-292. Dordrecht: Kluwer Academic Publishers, The Netherlands (2001).

Lam, I.H.Y. and I.J. Hodgkiss. 2001. A real time measurement system for red tides studies. Proceedings of *The Oceans 2001 MST/IEEE Conference*, 5-8 November, 2001, Honolulu, Hawaii. U.S.A., pp. 1151-1157.

Lee, J.H.W., K.T.M. Wong, Y. Huang and A.W. Jayawardena. 2000. A real time early warning and modelling system for red tides in Hong Kong. In *Stochastic Hydraulics 2000*, edited by Z.Y. Wang and S.X. Hu, 659- 669. Rotterdam: A.A. Balkema.

Lu, S. 2001. Ecological studies of phytoplankton and harmful algal blooms in Junk Bay, Hong Kong. Ph.D. Thesis, The University of Hong Kong.

Morton, B. and P.R. Twentyman. 1971. The occurrence and toxicity of a red tide caused by *Noctiluca scintillans* (Macartney) Ehrenb., in the coastal waters of Hong Kong. *Environmental Research* 4:544-557.

Murphy, J. and J.P. Riley. 1962 A modified single solution method for determination of phosphate in natural waters. *Analytica Chimica Acta* 27:31-36

Identifying Marine Phytoplankton, edited by C.R. Tomas. 1997. San Diego:Academic Press.

W.S. Ocean Systems Ltd. 2000. AutoLAB: automatic nutrient analysis system, operating manual. Issue A. Alton, Hants, UK and http://www.wsenvirotech.com/AutoLAB.htm, W.S. Ocean Systems Ltd.

Illustrations of the Marine Plankton of Japan, edited by I. Yamaji. 1984. Third edition. Osaka: Hoikusha Publications.

Yang, Z.B. 2000. Harmful algal blooms in selected Hong Kong coastal waters. Ph.D. Thesis. The University of Hong Kong.

REAL TIME PREDICTION OF PHYTOPLANKTON BLOOMS IN TANABE BAY

Yong Woo Park[1] and Takao Yamashita[2]

[1]Department of Civil Engineering, Graduate School of Engineering
Kyoto University, Uji, JAPAN
ywpark@rcde.dpri.kyoto-u.ac.jp

[2]Disaster Prevention Research Institute
Kyoto University, Uji, JAPAN

ABSTRACT

In the ecosystem problem of the coastal area, important research subjects for coastal engineering are the monitoring system, the comprehensive environmental database and the development of prediction methods using observational data for the environmental condition. The Observation by Kyoto University and several research groups, to reveal the seawater exchange mechanism and phytoplankton dynamics for the red tide blooms in Tanabe Bay, was started in 1998. Real-time prediction for the variation of phytoplankton species was conducted by using the observation data in Tanabe Bay and the artificial neural network (ANN) in this study. We changed the ANN input data for finding the optimum, limited input data which are necessary for a real time estimate. It is found that ANNs is able to predict real-time variation of phytoplankton with temperature, salinity, solar radiation, air temperature, and precipitation, without nutrients and current information improve the prediction accuracy.

INTRODUCTION

In generally, forecasting/prediction models can be divided into statistical and physical based approaches. Statistical approaches determine relationships between historical data sets, whereas physical based approaches model the underlying physical processes directly. Among methods for ecosystem prediction, multivariate statistics and machine learning approaches are very useful and practicable modeling methods for coastal ecosystem. Both methods can derive not only the general but also particular characteristics from ocean/coastal observed data.

Several modeling approaches have been developed in order to gain understanding on the dynamics of planktonic marine ecosystems. Probably, the most adopted approach was based upon a compartmental structure, each compartment representing a tropic level or taxonomic group and the interactions expressed by the different flows occurring among them. These models evolved from simple ones, only considering nutrients–phytoplankton-zooplankton interactions (Steele, 1974), to more complex ones, where components such as dissolved organic matter, detritus and bacteria are taken into account and size based models are implemented (Fasham et al., 1990; Moloney and Field, 1991).

Artificial Neural Networks (ANNs) are a practicable and useful method for predicting and elucidating information about ecology system, and the basic architecture of neural network can support the non-linear phenomenon. When using ANN for prediction, the modeling philosophy employed is similar to that used in traditional statistical approaches. The unknown model parameters (i.e., the connection weights in the case of ANN) are adjusted in order to obtain the best match between a historical set of model inputs and the corresponding outputs.

Observational data from several research group (DPRI, Kyoto Univ., Kinki Fishery Univ. and Tokyo Fishery Univ.) has started to reveal the seawater exchange mechanism and phytoplankton dynamics for the red tide blooms in Tanabe Bay, where the west boundary is located at the border of the Kii Channel and affected by Kuroshio currents (Fig. 1). Observations were carried out at the Station 1 every day and at 25 stations approximately once a week during summer transition season since 1998. Vertical profile and horizontal distribution of temperature, salinity density, chlorophyll-a and dissolved oxygen were recorded at every station with CTD (Sea bird 25). Solar radiation, wind, air temperature, and the other meteorological factors were observed at the Storm surge Observation Tower, DPRI, Kyoto University and current profile (ADCP), wave (Ultra sonic wave meter) and the time series of the temperature measurements with depth of thermistor chain were carried out around the Observation Tower.

The aim of this research is to apply the artificial neural network method to the real-time prediction of the phytoplankton variations and to find the optimum data for a real-time prediction of red tide. Because the ecosystem (including phytoplankton blooms) characteristics are very complicated due to diverse environmental changes, which control on the system, such as intrusion of low temperature and meteorological change, and other biological impacts.
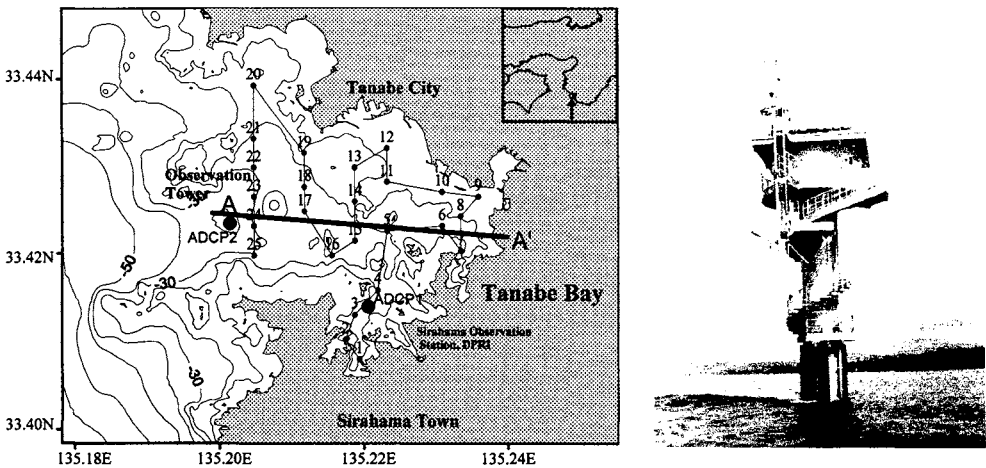

Figure 1. Study area and location of sampling stations: phytoplankton and CTD are sampled at Station 1 and storm surge Observation Tower (vertical water temperature, current profile (ADCP), solar radiation and wind around the mouth of Tanabe Bay

CHARACTERISTICS OF OBSERVED TIME SERIES DATA

Figure 2 shows the observed time series data of air temperature, precipitation, solar radiation and vertical time series water temperature at the bay mouth and interpolated vertical distribution of water temperature, salinity and dissolved oxygen at the station 1. The fluctuation of air temperature, solar radiation and sea surface temperature has a similar variation pattern. These seem to have 10-day period. The stratification caused by water temperature appeared in 2000 and 2001, but did not appear in 1999 (Figs. 2- a, b, c). Time-depth distribution of temperature, salinity and dissolved oxygen at station 1 are presented in Figures 2-d, e and f. The salinity structure show relatively stable, but the precipitation significantly influenced salinity of the surface waters. The low concentration of dissolved oxygen appeared at bottom layer, but vertically constant by mixing mechanism in 1999. The relatively low temperature waters (below 24℃ at 15 m in depth) coming from the Kii Channel had intruded through the bay mouth. Open seawater intrusion and other environmental condition (air temperature, salinity and currents) have affected the water exchange and phytoplankton bloom at Tanabe Bay in summer (Yoshioka et. al., 1998).
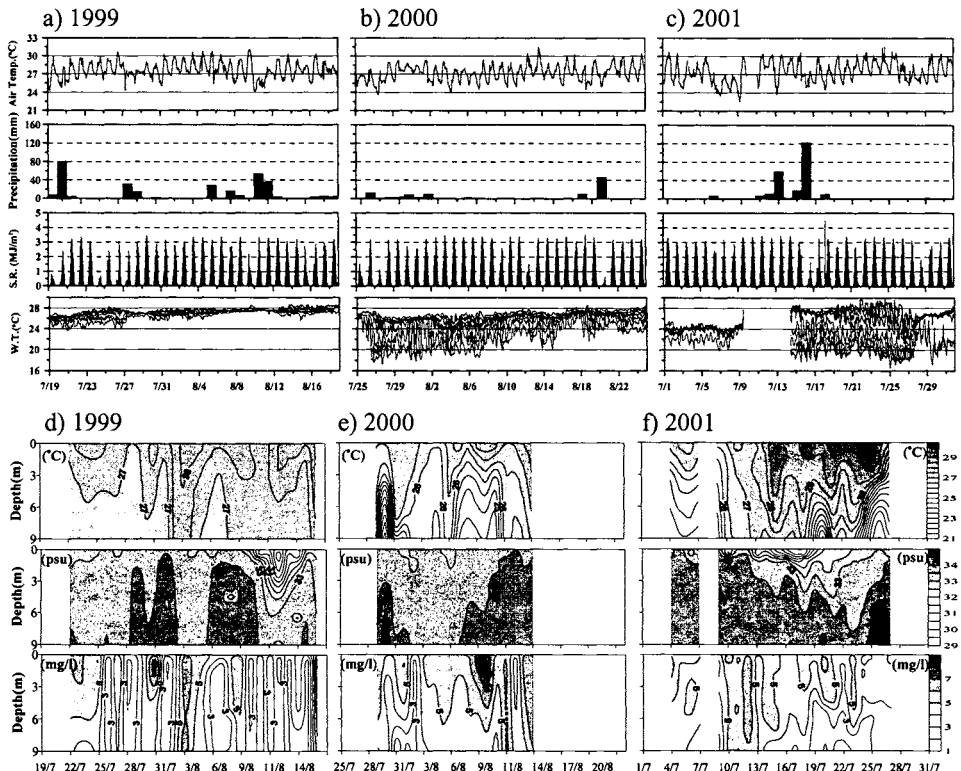

Figure 2. Time series of air temperature, precipitation, solar radiation and water temperature (2.5 m, 5 m, 10 m, 15 m, 20 m, 25 m, 30 m below the depth) around the Observation Tower, and time-depth distribution of temperature, salinity, and dissolved oxygen at station 1

The original 20-minute interval current data and 1hour interval temperature near the bay mouth were filtered by 49 hours low pass to remove the tidal components. The total phytoplankton cell concentration shows the periodic variation during observation period (Fig. 3). The period of phytoplankton was approximately 4 days in 1999, 4-7 days in 2000 and 4-8 days in 2001. The east component of current and water temperature appeared in the similar pattern.

To know the accurate period of the temperature and current, we used the spectrum analysis. Two spectra were calculated via Blackman-Tukey's method with 8 degrees of freedom. Spectral estimates were smoothed using a Turkey window. The prominent long period of temperature and current appeared 3-4 days and 7-9days.

Figure 4-b shows the correlation between phytoplankton concentration at the bay head and before-1 day lag of east component of current at the bay mouth. This indicates that the slow inflow velocity makes weakly water exchange movement and causes the phytoplankton bloom.
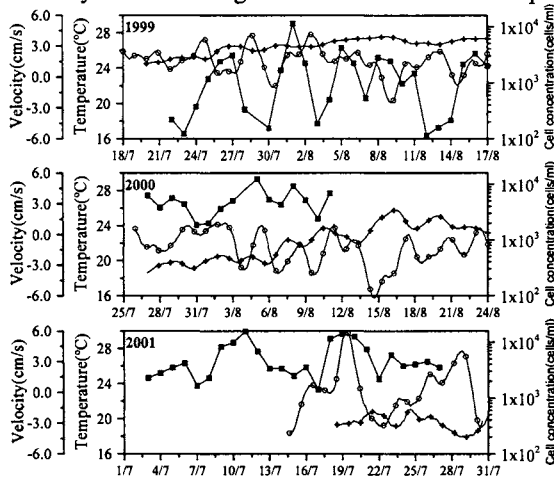

Figure 3. 49 hours low pass filtered water temperature (+), the east component of current (○) at the depth of 30 m around the bay mouth, and total phytoplankton concentration （ ■ ） in 1999, 2000, 2001.
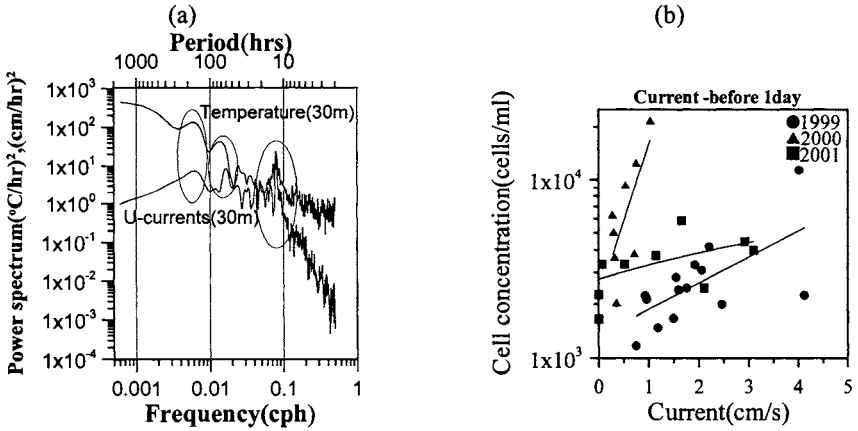
Figure 4. Power spectrum of temperature and the east component of current at the depth of 30 m (a). Correlation between phytoplankton cell concentration at the bay head and before-1 day lag of east component of current at the bay mouth (b)

Figures 2, 3, and 4 show that coastal time-series data is composed of a deterministic and a random component. The deterministic component changes over time in a regular and predictable way, caused by an underlying process. It can be characterized by a trend, periodicity and serial dependency. The random component is superimposed on the deterministic component and can be characterized by short-term fluctuations. Nature can be truly random or chaotic. Truly random components, such as the level of water, can be characterized by the statistical distribution function. Chaotic components of a time series are characterized by values that appear to be randomly distributed and non-periodic but are the result of a deterministic process due to underlying nonlinear dynamics (Recknagel, 1997).

NEURAL NETWORK APPROACH

The neural network approach, which has been developed in recently, is based on the concept of learning activities, such that, the procedure itself evolves an optimal model relating key variables.
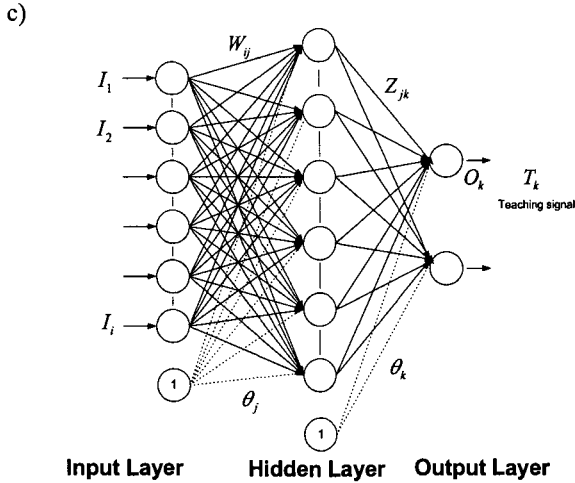

515

c)
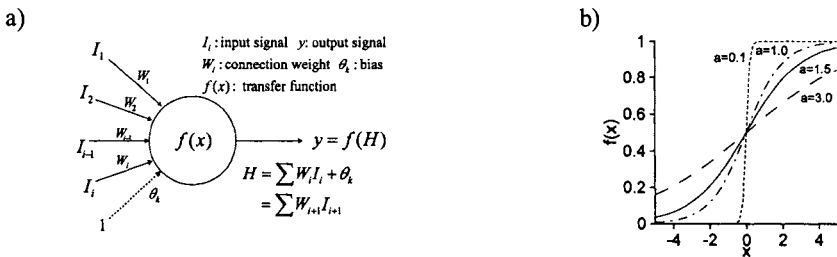
Figure 5. The architecture of a typical back-propagation neural network: The output cell of perceptron (a), sigmoid function (b), and simple 3-layer neural network (c).

Neural network computing differs from artificial intelligence and traditional computing in several important ways. Unlike traditional expert systems where the knowledge is made explicit in the form of rules, neural networks generate their own rules by learning from the examples shown to them. Learning is activated through a learning rule, which adapts or changes the connection weights of the network in response to the example inputs and the desired outputs to those inputs. Learning in neural networks refers to the processes of acquiring a desired behavior by changing the connection weights. Therefore, the advantage of neural networks is that no subjective information is required to determine the model structure or estimate parameters. Thus in analyzing large data sets with no a priori knowledge of processes or causality the neural network is more a pragmatic approach. However, in terms of representing processes neural networks will be severely limited. Only generalized process statements could be made from the neural network models and for a process interpretation of algal growth behavior the dynamic mass balance and growth equation approach will always be required. Whilst these models are essential to understand process interactions their predictive capability is not any better than the neural network approach. We propose here a red tide prediction model based on one of the principles of the neural network: the back-propagation algorithm (Rumelhart et al., 1986; Abdi, 1994).

The neural network was developed as a three-layer learning network, consisting of an input layer, a hidden layer and an output layer (Fig. 5c). Each layer is made up of several nodes, and the layers are connected by sets of connection weights. The nodes receive input from either outside the model (the initial inputs) or from the connections. Nodes operate on the input transforming it to produce an analogue output. The weights function to multiply an incoming signal prior to its arrival at the next layer. The transformation associated with each node is a sigmoid function (Fig. 5b).

NEURAL NETWORK ALGORITHM

$$U_j = \sum_i W_{ij} I_i - \theta_j \tag{1}$$

Here, θ_k is the bias value and W_{ij} are connection weights between the input layer and hidden layer. U_j, which is called the normalized logistic function between [0,1], is the output of response function f and transfers H_j to next hidden layer as follows

$$H_j = f(U_j) = \frac{1}{1 + \exp(-U_j / a)} \tag{2}$$

a is sigmoid shape parameter and changed gradient of sigmoid (Fig. 5-b). The sigmoid function is a differentiable function defined as follows:

$$f'(U_j) = (1/a) f(U_j) \{1 - f(U_j)\} \tag{3}$$

The relations among O_k (output from output unit), H_j (output from hidden layer) and Z_{jk} (connecting weights between hidden and output layer) are given by

$$O_k = f(X_k), \qquad X_k = \sum Z_{jk} H_j - \theta_k \tag{4}$$

The connection weights are modified step by step to minimize the mean square error between the observed value and the predicted value. This process is called learning procedure and use a gradient-descent method in order to minimize the mean square error (Rumelhart et al., 1986).

The sum of the square errors, E_p between the calculated output O_k and the observed data T_k, is described by

$$E_p = \frac{1}{2} \sum_k (O_k - T_k)^2 \tag{5}$$

E_p is minimized by a gradient-descent method as follows:

$$\Delta Z_{jk} = -\mu \frac{\partial E_p}{\partial Z_{jk}} = -\mu \frac{\partial E_p}{\partial O_k} \frac{\partial O_k}{\partial X_k} \frac{\partial X_k}{\partial Z_{jk}}$$
$$= \mu (T_k - O_k) f'(X_k) H_j \tag{6}$$

The errors between calculated and observed data are
$$\delta^* = T_k - O_k \tag{7}$$

used the differentiable sigmoid function, we can rewrite equation (6) as follows:

$$\Delta Z_{jk} = \mu \delta^* O_k (1 - O_k) H_j \tag{8}$$

$$\delta_k = -\frac{\partial E_p}{\partial X_k} = \delta^* O_k (1 - O_k) \tag{9}$$

To avoid the oscillation at learning rate μ, is to make the change in weight dependent of the past weight change by adding a momentum term (α).

$$\Delta Z_{jk} = \mu \delta_k H_j + \alpha \Delta Z_{jk} \qquad (10)$$

The differential of E_p with respect to W_{ij} is calculated as follows:

$$\Delta W_{ij} = -\mu \frac{\partial E_p}{\partial W_{ij}} = -\mu \frac{\partial E_p}{\partial X_k} \frac{\partial X_k}{\partial H_j} \frac{\partial H_j}{\partial U_j} \frac{\partial U_j}{\partial W_{ij}}$$

$$= \mu \left(\sum_k \delta_k W_{ij} \right) H_j (1 - H_j) I_i + \alpha \Delta W_{ij} \qquad (11)$$

REAL TIME PREDICTION OF PHYTOPLANKTON BLOOM

In this study, we have fixed one hidden layer and 15 nodes of hidden layer under same calculation condition for case study in order to find optimized real-time prediction of environmental factors.

To avoid over fitting, we took account of the stopping point of the training. In ANN, the stopping point of training must be fixed, i.e., the number of iterations calculated by the system. We calculated the mean sum of errors (MSE). At each iteration, the learning system modifies the weights to minimize because the MSE decreases after learning. At the end of some thousand of iterations, the MSE is practically nil. The result stabilized after 50,000 iterations in our computation. We used the internal network parameters include the learning rate (μ=0.2), momentum (α =0.8) and transfer function (a =3). The initial weights were randomly distributed between 0 and 1.

The water temperature, salinity, dissolved oxygen and meteorological data (solar radiation, precipitation, air temperature) at the Observation Tower are available for data set and two species of phytoplankton, diatom and dinoflagellate are used for output. In this study, we do not consider the effect of nutrient concentration, because a real-time measurement of these values is very difficult.

Before this experiment, we calculated the correlation between various environmental factors, as like wind, humidity et al., and phytoplankton, and choose high correlation values among these factors for prediction of phytoplankton using neural network.

In order to find the optimum limited data set, and to investigate the effect of using different data for training and predicting on the generalization ability, the neural network were trained using input and output data set (Table 1) of 1999, and 2000, and then predicted phytoplankton bloom only using input data set of 2001. Case 1~5 do not considered of east current trend, but case 6~10 do consider it.

Table 1. Decision of inputs and correlation coefficients between predicted and observed values.

	Input data	Dinoflagellate (R^2)	Diatom (R^2)
Case 1	Water temp, Salinity, A.T., SR, Precipitation, D.O.	0.734	0.636
Case 2	Water temp, Salinity, A.T., SR, Precipitation	0.827	0.597
Case 3	Water temp, Salinity, A.T., Precipitation	0.453	0.362
Case 4	Water temp, Salinity, SR, Precipitation	0.578	0.353
Case 5	Water temp, Salinity, A.T., SR	0.619	0.255
Case 6	Water temp, Salinity, A.T., SR, Precipitation, D.O., current	0.867	0.785
Case 7	Water temp, Salinity, A.T., SR, Precipitation, current	0.789	0.623
Case 8	Water temp, Salinity, A.T., Precipitation, current	0.897	0.390
Case 9	Water temp, Salinity, SR, Precipitation, current	0.451	0.534
Case 10	Water temp, Salinity, A.T., SR, flow	0.738	0.390

Table 1 and Figure 6 show the comparison of prediction and observation. The correlation coefficients of case 1 and case 2 are high for phytoplankton prediction. However these cases do not predict the peak point of observed phytoplankton concentration. To improve this weakness, we added current data as input data set (case 6 and case 7) resolution in more high correlation coefficients and predicting the peak period trend. As Figures 3 and 4, the current information, which has a period character and its transferring, should affect the ANN prediction of biological distribution. The high precision case for the prediction of dinoflagellate is case 8, which is also improved prediction accuracy by including the current whereas the prediction of diatom is not significantly improved.

Among the predicted results of cases, we divided the adaptable prediction system into two-group cases 1, 2, 6, 7 and the others. These results show it is able to predict real-time variation of phytoplankton with temperature, salinity, solar radiation, air temperature, and precipitation, and improve the prediction value adding currents.

To determine the relative significance of each input on the output, the following indicators is defined as a relative important parameter:

$$P_{ji} = |Z_{jk}| \times |W_{ij}|, \quad Q_{ji} = P_{ji}/\sum_i P_{ji}, \quad S_i = \sum_i Q_{ji}$$
$$S_i \times 100/\sum_i S_i \tag{12}$$

Figure 7 shows that the relative importance of the various input factors can be shown by examining these connection weights. These results indicate that the most important significant factors are changed according to input factors, and the neural network accuracy improved as more input variable are provided
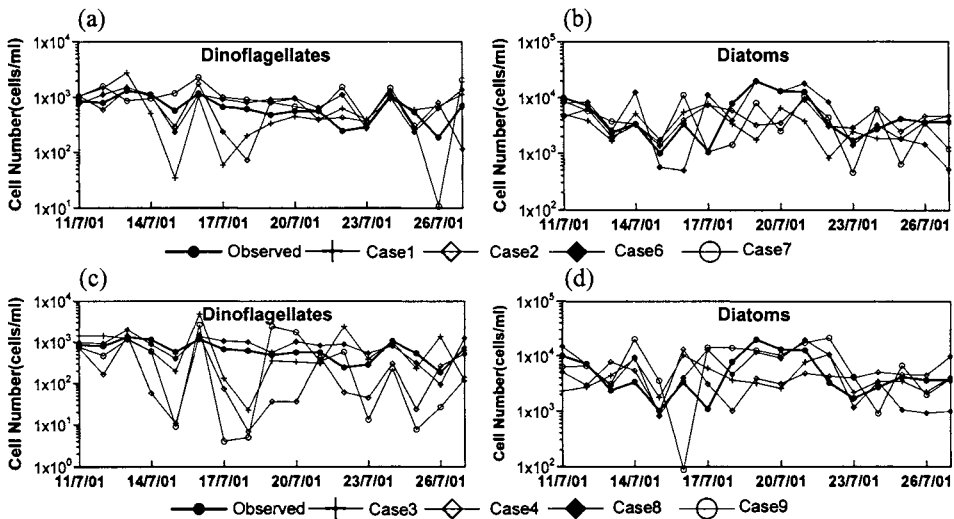
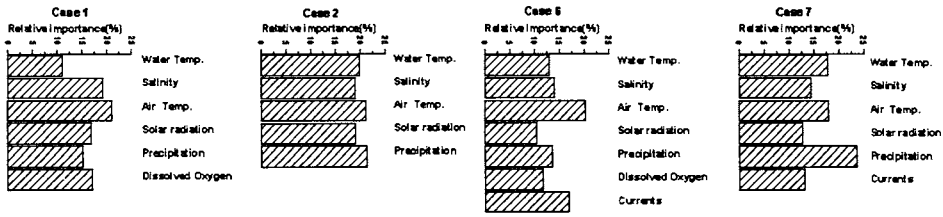Figure 6. Comparison of each case (1, 2, 6, 7, 3, 4 8, 9) predicted and observed results

Figure 7. Relative importance between input and output of case 1, 2 6 and 7

CONCLUSIONS

This study demonstrated that a generic ANN phytoplankton model structure in terms of inputs and outputs could be applied with different conditions in terms of water quality, climate, database characteristics, and achieve reasonable predictive accuracy. The ANNs model structured to forecast phytoplankton abundance proved to be successful for most, but not all, case studies investigated in this work.

Real-time prediction of the variation of phytoplankton species was conducted by using the observation data in Tanabe Bay and the artificial neural network (ANN) in this study. We changed the input data of ANN for finding the optimum, limited input data which is necessary for a real time estimate. It is found that ANNs is able to predict real-time variation of phytoplankton with temperature, salinity, solar radiation, air temperature, and precipitation, without nutrients and current information improve the prediction accuracy.

REFERENCES

Abdi, H. 1994. A neural network primer. *Journal of Biological Systems*. 2 (3), 247-283.

Fasham, M.J.R., H.W. Ducklow and S.M. McKelvie. 1990. A nitrogen-based model of phytoplankton dynamics in the oceanic mixed layer. *Journal of Marine Research*. 48: 591-639.

Moloney, C.L. and J.G. Field. 1991. The size-based dynamics of plankton food webs. I. A simulation model of carbon and nitrogen flow. *Journal of Plankton Research*. 13: 1003-1038.

Rumelhart, D.E., G.E. Hilton and R.J. Williams. 1986. Learning representations by back-propagating Errors. *Nature* 323. 533-536

Steele, J. 1974. Spatial heterogeneity and population stability. *Nature*. 248, 83.

Yoshioka, H. et.al 1998. The water exchange of Tanabe Bay in summer induced by internal kyucho. Proceedings of Coastal Engineering. JSCE, 45, 456-460.

HAITI WAITING FOR ITS DEEP OCEAN WATER SYSTEMS OR "FOUNTAINS OF PARADISE"

Gerard P. Pereira

Energies Naturelles (Energinat S.A.)
Port-au-Prince, HAITI
gerard.pereira@sympatico.ca

ABSTRACT

The Caribbean island Republic of Haiti is a country blessed with cold (4-6°C) deep ocean water (DOW) in close proximity to its entire coast. The Common Heritage Corporation (CHC) has been developing economic and environmentally sustainable, self-sufficient community habitat systems at the Natural Energy Laboratory of Hawaii Authority (NELHA) for more than a decade. A demonstration DOW system with pipelines, pumps and reservoirs to access the cold resource is now in operation which fully demonstrates the economic and environmental sustainability of such systems even for nations that are virtually devoid of capital, trained manpower and terrestrial resources. The systems do depend on the proximity of cold deep ocean water and high solar insolation.

Each DOW system has five potential profit centers: (1) generation of electricity with Ocean Thermal Energy Conversion (OTEC) and Thermal Electric Generator (TEG) systems; (2) air conditioning and industrial cooling; (3) fresh water production; (4) cold water agriculture; and (5) marine aquaculture. Two types of DOW systems can be designed to serve many purposes: Type 1 is a CHC basic system to provide an economically and environmentally sustainable habitat on a tropical coastal desert, while Type 2 is a system designed to focus on providing high market value recreational experiences, e.g. hotels, resorts, cold thalassotherapy and sports facilities in these tropical coastal desert locations.

The Haitian corporation, Energies Naturelles (Energinat S.A.), and CHC have negotiated a joint venture agreement for the purpose of establishing along the coast of Haiti a complete system of five DOW sites linked by sea transportation and submarine fiber optic telecommunications. Each site will be provided with a Type 1 or a Type 2 DOW system or a combination of the two. This paper describes the innovative technologies employed in the two types of DOW systems and how such ocean technologies can create paradise along much of the coastline of Haiti.

INTRODUCTION

When U.S. Senator Mike DeWine returned from his ninth trip to Haiti in January 2002, he reported in an article posted in the Miami Herald Web site on the 17th of March 2002 that the country - once a lush, tropical sanctuary - was now a "paradise lost" where he witnessed "devastation, destitution and desperation".

The Republic of Haiti is the leeward half of the trade wind Caribbean island of Hispaniola which it shares with the Domonican Republic and which the Windward Passage separates from Cuba itself located only 90 miles from the Florida Keys. Because of the trade winds, the coastal regions of the country are, for the most part, dry and barren, so that its topography is characterized mainly by coastal deserts and mountains.

Moreover, because peasants, of necessity, have stripped the land of its tree cover to produce charcoal (the country's primary fuel), today the thick forest that once blanketed the nation covers only 5% of the land area, 95% being deforested (Cobb, 1987). Once one of the world's most productive agricultural regions, agriculture in Haiti is now limited to scattered patches, being marginal or nonexistent in the remainder of the land. Yet Haiti is an essentially agricultural country with very few terrestrial resources. Does this mean that it is a hopeless case with no signs for optimism? Is there any hope that some day it will become in Milton's words a "paradise regained"?

This paper describes how a complete system utilizing innovative deep ocean water technologies can revitalize Haiti by creating paradise in at least five promising geographic sites identified along the coast of the country.

HAITI AND COLD OCEAN WATER

Fortuitously, Haiti is blessed with deep ocean water in close proximity to its entire coast. This is evident in a conventional map of Haiti on which the 1,000-meter isobath has been superimposed. Even its largest offshore island, Gonave Island, is surrounded by deep seawater. Thus, Haiti, by virtue of its land-sea configuration and its 200-nautical mile exclusive economic zone (EEZ), is the most favored nation in the Caribbean for access to deep ocean water.

In maps revealing the difference in temperature between the surface water and water at a depth of 1,000 meters in the world's oceans, this difference is more than 20°C in a band from latitudes of about 25° south and 32° north of the Equator extending from east to west (Penney and Daniel, 1988). Haiti is conveniently located at latitudes of 18° to 20° north of the Equator where it can take advantage of the earth's natural ocean thermal energy conversion system, which distributes cold deep ocean water to the tropical regions. Indeed, the country occupies a region where the temperature difference between the warm tropical surface seawater and the cold arctic or antarctic water at a depth of 1,000 meters is 22-24°C, a difference that can be exploited in various ways.

THE COMMON HERITAGE CORPORATION AND COLD DEEP OCEAN WATER

The Common Heritage Corporation (CHC) of Hawaii is a leader in the development and demonstration of new technologies for use of the Earth's most abundant and useful resource - deep ocean water (DOW). In addition to being cold, DOW is rich in dissolved inorganic nutrients (nitrates, phosphates and silicates) and free of surface pathogens. It is a renewable, abundant and inexhaustible resource that can be used continuously and in a non-polluting fashion. This virtually unlimited resource is also inexpensive. A simple calculation shows that,

while it costs US$0.10 to pump 1,000 gallons of DOW, it would cost US$3.00 to refrigerate the same volume of water. In the Kochi Prefecture of Japan, local residents have been encouraged to find commercial applications for pumped up deep seawater; one of the applications they have come up with is bottling the pure, nutrient rich seawater after desalinization (Hisatake, 1997). One 750-ml bottle of this pure water sells for US$10.00. No wonder Dr. John P. Craven, the CHC founder and Chief Scientist enjoys repeating that deep ocean water as "CLEAN, COOL, CASH".

The Natural Energy Laboratory of Hawaii Authority (NELHA), located at Keahole Point on the Big Island of Hawaii, operates a variety of polyethylene pipelines and pumping stations which access seawater from depths of 17 meters with a temperature of $26°$-$29°C$ and 700 meters with a temperature of $5°C$ (Daniel, 1994). At its Demonstration Site at the NELHA, which is a functional living habitat, the CHC has developed DOW technologies that encompass a number of revolutionary methods and applications. These technologies constitute the Deep Ocean Water Energy Recovery (DOWER) system that has three major components: (1) the Energy Utilization Subsystem, (2) the Cold Utilization Subsystem, and (3) the Nutrient Utilization Subsystem. As the water passes through each linked subsystem, it gradually warms before it is discharged into an injection well or wetland/park where it reaches ambient surface ocean temperature for final discharge. This paper will focus on how the use of DOW, either alone or in combination with warm surface seawater, in each of these subsystems can transform many of the barren coastal deserts of Haiti into oases of prosperity and plenty.

Energy Utilization Subsystem - OTEC and TEG Technology

Ocean Thermal Energy Conversion (OTEC) is a process which utilizes the temperature difference between warm surface seawater and cold deep ocean water to drive turbines to generate electricity. The OTEC process requires a temperature difference of at least $20°$ Celsius. This is achieved by using concentrated solar energy that has been absorbed by warm $24°$ to $29°C$ tropical surface seawater in combination with cold $6°C$ seawater pumped from a depth of at least 600 meters. Since the temperature of both the tropical surface seawater and the cold deep ocean water stays fairly constant daily and throughout the year, the $20°C$ temperature difference is always available both day and night and from season to season.

Basically, there are two different OTEC systems for the extraction of thermal energy from the oceans to generate electricity: the open-cycle system and the closed-cycle system. A summary of this technology is given by Penney and Daniel (1988).

Georges Claude, a French scientist who also invented the neon sign, first designed an open-cycle OTEC system, which he tested at Matanzas Bay in northern Cuba in 1930. Open Cycle OTEC exploits the scientific principle that water boils at low temperature in a vacuum. In this system, warm surface seawater (about $25°C$) is pumped into a vacuum chamber. The low pressure (1,400 pascals) of the chamber causes the seawater to boil and partially vaporize at that low temperature. The resulting low-pressure steam turns a turbine that drives an electrical generator. After it has passed through the turbine, the steam is then condensed either by "direct contact" with cold seawater or by passing it over a heat exchanger through which cold ocean water is pumped, thereby providing a cold surface to reliquefy the steam. The resultant condensate is a

bonus byproduct - desalinated water that has the purity of distilled water and a crisp taste and can therefore be used for drinking and irrigation. A 250 kW experimental open-cycle plant was built at NELHA in the early 1990s.

Jacques-Arsène d'Arsonval, a French engineer, first proposed the concept of a closed-cycle OTEC system in 1881. In the closed-cycle system, warm surface seawater is pumped into a heat exchanger (the evaporator) containing a low-boiling point "working" fluid such as ammonia. Heat transferred from the warm surface water via the heat exchanger vaporizes the working fluid. The expanding vapor turns a turbine driving an electrical generator. Cold deep ocean water pumped to a second heat exchanger (the condenser) provides a cold surface to reliquefy the ammonia vapor. The fluid is then returned to the first heat exchanger. It is proposed that a hybrid OTEC plant be used for desalinated water production; the hybrid plant would include a closed cycle component for electricity generation and a second stage, consisting of a separate vacuum "flash" evaporator and a surface condenser, for fresh water production.

It is estimated that a 1 MW hybrid cycle plant can produce one million gallons of fresh water per day (4,000 m^3/day), while a 50 MW plant can produce as much as 16 million gallons of water per day (62,000 m^3/day). That is sufficient to support a community of approximately 300,000 people in the developing world (Vega, 1992). The first OTEC plant to yield more electrical power than it consumed was "Mini-OTEC", a closed-cycle system mounted on a barge offshore of NELHA. One megawatt closed-cycle plants are under construction at NELHA and on an offshore platform in India. However, an OTEC generating plant is capital-intensive to construct and will make economic sense only if the costs of fossil fuels continue to rise and are passed on to the customers of utilities that generate their power from either diesel or oil-fired conventional generating plants. Ocean thermal energy power generation is expected to be very competitive as an alternative energy source to anticipated mean conventional utility costs as much as US$0.15/kWh or more.

Another promising and competitive electrical energy production system using DOW is the Thermal Electric Generator (TEG) developed by Dr. Maxwell Goldberger, which has no moving parts, creates no pollution discharge and is currently ready for commercial application. Basically, the TEG system generates an electrical potential by using the thermo-electric potential between dissimilar metals maintained at different temperatures. A prototype TEG utilizing solar parabolic mirrors as the heat source and DOW as the cold source was constructed at the CHC Demonstration Site. The TEG produces an effective temperature difference of 300°C with an electrical output of 1 kilowatt. To maintain electrical output during non-solar hours, a small reservoir of oil, heated by solar mirrors, is plumbed in the system as a heat sink. This system, which is estimated to produce electricity at a cost of US$0.15/kWh, can be expanded to generate 1 megawatt.

Cold Utilization Subsystem - Cooling Technology

One application for DOW technology is cost-effective air conditioning and industrial cooling. In warm climates and seasonally hot regions, air conditioning and industrial cooling consume an enormous amount of energy. For large buildings and hotels in tropical and subtropical climates, air conditioning represents the major source of energy demand for an entire complex. A single

hotel room requiring from 0.75 to 1.0 ton of air conditioning per day has an energy requirement of 0.9 kW of electricity. A hotel complex or resort with 1,000 rooms has a possible peak electrical demand of one megawatt just for air conditioning.

DOW air conditioning uses the pumped deep seawater directly or the residual cold water after it has been pumped up and run through an OTEC plant. The components that make up a centralized seawater air conditioning system include: an intake pipe to carry the deep ocean water, a pumping station to bring the water up, a cooling station (aluminum or titanium heat exchangers) to transfer the heat from the fresh water circulating internally through the buildings to the cold seawater, and a return line through which the deep seawater goes back to the ocean (Van Ryzin and Leraand, 1992).

The NELHA, which is located in a tropical coastal desert, has utilized DOW for cooling administration buildings since 1986 at substantial energy savings. A similar seawater air conditioning system exists at Purdy's Wharf in Halifax, Nova Scotia. Stockholm Energy has been cooling properties in central Stockholm with cold water from the Baltic Sea since 1995. Also, a nearby lake can be the source of the cold water resource. The first large-scale application of this cooling technology is at Ithaca, New York, where a 63-inch pipeline was installed to link Cornell University and nearby Lake Cayuga in 1999. The pipeline accesses 4°C water at a depth of 250 feet. The system, which can provide 20,000 tons of cooling, is supplying air conditioning to the Cornell University Campus and the Ithaca City Schools. Makai Ocean Engineering of Hawaii was involved in the design and construction of that facility. The second major application of the use of cold lake water may be the city of Toronto, Canada. Toronto city planners have been developing plans to utilize cold water from Lake Ontario to air condition the downtown district of the city.

It is calculated that utilizing DOW for cooling can save as much as 80% of the energy cost compared to typical compressor type cooling systems. A simple heat exchanger coupled with solar powered air fans can air condition schools, government buildings, sporting complexes, commercial buildings and residences cheaply. Dow cooling is both inexpensive and environmentally sound, for it uses no chemical compressor fluids and is sustainable with no emissions; it is a thermal process which generates no heat. It can be inexpensively distributed long distances horizontally along the shoreline. Moeover, commercial and residential unit systems using this technology cool and dry the interior air, creating an environment ideal for electronic equipment and dry storage. Additionally, coastal resort communities with large air conditioning demands can become more competitive by reducing operation and energy costs. One thousand gallons of DOW, which cost US10¢ to pump, can cool 2,500 ft³. Payback periods for initial capitalization costs are quite small for large systems (Davidson, 2001).

Cold Utilization Subsystem - Freshwater Technology

Innovative technologies are being developed to enhance and capture condensation from surfaces cooled by flows of DOW to provide lifesaving fresh water to many coastal desert communities. Indeed, a vast proportion of the world's coasline is desert, and the largest obstacle to sustaining life is the scarcity of fresh, usable water. Although evaporation takes place, it rarely rains in coastal regions. Moisture rising from the ocean is carried inland across coastal lowlands, seldom

falling as rain until it encounters a mountain range. DOW technology has provided innovative methods for producing fresh, potable water on tropical coastal deserts. The DOW developments that provide this most precious desert commodity are: desalinated water as a bonus byproduct of OTEC systems; fresh water rain from the Hurricane Tower; and condensate from pipes supplied with cold ocean water.

One method for producing large quantities of desalinated water is an adjacent function of the open-cycle OTEC system. As described previously, the system involves passing warm surface seawater into an area where the ambient pressure is reduced so that the seawater turns to steam. The resultant condensate is pure, salt-free fresh water that can be used for drinking or irrigation. In fact, the desalinated water produced by open-cycle plants is less saline than the water provided by most municipal water systems and is free of atmospheric and ground contaminants. The closed-cycle OTEC system can indirectly produce fresh water. The same cold ocean water that is employed to run the system can be transferred to a separate heat exchanger, and fresh water which condenses from the humid tropical air can be collected and stored as a potable water supply. Alternatively, a second stage consisting of a vacuum evaporator and a surface condenser can be added to the closed system for desalinated water production.

The discovery that large quantities of pure condensate are produced as a byproduct of both OTEC systems inspired Dr. John Craven and other DOW researches to invent a new exciting patented technology, christened the "Hurricane Tower^{TM}", which also uses temperature differences to produce pure condensate (Craven and Sullivan, 1998) . The Hurricane Tower is a micro-climate structure in which nature's hurricanes are simulated to generate rain.

The Hurricane Tower model was carefully designed and fitted with the components and ingredients necessary to simulate a real hurricane. Warm surface seawater, which has been further heated in a solar pond covered with plastic, is introduced into the bottom of a 20-foot high tower to simulate the surface of the sea. A lightweight rotor driven by a motor installed in the tower floor simulates the huricane vortex by spinning with a peripheral velocity of 100 mph. A heat exchanger made of tubing spiraled around the inside top of the tower and supplied with cold seawater simulates the lenticular cloud of ice of the tropopause (the upper limit of the troposphere). It has been determined that a tower of this size will be able to produce 10,000 gallons of pure fresh water per day.

Another method for producing desalinated water is the collection of fresh water condensate. CHC has shown that, as deep ocean water is passed through a heat exchanger, the amount of pure water condensate produced from the humid atmosphere is equal to 5% of the total quantity of cold water flowing through the system. In other words, if the relative humidity is over 80%, up to 5 liters of pure potable water can be produced for every 1,000 liters of deep seawater flowing through heat exchangers in the atmosphere. This is equivalent to approximately 4 inches of rain per day or 1,200 inches per year. Water can be captured at an elevation of 25 feet by utilizing a siphon which transports cold up where it can produce condensate. So far, the collection of condensate from an inexpensive heat exchanger with DOW in this manner is the most cost-effective method for producing fresh water. For example, freshwater condensation can drip from the heat exchanging coiled tubing supplied with DOW into a storage tank in the CHC's "Rasmussen Rainmaker". At a flow rate of 1.5 gallons per minute of DOW, this system produces from the atmospheric moisture 11.5 gallons of fresh water per day or some 4,200

gallons per year. The water is surprisingly cold, and the system requires no moving parts or additional energy to operate.

Cold Utilization Subsystem - ColdAg™ Technology

Of all the applications of DOW technologies to date, the unique CHC invention, cold water agriculture or ColdAg, is proving to be the most remarkable. The name "Blue-Green Revolution" was chosen to designate this new form of agriculture in order to express the possibility of a blue ocean creating life and greenery in a coastal desert.

By utilizing only the cold from deep ocean water, a year-round-spring-like microclimate for plant roots under tropical desert conditions is created which produces ideal conditions for growth of tropical, subtropical and temperate crops. Basically, DOW pumped to the surface is directed into plastic pipes embedded in the soil at a particular plant root depth for the purpose of cooling the ground, thereby creating a spring-like microclimate that extends from below the plant roots to the soil surface. Since the soil surface is below the dew point, which is in the 60 to 70°F range in tropical coastal regions, moisture in the warm tropical air is drawn down to the cool soil causing freshwater condensate to form and be carried onto the cold pipes and plant roots by gravity. The soil is therefore largely self-irrigating. Plants are able to capture thermal energy created by the temperature difference between the roots and the foliage. This added energy potential enables the plants to grow at an incredible rate seen elsewhere only in springtime - 365 days a year in a coastal desert.

CHC has grown more than one hundred varieties of fruits, vegetables and herbs, all showing surprisingly high sugar and aromatic content, with ColdAg. The salt water is confined to the pipes and does not touch the plants or the ground. ColdAg has been developed using organic gardening techniques and has enormous potential for developing countries with tropical coastal deserts adjacent to deep ocean.

This revolutionary new form of agriculture also allows gardener researchers to exploit and manipulate the biophysical applications of cold to force and break dormancy in seasonal and perennial plants.by turning off the cold water for a period and then restoring it, thereby simulating the effect of a temporary climate change. With the restoration of the cool root environment, dormancy is broken and the plant reenters its production cycle. This allows for the possibility of three or four annual harvest cycles in one year. The most convincing example of manipulating dormancy is with wine grapes. Subjecting grape vines to a short period of drought at local tropical desert temperatures by turning off the cold water and then restoring the water to break dormancy has resulted in a remarkable crop of the very best temperate grapes per vine every 110 days or a total of three crops a year.

One positive feature of ColdAg is that it requires no drainage; there is a complete absence of wastewater that threatens the environment by contributing run-off pesticides, herbicides and fertilizers as often occurs with traditional irrigation methods.

A particularly interesting spin-off has been the development of CHC Ecoturf ™ Technology. This will grow and maintain high quality turf consisting of grasses from virtually any climatic

zone under tropical desert conditions. As with other plants, these world-class turfs use ColdAg ^{TM} technology that produces fresh water condensate from deep ocean water, reducing watering by at least 80% compared to traditional irrigation methods. They consist of longer, deeper grass roots that make better playing surfaces; they are able to withstand impact and then come back for more by repairing themselves quickly. This technology makes possible the development of high quality low-cost landscaping and creates safer playing surfaces for sports, e.g., soccer, baseball, football, lawn tennis, golf and lawn bowling, in tropical coastal desert locations.

Nutrient Utilization Subsystem – Marine Aquaculture

In nature, an upwelling, usually caused by the wind, that transports pure, nutrient-rich DOW to the surface occurs regularly in the world's oceans and seas. Although DOW upwelling constitutes only 0.5% of all seawater, it supports nearly 50% of the ocean's food web, from phytoplankton and microscopic zooplankton to fish. DOW aquaculture imitates in warm coastal desert regions the upwelling phenomenon of the natural world by using the still-cold (about 11°C) seawater after it has run through other DOW subsystems. This seawater, which has elevated levels of inorganic nitrates, phosphates and silicates, can be used in its 'pathogen-free' state or combined with surface seawater in aquaculture farms to produce environments acceptable to many temperate and tropical species of marine life. Its high nutrient levels produce more rapid growth and higher protein content in microalgae and macroalgae. It also allows the growth of temperate shellfish (e.g., Maine lobster) and fin fish (e.g., flounder and salmon).

THE *SANSAQUA* PROJECT

One of the author's ancestors left Europe for the Island of Hispaniola in the late 17th century. According to Victor Perera (1995), this ancestor belonged to a group of Pere(i)ras who "envisioned themselves as architects of a grand design to move mountains, tame the seas and make the world habitable for rich and poor alike". It is in this tradition that the author founded Energies Naturelles (Energinat S.A.), a Haitian corporation dedicated to the optimal management of natural energy resources for the benefit of the people of Haiti. Energies Naturelles has negotiated a joint venture agreement with CHC for the purpose of establishing a DOW system in five geographic sites identified along the coast of the country, each of which is a promising location for a deep seawater development project. These sites are: Mole St. Nicolas (Mole's Cape), St. Marc's Bay (St. Marc's Point), Gonave Island (West Point), the northern coast of the Southern Peninsula (near Jeremie), and a coastal zone east of the city of Jacmel. Since these sites are removed from each other, they will be connected to the ports of the country by sea transportation comprising a fleet of high speed ferryboats for passengers and merchandise. They will also be linked to all coastal cities, towns and villages and to the transatlantic cables by a submarine necklace of fiber optics for telephone communications, the transfer of data and the Internet. Because the DOW system does not require fresh water from municipal systems, this sustainable socio-economic development project has been named the "*SANSAQUA* Project", a designation suggested by Admiral Ray Cohen, Chief of United States Naval Research.

Each DOW site will have its symbolic fountain (similar to the one at the NELHA) where visitors can feel for themselves the marked difference between the warm tropical surface seawater and

the cold arctic or antarctic deep seawater. This will serve to remind them that it is the temperature difference between these waters or between the cold DOW and the warm humid tropical air that makes it possible for each DOW system to provide: (1) fresh water for drinking, household and industrial use; (2) air conditioning and industrial cooling; (3) an abundance of temperate and tropical fruits, vegetables and herbs for food and for market; (4) Ecoturf to lay out high quality sports fields and recreational areas; (5) a nutrient-rich and pathogen-free medium for aquaculture; and (6) in the near future electricity. Because of all these quality of life benefits, which are gifts of the sea to humanity, it would be fitting to christen the fountains in the five DOW sites "The Fountains of Paradise". The latter differ from those described by Arthur C. Clarke (1979) in his famous science fiction book of the same name. Unlike Clarke's fountains, which are columns of fresh water that spring from buried pipes and leap toward the sky before falling on the ground, the seawater of the DOW site fountains is confined to pipes and does not touch the ground, but can make fresh water rain in an OTEC plant, a Hurricane Tower or a Rasmussen rainmaker.

Two main types of DOW systems can be designed to serve many purposes. Type 1 is a CHC basic DOW system for a self-sufficient tropical coastal desert community, which is economically, culturally and environmentally sustainable (Craven, J.P., 1995). It consists of:

- Two 24-inch polyethylene intake pipelines
- A pumping station (reservoirs and pumps)
- An administration building
- Fresh water production (Hurricane Towers)
- Air conditioning (A/C) for dwellings, offices and community buildings
- Cooling facilities for agriculture and aquaculture produce and fish catch
- 100 acres for cold water agriculture (farms, orchards and vineyard)
- 16 acres for marine aquaculture
- Reservation of space for a 1MW closed-cycle hybrid cycle OTEC plant and a TEG system

A Type 2 system focuses on providing high market value recreational experiences, e.g., hotels, resorts and sports facilities in tropical coastal desert locations. It may or may not include an adjacent village community with a DOW agriculture-aquaculture park for resort and market needs. It may be possible to combine a Type 2 system with a Type 1 facility to provide the fresh vegetables, fruits and fish products needed for the resort, local use and market, but also resort air conditioning and high quality landscaping and sports fields for soccer, tennis, bowling or golf courses with CHC DOW Ecoturf. Such a combined Type 1 and Type 2 system is very likely to be the first facility installed in Haiti on Gonave Island, the largest offshore island of the country. Indeed, the consortium formed by Energies Naturelles and CHC has been approached by a group of Haitian business leaders who are developing plans to build a beach resort and golf club plus low-income housing and luxurious residences in the proximity of the DOW site to be established in the West Point area of Gonave Island. The combination of nearby ocean, abundant sunshine, culture and history, together with mild climate will make this location a very attractive ecotourist destination.

Another benefit that ecotourists can derive from the combined system is cold thalassotherapy. It has long been known that seawater is effective for atopic dermatitis. However, because surface

seawater contains many bacteria and viruses, it is not recommended for daily application. Alternatively, pathogen-free DOW was tested for daily use with promising results (Nomura, 1995). Furthermore, in Finland, Russia and Canada, the so-called "polar bears" take to "Ice Swimming" in the ocean in the depths of winter because of its purported beneficial properties, such as increasing blood circulation, healing sports injuries and stimulating endorphin secretion. These polar bears will be able to enjoy the same benefits, all year-round, in pools of pumped up cold, pure DOW in a tropical coastal desert.

CONCLUSION

In 1962 the former Indian Prime Minister, Jawaharlal Nehru, went as far as stating in a speech to the Ceylon (now Sri Lanka) Association for the Advancement of Science: "Politics and religion are obsolete; the time has come for science and spirituality". For Haiti, however, the time has come for a happy marriage not only of religion and spirituality, but also of politics and science, in particular marine science and technology. During the first years of the 21st century, which has been called the "ocean century", growing numbers of Haitians are heading for the beach to await the arrival of the North Pacific albatross which will take off from the Big Island of Hawaii, fly between the Tropic of Cancer and a latitude of 15° north and follow, like Baudelaire's albatross, the fishing boats in the Pacific Ocean before traversing Mexico and the eastern corner of Cuba to land in Haiti, transporting on its large wings the CHC DOW systems.

These Haitians have come to realize that life of poverty and even misery will be their fate unless they use their DOW resource – the nation's most valuable natural energy resource. They know that these DOW systems can transform many of the coastal deserts of Haiti into oases of prosperity and plenty and, to paraphrase Arthur C. Clarke, create Paradise along much of the country's coastline, so that there will only remain to build Heaven on the summit of its mountains.

REFERENCES

Claude, G. 1930. Power from the tropical seas. *Mechanical Engineering.* 52(12): 1039-1044.

Clarke, A.C. 1979. The Fountains of Paradise. Published by Warner Books, New York.

Cobb, C.E., Jr. 1987. Haiti against all odds. *National Geographic.* 172(5): 644-671.

Craven, J.P. 1995. Realistic self-sufficient coastal complexes using deep ocean water as a resource. Presented at the Coastal Ocean Space Utilization (COSU) Conference '95, Yokohama, Japan, 1995.

Craven, J.P. and P.K. Sullivan 1998. Utilization of deep ocean water for seawater desalination. In *Proceedings of the International OTEC/DOWA Conference '98,* Vol. 9, No. 4/Winter 1998.

Daniel, T.H. 1994. Deep ocean water utilization at the Natural Energy Laboratory of Hawaii Authority. In *Proceeding of Oceanology International 94,* 8-11.

Davidson, J.R. 2001. California's energy future and cold ocean water? In *Recent Advances in Marine Science and Technology 2001,* edited by O. Bellwood, H. Choat and N. Saxena. San Francisco: PACON International, U.S.A.

Hisatake, R. 1997. Current and future situations of food industry using deep seawater in Kochi Prefecture. In *Proceeding of Kaiyo Shinsousui 97,* 107-111 (in Japanese).

Nomura, I. 1995. Medical treatment of atopic dermatitis using deep seawater. Magazine Kaigan. 34(2): 7-10 (in Japanese).

Penney, T.R. and T.H. Daniel. 1988. Energy from the ocean: A Resource for the Future. In *Science and the Future:1989 Yearbook,* 98-111. Chicago: Encyclopedia Britannica.

Perera, V. 1995. The French Pereiras. In *The Cross and the Pear Tree,* published by Alfred A. Knopf, Inc., New York, chapter 6, p.135.

Van Ryzin, J. and T. Leraand 1992. Air conditioning with deep sea water: A cost-effective alternative. *Sea Technology.* 33(8): 37-40.

Vega, L.A. 1992. Economics of Ocean Thermal Energy Conversion. In *Ocean Energy Recovery: The State of the Art,* published by the American Society of Civil Engineers and edited by R.J. Seymour, chapter 7.

ASSESSMENT ON ENVIRONMENTAL EFFECTS OF DEEP OCEAN WATER DISCHARGED INTO COASTAL SEA

Masatoshi Hayashi[1], Tomoji Ikeda[1], Koji Otsuka[2] and Masayuki Mac Takahashi[3]

[1]Kansai Environmental Engineering Center, Co., Ltd.
Azuchi-machi, JAPAN
hayashi_masatoshi@kanso.co.jp

[2]Osaka Prefecture University
Osaka, JAPAN

[3]Graduate School of Arts and Sciences, University of Tokyo
Tokyo, JAPAN

ABSTRACT

Deep ocean water (DOW) has some superior characteristics in comparison with surface seawater such as coldness, rich nutrients and cleanliness. Some of those characteristics of DOW have recently been used for many practical purposes. However environmental impacts due to DOW discharged into coastal sea after uses have not yet been evaluated. This will be one of the important subjects to be clarified for a possible great increase in DOW usage in the near future. Following points such as biological entrainment during pumping up of DOW, CO_2 emission into the atmosphere from DOW by pressure reduction and warming, fertilization of phytoplankton and seaweed and the other effects of DOW discharged into coastal sea have been given particular attention as probable impacts in this study. It is also intended to assess probable environmental impacts of pumping up and discharging used DOW into the natural environment.

INTRODUCTION

Deep ocean water (DOW) has recently received particular attention in Japan as a new natural resource having clean, cold and nutrient-rich characteristics (Takahashi, 2000), and many practical applications of DOW characteristics have now been made in various commercial uses such as foods, drinks, cosmetics and so on (Takahashi, 2002). There are nine pumping stations of DOW being operated in Japan, with pumping capacities ranging from 60 to 13,000 $t \cdot d^{-1}$. Two pumping stations, Mitsu and Takaoka in Kochi Prefecture, discharge DOW directly into the surrounding coastal sea without any special care, although actual amounts of discharge are part of DOW pumped up. At Namerikawa in Toyama Prefecture, most DOW of the ca 3000 $t \cdot d^{-1}$ pumped up is discharged into Namerikawa Harbor after being mixed with river water. While on Kume Island in Okinawa Prefecture, where the large quantity of 13,000 $t \cdot d^{-1}$ of DOW is pumped up, DOW is discharged using two pipes reaching beyond the coral reefs to avoid direct exposure of discharged DOW to corals.

Although existing pumping capacity at a given station is 13,000 $t \cdot d^{-1}$ or less in Japan, there is a possibility that the pumping capacity will be greatly increased in the near future, if we start to use the low temperature and nutrients contained in DOW resources commercially. For such a large use of DOW, we need to establish how to discharge DOW after use (Komatsu, 2000), and how to

make the necessary assessment of probable impacts of DOW discharge into the natural coastal environment (Otsuka, 2001).

One of the most probable impacts of DOW discharges will be local fertilization by the excess nutrients contained in DOW as well as lowering water temperature, which could give us some benefits if they could enhance local production of commercially valuable fish and shellfish (Ryther, 1969; Furuya, 1993; Ouchi, 2001; Matsuda, 2002). However, it could change the environment, which will be considered detrimental to the conservation of the existing natural environment. Furthermore, we have to evaluate not to fertilize the area will developing harmful red tide organisms and creating anoxic water.

There are also other possible impacts, such as entrainment of organisms living in deep depths by pumping up of DOW to the surface (Daniel, 1992) and probable CO_2 emission into the atmosphere (Harada, 2000). DOW contains higher concentrations of carbonic acid than that of surface seawater, and the excess CO_2 will be released into the atmosphere since DOW is reduced pressure and warmed at the surface. Since at least these two impacts cannot be avoided, we have to minimize the impacts. For the biological entrainment, we need to know what kinds of organisms might be entrained with DOW and their amounts. For the CO_2 release, we can minimize the impact or may change to a positive impact by absorbing excess CO_2 by accelerating the productivity of phytoplankton and seaweed using nutrients contained in DOW.

A national research project, in which a large quantity of DOW such as 1 million $t \cdot d^{-1}$ is planned for cooling a 600 MW commercial electric power generator, has been carried out since 1999 for the five-year program (Takahashi, 2002). The present study has been made a part of the national project mentioned above for making the necessary assessment of environmental impacts of DOW discharged into coastal area after uses. For establishing a suitable assessment, methodology on environmental impacts of large quantities of DOW is another target in this study, too.

This paper particularly focuses on probable impacts of the following factors: biological entrainment during pumping up of DOW, CO_2 emission into the atmosphere from DOW by warming, fertilization of phytoplankton and seaweed and several other effects of discharging DOW into coastal sea.

METHODS

Samples of biological entrainment were collected once a month (October 2000-September 2001) at the two prefectural deep seawater laboratories of Kochi and Toyama, and the Kinki University Fisheries Research Laboratory. DOW and surface seawater samples pumped up in the three DOW pumping stations were filtered through 92μm nylon gauze mesh for 24 hours. Three quarters of each sample was immediately fixed with 5% neutral formalin and then species were identified and the number of individuals was counted. The rest of the sample was filtered onto 50μm nylon gauze mesh filter and organic carbon of retained materials on the filter was then measured.

Samples to estimate CO_2 balance were collected once a month (October 2000-September 2001) at the two prefectural deep seawater laboratories mentioned above. The method for estimating CO_2 balance followed with Lewis and Wallace (1998). The hydraulic test was carried out in a horizontal flume being 7 m in length, 3 m in width and with 1/25 slope in bottom. Salinity of seawater in the tank was measured and for estimating the level of dilution.

Natural surface phytoplankton assemblages collected near the Kochi Prefectural Deep Seawater Laboratory were cultured in DOW mixed with surface seawater at levels of 90, 75, 50, 25 and 0% four times a year (May, August, November and February). Culture experiments for investigating possible effects of nutrients were also conducted by adding different amounts of nitrate, phosphate and silica to the surface water containing 1% of DOW. Possible effect of temperature was also examined. Specific growth rate was estimated based upon chlorophyll-a of phytoplankton assemblage determined every day. Culture of seaweed was examined in DOW mixed with surface seawater at levels of 100, 80, 60, 40, 20 and 0%. Relative growth rate of seaweed was estimated based upon wet weight measured every day.

RESULTS

Biological entrainment during pumping up of DOW

Biological entrainment due to pump up of DOW has been investigated by 24 hours accumulated sample monthly at three DOW pumping stations during one year. Kochi Prefectural Deep Seawater Research Laboratory pumped from ca.320 m by two pipes of inside diameter of 0.125m at 0.43 $m \cdot s^{-1}$ of pumping velocity, Toyama Prefectural Fisheries Research Laboratory from ca.320 m by a pipe of 0.25 m inside diameter at a pumping speed of 0.7 $m \cdot s^{-1}$ and Fisheries Research Laboratory in Toyama of the Kinki University from ca.100 m by a pipe of 0.45 m inside diameter at a pumping speed of 0.125 $m \cdot s^{-1}$. Entrainment surveys have also been performed for the surface seawater pumped.

Table 1. Particulate organic carbon (POC) retained on 50 μm netting in DOW and surface seawater samples during 24 hours continuous sampling once month throughout one year

	Kochi Prefectural Deep Seawater Research Laboratory		Toyama Prefectural Fishereis Research Laboratory		Fishereis Research Laboratory of Kinki Unversity	
	POC in DOW $(kgC \lrcorner 0^6 t^{-1})$	POC in Surface seawater $(kgC \lrcorner 0^6 n^{-1})$	POC in DOW $(kgC \lrcorner 0^6 t^{-1})$	POC in Surface seawater $(kgC \lrcorner 0^6 t^{-1})$	POC in DOW $(kgC \lrcorner 0^6 t^{-1})$	POC in Surface seawater $(kgC \lrcorner 0^6 t^{-1})$
Average	0.14	26.35	1.68	3.32	1.23	2.95
Maximam	0.25	42.24	3.97	7.11	2.28	5.47
Minimam	0.07	9.99	0.49	1.43	0.36	1.14

Monthly total amounts of biological entrainment during 24 hours continuous net sampling in DOW for each station were generally smaller than those for surface seawater. The main group of organisms collected from DOW was copepods of Arthropoda (Fig. 1). No actual entrainment of commercially valuable organisms was seen in the DOW samples collected during 24 hours in each month over one year at all three sampling stations. Organic carbon (POC) retained on 50μm mesh netting was lower in the DOW samples than that of the surface seawater samples at the three DOW pumping stations (Table 1). POC in DOW in Kochi was at least 1/10 of that in Toyama. These results show that the total amounts of entrainment in DOW pumped up were consistently low compared with the surface seawater. Although there is a possibility to entrain large size organisms such as fish, it has not been evaluated in the present study because of less frequency of sampling compared to probable entrainment probability of those large organisms.
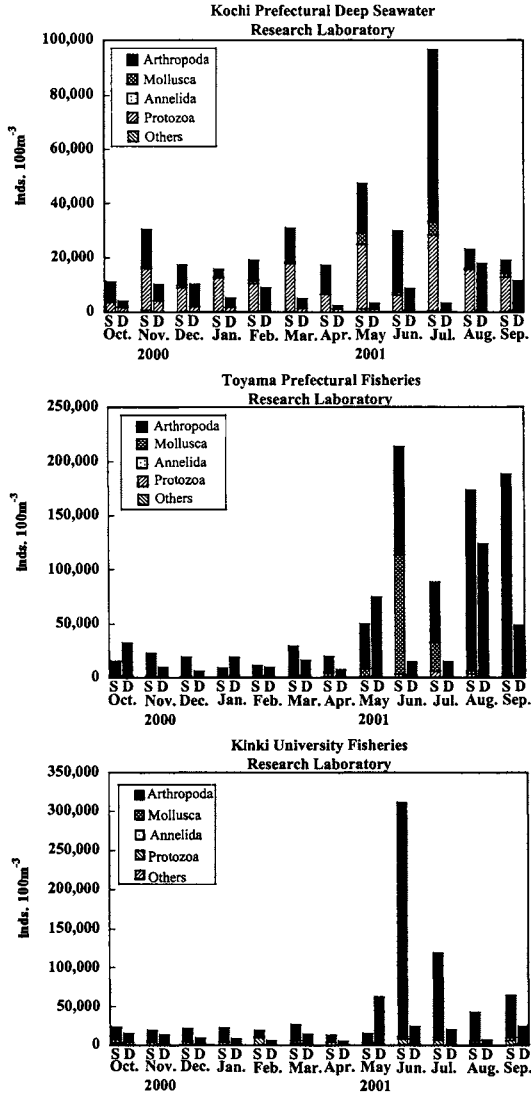
Figure 1. Biological entrainment expressed with individual numbers of different taxonomical groups due to pump up of DOW and of surface seawater; S: surface seawater, D: DOW

CO$_2$ emission from DOW at the surface

Total carbonic acid, total alkalinity, phosphoric acid, silicic acid and total inorganic nitrogen of DOW were measured once a month at all the three stations mentioned above. CO$_2$ emission caused by DOW being pumped up to the surface was estimated based on these measurements. Total carbonic acid concentrations of DOW pumped up from a depth of ca.320 m in Kochi and

Toyama were approximately 2,200 – 2,300 μmol·kg^{-1}, while they were around 1,900 - 2,000 μmol·kg^{-1} for surface water. This indicates a possibility that 200 – 300 μmol·kg^{-1} of CO_2 will be released into the atmosphere by warming the temperature of DOW to surface temperature after pumping up. Pumping up of one million t·d^{-1} of DOW for cooling a 600 MW LNG power plant might release 2,800 – 3,200 tCO$_2$·year^{-1}.

On the other hand, using cold DOW as a coolant for an electric power generator is highly likely to increase the power generation efficiency, which will reduce fuel consumption and CO_2 emissions from the power plant. According to Kadoyu (2000, 2001), it is estimated that the power generation efficiency of a power plant would increase by 3%. This improvement in power generation would reduce CO_2 release about 12,000 tCO$_2$·year^{-1} for a LNG power plant with a 50% duty cycle. This means that even if DOW pumped up releases CO_2 into the atmosphere, the total amount of CO_2 emissions would actually be reduced by saving fuel consumption through improved power generation efficiency (Table 2). Furthermore, if DOW is discharged into sea areas after use, growth of phytoplankton and seaweed will absorb CO_2 through photosynthesis by use of the excess nutrients in DOW, which can further contribute to reducing CO_2 in the atmosphere (Table 2).

Table 2. Estimates of CO_2 emission when 1 million t·d^{-1} of DOW is used for cooling a 600 MW LNG power plant with 50% duty cycle. Improvement of power generation efficiency is assumed to be 3% by using DOW for cooling.

	Kochi	Toyama
	(tCO$_2$·year^{-1})	
CO_2 release by pumping-up of DOW (A)	2,765	3,192
CO_2 fixation by photosynthesis of phytoplankton (B)	-1,634	-2,044
CO_2 reduction associated with power plant operation using DOW (C)	-12,212	
Total CO_2 reduction without photosynthesis effects (A+C)	-9,447	-9,020
Total CO_2 reduction with photosynthesis effects (A+B+C)	-11,081	-11,064

Possible effects on phytoplankton by discharged DOW

Since DOW has different characteristics than surface water, DOW after uses needs to be carefully discharged into the natural environment not to cause serious impacts. Our research was at first focused on the behavior of DOW water mass, in which DOW warmed in a power plant, was discharged into a coastal environment.

Hydraulic tests showed clear differences in the dispersal pattern of DOW depending upon differences in internal Froude number, where larger Froude numbers increased dilution of DOW (Fig. 2). This suggests how to discharge DOW after use for possible impacts of DOW such as low water temperature and some others on organisms living in the coastal regions. For enhancing phytoplankton productivity by excess nutrients of DOW after use, DOW needs to be discharged in order to stay in the euphotic zone.
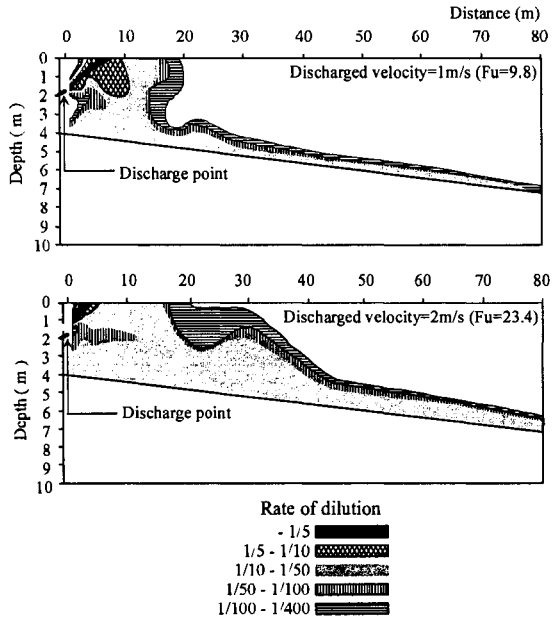
Figure 2. Model estimates of the diffusion pattern of discharged DOW watermass at two different internal Froude numbers (Fu).

Fertilization effects of DOW on phytoplankton

Since the actual evaluation of possible effects due to discharged DOW on phytoplankton under natural environment is not easy with the limited amount of DOW discharge currently occurring at each pumping station (Ishizaka et al., 1983; Furuya et al., 1993), we approached estimating the probable effects by culture experiments in the laboratory. We focused particularly attention on the specific growth rate of phytoplankton, using natural assemblages collected from surface at sites in Kochi Prefecture where DOW is actually discharged.

Culture experiments were conducted in a laboratory incubator under light with DOW mixed with the surface water containing natural phytoplankton assemblages in several different mixing proportions of 90, 75, 50, 25 and 0 percent. The specific growth rate of the total phytoplankton assemblage evaluated from chlorophyll a changes increased with the amounts of DOW up to 25% dilution. Specific growth rates of 1.16 to 1.80 d^{-1} in May and August, and 0.38 to 0.57 d^{-1} in November and February were obtained at 25% dilution of DOW (Fig. 3).
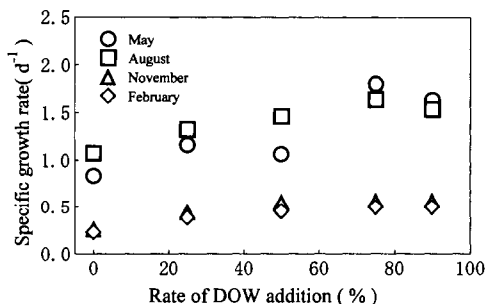
Figure 3. Changes of specific growth rate of surface natural phytoplankton assemblage cultured in a laboratory incubator under light with different additions of DOW

To evaluate possible effects of nutrients and temperature of DOW on phytoplankton, further culture experiments were conducted at two different temperatures, in which different amounts of NaNO$_3$ were added to the surface water. The following relationships were experimentally obtained between the specific growth rate of total phytoplankton (μ, d^{-1}) and the two environmental parameters, dissolved inorganic nitrogen (DIN) as nitrate and water temperature (WT).

For DIN (μ_S),

$$\mu_S = 1.09 \times S/(S + 7.57) \tag{1}$$

where S represents DIN concentration as nitrate in μM.

For WT (μ_T),

$$\mu_T = 1.02 \times (T/27 \times EXP(1 - T/27))^{16} \tag{2}$$

where T represents water temperature in °C.

Relationships between DOW discharged and the specific growth rate of total phytoplankton were estimated by use of equations (1) and (2), and the obtained results under an assumption that either nitrate concentration and/or temperature control the growth of the phytoplankton assemblage are graphically shown in Figure 4. Growth of the phytoplankton assemblage was enhanced both in the summer and in winter by the addition of DOW. It was also expected that DOW without warming could depress the growth of phytoplankton in the water even in winter because of lower temperature of DOW compared to the surface water.

DOW contains large amounts of nutrients and is characterized with high concentration of Si such as N:P:Si = 12:1:24. It has been reported that diatom species grow faster if the Si/P ratio is 10 or more in a mixed culture of a red tide alga of *Alexandrium tamarense* and a diatom species (Yamamoto *et al.*, 1999). Diatoms generally tend to dominate in our culture experiments using DOW even the surface phytoplankton assemblages were dominated by other phytoplankton species than diatoms at starting. Thus, it can be concluded that DOW could specifically accelerate the growth of diatoms in natural phytoplankton assemblages.
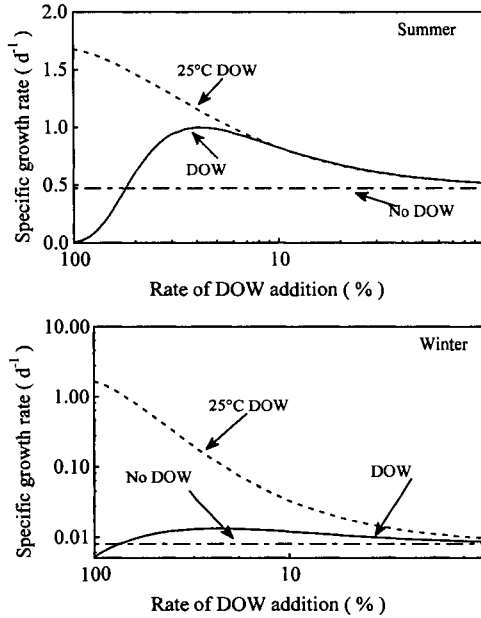
Figure 4.   Changes of specific growth rate of surface natural phytoplankton assemblage cultured in a laboratory incubator under light with different amounts of DOW

Fertilization effects on seaweed by discharged DOW

In the coastal sea in front of the Kochi Prefectural Deep Seawater Laboratory, several hundred t·d^{-1} of original and used DOW have been discharged over ten years.   Active developments of *Sargassum* spp. and *Ecklonia cave* have been noticed in the area around the outlets where DOW has been discharged particularly large coverage of *Sargassum* spp (Fig. 5).   This suggests a possibility for creating a seaweed bed by discharged DOW.   However, it is still not clear whether the growth of algae is due to nutrients or low temperature of DOW, yet.
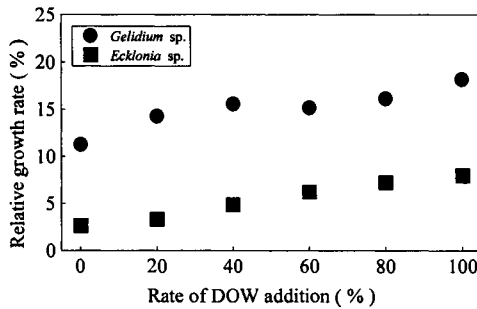
Figure 5. The observed distribution pattern of *Sargassum* spp. and *Ecklonia cave* nearby the Kochi Prefectural Deep Seawater Laboratory

542

"No DOW" represents the specific growth rates determined in surface seawater containing 2μM of DIN at 28°C for summer, and 2μM of DIN at 12°C for winter. "DOW" represents different additions of DOW containing 25μM at 10°C. "25°C DOW" represents DOW heated up to 25°C with different additions.

Then we conducted a culture experiment to determine possible relationships between the relative growth rate of algae and nutrient concentrations at a constant water temperature in an incubator under light in the laboratory. Nutrient concentrations were controlled by mixing DOW containing high concentrations of nutrients with surface seawater. *Gelidium* sp. showed almost similar growth rate above 40% additions of DOW although it gradually decreased with less amounts of DOW below 40% of DOW (Fig. 6). On the other hand, *Ecklonia* sp. showed a consistent increase of the relative growth rate with increasing proportion of DOW up to 100% (Fig. 6). These results indicate that nutrients in DOW could enhance the growth of seaweed. According to another culture, experiments conducted using *Gelidium* sp. and *Ecklonia* sp. at different temperatures, *Gelidium* sp. Showed the fastest growth rate at 23°C but *Ecklonia* sp. was at 15°C. Based on the results of the culture experiments, the following relations were obtained for the relative growth rates (%) of *Gelidium* sp. and *Ecklonia* sp. with dissolved inorganic nitrogen and water temperature.
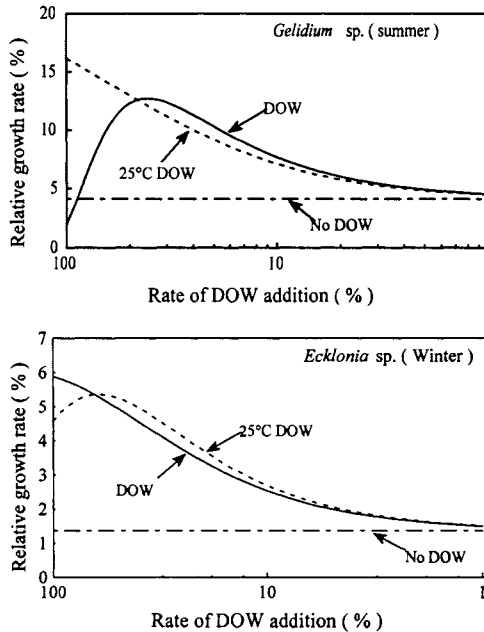
Figure 6. Changes of the relative growth rate of *Gelidium* sp. and *Ecklonia* sp. in different mixing proportions of DOW with the surface seawater

For *Gelidium* sp.,

$$\mu_S = 21.09 \times S/(S + 6.70) \tag{3}$$
$$\mu_T = 15.65 \times (T/23 \times EXP (1 - T/23))^8 \tag{4}$$

For *Ecklonia* sp.,

$$\mu_S = 11.14 \times S/(S + 13.15) \tag{5}$$
$$\mu_T = 5.07 \times (T/15 \times EXP (1 - T/15))^3 \tag{6}$$

where S represents DIN concentration in µM as nitrate and T represents water temperature in °C.

By using the relationships obtained, the growth of *Gelidium* sp. and *Ecklonia* sp. can be estimated under different DIN and temperature influenced by DOW (Fig. 7). Although the relative growth rates of *Gelidium* sp. and *Ecklonia* sp. were low under no addition of DOW but they generally increased their growth rate with the increase of DOW proportion. But the growth of *Gelidium* sp. was inhibited by the addition of too much DOW because of its low temperature, while DOW heated to 25°C enhanced the algal growth to the maximum at the highest proportion of DOW.
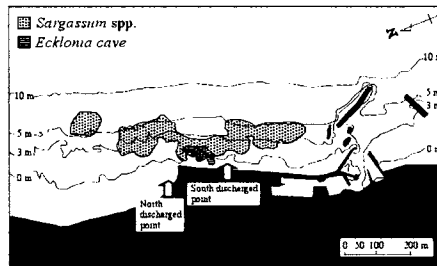
Figure 7. Changes of the relative growth rate of *Gelidium* sp. and *Ecklonia* sp. in different mixing proportions of DOW with surface seawater

"No DOW" represents relative growth rates determined in surface seawater containing 2µM of DIN at 28°C for summer, and 2µM of DIN at 12°C for winter. "DOW" represents different additions of DOW containing 25µM at 10°C. "25°C DOW" represents DOW heated up to 25°C.

DISCUSSION

Compared to using surface seawater varying temperature depending on season for a coolant of electric power plants, deep ocean water (DOW) having low temperature with no or small seasonal changes provides some improvements of power generating efficiency and results in reducing CO_2 emission as well as requiring small amount of cooling water with small size of heat exchangers (Kadoyu, 2000, 2001). It is also possible to eliminate low-temperature effects of DOW by warming up in power plants, and could be discharged at similar temperature around the surrounding environment.

Very little biological entrainment of DOW mainly small size zooplankton found in this study, as well as the characteristics of almost no biofouling of DOW which has been found in Japan and Hawaii (Daniel, 1992), are very helpful for its use as a coolant for power plants and other facilities. Although less frequent entrainment of large size organisms such as fish is still remained for future evaluation.

Another influences of DOW on the environment are enhancements of biological productivity of phytoplankton and seaweed. The specific growth rate of phytoplankton increased with the

increasing percentage of DOW. Thus there are possibilities to enhance biological production by DOW discharged which could lead into some increases of commercially valuable fish and shellfish production (Ouchi et al., 2001; Ogiwara et al., 2001). DOW discharge may also be effective for restoration and development of seaweed beds (Fujita, 2001; Watanabe et al., 2000). Increased biological production will also be beneficial for CO_2 absorption from the atmosphere.

Concerning a possible large increase of DOW utilization in the near future, it is important to study the environmental impacts of the pumping-up and discharge of DOW. We still need further considerations on most of the processes in this study and the other possible processes, which were not taken into account in the present study, finally, to put all the processes affecting the environment together by using a suitable approach such as an ecosystem model with sufficient hydrodynamic considerations for the thorough evaluation of effects by DOW.

ACKNOWLEDGMENT

REFERENCES

Daniel, T. H. 1992. An overview of ocean thermal energy conversion and its potential by-products. *Proc. Pacific Congress on Marine Science and Tech.*, PACON-92, pp. 263-272.

Fujita, D. 2001. Algal recovery on coralline-covered cobbles collected from an urchin-dominated barren ground in flowing deep-sea water. *Deep Ocean Water Research*. 2:57-64 (In Japanese with English summary).

Furuya, K., H. Tsuzuki, K. Iseki and A. Kawamura. 1993. Growth response of natural phytoplankton assemblages in artificially induced upwelling in Toyama Bay. Japan. *Bulletin of Plankton Society of Japan*. 40:109-125.

Harada, K. 2000. The problem about CO_2 due to utilize deep seawater. *Gekkann kaiyo*, Special volume 22:229-233 (In Japanese)

Ishizaka, J., M. Takahashi and S, Ichimura.1983. Evaluation of coastal upwelling effects on phytoplankton growth by simulated experiments, *Marine Biology*. 76:271-278.

Kadoyu, M. 2000. The possibility of deep seawater utilization for cooling water of thermal and nuclear power plant. *Gekkann kaiyo*, Special volume 22:56-61 (In Japanese).

Kadoyu, M. 2001. Research on deep ocean water utilization for cooling water of power plant. *Report of Central Research Institute of Electric Power Industry* (In Japanese).

Komatsu, M. 2000. The study on the deep ocean water discharge technology using a numerical simulation. *Deep Ocean Water Research*. 1: 5-11 (In Japanese with English summary)

Lewis E. and D. Wallace. 1998. Program development for CO_2 system calculations, ORNL/CDIAC 105, Carbon Dioxide Information Analysis Center, Oak Ridge National Laboratory, U.S. Department of Energy, Oak Ridge Tennessee.

Matsuda, F., T. Sakou, M. Takahashi, J. Szyper, J. Vadus and P. Takahashi. 2002. U.S.-Japan advances in development of open-ocean ranching. *UJNR Marine Facilities Panel.*

Ogiwara, S., Y. Awashima, H. Miyabe and K. Ouchi. 2001. Conceptual design of a deep ocean water upwelling structure for development of fisheries. Proc. 4th ISOPE Ocean Mining Symp. ISOPE-OMS-2001, pp.150-157.

Otsuka, K. 2000. Recent researches on deep ocean water applications in Japan. Proc. 4th ISOPE Ocean Mining Symp. ISOPE-OMS-2001, pp. 144-149.

Ouchi, K., T. Yamatogi and S. Jitsuhara. 2001. A feasibility study on the energy source for the ocean nutrient enhancer. Proc. 4th ISOPE Ocean Mining Symp., ISOPE-OMS-2001, pp.158-162.

Ryther, J.H. 1969. Photosynthesis and fish production in the sea. *Science* 166: 72-76.

Takahashi, M.M. 2000. DOW, Deep ocean water as our next natural resource. Terra Scientific Publishing Co., Tokyo. 99pp.

Takahashi, M.M. 2002. Deep ocean water utilization and future challenges toward sustainable society. Proceedings of PACON2002

Watanabe, M., M. Taniguchi, T. Ikeda, M. Komatsu, K. Takatsuki and S. Kanamaki. 2000. Fertilization at coastal zone using deep ocean water. *Gekkan kaiyo*, Special volume 22: 160-169 (In Japanese).

Yamamoto, T. and K. Tarutani. 1999. Effects of Si/P loading rate and supply modes on population dynamics of *Alexandrium tamarense. Can. Tech. Rep. Fish. Aquat. Sci.*, 2261:14-17.

A PARAMETRIC STUDY OF POWER PLANT PERFORMANCE USING DEEP-SEA WATER FOR STEAM CONDENSATION

M. Kadoyu, Y. Eguchi and F. Takeda

Central Research Institute of Electric Power Industry
Chiba, JAPAN
kadoyu@criepi.denken.or.jp

ABSTRACT

Power plant performance is parametrically evaluated in applying deep-sea water to a steam condenser as a heat sink. A 600 MWe fossil thermal plant is selected as a benchmark plant for the evaluation, and plant performance and hardware requirements are calculated under various conditions using a heat balance analysis code. The results show that, for an existing power plant designed for surface seawater, power generation can be improved by at most 3.5% in northern and central Japan in summer by applying deep-sea water. Moreover, the heat transfer area requirement of a steam condenser can be considerably reduced with the use of deep-sea water for optimally designed power plants, together with some improvement in plant efficiency.

INTRODUCTION

In steam power plants, power is generated by turbine rotation driven by the pressure difference between a boiler (turbine inlet) and a condenser (turbine outlet). Since the performance of a condenser has a direct impact on plant efficiency (or heat rate), intensive studies have been conducted on its improvement (Cooper, 1996; Tsou, 1991). Use of deep-sea water as a heat sink of the condenser would have a beneficial effect on plant efficiency, because (a) a high vacuum is realized in a condenser due to the coldness of the deep-sea water, (b) the inefficient off-design operation of a condenser can be avoided due to the dramatic reduction in seasonal temperature variations, and (c) the purity of deep-sea water prevents the pipeline from biologically fouling, thus saving on maintenance costs. If these positive effects pay for both the initial investment required for pipeline installation for deep-sea water and the additional running costs for pumping water up from the deep sea, the use of deep-sea water seems a promising option as a method of plant efficiency improvement.

In the present study, the authors have evaluated power plant performance with a numerical model, assuming the use of deep-sea water to condense the exhaust steam. A 600 MWe fossil thermal plant is selected as a benchmark plant for the evaluation. That evaluation was performed for an existing plant and a newly designed one, where hardware specifications are fixed in the former, but changeable in the latter. For an existing plant, whose hardware was originally designed for surface seawater cooling, plant performance is calculated using a heat balance analysis code, assuming deep-sea water-cooling. For a new plant designed for deep-sea water-cooling, the hardware requirements of a condenser and a seawater pump as well as plant performance are similarly calculated.

In what follows, the evaluation method is explained first. Then numerical results are presented, including the seasonal performance of a conventional plant, that of an existing plant with deep-sea water application, and the hardware specifications and performance of a newly designed plant. Finally, some concluding remarks are made.

EVALUATION METHOD

Plant Model

A 600 MWe fossil thermal plant is selected as a reference plant for the evaluation. The numerical model was constructed using the commercial plant analysis codes, STEAM-Pro and STEAM-Master (Thermoflow, Inc., 1997). The former code allows us to create a numerical model of a plant based upon the user input data of each primary component, and to estimate plant performance under the design condition. The latter code permits us to compute the plant performance under off-design conditions.

Though all the plant component models are well described in the manual, the condenser model merits a more detailed explanation here since the heat transfer character of the condenser is important in evaluating plant performance in the present analysis. The overall heat transfer coefficient of the condenser is computed by the reciprocal of the sum of four thermal resistances, i.e., the internal water convection, tube wall conduction, fouling, and the external condensation. The heat transfer of internal waterside convection is computed by the Dittus-Boelter correlation:

$$Nu = 0.023 Re^{0.8} Pr^{0.4} \qquad (1)$$

where Nu is the Nusselt numer, Re the Reynolds number, and Pr the Prandtl number. The tube wall thermal resistance, R_{tube}, is given by the theoretical formula as,

$$R_{tube} = (d_o/2K) \, ln(d_o/d_i) \qquad (2)$$

where d_o and d_i are the outer and inner tube diameters, while K denotes the thermal conductivity of the tube material. The condenser fouling coefficient is specified by the user. The heat transfer due to external condensation, h_{steam}, is modeled by the scaled Nusselt correlation, which was originally derived for static laminar condensation:

$$h_{steam} = 0.728 C (g\rho^2 \kappa^3 H/\mu \, d_o \Delta T)^{0.25} \qquad (3)$$

where C: correction factor, g: gravitational constant, ρ: water density, κ: water thermal conductivity, H: latent heat of condensation, μ: water viscosity, ΔT: condensation temperature difference. The correction factor is introduced to take the effects of turbulent vapor shear into account, and is usually set between 1 and 1.5. Though the Fujii's correlation (Fujii, 1979) includes the effect of vapor flow, the scale Nusselt correlation is used in the code because the velocity profile in a condenser is unknown.

Environmental and Operational Conditions

The temperatures of deep-sea water and surface seawater also vary from site to site. Therefore, in the present calculation, three sites (Site-N, Site-C and Site-S) are selected from northern, central and southern Japan, where the deep-sea water temperatures are assumed to be 3°C, 5°C and 9°C, respectively. The seasonal variations in the surface seawater at the sites are shown in Figures 1 (a), (b) and (c) with the discharged seawater temperatures in a conventional plant which vary in accordance with the seawater temperature, since the temperature rise in a condenser is usually kept constant (7°C) in Japan.

The performance of an existing plant was evaluated under constant heat input conditions for each site. On the other hand, the performance of a newly designed plant was estimated under constant electricity output conditions. The hardware requirements were also examined for a seawater circulation pump and a condenser in the newly designed plant.
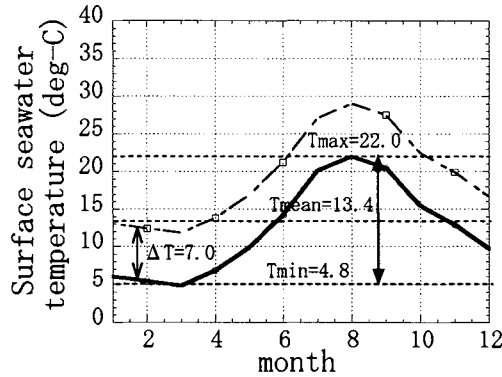
(a) Site-N
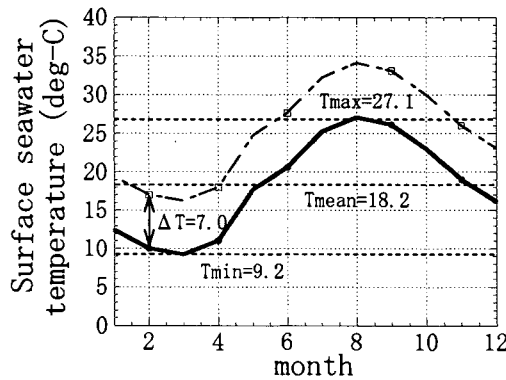
(b) Site-C
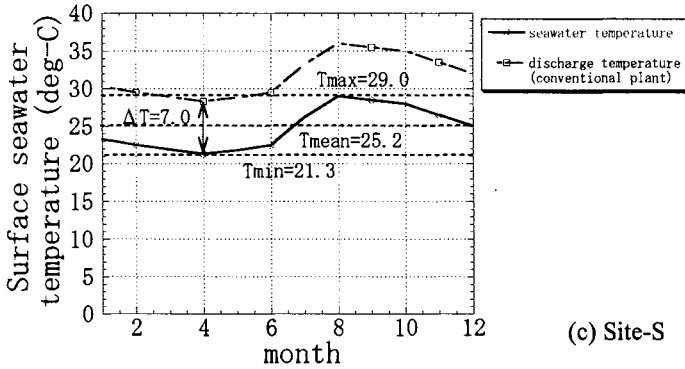
Figure 1. Seasonal temperature variation of surface seawater

NUMERICAL RESULTS

Performance of a Conventional Plant

The performance of a conventional plant varies seasonally depending on the seawater temperature. Figures 2 (a), (b) and (c) show monthly deviations in the electric power of a conventional plant located at Site-N, Site-C and Site-S, respectively, based upon the design electric power output. Poor performance, i.e., a deep dip in electric power output, can be found during summer in a plant at Site-N and Site-C due to the upsurge of seawater temperature in summer. The electric power output at Site-S is rather flat over all seasons due to fewer seasonal variations in seawater temperature.
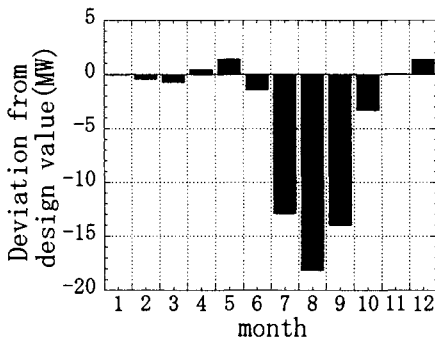
(a) Site-N
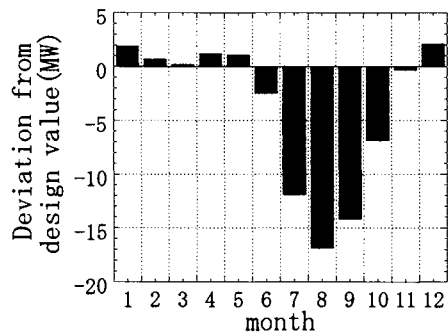
(b) Site-C
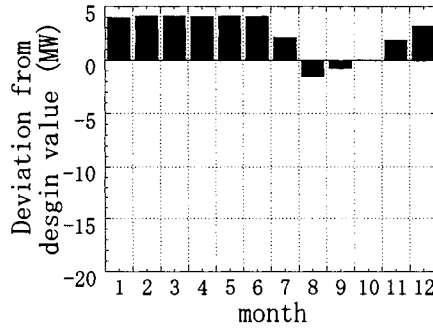
(c) Site-S

Figure 2. Monthly variation in electric power using surface seawater

Effect of deep-sea water usage in an existing plant

The effect of deep-sea water usage in an existing plant was examined, assuming that deep-sea water can be delivered using three parallel pipes of 5,000 m in length and 2.27 m in diameter. The temperatures of deep-sea water are assumed to be 3°C, 5°C and 9°C at Site-N, Site-C and Site-S, respectively. A key parameter, which has an impact on the performance of a deep-sea water plant, is the temperature rise of deep-sea water in a condenser. Therefore, the optimal value was analyzed by computing how performance varies with the temperature rise. Figures 3 (a), (b) and (c) depict the optimal temperature rises as 12.9°C, 15.6°C and 19.6°C at Site-N, Site-C and Site-S, respectively, and the corresponding discharge temperatures are 15.9°C, 20.6°C and 28.6°C. The flow rates of the deep-sea water are in almost inverse proportion to the temperature rise, being 1.13, 0.95 and 0.78 *million tons per day* at Site-N, Site-C and Site-S, respectively.

The reason why the electricity output has a peak as seen in Figure 3 is because the steam turbine blades are designed so that the exhaust loss is minimal for a specific steam velocity at the end of the turbine cascade. The steam velocity is obviously dependent on the back pressure of the turbine or the pressure in the condenser which is directly related to the steam temperature and, of course, to the rise in water temperature.
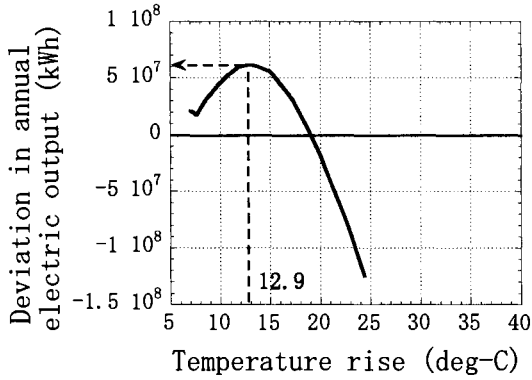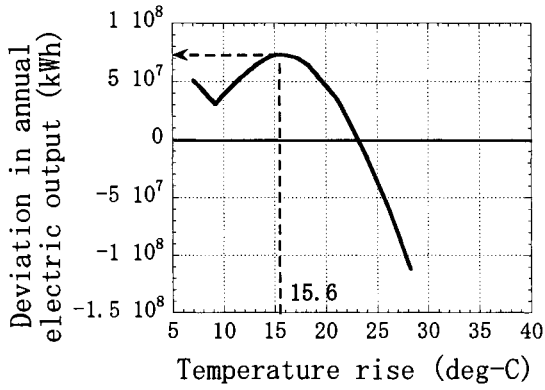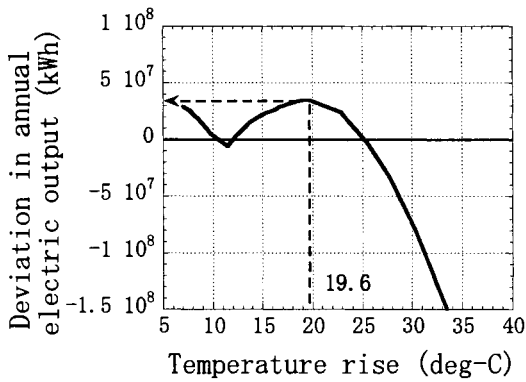
(a) Site-N

(b) Site-C

(c) Site-S

Figure 3.   Annual electrical output with full utility ratio (base: annual electrical output of a conventional plant using surface seawater)

The monthly deviations in electric power output of the deep-sea water plants at Site-N, Site-C and Site-S are shown in Figures 4 (a), (b) and (c), respectively, where the monthly electric power outputs of the conventional plants are used as the bases. The use of deep-seawater provides a gain of electric power over all seasons in comparison with a conventional plant, not only because the electric power outputs of the deep-sea water plants are constant over entire seasons, but because cold deep-sea water better heat sink for the condenser. The large gain in summer is explained by the comparatively poor performance of a conventional plant in summer. The results indicate that, for an existing power plant in central Japan, annual electric power output using deep-sea water possibly increases by 1.4% in comparison with a conventional operation using surface seawater. Especially in summer, the power generation is expected to improve by 3.5% at most in northern and central Japan.

(a) Site-N

(b) Site-C

(c) Site-S
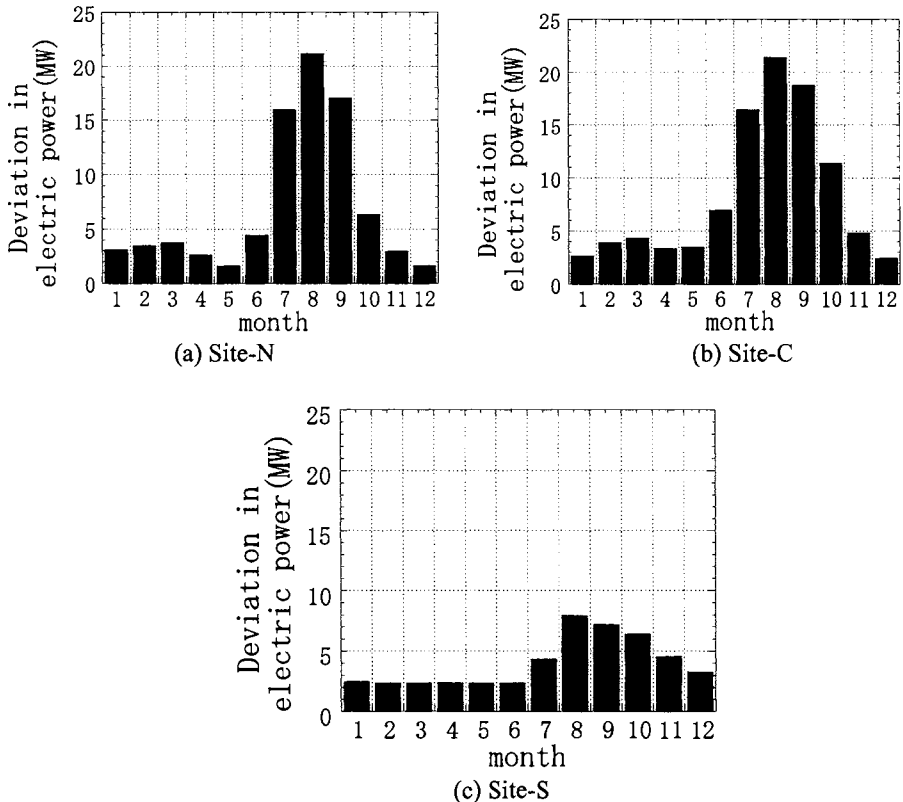
Figure 4. Monthly electrical power using deep-sea water (base: monthly power generation from a conventional plant using surface seawater)

Newly Designed Plants for Deep-sea Water Usage

In the previous section, deep-sea water usage in an existing plant was examined. In this section, we try to design a new plant suitable for the effective application of deep-sea water. Since the

seawater condition has a major impact on the condenser and pump designs, we restrict our design study to these components. The key design parameters of the condenser are the temperature rise in seawater, ΔT, and the steam temperature, T_s, both of which are so related that the discharge temperature of the seawater (original intake seawater temperature plus temperature rise) is lower than that of the steam temperature for a heat transfer from the steam side to the water side. In general, a larger heat transfer area of the condenser is required to realize a low steam temperature, because the temperature difference is then further reduced between the steam side and seawater side. On the other hand, a lower steam temperature tends to increase plant efficiency due to the larger steam pressure difference between the turbine inlet and outlet. Since the temperature rise is almost in inverse proportion to the flow rate of the seawater, it is obvious that any such rise has an impact on pump specifications and on the required electric power for intake. The effects of the two parameters are examined below, keeping the design net electric power at 600 MWe as a plant condition. Other conditions such as intake pipes and deep-sea water temperatures are the same as the previous ones.

Condenser and pump designs
Figure 5 shows the heat transfer area required for a new 600 MWe plant utilizing deep-sea water at Site-S. The results indicate that the condenser of the deep-sea water plant can be much smaller than that of the conventional plant, especially if the steam temperature is designed to be high and the temperature rise to be low. For example, the heat transfer area requirement can be reduced to as little as 30% of the present design under conditions of T_s= 38.5°C and ΔT= 7.0°C. Though the pump capacity requirement is 1.4 times larger at ΔT= 7.0°C, the results in Figure 6 indicate that the pump of the deep-sea water plant can be smaller than that of the conventional plant, if the temperature rise is designed to be larger. This is because the pump capacity required for the intake and discharge of deep-sea water is in inverse proportion to the temperature rise, being independent of the steam temperature.

The impacts of the temperature rise on the hardware requirements of the condenser and the pump are conflicting as seen in Figures 5 and 6, suggesting there is an optimal value to the temperature rise. A rough estimate indicates that the optimal temperature rise seems to fall between 10°C and 15°C. The impacts of the steam temperature on the hardware requirement of the condenser and the plant efficiency are expected to be conflicting also, since higher steam temperature tends to deteriorate the plant thermal efficiency. Such an effect of the steam temperature on the plant efficiency is examined in the next section.
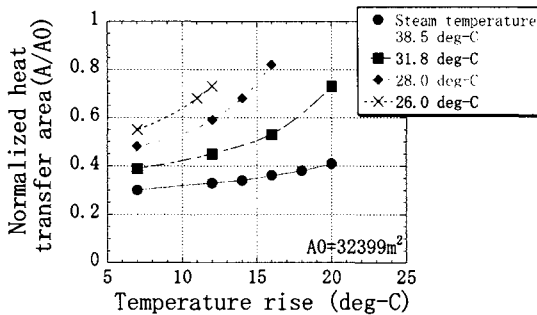

Figure 5. Required heat transfer area normalized by conventional plant value, A0
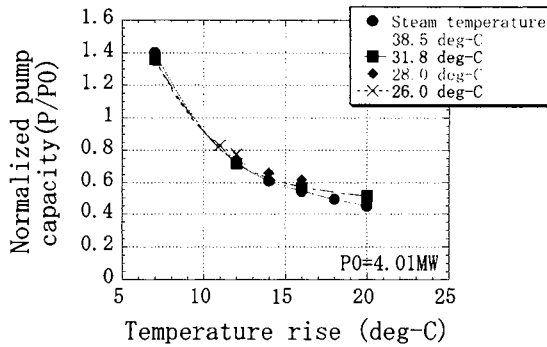
554

Figure 6. Required pump capacity normalized by conventional plant value, P0

Plant efficiency and economic feasibility

Since the design net electric power is kept at 600 MWe in the computation, the heat input requirement represents the reciprocal of the plant efficiency. Figure 7 shows the deviation in heat input from the conventional plant. The results suggest that a 3% saving in the heat input or fuel can be realized in the deep-sea water plant if a steam temperature of 26.0°C and a temperature rise of 12°C are adopted.

An evaluation of economic feasibility is impossible without a clear specification of the site conditions. In particular, the installation cost of the intake pipe for deep-sea water strongly depends on oceanographic factors such as wave and typhoon conditions. If the cost-savings of the condenser and pump compensate for the installation cost of the intake pipe for deep-sea water, the construction of a deep-sea water plant may be economically feasible. Further detailed study is needed for a concrete estimation, though that is not within the scope of the present study.
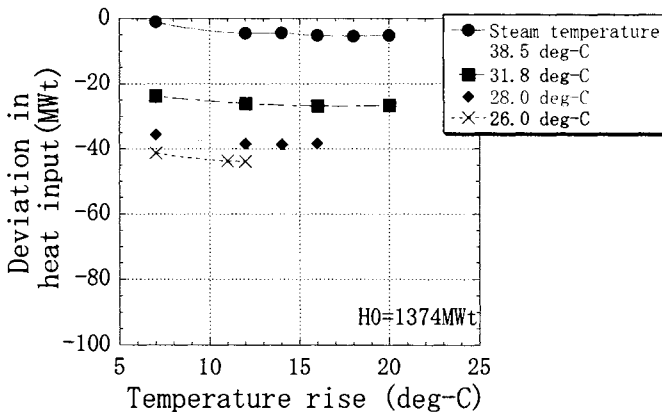
Figure 7. Heat input required for 600 *MWe* electrical output (base: H0=heat input of a conventional plant using surface seawater)

555

CONCLUSION

The present study shows the beneficial effects of deep-sea water on plant performance. In northern and central Japan, the use of deep-sea water seems effective in eliminating the dip in electric power generation during summer, which is a problem the conventional plants using surface seawater currently suffer from. In southern Japan, the use of deep-sea water seems effective in raising plant efficiency with a newly designed plant suitable for deep-sea water usage, because a cold heat sink is preferable for high plant performance. The use of deep-sea water in an existing plant in southern Japan did not prove very effective in that regard, because the seawater condition does not fit the condenser design which is optimized for a surface seawater condition, i.e., a much higher seawater temperature.

Perceived concerns about deep-sea water usage include biological and chemical issues, and the possible adverse effect of cold deep-sea water discharge, which can be lower than that of the environmental seawater temperature during summer. The unusual transport phenomena of such thermal flows may be of interest to fluid engineers and scientists.

REFERENCES

Cooper, W.H. 1996. Experimental Determination of Steam and Water Side Flows and Heat Transfer of a Surface Power Condenser. Master's thesis, The University of New Brunswick.

Fujii, T. 1979. Condensation of Steam on a Horizontal Tube --- The Influence of On-coming Velocity and Thermal Condition at the Tube Wall. In *Proceedings of the 18th US National Heat Transfer Conference*, 35-43, San Diego.

Thermoflow, Inc. 1997. STEAM Pro/Master manual.

Tsou, J.L. 1991. Condenser Performance Prediction Calculation Procedure. In *Proceedings of the American Power Conference*, 844-847, Chicago.

THE ADVANTAGE OF OTEC AS THE ENERGY SOURCE
FOR THE OCEAN NUTRIENT ENHANCER

Takayuki Watanabe[1], Kazuyuki Ouchi[2], Toshio Yamatogi[3] and Sadayuki Jitsuhara[4]

[1]Engineering Department, Xenesys, Inc.
Tokyo, JAPAN
watanabe@xenesys.com

[2]Ouchi Ocean Consultant, Inc.
Nagano, JAPAN

[3]Nakashima Propeller Co. Ltd.
Okayama, JAPAN

[4]Engineering Department, Xenesys, Inc.
Tokyo, JAPAN
watanabe@xenesys.com

ABSTRACT

For fertilizing the ocean by increasing primary production, the ocean nutrient enhancer (ONE) which pumps up the nutrient-rich deep ocean water (DOW) and discharges it into the euphotic zone has been studied. For establishing the entire concept of ONE, various requisite technologies have been evaluated because it is a completely new type of system that we have never had before. This paper focuses on the energy source for the ONE, which is one of the essentials for establishing the ONE.

According to feasibility studies, ocean thermal energy conversion (OTEC) has been chosen as the most suitable energy source for the ONE. The use of OTEC enables us not only to use low temperature of DOW, but also to adopt submerged floating structure which could stand for the rough sea conditions. Then actual possible field operation of the ONE was tested by simulating the conditions off the north of Okinawa in Japan, and has come out conclusion producing much more than enough electricity for pumping up the DOW for the ONE.

INTRODUCTION

Upwelling of deep ocean water (DOW), which contains rich nutrients such as nitrogen, phosphorus, etc. can fertilize the sea, because the poor nutrient conditions in the euphotic zone of the stratified sea can be improved and phytoplankton production can be enhanced. Actual fishing ground naturally developed in waters off Peru is one of the examples of the DOW upwelling area. Many experts are pointing out that sea can be fertilized by upwelling DOW artificially (Ryther, 1969), and this is one of possible solutions for overcoming food shortage in the future.

Marino-Forum 21, the subsidiary of the Fisheries Agency of Japan, awaited a research fund and organized the research and development project to design and test an ocean nutrient enhancer (ONE) which pumps up DOW, discharges it into the euphotic zone for the purpose to enhance primary production of the sea. The project has been started in April 2000 for five years.

The following four requisite technologies have been focused for establishing the ONE.
①How to pump up DOW and to discharge it into the euphotic zone.
②To find out a suitable energy source for pumping up and discharging DOW.
③ To design configuration of floating structure and riser pipe to stand against rough sea conditions in open ocean.
④ How to set up the system in the sea.

Regarding for the subject ① , density current generator was applied for discharging and plunging DOW horizontally into a certain layer of stratified water as density current (Ouchi et al., 1998). The concept and outline of the ONE operated by density current generator is shown schematically in Figure 1.

This concept has such advantages that intentional mixing of DOW with surface water makes density current which could stay in a certain layer in the euphotic zone (Ouchi, 1999). A prototype of density current generator is now operating in Gokasyo Bay, Mie Prefecture, 150 km of the south of Nagoya in Japan.
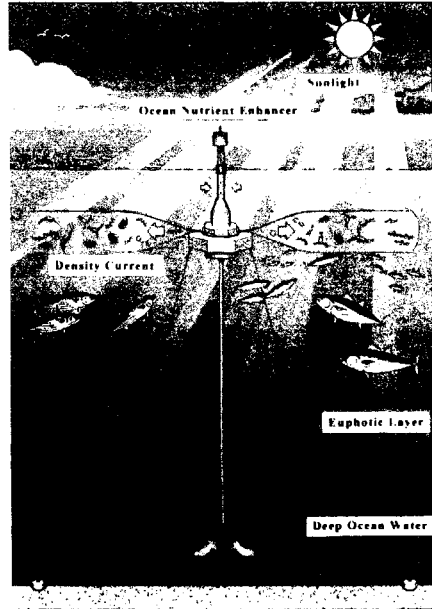
Figure 1. Schematic Design of the ocean nutrient enhancer

For establishing the ONE, it is essential to be reliable, low cost, easy maintenance, and highly efficient, and feasibility studies focusing on the subject ② and ③ are particularly essential. Choice of an energy source has a great impact on the entire design because it affects the configuration of the floating structure.

In this paper, an advantage of ocean thermal energy conversion (OTEC) for the energy source of the ONE is shown based on feasibility studies under considerations of various energy sources and a combined system of the ONE and OTEC is proposed.   Finally, the application of combined ONE operated by OTEC system was tested by simulation for the case waters off the north of Okinawa main island, and has come out a conclusion that this system can generate much more than sufficient electricity for pumping up DOW throughout the year.

FEASIBILITY STUDIES ON VARIOUS ENERGY SOURCES FOR THE ONE

The ONE is set in the open ocean far from the shore because DOW is pumped up from depth more than 300m.   Therefore, renewable energy available at site seems more competitive rather than conventional energy sources such as shore-based electric power, diesel engine, etc. Feasibility of various energy sources was evaluated under the following; for the next three cases, DOW is pumped up from 300 m depths and the location of the ONE is ten miles from the shore.

Case 1. Pumping DOW of $10^4 m^3$/day with riser pipe of 0.32m diameter, impeller diameter of 0.9 m, shaft power of 5 kw

Case 2. Pumping DOW of 10^5m^3/day with riser pipe of 1.0m diameter, impeller diameter of
    2.8 m, shaft power of 45 kw
Case 3. Pumping DOW of 10^6m^3/day with riser pipe of 3.2m diameter, impeller diameter of
    8.8 m, shaft power of 400 kw

Photovoltaics, wind, wave, OTEC, diesel, and shore-based electric power were evaluated as
possible energy source (Ouchi, 2001). The following points were particularly concerned;
maximum output power of system, system size, initial cost, running cost, total cost for ten
years operation, practicality level, suitable floating structure, and cost of floating structure.
Table 1 shows the summary, which includes analyses of two OTEC systems such as Rankine
cycle and Uehara cycle.

From this study, in terms of the total cost, which includes initial ten years running cost, wind
turbine, OTEC, and diesel engine were short-listed as the most feasible energy supply system
for the ONE.

Table 1. Summary of various energy supply systems for the ocean nutrient enhancer

Item		Unit	Photovoltaics			Wind			Wave			OTEC (Rankine) Uehara			Diesel			Shore-based electric power		
A	Amount of DOW to pump up	m3/day	0.4	10	100	1	10	100	1	10	100	1	10	100	1	10	100	1	10	100
B	Required power	kw	5	45	400	5	45	400	5	45	400	5	45	400	5	45	400	5	45	400
C	Required energy (kwh)	kwh/day	120	1080	9600	130	1080	9600	120	1080	9600	120	980	9600	120	1080	9600	120	1080	9600
	Max. Power output for the system	kw	45	400	3600	20	70	470	6	60	470	8	70	620	10	60	600	10	75	500
D	Assumption for the above calculation		Diameter of suriance 3.8m Conversion efficiency 0.12 Correction coefficient 0.3			Ave wind speed 5m/s Horizontal axis type			Significant wave height 1m Ave wave period 7 Heads turbine type			Temperature difference 20 C Net power in use 6% Titanium plate heat exchanger			2 sets 1set complete spare			Distance about 12 miles 3phase 3 line seal type power Reinforced cable $120/m		
E	System size: area	m2	370	3,350	29,800	1,000	2,000	5,000	780	4,000	28,000	10 8.5 20 17		60 51	56	90	210	30	30	40
	Weight	ton	9	80	720	30	74	120	1,000	3,590	24,500	3.25 20 17		80 88	2	13	23	1	3	6
F	Initial cost	10^6 US$	0.5	4.0	36.0	0.5	1.0	5.9	4.0	7.8	54.6	0.4 0.11 0.17		4.6	0.1	0.1	1.2	9.6	9.4	12.6
	Unit price for the above calculation	10^3 US$/kw	10	10	10	24	14	14	660	130	130	50	16	12	3.2	1.2	1.0	860	125	25.2
G	Running cost through 10 years	10^6 US$	0.1	0.2	0.3	0.2	0.3	0.5	0.2	0.3	0.8	0.2	0.3	0.5	1.0	2.2	7.9	0.3	0.6	3.6
	Bunker Lub oil Electric power	10^6 US$	0.0	0.0	0.0	0.0	0.0	0.0	0.0	0.0	0.0	0.0	0.0	0.0	0.3	1.7	6.6	0.1	0.4	3.4
	Manning Transportation	10^6 US$	0.0	0.0	0.0	0.0	0.0	0.0	0.0	0.0	0.0	0.0	0.0	0.0	0.2	0.2	0.7	0.0	0.0	0.0
	Maintenance	10^6 US$	0.1	0.2	0.3	0.2	0.3	0.5	0.2	0.3	0.8	0.2	0.3	0.5	0.5	0.8	1.1	0.7	0.7	0.2
H	Total cost F+G	10^6 US$	0.6	4.2	36.3	0.7	1.3	6.4	4.2	8.1	55.4	0.6	1.4	7.9	1.1	2.3	9.1	10.9	12.3	19.9
I	Practicality OO Plactical, O Actual experience, X No experience		OO	O	O	OO	OO	OO	O	x	x	O	O	O	OO	OO	OO	OO	OO	OO
J	Remarks Comments		Storage battery required Bigger output in summer Renewable energy.			Storage battery required Less output in summer Renewable enegy			Including air chamber in the frost Less output in summer Renewable energy.			temperature difference 15 C Renewable energy			FO price $380 kl Heavy A FO transport $15,000 year			Elec power price $0.1 kwh $570 kl light oil		
K	Suitable floating structure		Float of huge area			Float of huge area			Float of huge area			Buoy Spar			Buoy Spar			Buoy Spar		
L	Cost of floating structure		Large			Large			Large			Small			Small			Small		

EVALUATION OF THE ENERGY SUPPLY SYSTEM

The ONE is planned to be operated in Sagami Bay, Kanagawa, Japan, where there was a
counterclockwise surface voltex current often observed (Iwata et al., 1989). The voltex
current could help not to dilute nutrients supplied by DOW so quickly before enhancing
primary productivity in the euphotic zone, and this is the main reason to choose this site.
Pumping capacity of DOW is planned to be 500,000m^3/day from the depth of 450m.

Three energy systems such as wind turbine, OTEC, diesel engine, were then further evaluated
from the point of practicality in the ocean, initial cost, total life cost, float and mooring cost,
influence on environment, use of DOW property, adaptability in Sagami Bay, and scalability
to a large system (Ouchi, 2001). Table 2 shows the comparison of the evaluation of three
technologies. From this study, it is concluded that OTEC is the most feasible for the engine
of the ONE. The output of OTEC engine is affected by the vertical temperature distribution,

and the required power for pumping up DOW is affected by the vertical density distribution, so that the engine system of ONE should be designed according to these water quality data.

Table 2. Evaluation of energy system for the ocean nutrient enhancer ⊚:Good, ○:Fair, △:Poor

Items	Energy sources		
	Wind	OTEC	Diesel
Practicality in the ocean	○	○	⊚
Initial cost advantage	○	○	⊚
Total life cost advantage	○	○	△
Float and mooring cost advantage	△	⊚	⊚
Influence on environment	⊚	⊚	△
Utilization of DOW property	△	⊚	△
Adaptability in Sagami Bay	○	○	○
Scalability to large system	△	⊚	⊚
Overall evaluation	△	⊚	○

INITIAL DESIGN OF ENGINE SYSTEM
FOR THE OCEAN NUTRIENT ENHANCER

The components and arrangement of OTEC engine system is schematically shown in Figure 2 (Ouchi, 1999). Evaporators and condensers of plate type heat exchanger made by titanium closed piping system of ammonia, as the working fluid, and turbine with electric generator are the main components of the OTEC engine part of the ONE.
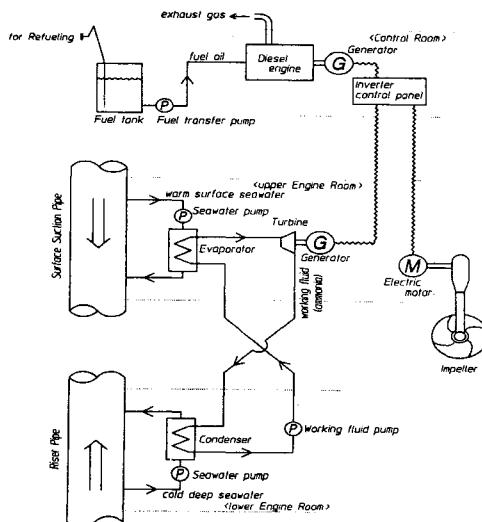
Figure 2. Schematic diagram of OTEC engine system

560

Figure 3 shows OTEC system in detail based on Uehara cycle, which is much more advanced system than Rankine cycle. The working fluid, which is the mixture of ammonia and water, is fed into evaporator to be warmed up by the warm surface seawater. After the working fluid evaporates, the vapor drives turbine 1 and triggers generator 1. One to five percent of the vapor in turbine 1 is diverted into heater, which warms up the working fluid arriving from tank 1, while the rest generates turbine 2. Finally, the vapor is routed to condenser to be cool off and condensed by deep cold seawater. At this stage, OTEC cycle is repeated from the beginning.
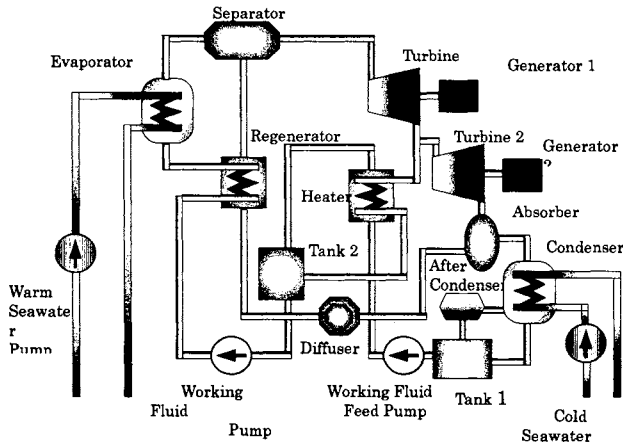
Figure 3. Schematic diagram of Uehara Cycle

Generally, Uehara cycle can attain a 30 to 50% higher efficiency compared with Rankine cycle. Moreover, due to more efficient plate heat exchangers developed by Saga University, the power consumption of pumps for cold and warm seawater can decrease to 30 to 40% of the conventional case. As shown in Table 1, regarding the same gross electric power output planed, the net power of Uehara cycle increase to 75% compared with 65% of Rankine cycle in case of 20°C temperature difference between warm seawater and cold one.

OTEC engine is probably ideal for the ONE. However, an auxiliary diesel engine, which is convenient and reliable, is needed in order to assist the OTEC engine for starting the OTEC engine and maintaining DOW pumping capacity when the OTEC output decreases due to insufficient temperature difference between DOW and surface water. Figure 2 also shows the schematic diagram of the entire engine system of the ONE.

Followed by the choice of OTEC and Diesel as a energy supply system, configuration of the floating structure was studied to be fitted with the engine, impeller pump, riser pipe, and discharge nozzle systems under considerations of severe sea condition at the center of Sagami Bay where there is 10 m significant wave height, 14 second average wave period, 50m/s wind velocity and 1.6 knot surface current. The ONE has then been designed with minimum small areas of water plane and the project above the water line, which resulted in little motion of the floating structure decreased riser pipe design scantling (Ogiwara et al., 2001). The principal characteristics of the ONE system designed for Sagami Bay is shown as Table 3 (Ouchi et al., 2001).

Table 3. The principal characteristics of the ONE system designed for Sagami Bay

Total height	470m	Depth of discharge nozzle	30m
Maximum breadth	30m	Diameter of impeller	6.1m
Draft (During operation)	450m	Motor capacity for impeller	80kw
Draft (During maintenance)	420m	Main engine (OTEC)	100kw
Displacement (During operation)	5,800t	Auxiliary engine (Diesel)	100kw
Diameter of riser pipe	2.50m	DOW rising capacity (m³/day)	500,000
Diameter of surface suction pipe	2.86m	Surface suction capacity (m³/day)	750,000
Diameter of discharge ring nozzle * slit clearance	25m*0.7m	Discharge capacity (m³/day)	1,250,000

APPLICATION OF COMBINED SYSTEM OF ONE OPERATED BY OTEC POWER IN CASE WATERS OFF THE NORTH OF OKINAWA MAIN ISLAND

The combined system of ONE operated by OTEC power has then been checked its operation in case waters off the north of Okinawa main island in Japan. Okinawa island locates in the subtropical area where is one of the suitable areas along Japan for OTEC, due to relatively higher temperature of the surface throughout the year. Figure 4 shows vertical temperature profile in waters off the north of Okinawa main island. Surface seawater temperature reached 28.5°C in summer and 21.0 °C in winter, while deep seawater temperature is almost constant at 5°C on average.
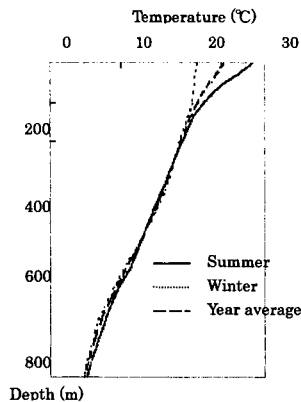
Figure 4. Temperature profile in waters off the north of Okinawa

It is assumed that DOW pumped up by the same ONE system as Sagami Bay is used for the present OTEC test simulation. In summer, which provides a temperature deference of 23℃ between the surface water and DOW, the OTEC system generates 5.1 MW electric power using 500,000 m3/day of DOW. In this temperature condition, net electricity production of OTEC increases up to 80%, so that this OTEC can provide 4.1 MW electric power for other uses than for the ONE. This surplus electric power can be used direct electricity use through the electric transmission by undersea cables, etc. It means that this combined system of the ONE operated by OTEC generates more electricity than needed for the ONE.

562

CONSIDERING SEASONAL CHANGES OF OTEC OUTPUTS

OTEC output is influenced by the temperature difference between surface and deep seawater, so that there are seasonal changes of OTEC outputs. Then it was evaluated in case waters off the north of Okinawa's main island (Fig. 5). Gross output of OTEC varies from 5.1 MW in summer to 2.8 MW in winter which is provided by temperature deference of 16° Celsius.
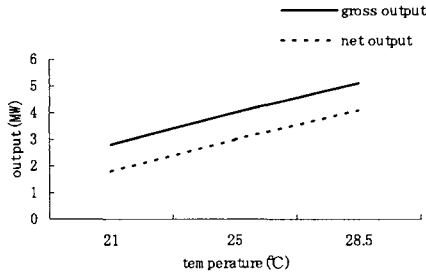
Figure 5. The output of electricity generated by OTEC due to changes in sea surface water temperature

This seasonal change is due to the change of surface water temperatures, which occurs every year, so that this change is easily predictable. Consequently, with a solid plan for electricity use in an every season, the electric power from OTEC could be used in the best way.

SUMMARY

Ocean Nutrient Enhancer (ONE for short) for creating a fishing ground by pumping up deep ocean water (DOW) in the open ocean is proposed.

By feasibility studies concerning various kind of energy supply source for the main engine system of the ONE, OTEC is found to be the most feasible.

A design of ONE applied with an OTEC / Diesel hybrid system is proposed for the project to be operated in Sagami Bay.

A simulating case study for the combined ONE and OTEC system in waters off the north of Okinawa main island suggests for producing enough electricity power.

Possible influences of seasonal change of surface water temperature on the output of OTEC are evaluated.

REFERENCES

Iwata, S. and M. Matsuyama. 1989. Surface circulation in Sagami Bay -the response to variations of the Kuroshio axis-, *Journal of the Oceanographical Society of Japan*. Vol. 45.

Kobayashi, H., S. Jitsuhara and H. Uehara. 2001. The present status and features of OTEC and recent aspects of thermal energy conversion technologies.

Ogiwara, S., Y. Awashima, H. Miyabe and K. Ouchi. 2001. Conceptual design of a deep ocean water upwelling structure for development of fisheries, Proc. of the ISOPE / OMS'01.

Ouchi, K. and H. Nakahara. 1999. A proposal of the deep ocean water upwelling machine using density current, Proc. of the ISOPE / OMS'99.

Ouchi, K., T. Yamatogi, K. Kobayashi and M. Nakamura. 1998. Density current generator -A new concept machine for agitating and upwelling a stratified water area-, Proc. of Ocean Community Conference '98 Baltimore USA, MTS.

Ouchi, K., T. Yamatogi and S. Jitsuhara. 2001. A feasibility study on the energy source for the ocean nutrient enhancer, Proc. of The Fourth (2001) Ocean Mining Symposium, Sept. 2001

Ryther, J.H., 1969. Photosynthesis and Fish Production in the Sea. *Science* Vol.166.

RECREATIONAL BOATS AND SUBMERGED MARINE DEBRIS IN SYDNEY HARBOUR, AUSTRALIA

Walter Martin Widmer

Centre for Research on Ecological Impacts of Coastal Cities – The University of Sydney
Sydney, New South Wales, AUSTRALIA
wwidmer@bio.usyd.edu.au

ABSTRACT

Although land-based activities are considered to be the main source of marine debris in coastal areas, marine-based sources may also be significant. This study tested the hypothesis that recreational boating is a contributing source of submerged marine debris. This was done by collecting information about the number of recreational boats anchored at six beaches in Sydney Harbour and the amount of benthic debris off these beaches. A significant positive correlation was found. The greatest amount of debris was found adjacent to the two beaches most visited by recreational boats, both situated inside a marine protected area. The most frequent types of litter were plastic bags, aluminium cans and glass bottles. Implications of these results to management and restoration attempts of littered areas are discussed.

INTRODUCTION

Marine debris is being increasingly recognised as a serious type of pollution (Stefatos et al., 1999) and the detrimental consequences of such debris have been widely documented. Marine debris represents a threat to an array of organisms, including turtles, mammals, birds and fish (Laist, 1987). Fouling invertebrates may also use marine litter as habitat, which may represent a new ecological niche for some species (Winston, 1982). Litter can also be a vector of transportation, with potential implications for the geographic distribution of some species (Gregory 1991; Barnes 2002). For humans, marine debris may be harmful (Dixon and Dixon, 1981) and is aesthetically repulsive (Williams and Nelson, 1997), which may have undesired consequences for areas where the local economy is based on tourism (Corbin and Singh, 1993).

Most studies about marine debris have been done on beaches or in pelagic environments (e.g. Frost and Cullen, 1997). Studies focussed on the presence of litter on the seabed were presented by Galil et al. (1995) and Stefatos et al. (1999), among others. Williams et al. (1993) and Backhurst and Cole (2000) have investigated benthic litter in sublitoral areas.

Although land-based activities are considered to be the main source of marine litter in coastal areas (Nollkaemper, 1994), marine-based sources may also be significant (Prutter, 1987). Among several marine-based activities, recreational boating has been suggested as having, in some cases, a significant role as a source of marine debris (Cahoon, 1990; Backhurst and Cole, 2000). Sydney Harbour (33° 50' S, 151° 16' E) is one of the main areas for recreational boating

in the southern hemisphere, with approximately 40 marinas and 35,000 recreational boats (Underwood and Chapman, 1999; DUAP, 1999).

Within the harbour, on its northern sector, lies the North Harbour Aquatic Reserve (NHAR). In the Australian State of New South Wales, aquatic reserves were designed to protect fish, habitats for fish, biodiversity and marine invertebrates (Fisheries, 1999). The NHAR was created in 1982 and, because it still lacks a formal plan of management (Bohm, 2000), its official aims are not clear. A placard located on the foreshore of the reserve says that *"divers and snorkellers are encouraged to enjoy the natural beauty of the reserve"*. Therefore, it seems reasonable to assume that the aims of the NHAR include protection of marine biota and the provision of a rewarding experience for visitors. Some of the beaches inside the reserve (Quarantine beach and Store beach) have been suggested as being popular anchorages for recreational boaters (Mathews, 1997). Considering the detrimental consequences of debris in marine environments, it is reasonable to consider that the presence of anthropogenic benthic litter in a reserve would be contrary to its conservational objectives.

Therefore, the aim of this study was to investigate the potential relationship between recreational boating and the amount of submerged litter inside the NHAR, by studying the anchoring patterns of recreational craft and the quantities of benthic litter off six beaches located in Sydney Harbour. Specifically, the following hypotheses were tested:

(i) Previous observations and literature (Mathews, 1997) suggest that some areas are preferred for anchoring when compared to others. The model proposed is that two beaches inside the NHAR (Quarantine beach and Store beach) are more used as an anchoring ground for recreational boats than are other beaches located inside (Reef beach and Washaway beach) and outside (Lady Bay beach and Obelisk beach) the reserve (Fig. 1). Therefore, if the number of recreational boats anchored in these beaches were counted, more boats would be expected to be anchored at the first two beaches than at the last four.

(ii) Literature evidence suggests that recreational boating may contribute to the presence of submerged litter in marine habitats (Cahoon, 1990; Backhurst and Cole, 2000). The model proposed is that this pattern is valid for the six beaches chosen for this study. Therefore, if the number of litter items in these beaches were representatively counted, a positive correlation between the mean number of anchored boats and the mean amount of debris items would be expected.

METHODS

Data on anchored boats

Three independent measurements were taken for each beach from vantage points during weekends in the austral summer of the year 2001 - December 2000 to March 2001, because previous observations indicated a significant increase in recreational boating during weekends. The independence of the data was obtained by taking only one replicate measurement per day. To avoid within-day variability, all measurements in a given month were taken during the mid-afternoon, defined as at three quarters of the time span between sunrise and sunset for the 15th

day of that month. Anchored boats were counted from vantage points using binoculars and classified into three categories, according to Adam et al.'s (1992) definitions of recreational boats: speed boats, motor cruisers and sailing yachts.

A few stranded craft on the beach, such as jet skis, rowing boats and sailing dinghies were not included, because they were not anchored. Commercial boats (identified by distinctive characteristics on the hull or on the rigging) were also not abundant and were not included, because this study is focused on recreational boating.

Data on marine debris

Benthic litter present off the six beaches was collected using a constant amount of search effort across beaches. Ten transects (10x4 m) were swum perpendicular to the beach (approximately at the 3 meter isobar) and distributed along the entire length of each beach. All visible submerged litter items along the transects were collected. The material was kept inside plastic bags and brought to the laboratory, where they were counted (e.g. Willoughby et al., 1997) and sorted into the following categories: plastic, metal, glass, paper and others.

Statistical treatment

Three types of beaches were defined, according to the proposed level of boat anchoring and their location. Quarantine beach and Store beach were labelled 'heavy anchoring – inside NHAR'; Reef beach and Washaway beach were labelled 'light anchoring – inside NHAR' and Obelisk beach and Lady bay beach were labelled 'light anchoring – outside NHAR'.

Mean numbers of anchored boats on the three types of beaches were compared using analysis of variance. The first, fixed factor was type of beach (with three levels); the second factor was replicate beaches (nested in the first factor and random). The homogeneity of variances was assured by appropriate transformations of data, if necessary. When a factor was found to be significant, Student-Newman-Keuls (SNK) tests were done to test differences between levels within that factor.

The significance of an eventual correlation between the number of anchored boats and the amount of marine debris was tested using Pearson's correlation index r.

Confounding sources of debris

The possibility that the litter found would originally come from sources other than recreational boats is considered to be small, because the six beaches were chosen in a way that their foreshores are protected by a national park (Sydney Harbour National Park, see Fig. 1), without residential developments and with restricted access from the land (only walking tracks, no car access). The beaches that were labelled 'heavy anchoring – inside NHAR' are particularly restricted for access other than by boat (only scheduled guided tours run by the National Parks and Wildlife Service for Quarantine beach and no walking tracks to Store beach).

567

Another possibility is that the litter found in a certain place might have been dumped elsewhere and transported to where it was collected by water currents. This is considered to be unlikely for material that will submerge rapidly as opposed to floating litter and it is reasonable to assume that any litter floating into the sites would represent similar amounts at the six beaches studied.
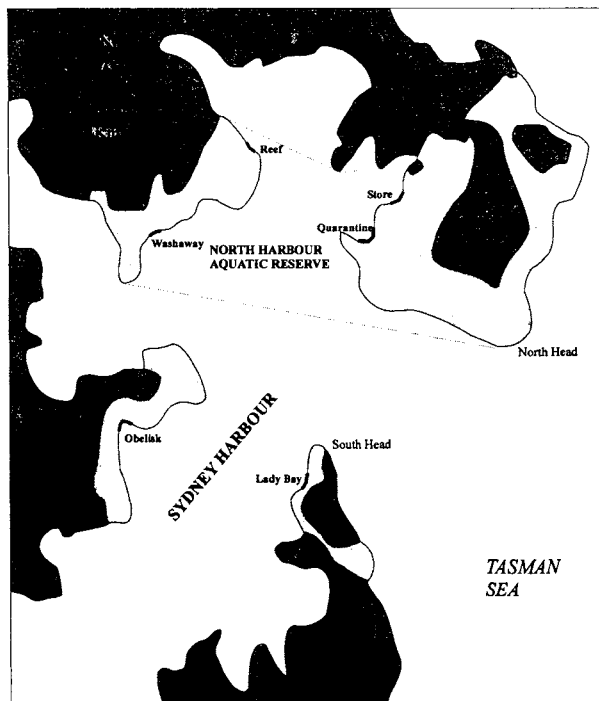
Figure 1. The entrance to Sydney Harbour, showing North Harbour Aquatic Reserve and the location of the six beaches used in this study (Light grey areas represent relevant parts of Sydney Harbour National Park)

RESULTS

Anchoring patterns

Store beach and Quarantine beach had 23.5 (± S.E. = 3) boats per beach, significantly more than the other two beaches inside the NHAR (1.16 ± 0.3 boats.beach[-1]), which had similar numbers of anchored boats compared to the two beaches outside the reserve (2.8 ± 1 boats.beach[-1]), as seen in Table 1 and Figure 2a. There was an average of 11.5 ± 1.4 sailing yachts and 9.8 ± 2.1 motor cruisers anchored at each of Quarantine and Store beach. The average number of speedboats in each of these two beaches was smaller (2.1 ± 0.4), as seen in Figure 2b.

Table 1: Analysis of variance of the mean number of anchored boats among beaches. Data were square root transformed to homogenise variances. Cochran's C = 0.57 after transformation, $P >$ 0.05. Untransformed data are presented in Figure 2a

Source of variation	DF	MS	F	P
Anchoring pattern	2	21.29	19.03	< 0.05
Beach (nested in anchoring pattern)	3	1.11	5.4	< 0.05
Residual	12	0.20		
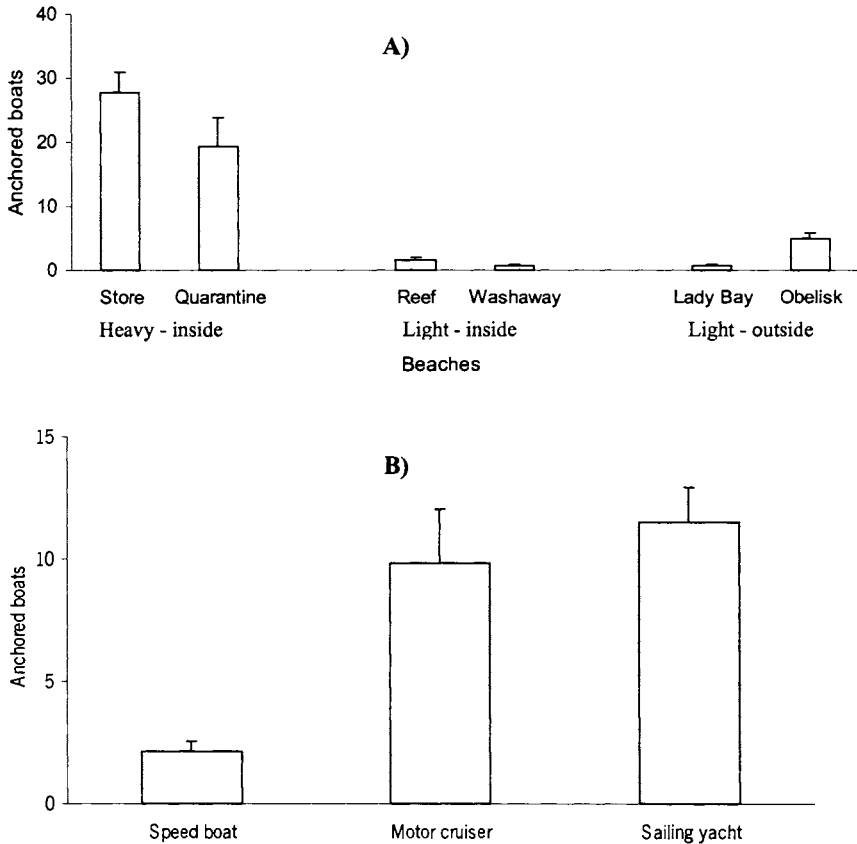
Figure 2. (a) Mean (+ S.E.) numbers of recreational boats anchored off the six beaches studied; (b) Mean (+ S.E.) numbers of different types of recreational boats anchored off Quarantine and Store beaches

Submerged debris

A total of 227 litter items were collected from the six beaches, representing an overall mean of 0.095 litter items per m^2 of seafloor. Plastic items accounted for almost half of all debris collected, followed by glass, metal and paper (Fig. 3). The majority of plastic items were supermarket-like plastic bags and the majority of the glass items were bottles for alcoholic drinks, such as beer, wine and sparkling wine (Fig. 4).

Large mean numbers of debris items.m^{-2} were found in waters adjacent to beaches associated with large mean numbers of anchored recreational boats (Fig. 5). This positive correlation was statistically significant (Pearson's $r = 0.96$, 4 df, $P < 0.01$).
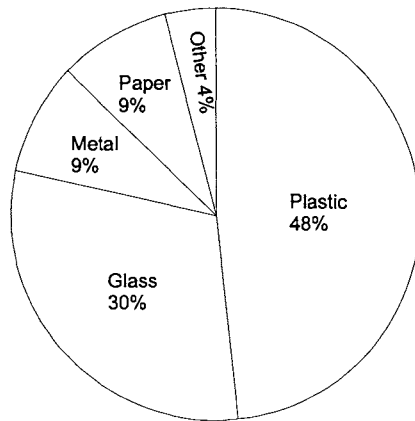
Figure 3. Proportion of types of debris items found on the seafloor off the beaches studied
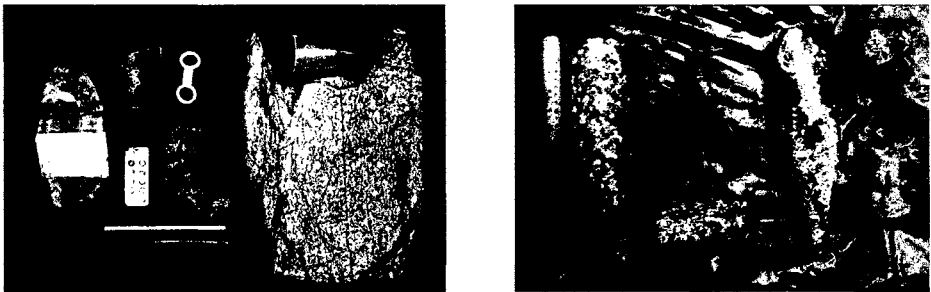
Figure 4. Examples of submerged marine debris found off the surveyed beaches. Left: selected plastic items; right: selected glass items. A 30 cm metallic ruler was added for scale reference
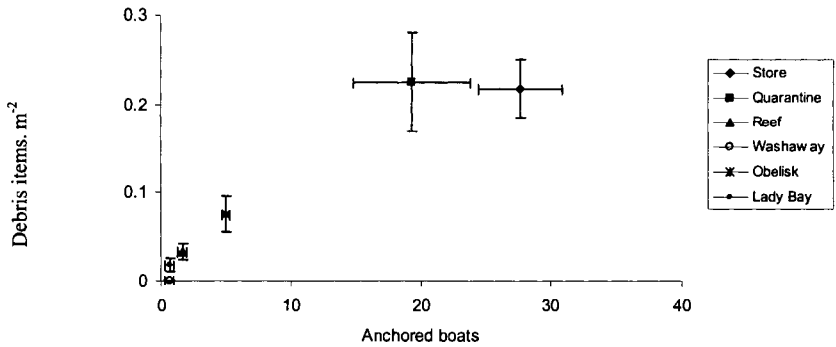
Figure 5. Relationship between the amount of submerged debris and the number of recreational boats anchored on the waters adjacent to the beaches studied. Plots represent mean ± S.E

DISCUSSION

This study showed that two beaches inside the NHAR (Quarantine beach and Store beach) support regularly large numbers of anchored boats, confirming the status of these areas as popular anchorages for recreational boats in Sydney Harbour. This finding is important because it provides unprecedented quantitative information about anchoring patterns within NHAR. Furthermore, it sets recreational boating as a major human activity in this aquatic reserve. Possible explanations for the popularity of these beaches among the boating community are their pristine character and the difficulty of access (for non-boaters).

The significant correlation between the number of anchored boats and the amount of debris items found in waters adjacent to the beaches where these boats were anchored does not demonstrate, by itself, a causal relationship between boating and littering. Because experimental manipulation of anchoring areas for recreational boats is a rare option, correlative analyses remain one of the best available approaches to identify contributing sources of marine debris. Considering that access other than by boat to these beaches (particularly to Quarantine and Store beach) is restricted coupled with the low level of residential development on the foreshores of these beaches, it is reasonable to consider that anchored boats contributed substantially to the amount of submerged debris found.

Two other aspects seem to support this idea. Anchored motor cruisers and sailing yachts were more abundant than speedboats. Cruisers and yachts normally have internal cabins (typically with a table, a stove, a refrigerator and cabinets) and it is conceivable that they can carry more goods aboard (and therefore more potential litter) than open-deck speedboats. In addition, it is probable that plastic bags and glass bottles, which were the litter items most commonly found, are part of the normal set of items aboard recreational boats. The majority of marine debris originated from anchored boats was probably dropped into the sea unintentionally, because

recreational boaters are considered to be reasonably sensitive to environmental issues (Gregory, 1991).

Previous research suggested that recreational boating is not publicly perceived as a significant cause of environmental disturbances to Sydney Harbour (Widmer et al., 2002). Indeed, it seems that recreational boating is not a main source of marine debris, when compared to other human activities. However, this study indicated that this leisure activity (when practiced intensely) can contribute locally to the amounts of submerged marine debris, particularly in areas where access by land is restricted. Because the methodology used here is inexpensive, further investigations of the role of recreational boating as a contributing source of marine debris can be performed in a wide range of locations where recreational boating is intense and where access to expensive technologies is limited (e.g. some Caribbean and South Pacific island-nations).

Of particular concern is the large number of glass bottles found on the seafloor of Store and Quarantine beaches. This material poses a potential risk for the health of the visitors of the reserve. Ecologically, marine debris has potential adverse effects that do not contribute to the conservation objective of the North Harbour Aquatic Reserve. The hypothesis that submerged marine debris provides novel habitat for biological fouling assemblages was experimentally tested and the results of such investigation will be presented in a forthcoming paper.

Haynes (1997), in a study about marine debris in the Great Barrier Reef Marine Park, argued that enforcement of regulations to control dumping of debris at sea is impractical. Other actions, such as clean-up, educational programme and pollution prevention initiatives should be considered (Ellis and Podlich, 1997). Among those, the deployment of public moorings could reduce the total number of anchored boats (and therefore the risk of litter being dropped overboard). It could also organise the spatial pattern of mooring, which is beneficial for boat users as it tends to reduce collisions and provides a more rational use of water space. It is not surprising that sectors of the boating community are receptive to the idea of public moorings at these two beaches (Lockwood, 2001). Other marine protected areas (e.g. Great Barrier Reef Marine Park) use public moorings to regulate recreational anchoring (GBRMPA, 1999). Such moorings, if wisely deployed, could also contribute to the reduction of the likelihood of anchor damage to *Posidonia australis*, a seagrass known to have a very limited capacity for recovery after physical disturbance (Meehan and West, 2000), which is present at the subtidal vicinity of these two beaches.

Sydney Harbour is a busy urban waterway where secluded areas are rare. Currently, the boating community has the informal privilege of access to the waters of Store and Quarantine beach. Visiting pristine areas is likely one of the attractions of recreational boating. In return for this privilege, if not for other reasons such as ethical considerations, it is reasonable to expect boaters to be caretakers for the area. Therefore, recreational boat users should commit themselves, with other stakeholders and regulatory agencies, to discuss managerial actions that, within an experimental framework, are aimed at reducing the amounts of submerged marine debris and improving the general environmental condition of this marine protected area.

ACKNOWLEDGMENTS

REFERENCES

Adams, C.E., R. Tippett, S. Nunn and G. Archibald. 1992. The utilization of a large waterway (Loch Lomond, Scotland) by recreational craft. *Scottish Geographical Magazine.* 108(2):113-118.

Backhurst, M.K. and R.G. Cole. 2000. Subtidal benthic marine litter at Kawau Island, north-eastern New Zealand. *Journal of Environmental Management.* 60:227-237.

Barnes, D.K.A. 2002. Invasions by marine life on plastic debris. *Science.* 416:808-809.

Bohm, C. 2000. *New South Wales Regional Ripples 7(3).* St. Leonards: Marine and Coastal Community Network.

Cahoon, L.B. 1990. Aluminum cans as litter in Masonboro Sound, North Carolina. *Journal of Coastal Research.* 6(3):479-483.

Corbin, C.J. and J.G. Singh. 1993. Marine debris contamination of beaches in St. Lucia and Dominica. *Marine Pollution Bulletin.* 26(6):325-328.

Dixon, T.R. and T.J. Dixon. 1981. Marine litter surveillance. *Marine Pollution Bulletin.* 12(9):289-295.

DUAP. 1999. *Sydney Harbour and tributaries - Discussion paper, towards a vision and strategic program.* Sydney: NSW Department of Urban Affairs and Planning.

Ellis, J. and M. Podlich. 1997. Recreational boaters and marine debris: how we can effectively reduce littering. In *Marine debris: sources, impacts and solutions,* edited by J. M. Coe and D. B. Rogers, 271-276. New York: Springer-Verlag.

Fisheries. 1999. *Policy and guidelines - aquatic habitat management and fish conservation.* Produced by A. K. Smith and D. A. Pollard. Port Stephens: NSW Fisheries.

Frost, A. and M. Cullen. 1997. Marine debris on Northern New South Wales beaches (Australia): Sources and the role of beach usage. *Marine Pollution Bulletin.* 34(5):348-352.

Galil, B.S., A. Golic and M. Turkay. 1995. Litter at the bottom of the sea: A sea bed survey in the eastern Mediterranean. *Marine Pollution Bulletin.* 30(1):22-24.

GBRMPA. 1999. High use shouldn't mean high abuse. *Reef Research (Great Barrier Reef Marine Park Authority)* 9(1):12-13.

Gregory, M.R. 1991. The hazards of persistent marine pollution: drift plastics and conservation islands. *Journal of the Royal Society of New Zealand.* 21(2):83-100.

Haynes, D. 1997. Marine debris on continental islands and sand cays in the far northern section of the Great Barrier Reef Marine Park, Australia. *Marine Pollution Bulletin.* 34(4):276-279.

Laist, D.W. 1987. Overview of the biological effects of lost and discarded plastic debris in the marine environment. *Marine Pollution Bulletin.* 18(6b):319-326.

Lockwood, D. 2001. Woeful harbour funding a worry. *Sydney Morning Herald,* p. 42. Sydney: 03/Feb/2001.

Mathews, P. 1997. The waterways of Sydney Harbour. Crowns Nest: Phillip Mathews Book Publishers.

Meehan, A.J. and R.J. West. 2000. Recovery times for a damaged *Posidonia australis* bed in south eastern Australia. *Aquatic Botany* 67:161-167.

Nollkaemper, A. 1994. Land-based discharges of marine debris: From local to global regulation. *Marine Pollution Bulletin* 28(11):649-652.

Prutter, A.T. 1987. Sources, quantities and distribution of persistent plastics in the marine environment. *Marine Pollution Bulletin.* 18(6b):305-310.

Stefatos, A., M. Charalampakis, G. Papatheodorou, and G. Ferentinos. 1999. Marine debris on the seafloor of the Mediterranean Sea: Examples from two enclosed gulfs in western Greece. *Marine Pollution Bulletin.* 36(5):389-393.

Underwood, A.J., and M.G. Chapman. 1999. The role of ecology in coastal zone management: perspectives from south east Australia. In *Perspectives on integrated coastal zone management,* edited by W. Salomons, R. K. Turner, L. A. Lacerda, and S. Ramachandran, 99-128. Berlin: Springer.

Widmer, W., A. Underwood and M. Chapman. 2002. Recreational boating on Sydney Harbour – Public perception of potential environmental impacts. *Natural Resource Management* 5(1):22-27.

Williams, A.T., S.L. Simmons and A. Fricker. 1993. Off-shore sinks of marine litter: a new problem. *Marine Pollution Bulletin.* 26(7):404-405.

Williams, A.T. and C. Nelson. 1997. The public perception of beach debris. *Shore and Beach.* 65(3):17-20.

Willoughby, N.G., H. Sangkoyo and B.O. Lakaseru. 1997. Beach litter: an increasing and changing problem for Indonesia. *Marine Pollution Bulletin.* 34(6):469-478.

Winston, J. 1982. Drift plastic-an expanding niche for a marine invertebrate? *Marine Pollution Bulletin.* 13(10):348-351.

.

MULTI-SATELLITE SENSOR APPROACH FOR PREDICTING SPILLED OIL IN JAPAN SEA

Katsutoshi Kozai

Kobe University of Mercantile Marine
Kobe, Hyogo, JAPAN
kouzai@cc.kshosen.ac.jp

ABSTRACT

Since January 1997, numerous investigations have been undertaken for predicting the path of spilled oil from the tanker Nakhodka by using physical models, satellite and ground-based remote sensing techniques. However, the optimal combination of satellite-derived products for predicting the path of spilled oil is not fully explored. The purpose of this study is to propose an approach for predicting the drifting path of spilled oil by using multi-satellite microwave sensors. Geostrophic current vectors are derived from TOPEX/Poseidon altimeter and surface wind vectors are derived from ADEOS/NSCAT scatterometer. These two satellite-derived products are used for predicting the drifting path of spilled oil from the tanker Nakhodka. Distribution of spilled oil is identified by sequential RADARSAT synthetic aperture radar images. Trajectories of spilled oil signature derived from the sequential RADARSAT images are evaluated by the combination of altimeter-derived geostrophic current vectors and the scatterometer-derived wind-induced drift vectors. It is found out that the estimated trajectory is agreed well with the one from the RADARSAT and is affected by the small scale cyclonic eddy appeared in the sea surface topography from TOPEX/Poseidon in the short temporal scale.

INTRODUCTION

In January 2, 1997 the tanker Nakhodka sank in the southern part of Japan Sea. The bow section of the tanker and associated spilled heavy oil were drifted to the coast of northern Japan and caused the worst oil spill disaster ever before. Furthermore the sunken tanker including about 6000 kilo litter of heavy oil at the time of accident continued to spill more than a couple of months. The study area with four TOPEX/Poseidon orbits and the locations of the sunken tanker and the JMA buoy 21002 are shown in Figure 1. Spilled oil has been monitored by various airborne and satellite sensors (NASDA, 1997, Kozai, 1999). However the use of satellite remote sensing techniques are limited in each sensor and the optimal combinations of satellite sensor for spilled oil are still under investigation. This study proposes an approach for predicting the drifting path of spilled oil by using multi-satellite microwave sensors, namely RADARSAT, TOPEX/Poseidon and ADEOS/ NSCAT.

SATELLITE AND IN SITU DATA

RADARSAT and spilled oil signature

RADARSAT launched in 1995 by the Canadian Space Agency is the first Canadian remote sensing satellite with C-band Synthetic Aperture Radar (SAR). Table 1 shows the characteristics of RADARSAT standard beam mode (Canadian Space Agency, 1994) and Figure 2 illustrates the RADARSAT image analysis procedure for extracting spilled oil signatures. One of the notable features of RADARSAT is the variable incidence angle which is ranging from 20 to 49 degrees.
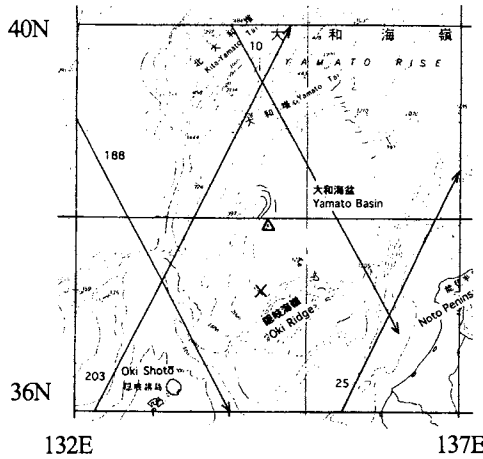
Figure 1. Study area with four TOPEX/Poseidon orbits (10, 25, 188, 203)
(X and △represents thelocation of sunken tanker Nakhodka and the buoy 21002 respectively)

Table 1.   Characteristics of RADARSAT Standard beam mode

Frequency	C band (5.3GHz)	Incidence angle	20~27° (beam position S1)
Polarization	HH		24~31° (beam position S2)
Swath	100km x 100km		30~37° (beam position S3)
Resolution/beams	30m/7		34~40° (beam position S4)
Orientation	Right		36~42° (beam position S5)
Altitude	798km		41~46° (beam position S6)
Orbit type	sun-synchronous		45~49° (beam position S7)
	dawn-dusk orientation		

Jan.11, 08h52m(UT)   Jan.11, 21h07m(UT)
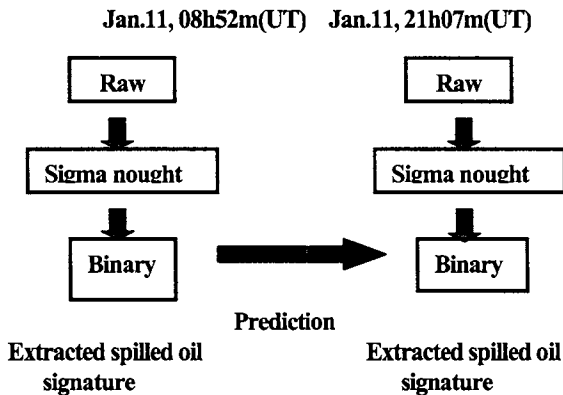
Figure 2.   RADARSAT image analysis procedure for extracting spilled oil signatures

578

In this study the SAR images taken at January 11, 08h 52m (UT) and January 11, 21h 07m (UT) are geometrically and radiometrically corrected and used with the standard beam positions S5 (ascending orbit) and S1 (descending orbit) respectively. According to Table 1 the incidence angle of the first image (January 11, 08h 52m) is about 16 degrees higher than the one of the second image (January 11, 21h 07m), which leads to the darker brightness values of the first image than the one of the second image shown in Figure 3. In general synthetic aperture radar images include inherent noise called speckle. In order to remove the speckle various methods have been developed (Lee, 1983). In this study the median filter with the window size 3x3 is applied for all images. After the speckle removal the conversion from raw digital counts of the images to normalized radar backscattering coefficient (sigma nought) is carried out as described below because the sigma nought is known as the representative of the physical feature of sea surface (Shepherd, 1997). Since the sigma nought α is derived from the beta nought (radar brightness value), extraction of beta nought β is also expressed as follows.

$$\beta_j = 10 \times \log_{10}\{(DN_j^2 + A3) / A2_j\}(dB) \tag{1}$$

where $A2_j$ is the scaling gain value for the jth pixel and A3 is the fixed offset.

$$\sigma_j = \beta_j + 10 \times \log_{10}(\sin l_j)(dB) \tag{2}$$

where l_j is the incidence angle at the jth range pixel. Figure 3 shows the extracted study areas expressed as sigma nought. Lower sigma nought values for each image are corresponding to spilled oil because of the damping effect of the radar illumination. In order to extract and compare spilled oil signature with different dates the binary classification is applied for both images based on the threshold values determined by the manual interpretation of the images. Figure 4 shows the histogram of the study areas of Figure 3 and Figure 5 illustrates the binary image extracted from Figure 3 based on the threshold values of −21 dB and −8 dB, respectively. A brighter curve-like spilled oil signature is clearly apparent in January 11, 08h 52m (UT) image. However, the curve-like signature seems to be diffused at the northern and eastern portion of the image (January 11, 21h 07m(UT)) after 12 hours. These two curve-like signatures are later used for the prediction approach.

(a)

Latitude (deg)

37.5
37.4
37.3
37.2
37.1

136.2 136.3 136.4 136.5 136.6
Longitude (deg)

-23   -20   -18   -15
Normalized Radar Backscattering Coefficient (dB)

(b)

Latitude (deg)

37.5
37.4
37.3
37.2
37.1

136.2 136.3 136.4 136.5 136.6
Longitude (deg)

-10   -8   -5   -3   0
Normalized Radar Backscattering Coefficient (dB)
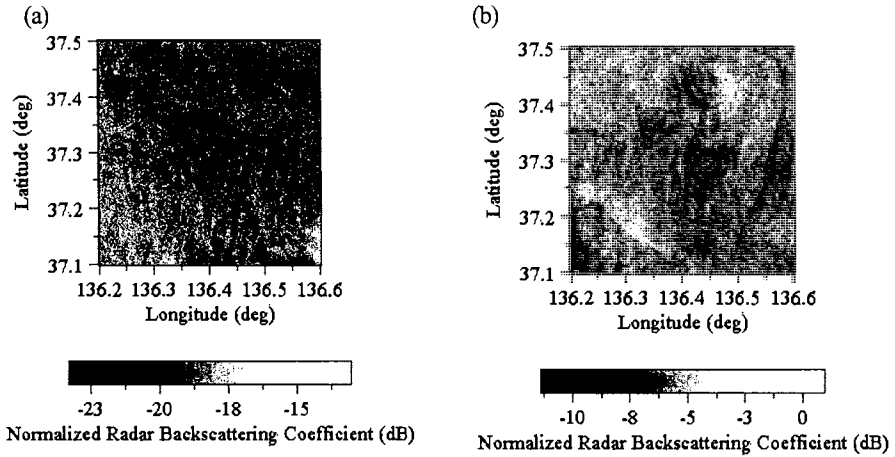
Figure 3. Spilled oil features observed by RADARSAT ((a) January 11, 08h 52m (UT), ascending orbit, beam position S5, (b) January 11, 21h 07m (UT), descending orbit, beam position S1).

TOPEX/Poseidon and geostrophic current vector

TOPEX/Poseidon launched in 1992 is a follow-on altimeter of Geosat and carries two altimeters shown in Table 2.   With its sea level measurement accuracy of 4.2 cm TOPEX/ Poseidon data have been utilized for investigating various phenomena (Menkes et al., 1995; Polito and Cornillon, 1997).   In general, the collinear method is used in order to calculate the dynamic sea surface height from the satellite altimeter data (Kuragano and Shibata, 1997; Jacobs et al., 1999).   In this study, the dynamic sea surface height is derived from the sum of the mean sea surface height from the model (GFDL MOM) (Hirose, 1999) and the temporal anomaly from the mean sea surface height from the altimeter.   Figures 6 and 7 show the sea surface topography analysis procedure and the comparison of various sea surface heights along the orbit. Precise corrections for the altimeter data such as tidal and atmospheric corrections are referred to the TOPEX/Poseidon user handbook (JPL, 1997).

580
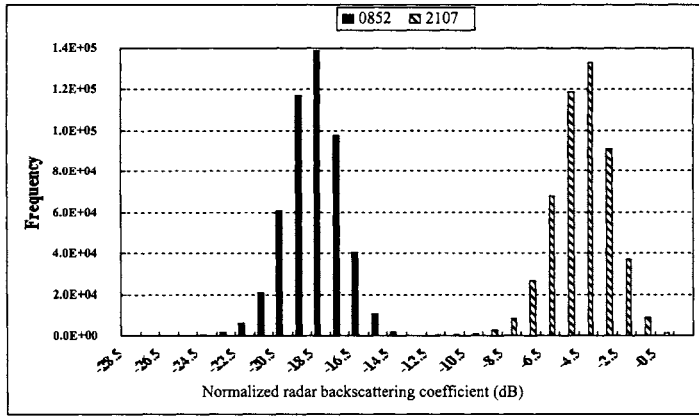
Figure 4. Histogram of Figure 3 (a) (January 11, 08h 52m (UT)) and (b) (January 11, 21h 07m (UT))
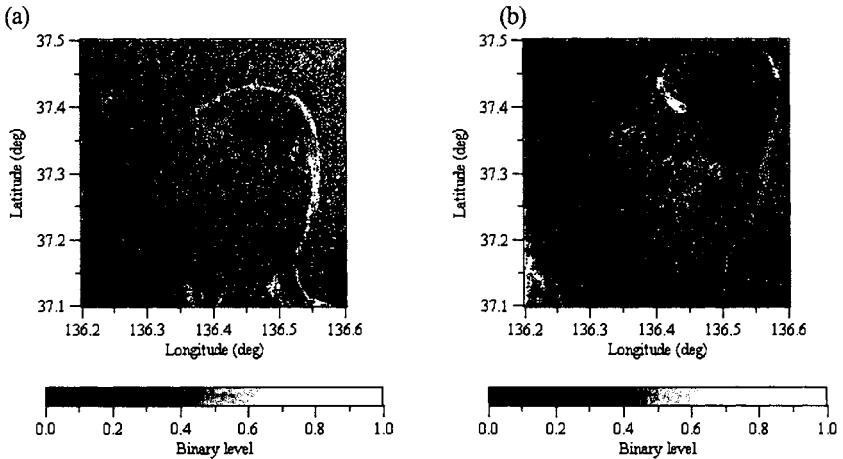
Figure 5.   Binary image extracted from RADARSAT images
((a) January 11, 08h 52m(UT), (b) January 11, 21h 07m(UT))

Based on the dynamic sea surface height along the four TOPEX/Poseidon orbits the sea surface topography of the study area is estimated.   Though the dynamic sea surface height along the orbits is available every 6.5 km, the distance between the orbit extends more than 200 km.   Furthermore, the time difference of one week exists between the orbit 10 and 203.   An objective analysis using the distance function (Thiebaux and Pedder, 1987) is carried out to estimate sea surface topography for the study area.   It is of characteristics that the estimated sea surface topography is an average in terms of spatial and temporal scales.   Figure 8 shows the estimated dynamic sea surface topography derived from TOPEX/Poseidon from January 7-14, 1997 including the two dates of spilled oil signatures extracted from RADARSAT.   It can be seen that the sea surface height increases toward the coast of Japan Sea and the sea surface gradient

581

is large around the extracted study area (rectangular hatched area in Fig. 8). Figure 9 shows the geostrophic current vectors derived from the dynamic sea surface topography from January 7-14, 1997. Most current directions are toward north and the current speed ranges from 4.1 to 23.4 cm/sec. Component geostrophic current speed Vc can be calculated as follows (Strub et al., 1997).

$$Vc(i) = \frac{g}{f}\frac{\partial h}{\partial s} = -\frac{g}{f}\left[\frac{h(i+n)-h(i-n)}{2n\Delta s}\right]$$

(3)

where Vc is the geostrophic current speed, g is the acceleration of gravity, f is the Coriolis parameter, h is the sea surface height, s is the coordinate along the orbit, i is the index of the coordinate grid point, and n is the half span of the centered difference. In this study a span of four TOPEX/Poseidon intervals (n=2) is used to produce a 26 km difference.

Table 2. Major specifications of TOPEX/ Poseidon

Sensors	NASA dual-frequency (C- and Ku-band) altimeter
	CNES single-frequency (Ku-band) solid-state altimeter
Orbit	1336-km, circular, 66 degrees inclination
	10-day repeat of ground track ($\pm$1km accuray)
Sea level measurement accuracy 4.2cm	

TOPEX/Poseidon sea surface height anomaly

Mean sea surface height from MOM (1993-1997)

Dynamic sea surface topography

Geostrophic current vector
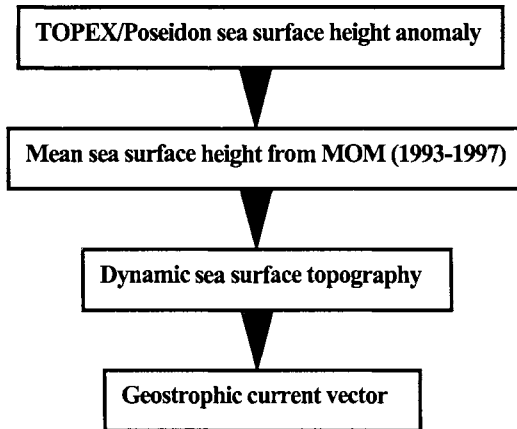
Figure 6. Sea surface topography analysis procedure for extracting geostrophic current vector
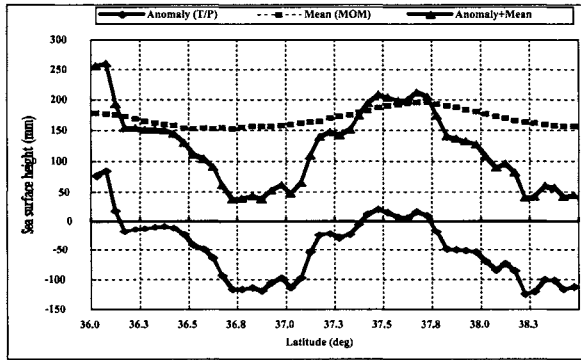
Figure 7. Comparison of various sea surface heights along the orbit 25, cycle 159 of TOPEX/POSEIDON, January 7, 1997.   Mean represents mean sea surface height simulated by the model (GFDL MOM).
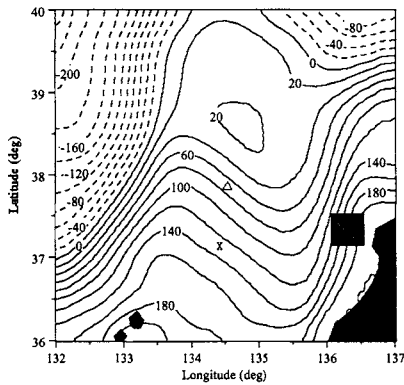
Figure 8. Estimated dynamic sea surface topography derived from TOPEX/Poseidon from January 7-14, 1997.   (Contour interval is 20mm. X and △ indicate the location of sunken tanker Nakhodka and the JMA buoy 21002, respectively.   Rectangular hatched area shows the extracted area including spilled oil signatures from RADARSAT.)

$\rightarrow = 2.0000e+01$
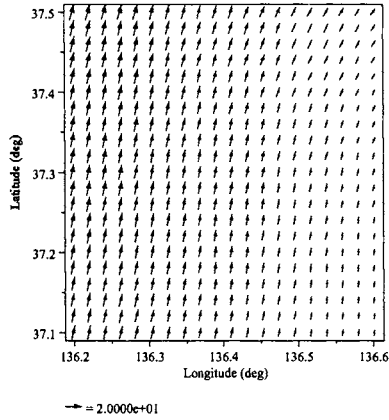
Figure 9. Geostrophic current vector derived from the dynamic sea surface topography from January 7-14, 1997.   (The maximum and minimum current speeds are 23.4 and 4.1cm/sec, respectively. Unit: cm/sec)

ADEOS/NSCAT and wind-induced drift vector

NSCAT is the abbreviation of NASA Scatterometer onboard ADEOS (Advanced Earth Observing Satellite) launched in 1996 and ceased its operation in June 1997 because of the power failure of ADEOS. Major mission requirements of NSCAT are listed in Table 3.   In this study W25 product with 25 km spatial resolution is used for the analysis. Since the W25 products along each orbit are not spatially gridded in terms of latitude and longitude, W25 products are resampled every 25 km by using the nearest neighbor method (Lillesand and Kiefer, 2000).   An example of wind vector distribution in January 11, 01h 53m (UT) is shown in Figure 10.   Wind directions are mostly north to northwest and the wind speeds range from 4.3 to 7.4 m/sec.   Based on the sea surface wind vectors the wind-induced drift vectors are derived from the wind drift model.

Table 3.   Major mission requirements of ADEOS/NSCAT

Wind speed	2m/s(rms) (for 3-20m/s)
Wind Direction	20deg.(rms) (for 3-30m/s)
Spatial Resolution	50km (Wind Cells)
Location Accuracy	25km(rms) (Absolute)
Coverage	90% of ocean every 2days

584

$\rightarrow$ = 1.0000e+01
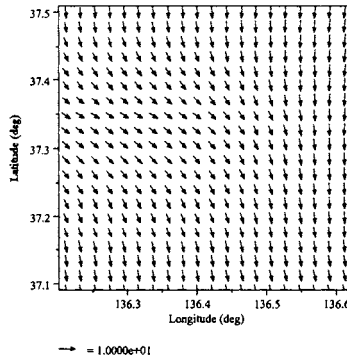
Figure 10. Example of wind vector distribution in January 11, 01h 53m. (The maximum and minimum wind speeds are 7.4 and 4.3m/sec, respectively. Unit: m/sec)

$\rightarrow$ = 2.5000e+01
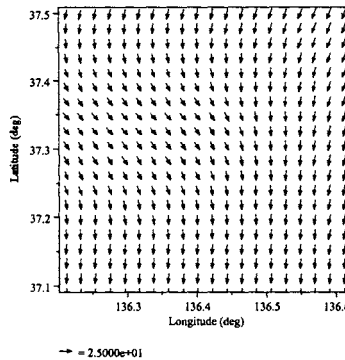
Figure 11. Example of wind-induced drift vector distribution in January 11, 01h 53m(UT). (The maximum and minimum speeds are 22.2 and 12.8 cm/sec, respectively. unit: cm/sec)

The wind drift model is defined as that the drift speed is 3% of the wind speed and the drift direction is 15 degrees to the right of the wind direction in the northern hemisphere (Espedal, 1999). Figure 11 shows an example of the wind-induced drift vector distribution in January 11, 01h 53m (UT). Drift directions are toward south to southeast and drift speeds range from 12.8 to 22.2cm/sec.

PREDICTION APPROACH

In order to quantitatively evaluate the drifting trajectories of spilled oil the synthesized surface current vector is defined as the sum of the geostrophic current vector and the wind-induced drift vector described as follows.

Synthesized surface current vector = geostrophic current vector + wind-induced drift vector   (4)

Figure 12 shows the variability of wind speed and direction at the buoy 21002 including the two RADARSAT times of data acquisition at January 11, 08h 52m and January 11, 21h 07m (UT). During the period of two RADARSAT overpasses the wind speeds are less than 4 m/sec and the wind directions

585

are variable. That means the wind stress is not effectively working on the spilled oil or can be negligible in terms of wind-induced drift vector. So the prediction approach is limited to the geostrophic current vector applied for the two extracted RADARSAT signatures. Figure 13 indicates the result of comparison between the spilled oil signatures extracted from RADARSAT and the estimated trajectory based on the geostrophic current vectors from TOPEX/Poseidon. Ten locations along the initial spilled oil signature at January 11, 08h 52m(UT) are extracted and the locations after 12 hours are estimated by the geostrophic current vectors corresponding to each location. Predicted spilled oil trajectory based on geostrophic current vectors closely approximates the spilled oil signature extracted from RADARSAT in the eastern part of the study area. However in the western part of the study area around 37.4N and 136.4E the estimated trajectory does not follow the spilled oil signature in January 11, 21h 07m (UT). This may be attributable to the existence of the low sea surface topography or small-scale cyclonic eddy appeared in the estimated dynamic sea surface topography derived from TOPEX/Poseidon shown in Figure 14. Although there is a time difference of three to four days between the estimated topography and the RADARSAT spilled oil signatures, a counterclockwise eddy is observed next to the spilled oil signature in the RADARSAT image in January 11, 21h 07m (UT) shown in Figure 3. This small scale eddy with a diameter less than 100km is not resolved in the estimated sea surface topography from January 7-14, 1997 shown in Figure 8. It is recommended that the spatial and temporal scale of sea surface topography should be taken into account for resolving the small-scale eddy.
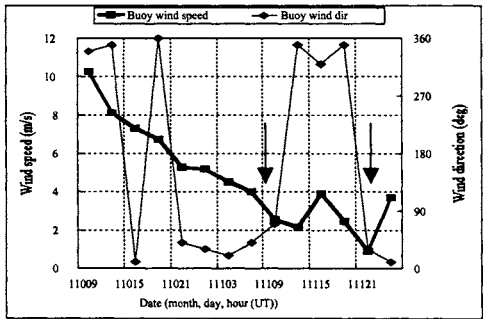
Figure 12. Variability of wind speed and direction at the buoy 21002 including the two RADARSAT times of data acquisition (January 11, 08h 52m and January 11, 21h 07m (UT) indicated as arrows)

586
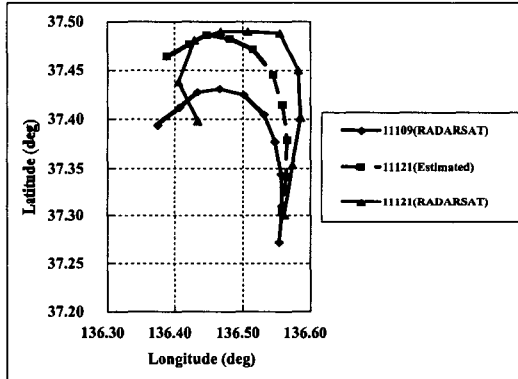
Figure 13. Comparison between the spilled oil signatures extracted from RADARSAT and the estimated trajectory based on geostrophic current vectors from TOPEX/Poseidon
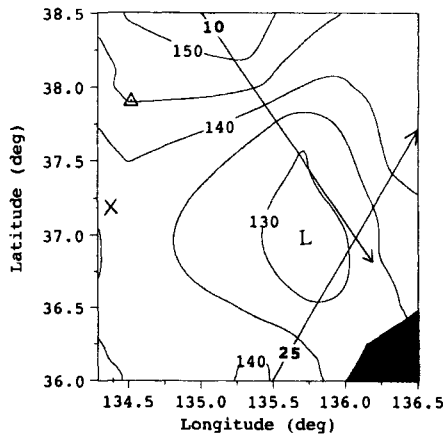
Figure 14. Estimated dynamic sea surface topography derived from TOPEX/Poseidon (cycle 159, orbit 10, 25) from January 7-8, 1997. (L represents relatively low dynamic sea surface height unit: mm)

SUMMARY

The results of the study above are summarized as follows.
(1) Spilled oil trajectory is estimated by the combination of multiple satellite microwave sensors, namely RADARSAT, TOPEX/ Poseidon and ADEOS/NSCAT.

(2) Predicted spilled oil trajectory based on geostrophic current vectors closely approximates the spilled oil signature extracted from RADARSAT.

(3) Small-scale cyclonic eddy appeared in the estimated sea surface topography from TOPEX/Poseidon in short temporal scale may affect the drifting path of spilled oil during the period of negligible wind influence.

ACKNOWLEDGEMENTS

REFERENCES

Canadian Space Agency, NASA and RADARSAT International. 1994. RADARSAT ADRO Program Announcement Volume II RADARSAT System Description.

Espedal, H.A. and T. Wahl. 1999. Satellite SAR oil spill detection using wind history information. INT. J. REMOTE SENSING, 20(1):49-65.

Hirose, N. 1999. Assimilation of Satellite Altimeter Data with Circulation Models of the Japan Sea. Ph.D thesis. Kyushu University.

Jacobs, G.A., P.J. Hogan and K.R. Whitmer. 1999. Effects of Eddy Variability on the Circulation of the Japan/East Sea. *J. Oceanography*. 55(2):247-256.

JPL Physical Oceanography Distributed Active Archive Center (PO.DAAC). 1997. MERGED GDR (TOPEX/Poseidon) Generation B USER'S HANDBOOK Version 2.0.

Kozai, K. 1999. Variation of satellite-derived sea surface topography in the southern part of the Japan Sea including the drifting period of Nakhodka bow section. J. of the Marine Meteorological Society (UMI TO SORA), 75(2):21-34. (in Japanese)

Kuragano, T. and A. Shibata. 1997. Sea Surface Dynamic Height of the Pacific Ocean Derived from TOPEX/Poseidon Altimeter Data: Calculation Method and Accuracy. *J. Oceanography*. 53(6):585-599.

Lee, J.S. 1983. A Simple Speckle Smoothing Algorithm for Synthetic Aperture Radar Imges. IEEE Trans. System, Man and Cybernetics. 13(1): 85-89.

Lillesand, T.M. and R.W. Kiefer. 2000. REMOTE SENSING AND IMAGE INTERPRETATION. 4th Edition. New York: John Wiley & Sons, Inc.

Menkes, C., J.P. Boulanger and A.J. Busalacchi. 1995. Evaluation of TOPEX and basin-wide Tropical Ocean and Global Atmosphere-Tropical Atmosphere Ocean sea surface topographies and derived geostrophic currents. J. Geophys. Res. 100, 25087-25099.

National Space Development Agency of Japan (NASDA) (ed.). 1997. Observation of spilled heavy oil from airborne and satellite sensors. A report of investigation by satellite remote sensing for the Nakhodka oil spill accident. (in Japanese).

Polito, P.S. and P. Cornillon. 1997. Long baroclinic Rossby waves detected by TOPEX/Poseidon. J. Geophys. Res. 102(C2):3215-3235.

Shepherd, N. 1997. Extraction of Beta Nought and Sigma Nought from RADARSAT CDPF Products, ALTRIX Systems.

Strub, T.P., T.K. Chereskin, P.P. Niiler, C. James and M.D. Levine. 1997. Altimeter-derived variability of surface velocities in the California Current System. *J. Geophys. Res.* 102(C6):12727-12748.

Thiebaux, H.J. and M.A. Pedder. 1987. SPATIAL OBJECTIVE ANALYSIS: with application in atmospheric science. Academic Press.

INDEX OF AUTHORS

INDEX OF AUTHORS